

**Faculty of Science and Engineering  
Department of Petroleum Engineering**

**Design of a small down hole motor for deep hard rocks mineral exploration  
drilling**

**Amir Mokaramian**

**This thesis is presented for the Degree of  
Doctor of Philosophy of  
Curtin University**

**April 2014**

***Declaration***

*To the best of my knowledge and belief this thesis contains no material previously published by any other person except where due acknowledgment has been made. This thesis contains no material which has been accepted for the award of any other degree or diploma in any university.*

Name: Amir Mokaramian

Signature:  Date: 4/04/2014

# Abstract

This research presents the potential for adopting existing technologies in oil and gas drilling practice to more efficiently drill deep hard rocks in mineral exploration applications. Coiled Tubing drilling technology has been proposed as a suitable technology for such applications but needs to be modified for small hole-size hard rock mineral exploration drilling. While advances have been made in coiled tubing (CT) technology in the oil and gas industry within the past few decades, introducing this system for mining applications is subjected to different challenges. In particular, this thesis aims to identify the most suitable down-hole rotary drive mechanism (motor) for small hole drilling in hard rocks using a CT assembly and proposes changes required to be made to the existing state of the art design used in petroleum drilling applications.

There are many special design criteria that are associated with the successful implementation of down-hole motors with CT drilling operations. When running a CT drilling operation it is often difficult to produce enough weight-on-bit (WOB) to maximize the rate of penetration (ROP) due to the low buckling resistance of the pipe. Since the ROP of a fixed cutter drill bit (impregnated diamond bit used here) is a product of the depth of cut (DOC) and the rotation speed (RPM) and that the DOC is primarily produced by the available WOB, in an environment where WOB is limited (as with CT drilling); high RPM is the key driver for ROP. This research proposes that turbodrills (turbine motors) are the best choice, amongst available down-hole motors, to be used for small size CT assemblies for hard rock drilling: this satisfies the high speed and low weight on bit drilling system and results in a smooth and good quality borehole with little vibrational effects during drilling.

Turbodrill design methodology and specifications are presented in this thesis and several small diameter turbodrill stage models with various geometries and configurations are designed specifically for the application in this study.

Comprehensive analyses are presented and discussed of fluid flow through the turbodrill stage using ANSYS® CFX solver software for CFD analyses and ANSYS® Mechanical APDL solver for the FSI analyses for various design specifications, fluid types and properties in different working conditions. As a result the optimum design specifications and operational

parameters are proposed for gaining the required power and rotation speed for a small and low weight-on-bit coiled tubing assembly in hard rock mineral exploration drilling.

# Published papers from this research thesis

1. Mokaramian, A., Rasouli, V. and Cavanough, G., 2013, Coiled Tube Turbodrilling: a proposed technology to optimise drilling deep hard rocks for mineral exploration, International Journal of Mining and Mineral Engineering, Vol. 4 (3), PP. 224-248. DOI: 10.1504/IJMME.2013.053171.
2. Mokaramian, A., Rasouli, V. and Cavanough, G., 2013, Fluid Flow Investigation through Small Turbodrill for optimal Performance: Mechanical Engineering Research, Vol. 3 (1), Canadian Center of Science and Education. DOI: 10.5539/mer.v3n1p1.
3. Roufail, R., Rasouli, V., Mokaramian, A., Kamyab, M., Lagat, C. and Cavanough, G., 2013, Utilizing Coiled tube rig for mineral exploration application, in Mapping the Future: Advances in Mining Engineering, 23rd World Mining Congress (WMC), 11-15 August 2013, Canada, Montreal: Canadian Institute of Mining, Metallurgy and Petroleum.
4. Mokaramian, A. and Rasouli, V. and Cavanough, G., 2012, CFD Simulations of Turbodrill Performance with Asymmetric Stator and Rotor Blades Configuration, Ninth International Conference on CFD in the Minerals and Process Industries, 10-12 December 2012, CSIRO, Melbourne, Australia.
5. Mokaramian, A. and Rasouli, V. and Cavanough, G., 2012, Fluid Flow Simulations and Performance Analysis of Turbodrills, 18th Australasian Fluid Mechanics Conference, 3-7 December 2012, Launceston, Australia.
6. Mokaramian, A. and Rasouli, V. and Cavanough, G., 2012, Turbodrills design and performance analysis for efficient drilling in hard rocks, in 1st International Conference on Petroleum and Mineral Resources, 3-5 December 2012, Kurdistan, Iraq: University of Koya, Transactions of the Wessex Institute, DOI: 10.2495/PMR120111.
7. Mokaramian, A. and Rasouli, V. and Cavanough, G., 2012, Quality sampling using coiled tubing drilling in deep mineral exploration, in Proceedings of Sampling 2012: The critical role of sampling, 21-22 August 2012, PP. 73-79, The Australasian Institute of Mining and Metallurgy (AusIMM), Perth, Western Australia.
8. Mokaramian, A. and Rasouli, V. and Cavanough, G., 2012, A hydraulic specific energy performance indicator for coiled tube turbodrilling, 46th US Rock Mechanics/Geomechanics Symposium, 24-27 June 2012, American Rock Mechanics Association (ARMA), Chicago, USA.

9. Mokaramian, A. and Rasouli, V. and Cavanough, G., 2012, A feasibility study on adopting coiled tubing drilling technology for deep hard rock mining exploration, in Deep Mining 2012: Proceedings of the Sixth International Seminar on Deep and High Stress Mining, 28-30 March 2012, PP. 487-499, Australian Centre for Geomechanics, Perth, Western Australia.
10. Mokaramian, A. and Rasouli, V. and Cavanough, G., 2012, Adapting oil and gas downhole motors for deep mineral exploration drilling, in Deep Mining 2012: Proceedings of the Sixth International Seminar on Deep and High Stress Mining, 28-30 March 2012, PP. 475-486, Australian Centre for Geomechanics, Perth, Western Australia.

# Acknowledgements

It is my pleasure to express my gratitude to my supervisors, Associate Professor Vamegh Rasouli the head of the Department of Petroleum Engineering, and Dr Gary Cavanough for their supervision and support. I would like to thank Professor Brian Evans, and Kelvin Brown for their great supports during my study.

The work has been supported by the Deep Exploration Technologies Cooperative Research Centre whose activities are funded by the Australian Government's Cooperative Research Centre Programme. The author would like to express his sincere thanks to the Deep Exploration Technologies Cooperative Research Centre (DET CRC) for their financial supports towards this project.

*"TO God belongs the East and the West,  
Wheresoever you look is the face of God. Indeed, God is all-Encompassing and Knowing"*

# Contents

	<i>Page</i>
<b>Abstract.....</b>	iii
<b>Published papers from this research thesis .....</b>	iv
<b>Acknowledgements.....</b>	vi
<b>Contents .....</b>	viii
<b>List of Figures.....</b>	xiii
<b>List of Tables .....</b>	xxvii
 <b>Chapter 1 Down hole rotary drive mechanism for hard rocks drilling</b>	
<b>1.1 Hard rocks exploration drilling .....</b>	1
<b>1.2 Down hole drive mechanism for coiled tubing drilling.....</b>	3
<b>1.3 Objectives of this thesis.....</b>	6
<b>1.4 Significance of this research .....</b>	7
<b>1.5 Thesis structure .....</b>	8
 <b>Chapter 2 Deep hard rocks mineral exploration drilling</b>	
<b>2.1 Mineral exploration versus petroleum drilling .....</b>	11
<b>2.2 Coiled tubing drilling .....</b>	15
<b>2.3 Drilling fluid in coiled tubing operation.....</b>	18
<b>2.4 Adopting coiled tubing drilling for deep hard rocks mineral exploration...21</b>	
2.4.1 Drill bit .....	21
2.4.2 Weight on bit sub.....	23
2.4.3 Anti-stall tool sub .....	23
2.4.4 Micro-hole drilling tractor .....	23
2.4.5 Isolation sub.....	24
2.4.6 Bottom hole assembly .....	24
2.4.7 Intelligent wireless down hole orienter .....	24

2.4.8	Down hole rotary drive mechanism .....	25
<b>2.5</b>	<b>Down hole motors.....</b>	<b>26</b>
2.5.1	Electric motor .....	27
2.5.2	Positive displacement motor.....	29
2.5.3	Turbine down hole motor .....	38
<b>2.6</b>	<b>Motor selection for hard rocks small CT drilling .....</b>	<b>45</b>
2.6.1	Turbodrill versus PDM.....	46
<b>2.7</b>	<b>Coiled Tube Turbodrilling system.....</b>	<b>47</b>
<b>2.8</b>	<b>Summary .....</b>	<b>50</b>

## Chapter 3 Turbodrill design and specifications

<b>3.1</b>	<b>Power requirements for hard rocks drilling.....</b>	<b>51</b>
<b>3.2</b>	<b>Turbodrill as an axial Turbomachine .....</b>	<b>55</b>
3.2.1	Efficiency of Turbodrill .....	56
<b>3.3</b>	<b>Turbodrill material .....</b>	<b>58</b>
3.3.1	Cavitation .....	60
<b>3.4</b>	<b>Turbodrill design.....</b>	<b>60</b>
3.4.1	Design Flow Coefficient.....	63
3.4.2	Stage Loading Coefficient.....	63
3.4.3	Stage Reaction .....	64
3.4.4	Preliminary Turbodrill stage design .....	65
3.4.5	Effect of Reaction on Turbodrill performance .....	68
<b>3.5</b>	<b>Turbodrill design with ANSYS® .....</b>	<b>69</b>
3.5.1	Turbodrill stage geometry .....	69
<b>3.6</b>	<b>Turbodrill stage models .....</b>	<b>69</b>
3.6.1	A1 stage models .....	71
3.6.2	A2 stage models .....	77
3.6.3	A3 stage models .....	79
3.6.4	B1 stage models.....	82
3.6.5	B2 stage models.....	84
<b>3.7</b>	<b>Summary .....</b>	<b>86</b>

## **Chapter 4 Turbodrill fluid flow analysis**

<b>4.1</b>	<b>Computational Fluid Dynamics .....</b>	<b>87</b>
4.1.1	CFD software.....	90
<b>4.2</b>	<b>Basic equations of fluid dynamics.....</b>	<b>91</b>
4.2.1	Conservation of mass .....	91
4.2.2	Conservation of momentum .....	92
4.2.3	Conservation of energy.....	94
4.2.4	Convection–Diffusion form of a conservation law .....	96
<b>4.3</b>	<b>Navier–Stokes equations for a Newtonian fluid .....</b>	<b>97</b>
<b>4.4</b>	<b>Iterative solution method.....</b>	<b>98</b>
<b>4.5</b>	<b>Reynolds-Averaged Navier–Stokes equations .....</b>	<b>100</b>
<b>4.6</b>	<b>Turbulence models .....</b>	<b>101</b>
4.6.1	Boussinesq approximation.....	103
4.6.2	The $k$ –epsilon turbulence model.....	103
4.6.3	Wilcox $k$ –omega turbulence model .....	106
4.6.4	Shear Stress Transport (SST) turbulence model .....	107
<b>4.7</b>	<b>Modelling flow near the wall.....</b>	<b>108</b>
4.7.1	Wall functions .....	109
4.7.2	Blended high/low Reynolds number formulation .....	110
<b>4.8</b>	<b>Numerical schemes.....</b>	<b>110</b>
4.8.1	Shape functions .....	111
4.8.2	Advection term .....	111
<b>4.9</b>	<b>Physical models.....</b>	<b>113</b>
4.9.1	Steady state and transient flows .....	113
4.9.2	Automatic timescale .....	114
4.9.3	Heat transfer .....	115
4.9.4	Buoyancy .....	115
4.9.5	Non-Newtonian flow .....	116
<b>4.10</b>	<b>Multiphase flow modelling .....</b>	<b>116</b>
<b>4.11</b>	<b>Lagrangian Particle Transport.....</b>	<b>117</b>
4.11.1	Particle-wall interaction.....	122
<b>4.12</b>	<b>Boundary conditions .....</b>	<b>122</b>

4.12.1	Inlet (subsonic) .....	122
4.12.2	Outlet (subsonic) .....	123
4.12.3	Wall boundary .....	124
4.12.4	Counter-rotating wall and rotating wall .....	124
4.12.5	Symmetry plane.....	124
<b>4.13</b>	<b>Interface models .....</b>	<b>124</b>
4.13.1	Frame change/mixing model .....	126
4.13.2	Transient blade row modelling.....	127
<b>4.14</b>	<b>Grid properties .....</b>	<b>127</b>
4.14.1	TurboGrid .....	132
<b>4.15</b>	<b>Errors and uncertainty in CFD modelling.....</b>	<b>133</b>
4.15.1	Numerical errors.....	133
4.15.2	Numerical schemes and errors.....	136
<b>4.16</b>	<b>Verification and validation.....</b>	<b>139</b>
4.16.1	Verification.....	139
4.16.2	Validation .....	141
<b>4.17</b>	<b>Fluid-Structural Interaction analysis .....</b>	<b>143</b>
<b>4.18</b>	<b>Summary .....</b>	<b>148</b>

## Chapter 5 Numerical simulation results and discussions

<b>5.1</b>	<b>CFD simulation process .....</b>	<b>149</b>
5.1.1	Fluid type.....	150
5.1.2	Boundary conditions.....	151
<b>5.2</b>	<b>Grid convergence study for CFD simulations .....</b>	<b>154</b>
5.2.1	Water flow grid convergence study.....	155
5.2.2	Air flow grid convergence study .....	165
<b>5.3</b>	<b>FSI simulation process .....</b>	<b>168</b>
<b>5.4</b>	<b>Grid convergence study for FSI simulations .....</b>	<b>170</b>
<b>5.5</b>	<b>Water flow simulation results .....</b>	<b>175</b>
5.5.1	Water flow simulation results for Turbodrill stage model “A1” .....	175
5.5.2	Water flow simulation results for Turbodrill stage model “A2” .....	202
5.5.3	Water flow simulation results for Turbodrill stage model “A3” .....	217

5.5.4	Water flow simulation results for Turbodrill stage model “B1” .....	228
5.5.5	Water flow simulation results for Turbodrill stage model “B2” .....	239
<b>5.6</b>	<b>Air and mist flow simulation results.....</b>	<b>254</b>
5.6.1	Air and mist flow simulation results for Turbodrill stage model “A1”.	254
5.6.2	Conclusion remarks for air and mist flow simulation results.....	273
<b>5.7</b>	<b>Summary .....</b>	<b>274</b>
<b>Chapter 6     Conclusion and future work</b>		
<b>6.1</b>	<b>Proposed Turbodrill stage models .....</b>	<b>275</b>
<b>6.2</b>	<b>Turbodrill stage prototype .....</b>	<b>278</b>
<b>6.3</b>	<b>Recommendations for future work.....</b>	<b>280</b>
<b>References .....</b>		<b>282</b>

# List of Figures

	<i>Page</i>	
<b>Figure 1.1</b>	A schematic coiled tubing unit with BHA assembly for hard rocks mineral exploration drilling.....	3
<b>Figure 1.2</b>	Structure of the thesis.....	10
<b>Figure 2.1</b>	A typical diamond coring system in mineral exploration (after Atlas-Copco, 2010).....	13
<b>Figure 2.2</b>	Down hole drilling assembly for diamond coring system in mineral exploration (after Atlas-Copco, 2010).....	14
<b>Figure 2.3</b>	A typical coiled tubing drilling assembly (after CTES, 2005).....	16
<b>Figure 2.4</b>	Basic design components of a PMSM electric motor (after IT, 2007).....	29
<b>Figure 2.5</b>	Basic positive displacement motor design principle (courtesy of Smith International, Inc.) .....	30
<b>Figure 2.6</b>	PDM components, (courtesy of China-Ogpe) .....	31
<b>Figure 2.7</b>	Power section assembly, Lobe configurations and conventional and pre-contoured stator cross section (after Cavo, 2005; Regener <i>et al.</i> , 2005).....	33
<b>Figure 2.8</b>	Coupling assembly in the left, bearing assembly in the right (after Cavo, 2005) .....	35
<b>Figure 2.9</b>	PDM performance curve, 43 mm (1.69 in.) outside diameter, 5/6 lobe profile, 5 stages, (NOV, 2011).....	36
<b>Figure 2.10</b>	Turbodrill assembly and schematic fluid flow through turbine stages (after Beaton and Seale, 2004) .....	40
<b>Figure 2.11</b>	Turbine motor characteristics versus mud weight (Reich <i>et al.</i> , 2000).....	42
<b>Figure 2.12</b>	The only published computational fluid dynamics result for NASA blades turbodrill design (Radtke <i>et al.</i> , 2011) .....	49
<b>Figure 2.13</b>	Turbodrill performance from lab experiments with the NASA blades with the PDC cutter drill (Radtke <i>et al.</i> , 2011).....	49
<b>Figure 3.1</b>	Conceptual drilling response of the bit-rock interaction (after Detournay and Defourny, 1992; Detournay <i>et al.</i> , 2008).....	53
<b>Figure 3.2</b>	Turbine Isentropic efficiency against pressure ratio for various polytropic efficiencies ( $\gamma = 1.4$ ) (Dixon and hall, 2010) .....	57

<b>Figure 3.3</b>	Schematic of turbodrill stage geometry (after Eskin and Maurer, 1997) .....	62
<b>Figure 3.4</b>	Turbine stage velocity diagrams and relative velocities (after Dixon and Hall, 2010) .....	62
<b>Figure 3.5</b>	A BladeGen snapshot of the rotor blade row design process.....	70
<b>Figure 3.6</b>	Description of the blade row model of “A1W20S11”.....	71
<b>Figure 3.7</b>	Geometrical specifications of the turbodrill stage model “A1” .....	72
<b>Figure 3.8</b>	Blade Alpha and Beta angles versus meridional length for the stator row model of “A1W20S11” .....	73
<b>Figure 3.9</b>	Blade angles and normal thickness versus camber length of the blade for stator model “A1W20S11” at span surface 0.5 .....	73
<b>Figure 3.10</b>	Blade Alpha and Beta angles versus meridional length for the stator row model of “A1W20S12” .....	74
<b>Figure 3.11</b>	Blade angles and normal thickness versus camber length of the blade for stator model “A1W20S12” at span surface 0.5 .....	74
<b>Figure 3.12</b>	Blade Alpha and Beta angles versus meridional length for the rotor row model of “A1W20R23”.....	75
<b>Figure 3.13</b>	Blade angles and normal thickness versus camber length of the blade for rotor model “A1W20R23” at span surface 0.5 .....	75
<b>Figure 3.14</b>	Blade Alpha and Beta angles versus meridional length for the rotor row model of “A1W20R24” .....	76
<b>Figure 3.15</b>	Blade angles and normal thickness versus camber length of the blade for rotor model “A1W20R24” at span surface 0.5 .....	76
<b>Figure 3.16</b>	Blade Alpha and Beta angles versus meridional length for the rotor row model of “A1G25R15” .....	77
<b>Figure 3.17</b>	Blade angles and normal thickness versus camber length of the blade for rotor model “A1G25R15” at span surface 0.5 .....	77
<b>Figure 3.18</b>	Geometrical specifications of the turbodrill stage model “A2” .....	78
<b>Figure 3.19</b>	Geometrical specifications of the turbodrill stage model “A3” .....	80
<b>Figure 3.20</b>	Blade Alpha and Beta angles versus meridional length for the stator row model of “A3W22S46” .....	81
<b>Figure 3.21</b>	Blade angles and normal thickness versus camber length of the blade for stator model “A3W22S46” at span surface 0.5 .....	81

<b>Figure 3.22</b>	Blade Alpha and Beta angles versus meridional length for the rotor row model of “A3W22R57” .....	82
<b>Figure 3.23</b>	Blade angles and normal thickness versus camber length of the blade for rotor model “A3W22R57” at span surface 0.5 .....	82
<b>Figure 3.24</b>	Geometrical specifications of the turbodrill stage model “B1” .....	83
<b>Figure 3.25</b>	Geometrical specifications of the turbodrill stage model “B2” .....	85
<b>Figure 4.1</b>	2D Mesh element and control volume surface (ANSYS <sup>®</sup> , 2011b) .....	91
<b>Figure 4.2</b>	Structured curvilinear body-fitted grid of the H-type (Hirsch, 2007) .....	128
<b>Figure 4.3</b>	Structured curvilinear body-fitted grid of the C-type (Hirsch, 2007) .....	129
<b>Figure 4.4</b>	Structured curvilinear body-fitted grid of the O-type (Hirsch, 2007) .....	129
<b>Figure 4.5</b>	Structured curvilinear body-fitted grid of the I-type (Hirsch, 2007) .....	129
<b>Figure 4.6</b>	Structured curvilinear body-fitted grid of the C-H-type (Hirsch, 2007) ....	130
<b>Figure 4.7</b>	Structured curvilinear body-fitted grid of the O-H-type (Hirsch, 2007) ....	131
<b>Figure 4.8</b>	Example of an unstructured triangular grid (Hirsch, 2007) .....	131
<b>Figure 4.9</b>	Relations between consistency, stability and convergence (Hirsch, 2007).....	138
<b>Figure 4.10</b>	Phases of modelling and simulation and the role of verification and validation (AIAA, 2002) .....	140
<b>Figure 4.11</b>	Verification process (AIAA, 2002).....	140
<b>Figure 4.12</b>	Validation phases (AIAA, 2002).....	142
<b>Figure 4.13</b>	Deformation caused by applying loads on a body (ANSYS <sup>®</sup> , 2011d) .....	146
<b>Figure 4.14</b>	The stress vectors (ANSYS <sup>®</sup> , 2011d).....	146
<b>Figure 5.1</b>	Geometrical domain (one blade of stator and rotor) in green for one of the Turbodrill stage models used in this study for simulation purposes .....	150
<b>Figure 5.2</b>	Boundary conditions set in CFX for this study, (part 1) .....	152
<b>Figure 5.3</b>	Boundary conditions set in CFX for this study, (part 2) .....	153
<b>Figure 5.4</b>	Mesh model with N=1 and F=1 for the stator blade at span surface 0.5....	156
<b>Figure 5.5</b>	Mesh model with N=1 and F=2 for the stator blade at span surface 0.5....	156
<b>Figure 5.6</b>	Mesh model with N=1 and F=3 for the stator blade at span surface 0.5....	156
<b>Figure 5.7</b>	Mesh model with N=2 and F=1 for the stator blade at span surface 0.5....	157
<b>Figure 5.8</b>	Mesh model with N=2 and F=2 for the stator blade at span surface 0.5....	157
<b>Figure 5.9</b>	Mesh model with N=2 and F=3 for the stator blade at span surface 0.5....	157
<b>Figure 5.10</b>	Mesh model with N=4 and F=1 for the stator blade at span surface 0.5....	158

<b>Figure 5.11</b>	Mesh model with N=4 and F=2 for the stator blade at span surface 0.5....	158
<b>Figure 5.12</b>	Mesh model with N=4 and F=3 for the stator blade at span surface 0.5....	158
<b>Figure 5.13</b>	Mesh model with N=8 and F=1 for the stator blade at span surface 0.5....	159
<b>Figure 5.14</b>	Mesh model with N=8 and F=2 for the stator blade at span surface 0.5....	159
<b>Figure 5.15</b>	Mesh model with N=8 and F=3 for the stator blade at span surface 0.5....	159
<b>Figure 5.16</b>	Mesh model with N=20 and F=1 for the stator blade at span surface 0.5 .....	160
<b>Figure 5.17</b>	Mesh model with N=20 and F=2 for the stator blade at span surface 0.5 .....	160
<b>Figure 5.18</b>	Mesh model with N=20 and F=3 for the stator blade at span surface 0.5 .....	160
<b>Figure 5.19</b>	Mesh model with N=40 and F=1 for the stator blade at span surface 0.5 .....	161
<b>Figure 5.20</b>	Mesh model with N=40 and F=2 for the stator blade at span surface 0.5 .....	161
<b>Figure 5.21</b>	Mesh model with N=40 and F=3 for the stator blade at span surface 0.5 .....	161
<b>Figure 5.22</b>	Mesh model with N=80 and F=1 for the stator blade at span surface 0.5 .....	162
<b>Figure 5.23</b>	Mesh model with N=80 and F=2 for the stator blade at span surface 0.5 .....	162
<b>Figure 5.24</b>	Mesh model with N=80 and F=3 for the stator blade at span surface 0.5 .....	162
<b>Figure 5.25</b>	CFD simulation results of water flow grid convergence study for one stage power with different mesh and turbulence models and steady state analysis.....	165
<b>Figure 5.26</b>	CFD simulation results of air flow grid convergence study for one stage power with different mesh models with SST turbulence and steady state analysis.....	168
<b>Figure 5.27</b>	Geometry domain of the turbodrill model “A1W20” used for structural analysis, with one blade of stator and rotor in green with the blends on their interfaces with hub and shroud .....	170

<b>Figure 5.28</b>	Mesh model for FSI grid convergence study with zero refinement on the blades body (mesh model 0).....	171
<b>Figure 5.29</b>	Mesh model for FSI grid convergence study with one level refinement on the blades body (mesh model 1).....	172
<b>Figure 5.30</b>	Mesh model for FSI grid convergence study with two level refinements on the blades body (mesh model 2).....	173
<b>Figure 5.31</b>	Mesh model for FSI grid convergence study with three level refinements on the blades body (mesh model 3).....	174
<b>Figure 5.32</b>	CFD simulation results for one stage turbodrill model “A1W20” with water flow rate of 3 L/s at reference radius of 22.5987 mm .....	176
<b>Figure 5.33</b>	CFD simulation results for one stage turbodrill model “A1W20” with water flow rate of 3 L/s at 4,000 rpm rotation speed.....	177
<b>Figure 5.34</b>	Velocity profile versus normalized streamwise for water flow rate of 3 L/s at 4,000 rpm rotation speed through turbodrill stage model “A1W20” .....	178
<b>Figure 5.35</b>	Pressure profile versus normalized streamwise for water flow rate of 3 L/s at 4,000 rpm rotation speed through turbodrill stage model “A1W20” .....	178
<b>Figure 5.36</b>	Equivalent (Von-Mises) stress profile for water flow rate of 3 L/s at 4,000 rpm rotation speed through turbodrill stage model “A1W20” with blend radius of 0.5 mm.....	180
<b>Figure 5.37</b>	Equivalent elastic strain profile for water flow rate of 3 L/s at 4,000 rpm rotation speed through turbodrill stage model “A1W20” with blend radius of 0.5 mm.....	181
<b>Figure 5.38</b>	Total deformation profile for water flow rate of 3 L/s at 4,000 rpm rotation speed through turbodrill stage model “A1W20” with blend radius of 0.5 mm.....	182
<b>Figure 5.39</b>	CFD simulation results for one stage turbodrill model “A1W20” with water flow rate of 3 L/s at 100 rpm rotation speed.....	183
<b>Figure 5.40</b>	Velocity profile versus normalized streamwise for water flow rate of 3 L/s at 100 rpm rotation speed through turbodrill stage model “A1W20” .....	184

<b>Figure 5.41</b>	Pressure profile versus normalized streamwise for water flow rate of 3 L/s at 100 rpm rotation speed through turbodrill stage model “A1W20” .....	184
<b>Figure 5.42</b>	CFD simulation results for one stage turbodrill model “A1W20” with water flow rate of 3 L/s at 8,000 rpm rotation speed.....	185
<b>Figure 5.43</b>	Velocity profile versus normalized streamwise for water flow rate of 3 L/s at 8,000 rpm rotation speed through turbodrill stage model “A1W20” .....	186
<b>Figure 5.44</b>	Pressure profile versus normalized streamwise for water flow rate of 3 L/s at 8,000 rpm rotation speed through turbodrill stage model “A1W20” .....	186
<b>Figure 5.45</b>	CFD simulation results for one stage turbodrill model “A1W20” with water flow rate of 4 L/s at reference radius of 22.5987 mm .....	188
<b>Figure 5.46</b>	CFD simulation results for one stage turbodrill model “A1W20” with water flow rate of 4 L/s at 6,000 rpm rotation speed.....	189
<b>Figure 5.47</b>	Velocity profile versus normalized streamwise for water flow rate of 4 L/s at 6,000 rpm rotation speed through turbodrill stage model “A1W20” .....	190
<b>Figure 5.48</b>	Pressure profile versus normalized streamwise for water flow rate of 4 L/s at 6,000 rpm rotation speed through turbodrill stage model “A1W20” .....	190
<b>Figure 5.49</b>	CFD simulation results for one stage turbodrill model “A1W20” with water flow rate of 4 L/s and various viscosity models at reference radius of 22.5987 mm.....	194
<b>Figure 5.50</b>	CFD simulation results for one stage turbodrill model “A1W20” with water flow rate of 4 L/s and with stator outlet blade angle of 60 degree at reference radius of 22.5987 mm .....	195
<b>Figure 5.51</b>	CFD simulation results for one stage turbodrill model “A1W20” with water flow rate of 4 L/s and stator outlet blade angle of 60 degree at 5,000 rpm rotation speed .....	196
<b>Figure 5.52</b>	Velocity profile versus normalized streamwise for water flow rate of 4 L/s at 5,000 rpm rotation speed through turbodrill stage model “A1W20” with stator blade outlet angle of 60 degree .....	197

<b>Figure 5.53</b>	Pressure profile versus normalized streamwise for water flow rate of 4 L/s at 5,000 rpm rotation speed through turbodrill stage model “A1W20” with stator blade outlet angle of 60 degree .....	197
<b>Figure 5.54</b>	CFD simulation results for one stage turbodrill model “A1W16” with water flow rate of 4 L/s at reference radius of 22.5972 mm .....	198
<b>Figure 5.55</b>	CFD simulation results for one stage turbodrill model “A1W16” with water flow rate of 4 L/s at 4,000 rpm rotation speed.....	199
<b>Figure 5.56</b>	Velocity profile versus normalized streamwise for water flow rate of 4 L/s at 4,000 rpm rotation speed through turbodrill stage model “A1W16” .....	200
<b>Figure 5.57</b>	Pressure profile versus normalized streamwise for water flow rate of 4 L/s at 4,000 rpm rotation speed through turbodrill stage model “A1W16” .....	200
<b>Figure 5.58</b>	CFD simulation results of water flow through one stage turbodrill stage model “A1” .....	201
<b>Figure 5.59</b>	CFD simulation results for one stage turbodrill model “A2W20” with water flow rate of 3 L/s at reference radius of 21.2716 mm .....	202
<b>Figure 5.60</b>	CFD simulation results for one stage turbodrill model “A2W20” with water flow rate of 3 L/s at 3,000 rpm rotation speed.....	203
<b>Figure 5.61</b>	Velocity profile versus normalized streamwise for water flow rate of 3 L/s at 3,000 rpm rotation speed through turbodrill stage model “A2W20” .....	204
<b>Figure 5.62</b>	Pressure profile versus normalized streamwise for water flow rate of 3 L/s at 3,000 rpm rotation speed through turbodrill stage model “A2W20” .....	204
<b>Figure 5.63</b>	Equivalent (Von-Mises) stress profile for water flow rate of 3 L/s at 3,000 rpm rotation speed through turbodrill stage model “A2W20” with different blend radius.....	206
<b>Figure 5.64</b>	Equivalent elastic strain profile for water flow rate of 3 L/s at 3,000 rpm rotation speed through turbodrill stage model “A2W20” with different blend radius.....	207

<b>Figure 5.65</b>	Total deformation profile for water flow rate of 3 L/s at 3,000 rpm rotation speed through turbodrill stage model “A2W20” with different blend radius .....	208
<b>Figure 5.66</b>	CFD simulation results for one stage turbodrill model “A2W20” with water flow rate of 4 L/s at reference radius of 21.2716 mm .....	209
<b>Figure 5.67</b>	CFD simulation results for one stage turbodrill model “A2W20” with water flow rate of 4 L/s at 5,000 rpm rotation speed.....	210
<b>Figure 5.68</b>	Velocity profile versus normalized streamwise for water flow rate of 4 L/s at 5,000 rpm rotation speed through turbodrill stage model “A2W20” .....	211
<b>Figure 5.69</b>	Pressure profile versus normalized streamwise for water flow rate of 4 L/s at 5,000 rpm rotation speed through turbodrill stage model “A2W20” .....	211
<b>Figure 5.70</b>	CFD simulation results for one stage turbodrill model “A2W20” with water flow rate of 5 L/s at reference radius of 21.2716 mm .....	213
<b>Figure 5.71</b>	CFD simulation results for one stage turbodrill model “A2W20” with water flow rate of 5 L/s at 6,000 rpm rotation speed.....	214
<b>Figure 5.72</b>	Velocity profile versus normalized streamwise for water flow rate of 5 L/s at 6,000 rpm rotation speed through turbodrill stage model “A2W20” .....	215
<b>Figure 5.73</b>	Pressure profile versus normalized streamwise for water flow rate of 5 L/s at 6,000 rpm rotation speed through turbodrill stage model “A2W20” .....	215
<b>Figure 5.74</b>	CFD simulation results of water flow through one stage turbodrill stage model “A2” .....	216
<b>Figure 5.75</b>	CFD simulation results for one stage turbodrill model “A3W22” and 65 degree stator outlet blade angle with water flow rate of 5 L/s at reference radius of 19.6776 mm.....	217
<b>Figure 5.76</b>	CFD simulation results for one stage turbodrill model “A3W22” and 65 degree stator outlet blade angle with water flow rate of 5 L/s at 4,000 rpm rotation speed .....	218

<b>Figure 5.77</b>	Velocity profile versus normalized streamwise for water flow rate of 5 L/s at 4,000 rpm rotation speed through turbodrill stage model “A3W22” and 65 degree stator outlet blade angle .....	219
<b>Figure 5.78</b>	Pressure profile versus normalized streamwise for water flow rate of 5 L/s at 4,000 rpm rotation speed through turbodrill stage model “A3W22” and 65 degree stator outlet blade angle .....	219
<b>Figure 5.79</b>	CFD simulation results for one stage turbodrill model “A3W22” and 65 degree stator outlet blade angle with water flow rate of 6 L/s at reference radius of 19.6776 mm.....	221
<b>Figure 5.80</b>	CFD simulation results for one stage turbodrill model “A3W22” and 65 degree stator outlet blade angle with water flow rate of 6 L/s at 5,000 rpm rotation speed .....	222
<b>Figure 5.81</b>	Velocity profile versus normalized streamwise for water flow rate of 6 L/s at 5,000 rpm rotation speed through turbodrill stage model “A3W22” and 65 degree stator outlet blade angle .....	223
<b>Figure 5.82</b>	Pressure profile versus normalized streamwise for water flow rate of 6 L/s at 5,000 rpm rotation speed through turbodrill stage model “A3W22” and 65 degree stator outlet blade angle .....	223
<b>Figure 5.83</b>	CFD simulation results for one stage turbodrill model “A3W22” and 50 degree stator outlet blade angle with water flow rate of 6 L/s at reference radius of 19.6734 mm.....	224
<b>Figure 5.84</b>	CFD simulation results for one stage turbodrill model “A3W22” and 50 degree stator outlet blade angle with water flow rate of 6 L/s at 3,000 rpm rotation speed .....	225
<b>Figure 5.85</b>	Velocity profile versus normalized streamwise for water flow rate of 6 L/s at 3,000 rpm rotation speed through turbodrill stage model “A3W22” and 50 degree stator outlet blade angle .....	226
<b>Figure 5.86</b>	Pressure profile versus normalized streamwise for water flow rate of 6 L/s at 3,000 rpm rotation speed through turbodrill stage model “A3W22” and 50 degree stator outlet blade angle .....	226
<b>Figure 5.87</b>	CFD simulation results of water flow through one stage turbodrill stage model “A3” .....	227

<b>Figure 5.88</b>	CFD simulation results for one stage turbodrill model “B1W20” with water flow rate of 2 L/s at reference radius of 18.5438 mm .....	228
<b>Figure 5.89</b>	CFD simulation results for one stage turbodrill model “B1W20” with water flow rate of 2 L/s at 10,000 rpm rotation speed.....	229
<b>Figure 5.90</b>	Velocity profile versus normalized streamwise for water flow rate of 2 L/s at 10,000 rpm rotation speed through turbodrill stage model “B1W20” .....	230
<b>Figure 5.91</b>	Pressure profile versus normalized streamwise for water flow rate of 2 L/s at 10,000 rpm rotation speed through turbodrill stage model “B1W20” .....	230
<b>Figure 5.92</b>	CFD simulation results for one stage turbodrill model “B1W16” with water flow rate of 2 L/s at reference radius of 18.5431 mm .....	232
<b>Figure 5.93</b>	CFD simulation results for one stage turbodrill model “B1W16” with water flow rate of 2 L/s at 8,000 rpm rotation speed.....	233
<b>Figure 5.94</b>	Velocity profile versus normalized streamwise for water flow rate of 2 L/s at 8,000 rpm rotation speed through turbodrill stage model “B1W16” .....	234
<b>Figure 5.95</b>	Pressure profile versus normalized streamwise for water flow rate of 2 L/s at 8,000 rpm rotation speed through turbodrill stage model “B1W16” .....	234
<b>Figure 5.96</b>	CFD simulation results for one stage turbodrill model “B1W16” with water flow rate of 3 L/s at reference radius of 18.5431 mm .....	236
<b>Figure 5.97</b>	CFD simulation results for one stage turbodrill model “B1W16” with water flow rate of 3 L/s at 10,000 rpm rotation speed.....	237
<b>Figure 5.98</b>	Velocity profile versus normalized streamwise for water flow rate of 3 L/s at 10,000 rpm rotation speed through turbodrill stage model “B1W16” .....	238
<b>Figure 5.99</b>	Pressure profile versus normalized streamwise for water flow rate of 3 L/s at 10,000 rpm rotation speed through turbodrill stage model “B1W16” .....	238
<b>Figure 5.100</b>	CFD simulation results of water flow through one stage turbodrill stage model “B1”.....	239

<b>Figure 5.101</b>	CFD simulation results for one stage turbodrill model “B2W20” with water flow rate of 2 L/s at reference radius of 17.6290 mm .....	240
<b>Figure 5.102</b>	CFD simulation results for one stage turbodrill model “B2W20” with water flow rate of 2 L/s at 8,000 rpm rotation speed.....	241
<b>Figure 5.103</b>	Velocity profile versus normalized streamwise for water flow rate of 2 L/s at 8,000 rpm rotation speed through turbodrill stage model “B2W20” .....	242
<b>Figure 5.104</b>	Pressure profile versus normalized streamwise for water flow rate of 2 L/s at 8,000 rpm rotation speed through turbodrill stage model “B2W20” .....	242
<b>Figure 5.105</b>	CFD simulation results for one stage turbodrill model “B2W16” with water flow rate of 2 L/s at reference radius of 17.6266 mm .....	243
<b>Figure 5.106</b>	CFD simulation results for one stage turbodrill model “B2W16” with water flow rate of 2 L/s at 5,000 rpm rotation speed.....	244
<b>Figure 5.107</b>	Velocity profile versus normalized streamwise for water flow rate of 2 L/s at 5,000 rpm rotation speed through turbodrill stage model “B2W16” .....	245
<b>Figure 5.108</b>	Pressure profile versus normalized streamwise for water flow rate of 2 L/s at 5,000 rpm rotation speed through turbodrill stage model “B2W16” .....	245
<b>Figure 5.109</b>	CFD simulation results for one stage turbodrill model “B2W16” with water flow rate of 3 L/s at reference radius of 17.6266 mm .....	247
<b>Figure 5.110</b>	CFD simulation results for one stage turbodrill model “B2W16” with water flow rate of 3 L/s at 7,000 rpm rotation speed.....	248
<b>Figure 5.111</b>	Velocity profile versus normalized streamwise for water flow rate of 3 L/s at 7,000 rpm rotation speed through turbodrill stage model “B2W16” .....	249
<b>Figure 5.112</b>	Pressure profile versus normalized streamwise for water flow rate of 3 L/s at 7,000 rpm rotation speed through turbodrill stage model “B2W16” .....	249
<b>Figure 5.113</b>	CFD simulation results for one stage turbodrill model “B2W16” with water flow rate of 4 L/s at reference radius of 17.6266 mm .....	250

<b>Figure 5.114</b>	CFD simulation results for one stage turbodrill model “B2W16” with water flow rate of 4 L/s at 10,000 rpm rotation speed.....	251
<b>Figure 5.115</b>	Velocity profile versus normalized streamwise for water flow rate of 4 L/s at 10,000 rpm rotation speed through turbodrill stage model “B2W16” .....	252
<b>Figure 5.116</b>	Pressure profile versus normalized streamwise for water flow rate of 4 L/s at 10,000 rpm rotation speed through turbodrill stage model “B2W16” .....	252
<b>Figure 5.117</b>	CFD simulation results of water flow through one stage turbodrill stage model “B2”.....	253
<b>Figure 5.118</b>	CFD simulation results for one stage turbodrill model “A1G25” for mist flow with air mass flow rate of 0.05 Kg/s and water flow rate of 12 L/s for PRC=1 at 10,000 rpm rotation speed.....	256
<b>Figure 5.119</b>	Velocity profile versus normalized streamwise for mist flow with air mass flow rate of 0.05 Kg/s and water flow rate of 12 L/s for PRC=1 at 10,000 rpm rotation speed through turbodrill stage model “A1G25” ....	257
<b>Figure 5.120</b>	Pressure profile versus normalized streamwise for mist flow with air mass flow rate of 0.05 Kg/s and water flow rate of 12 L/s for PRC=1 at 10,000 rpm rotation speed through turbodrill stage model “A1G25” ....	257
<b>Figure 5.121</b>	CFD simulation results for one stage turbodrill model “A1G25” for mist flow with air mass flow rate of 0.1 Kg/s and water flow rate of 12 L/s for PRC=1 at 10,000 rpm rotation speed.....	259
<b>Figure 5.122</b>	Velocity profile versus normalized streamwise for mist flow with air mass flow rate of 0.1 Kg/s and water flow rate of 12 L/s for PRC=1 at 10,000 rpm rotation speed through turbodrill stage model “A1G25” .....	260
<b>Figure 5.123</b>	Pressure profile versus normalized streamwise for mist flow with air mass flow rate of 0.1 Kg/s and water flow rate of 12 L/s for PRC=1 at 10,000 rpm rotation speed through turbodrill stage model “A1G25” .....	260
<b>Figure 5.124</b>	CFD simulation results for one stage turbodrill model “A1G25” for mist flow with air mass flow rate of 0.07 Kg/s and water flow rate of 6 L/s for PRC=1 at 10,000 rpm rotation speed.....	262

- Figure 5.125** Velocity profile versus normalized streamwise for mist flow with air mass flow rate of 0.07 Kg/s and water flow rate of 6 L/s for PRC=1 at 10,000 rpm rotation speed through turbodrill stage model “A1G25” .....263
- Figure 5.126** Pressure profile versus normalized streamwise for mist flow with air mass flow rate of 0.07 Kg/s and water flow rate of 6 L/s for PRC=1 at 10,000 rpm rotation speed through turbodrill stage model “A1G25” .....263
- Figure 5.127** CFD simulation results for one stage turbodrill model “A1G25” for mist flow with air mass flow rate of 0.07 Kg/s and water flow rate of 12 L/s for PRC=1 at 10,000 rpm rotation speed.....264
- Figure 5.128** CFD simulation results for one stage turbodrill model “A1G25” for mist flow with air mass flow rate of 0.07 Kg/s and water flow rate of 12 L/s for PRC=0.5 at 10,000 rpm rotation speed.....266
- Figure 5.129** Velocity profile versus normalized streamwise for mist flow with air mass flow rate of 0.07 Kg/s and water flow rate of 12 L/s for PRC=0.5 at 10,000 rpm rotation speed through turbodrill stage model “A1G25” ....267
- Figure 5.130** Pressure profile versus normalized streamwise for mist flow with air mass flow rate of 0.07 Kg/s and water flow rate of 12 L/s for PRC=0.5 at 10,000 rpm rotation speed through turbodrill stage model “A1G25” ....267
- Figure 5.131** CFD simulation results for one stage turbodrill model “A1G25” for mist flow with air mass flow rate of 0.07 Kg/s and water flow rate of 12 L/s for PRC=0.1 at 10,000 rpm rotation speed.....269
- Figure 5.132** Velocity profile versus normalized streamwise for mist flow with air mass flow rate of 0.07 Kg/s and water flow rate of 12 L/s for PRC=0.1 at 10,000 rpm rotation speed through turbodrill stage model “A1G25” ....270
- Figure 5.133** Pressure profile versus normalized streamwise for mist flow with air mass flow rate of 0.07 Kg/s and water flow rate of 12 L/s for PRC=0.1 at 10,000 rpm rotation speed through turbodrill stage model “A1G25” ....270
- Figure 5.134** CFD simulation results for one stage turbodrill model “A1G22” for mist flow with air mass flow rate of 0.1 Kg/s and water flow rate of 12 L/s for PRC=1 at 10,000 rpm rotation speed.....272
- Figure 5.135** Velocity profile versus normalized streamwise for mist flow with air mass flow rate of 0.1 Kg/s and water flow rate of 12 L/s for PRC=1 at 10,000 rpm rotation speed through turbodrill stage model “A1G22” .....273

<b>Figure 5.136</b>	Pressure profile versus normalized streamwise for mist flow with air mass flow rate of 0.1 Kg/s and water flow rate of 12 L/s for PRC=1 at 10,000 rpm rotation speed through turbodrill stage model “A1G22” .....	273
<b>Figure 6.1</b>	Prototyped turbodrill stage model with 3D printing.....	277

# List of Tables

	<i>Page</i>
<b>Table 3.1</b> Geometry specifications for the turbodrill stage models designed and used for simulation purposes in this study .....	70
<b>Table 3.2</b> Geometrical specifications for turbodrill stage models with 50 mm shroud diameter and blade height or span of 5 mm (A1 stage models) .....	71
<b>Table 3.3</b> Geometrical specifications for turbodrill stage models with 50 mm shroud diameter and blade height or span of 8 mm (A2 stage models) .....	79
<b>Table 3.4</b> Geometrical specifications for turbodrill stage models with 50 mm shroud diameter and blade height or span of 12 mm (A3 stage models) .....	79
<b>Table 3.5</b> Geometrical specifications for turbodrill stage models with 40 mm shroud diameter and blade height or span of 3 mm (B1 stage models) .....	84
<b>Table 3.6</b> Geometrical specifications for turbodrill stage models with 40 mm shroud diameter and blade height or span of 5 mm (B2 stage models) .....	84
<b>Table 5.1</b> Mesh models generated for water flow grid convergence study .....	155
<b>Table 5.2</b> CFD simulation results for water flow grid convergence study with 4 Kg/s mass flow rate and 6,000 rpm rotation speed and with the $k-\varepsilon$ turbulence model.....	163
<b>Table 5.3</b> CFD simulation results for water flow grid convergence study with 4 Kg/s mass flow rate and 6,000 rpm rotation speed and with the SST turbulence model.....	164
<b>Table 5.4</b> Transient CFD simulation results for water flow grid convergence study with 4 Kg/s mass flow rate and 6,000 rpm rotation speed and with the SST turbulence model.....	164
<b>Table 5.5</b> Mesh models generated for air flow grid convergence study.....	166
<b>Table 5.6</b> CFD simulation results for air flow grid convergence study with 0.07 Kg/s mass flow rate at 100 psi (6.89 bar) inlet pressure and 10,000 rpm rotation speed and with the SST turbulence model .....	167
<b>Table 5.7</b> Transient CFD simulation results for air flow grid convergence study with 0.07 Kg/s mass flow rate at 100 psi (6.98 bar) inlet pressure and 10,000 rpm rotation speed and with the SST turbulence model .....	167
<b>Table 5.8</b> Simulation results for FSI grid convergence study for four mesh models .....	175
<b>Table 5.9</b> CFD simulation results for one stage turbodrill model “A1W20” with water flow rate of 3 L/s .....	175

<b>Table 5.10</b>	FSI simulation results for water flow rate of 3 L/s at 4,000 rpm rotation speed through turbodrill stage model “A1W20” .....	179
<b>Table 5.11</b>	FSI simulation results for water flow rate of 3 L/s at 100 rpm rotation speed through turbodrill stage model “A1W20” .....	185
<b>Table 5.12</b>	FSI simulation results for water flow rate of 3 L/s at 8,000 rpm rotation speed through turbodrill stage model “A1W20” .....	187
<b>Table 5.13</b>	CFD simulation results for one stage turbodrill model “A1W20” with water flow rate of 4 L/s .....	187
<b>Table 5.14</b>	FSI simulation results for water flow rate of 4 L/s at 6,000 rpm rotation speed through turbodrill stage model “A1W20” .....	191
<b>Table 5.15</b>	CFD simulation results for one stage turbodrill model “A1W20” with water flow rate of 4 L/s and using the base viscosity model.....	192
<b>Table 5.16</b>	CFD simulation results for one stage turbodrill model “A1W20” with water flow rate of 4 L/s and using the base viscosity model with $n=0.5$ .....	192
<b>Table 5.17</b>	CFD simulation results for one stage turbodrill model “A1W20” with water flow rate of 4 L/s and using the base viscosity model with $n=0.9$ .....	192
<b>Table 5.18</b>	CFD simulation results for one stage turbodrill model “A1W20” with water flow rate of 4 L/s and using the base viscosity model with $K=0.2$ Pa.s .....	193
<b>Table 5.19</b>	CFD simulation results for one stage turbodrill model “A1W20” with water flow rate of 4 L/s and using the base viscosity model with $K=0.05$ Pa.s .....	193
<b>Table 5.20</b>	CFD simulation results for one stage turbodrill model “A1W20” with water flow rate of 4 L/s and stator outlet blade angle of 60 degree .....	194
<b>Table 5.21</b>	FSI simulation results for water flow rate of 4 L/s at 5,000 rpm rotation speed through turbodrill stage model “A1W20” with stator outlet blade angle of 60 degree.....	198
<b>Table 5.22</b>	CFD simulation results for one stage turbodrill model “A1W16” with water flow rate of 4 L/s .....	198
<b>Table 5.23</b>	FSI simulation results for water flow rate of 4 L/s at 4,000 rpm rotation speed through turbodrill stage model “A1W16” .....	201
<b>Table 5.24</b>	CFD simulation results for one stage turbodrill model “A2W20” with water flow rate of 3 L/s .....	202
<b>Table 5.25</b>	FSI simulation results for water flow rate of 3 L/s at 3,000 rpm rotation speed through turbodrill stage model “A2W20” .....	205
<b>Table 5.26</b>	CFD simulation results for one stage turbodrill model “A2W20” with water flow rate of 4 L/s .....	209

<b>Table 5.27</b>	FSI simulation results for water flow rate of 4 L/s at 5,000 rpm rotation speed through turbodrill stage model “A2W20” .....	212
<b>Table 5.28</b>	CFD simulation results for one stage turbodrill model “A2W20” with water flow rate of 5 L/s .....	212
<b>Table 5.29</b>	FSI simulation results for water flow rate of 5 L/s at 6,000 rpm rotation speed through turbodrill stage model “A2W20” .....	216
<b>Table 5.30</b>	CFD simulation results for one stage turbodrill model “A3W22” and 65 degree stator outlet blade angle with water flow rate of 5 L/s .....	217
<b>Table 5.31</b>	FSI simulation results for water flow rate of 5 L/s at 4,000 rpm rotation speed through turbodrill stage model “A3W22” and 65 degree stator outlet blade angle .....	220
<b>Table 5.32</b>	CFD simulation results for one stage turbodrill model “A3W22” and 65 degree stator outlet angle with water flow rate of 6 L/s .....	220
<b>Table 5.33</b>	FSI simulation results for water flow rate of 6 L/s at 5,000 rpm rotation speed through turbodrill stage model “A3W22” and 65 degree stator outlet blade angle .....	224
<b>Table 5.34</b>	CFD simulation results for one stage turbodrill model “A3W22” and 50 degree stator outlet blade angle with water flow rate of 6 L/s .....	224
<b>Table 5.35</b>	FSI simulation results for water flow rate of 6 L/s at 3,000 rpm rotation speed through turbodrill stage model “A3W22” and 50 degree stator outlet blade angle .....	227
<b>Table 5.36</b>	CFD simulation results for one stage turbodrill model “B1W20” with water flow rate of 2 L/s .....	228
<b>Table 5.37</b>	: FSI simulation results for water flow rate of 2 L/s at 10,000 rpm rotation speed through turbodrill stage model “B1W20” .....	231
<b>Table 5.38</b>	CFD simulation results for one stage turbodrill model “B1W16” with water flow rate of 2 L/s .....	231
<b>Table 5.39</b>	FSI simulation results for water flow rate of 2 L/s at 8,000 rpm rotation speed through turbodrill stage model “B1W16” .....	235
<b>Table 5.40</b>	CFD simulation results for one stage turbodrill model “B1W16” with water flow rate of 3 L/s .....	235
<b>Table 5.41</b>	FSI simulation results for water flow rate of 3 L/s at 10,000 rpm rotation speed through turbodrill stage model “B1W16” .....	239
<b>Table 5.42</b>	CFD simulation results for one stage turbodrill model “B2W20” with water flow rate of 2 L/s .....	240

<b>Table 5.43</b>	FSI simulation results for water flow rate of 2 L/s at 8,000 rpm rotation speed through turbodrill stage model “B2W20” .....	243
<b>Table 5.44</b>	CFD simulation results for one stage turbodrill model “B2W16” with water flow rate of 2 L/s .....	243
<b>Table 5.45</b>	FSI simulation results for water flow rate of 2 L/s at 5,000 rpm rotation speed through turbodrill stage model “B2W16” .....	246
<b>Table 5.46</b>	CFD simulation results for one stage turbodrill model “B2W16” with water flow rate of 3 L/s .....	246
<b>Table 5.47</b>	FSI simulation results for water flow rate of 3 L/s at 7,000 rpm rotation speed through turbodrill stage model “B2W16” .....	250
<b>Table 5.48</b>	CFD simulation results for one stage turbodrill model “B2W16” with water flow rate of 4 L/s .....	250
<b>Table 5.49</b>	FSI simulation results for water flow rate of 4 L/s at 10,000 rpm rotation speed through turbodrill stage model “B2W16” .....	253
<b>Table 5.50</b>	CFD simulation results for one stage turbodrill model “A1G25” with air mass flow rate of 0.05 Kg/s.....	254
<b>Table 5.51</b>	CFD simulation results for one stage turbodrill model “A1G25” for mist flow with air mass flow rate of 0.05 Kg/s and different water flow rate for PRC=1 at 10,000 rpm rotation speed .....	255
<b>Table 5.52</b>	CFD simulation results for one stage turbodrill model “A1G25” with air mass flow rate of 0.1 Kg/s.....	258
<b>Table 5.53</b>	CFD simulation results for one stage turbodrill model “A1G25” for mist flow with air mass flow rate of 0.1 Kg/s and different water flow rate for PRC=1 at 10,000 rpm rotation speed .....	258
<b>Table 5.54</b>	CFD simulation results for one stage turbodrill model “A1G25” for mist flow with air mass flow rate of 0.07 Kg/s and different water flow rate for PRC=1 at 10,000 rpm rotation speed .....	261
<b>Table 5.55</b>	CFD simulation results for one stage turbodrill model “A1G25” for mist flow with air mass flow rate of 0.07 Kg/s and different water flow rate for PRC=0.5 at 10,000 rpm rotation speed .....	265
<b>Table 5.56</b>	CFD simulation results for one stage turbodrill model “A1G25” for mist flow with air mass flow rate of 0.07 Kg/s and different water flow rate for PRC=0.1 at 10,000 rpm rotation speed .....	268
<b>Table 5.57</b>	CFD simulation results for one stage turbodrill model “A1G22” for mist flow with air mass flow rate of 0.1 Kg/s and different water flow rate for PRC=1 at 10,000 rpm rotation speed .....	271

# 1

# Down hole rotary drive mechanism for hard rocks drilling

Since the inception of rotary drilling more than 100 years ago, improving drilling performance and technologies have been in the subject of many scientific research and inventions. While drilling deeper and in more complex conditions have become necessary, delivering required power directly to the bit, independent of rotating the drill string, appears to be necessary. The main objective of this research is to identify and design specifically the best suitable and applicable down hole rotary drive mechanism with current technology for drilling deep and small diameter holes through hard rocks for the purpose of mineral exploration. Providing the required power by a down hole drive mechanism for drilling deep hard rocks and small holes for mineral exploration is subjected to various challenges. Therefore, a systematic approach should be used for selection, adoption and/or development of an appropriate down hole rotary drive mechanism for efficient drilling for the applications of this study. In this Chapter, after a brief description of the research background in this topic, the most suitable down hole rotary drive mechanism for this application is proposed, various design specifications are listed and the need for future study around this topic will be highlighted. The remaining of this Chapter summarises the outline, objectives and significance of this research work and the thesis structure.

## 1.1 Hard rocks exploration drilling

The Deep Exploration Technologies Cooperative Research Centre (DET CRC) was established under the Australian Government's CRC program to address the most significant challenges to the future of the minerals industry. It means the reduction in the mineral resources inventory due to high production rates and low mineral exploration success. To ensure the future of the minerals industry, new technologies must be developed to explore to greater depths in the vast areas of deep, covered prospective basement. The flagship project for the DET CRC program is the next

generation drilling technologies which plans for the development and/or adaptation of transformational technologies for mineral exploration drilling.

Drilling for petroleum and for mineral deposits are very similar activities with quite different targets. In mineral exploration, drilling is used to obtain very detailed information about rock types, mineral content, rock genesis and the relationships between rock layers close to the surface and at depth. Drilling is only used in areas that have been selected as targets from geological, geophysical and geochemical methods and the most important reason for drilling is to collect samples of rock to obtain information about the vertical and lateral distribution of the geological formations, the structural regime, ore and its grade. This would determine if the site is feasible for further investigations and studies. With this in mind, obtaining core samples over whole overburden is not always essential and having cuttings of small sizes could be used for the analyses needed during the exploration phase. Therefore drilling small size holes as fast as possible and obtaining the samples to the surface would be a good alternative with several advantages over conventional drilling methods for deep hard rocks mineral exploration.

Currently, reverse circulation (RC) and diamond core drilling are the two principal methods of drilling in mineral exploration. The RC method is faster and more flexible than coring and provides virtually uncontaminated cuttings suitable for geochemical anomalies, and diamond coring produces core samples to increase the level of geological knowledge and the 3D extension and distribution of the ore body. However, both of these methods are subjected to certain limitations and inefficiencies in reaching deeper depths and drilling complex hole geometries. Examples of such shortcomings include the inability to provide enough air pressure for RC drilling and high friction between drill pipe and the hole wall and drill string “twist-off” in deep diamond core drilling.

Drilling deep wells of the order of few kilometres is however a very common practice in oil and gas industry: this justifies the idea of adopting the existing oil and gas drilling technologies into mineral exploration drilling. The geological environments for the proposed deep hard rocks mineral depositions are quite different than that of hydrocarbon reserves. While oil and gas are accumulated in sedimentary source rocks (porous rocks with pore pressure) during years of deposition of organic material, most of the proposed deep hard rocks mineral resources are found in the form of various size lenses or veins within the igneous and metamorphic source rocks. On the other hand, by

nature, the host rocks for the proposed deep hard rocks mineral depositions are stronger and harder to drill than oil and gas bearing formations.

Considering that delivering large volume of reliable samples from deep zones to the surface in shortest possible time is of paramount importance in mineral exploration, coiled tubing (CT) drilling is proposed in this study for these applications. Coiled tubing (CT) is a continuous length of carbon steel or composite tube that is stored and transported over a large reel. While advances have been made in the CT technology in the oil and gas industry within past few decades, introducing this system for mining applications is subjected to different challenges. Considering the fundamental differences in drilling hard rocks in mineral exploration comparing to oil and gas wells, the bottom hole assembly (BHA) should be specifically adapted for CT drilling in mineral exploration applications. Figure 1.1 shows a schematic CT unit with main components proposed for hard rocks mineral exploration drilling.

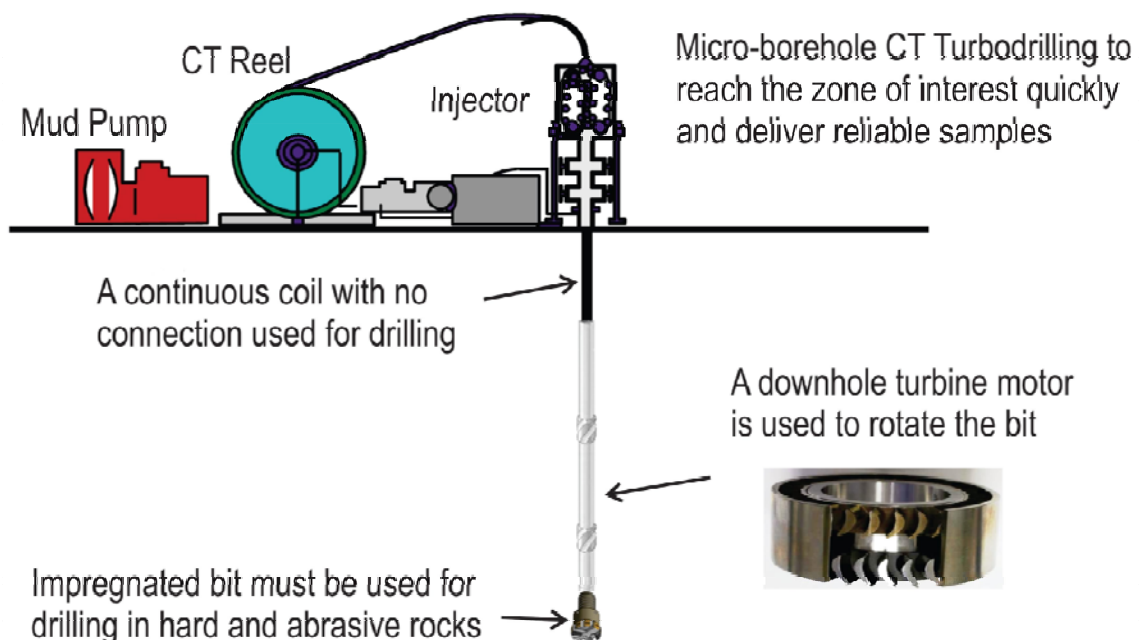


Figure 1.1 A schematic coiled tubing unit with BHA assembly for hard rocks mineral exploration drilling.

## 1.2 Down hole drive mechanism for coiled tubing drilling

Coiled tubing is a continuous pipe and therefore a down hole drive mechanism is needed to provide rotation and mechanical power to the bit. Here, in CT drilling, the whole required mechanical power for the bit is generated by the down hole rotary drive mechanism (motor) which plays a critical role in drilling efficiency. There are many special design criteria that are associated with the successful implementation of down hole motors with CT drilling operations. Since CT is not very resistant to buckling

loads, one major concern when running a CT job is that it is often difficult to get enough weight on bit (WOB) to maximize the rate of penetration (ROP) through the drilling interval (Sanchez *et al.*, 1996; Blount *et al.*, 1998; Maehs *et al.*, 2005; Newman *et al.*, 2007). Since the ROP of a fixed cutter drill bit is a product of the depth of cut (DOC) and the rotation speed (RPM) and that the DOC is primarily produced by the available WOB, in an environment where WOB is limited (as with CT drilling); high RPM is the key driver for ROP (Beaton and Seale, 2004; Seale *et al.*, 2004; Judzis *et al.*, 2006; IT, 2007; APS, 2008; Grigor *et al.*, 2008; Mushovic *et al.*, 2009; Schlumberger, 2010; Radtke *et al.*, 2011; Staley *et al.*, 2011). Commercial introduction of coiled tubing technology to the mining hard rocks drilling industry requires an effective down hole drive mechanism which operates efficiently at high RPM and low weight on bit (very low depth of cut) for delivering efficient power to the special high RPM drill bit for ensuring both high penetration rate and long bit life.

There are currently three main types of down hole drilling motors available in the market. These are electric motor, Positive Displacement Motor (PDM), and turbine motor (turbodrill). Based on the requirements of CT drilling, amongst available down hole motors, turbodrills (turbine motors) are the best choice to be used for small size CT drilling hard rocks (Mokaramian *et al.*, 2012a): this satisfies the high speed and low weight on bit drilling system and results in a smooth and good quality borehole with little vibrational effects during drilling.

In general, the down hole turbine motor is composed of two sections: the turbine motor section and the bearing section (thrust-bearing and radial support bearing). The turbine motor section has multistage of stators and rotors which converts the hydraulic power provided by the drilling fluid (pumped from surface) to mechanical power with diverting the fluid flow through the stator vanes to rotor vanes. Several new turbodrill designs and modifications are currently underway to extend the applicability of turbodrilling to coiled tubing operations for petroleum drilling applications (Seale *et al.*, 2004; Grigor *et al.*, 2008; Radtke *et al.*, 2011). One of the most significant developments in progress is the creation of a turbodrill that is much shorter in length than existing designs in order to enhance compatibility with coiled tubing rig and to maximize power output in the shortest possible tool configurations (Calnan *et al.*, 2007; Natanael *et al.*, 2008; Radtke *et al.*, 2011). Blade shapes and angle of attack into the hydraulic fluid stream are critical. Inefficient blade shapes generate losses in the process of converting hydraulic to mechanical energy.

Although many research have been focused on developing new down hole motors with enhanced performance for drilling oil and gas wells, there is no available high speed small down hole motor ( $< 73$  mm) suitable for small borehole hard rocks mineral exploration drilling. As a result, design and manufacturing of small size and high speed turbodrill is a needed development in this area. In this study based on down hole power and speed requirements for small size coiled tubing drilling for deep hard rocks mineral exploration, a small diameter turbodrill is designed specifically to provide following requirements for this specific application:

1. The turbodrill should has a small diameter (OD  $\leq 60$  mm); The reason is that with small diameter, higher speeds can be applied to smaller bit and it needs less WOB as well. Also drilling small holes with small drilling assemblies has certain benefits for mineral exploration applications.
2. This down hole tool should has a relatively short length (total length of less than 3 m). The purpose of this is that with shorter tools, drilling operation is much easier, faster and safer for small size coiled tubing assembly that may not have an adequate derrick height suitable for a long motor to be tripped in and out of the hole easily.
3. The motor should have high optimum rotation speed ( $N \approx 5,000$  to  $10,000$  revolutions per minute, rpm). In this way with low depth of cut impregnated diamond bits, with less WOB, acceptable ROP can be reached.
4. The design needs to be optimized for minimum drilling fluid flow rate, while generating required power and speed. The turbodrill performance is very sensitive to the flow rate and its power changes according to the changes in the flow rate to the power of three. In the small diameter drilling assembly and hole size, reducing the flow rate as much as possible results in less pressure losses in the system and therefore less energy will be lost.
5. Software platform capable of predicting turbodrill performance and flow properties passing through the motor, for any complex drilling fluid (multiphase flow, multi-components fluid) in any possible conditions is required for such this design. This makes the drilling optimization more straightforward in comparison with the previous platforms that are passive and only check the turbodrill performance through limited lab experiment flow test with limited fluid properties and with few flow observations.
6. Extending the life of turbodrill with finite element structural analysis of loads applied to the blade due to the fluid flow, is the second stage in the design of the motor

which should be performed. This is another novelty in this study which, has not previously been considered during the design process (despite an extensive review of literature made by the Author).

In this study ANSYS® TurboSystem software tool is utilized to first design small turbodrill stages with specific requirements for this application and then investigate the effect of various design parameters and fluid flow properties on the turbodrill performance through Computational Fluid Dynamics (CFD) analyses. In the design methodology presented in this study, CFD code is used at the first stage to optimise the fluid flow performance through turbodrill and then Fluid-Structural Interaction (FSI) analyses are conducted to calculate the amount of the mechanical stresses and deformations caused by the fluid flow and interactions with the blades.

### **1.3 Objective of this thesis**

Based on the application of this study, the objectives of this PhD thesis can be summarised as below.

1. Identify and introduce various possible adoptions from the existing technologies in petroleum drilling to deep hard rocks mineral exploration drilling, through a comprehensive review of the literature.
2. Identify and propose the appropriate down hole rotary drive mechanism (motor) for application of this study, with a comprehensive critical review of the literature.
3. Propose and describe design methodology and various design specifications for the appropriate down hole motor.
4. Describe and specify the numerical method for fluid flow analysis through the down hole motor using Computational Fluid Dynamics (CFD) for different drilling conditions.
5. Error quantification in the numerical method and applying verification and validation process to ensure high quality numerical results suitable for application of this study are presented.
6. Comprehensive full scale (3D) fluid flow analyses with ANSYS® CFD code (CFX) using Finite Volume Method (FVM) to evaluate the performance of the turbodrill stage with different design specifications, fluid types and properties, and flow properties.

7. Calculate the amount of the mechanical stresses and deformations caused by the fluid flow through Fluid-Structural Interaction (FSI) analyses using ANSYS® Mechanical APDL solver with the Finite Element Method (FEM).
8. Propose the most appropriate design specifications for the small diameter and high speed down hole motor for the application of this study and provide the motor performance curves with different fluid and flow properties.

## 1.4 Significant of this research

As stated in the previous sections, in this study a small size down hole motor was designed to be used with a Coiled Tubing rig system for drilling hard rocks mineral exploration boreholes faster, cheaper and safer. This study is unique in different ways, some of which are listed below:

1. Although several research studies have been focused (mostly through lab experiments) on developing new down hole motors with enhanced performance for drilling oil and gas wells, there is no available small diameter ( $< 73$  mm) and high speed down hole motor suitable for small borehole hard rocks mineral exploration drilling. As a result, design and manufacturing of small size (5-6 cm OD) and high speed (5 to 10 thousand rpm) turbodrill specifically for these applications is a new development presented in this study.
2. In this research high speed turbodrill is proposed as the preferred rotary drive mechanism for hard rocks mineral exploration drilling. Turbodrill is an axial hydraulic turbomachinery and the basic design methodology of general axial turbomachinery can be adopted for turbodrill design and optimization for application of this study. In this study, several small diameter turbodrill models were designed specifically to produce highest amount of power and speed in the shortest possible length. Here, in comparison to the oil and gas design specifications, the higher optimum rotation speed is more attractive and the drilling operation is managed to be on the higher speed side of the turbodrill performance curve that we have less torque and then less WOB (less DOC) is required to reach relatively high ROP.
3. For the first time, comprehensive full scale (3D) numerical fluid flow analyses at this scale under real drilling conditions were performed in this work to investigate the effect of various design specifications, fluid types and properties on the turbodrill performance. The design platform and approach in this study is applicable to any turbodrill size and specifications to be optimised for any complex fluid flow

properties for both petroleum and mining drilling applications. Using state of the art Computational Fluid Dynamics (CFD) simulation techniques and Fluid-Structural Interaction (FSI) analyses ensure comprehensive optimization of the turbodrill to provide the required output mechanical power to the bit with extending the working life with respect to the material used for turbodrill manufacturing.

The above are all innovative steps which will be practiced for the first time in this research work and the results are expected to advance the fundamental science in this subject.

## 1.5 Thesis structure

Based on the objectives of this study, this thesis is structured in different Chapters which are explained briefly below. Figure 1.2 shows a brief overview of this thesis structure.

In Chapter 2, typical differences between drilling practices in petroleum and mineral exploration applications are discussed and transfer of coiled tubing (CT) drilling technology from its current applications in petroleum industry to hard rocks mineral explorations is proposed and described. Based on the different drilling environments, possible adoptions to CT drilling assembly are proposed. In particular, various down hole rotary drive mechanisms currently available in the market are discussed in detail with their performance characteristics. Finally in this Chapter, according to the performance requirements for application of this study, the most appropriate down hole motor is identified and the required changes and adoptions in compare to available designs are discussed.

Turbodrill design methodology and specifications are presented in Chapter 3. In the first section of this Chapter, power requirement for hard rocks drilling is discussed. In the following sections of this Chapter, basic turbodrill design concepts as an axial Turbomachine are described, and then drawings of the basic specifications for each geometry models are reported with real design dimensions for the simulation purposes.

A detailed introduction to the numerical method and Computational Fluid Dynamics (CFD) code which is used by ANSYS<sup>®</sup> CFX software in fluid flow analysis of turbine motor will be covered in Chapter 4 with detailed turbulence models and boundary conditions used in this study. Errors and uncertainty in CFD modelling and verification and validation process in assessing the quality of a CFD model are

## **Chapter 1** *Down hole rotary drive mechanism for hard rocks drilling*

discussed next in this Chapter. Finally, the basic concepts for Fluid-Structural Interaction (FSI) analysis used in this study are presented.

In Chapter 5, comprehensive analyses of fluid flow through turbodrill stage using ANSYS® CFX and ANSYS® Mechanical APDL solvers for various design specifications, fluid types and properties in different working conditions will be reported and discussed. Detailed performance curves for various turbodrill models and flow conditions are presented and the numerical simulation results will be compared in various aspects.

In Chapter 6, the conclusions drawn and recommendations proposed as a result of this PhD thesis will be presented.

**Chapter 1: Down hole rotary drive mechanism for hard rocks drilling**

A brief introduction to hard rocks exploration drilling and proposed down hole rotary drive mechanism (motor) for application of this study.

**Chapter 2: Deep hard rocks mineral exploration drilling**

- A review of existing drilling practices in mineral exploration in compare to the common drilling technologies in petroleum industry.
- Proposing coiled tubing rig, with its main application in oil and gas industry to hard rocks mineral exploration drilling and discussing possible adoptions for this technology transfer.
- Various down hole rotary drive mechanisms currently available in the market are discussed in detail with their performance characteristics.
- Identifying the most appropriate down hole motor for application of this study and discussing the required changes and adoptions in compare to the available motor designs.

**Chapter 3: Turbodrill design and specifications**

- Turbodrill design methodology and specifications are presented.
- Basic specifications for each geometry models are reported with real design dimensions for the simulation purposes.

**Chapter 4: Turbodrill fluid flow analysis**

- A detailed introduction to the numerical method and Computational Fluid Dynamics (CFD) code used by ANSYS® CFX software in fluid flow analysis of turbine motor.
- Discussion on errors and uncertainty in CFD modelling and verification and validation process in assessing the quality of a CFD model.
- Basic concepts for Fluid-Structural Interaction (FSI) analysis used in this study.

**Chapter 5: Numerical simulation results and discussions**

- Grid convergence study of the model in numerical simulations.
- Comprehensive numerical analyses of fluid flow through turbodrill stage using ANSYS® CFX and APDL solvers.
- Detailed performance curves for various turbodrill models and flow conditions.

**Chapter 6: Conclusions and future work**

**References**

Figure 1.2 Structure of the thesis.

# 2

# Deep hard rocks mineral exploration drilling

In the previous Chapter, the importance of adopting drilling technologies from oil and gas to mineral exploration was briefly reviewed. In this Chapter, to identify potential adoptions required to be applied to the existing technologies, these two different drilling environments are compared and based on the objectives of this study, applicable adoptions are proposed. The focus in technology transfer will be on coiled tubing (CT) assembly as it was suggested that it would be the method of choice for drilling deep small size boreholes in hard rocks as fast as possible. In particular, different down hole rotary drive mechanisms (motors) are compared later in this Chapter to identify first most appropriate down hole motor and then propose suitable adoptions to existing designs used in petroleum drilling to optimise for the application of this study.

## 2.1 Mineral exploration versus petroleum drilling

In mineral exploration, the main purpose of drilling is to obtain information about the vertical and lateral distribution of the geological formations, the structural regime, ore and its grade (Marjoribanks, 2010). This would determine if the site is feasible for further investigations and studies. On the other hand, taking samples at different depths is a side purpose in drilling oil and gas wells. An oil and gas well provides long term services and taking samples is for the purpose of various lab analyses, including chemical and mechanical tests. Cuttings are also used in some occasions for special kind of analysis known as mud logging which is beneficial to field geologists for their studies; however most of the tests on reservoir rocks are performed on intact samples acquired down hole (Santarelli and Dusseault, 1991; Fleckenstein and Eustes, 2003).

The geological environments for the proposed deep hard rocks mineral depositions are quite different than that of hydrocarbon reserves. While oil and gas are accumulated in sedimentary source rocks (porous rocks with pore pressure) during years of deposition of organic material, most of the proposed deep hard rocks mineral resources are found in the form of various size lenses or veins within the igneous and

metamorphic source rocks. On the other hand, by nature, the host rocks for the proposed deep hard rocks mineral depositions are stronger and harder to drill than oil and gas bearing formations.

Drilling deviated or horizontal wells in hydrocarbon reservoirs is with the purpose of enhanced recovery and commonly larger curvatures – in comparison with mineral exploration applications – are used for deviated sections below the kick off point. The only reasons for drilling deviated boreholes in mining exploration are to correct the hole trajectory to get access to the minerals which are formed as small veins or a pocket or to cross the specific layers in a certain direction and dip and this is for the purpose of sampling and reserve determination. In this case it is more practical to use short radius for the curved section of the borehole.

In oil and gas drilling both mechanical and chemical related well instabilities are very likely to be observed during drilling or the course of production. It can be seen that the pore pressure inside the reservoir would play a significant role in balancing the bottom hole pressure and changing the failure status. Also, as the size of the wells are larger in oil and gas than mining applications the failure potential would increase accordingly due to the possibility of intersecting more natural fractures and having less homogenous rocks. In hard rock mining drilling, however, the rocks are stronger and generally there is no pore pressure, hence borehole integrity is of much less concern. While the wells drilled for oil and gas production are expected to provide a long term service till abandonment stage, integrity of the borehole is considered critical and hence casing and cementing operations are necessary. In mining exploration the main purpose of drilling is to obtain samples for various analyses and therefore the integrity of the borehole is important as long as it serves this purpose and usually it is not a long term function. Consequently, time dependent instabilities may not be of any concern in mining exploration applications and also due to the small borehole size the potential for structural failures is lower than wells drilled in oil and gas industry.

Currently, reverse circulation (RC) and diamond coring are the two typical drilling methods which are used in mining applications (Atlas-Copco, 2010; Marjoribanks, 2010). The first method provides small size to powder like samples, whereas with the latter technique cores can be retrieved. In the RC method the energy is provided by the hammer through pneumatic percussion action to the bit instead of rotating the entire drilling rods, and is faster and more flexible than coring and provides virtually uncontaminated cuttings (ranges from dust to 25 mm chips) suitable for geochemical

anomalies. In diamond coring, a hollow bit, usually impregnated diamond, is used to cut the rock through rotary motion with the purpose of extracting core to increase our knowledge about the geology of the rocks and the 3D extension and distribution of the ore body. Figure 2.1 and Figure 2.2 show respectively a typical diamond coring drilling and the main drilling assembly for such drilling system.

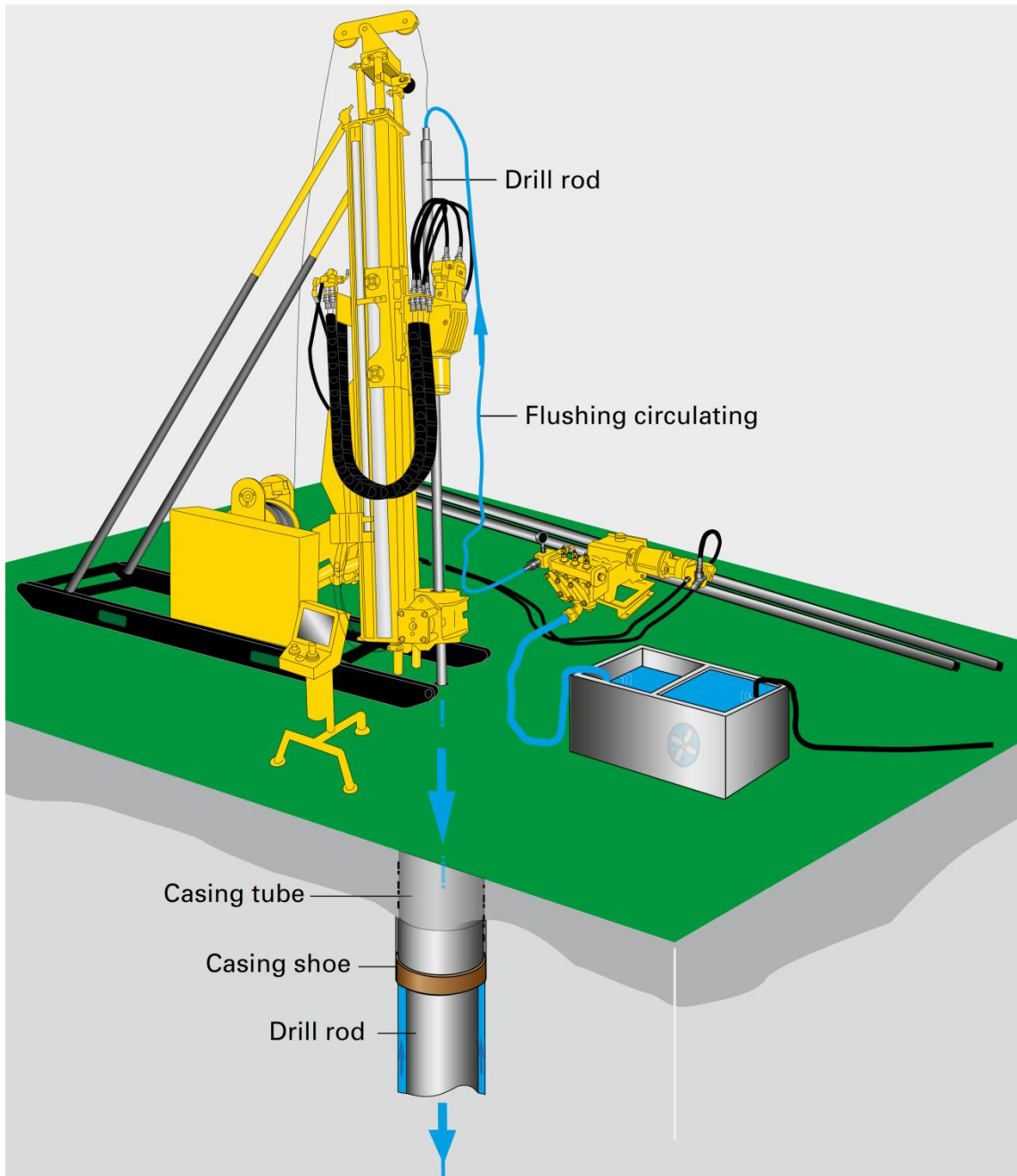


Figure 2.1 A typical diamond coring system in mineral exploration (after Atlas-Copco, 2010).

RC drilling, compared to core drilling, has two shortcomings. Firstly, because of the increase in air pressure required with hole depth there is a limit to drilling up to the depth of 800 m using multiple air compressors to supply the drill rig. Secondly, RC drilling yields less information about geological structure of the ore body.

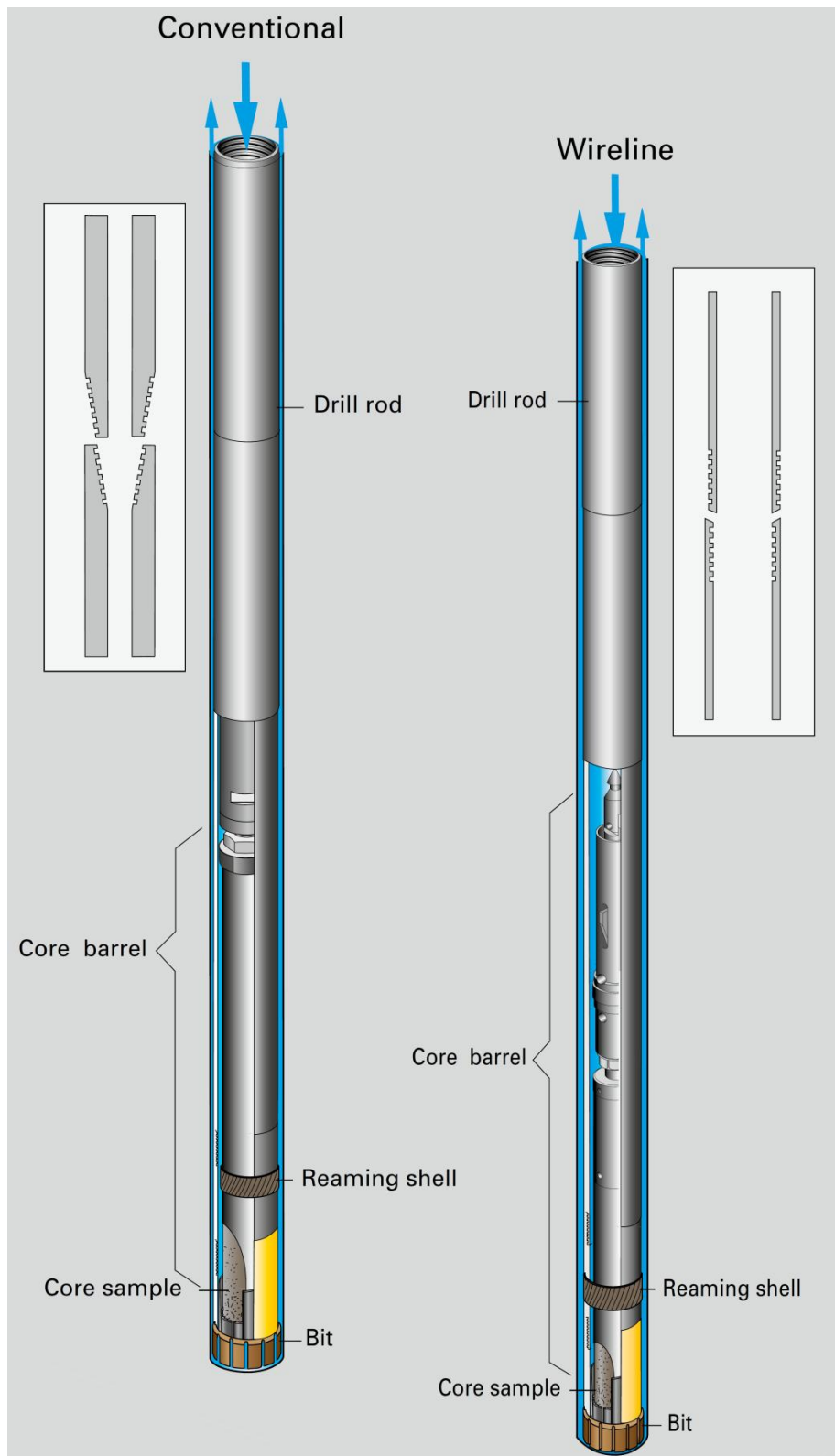


Figure 2.2 Down hole drilling assembly for diamond coring system in mineral exploration (after Atlas-Copco, 2010).

Diamond drilling can routinely achieve depths in excess of 1,200 m, and as it goes deeper, twist-offs of the small-diameter drill pipe is a major problem with this system. The depth capacity of the diamond coring rig is set by at least two factors: pull force and torque (Atlas-Copco, 2010). When drilling to deep depths with diamond coring

system, the drill pipes will encounter intense friction due to larger contacts between drill pipes and the hole wall, so that drill bit efficiency will be lost as power from the rig-surface top drive system lessens. Drilling efficiency and core recovery will also decrease and the core sample damaged by problems such as the stick-slip phenomenon. Thus, more power at the bottom of the borehole will be required for relatively deep hard rock formations. In conventional drilling this power is provided through the rotation of the drill string.

Currently, mine operators mostly use RC for drilling shallow holes and in-pit grade control to clearly define surface geochemical anomalies, and core drilling for deeper holes to identify future resources if the area is geologically complex or the exposure is poor (Marjoribanks, 2010). Selecting the right technique or combination of techniques is always a trade-off between speed, cost, required sample quality, sample volume; logistics and environmental considerations. However, the best method for drilling is the one which reduces the sampling time and costs and achieves the best quality samples (Atlas-Copco, 2010).

With respect to the purpose of mineral exploration, drilling small size holes as fast as possible and obtaining the samples to the surface would be a good alternative with several advantages over conventional drilling methods. As a result, the use of coiled tubing (CT), which is a continuous length of pipe with no connection, is proposed for mining drilling applications. CT has been initially used in oil and gas industry for stimulation and work-over operations but its applications was extended to drilling micro-boreholes recently (Albright *et al.*, 2003a; Albright *et al.*, 2003b; Cohen and Deskins, 2005; Galbierz and Oglesby, 2005; Theimer and Kollé, 2007; Dietrich *et al.*, 2009). Considering the fundamental differences in drilling hard rocks in mineral exploration comparing to oil and gas wells, the drilling assembly especially bottom hole assembly (BHA) should be adapted for CT drilling in mineral exploration applications.

## **2.2 Coiled tubing drilling**

Coiled tubing (CT) is a continuous length of ductile steel or composite tube that is stored and transported over a large reel (see Figure 2.3), in which the reel diameter must be at least 40-48 times the diameter of the tubing, to avoid excessive stress (CTES, 2005; ICoTA, 2005; NETL, 2005). The CT Unit (CTU) consists of four basic elements: 1) Reel, for storage and transport of the CT, 2) Injector Head, to provide the surface drive force to run and retrieve the CT, 3) Control Cabin, from which the equipment

operator monitors and controls the CT, and 4) Power Pack, to generate hydraulic and pneumatic power required to operate the CT unit. Tube sizes for drilling purposes range from 2.54 cm (1 in.) to 11.4 cm (4 ½ in.), and with an average yield strength of 344.7 MPa (50,000 psi) to 827.4 MPa (120,000 psi) (NETL, 2005). The bigger the CT diameter, the deeper it can be used but the more it weighs and the less its life would be. It can be uncoiled in the well and returned back to the reel up a limited times (ex. 50 times) depending to the drilling conditions before metal fatigue forces retirement (CTES, 2005; NETL, 2005). In oil and gas industry, the basic micro-drilling rig concept was developed by the U.S. Los Alamos National Laboratory LANL (Albright *et al.*, 2003a; NETL, 2005) to achieve a readily automated coiled tubing deployed drilling model to provide an inexpensive, reliable, and field demonstrated in range of 4.45 to 6.03 cm diameter holes to the depth of 200-300 m.

The maximum stall torque of the motor should not exceed 80% of the nominal torsional yield of the tubing for vertical drilling, and 50% of the nominal yield for drilling directional boreholes (CTES, 2005). The required mast height for handling the BHA components for CT drilling is dictated by the maximum anticipated drilling motor length since these are likely to be the longest components that will need to be inserted.

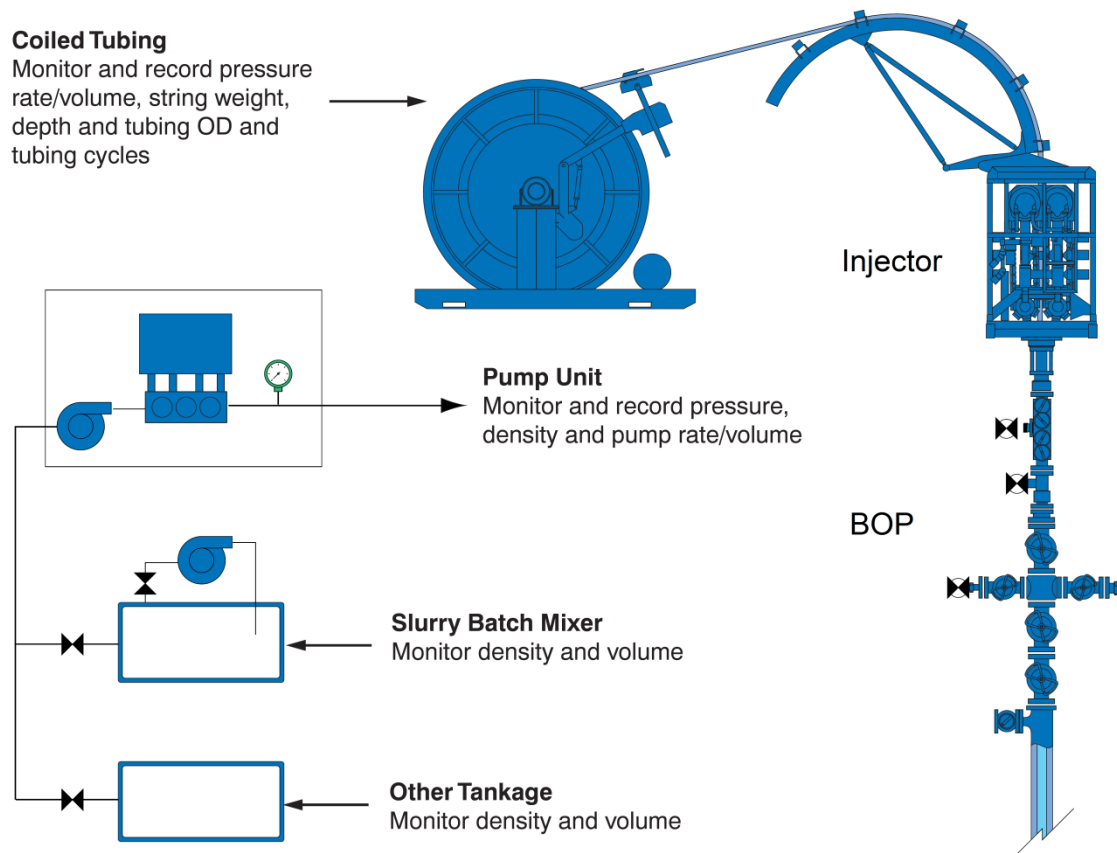


Figure 2.3 A typical coiled tubing drilling assembly (after CTES, 2005).

CT drilling has several advantages and limitations in comparison to conventional drilling method in oil and gas industry (Pierce *et al.*, 1996; Byrom, 1999; NETL, 2005). Some of these advantages are listed below with reference to mineral exploration applications.

- Fast tripping, up to 2.5 times faster than with drill pipe (with world record above 200 m/hr), also set-up time is greatly reduced,
- A big derrick is not required for handling drill pipes, so surface equipment and its footprint can be reduced. The units require about half the surface area that a conventional drilling rig requires,
- Fewer crews required for operation (2 man crew can manage the drilling operation),
- Smaller volumes of drilling mud are needed, and a smaller volume of rock cuttings is created during drilling due to smaller diameter hole drilled,
- It would be relatively simple to incorporate an electrical conductor into coiled tubing. This would facilitates drilling with electric motors, using active down hole steering tools, and collecting real-time, high-bit-rate down hole data (Anderson *et al.*, 1997; Turner *et al.*, 1999a; Turner *et al.*, 1999b),
- More effective in precise positioning of tools in horizontal and vertical wells,
- Drilling fluid can be pumped continuously without any interruption due to the rod handling and this reduce the cuttings transport problem and consequently it is possible to reach higher ranges of ROP (Elsborg *et al.*, 1996),

On the other hand some of the disadvantages and limitations of CT system can be listed as followings:

- Since the CT does not rotate, a down hole motor (which is expensive) must be used for drilling,
- Lack of pipe rotation also increases the possibility of differential sticking,
- Hole size and down hole hydraulics are limited by currently available tubing sizes (Blount, 1994),
- Weight-on-bit and torque are limited,
- The tubing is deformed plastically in bending around a relatively small radius, so pipe fatigue limits the number of trips for any piece of tubing. The tubing life limits cycling,
- CT hoisting capacity is limited by the injector that controls the penetration rate and insures the tubing is in tension, not compression,
- Rig dimensions are limited by highway regulations,

- Limitation on how far the CT can be pushed (pulled) horizontally, even with tractors and equalizers.

Various parameters may affect the life of a CT unit. The number of times in which CT is subjected to stresses higher than the minimum yield stress will affect when travelling from the reel to the gooseneck and from the gooseneck into the injector. Internal CT pressure induces further hoop (circumferential) and radial stresses and could affect CT life. Also, the size of the CT unit and the radius of curvature over which the CT is being bent (CT reel diameter) could affect its life (CTES, 2005).

Both fatigue testing and computer modelling show that CT working life increases with (CTES, 2005):

- Increasing tubing wall thickness,
- Decreasing tubing outer diameter (OD),
- Increasing guide arch radius,
- Using the largest reel diameter available,
- Reducing CT internal pressure during trips,
- Increasing material yield strength (at low pressure, higher stresses are generated in higher strength tubing that can cause shorter fatigue lives).

The CT manufacturing companies have been working for years on corrosion resistant alloy (CRA) CT materials. The fatigue life of the CRA material is approximately triples the life of conventional steel CT (CTES, 2005). Another alternative to steel for manufacturing CT is a composite made of carbon fibres embedded in a resin matrix. In comparison to carbon steel, composite CT has high resistance to fatigue damage, capability to include electrical conductors or optical fibres, and also is impervious to corrosion and significantly lighter than steel CT. However, it is 3-5 times more expensive and has maximum operating temperature of 120 °C (250 °F) and significantly lower stiffness than carbon steel, which means critical buckling force is much lesser (CTES, 2005).

## **2.3 Drilling fluid in coiled tubing operation**

The drilling fluid, or mud, is a crucial component in the success of any drilling operation. The three main categories of drilling fluids are water-based muds (which can be dispersed and non-dispersed), non-aqueous muds, usually called oil-based mud, and gaseous drilling fluid, in which a wide range of gases can be used. The basic functions of drilling fluids in general are: cuttings transport, cooling and lubrication of the bit and

motor, wellbore stability, and transmitting hydraulic power to the down hole motor and tools.

To determine the fluid flow characteristics, one of the major elements is the rheological properties of the drilling fluid. Rheology is the study of flow characteristics of a drilling fluid and how these characteristics affect movement of the fluid. Specific measurements are made on a fluid to determine rheological parameters under a variety of conditions. From this information the circulating system can be designed or evaluated for the desired objectives. Many mathematical models have been proposed for mud rheology to fit the experimental shear rate ( $\gamma$ ) – shear stress ( $\tau$ ) data. Amongst these models, Herschel–Bulkley (1926) model yields better estimation of pressure loss inside the drill string (with 96% accuracy) whereas the Power Low model (Govier and Aziz, 1972) being more accurate for pressure loss estimation in the annulus section (93% accuracy) (APIRP-13D, 2010). This is due to the fact that in oil and gas drilling, fluid velocity is higher inside the drill pipe section than that of the annulus space and this will result in higher shear rates. Published models are not very accurate in the turbulent flow regime, and empirical annular-flow correction factors are untested for the small sized CT Drilling (CTES, 2005). For instance in a reference, the minimum borehole diameter to drill is identified to be limited to an order of 5.08 cm (2 in) to 7.62 cm (3 in) at depths deeper than 1000 m. This is due to the limitations of the hydraulic system (Dietrich *et al.*, 2009).

The behaviour of a fluid is determined by the flow regime which has a direct effect on the ability of that fluid to perform its basic functions. The flow can be either laminar or turbulent, depending on the fluid velocity, size and shape of the flow channel, fluid density, and viscosity according to the Reynolds number. It is important to know which of the flow regimes is present in a particular situation to evaluate the performance of a fluid.

The roles of drilling fluid type, flow rate and the flow regime on efficient cuttings transport have been investigated numerously in the literature (Leising and Walton, 2002). There are many criteria associated with drilling fluid selection and properties appropriate for CT drilling and delivering reliable chip samples for mineral exploration. The drilling fluid should have enough density to generate enough torque and power to run the desired down hole motor and enough viscosity to hold and carry the cuttings in suspension throughout the annulus. In a study by Leising and Walton (2002) it was shown that, in many circumstances, hole cleaning is more efficient if a low-viscosity

fluid is pumped in turbulent flow rather than a high-viscosity fluid in laminar flow. In addition, the flow rate and its flow regime should be engineered accurately in such a way that it satisfies down hole motor requirements and proper flow velocity resulting in an operationally safe total pressure loss for CT drilling.

When using hydraulic down hole motors, one of the key strengths is that the hydraulic fluid provides cooling to the bit. Compressible fluids such as air or nitrogen, while providing some cooling to the bit, do not provide enough to have a practical effect. Foam provides greater lubricity and cooling than either air or nitrogen, but doesn't provide the same cooling capabilities that a hydraulic fluid such as water does. Use of compressible fluids does however have some major benefits that make it a viable drilling option. The major advantage is that it is extremely successful in underbalanced drilling. The pressure when using a compressible fluid as a drilling fluid is less than the reservoir pressure. This helps prevent damage to the formation and thus increase productivity of the well. Another advantage is that compressible fluids such as air and nitrogen are more environmentally safe than drilling fluids composed of water, chemicals and other minerals. Air and nitrogen will not contaminate a formation while another drilling fluid could (RIO, 2004).

In CT drilling operations, the geometry of the CT string present many challenges to drilling fluid performance. For all CT operations, the fluid travels through the entire tubing string regardless of the depth. Moreover, the frictional pressure loss for CT on the reel is considerably greater than for straight tubing. For optimum hydraulic performance, the drilling fluid must behave as a low viscosity fluid inside the CT to reduce the pressure drop through drilling assembly. Increasing the CT size has two advantages: 1) it reduces the frictional pressure losses inside the CT and so higher pump flow rates achieves; 2) And also it narrows down the annulus section that increases the turbulent intensity for efficient cuttings transport (Leising and Newman, 1993).

A good drilling fluid for coiled tubing operation is the one which is relatively free of lost circulation type materials to avoid detrimental effect on down hole motor performance. The drilling fluid must be thin enough to pass through the coiled tubing, yet have the ability to lift cuttings back to surface at flow rates compatible with the coiled tubing and down hole motor. As the annular gap between the drill string and the borehole is decreased, the maximum allowable drill-cuttings particle size must be decreased proportionally. Cleaning below the 20 micron particle size range must be accomplished with a centrifuge, ultra-small hydro cyclones. Centrifuges are heavy,

expensive to buy and operate and hard to maintain (Galbierz and Oglesby, 2005). As a general practice, the volumetric cuttings concentration must be kept well below 5% to maintain a continuous liquid phase and avoid the high pressure losses (Albright *et al.*, 2003a). High concentrations will result in excessive pressure losses due to particle interactions. Determining the optimum circulation rate to produce the optimum penetration rate is a complex, non-linear optimization problem that will require a computationally sophisticated systems analysis (Albright *et al.*, 2003a).

To evaluate a rig's hydraulic system it is necessary to know, amongst other parameters, the pressure losses through surface equipment, size and length of BHA components, number and size of drill collars, and, of course, the pressure drop through the down hole motor and bit. Detailed system pressure losses calculations and equations are provided in two references including: "Coiled Tubing Manual" (CTES, 2005) and "Rheology and Hydraulics of Oil-well Fluids: API Recommended Practice 13D" (APIRP-13D, 2010).

## **2.4 Adopting coiled tubing drilling for deep hard rocks mineral exploration**

Considering the fundamental differences in drilling hard rocks in mineral exploration comparing to oil and gas wells, the CT drilling assembly should be adapted specifically for mineral exploration applications. The design should be with the objective of delivering reliable samples to the surface with faster, cheaper and safer drilling. Accordingly, the main components of a drilling assembly, from bit up to the CT unit at the surface are proposed in the following subsections.

### **2.4.1 Drill bit**

An impregnated diamond bit with low depth of cut (DOC) which is designed for high rotary speed and low WOB drilling should be used to be compatible with formation properties, the coil and the motor. Diamond impregnated bits, commonly referred to as impregs, drill rocks by grinding action. Impregnated diamond bits are the most commonly used bits in mineral exploration drilling. Diamonds smaller than a few millimetres are imbedded in a tungsten carbide binder, allowing them enough exposure to grind away a small amount of formation at a time, until the dull, break out, and fresh diamonds are exposed. The most obvious optimization of this is the volume of diamond impregnated material exposed to the bottom hole at a given time, normally by the

number and width of blades. However, diamond size, type, concentration within the substrate, and alloy properties of the substrate should be optimized. In addition, recent technology allows diamonds to be spatially oriented within the substrate, mitigating inconsistencies created by having high and low concentration regions within the substrate (Langille *et al.*, 2009; Franca and Lamine, 2010). As a result, matrix hardness, diamond size and dosing can be varied according to the rock which must be cut.

For the applications with high speed motors, bits with a long gauge should be used to prevent a spiral hole and to replace the near bit stabilizer which is used to wear down very quickly at high RPM, especially in deviated wells (Chen *et al.*, 2002). In high rotation speed, cooling improvement of impregnated bit is very important. The nozzles allow water to be delivered to the cutting face. This provides three essential functions: lubrication, cooling, and removal of drill cuttings from the hole (Atlas-Copco, 2010). Proper flow rate and bit hydraulics calculations are essential to obtain desired depth of cut and should have a proper relation with the bit speed (RPM). At high bit RPM, the flow rate must be sufficient to clean the cuttings bed before the subsequent segment of the impregnated bit re-drills the cuttings. An increase in flow rate leads to clean out of this bed, resulting in a higher depth of cut.

The cutting elements and holding methodology are the limiting elements for available bits to reach high rotation speeds. Finite Element (FE) thermal modelling of the bit should be performed to predict cutter temperatures while drilling hard and abrasive rocks at high RPM and various parameters should be considered including: cutter forces, cutter temperatures, cutter wear rates, weight-on-bit, drilling torque, rock type, fluid temperature, fluid cooling rate, rotary speed, and penetration rate.

It is also interesting to note that for a given cutter as the radius decreases to the centre, the cutter velocity decreases to zero, independent of the bit size or rotating speed. Thus, it should be recognized that different cutting mechanism must exist as a function of radii and RPM. For high velocities, the outer high speed cutting edge can be a shearing cutting mechanism and for the middle can be a gouging method (IT, 2007). But still the bit cutting mechanism at and near the centre where the cutter speed is near zero is under question. The centre must be more of a crushing column method than a grinding mechanism. The cutting method's efficiency at the centre is not clear. If the centre column were cut by water jetting or abrasive jetting then improvements in drilling rate may be improved. This changing cutting mechanism should be studied further.

### **2.4.2 Weight on bit sub**

The weight on bit (WOB) sub records the tension, torque and the temperature near the bit whereas separate transducers record inside pipe and annular space pressures. Data from these devices are recorded down hole and will be transferred to a computer at the surface during the BHA trips (Blount *et al.*, 1998). The capability to make accurate, real-time, bottom hole measurements of WOB and torque is a critical element for a deep CT deployed drilling system, especially for maintaining low depth of cut.

### **2.4.3 Anti-stall tool sub**

Anti-stall tool (AST) is a mechanical down hole tool that aims to adjust the drilling torque automatically in real time. Originally, the tool was developed by “Tomax AS” for CT applications where it has proven its ability to successfully reduce vibrations, motor stalls, equipment failures, and general wear, in addition to increasing the penetration rate and run length (Dagestad *et al.*, 2006). The main idea behind the AST is to provide active down hole control of the rock-cutting process by diverting energy from the drilling process and using it to prevent dynamic forces from reaching destructive levels and thereby preserving the CT components and optimizing rock-cutting efficiency. The AST is placed as close to the bit as possible. AST will reduce stick-slip effects and bit stalls caused by the formations drilled. This has led to a significant reduction in symptoms of drill string overload and a measurable improvement in penetration rate (Selnes *et al.*, 2009).

### **2.4.4 Micro-hole drilling tractor**

The Micro-hole drilling tractor (MDT) is a down hole tool that facilitates running heavy bottom hole assemblies and extends maximum achievable horizontal hole by exerting additional force onward. The MDT is powered by differential pressure of the drilling fluid between the bore and the annulus and controlled by the surface pump and coiled tubing injector. Specific features of the MDT that increase its effectiveness are: 1) Operation on differential pressure of the drilling fluid, 2) On/Off capability, 3) High strength and flexibility, and 5) Compatibility to existing CT drilling equipment and operations (WWT, 2007).

#### **2.4.5 Isolation sub**

This sub will isolate the other instrument subs and coiled tubing from vibration, the rotary motor and bit-induced resonance, and other detrimental forces resulted in the bottom hole conditions (Melamed *et al.*, 2000; Staley *et al.*, 2011).

#### **2.4.6 Bottom hole assembly**

Two types of bottom hole assembly (BHA) assembly are needed to be used with CT unit for different sampling purposes, one for coring and another for full bit face drilling. The drilling BHA will provide reliable cutting samples even with depth accuracy of less than 1 metre depending on the drill depth, annular velocity, mud viscosity etc. (Georgi *et al.*, 1993). However, some degree of cuttings dispersion and contamination of the sample is inevitable. The coring BHA is only used for particular intervals which are crucial to be cored due to CT susceptibility to number of trips for retrieving the cores. Coring during turbine drilling with conventional core barrels attached to the turbodrill shaft proved to be very difficult, and high vibration levels often breaks the core in the core barrel (Eskin and Maurer, 1997). As a result, special Turbo-corer is needed. This consists of a turbodrill fitted with a hollow shaft which houses a detachable core holder (Eskin and Maurer, 1997). An area for CT development which would potentially result in significant performance and cost improvement is using Hybrid CT (Littleton *et al.*, 2010). It is especially effective in coring operation in providing enough mast height to pull out the core barrel and lay down to its carrier.

Proper BHA design for CT drilling is essential in keeping the hole straight and cause lower vibration and better hole quality which means better tool face control, better steerability, improved weight transfer to the bit, and more constant bit-rock interactions (Maranuk *et al.*, 2000; Maehs *et al.*, 2005; Newman *et al.*, 2007; Staley *et al.*, 2011). Hole spiralling can occur with both steerable motor assemblies and rotary assemblies (DeLucia, 1989). To mitigate or reduce this the best way to drill a high-quality wellbore is to use extended-gauge bits (Gaynor, 1988; Chen *et al.*, 2002).

#### **2.4.7 Intelligent wireless down hole orienter**

Directional drilling with CT requires a reliable down hole means to manipulate the orientation of the mud motor bend and changing the tool-face. Traditionally, hydraulic and wired orienters have been used with CT bottom hole assembly (BHA). In hydraulic ones, cycling of the flow rate while bit off-bottom will actuate them to offer right-hand

indexing of the BHA tool-face in 20° (or larger) increments with each cycle of the mud pumps (Gleitman *et al.*, 1998; Zegarra *et al.*, 2002). Once the desired tool-face has been attained and confirmed using directional MWD data, drilling can resume. Another category of CT orienter is powered from surface using a wireline inside the CT. Orienting while on bottom with the e-line system allows for a smoother well path because tool face changes are made over the length of the curve, and not in abrupt directional changes (Ohlinger *et al.*, 2002). These wired orienters produce higher torque and operate independently of flow rate while drilling. However, wireline impose certain logistical and operational difficulties in CT drilling (Zegarra *et al.*, 2002).

An intelligent orienter has been designed to address many of the limitations of standard hydraulic orienters (Zegarra *et al.*, 2002). This turbine-powered intelligent orienter offers the high torque rating of the wired orienters but does not require a wireline or link to surface, and reduces the orienting time significantly via continuous closed loop correction. The turbine orienter consists of two basic modules, the power and control module and the orienter module; the power and control module is composed of a fluid turbine, for converting the mud flow through the tool into electrical energy sufficient to power the electronics and a central processing unit (CPU) to receive commands from surface and control the tool operation. The orienter module consists of the electric orienter motor and associated electronics for performing all orienting functions (Zegarra *et al.*, 2002). Orienting is achieved by sending accurate commands with a computer from the surface to the tool by varying the mud flow rate between a nominal rate and 10% below the nominal rate. This action results in down hole changes of the turbine rotational speed. By changing the flow rate in a series of steps, commands are built and interpreted by the turbine orienter CPU to control the orientation (Zegarra *et al.*, 2002).

#### 2.4.8 Down hole rotary drive mechanism

Contrary to conventional drilling, in CT drilling the tube cannot rotate and hence a down hole motor is required to provide the rotation and power to the bit. There are many special design criteria that are associated with the successful implementation of down hole motors with CT drilling operations. Since CT is not very resistant to buckling loads, one major concern when running a CT job is that it is often difficult to get enough weight on bit (WOB) to maximize the rate of penetration (ROP) through the drilling interval (Sanchez *et al.*, 1996; Blount *et al.*, 1998; Maehs *et al.*, 2005; Newman

*et al.*, 2007). Since the ROP of a fixed cutter drill bit (impregnated diamond bit used here) is a product of the depth of cut (DOC) and the rotation speed (RPM) and that the DOC is primarily produced by the available WOB, in an environment where WOB is limited (as with CT drilling); high RPM is the key driver for ROP, especially in hard rocks drilling (Beaton and Seale, 2004; Seale *et al.*, 2004; Judzis *et al.*, 2006; IT, 2007; APS, 2008; Grigor *et al.*, 2008; Mushovic *et al.*, 2009; Schlumberger, 2010; Radtke *et al.*, 2011; Staley *et al.*, 2011). As a result a high power and ultra-high rotation speed down hole motor is required for hard rocks CT drilling. This high speed down hole motor has a critical role in the CT drilling performance. Consequently, the main objective of this study is design of a small down hole motor suitable for small hole size CT drilling for deep hard rocks mineral exploration drilling. In the next sections the various types of down hole motors are presented and then based on their specifications and the small CT drilling requirements, the best down hole motor type that satisfy this condition is identified and certain modifications or adaptions to be fit to this application are discussed.

## 2.5 Down hole motors

The invention of down hole motors goes back to 1920s with the first single-stage turbine motor developed by the Russian engineer Matvey Kapelyushnikov. Some major advantages in using down hole motors are to significantly increase penetration rates compared to conventional drilling techniques, and reduction of friction between drill string and borehole, which is very important, especially in drilling directional holes. This can result in smoother drilling operations and less rig trip time because of reduced possibilities of “twist-offs”.

There are currently three main types of down hole drilling motors available in the market. The three motor types are 1) Electric motor 2) Positive Displacement Motor (PDM), and 3) Turbine motor (turbodrill). Down hole drilling motors can be also classified into the hydraulic drive type (mud motor) and the electrical drive type from the actuating mechanism standpoint. Also mud motors themselves can be classified as 1) hydraulic (incompressible fluid) 2) compressible based on the drilling fluid used whether it is non-compressible drilling fluid or compressible (i.e., air, nitrogen, foam, etc.), respectively.

The hydraulic drive down hole motor (mud motor) converts hydraulic energy provided by the drilling fluid into the mechanical energy to rotate the bit. Drilling fluid

pushed through the power section creates the necessary power for the drilling motor. On the other hand an electric motor is controlled directly by the operator as commands are sent through the surface electrical controller and computer whereas a mud motor is controlled indirectly via variations in the mud flow. In the next sections detailed information's about the basis and performance of each motor type are presented.

### 2.5.1 Electric motor

The idea of electric drive drilling is not new. Electric motors have been used to great extent for horizontal well drilling in the former Soviet Union. In the U.S., General Electric worked on down hole electric motors for drilling in a project, cumulating in a final report in 1977. Several problems were noted, most notably the lack of a high capacity, reliable electrical link to the bottom hole assembly via the jointed drill pipe. The electric motor allows complete, and direct, control of the motor. The motor speed may be increased or decreased with a joystick. In this case hydraulic power by drilling fluid is required solely for bit cooling, cuttings clearance and transport and not for generating mechanical power required by the bit. This provides for better control of the drilling process while allowing circulation flexibility. Another advantage of the electric drilling motor is that the bottom hole assembly (BHA) is insensitive to aerated or energized drilling mediums. Air drilling may even be considered with the electric motor. This allows for the use of a full range of underbalanced drilling techniques (RIO, 2004).

There are a number of difficulties associated with electric motors. One of their problems is a low starting torque. Another difficulty is with both motor and electrical shorts during operation and it cause insulation problems. In this case rotating seals provide the primary protection for motor electrical wiring. Recent attempts to integrate electric motors into a rotary drilling assembly have had limited success, mainly due to the difficulties of providing a high capacity electric link to the down hole drilling assembly (RIO, 2004). Coiled tubing has provided an excellent means of achieving this through the installation of high capacity power cables within the coil to enable electric coiled tubing drilling (E-CTD) (Turner *et al.*, 1999a; Turner *et al.*, 1999b).

The new electric motor is an encapsulated permanent magnet motor instead of being an induction motor. The new electric motor is expected to address the major weaknesses of the current electric motor. It is expected to have high starting torque compared to the starting torque of current electric motors, and is expected to be totally

encapsulated, with no rotating seals, no motor oil, and no pressure compensation chamber (RIO, 2004).

In the latest effort toward developing new electrical motors in a project sponsored by United States Department of Energy (DOE), Three models have been designed by finite element analysis (FEA) for two sizes, 6.91 cm (2.72 inch) and 4.29 cm (1.69 inch) outer diameters, of a patented inverted configured “Permanent Magnet Synchronous Machines (PMSM)” electric motor specifically for drilling at ultra-high rotational speeds (10,000 rpm) (IT, 2007). Key features of the final designed motors are: fixed non-rotating shaft with stator coils attached channelled for mud circulation, rotating housing with permanent magnet (PM) rotor attached which connected to the bit, and electric components that are hydrostatically isolated from high internal pressure circulating fluids by static metal to metal seals (see Figure 2.4). With operating conditions of 300 voltage AC and 3 phase system at the motor leads, the 6.91 cm (2.72 inch) OD axial inverted motor can generate 4.18 KW (5.61 hp) power at 10,000 rpm with a 4 N.m (2.95 ft-lbs) of torque for every 30.48 cm (12 inches) of power section. The 6.91 cm (2.72 inch) OD radial inverted motor can generate 5.03 KW (6.74 hp) with 4.8 Nm (3.54 ft-lb) torque at 10,000 rpm for the same length of power section. The 4.29 cm (1.69 inch) OD radial inverted motor can generate 2.56 KW (3.43 hp) power with 2.44 Nm (1.8 ft-lb) torque at full speed 10,000 rpm for every 30.48 cm (12 inches) of power section. These types of motors were not built because of high tip velocities at the bit face and there is no available cutting element suitable for this high speed application (IT, 2007). However, a 7.62 cm (3 inch) OD, low speed, PMSM radial electric motors based on this project design was going to be built under a 2006 Oklahoma Centre for the Advancement of Science and Technology “proof of concept” grant. Only low rotational speeds (less than 1000 rpm) electrical motors for drilling have been tested to date (IT, 2007). In this project, many bearings and seals were investigated, but most of them were discarded due to such high speeds and the inverted configuration. No rolling bearing type can be used at these speeds. Hydrodynamic types were preferred due to ruggedness in the drilling operation, but none were available specifically for inverted configurations. Due to concern about variable film thickness, Metal to metal bearings was needed to maintain the 2 mm air-gap between rotating elements.

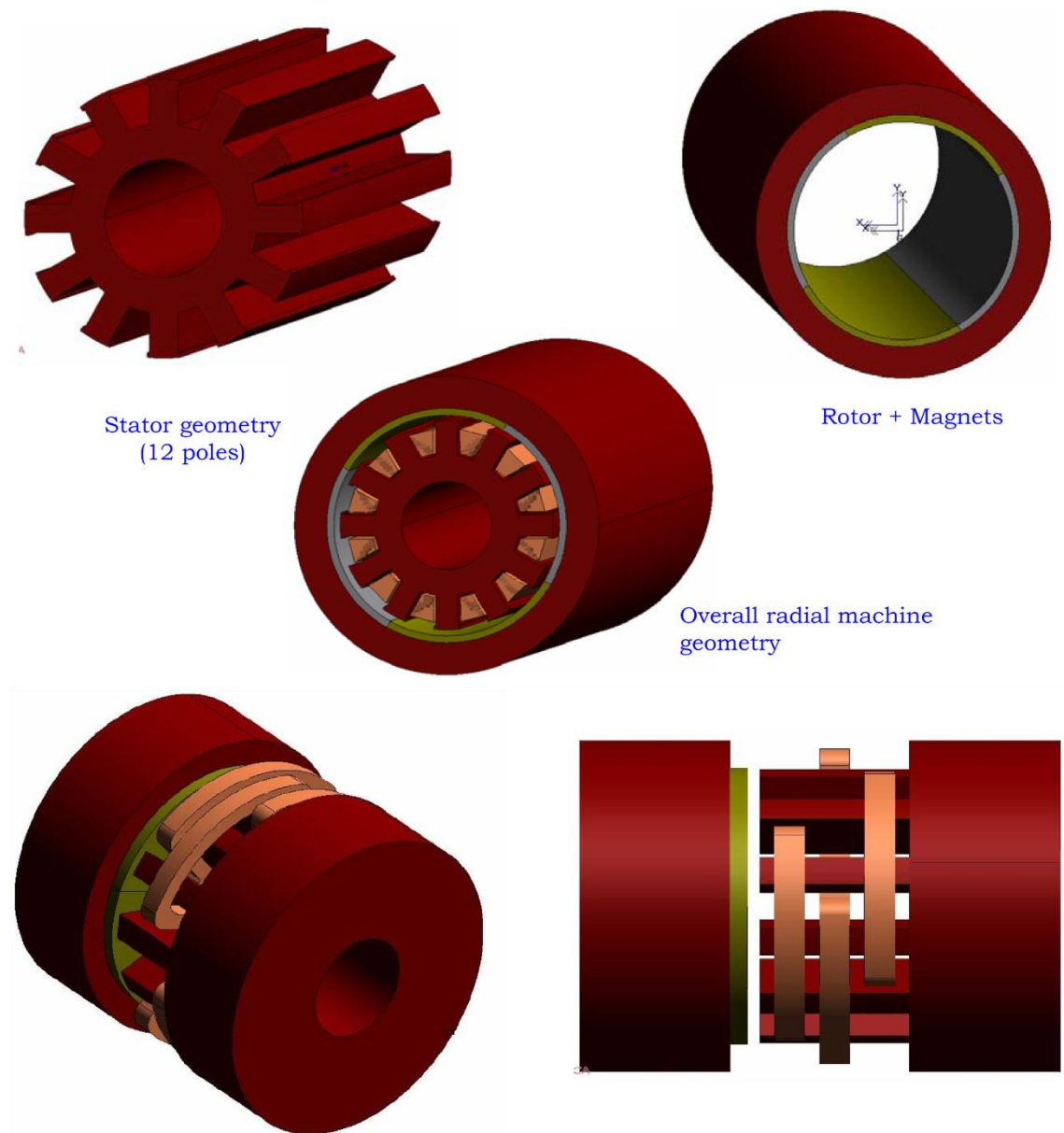


Figure 2.4 Basic design components of a PMSM electric motor (after IT, 2007).

### 2.5.2 Positive displacement motor

The development of positive displacement down hole motors (PDM) began in the late 1950s. The initial development was the result of a United States patent filed by W. Clark in 1957. The design of this down hole motor was based on the original work of a French engineer, René Moineau, and is classified as a helimotor. The motor is actuated by drilling mud pumped from the surface and converts hydraulic energy provided by the drilling fluid into mechanical energy. There are two other types of PDMs that have been used, or are at present in use today: the vane motor and the reciprocating motor. However, by far the most widely used PDM is the helimotor which uses a stator made of an elastomer (Lyons and Plisga, 2005) and this is the most common motor in use in

both petroleum and mining drilling. In general, most of the recent development work in helimotors has centred on multi-lobe motors. The higher the lobe system, the lower the motor speed and the higher the operating torque (Lyons and Plisga, 2005). Figure 2.5 shows a single chamber of a multi-chambered down hole positive displacement motor (a chamber is a lengthwise repeat of the motor). The rotor is made of rigid material such as steel and is fabricated in a helical shape. The activating drilling fluid (mud) is pumped at high velocity through the motor section, which, because of the eccentricity of the rotor and stator configuration, and the flexibility of the stator, allows the hydraulic pressure of the flowing fluid to cause a rotating torque to the rotor. As the rotor rotates the fluid passes from chamber to chamber. These chambers are separate entities and as one opens up to accept the mud from the preceding, the preceding closes up (Lyons and Plisga, 2005).

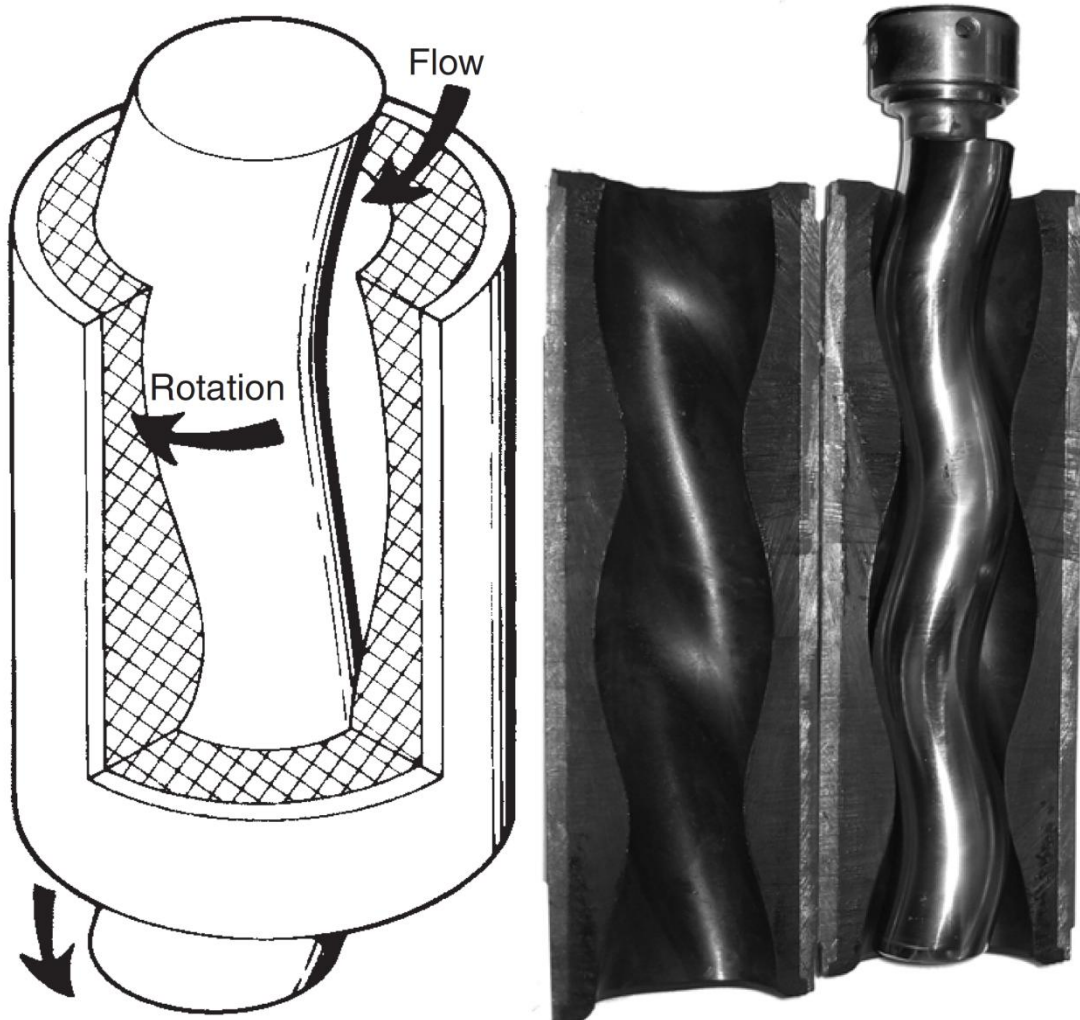


Figure 2.5 Basic positive displacement motor design principle (courtesy of Smith International, Inc.).

In general, the down hole positive displacement motor constructed on the Moineau principle is composed of 5 basic basic components (Cavo, 2005):

- Crossover sub or dump valve (optional)
- Safety catch sub (optional)
- Power-section assembly
- Coupling assembly (trains mission)
- Bearing assembly

Figure 2.6 is a cutaway view of the entire motor and shows these basic components.

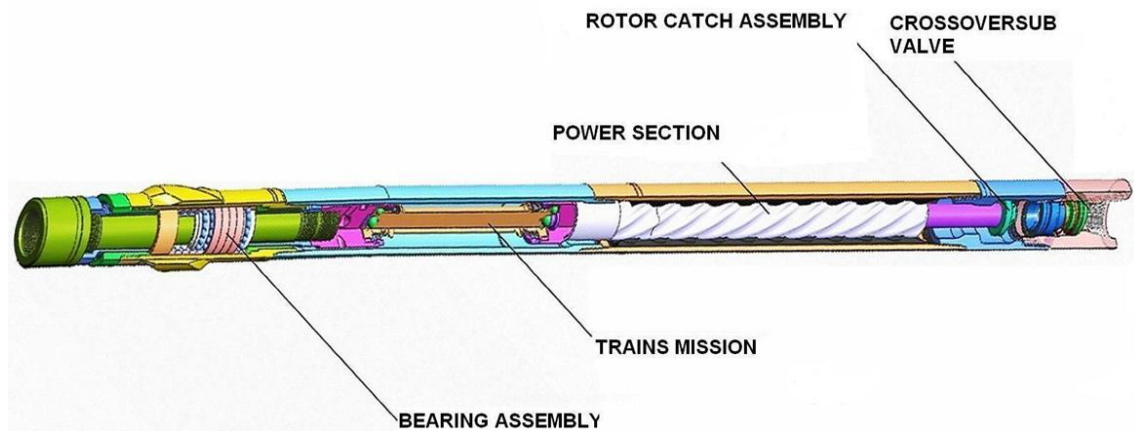


Figure 2.6 PDM components (courtesy of China-Ogpe).

The main advantages of the down hole PDM are (Lyons and Plisga, 2005):

- Capable of drilling soft, medium and hard rocks formations using nearly all type of rock bits,
- Relatively moderate flow rates and pressures are required to operate the PDM, and then most typical surface pumps can be used to operate these PDMs,
- Rotary speed of the PDM is directly proportional to flow rate. Torque is directly proportional to the pressure drop. Therefore, normal surface instruments can be used to monitor the operation of the PDM,
- High torques and low speeds are obtainable with certain PDM designs,
- PDMs can be also operated with aerated muds, foam and air mist.

The main disadvantages of the PDMs are (Lyons and Plisga, 2005):

- When the rotor shaft of the PDM is not rotating, the surface pump pressure will rise sharply and little fluid will pass through the motor,
- The elastomer of the stator can be damaged by high temperatures and some hydrocarbons,
- Short motor run life (especially in small diameter holes).

#### **Dump valve**

A crossover sub is used generally to connect the motor to the drill string. Optionally, a dump valve can be used instead of the crossover sub. The dump valve assembly enables filling and draining the drill string with drilling fluid from the annulus while tripping into the hole or out of the hole (Cavo, 2005). The valve uses a spring-loaded piston to close the ports separating the inside of the tool from the annulus. When drilling fluid is not circulating, this valve allows the fluid to enter or exit the drill string through the valve ports and bypass the motor. When the mud pumps are turned on and the circulating drilling fluid reaches the minimum velocity needed to overcome the spring force holding the piston in the up position, the dump valve is forced into the down, or closed-port, position. The fluid then flows through the motor, providing the power to turn the bit. The PDM does not permit fluid to flow through the motor unless the motor is rotating. Therefore, a dump valve plays an important role at the top of the motor allowing drilling fluid to be circulated to the annulus even if the motor is not rotating.

#### **Safety catch sub**

The safety catch sub is an optional PDM component that provides the ability to retrieve the motor components including the rotor and lower assembly in the case of a motor connection failure. It is generally used on a motor when tool joints are exposed to excessive loads from harsh drilling operations.

#### **Power section assembly**

The power section is the section of the motor that converts hydraulic power into mechanical power, resulting in bit rotation. The PDM power section (shown in Figure 2.7) consists of only two parts, the rotor and the stator. When assembled, these two components form continuous seal cavities along their contact points. The rotor is made of steel with a helical (multi-lobed) pattern, and is chromed plated to reduce friction, wear, and corrosion (Cavo, 2005). The stator is a length of tubular steel covered with an elastomer compound with a helical pattern to mate with the rotor. Various elastomers are available, depending on drilling-fluid type and bottom hole temperature (Cavo, 2005). It is the pattern of the lobes and the length of the helix that dictate what output performance will be developed by the power section. The stator always has one more lobe than the rotor (see Figure 2.7). Generally, more lobes yield higher torque and slower speed while fewer lobes yield higher speed and lower torque (PES, 2000; Cavo, 2005).

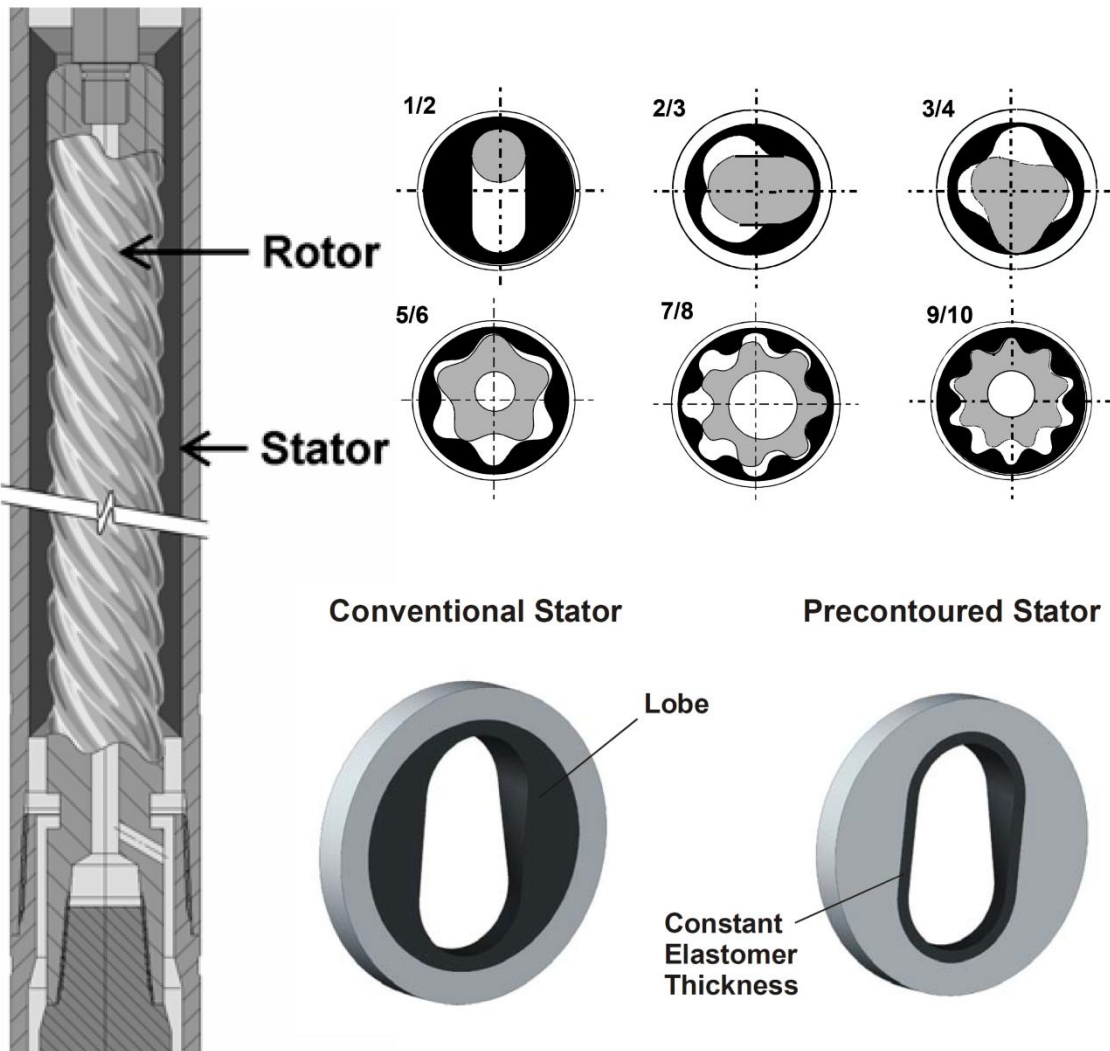


Figure 2.7 Power section assembly, Lobe configurations and conventional and pre-contoured stator cross section (after Cavo, 2005; Regener et al., 2005).

The second control on power section output characteristics is length. A stage is defined as a full helical rotation of the lobed stator. With more stages, the power section is capable of greater overall pressure differential, which in turn provides more torque to the rotor and the bit (Cavo, 2005).

With increased temperatures, or running with certain drilling fluids, the stator elastomer may expand and form a tighter seal between the stator and rotor and creates more of an interference fit, which may result in stator elastomer damage. Special stator materials or interference fit can be requested for these conditions (PES, 2000).

Positive displacement mud motors are more cost effective and show much better efficiencies, even at lower flow rates, but used to survive fewer hours on bottom and tended to fail at higher bottom hole temperatures (Regener et al., 2005). Current manufacturing technologies, especially the capability to manufacture pre-contoured stator tubes covered with a thin layer of elastomer, have helped to overcome the above

mentioned problems (see Figure 2.7). This allows the design of a stator with constant elastomer thickness resulting in benefits as described below. Power sections of the new design can provide much higher volumetric and mechanical efficiencies and therefore deliver substantial performance improvement. The torque output of a positive displacement down hole motor is proportional to the differential pressure across its power section. With conventional power sections the hydraulic forces start to deform the stator elastomer under increased differential pressure (Regener *et al.*, 2005).

#### **Coupling assembly**

There is an eccentric rotation of the rotor inside of the stator, due to the design nature of the PDM power section. To compensate for this eccentric motion and to convert it to a purely concentric rotation drilling motors, it needs a high strength coupling assembly (see Figure 2.8) attached to the lower end of the rotor and transmits motor rotational torque and speed to the drive shaft and bit (Cavo, 2005).

#### **Bearing assembly**

The bearing section of the PDM contains two types of bearings and bushings: thrust and radial (see Figure 2.8). They transfer the axial and radial loads from the bit to the drill string while providing power to rotate the bit. Drilling parameters, such as WOB, circulation rate, and bit pressure drop, directly affects the bearing assembly (Cavo, 2005). The thrust bearings support the downward force resulting from the WOB and the loads from the combination of hydraulic thrust and weight loads of internal motor components. Radial support bearings support the radial loads on the drive shaft (Cavo, 2005). The radial support bearings, usually located above the thrust bearings, ensure that the main drive shaft rotates about a fixed centre.

The bearing section may utilize sealed, oil filled, or mud lubricated bearings. With a sealed assembly the bearings are not subjected to drilling fluid and provide extended, reliable operation with minimal wear (PES, 2000). The mud lubricated bearings typically use tungsten carbide-coated sleeves to provide the radial support, and usually 4% to 10% of the drilling fluid is diverted pass this assembly to cool and lubricate the shaft, radial and thrust bearings (PES, 2000).

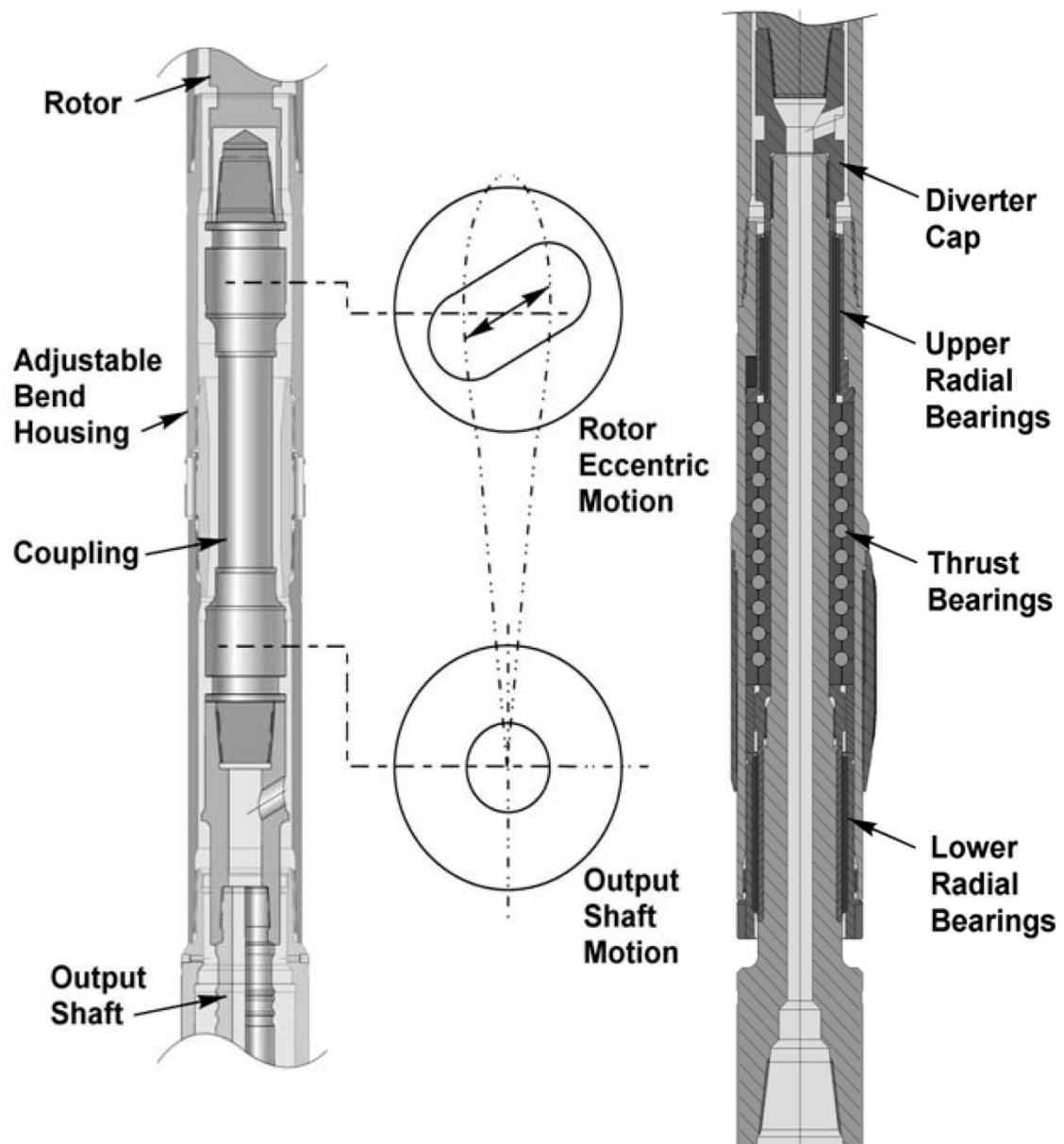


Figure 2.8 Coupling assembly in the left, bearing assembly in the right (after Cavo, 2005).

#### PDM operation

In the PDM, the rotor when assembled into the stator, provides continuous seal at contact points between the outside surface of the rotor and the inside surface of the stator. The rotor is made up of  $n_r$  lobes and the stator is made up of  $n_s$  lobes, which is equal to one lobe more than the rotor ( $n_s = n_r + 1$ ). As drilling fluid is pumped through the cavities in each chamber, the differential pressure of the flowing fluid causes the rotor to rotate within the stator. The main performance parameters of PDMs are: output power, torque, and pressure drop. Figure 2.9 gives the typical performance characteristics of a positive displacement motor. The example in this figure is for a 43 mm (1.69 in.) outside diameter PDM having 5 stages activated by three different flow rates of drilling mud.

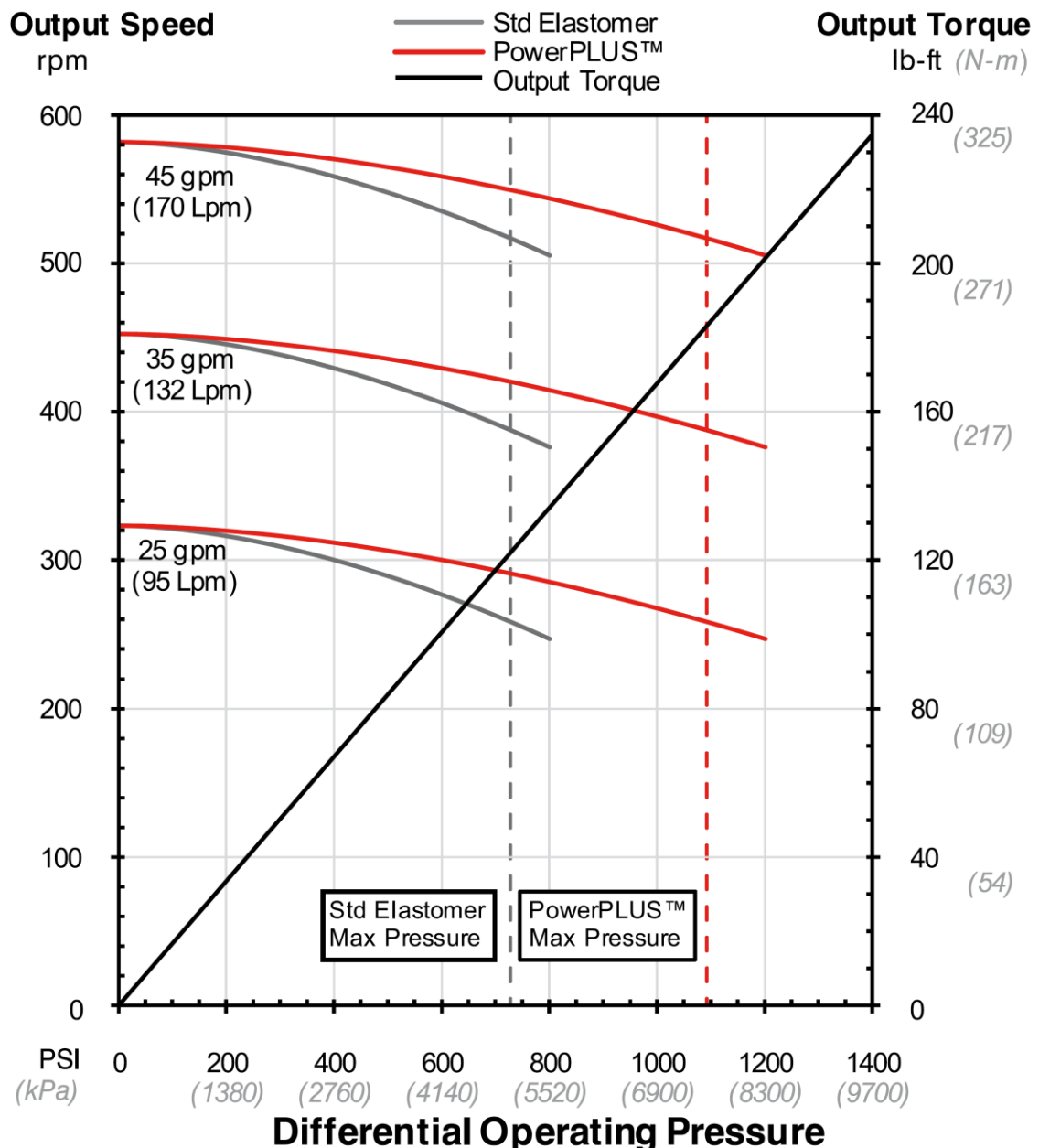


Figure 2.9 PDM performance curve, 43 mm (1.69 in.) outside diameter, 5/6 lobe profile, 5 stages (NOV, 2011).

The torque and the power of the PDM are both linear with the pressure drop across the motor. Therefore, as more weight is applied on the drill bit and the motor, the greater is the resisting torque of cutting the rock. The mud pumps can compensate for this increased torque by increasing the pressure on the constant flow rate through the motor. In this example the limit in pressure drop across the motor is about 5,019 KPa (728 psi) for standard elastomer and 7,529 KPa (1,092 psi) for PowerPLUS design. Beyond this limit there will be either extensive leakage or damage to the motor, or both. The amount of torque and power can be simply determined by the pressure change at the standpipe pressure gage at the surface between the unloaded condition and the loaded condition. If too much weight is placed on the motor, the differential pressure

limit for the motor will be reached and there will be leakage or a mechanical failure in the motor.

The rotor pitch is equivalent to the wavelength of the rotor. The rotor pitch  $t_r$  and the stator pitch  $t_s$  are equal. The rotor lead is the axial distance that a wave advances during one full revolution of the rotor. The rotor lead ( $L_r = n_r t_r$ ) and stator lead ( $L_s = n_s t_s$ ) are proportional to their respective number of waves. The specific displacement per revolution of the rotor is equal to the cross-sectional area of the fluid multiplied by the distance the mud advances. The specific displacement  $s$  is obtained from (Lyons and Plisga, 2005):

$$s = n_r n_s t_r A, \quad (2.1)$$

where,  $A$  is the fluid cross-sectional area which is approximately:

$$A \approx 2ne_r^2(n_r^2 - 1), \quad (2.2)$$

where  $e_r$  is the rotor rotation eccentricity. For instance in the special case of a 1:2 lobe profile, motor has a fluid cross-sectional area as following (Lyons and Plisga, 2005):

$$A \approx 2e_r d_r. \quad (2.3)$$

For the 1:2 lobe profile motor, the reference diameter is approximately equal to the diameter of the rotor shaft. The instantaneous torque of the positive displacement motor  $T$  in (ft-lb) is (Lyons and Plisga, 2005):

$$T = 0.133 s \Delta p \eta, \quad (2.4)$$

where:

$\Delta p$  = differential pressure loss through the motor in (psi),

$\eta$  = total efficiency of the motor.

The 1:2 lobe profile motors have efficiencies around 0.80. The higher lobe profile motors have efficiencies that are lower (i.e., of the order of 0.70 or less) (Lyons and Plisga, 2005). The instantaneous speed of the PDM,  $N$  (rpm) is (Lyons and Plisga, 2005):

$$N = \frac{231.016 q}{s}, \quad (2.5)$$

where  $q$  is the circulation flow rate (gal/min). The positive displacement motor power  $P$  (hp) for any speed is (Lyons and Plisga, 2005):

$$P = \frac{q \Delta p}{1714} \eta. \quad (2.6)$$

The number of positive displacement motor chambers  $n_c$  is obtained as (Lyons and Plisga, 2005):

$$n_c = \frac{L}{t_s} - (n_s - 1), \quad (2.7)$$

where  $L$  is the length of the actual motor section. The maximum torque  $T_{max}$  will be at the maximum differential pressure  $\Delta p_{max}$  which is obtained from (Lyons and Plisga, 2005):

$$T_{max} = 0.133 s \Delta p_{max} \eta. \quad (2.8)$$

The maximum power  $P_{max}$  will also be at the maximum differential pressure  $\Delta p_{max}$ , which is obtained from:

$$P_{max} = \frac{q \Delta p_{max}}{1714} \eta. \quad (2.9)$$

It should be noted that the PDM performance parameters are independent of the drilling mud weight. Thus, these performance parameters only will change with motor design values and the circulation flow rate. If the above performance parameters for a PDM design are known for a given circulation flow rate (denoted as 1), the performance parameters for the new circulation flow rate (denoted as 2) can be found by the following relationships (Lyons and Plisga, 2005):

Torque:

$$T_2 = T_1, \quad (2.10)$$

Speed:

$$N_2 = \left( \frac{q_2}{q_1} \right) N_1, \quad (2.11)$$

Power:

$$P_2 = \left( \frac{q_2}{q_1} \right) P_1. \quad (2.12)$$

### 2.5.3 Turbine down hole motor

Amongst the technical breakthroughs in the oil and gas drilling industry in the 1920s, a special place is held by an invention in 1922 of a single-stage down hole turbine motor (turbodrill) by the Russian engineer Matvey Kapelyushnikov. The first turbodrills adopted commercially and tested for drilling in the USSR were developed between 1923 and 1932. These single-stage turbines produced rotary speeds up to 3000 rpm and

above (Eskin and Maurer, 1997). In 1932-1934, P.P. Shumilov developed the major theory of multistage axial turbines (Eskin and Maurer, 1997), which was a major step forward in turbodrill construction. The Soviet Union continued the development of the down hole turbine motor and utilized the technology to drill the majority of its oil and gas wells. By the 1950s the Soviet Union was drilling nearly 80% of their wells with the down hole turbine motors (Lyons and Plisga, 2005).

In general, the down hole turbine motor (turbodrill) is composed of two sections: turbine motor section and bearing section i.e. thrust-bearing and radial support bearing (Eskin and Maurer, 1997). Figure 2.10 shows a typical turbodrill assembly and the fluid flow path through turbine stages. The turbine motor section has multistage of rotors and stators and plurality of rotor and stator vanes on each rotor and stator. Sometimes a special section is used at the top of the motor to provide a filter to clean up the drilling mud flow before it enters the motor, or to provide a by-pass valve. The lower end of the rotating shaft of the turbine motor section is attached to the upper end of the main shaft. The drilling fluid after passing through the turbine motor section is channelled into the centre of the shaft through large openings in the main shaft. The drill bit is attached to the lower end of the main shaft. The weight on the bit is transferred to the down hole turbine motor housing via the thrust-bearing section. This bearing section provides for rotation while transferring the weight on the bit to the down hole turbine motor housing (Lyons and Plisga, 2005). One of the most important developments in bearing technology has been the optimization of PDC thrust bearings that through diamond to diamond contact support the axial thrust and rotation created by the turbine blades (Radtke *et al.*, 2011). PDC bearings have many advantages, but having a very low coefficient of friction and a very long life are the main ones. Diamond-to-diamond interfaces, produce very little friction specially when lubricated by the drilling mud, and absorb axial thrust with very little energy lost in the process, causing higher overall tool efficiency (Radtke *et al.*, 2011). Water passing through the bearing section is intended to cool and lubricate the bearings. In addition, the flow-through bearing package may offer the advantage of longer service intervals.

Turbodrills may be used either as “direct drive” or with gear between the rotor and the shaft connected to the bit to reduce the rotation speed and increase the power and torque capability of the turbodrill. Turbodrills that have direct linkages between the rotor and the shaft are said to be “direct drive” turbodrills.

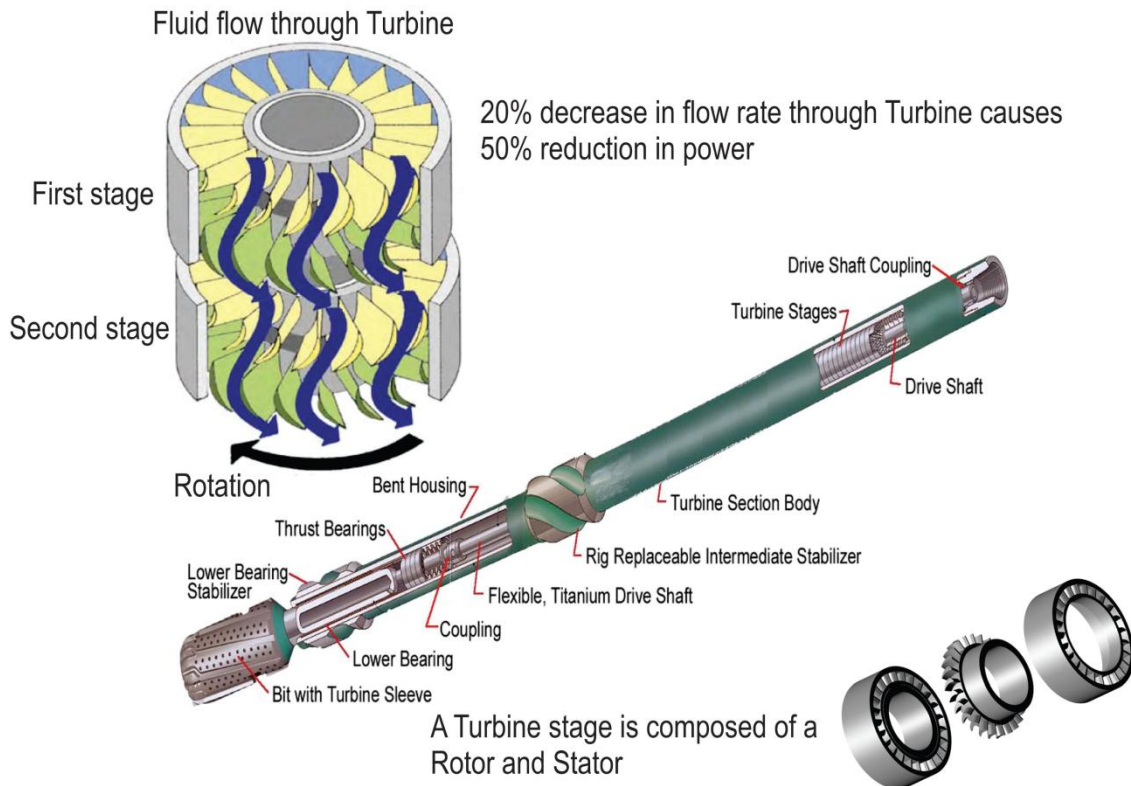


Figure 2.10 Turbodrill assembly and schematic fluid flow through turbine stages (after Beaton and Seale, 2004).

The activating drilling mud or water is pumped at high velocity through the motor section, which, because of the vane angle of each rotor and stator (one stage), causes the rotor to rotate the shaft of the motor which is connected to the bit. The energy required to change the rotational direction of the drilling fluid is transformed into rotational and axial (thrust) force. This energy transfer is seen as a pressure drop in the drilling fluid. The thrust is typically absorbed by thrust bearing. The rotational force causes the rotor to rotate relative to the housing. In practice, multiple stages are stacked coaxially until the desired power and torque is achieved.

The primary role of the stator is to swirl the drilling fluid prior to entering the rotor. The stator is rotationally fixed relative to the housing of the turbodrill and any rotational force generated is absorbed by the housing and is therefore wasted. The primary role of the rotor is to transform the energy of the drilling fluid into rotational energy for rotating the drill bit. This is achieved by changing the direction of the fluid flow. The force required to turn the fluid causes a reaction force on the rotor vanes resulting in turning the rotor row.

The main advantages of the turbodrills are (Lyons and Plisga, 2005):

- Capable of drilling hard to extremely hard rocks formations using impregnated diamond or polycrystalline diamond bits,

- Rather high rates of penetration can be achieved since bit rotation speeds are high,
- High reliability and long running Life,
- Extreme temperature capability,
- Reduced shock and vibration that cause smooth drilling and improve hole quality,
- Mud circulation regardless of motor condition. Circulation can even take place when the motor is stalled,
- Improved steerability with controllable tool face and high slide mode ROP.
- Lower reactive torque for improved directional control.

The main disadvantages of the turbodrills are (Lyons and Plisga, 2005):

- The high required flow rate and the resulting pressure drop through the motor require large surface pump systems,
- The rotation speed and/or torque cannot be measured using normal surface data (i.e., standpipe pressure, weight on bit), therefore a measure while drilling instrument should be used to ascertain whether the turbine motor is operating efficiently,
- Because of the necessity to use many stages in the turbine motor to obtain the needed power to drill, The down hole turbine motor is often quite long, because of the using many stages in the turbine motor to obtain the required power for drill bit,
- Down hole turbine motors are sensitive to the fouling agents in the mud; therefore, when running a turbine motor we should provide particle-free drilling mud.

#### **Down hole pneumatic turbine motor**

The internal energy of the air flow delivered by the surface compressors is changed to kinetic energy at the nozzle (stator row). As the high-velocity air flows through the rotor, the kinetic energy of the air stream is changed to kinetic energy of the rotor. A bypass valve assembly with an air filter can be located above the turbine to allow the air flow to be vented from the interior of the drill string to the annulus of the hole. By venting some of the air to the annulus, the turbine maximum rotary speed is reduced, preventing gearbox damage during operation with little or no WOB.

The down hole pneumatic turbine motors must be operated with a junk screen above the turbine section when drilling deep wells. This screen will catch any large particles of pipe scale or other foreign matter before they can lodge in the turbine stator and rotor.

### Turbodrill operation

The basic performance characteristics for a turbine motor ( $OD = 17.1\text{cm}$ ) are shown in Figure 2.11 for a constant flow rate. For a specific weight of 1.5 SG of the mud system the torque/speed relationship and the corresponding power output are shown by solid lines. To generate the optimum output mechanical power, the turbine motor has to be operated at the maximum efficiency which occurs at a bit speed of about 1,000 rpm. Operating the turbine at higher speed levels will increase the likelihood of early wear of the diamond bit and might damage the internal or external components of the turbine within a short period of time (Reich *et al.*, 2000).

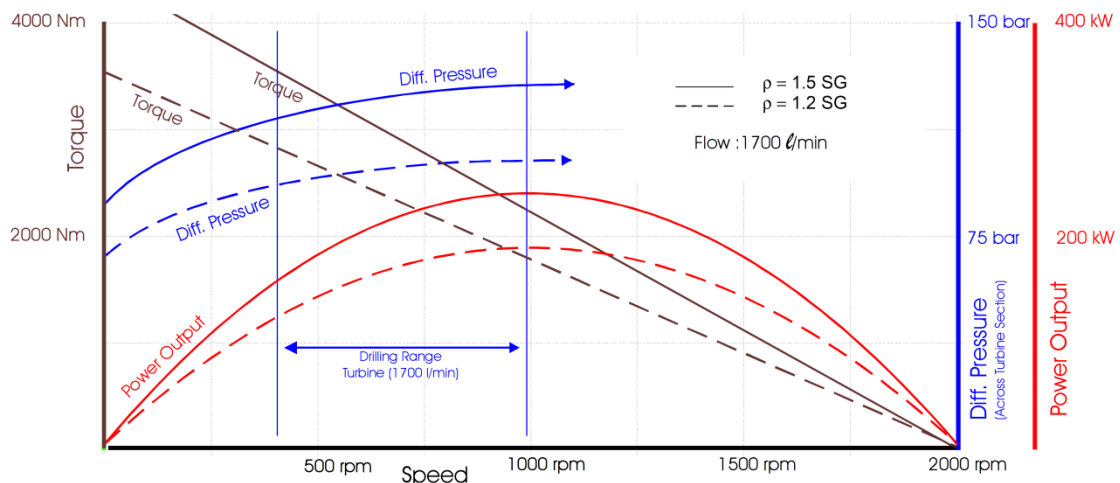


Figure 2.11 Turbine motor characteristics versus mud weight (Reich *et al.*, 2000).

The main operating parameters that dictate the size of the turbine motors are torque, speed, and mud weight (Sanchez *et al.*, 1996). Due to hydrodynamics function, the output power of a turbine motor is not linear with the mud flow rate and 20% decrease in the flow rate causes a 50% reduction in the turbine motor output power (Reich *et al.*, 2000). A turbine motor has the unique characteristic that it will allow mud circulation independent of what torque or power the motor is producing. If the turbine motor is lifted off the bottom of the borehole and mud circulation continues, the motor will speed up to the runaway speed. In this situation the motor produces no drilling torque or power. As the turbine motor is lowered and weight is placed on the motor and thus the bit, the motor begins to slow its speed and produce torque and power. When sufficient weight has been applied on the turbine motor, the motor will produce its maximum possible power. If more weight is added to the turbine motor and the bit, the motor speed and output power will continue to decrease and torque continuously will increase till the motor cease to rotate and the motor is described as being stalled. At this

condition, the turbine motor produces its maximum possible torque (Lyons and Plisga, 2005). Even when the motor is stalled, the drilling mud is still circulating.

It is almost impossible to determine formulae for turbine motors under working conditions (Eskin and Maurer, 1997). Laboratory experiments using drilling dynamometer test stand have to be conducted to determine nominal data on turbodrills. If the performance parameters for a turbine motor design are known for a given circulation flow rate and mud weight, the performance parameters for other circulation flow rate and mud weight can be found by the following mathematical relationships (Eskin and Maurer, 1997):

$$N \propto Q; T \propto Q^2; \Delta p \propto Q^2; P \propto Q^3; \eta \propto \frac{1}{Q}, \quad (2.13)$$

$$N \propto \frac{1}{\rho}; T \propto \rho; \Delta p \propto \rho; P \propto \rho; \eta \propto \frac{1}{\rho}, \quad (2.14)$$

where:

$N$  = Turbodrill output rotation speed (revolution per minute),

$\rho$  = Drilling fluid (mud) density,

$P$  = Turbodrill output power,

$T$  = Turbodrill output Torque,

$Q$  = Flow rate,

$\Delta p$  = Turbodrill differential pressure,

$\eta$  = Turbodrill efficiency.

Some turbodrill performance parameters are described as following (Lyons and Plisga, 2005):

The stall torque  $T_s$  (ft-lb) for any turbine motor can be determined from:

$$T_s = 1.38386 \times 10^{-5} \frac{\eta_h \eta_m n_s \bar{\gamma}_m q^2 \tan \beta}{h}, \quad (2.15)$$

where:

$\eta_h$  = Hydraulic efficiency,

$\eta_m$  = Mechanical efficiency,

$n_s$  = Number of stages,

$\bar{\gamma}_m$  = Specific weight of mud in lb/gal,

$q$  = Circulation flow rate in gal/min,

$\beta$  = Exit blade angle in degrees,

$h$  = Radial width of the blades in inch.

The runaway speed  $N_r$  (rpm) for any turbine motor can be determined from:

$$N_r = 5.85 \frac{\eta_v q \tan \beta}{r_m^2 h}, \quad (2.16)$$

where:

$\eta_v$  = Volumetric efficiency,

$r_m$  = Mean blade radius in inch,

Depending on the skills of the turbodrill operator the speed may vary from zero rpm to the runaway speed. The turbine motor instantaneous torque  $T$  (N.m) for any rotation speed  $N$  (rpm) is obtained as:

$$T = T_s \left( 1 - \frac{N}{N_r} \right), \quad (2.17)$$

where:

$T_s$  = Stalled torque (maximum torque),

$N_r$  = Runaway rotation speed (maximum speed).

The turbine motor horsepower  $P$  (hp) for any speed is obtained from:

$$P = \frac{2\pi T_s N}{33,000} \left( 1 - \frac{N}{N_r} \right). \quad (2.18)$$

The maximum turbine motor power is at the optimum speed,  $N_o$ , which is one-half of the runaway speed. This is:

$$N_o = \frac{N_r}{2}. \quad (2.19)$$

The torque at the optimum speed  $T_o$  is one-half the stall torque. Thus:

$$T_o = \frac{T_s}{2}. \quad (2.20)$$

The pressure drop  $\Delta p$  (psi) through a given turbine motor design is usually obtained empirically. Once this value is known for a circulation flow rate and mud weight, the pressure drop for other circulation flow rates and mud weights can be estimated. If the above performance parameters for a turbine motor design are known for a given circulation flow rate and mud weight (denoted as 1), the performance parameters for the new circulation flow rate and mud weight (denoted as 2) can be found by the following relationships (Lyons and Plisga, 2005):

Torque:

$$T_2 = \left( \frac{q_2}{q_1} \right)^2 T_1, \quad (2.21)$$

$$T_2 = \left( \frac{\bar{\gamma}_2}{\bar{\gamma}_1} \right) T_1, \quad (2.22)$$

Speed:

$$N_2 = \left( \frac{q_2}{q_1} \right) N_1, \quad (2.23)$$

Power:

$$P_2 = \left( \frac{q_2}{q_1} \right)^3 P_1, \quad (2.24)$$

$$P_2 = \left( \frac{\bar{\gamma}_2}{\bar{\gamma}_1} \right) P_1, \quad (2.25)$$

Pressure drop:

$$\Delta p_2 = \left( \frac{q_2}{q_1} \right)^2 \Delta p_1, \quad (2.26)$$

$$\Delta p_2 = \left( \frac{\bar{\gamma}_2}{\bar{\gamma}_1} \right) \Delta p_1. \quad (2.27)$$

## 2.6 Motor selection for hard rocks small CT drilling

There are many special criteria that are associated with the successful implementation of down hole motors with CT operations. Since we cannot apply much of WOB in CT hard rocks drilling, therefore the best way to increase the ROP is that a system of very low depth of cut (DOC) and high rotation speed should be adopted for small size hard rocks mineral exploration drilling. In this application a very low depth of cut impregnated diamond bit with depth of cut of around 0.01-0.1 (mm/rev.) should be adapted in such a way that survive under high temperature caused by bit rock interactions on the bit face. For selecting a motor type to be fit for the small hole size (<= 76 mm (3 in)), their specifications should satisfy the whole drilling system. Electric motors need a high capacity (3 phase) and reliable electrical link (wireline) to the

bottom hole. This may happen in 2 ways with the CT assembly. The first way is to pass the wireline inside the tube itself that in this case further hydraulic and insulation problems will arise. Because of reducing the flow area inside the tube caused by the wireline, especially due to small diameter CT, the pressure drop through the tube will increase significantly. In the second way, the electric link should be embedded inside the body of the tube itself and in this way we actually trying not to block the area for the fluid flow inside the tube. This way could be possible with composite or carbon fibre tube, which up to now their capacity for mechanical stability and their operational feasibility has not been studied yet in this project and another project in parallel for DET CRC, is in progress now trying to find the best material for CT tube in which capable of including electric wires and sensors while maintain the mechanical properties required for the harsh drilling environments. Therefore at this stage, the choice of electric motors is neglected and tries to find most appropriate one between hydraulic motor types. In the following section two main types of hydraulic motor are compared with each other to identify which type is the most appropriate one for the proposed conditions.

### 2.6.1 Turbodrill versus PDM

In general, turbodrills are capable of more than double the RPM of the highest speed PDMs available on the market. In addition to the increased RPM potential, turbodrills are also capable of much higher torque for a given RPM than a PDM. Turbodrills are capable of sustaining very high pressures because the mechanism of converting hydraulic power to mechanical power in a turbodrill is done entirely with metallic components, therefore they are much more powerful drilling tools than PDMs and having no elastomers in their system, the turbodrill is also well suited for performing in high temperature environments (Beaton and Seale, 2004). In considering the fact that high RPM is beneficial to increased ROP for CT applications, turbodrills are actually capable of much higher output torque when operating at high RPM than are PDMs (Beaton and Seale, 2004). The concentric design of the turbodrill power shaft also makes for efficient use with CT that because of reducing vibration, so there is little energy lost in the system (Beaton and Seale, 2004).

In addition to the smooth running nature of a turbodrill as a result of high RPM and low DOC, the design of the turbodrill itself also tends to very smooth torque response, and with a turbodrill, stalling is not an issue. It just means that the hydraulic energy by

the mud isn't high enough to produce the torque required at that moment, so the tool stops rotating. In comparison, the practice of stalling with PDM is actually very severe on the motor and BHA, and creates a very sizeable pressure spike in the system which can lead to the damage of other components associated with the drilling job (Beaton and Seale, 2004).

PDMs are more cost effective and show much better efficiencies, even at lower flow rates, but used to survive fewer hours on bottom and tended to fail at higher bottom hole temperatures. A PDM has multi-chambers, however, the number of chambers in a positive displacement motor is much less than the number of stages in a turbine motor. A typical positive displacement motor has from two to seven chambers. Therefore the overall length of PDMs is generally less than the turbodrills.

Having no elastomers in the system, the turbodrill is also well suited for performing in high temperature environments, where other down hole motors frequently fail. The concentric design of the turbodrill power shaft also makes it more efficient for use with CT. When drilling or milling, the turbodrill has little vibration, so there is little lost energy in the system (Maurer *et al.*, 1977; DeLucia and Herbert, 1984; Reich *et al.*, 2000; Beaton and Seale, 2004; RIO, 2004; Regener *et al.*, 2005; Seale and Conroy, 2005; Langille *et al.*, 2009; Mushovic *et al.*, 2009; Barton *et al.*, 2011).

## **2.7 Coiled Tube Turbodrilling system**

According to the comparison made between the turbine down hole motor and PDM in previous section, in summary, since RPM is such a significant factor in promoting good ROP in areas where weight transfer to the bit is difficult, as in CT drilling, and also the preference in this application for a low weight on bit (very low depth of cut) and high rotation speed resulting at high quality hole, therefore the turbodrill is an excellent tool and proposed here for the long term objective of DET CRC for deep hard rocks CT drilling.

Extending the applicability of turbodrilling to coiled tubing in petroleum drilling operations, several new turbodrill designs and modifications are currently underway. One of the most significant developments in progress is the creation of a turbodrill that is much shorter than existing designs in order to enhance compatibility with CT equipment. Other developments currently underway to improve compatibility with CT drilling applications include specially designed turbine blades for these applications. These blades are being designed to maximize power output in the shortest possible tool

configurations (Beaton and Seale, 2004; Seale *et al.*, 2004; Grigor *et al.*, 2008; Radtke *et al.*, 2011).

In the latest effort to optimise a high power turbodrill for CT operation for petroleum drilling applications, Technology International, Inc. submitted the final report of a project for United States Department of Energy and National Energy Technology Laboratory entitled as “High-Power Turbodrill and Drill Bit for Drilling with Coiled Tubing” at 2011 (Radtke *et al.*, 2011). This project teamed Schlumberger® Smith Neyrfor and Smith Bits, and NASA AMES Research Center with Technology International, Inc (TII), to deliver a down hole, hydraulically-driven turbine motor (with OD = 73 mm or 2-7/8 in.), matched with a custom drill bit designed to drill 10.5 cm (4-1/8 in.) boreholes with a purpose-built coiled tubing rig. The new optimised high power turbodrill is shorter, delivers power more efficiently, operates at relatively high RPM, and requires low weight on bit. NASA AMES Laboratory was contracted to increase the hydraulic efficiency of the existing Smith Neyrfor baseline SII MK2 turbine blades. The only outcome published and released is this statement that, “NASA blade design ultimately improved Smith Neyrfor commercial turbodrill efficiency (which is 50%) by approximately 13% increase in each stage power and increase the overall turbodrill power by 29%”. Figure 2.12 shows the only published Computational Fluid Dynamics results for this design that even shows separation and inefficiencies in the trailing edge of the blade. Also flow tests run by Smith Neyrfor proved the improved efficiency of the NASA designed blades. In this project two turbodrill prototype (OD = 73 mm) were manufactured by Smith Neyrfor, one with a new Heat™ turbine blade design by Smith Neyrfor using conventional physical hydraulic models and the second one with NASA designed turbine blades designed by NASA AMES using CFD analysis and response surface methodology for the first time to petroleum down hole turbodrills. Both were considered improved blade designs for increased efficiency. The free-wheeling blade speeds (run-away speed) were as much as 4,000 RPM (Radtke *et al.*, 2011). As part of this project, Cutter temperatures and wear rates as well as overall bit performance parameters were estimated with a thermally stable diamond (TSP) bit (OD = 10.5 cm) for rotary speeds up to 2,000 RPM in order to simulate drilling with the improved turbodrill. Thermal modelling of the TSP cutters (OD = 10.5 or 4-1/8 in) revealed that they are able to be rotated at speeds of 2,000 to 4,000 rpm without excessive wear, due to their high thermal conductivity (Radtke *et al.*, 2011). Figure 2.13 shows the turbodrill performance with the NASA blades with the PDC cutter drill bit.

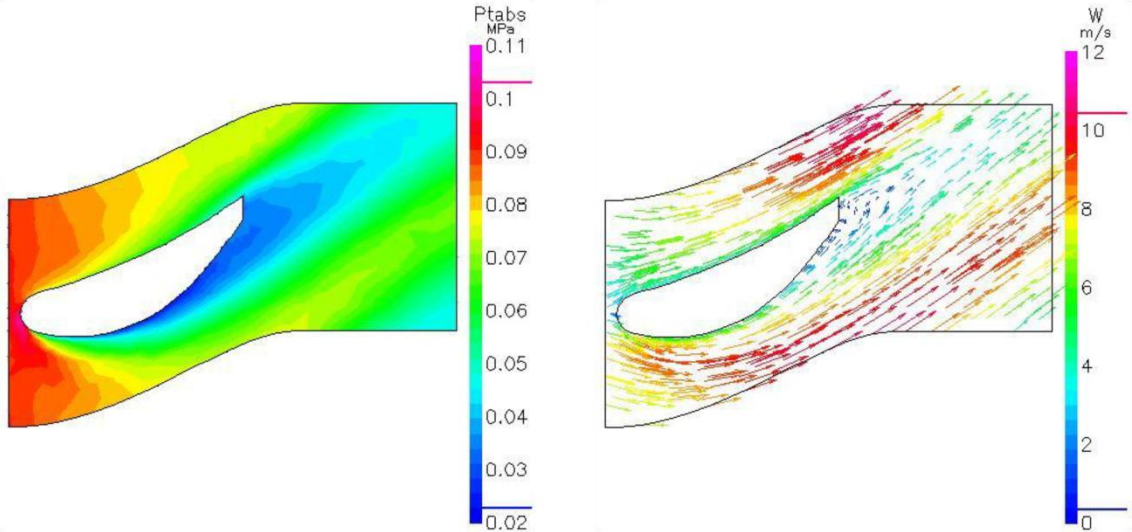


Figure 2.12 The only published computational fluid dynamics result for NASA blades turbodrill design (Radtke et al., 2011).

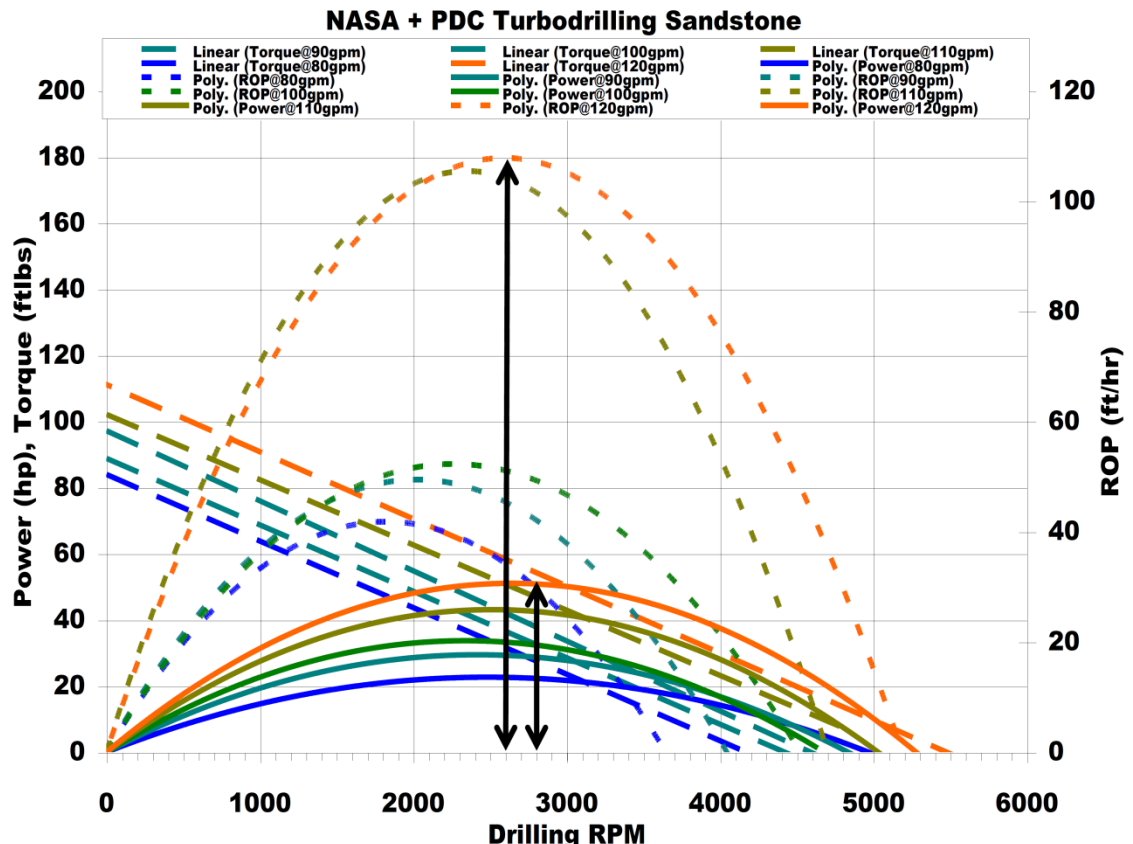


Figure 2.13 Turbodrill performance from lab experiments with the NASA blades with the PDC cutter drill (Radtke et al., 2011).

Currently there is no small size turbodrill ( $< 7$  cm) available in the market suitable for small borehole mineral exploration drilling and the smallest size turbodrill available in the market is 73 mm (2-7/8 in.) by Schlumberger® (Neyfor). It is optimised for petroleum drilling applications and their optimum speed is between 1,000-2,000 rpm. As a result, for the application of this study, design and manufacturing of a smaller size turbodrill optimised for higher optimum rotation speed ( $N > 2,000$  rpm) is a needed

development in this area. The main objective of this study is designing a small turbodrill specifically optimised for coiled tubing drilling deep hard rocks mineral exploration based on both fluid flow analyses and structural analyses. In the design methodology presented in this study, CFD code is used at the first stage to optimise the fluid flow performance through turbodrill and then Fluid-Structural Interaction (FSI) analyses are used to calculate the amount of the mechanical stresses and deformations caused by the fluid flow and interactions with the blades.

## **2.8 Summary**

The first part of this Chapter presented the differences between petroleum drilling and hard rocks mineral exploration drilling. Small size coiled tubing drilling was proposed for application of this study. The possible adoptions to the coiled tubing assembly were proposed transferring from current applications in petroleum industry to deep hard rocks mineral exploration. The various types of down hole motors were discussed and turbine down hole motor (turbodrill) was proposed as the most appropriate down hole rotary drive mechanism for small size and low weight on bit CT drilling. In the next Chapter, turbodrill design process and the models for this study will be presented.

# 3

## Turbodrill design and specifications

In the previous Chapter, potential adoptions to the coiled tubing (CT) drilling assembly from existing drilling practices in petroleum industry to deep hard rocks mineral exploration applications were discussed. In particular, turbodrill was proposed as the preferred down hole rotary drive mechanism for applications of this study. In this Chapter, using the bit-rock interaction laws the calculations of required down hole power for drilling into a typical hard rock formation are presented. This is followed by discussing turbodrill manufacturing material. Finally, based on down hole power and speed requirements for small size CT drilling for deep hard rocks mineral exploration, several small diameter turbodrill stage models are designed.

### 3.1 Power requirements for hard rocks drilling

Efficient drilling of hard rocks requires a comprehensive knowledge of the energy spent at the bit. The bit-rock interface and interaction laws determine the amount of the mechanical power that an impregnated diamond bit requires for efficient drilling and delivering the desired range of ROP. In a model of the drilling response for drag bits, a set of relations between the WOB ( $W$ ), the torque-on-bit, TOB ( $T$ ), the ROP ( $V$ ), and the angular velocity ( $\Omega$ ) characterize the bit-rock interactions (Detournay and Defourny, 1992; Detournay *et al.*, 2008). This model proposes three successive regimes in the drilling response of the bit. Phase I, at low DOC per revolution, is identified by dominance of the frictional contact process and by an increase in the contact forces with the DOC ( $d$ ). Phase II refers to the regime where the contact forces are fully mobilized and the desired range of DOC are achieved. In phase III, the actual contact length increases, due to poor cleaning or excessive DOC. The drilling response model for a typical mode consists of a set of relationships between  $W$ ,  $T$ ,  $V$ , and  $\Omega$ . In this method, The rate-independent bit-rock interface laws is expressed in terms of dynamic quantities, a scaled weight  $w$  and torque  $t$ , and on the DOC per revolution,  $d$ , which is proportional to the velocity ratio  $V/\Omega$ . These three basic state variables are defined as:

$$w = \frac{W}{a}, \quad (3.1)$$

$$t = \frac{2T}{a^2}, \quad (3.2)$$

$$d = \frac{2\pi V}{\Omega}, \quad (3.3)$$

where  $a$  is the bit radius. Scaling of the weight and torque removes the influence of the bit dimension from the interface laws. The scaled quantities  $w$  and  $t$ , which have dimensions of force/length (a convenient unit is the N.mm<sup>-1</sup>), can conveniently be interpreted as the normal and shear forces per unit length on a two-dimensional cutter removing material over a DOC ( $d$ ). Figure 3.1 shows a conceptual drilling response characterized by three distinct phases as explained before in the plot of  $w$  and  $t$  versus  $d$ . The extent of phase I ( $d_*$ ) is controlled by the tool state of wear ( $d_* = d_*(l)$ ) in which  $l$  is the length of wear contact, and various experimental results suggest that ( $l/20 < d_* < l$ ). In phase 2, where the desired range of DOC is achieved, the rubbing force is assumed constant and the governing equations for this phase are:

$$w = \zeta \varepsilon d + \sigma l, \quad (3.4)$$

$$t = \varepsilon d + \mu \gamma \sigma l, \quad (3.5)$$

Where  $\varepsilon$  is the intrinsic specific energy (the minimum amount of energy required to remove a unit volume of rock). The information provided here for the bit-rock interaction are taken from the internal reports to DET CRC submitted by CSIRO (Commonwealth Scientific and Industrial Research Organisation). For impregnated bits  $\varepsilon$  is assumed to be  $5q$ , where  $q$  is the rock uniaxial compressive strength. Also  $\zeta$  is a number that characterises the inclination of the cutting or fragmenting force, which usually for impregnated bits is assumed to be 3-4, and here is assumed to be 4. Here,  $\sigma$  is the contact stress, which is equivalent to  $q$ . In this equation  $\mu$  is the friction coefficient, which for impregnated bits it is assumed to be in the range of 0.05-0.2. Also,  $\gamma$  is the bit number, which for the sake of simplicity, it is assumed to be 1.

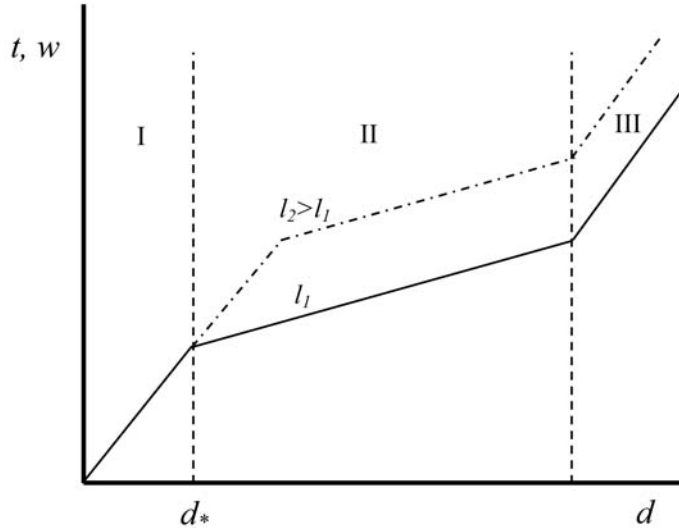


Figure 3.1 Conceptual drilling response of the bit-rock interaction (after Detournay and Defourny, 1992; Detournay *et al.*, 2008).

For full bit face CT drilling in hard rocks, it is preferred to design the drilling system for high optimum rotation speeds (i.e.  $N > 2,000$  rpm) and very low DOCs in the range of 0.01-0.1 mm/rev. For calculation purposes we assume  $ROP \approx 10$  m/hr at an optimum rotation speed of  $N \cong 4,000$  rpm (418.9 rad/s). This results in a DOC of:

$$d\left(\frac{mm}{rev}\right) = \frac{ROP\left(\frac{m}{hr}\right) \times 16.7}{N(rpm)} = \frac{10 \times 16.7}{4000} = 0.042 \frac{mm}{rev}.$$

To be on the conservative side, for a typical hard rock ( $UCS \approx 200$  MPa), the range of parameters mentioned above and assuming  $l \approx 0.1$  mm, the scaled weight and torque is considered to be:

$$w \approx 200\left(\frac{N}{mm}\right); t \approx 50\left(\frac{N}{mm}\right).$$

Here, if the bit radius ( $a$ ) assumed to be 30 mm, therefor WOB ( $W$ ) and torque ( $T$ ) are calculated as:

$$w = \frac{W}{a} \Rightarrow WOB = 200 \times 30 = 6 KN,$$

$$t = \frac{2T}{a^2} \Rightarrow T = \frac{50 \times (30)^2}{2} = 22.5 N.m.$$

And if the bit radius ( $a$ ) assumed to be 35 mm, therefor WOB ( $W$ ) and torque ( $T$ ) are calculated as:

$$w = \frac{W}{a} \Rightarrow WOB = 200 \times 35 = 7 KN,$$

$$t = \frac{2T}{a^2} \Rightarrow T = \frac{50 \times (35)^2}{2} = 30.6 \text{ N.m.}$$

It is assumed here that the cutting processes are not intrinsically affected by down hole condition in particular the down hole mud pressure. In this way, the angular power  $P$  at the bit required to drill is simply given by:

$$P = T\Omega, \quad (3.6)$$

where,  $\Omega$  is the bit angular velocity (expressed in rad.s<sup>-1</sup>). This equation can be written in the following form, (Bourgoyn *et al.*, 1986):

$$P_m (\text{KW}) = \frac{T(\text{N.m}) \times N(\text{rpm})}{9,550}. \quad (3.7)$$

If the optimum rotation speed is assumed to be  $N \cong 4,000$  (rpm), then:

If  $a = 30 \text{ mm}$ ,

$$P_m = \frac{22.5 \times 4,000}{9,550} = 9.4 \text{ KW (12.6 hp)}.$$

If  $a = 35 \text{ mm}$ ,

$$P_m = \frac{30.6 \times 4,000}{9,550} = 12.8 \text{ KW (17.2 hp)}.$$

The down hole motor output power should be adequate to provide the required power by the bit. This is to say that:

$$P_{hyd} \geq P_m, \quad (3.8)$$

The hydraulic power generated by turbodrill ( $P_{hyd}$ ) is calculated as:

$$P_{hyd} (\text{hp}) = \frac{Q(\text{gpm}) \times \Delta P(\text{psi})}{1714} \times \eta_m = P_t \times \eta_m, \quad (3.9)$$

Where,  $Q$  is the flow rate,  $\Delta P$  is the pressure drop across the turbine motor,  $P_t$  is the net generated power by the turbine motor section by fluid flow and  $\eta_m$  is the turbodrill efficiency, which is usually considered 0.5-0.6 (Eskin and Maurer, 1997). Here, we use  $\eta_m=0.6$  for power estimation generated by turbine down hole motor section ( $P_t$ ) as following:

If  $a = 30 \text{ mm}$ ,

$$P_t = \frac{P_m}{\eta_m} = \frac{9.4(\text{KW})}{0.6} = 15.7 \text{ KW}.$$

If  $a = 35$  mm,

$$P_t = \frac{P_m}{\eta_m} = \frac{12.8(KW)}{0.6} = 21.3KW,$$

and if the mud flow rate for the current application is considered to be 4 L/s ( $Q = 63.4$  gpm). This would lead to the turbodrill pressure drop ( $\Delta P$ ) of:

If  $a = 30$  mm,

$$12.6 \text{ hp} = \frac{63.4 \times \Delta P}{1714} \times 0.6 \Rightarrow \Delta P = 568 \text{ psi (39.2 bar)}.$$

If  $a = 35$  mm,

$$17.2 \text{ hp} = \frac{63.4 \times \Delta P}{1714} \times 0.6 \Rightarrow \Delta P = 775 \text{ psi (53.4 bar)}.$$

### 3.2 Turbodrill as an axial Turbomachine

All the devices in which energy is transferred either to, or from, a continuously flowing fluid by the dynamic action of one or more moving blade rows, are called turbomachines (Dixon and hall, 2010). In these machines, the stagnation enthalpy of the fluid changes by the rotating blade row (rotor) and this enthalpy changes are linked with the pressure changes occurring in the fluid. Two principal categories of turbomachine are identified: firstly, those that absorb power to increase the fluid pressure or head (fans, compressors, and pumps); secondly, those that produce power by expanding fluid to a lower pressure or head (wind, hydraulic, steam, and gas turbines) (Dixon and hall, 2010). Turbomachines are also categorised based on the nature of the flow path through them. When the path of the through-flow is mainly parallel to the axis of rotation, the device is termed an axial flow turbomachine. When the path of the through-flow is mainly in a plane perpendicular to the rotation axis, the device is termed a radial flow turbomachine, and when the direction of the through-flow has both radial and axial velocity components in significant amounts, the device is termed a mixed flow turbomachine (Dixon and hall, 2010). As a result, because the path of the through-flow is mainly parallel to the axis of rotation of the turbodrill, it is belong to the axial flow turbomachine category and all the rules in this category are applied to the design of a turbodrill. Methods of analysing the flow processes differ depending upon the geometrical configuration of the machine and whether the fluid can be regarded as incompressible or not.

### 3.2.1 Efficiency of Turbodrill

Turbodrills are designed to convert the available energy in the flowing fluid into useful mechanical work delivered at the coupling of the shaft. Therefore, the overall efficiency  $\eta_0$ , is defined as (Dixon and hall, 2010):

$$\eta_0 = \frac{\text{mechanical energy available at coupling of output shaft in unit time}}{\text{maximum energy difference possible for the fluid in unit time}}. \quad (3.10)$$

Mechanical energy losses occur between the turbodrill rotor and the shaft coupling as a result of the work done against friction at the bearings. The magnitude of this loss as a fraction of the total energy transferred to the rotor is difficult to estimate as it varies with the size and design of turbomachine. For small machines (several kilowatts) it may reach to 5% or more, but for medium and large machines this loss ratio may become as little as 1% (Dixon and hall, 2010). The isentropic efficiency  $\eta_t$  or hydraulic efficiency  $\eta_h$  for a turbine is (Dixon and hall, 2010):

$$\begin{aligned} \eta_t (\text{or } \eta_h) &= \frac{\text{mechanical energy supplied to the rotor in unit time}}{\text{maximum energy difference possible for the fluid in unit time}} \\ \eta_t (\text{or } \eta_h) &= \frac{\text{actual work}}{\text{ideal (maximum) work}} = \frac{\Delta W_t}{\Delta W_{\max}} \end{aligned} \quad (3.11)$$

For turbodrill using the definition of the stagnation enthalpy, the actual work can be determined as:

$$\Delta W_t = \frac{\dot{W}_t}{\dot{m}} = (h_{01} - h_{02}). \quad (3.12)$$

The ideal work is a bit complicated to determine depending on how the ideal process is defined. The steady flow energy equation can be written in differential form for an adiabatic turbodrill as:

$$d\dot{W}_t = \dot{m} \left[ dh + \frac{1}{2} d(c^2) + gdz \right]. \quad (3.13)$$

For an isentropic process,  $Tds = 0 = dh - dp/\rho$ . The maximum work output is therefore:

$$\dot{W}_{\max} = \dot{m} \left[ \int_1^2 \frac{1}{\rho} dp + \frac{1}{2} (c_1^2 - c_2^2) + g(z_1 - z_2) \right]. \quad (3.14)$$

For an incompressible fluid, the maximum work output is:

$$\dot{W}_{\max} = \dot{m} \left[ \frac{1}{\rho} (p_1 - p_2) + \frac{1}{2} (c_1^2 - c_2^2) + g(z_1 - z_2) \right] = \dot{m}g(H_1 - H_2), \quad (3.15)$$

where,  $gH = p/\rho + \frac{1}{2}c^2 + gz$  and  $\dot{m} = \rho Q$ . Finally it can be obtained as:

$$\eta_t (\text{or } \eta_h) = \frac{\dot{W}_t}{\dot{W}_{\max}} = \frac{\Delta W_t}{g[H_1 - H_2]} = \frac{\Delta h_0}{g \Delta H}. \quad (3.16)$$

If each small stage has the same efficiency, then the isentropic efficiency of the whole machine may be different from the small stage efficiency, the difference depends upon the pressure ratio of the machine (Dixon and hall, 2010). The turbodrill is divided into a large number of small stages of equal efficiency. Figure 3.2 shows the “Overall” isentropic efficiencies have been calculated for a range of pressure ratios and polytropic efficiencies. It shows that overall isentropic efficiency exceeds small stage efficiency with increasing the pressure ratio. Because in this study the pressure ratio for each stage is very close to 1, then the overall isentropic efficiency is assumed to be equal to small stage efficiency.

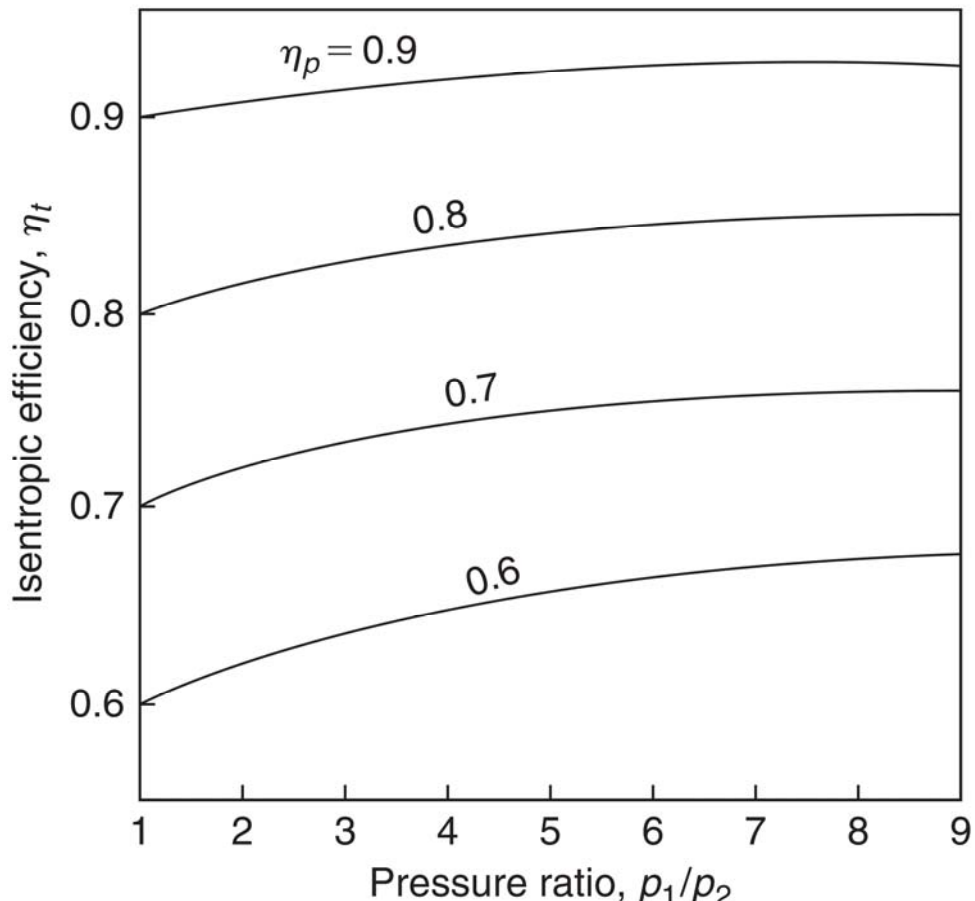


Figure 3.2 Turbine Isentropic efficiency against pressure ratio for various polytropic efficiencies ( $\gamma = 1.4$ ) (Dixon and hall, 2010).

For more general information for hydraulic turbine efficiencies and workflow, a good reference is a book by Dixon and hall (2010) named as “Fluid Mechanics and Thermodynamics of Turbomachinery”, especially refer to chapter 4 and chapter 6.

### **3.3 Turbodrill material**

Generally, stainless steel is used for manufacturing of turbodrill stages. There is a large variety of stainless steel available in the market. For instance for a Geothermal drilling project (Maurer Engineering Inc., 2000), the stators and rotors of the turbodrill were made from 17-4 PH (Precipitation Hardening) stainless steel. The 17-4 Precipitation Hardening also known as type 630 is a chromium-copper precipitation hardening stainless steel used for applications requiring high strength and a moderate level of corrosion resistance. In this case, high strength is maintained to approximately 316 degrees Celsius (600 degrees Fahrenheit). Their mechanical properties can be optimized with heat treatment and very high yield strength up to 1,100-1,300 MPa can be achieved.

Stainless steel does not corrode, rust or stain with water as ordinary steel does. Stainless steel is used where both the properties of steel and resistance to corrosion are required. Stainless steel differs from carbon steel by the amount of chromium present. Stainless steels contain sufficient chromium to form a passive film of chromium oxide, which prevents further surface corrosion and blocks corrosion from spreading into the metal's internal structure.

There are different types of stainless steels. The traditional AISI (American Iron and Steel Institute) numbering system categorizes stainless steels into 300, 400 etc. series, such as type 304, and type 430 etc. The newer UNS (Unified Numbering System) uses numbers of the form S30400 and S43000 for these same grades.

The basic and simplest composition of stainless steel is iron (Fe) and chromium (Cr), which is known as the ferritic stainless steels because their crystal structure is called ferrite. The ferritic stainless steels are magnetic like ordinary steel, least expensive but can be more difficult to form and weld. A commonly used grade is type 430 (S43000). For greater hardness and strength, more carbon is added. When nickel is added, the austenite structure of iron is stabilized. This crystal structure makes the steels virtually non-magnetic and less brittle at low temperatures. Austenitic stainless steels are ductile, tough, easy to form and weld, and are not magnetic in the annealed condition. The most common example is type 304 (S30400) or the most widely used

stainless steel in the world. Manganese preserves an austenitic structure in the steel, similar to nickel, but at a lower cost. Molybdenum (Mo) is added to some stainless steels to increase their corrosion resistance, particularly in marine and acidic environments.

Halfway between the ferritic and austenitic stainless steels is a family called the duplex stainless steels, which are about 50% ferrite and 50% austenite. Because of this duplex structure, they are resistant to stress corrosion cracking, this can affect the austenitic stainless steels in hot waters containing chlorides. The most common duplex stainless steel is 2205 and it is used in many applications such as hot water tanks.

The precipitation hardening stainless steels is a specialised family which has very high strength achieved by adding elements such as copper, which form very fine particles during heat treatment. They generally have slightly higher corrosion resistance than the martensitic stainless steels but, at best, they have slightly less resistance than type 304. They are commonly used in the aerospace and defence industries, but also find use in items such as pump shafts. In this category, 17-4PH (S17400) is a typical example.

The particular and interesting group of materials which are proposed here for manufacturing of turbodrill stages are steels with “Surface Hardening”. Surface hardening is a process for obtaining desired characteristics on the exterior of a steel component which improve: wear resistance, fracture toughness, fatigue resistance, resistance to high contact stresses and sometimes to improve corrosion resistance. Two general methods for surface hardening process are: 1) processes that change surface composition, 2) processes that preserve surface composition. Among the methods that involve changing surface composition (Heat-Treating methods), carburizing, nitriding, carbonitriding, nitrocarburizing, boronizing, and chromizing are more famous. For instance, carburizing is the process of adding carbon to the surface of steels by exposing the part to a carbon-rich atmosphere at an elevated temperature and allowing diffusion to transfer the carbon atoms into steel. Carburizing is the best method for low carbon steels (Davis, 2002). The longer the package is held at the high temperature, the deeper the carbon will diffuse into the surface. Different depths of hardening is desirable for different purposes: sharp tools need deep hardening to allow grinding and resharpening without exposing the soft core, while machine parts like gears might need only shallow hardening for increased wear resistance (Davis, 2002). By the use of high-quality alloy steels, great strength and toughness in the core can be combined with extreme surface

hardness, resulting in a composite structure capable of withstanding certain kinds of stress to a high degree. For less priced steel, there are many applications where low or moderate core properties, together with a high degree of surface hardness, can be obtained.

However, today completely different surface hardening technologies are being applied to and developed for steels. The objective remains the same, that is, enhanced surface performance, but technologies that incorporate high energy beams, plasmas, magnetic and electrical fields, and vacuums are being applied (Davis, 2002).

On the manufacturing point of view, the investment casting method is the preferred one that allows significant improvement in turbine performance due to achieving precise geometric dimensions and relative surface smoothness. Investment casting is based on lost-wax casting, one of the oldest known metal-forming techniques. It can produce complicated shapes that would be difficult or impossible with die casting and requires little surface finishing and only minor machining.

### 3.3.1 Cavitation

Cavitation is the boiling of a liquid at normal temperature when the static pressure is made sufficiently low (Dixon and hall, 2010). It may occur at the exit from hydraulic turbines in the vicinity of the moving blades. The dynamic motion of the blades in very high rotation speeds needs to reduce the static pressure locally to below atmospheric pressure for the cavitation to be commenced. The phenomenon is emphasized by the presence of dissolved gases that are released with a reduction in pressure below the vapour pressure corresponding to the liquid's temperature. In general the liquids flowing through turbodrill will contain some dust and dissolved gases and under these conditions negative pressure does not arise. Also, in contrast to pumps and other hydraulic turbines, the flow in turbodrill, due to low pressure ratio, does not reach to the negative pressure conditions (vapour pressure) as long as the motor is working steadily and therefore in this study the cavitation condition was not considered.

## 3.4 Turbodrill design

In turbodrill, turbine motor section composed of multistage of stator and rotor. In turbodrill, the hub (shaft) and shroud (housing) diameter are identical for all the stages. When designing a hydraulic multistage turbodrill, it is assumed that each turbine stage

is identical in which the flow rate, pressure drop, rotary speed, generated torque, and power transmitted to the shaft are the same for each of the stages.

The basic design of a turbodrill stage is shown in Figure 3.3. In stator and rotor, the drilling fluid flows between two coaxial cylindrical layer with diameter D2 and D5. The simplest approach for turbine stage analysis is to assume that the flow conditions at a mean radius, called the pitchline, represent the flow at all radii (Dixon and hall, 2010). As a result, in order to facilitate the process of design, the diameter of Dcp cylinder layer is defined as characteristic cylinder layer with the average flow conditions. From now on, all the turbodrill performance parameters are provided or from simulation results are based on the reference radius which is equal to Dcp/2.

The well-known method of building velocity triangles (and polygons) is used when designing the blade unit profile (see Figure 3.4). This method is useful for visualizing changes in the magnitude and direction of the fluid flow due to its interaction with the blade system. Fluid enters the stator with an absolute velocity  $c_1$  and at an absolute velocity angle  $\alpha_1$  and accelerates to an absolute velocity  $c_2$  at angle  $\alpha_2$ . All angles are measured from the axial direction ( $x$ ). From the velocity diagram, the rotor inlet relative velocity  $w_2$ , at a relative velocity angle  $\beta_2$ , is found by subtracting, vectorially, the blade speed,  $U$ , from the absolute velocity  $c_2$ . The relative flow within the rotor accelerates to a relative velocity  $w_3$  at an angle  $\beta_3$  at rotor outlet. The analysis of the flow field within the rotating blades of a turbodrill is performed in a frame of reference that is stationary relative to the blades. In this frame of reference the flow field appears as steady, whereas in the absolute frame of reference it is unsteady. This makes any calculations more straightforward and therefore relative velocities and relative flow quantities are used in this study.

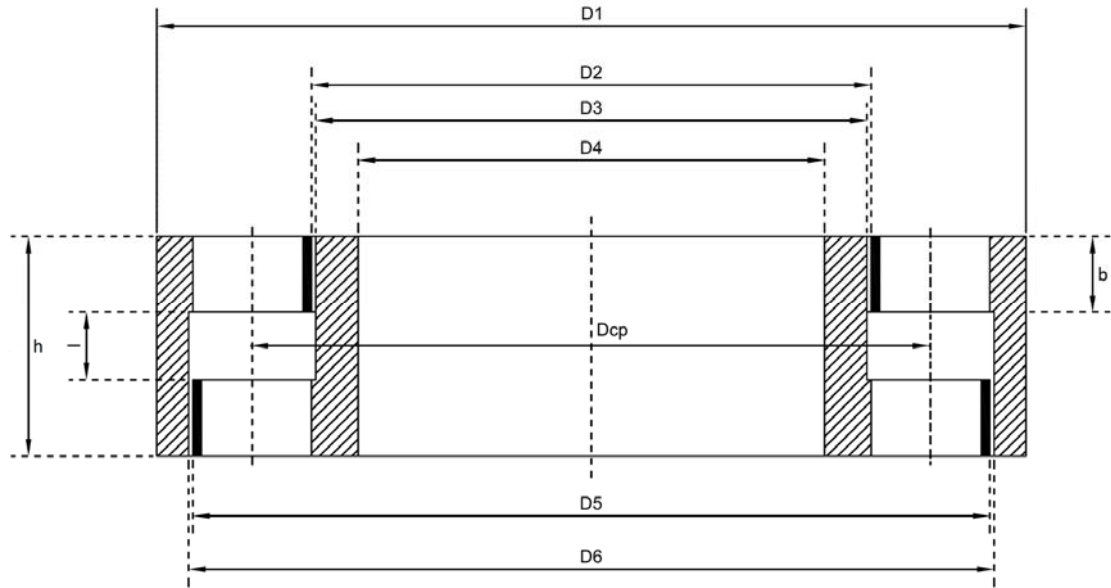


Figure 3.3 Schematic of turbodrill stage geometry (after Eskin and Maurer, 1997).

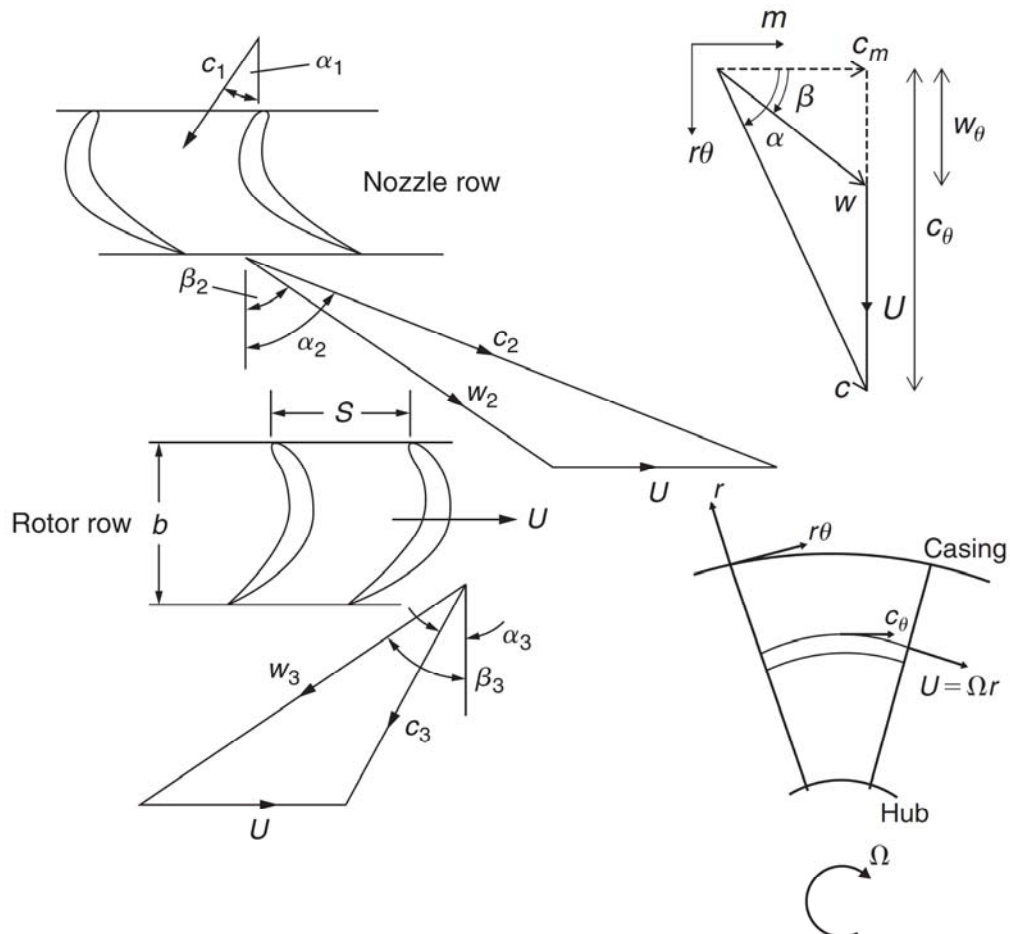


Figure 3.4 Turbine stage velocity diagrams and relative velocities (after Dixon and Hall, 2010).

The relative velocity is simply the absolute velocity minus the local velocity of the blade (see Figure 3.4). The blade has velocity only in the tangential direction, and therefore the relative components of velocity can be written as:

$$w_\theta = c_\theta - U, \quad w_x = c_x, \quad w_r = c_r, \quad (3.17)$$

$$\tan \beta = \tan \alpha - U / c_m. \quad (3.18)$$

Three key non-dimensional parameters are related to the shape of the turbine velocity triangles and are used in fixing the preliminary design of a turbine stage. These are described in the following sections.

### 3.4.1 Design Flow Coefficient

Design flow coefficient is defined as the ratio of the meridional flow velocity to the blade speed,  $\phi=c_m/U$  (Dixon and hall, 2010). In general, the flow in a turbomachine has components of velocity along all three cylindrical axes (axial  $x$ , radial  $r$ , and tangential  $r_\theta$  axes). However, for turbodrill as an axial turbomachinery, to simplify the analysis it is assumed that the flow does not vary in the tangential direction. In this case, the flow moves through the machine on axi-symmetric stream surfaces. The component of velocity along an axi-symmetric stream surface is called the meridional velocity ( $c_m$ ), expressed as:

$$c_m = \sqrt{c_x^2 + c_r^2}. \quad (3.19)$$

Also in purely axial-flow machines such as turbodrill, the radius of the flow path is constant and therefore, the radial flow velocity will be zero and  $c_m = c_x$ . Therefore, the flow coefficient for turbodrill is defined as:

$$\phi = \frac{c_x}{U}. \quad (3.20)$$

The value of  $\phi$  for a stage indicates the relative flow angles. A stage with a low value of  $\phi$  implies highly staggered blades and relative flow angles close to tangential axis, whereas high values imply low stagger and flow angles closer to the axial axis (Dixon and hall, 2010).

### 3.4.2 Stage Loading Coefficient

The stage loading coefficient is defined as the ratio of the stagnation enthalpy change through a turbine stage to the square of the blade speed,  $\psi = \Delta h_0/U^2$  (Dixon and hall, 2010). In turbodrill that is assumed to be an adiabatic turbine, the stagnation enthalpy change is equal to the specific work,  $\Delta W$ , and because it is a purely axial turbine with constant radius, we can use the Euler work equation ( $\Delta W = U \times \Delta c_\theta$ ) to write,  $\Delta h_0 =$

$U \times \Delta c_\theta$  (Dixon and hall, 2010). As a result, the stage loading for turbodrill can be written as:

$$\psi = \frac{\Delta c_\theta}{U}, \quad (3.21)$$

where  $\Delta c_\theta$  is equal to the change in the tangential component of absolute velocity through the rotor. Therefore, high stage loading means large flow turning and leads to highly “skewed” velocity triangles to achieve this turning. Since the stage loading is a non-dimensional measure of the work produced per stage, a high stage loading is desirable because it means fewer stages needed to produce a required work output (Dixon and hall, 2010). As a result, with designing blades leading to large flow turning, the stage loading coefficient will be higher and smaller turbodrill with less stages can result to the required power as long as being limited by the effects that high stage loadings have on efficiency.

### 3.4.3 Stage Reaction

The stage reaction is expressed as the ratio of the static enthalpy drop in the rotor to the static enthalpy drop across the turbine stage (Dixon and hall, 2010):

$$R = \frac{h_2 - h_3}{h_1 - h_3}. \quad (3.22)$$

Assuming the flow through a turbodrill as isentropic, the equation of the second law of thermodynamics,  $Tds = dh - dp/\rho$  can be approximated by  $dh = dp/\rho$ , and by ignoring compressibility effects, the reaction can then be obtained as (Dixon and hall, 2010):

$$R = \frac{p_2 - p_3}{p_1 - p_3}. \quad (3.23)$$

The reaction represents the drop in pressure across the rotor compared to that of the stage. It describes the asymmetry of the velocity triangles and is therefore a statement of the blade geometries (Dixon and hall, 2010). For example, a 50% reaction turbodrill implies velocity triangles that are symmetrical, which leads to similar stator and rotor blade shapes. Typically, in prior turbodrills design a 50% reaction were selected (i.e. the stator blades and the rotor blades are symmetric) (Natanael *et al.*, 2008). In contrast, a zero reaction turbodrill stage implies a little pressure change through the rotor, which requires rotor blades to be highly cambered, that do not accelerate the relative flow greatly, and low cambered stator blades that produce highly accelerating flow. Axial

thrust resulting from the reaction on the rotor blade is typically absorbed by thrust bearings. A higher reaction therefore increases the thrust created by the rotor blade, which must then be absorbed by thrust bearings. The efficiency of the turbodrill will increase by decreasing the amount of axial thrust absorbed by the thrust bearings thereby decreasing resistance to rotation of the shaft.

### 3.4.4 Preliminary Turbodrill stage design

The process of designing the best turbodrill for a given application involves juggling several parameters that may be of equal importance. As a result, a simple presentation can hardly satisfy the real problem of an integrated design. The main goal in the preliminary stage design of a turbodrill is to fix the shapes of the velocity triangles, either by setting the flow angles or by choosing values for the three dimensionless design parameters,  $\phi$ ,  $\psi$ , and  $R$ .

In normal multistage turbodrill, with identical mean velocity triangles for all stages, the axial velocity and the mean blade radius must remain constant throughout the turbodrill, therefore  $c_x = c_m = \text{constant}$ ,  $\alpha_1 = \alpha_2$ , and we have:

$$r_m = r_{rms} = \sqrt{\frac{r_{sh}^2 + r_h^2}{2}}, \quad (3.24)$$

where:

$r_{sh}$  = shroud radius,

$r_h$  = hub radius.

If the mass flow rate through the turbodrill is specified the annulus area,  $A_n$ , can be determined from the continuity equation combined with the flow coefficient, as following:

$$A_n = \frac{\dot{m}}{\rho\phi U} \approx 2\pi \times r_m H. \quad (3.25)$$

In all cases, an accurate expression for the annulus area is given by:

$$A_n = \pi \times r_{sh}^2 \left[ 1 - \left( \frac{r_h}{r_{sh}} \right)^2 \right]. \quad (3.26)$$

The spanwise height required for the blades can then be determined from:

$$r_{sh} - r_h = H \approx \frac{\dot{m}}{\rho\phi U 2\pi \times r_m}. \quad (3.27)$$

From the specification of the turbodrill, the design will usually have a known mass flow rate of the drilling fluid and a required power output. As a result, the specific work per stage can be determined from the stage loading and the blade speed and, consequently, the required number of stages can be found as following:

$$n_{stage} \geq \frac{\Delta \dot{W}_t}{\psi U^2}. \quad (3.28)$$

An inequality is used in this equation, because the number of stages must be an integer value. The equation here shows how a large stage loading can reduce the number of stages required and also shows that a high blade speed,  $U$ , is desirable as well.

For turbodrills, several useful relationships can be derived relating the shapes of the velocity triangles to the three dimensionless design parameters. These relationships are important for the preliminary design. Starting with the definition of the stage reaction, and accepting no work is done through the stator, so the stagnation enthalpy remains constant across it and after a few substitutions, finally the relations between flow coefficients and angles are obtained as following:

$$R = \frac{\phi}{2}(\tan \beta_3 - \tan \beta_2) = 1 - \frac{\phi}{2}(\tan \alpha_2 - \tan \alpha_1). \quad (3.29)$$

Also it can be obtained that:

$$\psi = 2(1 - R + \phi \tan \alpha_1). \quad (3.30)$$

Two important angles in the geometry of a rotor blade are  $\beta_2$  and  $\beta_3$ . These two angles are important factors in the performance of the rotor blade because they determine the change in the direction of the drilling fluid passing through the rotor blade.  $\beta_2$  plus  $\beta_3$  is preferably less than 120 degree to avoid excessive blade turning, which can damage the rotor vanes (Natanael *et al.*, 2008). To determine  $\beta_2$  and  $\beta_3$  from Equation (3.29) we can write:

$$R = \frac{c_x}{2U}(\tan \beta_3 - \tan \beta_2), \quad (3.31)$$

then,

$$\beta_3 = \tan^{-1} \left( \frac{2UR}{c_x} + \tan \beta_2 \right). \quad (3.32)$$

Also the work done on the rotor by unit mass of fluid, i.e. the specific work, equals the stagnation enthalpy drop caused by the fluid passing through the stage. According to the Euler work equation this can be written mathematically as:

$$\Delta W = \Delta h_0 = U\Delta c_\theta = Uc_x (\tan \beta_2 + \tan \beta_3). \quad (3.33)$$

The output power of each stage is obtained as following:

$$P = \rho Q \Delta W = \rho Q U c_x (\tan \beta_2 + \tan \beta_3). \quad (3.34)$$

Also the output torque of each stage is:

$$T = \rho Q r_m c_x (\tan \beta_2 + \tan \beta_3). \quad (3.35)$$

Solving for  $\beta_3$  results in:

$$\beta_3 = \tan^{-1} \left( \frac{P}{\rho Q U c_x} - \tan \beta_2 \right). \quad (3.36)$$

Equations (3.32) and (3.36) can be combined to solve for  $\beta_2$ . This yields:

$$\beta_2 = \tan^{-1} \left( \frac{P}{2 \rho Q U c_x} - \frac{U R}{c_x} \right). \quad (3.37)$$

The fluid exiting from the stator blade should leave with a close angle to the inlet angle  $\beta_2$  of the rotor blade. This helps in avoiding an abrupt direction change of the fluid, which can result in the fluid separation on the rotor blade. Fluid separation results in more energy losses. Fluid separation also occurs at the trailing edges of the stator and rotor blades (Natanael *et al.*, 2008).

After calculating  $\beta_2$  and  $\beta_3$ , a stagger angle ( $\xi$ ) can be determined that is the angle between the chord line and the axial flow direction. After determining the stagger angle, the ideal length of the chord can be calculated based on the angle and desired length of the rotor blade. With the basic profile of the rotor blade determined, the stator exit angle can be calculated. The stator exit angle,  $\alpha_2$ , may be selected to be substantially similar to the rotor inlet swirl angle and is calculated as:

$$\alpha_2 = \tan^{-1} \left( \frac{c_x \tan \beta_2 + U}{c_x} \right). \quad (3.38)$$

With the profile of the stator and rotor blades being defined, an optimum number of blades on each row and the chord lengths of the blades can also be estimated during the preliminary design. The aspect ratio of a blade row is the height, or blade span, divided by the axial chord,  $H/b$ . A suitable value of this is set by mechanical and manufacturing

considerations and will vary between applications. Typically, in prior turbodrills design the aspect ratio for rotor blades was 0.5. It has been found that energy losses may be reduced by increasing the aspect ratio of the stator and/or rotor blades (Natanael *et al.*, 2008). To find the ratio of blade pitch to axial chord,  $S/b$ , the Zweifel criterion for blade loading can be applied. The Zweifel criterion states that for turbine blades there is an optimum space-chord ratio that gives a minimum overall loss. Typically, the Zweifel criterion,  $Z$ , is assumed to be between 0.5 and 1.2 (Dixon and Hall, 2010). If the spacing between the blades is made small, the fluid receives the maximum amount of guidance from the blades, but the friction losses will be large. On the other hand, with the same blades spaced well apart, friction losses are small but, because of poor fluid guidance, the losses resulting from flow separation are high (Dixon and Hall, 2010). For a known axial chord, knowing  $S/b$  fixes the number of blades on each stator and rotor row as (Dixon and Hall, 2010):

$$N_B = \frac{4\pi r_m \times \cos^2 \beta_3 (\tan \beta_2 + \tan \beta_3)}{Z \times b}. \quad (3.39)$$

### 3.4.5 Effect of Reaction on Turbodrill performance

Consider the case that the mean blade speed  $U$ , the stage loading,  $\psi$  (or  $\Delta W/U^2$ ), and the flow coefficient  $\phi$  (or  $c_x/U$ ) have already been selected. The only remaining parameter required to completely define the velocity triangles is Reaction ( $R$ ) or the inter-stage swirl angle,  $\alpha_1$ , since we have:

$$\psi = 2(1 - R + \phi \tan \alpha_1). \quad (3.40)$$

For different values of  $R$  the velocity triangles can be constructed, the loss coefficients determined and the efficiencies calculated. In the plot of efficiencies versus Reaction range, we can find the Reaction value in which the efficiencies are highest.

Any diffusion of the fluid flow through turbine blade rows is undesirable and must, at the design stage, be avoided at any costs (Dixon and Hall, 2010). The negative values of reaction indicates diffusion of the rotor relative velocity (i.e., for  $R < 0$ ,  $w_3 < w_2$ ). If  $R > 1$ , diffusion of the stator absolute velocity is occurred and  $c_2 < c_1$ . When  $\alpha_3 = \alpha_2$  the reaction is unity (also  $c_2 = c_3$ ). If  $R = 0$ , then we have  $w_2 = w_3$  and  $\beta_2 = \beta_3$ . Also when  $R = 0.5$ , then we have  $c_2 = w_3$ ,  $w_2 = c_3 = c_1$  and  $\alpha_1 = \alpha_3 = \beta_2$ .

### 3.5 Turbodrill design with ANSYS®

ANSYS® is an engineering simulator (computer-aided engineering, or CAE) including general-purpose finite element analysis and computational fluid dynamics software. TurboSystem is a set of software applications and tools for designing turbomachinery in the ANSYS® Workbench environment. In this study some of these tools have been used for turbodrill design and simulation which include: BladeGen (a geometry creation tool for turbomachinery blades design), TurboGrid (a meshing tool for turbomachinery blade rows), CFX (a general purpose CFD software suite that combines an advanced solver with powerful pre- and post-processing capabilities).

For the turbodrill stage modelling, the shroud (housing) and hub (shaft) diameter of the turbodrill need to be set in BladeGen first. For the applications of this study as it needs to be utilized by the small size CT for fast drilling, several sets of shroud and hub diameters were set for stage models. Here, because the blades are connected to the hub and shroud, then no hub and shroud tips were set in the design process.

There are two models for geometry generation of the blades in BladeGen: Angle/Thickness mode and Pressure/Suction mode, in which blades profile properties are displayed and defined in various views and blade sections. In the Angle/Thickness mode which is the preferred mode used in this study, the Angle and Thickness are available to see and modify the Camberline/Thickness definitions. The Angle view displays a graph of the Theta and/or Beta angle definition for the selected layer. The Thickness view displays a graph of the thickness definition for the selected layer. Figure 3.5 shows a BladeGen snapshot of the rotor blade row design process.

### 3.6 Turbodrill stage models

Table 3.1 shows the geometry specifications for the turbodrill stage models designed and used for simulation purposes in this study.

### Chapter 3 Turbodrill design and specifications

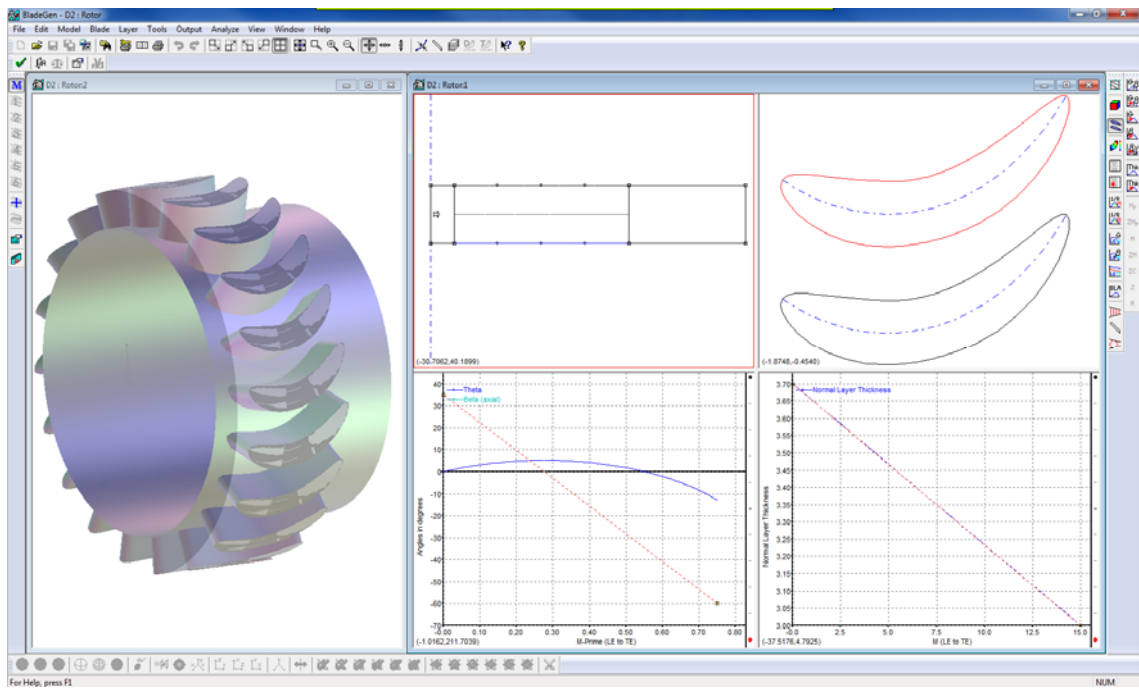


Figure 3.5 A BladeGen snapshot of the rotor blade row design process.

Table 3.1: Geometry specifications used for the design and simulations of turbodrill stage in this study.

Shroud Diameter (mm)	Model: Blade Height (mm)	Fluid Type	No. of Blades	Stator (S) or Rotor (R)	Normal Blade Thickness Model: LE – TE (mm)	Beta Model: Inlet – Outlet Angle
Model A: 50 mm Shroud Diameter	1: 5 mm	Water	20	S	1: 3.5 – 3.0	1: (-5) – 65
				R	2: 3.7 – 3.0	2: (-5) – 60 3: 35 – (-60) 4: 20 – (-60)
		Gas	16	S	1: 3.5 – 3.0	1: (-5) – 65
			R	2	3.7 – 3.0	3: 35 – (-60)
	2: 8 mm	Water	20	S	3: 3.2 – 2.0	1: (-5) – 65
				R	1: 3.5 – 3.0	5: 50 – (-65)
		Gas	25	S	3: 3.2 – 2.0	1: (-5) – 65
			R	2	3.5 – 3.0	5: 50 – (-65)
	3: 12 mm	Water	22	S	1: 3.5 – 3.0	1: (-5) – 65
				R	2: 3.7 – 3.0	3: 35 – (-60)
		Gas	20	S	4: 3.0 – 2.0	4: (-5) – 65
			R	5	3.0 – 1.7	6: (-5) – 50 7: 30 – (-60)
Model B: 40 mm Shroud Diameter	1: 3 mm	Water	20	S	4: 3.0 – 2.0	6: (-5) – 50
				R	5: 3.0 – 1.7	7: 30 – (-60)
		Gas	16	S	4: 3.0 – 2.0	6: (-5) – 50
			R	5	3.0 – 1.7	7: 30 – (-60)
	2: 5 mm	Water	20	S	4: 3.0 – 2.0	1: (-5) – 65
				R	5: 3.0 – 1.7	7: 30 – (-60)
		Gas	16	S	1: 3.5 – 3.0	1: (-5) – 65
			R	2	3.7 – 3.0	3: 35 – (-60)

Each model is identified in this study according to Table 3.1 and based on the following description. Here, for example blade row model of “A1W20S11” described in Figure 3.6.

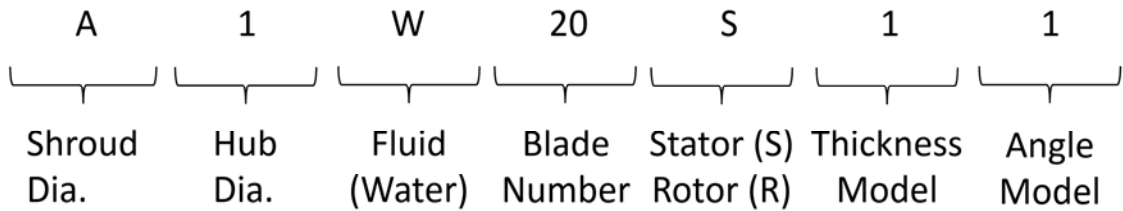


Figure 3.6 Description of the blade row model of “A1W20S11”.

In the following sections, basic drawings and geometry specifications for each turbodrill stage models are reported with real design dimensions for the simulation purposes.

### 3.6.1 A1 stage models

Table 3.2 shows the geometrical specifications for turbodrill stage models with 50 mm shroud diameter and blade height or span of 5 mm. Figure 3.7 shows the geometrical specifications of the turbodrill stage model “A1”.

Table 3.2: Geometrical specifications for turbodrill stage models with 50 mm shroud diameter and blade height or span of 5 mm (A1 stage models).

Model	TE Pitch (S) (mm)	Chord Length (C) (mm)	Meridional Length (M) (mm)	Stagger Angle	Pitch Chord Ratio (S/C)
A1W20S11	7.06858	18.3174	15.0	35.0	0.385894
A1W20S12	7.06858	17.5472	15.0	31.3	0.402833
A1W20R23	7.06858	15.6504	15.0	-16.6	0.451655
A1W20R24	7.06858	16.4588	15.0	-24.3	0.429471
A1W16S11	8.83573	18.3174	15.0	35.0	0.482368
A1W16R23	8.83573	15.6504	15.0	-16.6	0.564568
A1G25S31	5.65487	18.3174	15.0	35.0	0.308715
A1G25R15	5.65487	15.3238	15.0	-11.8	0.369025
A1G22S31	6.42598	18.3174	15.0	35.0	0.350813
A1G22R15	6.42598	15.3238	15.0	-11.8	0.419347

#### A1W20S11 stator blade row model

Figure 3.8 shows the blade Theta and Beta angles versus meridional length for the stator blade row model “A1W20S11” for water flow simulations at three span surfaces. Figure 3.9 shows the blade angles and normal thickness versus camber length of the blade for this stator model at span surface of 0.5. When using Camberline/Thickness design mode, the Angle and Thickness views are available to modify the blade shape. The blade design parameters shown in Figure 3.8 and Figure 3.9 are the controlling parameters of the blade shape and are set in “BladeGen” software specifically for each of turbodrill stage models presented in this study.

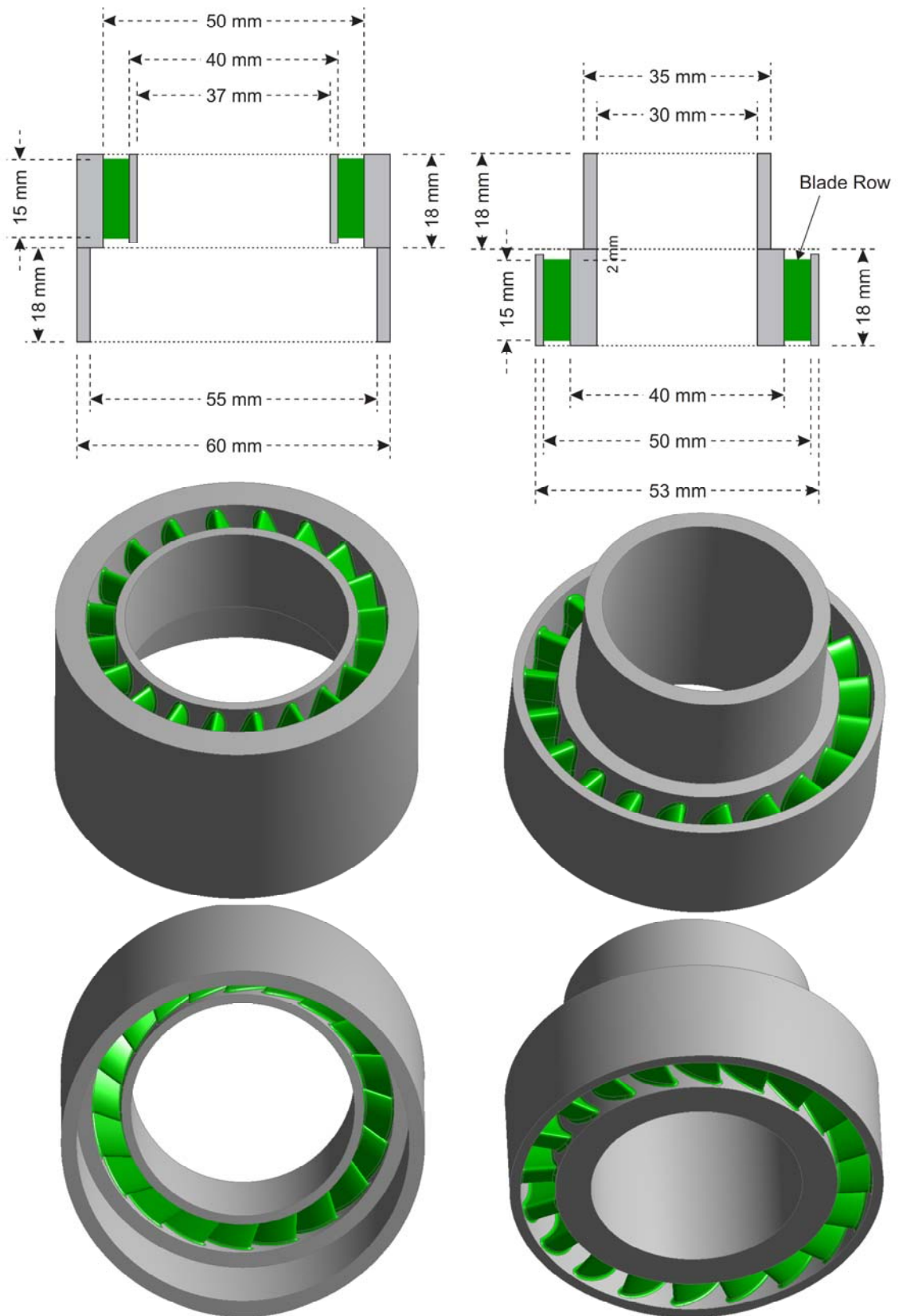


Figure 3.7    Geometrical specifications of the turbodrill stage model "A1".

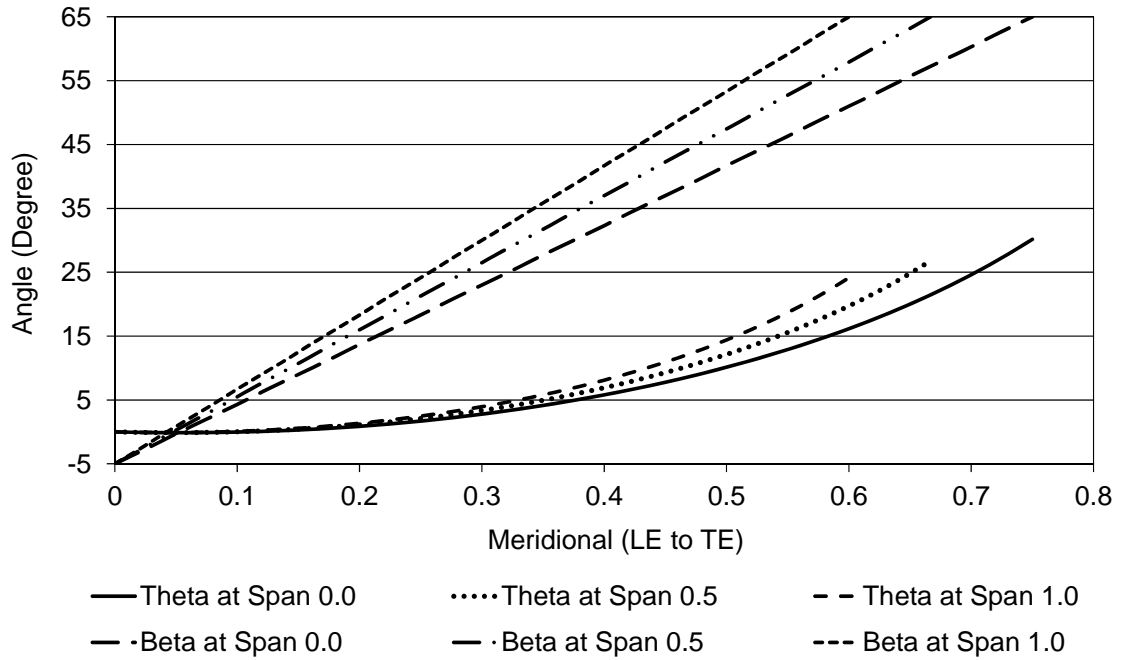


Figure 3.8 Blade Theta (blade location) and Beta (blade angle) angles versus meridional length for the stator row model "A1W20S11".

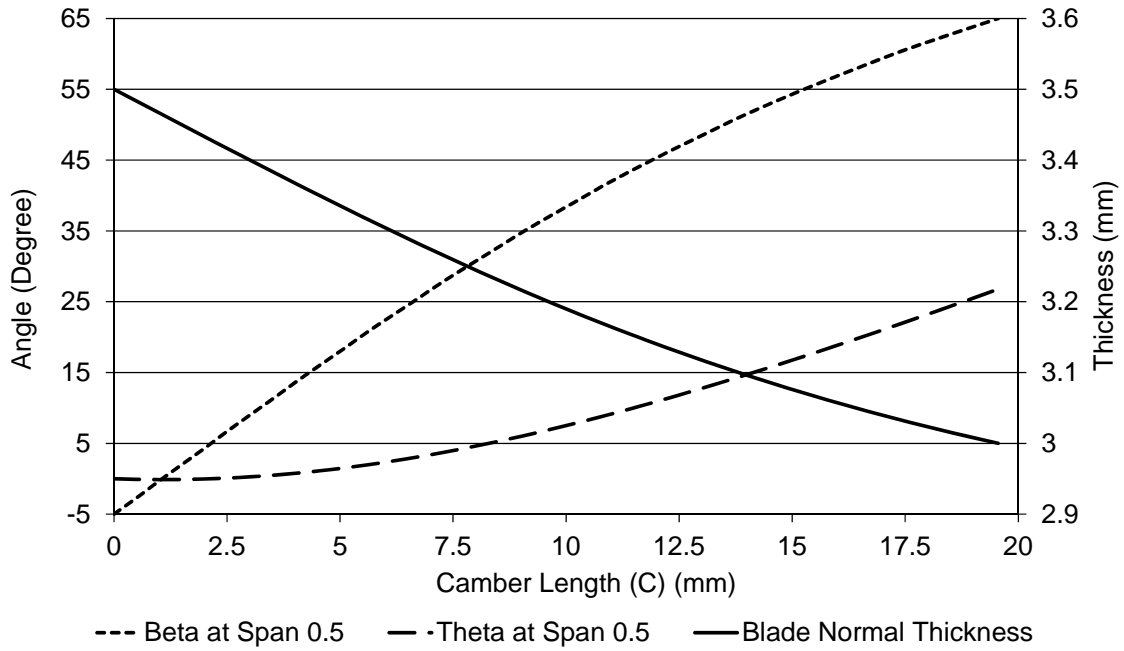


Figure 3.9 Blade angles and normal thickness versus camber length of the blade for stator model "A1W20S11" at span surface 0.5.

#### A1W20S12 stator blade row model

Figures 3.10 shows the blade Theta and Beta angles versus meridional length for the stator blade row model of "A1W20S12" for water flow simulations at three span surfaces. Figure 3.11 shows the blade angles and normal thickness versus camber length of the blade for this stator model at span surface of 0.5.

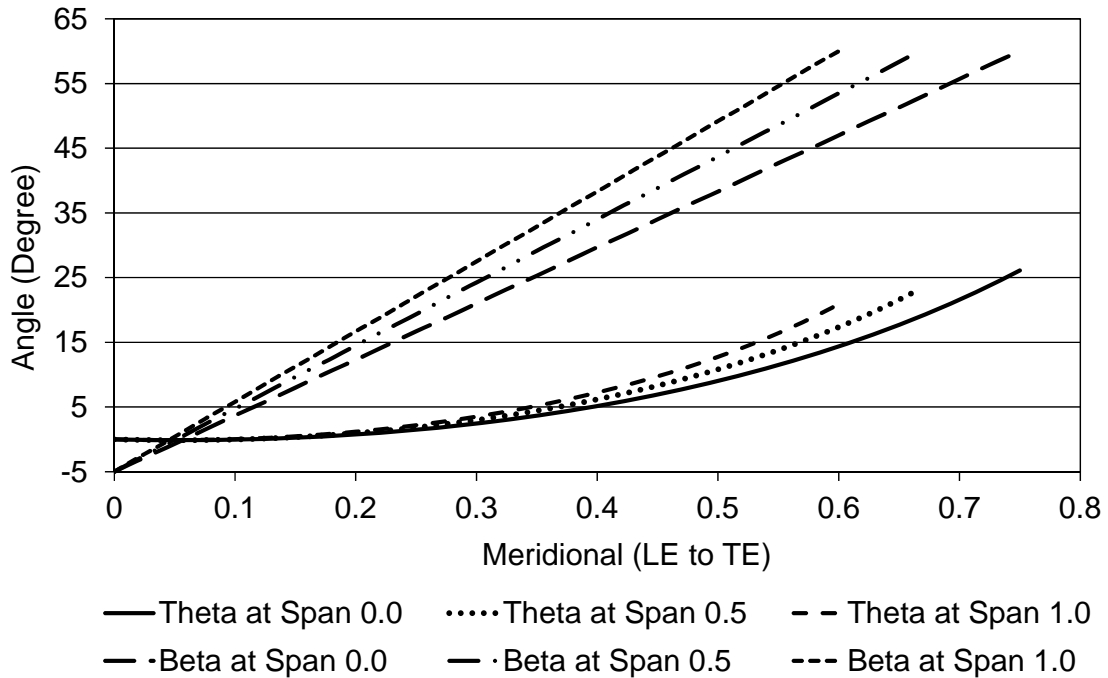


Figure 3.10 Blade Theta and Beta angles versus meridional length for the stator row model of "A1W20S12".

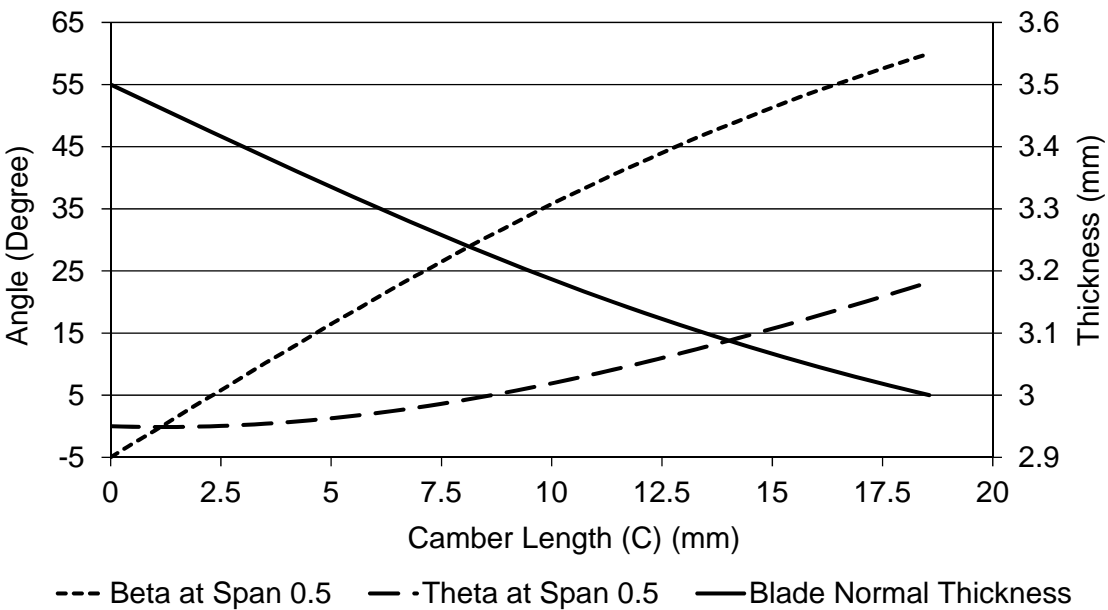


Figure 3.11 Blade angles and normal thickness versus camber length of the blade for stator model "A1W20S12" at span surface 0.5.

#### A1W20R23 rotor blade row model

Figures 3.12 shows the blade Theta and Beta angles versus meridional length for the rotor blade row model of "A1W20R23" for water flow simulations at three span surfaces. Figure 3.13 shows the blade angles and normal thickness versus camber length of the blade for this rotor model at span surface of 0.5.

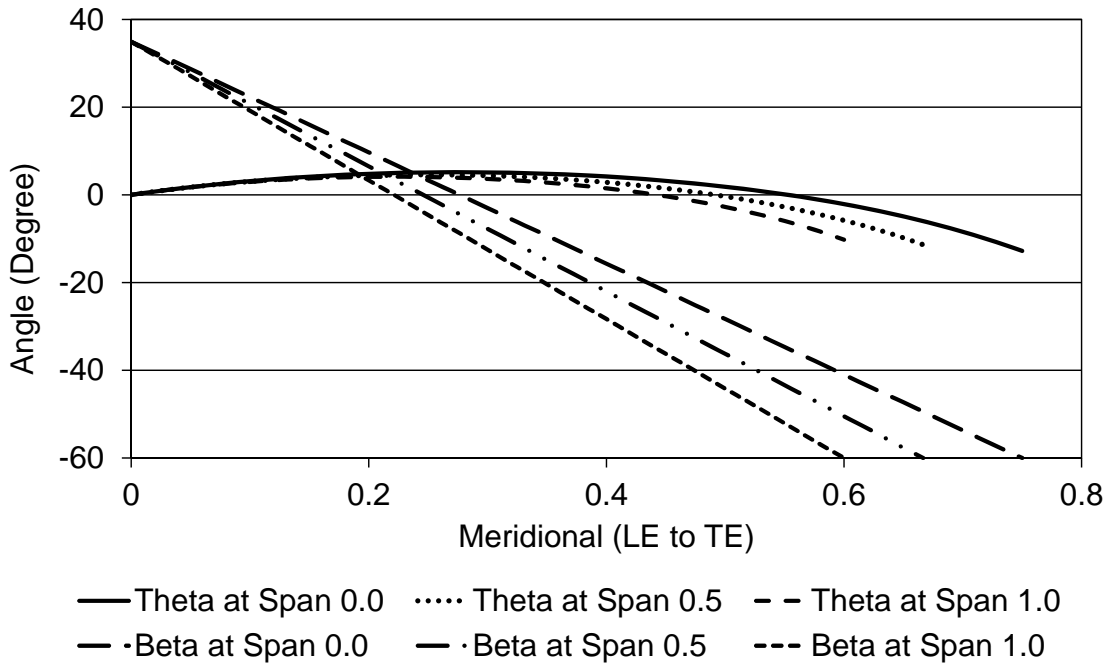


Figure 3.12 Blade Theta and Beta angles versus meridional length for the rotor row model of "A1W20R23".

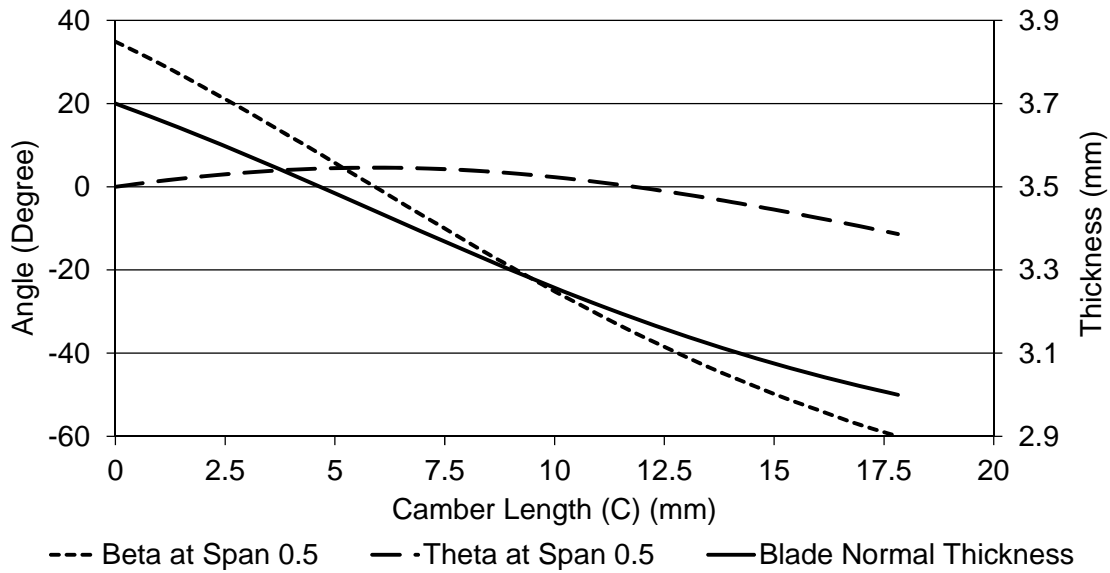


Figure 3.13 Blade angles and normal thickness versus camber length of the blade for rotor model "A1W20R23" at span surface 0.5.

#### A1W20R24 rotor blade row model

Figures 3.14 shows the blade Theta and Beta angles versus meridional length for the rotor blade row model of "A1W20R24" for water flow simulations at three span surfaces. Figure 3.15 shows the blade angles and normal thickness versus camber length of the blade for this rotor model at span surface of 0.5.

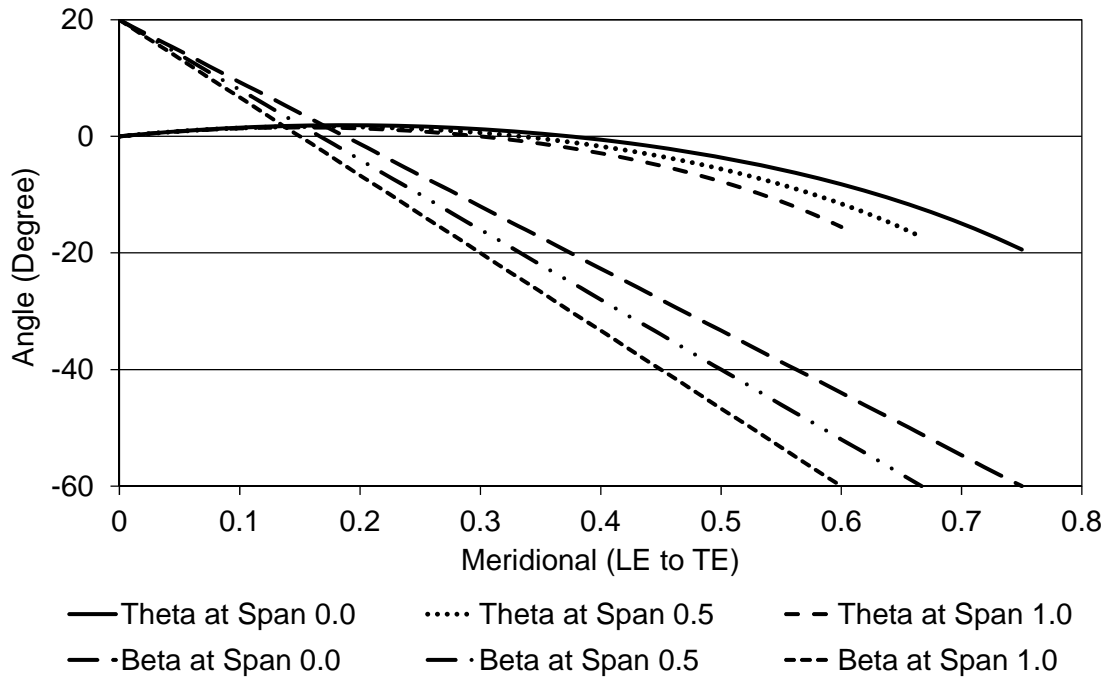


Figure 3.14 Blade Theta and Beta angles versus meridional length for the rotor row model of "A1W20R24".

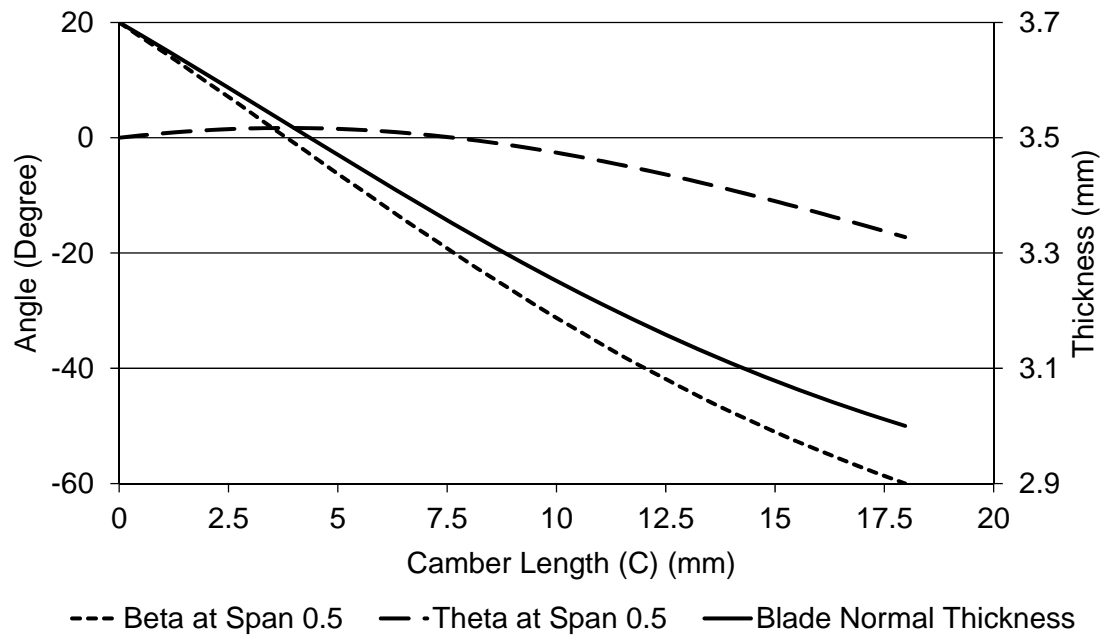


Figure 3.15 Blade angles and normal thickness versus camber length of the blade for rotor model "A1W20R24" at span surface 0.5.

#### A1G25R15 rotor blade row model

Figures 3.16 shows the blade Theta and Beta angles versus meridional length for the rotor blade row model of "A1G25R15" for gas flow simulations at three span surfaces. Figure 3.17 shows the blade angles and normal thickness versus camber length of the blade for this rotor model at span surface of 0.5.

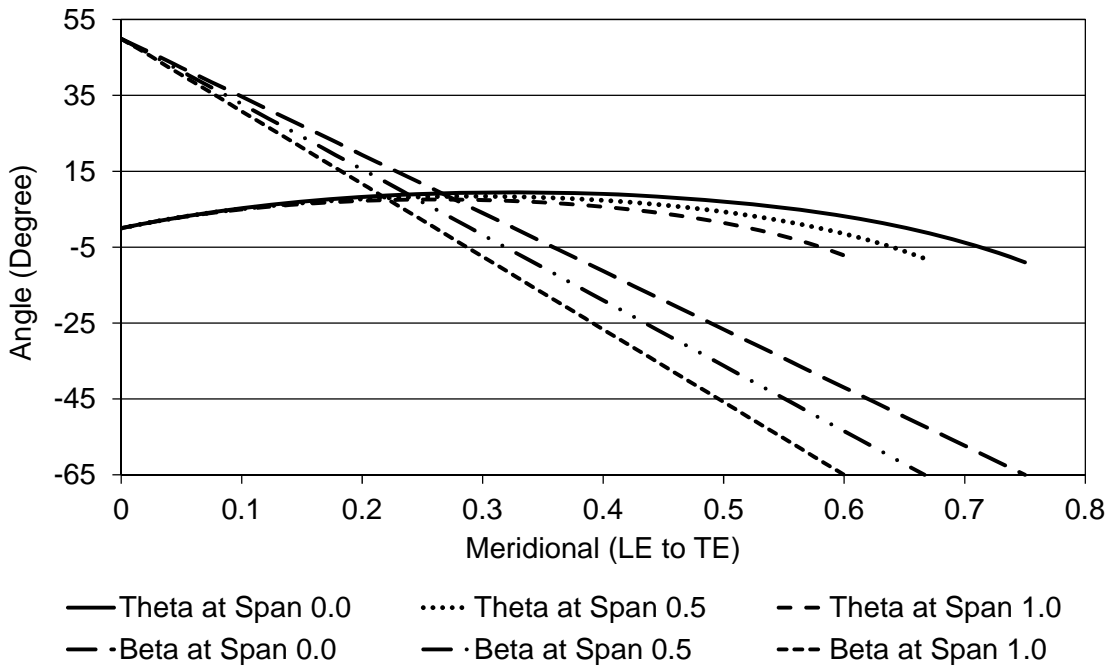


Figure 3.16 Blade Theta and Beta angles versus meridional length for the rotor row model of "A1G25R15".

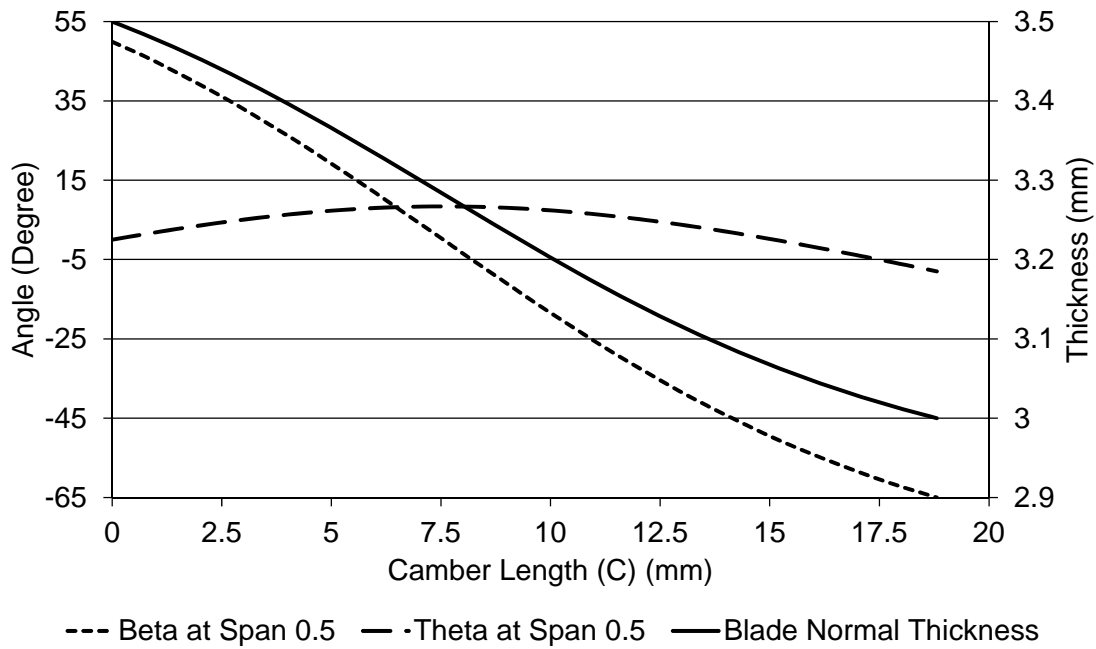


Figure 3.17 Blade angles and normal thickness versus camber length of the blade for rotor model "A1G25R15" at span surface 0.5.

### 3.6.2 A2 stage models

Figure 3.18 shows the geometrical specifications of the turbodrill stage model "A2". Table 3.3 shows the geometrical specifications for turbodrill stage models with 50 mm shroud diameter and blade height or span of 8 mm.

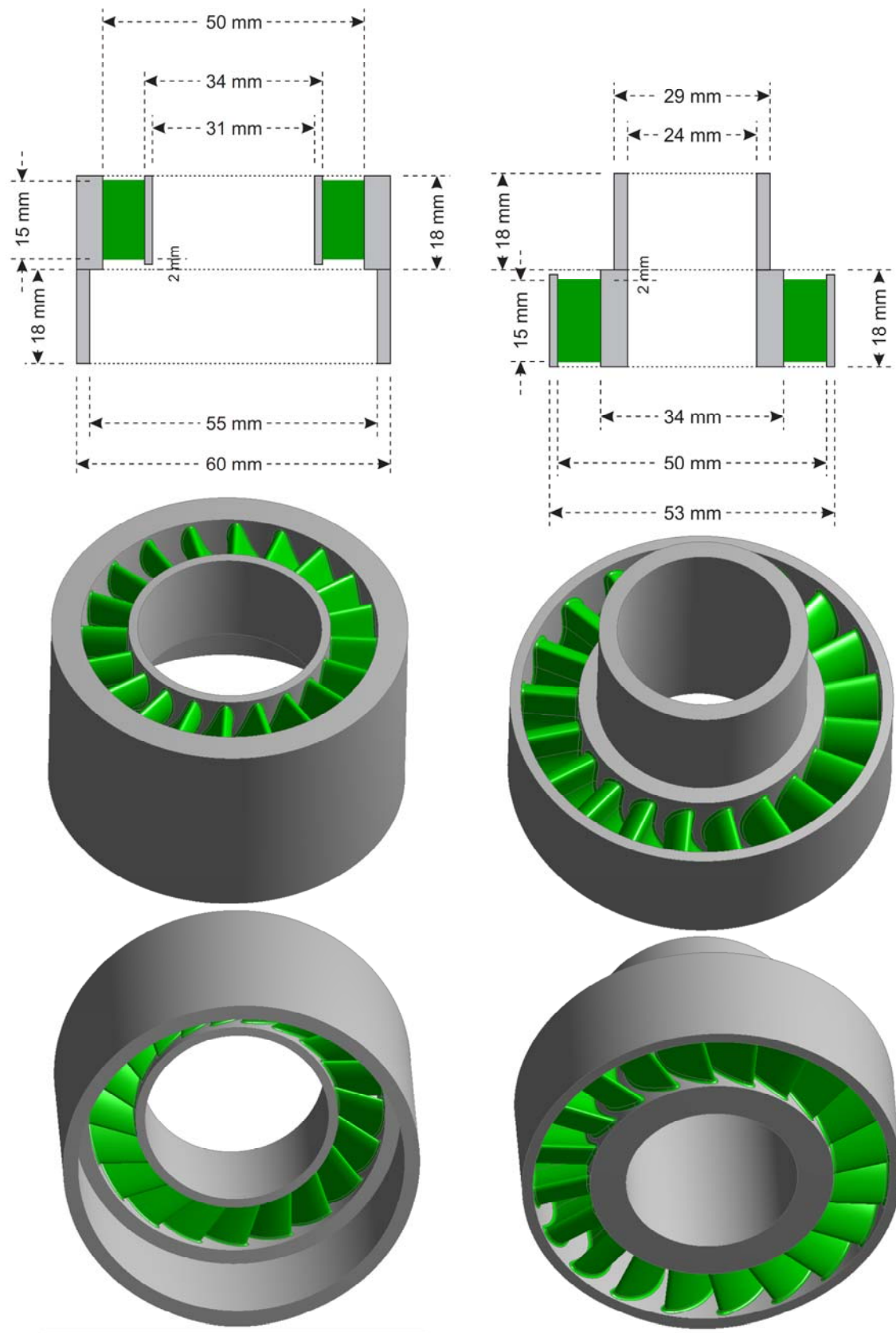


Figure 3.18 Geometrical specifications of the turbodrill stage model "A2".

Table 3.3: Geometrical specifications for turbodrill stage models with 50 mm shroud diameter and blade height or span of 8 mm (A2 stage models).

Model	TE Pitch (S) (mm)	Chord Length (C) (mm)	Meridional Length (M) (mm)	Stagger Angle	Pitch Chord Ratio (S/C)
A2W20S11	6.59734	18.2967	15.0	34.9	0.360576
A2W20R23	6.59734	15.6496	15.0	-16.6	0.421566

### 3.6.3 A3 stage models

Table 3.4 shows the geometrical specifications for turbodrill stage models with 50 mm shroud diameter and blade height or span of 12 mm. Figure 3.19 shows the geometrical specifications of the turbodrill stage model “A3”.

Table 3.4: Geometrical specifications for turbodrill stage models with 50 mm shroud diameter and blade height or span of 12 mm (A3 stage models).

Model	TE Pitch (S) (mm)	Chord Length (C) (mm)	Meridional Length (M) (mm)	Stagger Angle	Pitch Chord Ratio (S/C)
A3W22S41	5.42639	18.2191	15.0	34.6	0.297841
A3W22S46	5.42639	16.4669	15.0	24.4	0.329533
A3W22R57	5.42639	15.8829	15.0	-19.2	0.341649
A3W20S46	5.96903	16.4669	15.0	24.4	0.362487
A3W20R57	5.96903	15.8829	15.0	-19.2	0.375814
A3G22S41	5.42639	18.2191	15.0	34.6	0.297841
A3G22R57	5.42639	15.8829	15.0	-19.2	0.341649

#### A3W22S46 stator blade row model

Figures 3.20 shows the blade Theta and Beta angles versus meridional length for the stator blade row model of “A3W22S46” for water flow simulations at three span surfaces. Figure 3.21 shows the blade angles and normal thickness versus camber length of the blade for this stator model at span surface of 0.5.

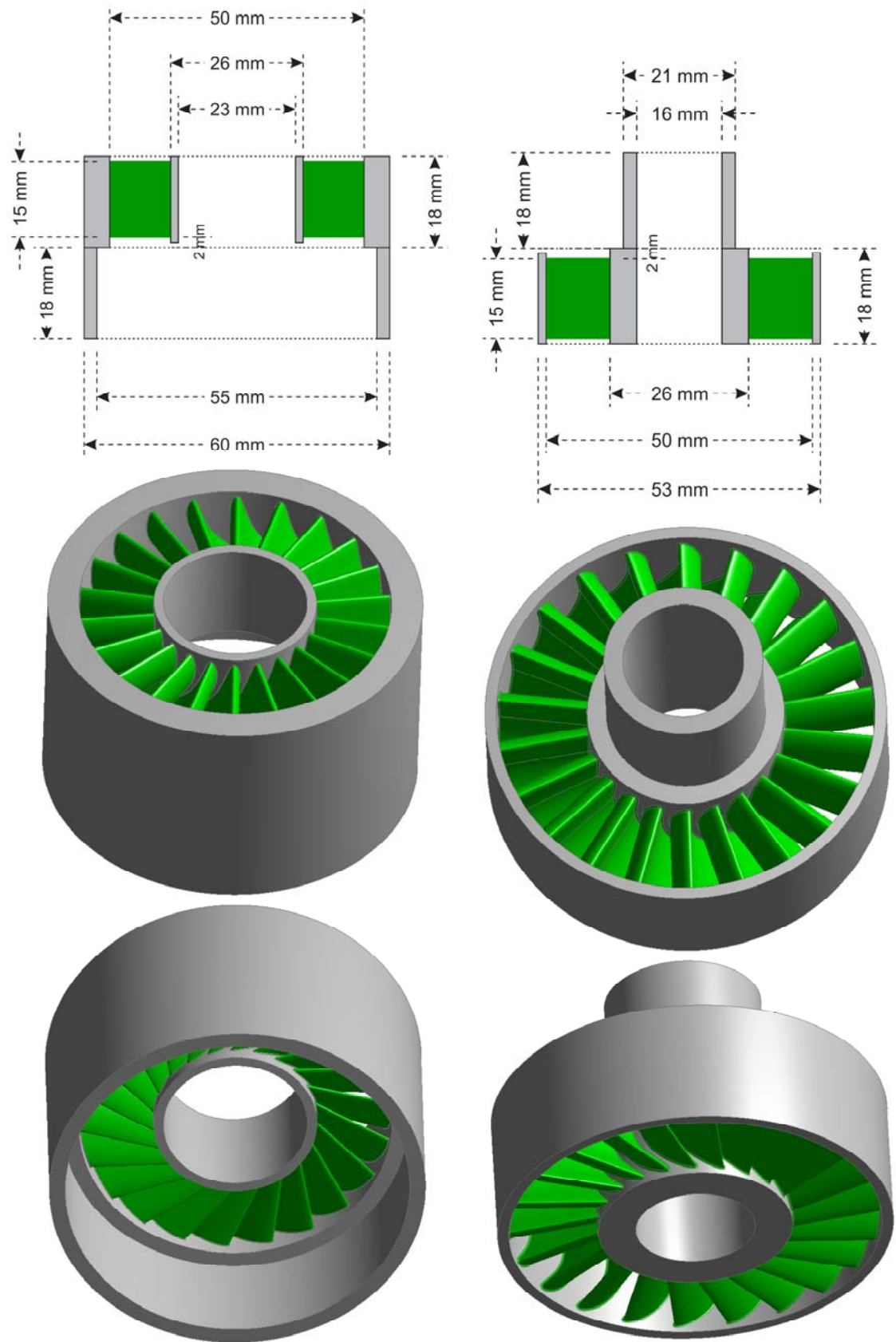


Figure 3.19 Geometrical specifications of the turbodrill stage model "A3".

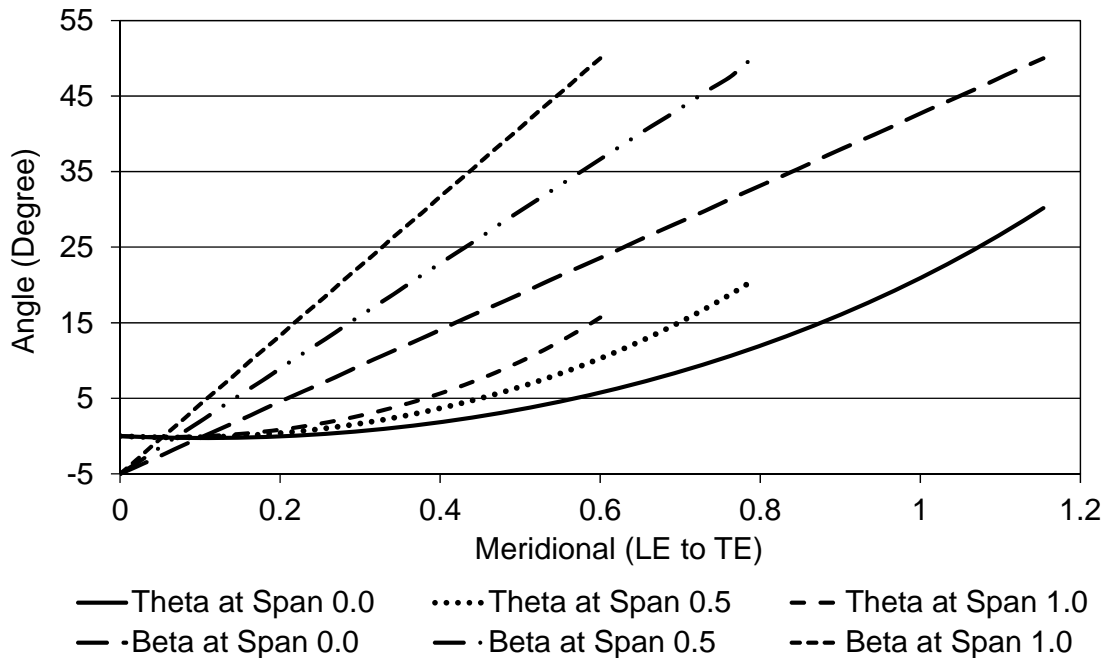


Figure 3.20 Blade Theta and Beta angles versus meridional length for the stator row model of "A3W22S46".

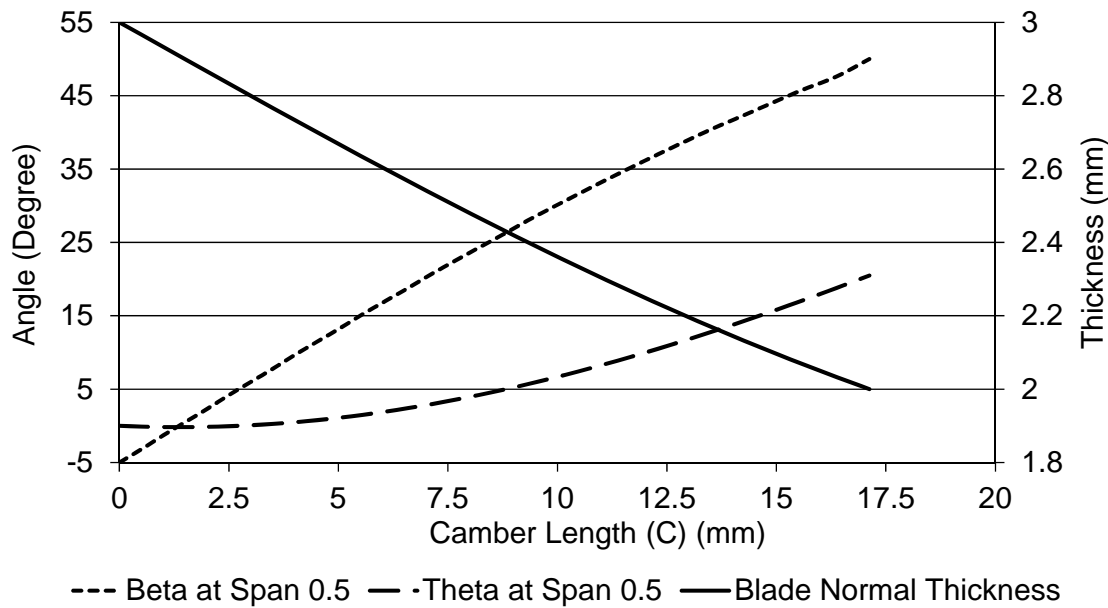


Figure 3.21 Blade angles and normal thickness versus camber length of the blade for stator model "A3W22S46" at span surface 0.5.

#### A3W22R57 rotor blade row model

Figures 3.22 shows the blade Theta and Beta angles versus meridional length for the rotor blade row model of "A3W22R57" for water flow simulations at three span surfaces. Figure 3.23 shows the blade angles and normal thickness versus camber length of the blade for this rotor model at span surface of 0.5.

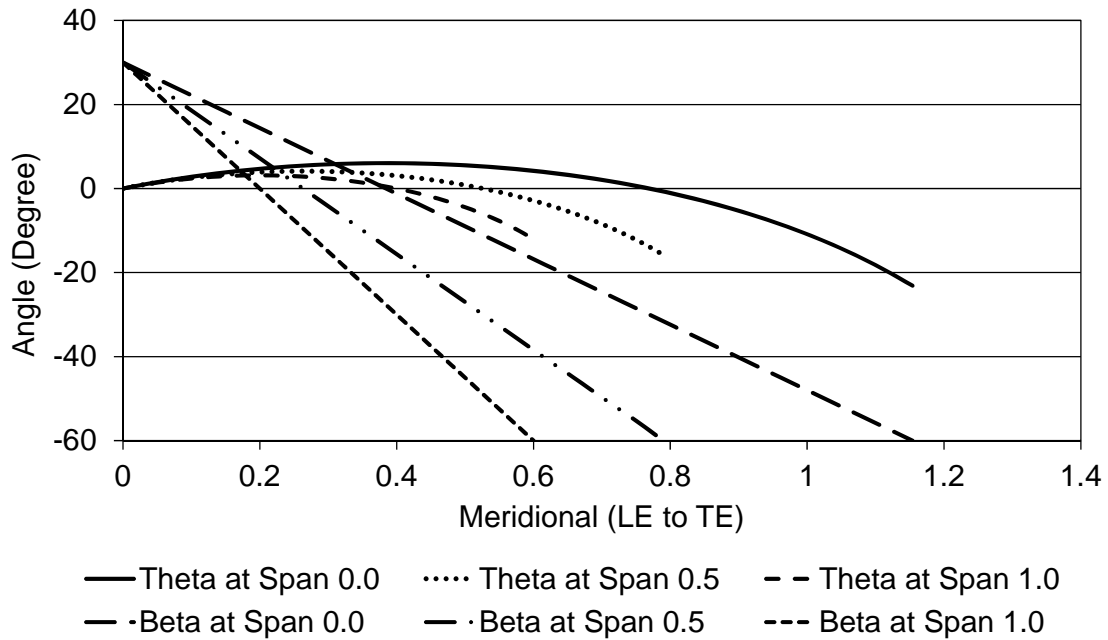


Figure 3.22 Blade Theta and Beta angles versus meridional length for the rotor row model of "A3W22R57".

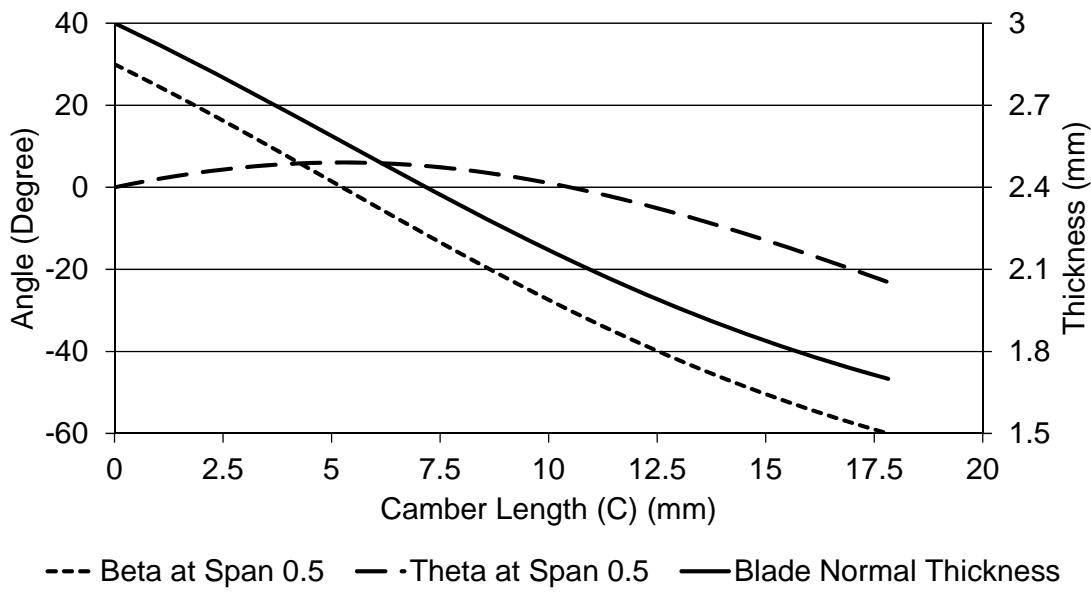


Figure 3.23 Blade angles and normal thickness versus camber length of the blade for rotor model "A3W22R57" at span surface 0.5.

### 3.6.4 B1 stage models

Figure 3.24 shows the geometrical specifications of the turbodrill stage model "B1". Table 3.5 shows the geometrical specifications for turbodrill stage models with 40 mm shroud diameter and blade height or span of 3 mm.

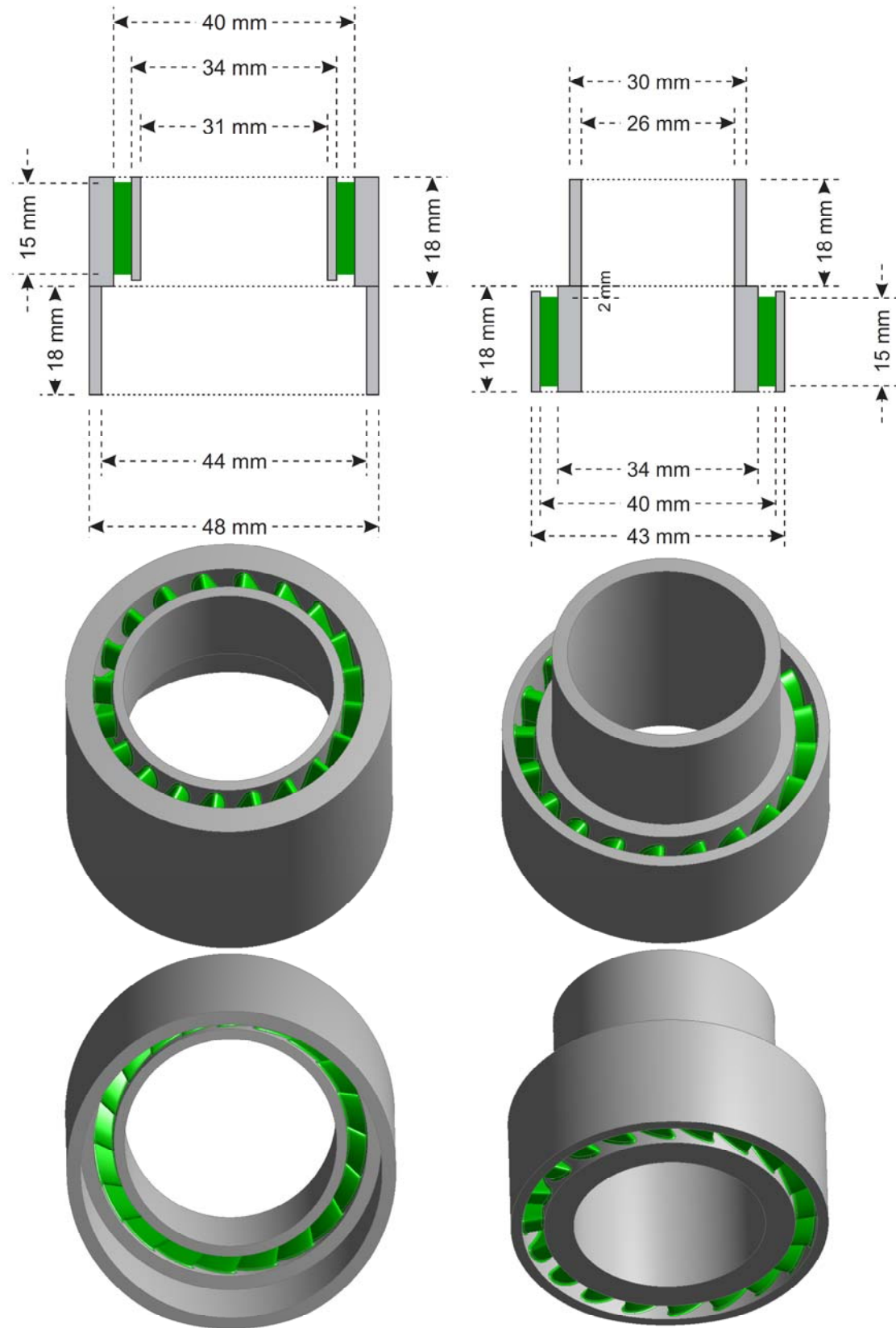


Figure 3.24 Geometrical specifications of the turbodrill stage model "B1".

Table 3.5: Geometrical specifications for turbodrill stage models with 40 mm shroud diameter and blade height or span of 3 mm (B1 stage models).

Model	TE Pitch (S) (mm)	Chord Length (C) (mm)	Meridional Length (M) (mm)	Stagger Angle	Pitch Chord Ratio (S/C)
B1W20S11	5.81195	18.3192	15.0	35.0	0.317259
B1W20R23	5.81195	15.6505	15.0	-16.6	0.371359
B1W16S11	7.26493	18.3192	15.0	35.0	0.396574
B1W16R23	7.26493	15.6505	15.0	-16.6	0.464199
B1G20S61	5.81195	18.3192	15.0	35.0	0.317259
B1G20R15	5.81195	15.3238	15.0	-11.8	0.379276

### 3.6.5 B2 stage models

Table 3.6 shows the geometrical specifications for turbodrill stage models with 40 mm shroud diameter and blade height or span of 5 mm. Figure 3.25 shows the geometrical specifications of the turbodrill stage model “B2”.

Table 3.6: Geometrical specifications for turbodrill stage models with 40 mm shroud diameter and blade height or span of 5 mm (B2 stage models).

Model	TE Pitch (S) (mm)	Chord Length (C) (mm)	Meridional Length (M) (mm)	Stagger Angle	Pitch Chord Ratio (S/C)
B2W20S11	5.49779	18.1945	15.0	34.5	0.302168
B2W20R23	5.49779	15.6499	15.0	-16.6	0.351299
B2W16S11	6.87223	18.1945	15.0	34.5	0.377710
B2W16R23	6.87223	15.6499	15.0	-16.6	0.439124
B2G20S61	5.49779	18.2331	15.0	34.6	0.301528
B2G20R15	5.49779	15.3237	15.0	-11.8	0.358778

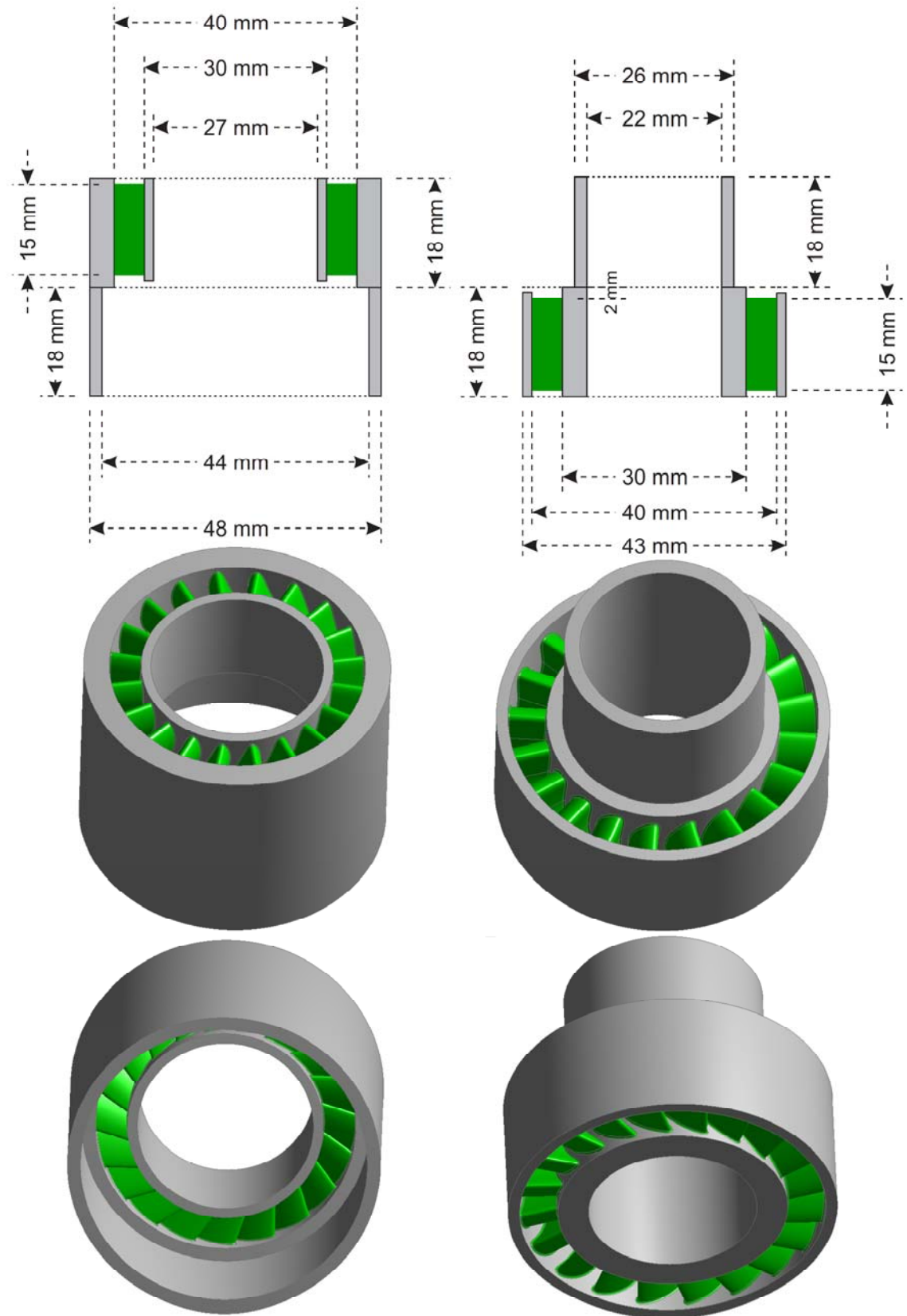


Figure 3.25 Geometrical specifications of the turbodrill stage model "B2".

### **3.7 Summary**

In this Chapter, the detailed design processes of the turbodrill as an axial turbomachine were presented. The amount of output power and rotation speed required, which in turn defines the turbine motor length, diameter and other specifications, is dependent to several drilling conditions and rock properties. Therefore, several small diameter turbodrill stage models were designed with specific blade configurations for the numerical simulation purposes. In the next Chapter, numerical simulation process and the theories of fluid flow analysis through turbodrill will be discussed in detail.

# 4

## Turbodrill fluid flow analysis

In the previous Chapter, basic design specifications for each turbodrill stage geometry models were reported with real design dimensions for the fluid flow simulation purposes. In this Chapter, with the objective of fluid flow analysis through turbine down hole motor, detailed numerical methodologies and equations of fluid dynamics related to this study are presented followed by quantification methodologies used for simulation accuracy and uncertainty assessments. Moreover, Fluid-Structural Interaction (FSI) is described as another main stage of numerical analysis of turbodrill performance and design optimization.

Conventionally assessment of turbine motors performance are carried out by conducting model experiments which are costly and time consuming for analysing several design alternatives and especially for design optimization. Recently, numerical simulations using Computational Fluid Dynamics (CFD) software applications has become a more cost effective tool for predicting detailed flow information through turbines (in general) to enable the selection of the best design. With the fast growth of the computational mechanics and techniques, the virtual hydraulic machines are becoming more and more realistic to get minor details of the fluid flow, which are not possible in model testing. The fluid flow in a hydraulic turbine motor is extremely complex, since it is generally turbulent, unsteady and three-dimensional (3D) in nature with strong effects from rotation and curvature. For a hydraulic turbine down hole motor the fluid flow analyses are the same as in other axial turbomachinery and the optimization of the hydraulic turbine needs huge computation and is a time consuming job.

### 4.1 Computational Fluid Dynamics

Computational Fluid Dynamics (CFD) is a computer-based numerical analysis tool for simulating the behaviour of systems involving fluid flow, heat transfer, and other related physical processes. It works by solving numerically the laws that govern the movement of fluids throughout a region of interest, with specified imposed initial and boundary conditions on that region. In this manner a set of partial differential equations

that describe the processes of mass, momentum and heat transfer which are known as the Navier–Stokes equations are solved numerically. These equations were derived in the early nineteenth century and have no known general analytical solution. Basic steps of any CFD simulations are defined as followings (Hirsch, 2007):

- Defining the mathematical model and the level of the approximation to the reality that is to be simulated.
- Discretization phase composing of space discretization defined by the grid generation and discretization of the equations, known as the numerical scheme.
- Analysis the numerical scheme for stability, accuracy and etc.
- Solving the numerical scheme, including choosing the most appropriate time integration method, convergence acceleration techniques and other resolution methods in related to the algebraic systems.
- Post-processing and data interpretation of numerical results.

The first step in CFD simulations is to define the physical properties and limitations of the accepted models that we want to simulate. Mathematical model based on fluid mechanics laws form a system of nonlinear partial differential equations are extremely complicated. Consequently, with the exception of Direct Numerical Simulation (DNS) of the Navier–Stokes equations, we need to define appropriate modelling assumptions and simplifications. It is worth mentioning here that sometimes discrepancies between CFD predictions and experiment results are not due to the errors in experimental or numerical data, but are due to the fact that the physical model assumed in the computations is not an adequate description of the real physics.

Once a mathematical model is defined, we start with the major process of a simulation known as the discretization process. The process of translating our geometrical and mathematical models into numbers to be recognized by computers is called discretization. The first step in discretization process is space discretization, including the geometries (fluid and solid bodies) present in the flow domain which is called a grid or a mesh. Grid generation is a major step in setting up a CFD analysis as the result of a CFD simulation and its accuracy can be extremely dependent on the grid properties and quality. It is accepted that the error of a numerical simulation has to tend to zero when the mesh size tends to zero. In general there are two types of mesh: structured and unstructured. Structured grids are formed by groups of lines (one for each space dimension), each mesh point locates at the intersection of one line of each line family and correspond to Cartesian grids in the mathematical space of the curvilinear

coordinates. In unstructured grids, the mesh point distribution is arbitrary since they are not fixed on identified lines and they can be connected through various polynomials in 2D or polyhedrals in 3D. In the second step of discretization process, after grid generation as the first step, we initiate discretization of the mathematical model equations. In this step because the mesh point values are the only quantities available to the computer, all mathematical formulas, such as partial derivatives of the various quantities, will have to be transformed into arithmetic operations on the mesh point values. The basis of all numerical methods is the transformation of the mathematical model into an algebraic, linear or nonlinear, system of equations for the mesh-related unknown quantities. By the end of this process, a set of algebraic relations between neighbouring mesh point values is obtained, one relation for each mesh point. These relations are called a numerical scheme.

The numerical scheme must satisfy a certain number of conditions to be accepted for the specified simulation purposes and subsequently it must be analysed to establish the associated level of accuracy for simulation results. The replacement of the continuum model by its discrete representation of algebraic system of equations will automatically generate errors as result of discretization process. The concepts of consistency, stability and convergence of a numerical scheme, including the quantitative evaluation of the errors associated to the selected scheme should be studied with great attention.

The next step in the CFD simulation process is solving the numerical scheme to obtain the mesh point values of the main flow variables. The solution algorithms depend on the type of problem we are analysing, i.e. time-dependent or steady flows. This will require numerical techniques either to solve a set of ordinary differential equations in time, or to solve an algebraic system. Consequently, a very important aspect in the definition of an algorithm is the choice to be made between a time-dependent or steady state model for the flow equations.

In the last step of CFD simulations, once the solution is obtained, we need to manipulate and interpret considerable amount of numerical data to analyse and understand the computed flow field. This can only be achieved through powerful visualization systems, which provide various software tools to study, qualitatively and quantitatively, the obtained results.

### 4.1.1 CFD software

In this study, for the fluid flow simulations through the turbine down hole motor, ANSYS® CFX 14.0 is utilised which is a general purpose Computational Fluid Dynamics (CFD) software suite that combines an advanced solver with powerful pre- and post-processing capabilities. ANSYS® CFX is capable of modelling (ANSYS®, 2011a):

- Steady-state and transient flows,
- Laminar and turbulent flows,
- Subsonic, transonic and supersonic flows,
- Heat transfer and thermal radiation,
- Buoyancy,
- Non-Newtonian flows,
- Transport of non-reacting scalar components,
- Multiphase flows,
- Combustion,
- Flows in multiple frames of reference,
- Particle tracking.

There are three distinct methods of numerical solution techniques: Finite Difference (FD), Finite Element (FE) and spectral methods (Versteeg and Malalasekera, 2007). The most common, and the one on which CFX is based, is known as the Finite Volume Method (FVM) which is a special finite difference formulation that is central to the most well-established CFD codes. In this technique, the region of interest is divided into small sub-regions, called control volumes. The control volumes are formed around mesh element nodes shown in Figure 4.1. The equations are discretised utilizing finite element shape functions and solved iteratively for each control volume. As a result, an approximation of the value of each variable at specific points throughout the domain can be obtained. In this way a full picture of the fluid flow behaviour can be derived.

The FVM is based on cell-averaged values, which is a most fundamental quantity in CFD tools. This distinguishes the FVM from the finite difference and finite element methods, where local function values at the mesh points are the main numerical quantities. The FVM has the great advantage that the conservative discretization is automatically satisfied, through the direct discretization of the integral form of the conservation laws.

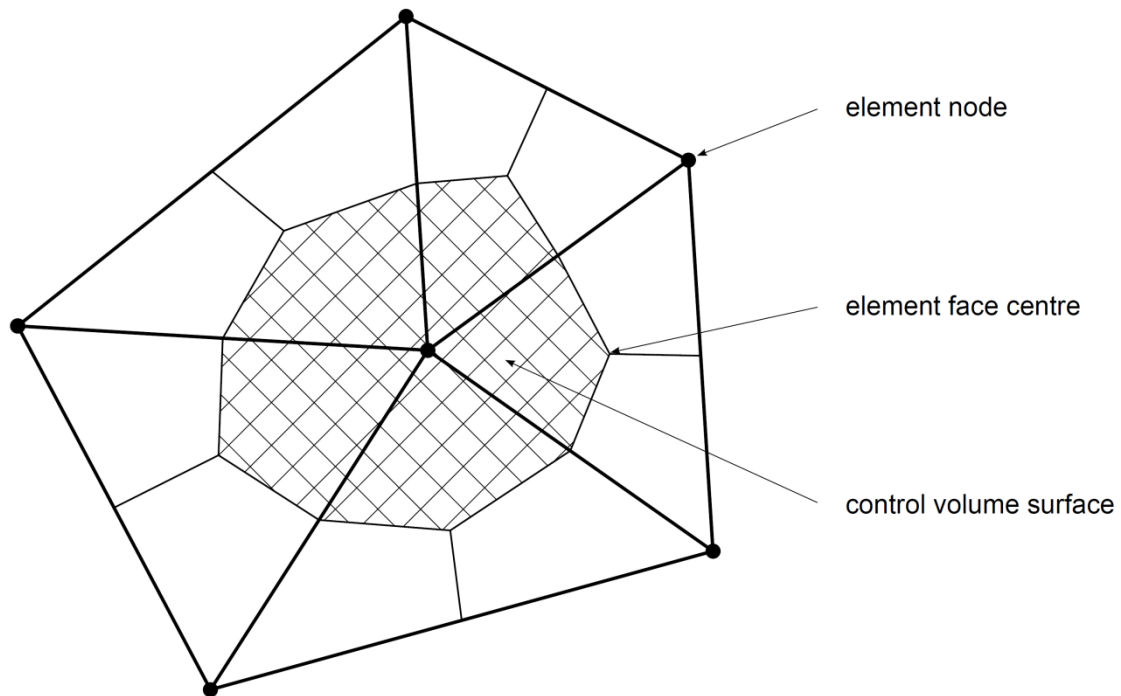


Figure 4.1 2D Mesh element and control volume surface (ANSYS®, 2011b).

## 4.2 Basic equations of fluid dynamics

Fluid dynamics is the study of the behaviour of averaged quantities and properties of a large number of interacting fluid elements. An essential step in fluid dynamics is therefore the averaging process. The governing equations of fluid mechanics represent mathematical statements of the conservation laws of physics. Conservation law states that the variation of the total amount of a quantity  $U$  inside a given domain is equal to the balance between the amount of that quantity entering and leaving the considered domain, plus the contributions from the sources generating that quantity (Hirsch, 2007).

The basic equations of fluid flow are three conservation laws:

1. Conservation of mass (continuity),
2. Conservation of momentum (Newton's second law, equation of motion),
3. Conservation of energy (first law of thermodynamics).

When the equations of conservation laws are applied to a viscous fluid, the set of these equations are known as the Navier–Stokes equations, while they are known as the Euler equations when applied to a perfect, inviscid fluid (Hirsch, 2007).

### 4.2.1 Conservation of mass

The mass of a fluid is conserved. The conservation of mass for a compressible fluid can be stated as:

$$\frac{\partial \rho}{\partial t} + \nabla \cdot (\rho \mathbf{u}) = 0. \quad (4.1)$$

The first term on the left hand side is the rate of change in time of the density (mass per unit volume). The second term describes the net mass flow across the element boundaries and is called the convective term. Divergence ( $\nabla$ ) is a vector operator that measures the magnitude of a vector field's source or sink at a given point, and represents the volume density of the outward flux of a vector field from an infinitesimal volume around a given point. It is defined as following:

$$\nabla \cdot \mathbf{v} = \frac{\partial}{\partial x} + \frac{\partial}{\partial y} + \frac{\partial}{\partial z}. \quad (4.2)$$

For an incompressible fluid (i.e. water) the density  $\rho$  is constant and Equation (4.1) simplifies to:

$$\nabla \cdot \mathbf{u} = 0. \quad (4.3)$$

#### 4.2.2 Conservation of momentum

Momentum is a vector quantity defined as the product of mass and velocity, and when expressed per volume unit, becomes the product of density and velocity. In fluid dynamics we distinguish two types of forces on fluid particles:

- Surface forces (ex. pressure force, viscous force),
- Body forces (ex. gravity force, centrifugal force, Coriolis force, electromagnetic force).

The contributions due to the surface forces is highlighted as separate terms in the momentum equation and the effects of body forces is defined and added as source terms ( $S_M$ ). The momentum and energy conservation laws make statements regarding changes of fluid properties as a function of the fluid particle position ( $x, y, z$ ) and time  $t$ . If a property per unit mass be denoted by  $\phi$ , the total derivative of  $\phi$  with respect to time following a fluid particle, written as  $D\phi/Dt$ , is:

$$\frac{D\phi}{Dt} = \frac{\partial \phi}{\partial t} + \frac{\partial \phi}{\partial x} \frac{dx}{dt} + \frac{\partial \phi}{\partial y} \frac{dy}{dt} + \frac{\partial \phi}{\partial z} \frac{dz}{dt}, \quad (4.4)$$

$$\frac{D\phi}{Dt} = \frac{\partial \phi}{\partial t} + u \frac{\partial \phi}{\partial x} + v \frac{\partial \phi}{\partial y} + w \frac{\partial \phi}{\partial z} = \frac{\partial \phi}{\partial t} + \mathbf{u} \cdot \nabla \phi. \quad (4.5)$$

$D\phi/Dt$  is the rate of change of property  $\phi$  per unit mass. The rate of change of property  $\phi$  per unit volume for a fluid particle is given by the product of  $D\phi/Dt$  and density  $\rho$ , hence:

$$\rho \frac{D\phi}{Dt} = \rho \left( \frac{\partial \phi}{\partial t} + \mathbf{u} \cdot \nabla \phi \right). \quad (4.6)$$

Newton's second law states that the rate of change of momentum of a system is equal to the sum of the forces on the system. For a fluid system, this can be stated as:

$$\rho \frac{D\mathbf{u}}{Dt} = \nabla \cdot \tau_{ij}, \quad (4.7)$$

where the left hand side of the equation uses the particle derivative which is defined as:

$$\frac{D}{Dt} = \frac{\partial}{\partial t} + (\mathbf{u} \cdot \nabla). \quad (4.8)$$

On the right hand side, the stress tensor  $\tau_{ij}$  on the right hand side can be split into pressure and viscous terms:

$$\tau_{ij} = -p\delta_{ij} + \tau_{ij}^v, \quad (4.9)$$

where,  $\delta_{ij}$  is the Kronecker delta function ( $\delta_{ij}=1$  if  $i=j$  and  $\delta_{ij}=0$  if  $i \neq j$ ). As a result, it becomes:

$$\rho \frac{D\mathbf{u}}{Dt} = -\nabla p + \nabla \cdot \tau_{ij}^v. \quad (4.10)$$

In the Newtonian fluids the viscous stresses are linearly related to the strain rates, and then the following deformation law may be derived, as first given by Stokes in 1845:

$$\tau_{ij} = -p\delta_{ij} + \mu \left( \frac{\partial u_i}{\partial x_j} + \frac{\partial u_j}{\partial x_i} \right) + \delta_{ij}\lambda \nabla \cdot \mathbf{u}, \quad (4.11)$$

$$\rho \frac{D\mathbf{u}}{Dt} = -\nabla p + \frac{\partial}{\partial x_j} \left[ \mu \left( \frac{\partial u_i}{\partial x_j} + \frac{\partial u_j}{\partial x_i} \right) + \delta_{ij}\lambda \nabla \cdot \mathbf{u} \right]. \quad (4.12)$$

The coefficient of bulk viscosity ( $\lambda$ ) is often assumed to be related to the viscosity by following Stokes' hypothesis (1845):

$$\lambda + \frac{2}{3}\mu = 0. \quad (4.13)$$

The term ( $\delta_{ij} \lambda \nabla \cdot \mathbf{u}$ ) is not included by default in the CFX solver (ANSYS<sup>®</sup>, 2011b). If we assume that both density and viscosity are constant we arrive at the much simpler equation:

$$\rho \frac{D\mathbf{u}}{Dt} = -\nabla p + \mu \nabla^2 \mathbf{u}. \quad (4.14)$$

The Laplacian vector operator used here is defined as:

$$\nabla^2 \mathbf{u} = \nabla(\nabla \cdot \mathbf{u}) - \nabla \times (\nabla \times \mathbf{u}). \quad (4.15)$$

In Cartesian coordinates this reduces to:

$$\nabla^2 \mathbf{u} = \nabla^2 u \mathbf{i} + \nabla^2 v \mathbf{j} + \nabla^2 w \mathbf{k}. \quad (4.16)$$

For the case of incompressible fluids or compressible fluid flow under isothermal conditions, equation of motion (4.14) coupled with the continuity equation (4.3), may be solved for the velocity and pressure. If the temperature field is required to be solved, i.e. where the density and/or the viscosity is related to the temperature, then the energy equation (described in the next section) should be solved with the mass and momentum equations.

### 4.2.3 Conservation of energy

The first law of thermodynamics states that the rate of energy change of a system is equal to the rate of heat addition to the system plus the rate of work done on the system. The rate of work done on the fluid system by a surface force is equal to the product of the force and velocity component in the direction of the force. It can be stated as:

$$-\nabla \cdot (\rho \mathbf{u}) + \frac{\partial (u_i \tau_{ij}^v)}{\partial x_j}. \quad (4.17)$$

Energy flux due to heat conduction has three components:  $q_x$ ,  $q_y$  and  $q_z$ . The total rate of heat added to the fluid particle per unit volume due to heat flow across its boundaries is:

$$-\frac{\partial q_x}{\partial x} - \frac{\partial q_y}{\partial y} - \frac{\partial q_z}{\partial z} = -\operatorname{div} \mathbf{q}. \quad (4.18)$$

Fourier's law of heat conduction relates the heat flux to the local temperature gradient. As a result, the heat vector components are defined as:

$$q_x = -k \frac{\partial T}{\partial x} \quad q_y = -k \frac{\partial T}{\partial y} \quad q_z = -k \frac{\partial T}{\partial z}. \quad (4.19)$$

where  $T$  is the absolute temperature, and  $k$  is the thermal conductivity coefficient. This can be written in vector form as follows:

$$\mathbf{q} = -k \operatorname{grad} T. \quad (4.20)$$

Also we have, according to the following definition:

$$k = \rho c_p \kappa = \mu c_p / \operatorname{Pr}, \quad (4.21)$$

where  $\kappa$  is the diffusivity coefficient, and  $\operatorname{Pr}$  is the Prandtl number. It also can be stated as:

$$\operatorname{Pr} = \nu / \kappa = \mu c_p / k. \quad (4.22)$$

Combining together yields the final form of the heat addition rate to the fluid particle due to heat conduction across element boundaries:

$$-\operatorname{div} \mathbf{q} = \operatorname{div}(k \operatorname{grad} T). \quad (4.23)$$

Finally for a fluid system the energy equation can be stated mathematically as:

$$\rho \frac{DE}{Dt} = \nabla \cdot (k \nabla T) - \nabla \cdot (\rho \mathbf{u}) + \frac{\partial (u_i \tau_{ij}^v)}{\partial x_j} + S_E, \quad (4.24)$$

where  $E$  is the specific energy (total energy) of a fluid. As used here, this is the sum of the internal (thermal) energy  $e$  and the kinetic energy ( $\frac{1}{2} u_i u_i$ ) i.e.  $E = e + \frac{1}{2} u_i u_i$ . Equation (4.24) also incorporates Fourier's law for the heat conduction term.

In CFX, the energy conservation equation is used in either of two alternative forms: as the 'total energy' equation (actually the total enthalpy) or the thermal energy equation. First the total enthalpy equation is considered by taking the definitions of the static and total enthalpy:

$$h = e + \frac{P}{\rho}, \quad (4.25)$$

$$h_0 = h + \frac{1}{2} (u_i u_i). \quad (4.26)$$

and the definition of the specific energy  $E$ , it results at:

$$h_0 = E + \frac{P}{\rho}. \quad (4.27)$$

Substitution of equation (4.27) inside equation (4.24) yields after some rearrangement the total energy (total enthalpy) equation:

$$\frac{\partial(\rho h_0)}{\partial t} + \nabla \cdot (\rho h_0 \mathbf{u}) = \nabla \cdot (k \nabla T) + \frac{\partial p}{\partial t} + \frac{\partial(u_i \tau_{ij}^v)}{\partial x_j} + S_h. \quad (4.28)$$

The thermal energy equation is derived as a kinetic energy equation resulted from the energy equation (4.24). This kinetic energy equation is found by taking the scalar product of the velocity and the momentum equation to give:

$$\rho \frac{D}{Dt} \left[ \frac{1}{2} (u_i u_i) \right] = -\mathbf{u} \cdot \nabla p + \mathbf{u} \cdot \nabla \cdot \tau_{ij}^v. \quad (4.29)$$

Subtracting above equation from equation (4.24) yields the thermal energy equation as following:

$$\rho \frac{De}{Dt} = \nabla \cdot (k \nabla T) - p \nabla \cdot \mathbf{u} + \tau_{ij}^v \frac{\partial u_i}{\partial x_j} + S_e. \quad (4.30)$$

In CFX the term ( $p \nabla \cdot \mathbf{u}$ ) is neglected which will be non-zero in variable density flows. Different results will thus produce from use of the thermal energy equation versus the total enthalpy equation. The CFX-Solver Theory Guide suggests use of the thermal energy equation for low speed flows where compressibility effects are minimal. It is also suggested for cases where the total enthalpy equation may experience robustness issues due to the pressure transient and the  $p/\rho$  contribution to enthalpy.

#### 4.2.4 Convection–Diffusion form of a conservation law

In the conservation laws, the amount of the quantity which is crossing the boundary surface is called the flux and its expression results from the mechanical and thermodynamic properties of the fluid. The fluxes are vectors for a scalar quantity and tensors for a vector quantity like momentum. They are generated from two contributions: one due to the convective transport of the fluid and another due to the molecular agitation, which can be present even when the fluid is at rest. The first contribution, which is always present, is the convective flux ( $\vec{F}_c$ ), attached to the quantity  $U$  in a flow of velocity ( $\mathbf{u}$ ). It represents the amount of  $U$  that is carried away or transported by the flow and is defined as (Hirsch, 2007):

$$\vec{F}_C = U \mathbf{u} . \quad (4.31)$$

A convective flux cannot provide a contribution in a direction transverse or opposite to the flow direction, and it appears in the conservation law as a first order partial derivative term. The local contribution of the convective flux through a surface element  $d\vec{S}$ ,  $(\vec{F}_C \cdot d\vec{S})$  has an important physical significance (Hirsch, 2007). For  $U=\rho$  (fluid density), it is equal to the local mass flow rate, where the mass flow rate is known by  $\dot{m}$ :

$$\rho \mathbf{u} \cdot d\vec{S} = d\dot{m} . \quad (4.32)$$

This quantity represents the amount of mass flowing through the surface  $dS$ , per unit of time, and is expressed in kg/s. The second contribution is a diffusive flux  $\vec{F}_D$ , defined as the contribution present in fluids at rest, due to the macroscopic effect of the molecular thermal agitation. Diffusive fluxes do not always exist; and in a single-phase fluid at rest, no diffusion of specific mass is possible. Therefore, there will be no diffusive flux contribution to the mass conservation equation. The diffusive flux is expressed as (Hirsch, 2007):

$$\vec{F}_D = -\kappa \rho \vec{\nabla} u , \quad (4.33)$$

where  $\kappa$  is the diffusivity coefficient and has units of  $\text{m}^2/\text{s}$  for any quantity. The diffusion effects appear in the conservation law as a second order partial derivative term.

### 4.3 Navier–Stokes equations for a Newtonian fluid

The most useful forms of the conservation equations are obtained by introducing a suitable model for the viscous stresses  $\tau_{ij}$ . In a Newtonian fluid the viscous stresses are proportional to the rates of deformation. In three-dimensional flows the local rate of deformation is composed of the linear deformation rate and the volumetric deformation rate. The three-dimensional form of Newton's law of viscosity for compressible flows involves two constants of proportionality: the first (dynamic) viscosity,  $\mu$ , to relate stresses to linear deformations, and the second viscosity,  $\lambda$ , to relate stresses to the volumetric deformation. The six viscous stress components, out of nine, are independent and are expressed as (Hirsch, 2007):

$$\begin{aligned}\tau_{xx} &= 2\mu \frac{\partial u}{\partial x} + \lambda \operatorname{div} \mathbf{u} & \tau_{yy} &= 2\mu \frac{\partial v}{\partial y} + \lambda \operatorname{div} \mathbf{u} & \tau_{zz} &= 2\mu \frac{\partial w}{\partial z} + \lambda \operatorname{div} \mathbf{u} \\ \tau_{xy} = \tau_{yx} &= \mu \left( \frac{\partial u}{\partial y} + \frac{\partial v}{\partial x} \right) & \tau_{xz} = \tau_{zx} &= \mu \left( \frac{\partial u}{\partial z} + \frac{\partial w}{\partial x} \right) & \tau_{yz} = \tau_{zy} &= \mu \left( \frac{\partial v}{\partial z} + \frac{\partial w}{\partial y} \right)\end{aligned}\quad (4.34)$$

Liquids are incompressible so the mass conservation equation is  $\operatorname{div} \mathbf{u} = 0$  and the viscous stresses are defined as twice the local rate of linear deformation times the dynamic viscosity. Substitution of the derived shear stresses into conservation equation yields the so-called Navier–Stokes equations, named after the two nineteenth-century scientists who derived them independently, and can be written in the most useful form for the development of the finite volume method as following (Hirsch, 2007):

$$\rho \frac{Du}{Dt} = -\frac{\partial p}{\partial x} + \operatorname{div}(\mu \operatorname{grad} u) + S_{Mx}, \quad (4.35)$$

$$\rho \frac{Dv}{Dt} = -\frac{\partial p}{\partial y} + \operatorname{div}(\mu \operatorname{grad} v) + S_{My}, \quad (4.36)$$

$$\rho \frac{Dw}{Dt} = -\frac{\partial p}{\partial z} + \operatorname{div}(\mu \operatorname{grad} w) + S_{Mz}. \quad (4.37)$$

If we introduce a general variable  $\phi$  the conservative form of all fluid flow equations can usefully be written in the following form (Hirsch, 2007):

$$\frac{\partial(\rho\phi)}{\partial t} + \operatorname{div}(\rho\phi\mathbf{u}) = \operatorname{div}(\Gamma \operatorname{grad} \phi) + S_\phi. \quad (4.38)$$

This equation is the transport equation for property  $\phi$ . It highlights the various transport processes: the rate of change term and the convective term on the left hand side and the diffusive term ( $\Gamma$  = diffusion coefficient) and the source term respectively on the right hand side. This equation is used as the starting point in the finite volume method. By setting  $\phi$  equal to 1,  $u$ ,  $v$ ,  $w$  and  $e$  and selecting appropriate values for diffusion coefficient  $\Gamma$  and source terms, we obtain special forms of PDEs for mass, momentum and energy conservation.

## 4.4 Iterative solution method

The system of Navier–Stokes equations, expressing the conservation of the three fundamental quantities, mass, momentum and energy, contain many levels of complexity. They form a system of five (in 3D space) fully coupled nonlinear time-dependent partial differential equations for the five unknowns, velocity vector (three unknowns), and two thermodynamic quantities, such as for example pressure and

density, or pressure and temperature. These complexities in fluid dynamics introduce considerable challenges for CFD simulations, in particular for turbulent flows. The linear system of equations described in the previous sections could in principle be solved using a direct method such as Gaussian elimination. This forms the basis of the growing development of Direct Numerical Simulation (DNS) which are computationally far too expensive. The computer requirements for DNS simulations of turbulent flows are out of reach in the foreseeable future for industrial applications. Therefore iterative methods are needed to be used. The highest approximation, with good prospects for reaching the industrial stage in the near future is the approximation known as Large Eddy Simulation (LES). This LES approach is similar to DNS, in its objective to simulate directly the turbulent fluctuations, but restricted to the larger scales with the smaller scales being modelled.

The iterative methods are well suited to the solution of the discretised mass and momentum equations. The basis of iterative methods is to perform a small number of operations on the matrix elements of the algebraic system in an iterative way, with the aim of approaching the exact solution, within a pre-set accuracy, in a finite number of iterations.

The most efficient of the iterative techniques is the Multi-grid Method (Hirsch, 2007). It is the most general method available to obtain fast convergence rates. CFX uses a multi-grid accelerated Incomplete Lower Upper (ILU) factorization technique to solve the linear equation system (ANSYS<sup>®</sup>, 2011b). The multi-grid method involves the use of solutions on a series of coarser grids to speed up the solution on the original (fine) grid.

Many discrete approximations developed for CFD are based on series expansion approximations of continuous functions (such as the Taylor series). The order of accuracy of the approximation is determined by the exponent on the mesh spacing or time step factor of the largest term in the truncated part of the series expansion, which is the first term excluded from the approximation (Hirsch, 2007). Increasing the order-accuracy of an approximation generally causes that errors are reduced more quickly with mesh or time step size refinement. Unfortunately, in addition to increasing the computational expenses, high-order approximations are generally less robust (that is, less numerically stable) than their low-order counterparts (Hirsch, 2007). CFX uses second order accurate approximations as much as possible.

One of the most significant approximations that must be made in order to use CFD and to solve the Navier–Stokes equations for turbomachinery flows is a time averaging technique called Reynolds Averaging. Without this approximation, the computational resources needed to directly simulate the Navier–Stokes equations for turbomachinery are only available at large supercomputing facilities (Hirsch, 2007). The Reynolds Averaged Navier–Stokes (RANS) model is restricted to the computation of the averaged turbulent flow. This needs the RANS equations to be supplemented by models for the Reynolds stresses. These models can range from simple eddy viscosity or mixing length models to transport equations for the turbulent kinetic energy and dissipation rates.

## 4.5 Reynolds-Averaged Navier–Stokes equations

In the classical approaches of turbulence modelling we substitute the Reynolds decomposition for each of the relevant flow variables into the (instantaneous) conservations equations, followed by time-averaging of the equations. This splits the instantaneous value of a flow variable - into the sum of a steady mean component  $\Phi$  and a time varying fluctuating component  $\phi'$  with zero mean value. To derive the time-averaged mass and momentum equations for an incompressible fluid with constant viscosity we first substitute (Hirsch, 2007):

$$\phi = \Phi + \phi', \quad (4.39)$$

$$\rho \frac{D\mathbf{u}}{Dt} = -\nabla p + \nabla \cdot \tau_{ij}, \quad (4.40)$$

$$\tau_{ij} = \mu \left( \frac{\partial U_i}{\partial x_j} + \frac{\partial U_j}{\partial x_i} \right) - \rho \overline{u'_i u'_j}. \quad (4.41)$$

In principle, the Navier–Stokes equations describe both laminar and turbulent flows without the need for additional information. However, turbulent flows at realistic Reynolds numbers produce a large range of turbulent length and time scales, and involve length scales much smaller than the smallest finite volume mesh, which used in a numerical analysis. The Reynolds Averaged Navier–Stokes (RANS) equations, on the other hand, represent the mean flow quantities only, while modelling turbulence effects without a need for the resolution of the turbulent fluctuations. Turbulence models based on the RANS equations are known as Statistical Turbulence models due to the statistical averaging procedure employed to obtain the equations (Hirsch, 2007). The averaging procedure introduces additional unknown terms containing products of the fluctuating

quantities, which act like additional stresses in the fluid. These terms, called ‘turbulent’ or ‘Reynolds’ stresses, are difficult to determine directly and so become further unknowns. Therefore unlike the Navier–Stokes equations for incompressible flow which are close and consist of four equations for four unknowns, the RANS equations are not closed due to the addition of six unknowns in the form of the Reynolds stresses. Two approaches exist to develop a closed system of equations (Hirsch, 2007). First, the Reynolds stresses may be related to the mean flow gradients and this is called eddy viscosity models. Second, we develop conservation equations for the Reynolds stresses, involving further conservation equations for additional variables, which are called Reynolds stress equation models. As a result, The Reynolds (turbulent) stresses need to be modelled by additional equations of known quantities in order to achieve “closure”. Closure means that there are a sufficient number of equations for all the unknowns, including the Reynolds-Stress tensor resulting from the averaging procedure (Hirsch, 2007). The equations used to close the system define the type of turbulence model. The most common RANS turbulence models are classified on the basis of the number of additional transport equations that need to be solved along with the RANS flow equations.

## 4.6 Turbulence models

Turbulence consists of fluctuations in the flow field in time and space. All flows become unstable above a certain Reynolds number (which is equal to  $UL/v$  where  $U$  and  $L$  are characteristic velocity and length scales of the mean flow and  $v$  is the kinematic viscosity). At low Reynolds numbers flows are laminar. At higher Reynolds numbers flows become turbulent. It is a complex process, mainly because it is three dimensional, unsteady, unpredictable and consists of many scales. It can have a significant effect on the characteristics of the flow. Turbulence occurs when the inertia forces in the fluid become significant compared to viscous forces, and is characterized by a high Reynolds Number. Rotational flow structures termed ‘eddies’ are readily observable in turbulent flow. For transient flows, the equations are ensemble-averaged. This allows the averaged equations to be solved for transient simulations as well (ANSYS<sup>®</sup>, 2011b). The resulting equations are sometimes called URANS (Unsteady Reynolds Averaged Navier–Stokes equations).

CFX turbulence models can be broadly divided into two classes based on the RANS equations: eddy viscosity models ( $k-\varepsilon$ ,  $k-\omega$  and SST) and Reynolds stress

models. CFX also provides the Large Eddy Simulation (LES) and Detached Eddy Simulation (DES) turbulence models, which are not based on the RANS equations.

In this study, only the eddy viscosity turbulence models are used. Eddy viscosity models suggests that turbulence consists of small eddies which are continuously forming and dissipating, and in which the Reynolds stresses are assumed to be proportional to mean velocity gradients, expressed as following (ANSYS®, 2011b):

$$-\rho \overline{u'_i u'_j} = \mu_t \left( \frac{\partial U_i}{\partial x_j} + \frac{\partial U_j}{\partial x_i} \right) - \frac{2}{3} \delta_{ij} \left( \rho k + \mu_t \frac{\partial U_k}{\partial x_k} \right), \quad (4.42)$$

where,  $\mu_t$  = is the eddy viscosity or turbulent viscosity,  $k$  = turbulent kinetic energy which is defined as:

$$k = \frac{1}{2} \overline{u'_i u'_j}. \quad (4.43)$$

Similar to the eddy viscosity hypothesis is the eddy diffusivity hypothesis in which the Reynolds fluxes of a scalar are linearly related to the mean scalar gradient, expressed as following (ANSYS®, 2011b):

$$-\rho \overline{u_i \phi} = \Gamma_t \frac{\partial \Phi}{\partial x_i}, \quad (4.44)$$

where,  $\Gamma_t$  is the eddy diffusivity and has to be prescribed. The eddy diffusivity can be written as:

$$\Gamma_t = \frac{\mu_t}{Pr_t}, \quad (4.45)$$

where  $Pr_t$  is the turbulent Prandtl number. Eddy diffusivities are then prescribed using the turbulent Prandtl number.

Standard mathematical descriptions of turbulence begin with the concept of the Reynolds decomposition (i.e. for velocity  $u(t)=U+u'(t)$ ), in which  $U$  is a steady mean component defined as following:

$$U = \frac{1}{\Delta t} \int_0^{\Delta t} u(t) dt, \quad (4.46)$$

One-half of the sum of the variances of the fluctuating velocity components is defined as the turbulent kinetic energy per unit mass, as following (ANSYS®, 2011b):

$$k = \frac{1}{2} (\overline{u'^2} + \overline{v'^2} + \overline{w'^2}), \quad (4.47)$$

It has dimensions of ( $L^2 T^{-2}$ ); for example,  $m^2/s^2$ . The turbulence eddy dissipation ( $\varepsilon$ ) is the rate at which the velocity fluctuations dissipate, and has dimensions of  $k$  per unit time ( $L^2 T^{-3}$ ); for example,  $m^2/s^3$ .

#### 4.6.1 Boussinesq approximation

Eddy viscosity turbulence models such as the mixing length,  $k-\varepsilon$  and  $k-\omega$  models begin with Boussinesq's assumption (1877) that the Reynolds stresses are proportional to the mean flow gradients, expressed as following (ANSYS®, 2011b):

$$\tau'_{ij} = -\rho \overline{u'_i u'_j} = \mu_t \left( \frac{\partial U_i}{\partial x_j} + \frac{\partial U_j}{\partial x_i} \right) - \frac{2}{3} \rho k \delta_{ij}. \quad (4.48)$$

In the CFX the term  $\frac{2}{3} \rho k \delta_{ij}$  is not included by default in the momentum equation expressed as following (ANSYS®, 2011b):

$$\rho \frac{D\mathbf{u}}{Dt} = -\nabla p + \frac{\partial}{\partial x_j} \left[ \mu_{eff} \left( \frac{\partial u_i}{\partial x_j} + \frac{\partial u_j}{\partial x_i} \right) \right], \quad (4.49)$$

where the effective viscosity is the sum of molecular and turbulent viscosities:  $\mu_{eff} = \mu + \mu_t$ .

#### 4.6.2 The $k$ -epsilon turbulence model

The  $k-\varepsilon$  model is termed a two-equation turbulence model as it involves the solution of conservation equations for the two turbulence quantities, i.e.  $k$  and  $\varepsilon$ . The  $k-\varepsilon$  model is the most widely used and validated turbulence model. The model performs particularly well in confined flows where the Reynolds shear stresses are most important. The instantaneous kinetic energy  $k(t)$  of a turbulent flow is the sum of the mean kinetic energy  $K=1/2 (U^2 + V^2 + W^2)$  and the turbulent kinetic energy is defined as:

$k = \frac{1}{2} (\overline{u'^2} + \overline{v'^2} + \overline{w'^2})$ . An equation for the mean kinetic energy  $K$  can be obtained as (ANSYS®, 2011b):

$$\frac{\partial(\rho K)}{\partial t} + \operatorname{div}(\rho K \mathbf{U}) = \operatorname{div}(-P \mathbf{U} + 2\mu \mathbf{U} \mathbf{S}_{ij} - \rho \mathbf{U} \overline{u'_i u'_i}) - 2\mu S_{ij} \cdot S_{ij} + \rho \overline{u'_i u'_i} \cdot S_{ij}, \quad (4.50)$$

where  $S_{ij}$  is the deformation tensor. Another equation for the turbulent kinetic energy  $K$  can be obtained by multiplication of each of the instantaneous Navier–Stokes equations by the appropriate fluctuating velocity components, expressed as (ANSYS®, 2011b):

$$\frac{\partial(\rho k)}{\partial t} + \operatorname{div}(\rho k \mathbf{U}) = \operatorname{div}\left(-\overline{p' \mathbf{u}'} + 2\mu \overline{\mathbf{u}' s'_{ij}} - \rho \frac{1}{2} \overline{u'_i \cdot u'_j u'_j} - 2\mu \overline{s'_{ij} \cdot s'_{ij}} - \rho \overline{u'_i u'_i} \cdot S_{ij}\right). \quad (4.51)$$

These equations look very similar in many aspects; however, the appearance of primed quantities on the right hand side of the  $k$ –equation shows that changes to the turbulent kinetic energy are mainly governed by turbulent interactions (ANSYS®, 2011b).

The dissipation of turbulent kinetic energy is caused by work done by the smallest eddies against viscous stresses. The rate of dissipation per unit volume is normally written as the product of the density  $\rho$  and the rate of dissipation of turbulent kinetic energy per unit mass defined as  $\varepsilon$ , and expressed as (ANSYS®, 2011b):

$$\varepsilon = 2\nu \overline{s'_{ij} \cdot s'_{ij}}. \quad (4.52)$$

The dimensions of  $\varepsilon$  are  $m^2/s^3$ . This quantity is of vital importance in the study of turbulence dynamics. We use  $k$  and  $\varepsilon$  to define velocity scale  $\vartheta$  and length scale  $l$  representative of the large-scale turbulence as follows (ANSYS®, 2011b):

$$\vartheta = k^{1/2}, \quad l = \frac{k^{3/2}}{\varepsilon}, \quad (4.53)$$

The standard  $k$ – $\varepsilon$  model uses the following transport equations for  $k$  and  $\varepsilon$  (ANSYS®, 2011b):

$$\frac{\partial(\rho k)}{\partial t} + \operatorname{div}(\rho k \mathbf{U}) = \operatorname{div}\left[\frac{\mu_t}{\sigma_k} \operatorname{grad} k\right] + 2\mu_t S_{ij} \cdot S_{ij} - \rho \varepsilon, \quad (4.54)$$

$$\frac{\partial(\rho \varepsilon)}{\partial t} + \operatorname{div}(\rho \varepsilon \mathbf{U}) = \operatorname{div}\left[\frac{\mu_t}{\sigma_\varepsilon} \operatorname{grad} \varepsilon\right] + C_{\varepsilon 1} \frac{\varepsilon}{k} 2\mu_t S_{ij} \cdot S_{ij} - C_{\varepsilon 2} \rho \frac{\varepsilon^2}{k}. \quad (4.55)$$

In words the equations are described as:

Rate of change of	+	Transport of $k$ or $\varepsilon$ by convection	=	Transport of $k$ or $\varepsilon$ by diffusion	+	Rate of production of $k$ or $\varepsilon$	-	Rate of destruction of $k$ or $\varepsilon$
----------------------	---	---	---	--	---	--	---	---

This is the standard  $k$ – $\varepsilon$  turbulence model. In the CFX solver a slightly modified version is used as following (ANSYS®, 2011b):

$$\mu_t = \rho C_\mu \frac{k^2}{\varepsilon}, \quad (4.56)$$

$$\frac{\partial(\rho k)}{\partial t} + \nabla \cdot (\rho k \mathbf{U}) = \nabla \cdot \left[ \left( \mu + \frac{\mu_t}{\sigma_k} \right) \nabla k \right] + P - \rho \varepsilon, \quad (4.57)$$

$$\frac{\partial(\rho \varepsilon)}{\partial t} + \nabla \cdot (\rho \varepsilon \mathbf{U}) = \nabla \cdot \left[ \left( \mu + \frac{\mu_t}{\sigma_\varepsilon} \right) \nabla \varepsilon \right] + C_{\varepsilon 1} \frac{\varepsilon}{k} P - C_{\varepsilon 2} \rho \frac{\varepsilon^2}{k}, \quad (4.58)$$

$$C_\mu = 0.09, \quad \sigma_k = 1.0, \quad \sigma_\varepsilon = 1.3, \quad C_{\varepsilon 1} = 1.44, \quad C_{\varepsilon 2} = 1.92, \quad (4.59)$$

Where  $P$  is the rate of production of turbulent kinetic energy, defined as (ANSYS®, 2011b):

$$P = 2\mu_t S_{ij} \cdot S_{ij} - \frac{2}{3}(3\mu_t \nabla \cdot \mathbf{U} + \rho k) \nabla \cdot \mathbf{U}. \quad (4.60)$$

Here, the molecular viscosity is included in the gradient-diffusion term in both the  $k$ - and  $\varepsilon$ -equations. This modification is usually made to allow the  $k-\varepsilon$  model to be applied at grid points within the viscous sub-layer of the boundary layers. However, wall damping functions must also be added to the model to allow its use in the viscous sub-layer. Therefore  $k-\varepsilon$  model can only be used in CFX in conjunction with wall functions. Within CFX, the  $k-\varepsilon$  turbulence model uses the scalable wall function approach to improve robustness and accuracy when the near-wall mesh is very fine. The scalable wall functions allow solution on arbitrarily fine near wall grids, which is a significant improvement over standard wall functions. The standard  $k-\varepsilon$  model assessment is provided as following (ANSYS®, 2011b):

Advantages:

- Simplest turbulence model for which only initial and/or boundary conditions need to be supplied,
- Acceptable performance for many industrially applications,
- Well established, the most widely validated turbulence model,

Disadvantages:

- More expensive to implement than mixing length model (two extra PDEs),
- The  $k-\varepsilon$  model predicts excessive levels of turbulent shear stress, particularly in the presence of adverse pressure gradients leading to suppression of separation on curved walls,

- Poor performance in a variety of important cases such as: unconfined flows, flows with large extra strains, rotating flows and flows driven by anisotropy of normal Reynolds stresses.

#### 4.6.3 Wilcox $k$ -omega turbulence model

Among many two-equation turbulent models proposed, most of them use  $k$  as one of the variables, but choice of the second variable is more diverse. Next to  $\varepsilon$ , the most prominent is omega ( $\omega$ ), or the dissipation per unit kinetic energy, often called the turbulence frequency. It is defined as  $\omega = \varepsilon / (\beta^* k)$  where  $\beta^*$  is a constant (ANSYS®, 2011b).

In the  $k$ - $\varepsilon$  model the kinematic eddy viscosity  $\nu_t$  is expressed as the product of a velocity scale  $\vartheta = k^{1/2}$  and a length scale  $l = \frac{k^{3/2}}{\varepsilon}$ . The rate of dissipation of turbulence kinetic energy  $\varepsilon$  is not the only possible length scale determining variable. In the  $k$ - $\omega$  model proposed by Wilcox, which uses the turbulence frequency  $\omega = \varepsilon/k$  (dimensions  $s^{-1}$ ) as the second variable, the transport equation for  $k$  and  $\omega$  for turbulent flows at high Reynolds implemented in CFX defined as follows (ANSYS®, 2011b):

$$\mu_t = \rho \frac{k}{\omega}, \quad (4.61)$$

$$\frac{\partial(\rho k)}{\partial t} + \nabla \cdot (\rho k \mathbf{U}) = \nabla \cdot \left[ \left( \mu + \frac{\mu_t}{\sigma_k} \right) \nabla k \right] + P - \beta^* \rho k \omega, \quad (4.62)$$

$$\frac{\partial(\rho \omega)}{\partial t} + \nabla \cdot (\rho \omega \mathbf{U}) = \nabla \cdot \left[ \left( \mu + \frac{\mu_t}{\sigma_\omega} \right) \nabla \omega \right] + \alpha \frac{\omega}{k} P - \beta \rho \omega^2, \quad (4.63)$$

$$\sigma_k = 2.0, \quad \sigma_\omega = 2.0, \quad \alpha = 5/9, \quad \beta = 0.075, \quad \beta^* = 0.09. \quad (4.64)$$

At inlet boundaries the values of  $k$  and  $\omega$  must be specified, and at outlet boundaries the usual zero gradient conditions are used. The boundary condition of  $\omega$  in a free stream, where turbulence kinetic energy  $k \rightarrow 0$  and turbulence frequency  $\omega \rightarrow 0$ , is the most problematic one (ANSYS®, 2011b). The primary advantage of the  $k$ - $\omega$  model over the  $k$ - $\varepsilon$  is in its ability to be applied throughout the boundary layer without the use of wall damping functions. For such boundary layer flows, and especially adverse pressure gradient boundary layer flows, its results are superior over the  $k$ - $\varepsilon$  model (ANSYS®, 2011b).

#### 4.6.4 Shear Stress Transport (SST) turbulence model

One of the main problems in turbulence modelling is the accurate prediction of flow separation from a smooth surface. Standard two-equation turbulence models often fail to predict the onset and the amount of flow separation under adverse pressure gradient conditions (Menter *et al.*, 2003). The starting point for the development of the SST model was the need for the accurate prediction of aeronautics flows with strong adverse pressure gradients and separation (Menter *et al.*, 2003). Menter suggest a hybrid model using 1) a transformation of the  $k-\varepsilon$  model into a  $k-\omega$  model in the near-wall region and 2) the standard  $k-\varepsilon$  model in the fully turbulent region far from the wall (Menter, 1994). Therefore in order to solve the problem, a blending between the model near the surface and the model in the outer region was developed by Menter. The zonal formulation is based on blending functions, which ensure a proper selection of the  $k-\omega$  and  $k-\varepsilon$  zones without user interaction. The Wilcox model is thereby multiplied by a blending function  $F_1$  and the transformed  $k-\varepsilon$  model by a function  $1-F_1$ . Here,  $F_1$  is equal to one near the surface and decreases to a value of zero outside the boundary layer (that is, a function of the wall distance). The Reynolds stress computation and the  $k$ -equation are the same as in Wilcox's original  $k-\omega$  model, but the  $\varepsilon$ -equation is transformed into an  $\omega$ -equation by substituting  $\varepsilon = \beta^* k \omega$ . This yields transformed  $k-\varepsilon$  model as following (ANSYS<sup>®</sup>, 2011b):

$$\frac{\partial(\rho k)}{\partial t} + \nabla \cdot (\rho k \mathbf{U}) = \nabla \cdot \left[ \left( \mu + \frac{\mu_t}{\sigma_{k2}} \right) \nabla k \right] + P - \beta^* \rho k \omega, \quad (4.65)$$

$$\frac{\partial(\rho \omega)}{\partial t} + \nabla \cdot (\rho \omega \mathbf{U}) = \nabla \cdot \left[ \left( \mu + \frac{\mu_t}{\sigma_{\omega2}} \right) \nabla \omega \right] + \gamma_2 \frac{\omega}{k} P - \beta_2 \rho \omega^2 + 2\rho \frac{1}{\sigma_{\omega2} \omega} \nabla k \nabla \omega. \quad (4.66)$$

Then for SST model, this can expressed as (ANSYS<sup>®</sup>, 2011b):

$$\frac{\partial(\rho \omega)}{\partial t} + \nabla \cdot (\rho \omega \mathbf{U}) = \nabla \cdot \left[ \left( \mu + \frac{\mu_t}{\sigma_{\omega}} \right) \nabla \omega \right] + \gamma \frac{\omega}{k} P - \beta \rho \omega^2 + 2(1-F_1)\rho \frac{1}{\sigma_{\omega2} \omega} \nabla k \nabla \omega. \quad (4.67)$$

The blending function is defined as (ANSYS<sup>®</sup>, 2011b):

$$F_1 = \tanh(\arg_1^4), \quad (4.68)$$

$$\arg_1 = \min \left[ \max \left( \frac{\sqrt{k}}{\beta^* \omega y} \left| \frac{500\nu}{y^2 \omega} \right| \right) \left| \frac{4\rho k}{CD_{k\omega} \sigma_{\omega2} y^2} \right| \right], \quad (4.69)$$

$$CD_{k\omega} = \max \left( 2\rho \frac{1}{\sigma_{\omega 2} \omega} \nabla k \nabla \omega \Big| 10^{-10} \right). \quad (4.70)$$

The set of constants from the transformed  $k-\varepsilon$  model are (ANSYS®, 2011b):

$$\sigma_{k2} = 1.0, \quad \sigma_{\omega 2} = 1/0.856 = 1.168, \quad \gamma_2 = 0.44, \quad \beta_2 = 0.0828, \quad \beta^* = 0.09. \quad (4.71)$$

The shear stress transport (SST) model adds a function to these set of formulae to limit the turbulent shear stress (Menter, 1994). In this way, the turbulent eddy viscosity is calculated as:

$$\nu_t = \min \left( \frac{k}{\omega} \left| \frac{a_1 k}{S F_2} \right. \right). \quad (4.72)$$

This term uses an invariant measure of the shear strain rate  $S = \sqrt{2S_{ij}S_{ij}}$ , with  $S = \partial U / \partial y$  for boundary layer flows, and the function  $F_2$  that is one in boundary layers and zero outside. The blending function ensures that the original formulation  $\nu_t = k / \omega$  is used outside of boundary layers. This function is defined as (ANSYS®, 2011b):

$$F_2 = \tanh(\arg_2^2), \quad (4.73)$$

$$\arg_2 = \max \left( \frac{2\sqrt{k}}{\beta^* \omega y} \left| \frac{500\nu}{y^2 \omega} \right. \right). \quad (4.74)$$

## 4.7 Modelling flow near the wall

Near a non-slip wall, there are strong gradients in the flow variables. In addition, viscous effects on the transport processes are large. Experiments and mathematical analysis have shown that the near-wall region can be divided into two sub-layers. In the innermost layer, the so-called viscous sub-layer, the flow is almost laminar, and the molecular viscosity plays a dominant role in momentum and heat transfer. Further away from the wall, in the logarithmic layer, turbulence dominates the mixing process. Finally, there is a region between the viscous sub-layer and the logarithmic layer called the buffer layer, where the effects of molecular viscosity and turbulence are of equal importance (ANSYS®, 2011a).

Two approaches exist to the modelling of turbulent boundary layers. The first is termed the ‘low Reynolds number’ approach, in which the first grid point from the wall (point  $P$ ) must be in the viscous sub-layer (with  $y_P^+ < 2$ ) and where the velocity boundary condition is  $U_w = 0$ .  $y^+$  is the dimensionless distance from the wall. It

is used to check the location of the first node away from a wall. The second approach is termed the ‘high Reynolds number’ or wall function approach, in which the first grid point from the wall must be outside the viscous sub-layer (with  $y_P^+ > 35$ ), and where we prescribe the wall shear stress based on the velocity at point  $P$  using the log-law. The primary benefit of the wall function approach is that the high gradient shear layers near walls can be modelled with relatively coarse meshes, yielding substantial savings in CPU time and storage. It also avoids the need to account for viscous effects in the turbulence model. The wall function approach, then a blended high/low Reynolds number approach is discussed in the next sections. The both methods are implemented in CFX for  $k-\omega$  based models.

#### 4.7.1 Wall functions

Wall functions are the most popular way to account for wall effects. In CFX, scalable wall functions are used for all turbulence models based on the  $\varepsilon$ -equation. For  $k-\omega$  based models (including the SST model), an Automatic near-wall treatment method is applied. Within the overlap region of the boundary layer  $35 < y^+ < 350$ , corresponding roughly to the range  $0.02 < y/\delta < 0.2$ , the famous log-law applies (ANSYS<sup>®</sup>, 2011b):

$$\frac{U}{u_\tau} = \frac{1}{\kappa} \ln \left( \frac{yu_\tau}{\nu} \right) + B, \quad (4.75)$$

with the friction velocity  $u_\tau$  defined as:

$$u_\tau = \sqrt{\frac{\tau_w}{\rho}}, \quad (4.76)$$

where,  $U$  is the velocity tangential to the wall at a distance  $y$  normal to the wall and  $\tau_w$  is the wall shear stress. The commonly used values for the constants  $\kappa$  and  $B$  are 0.41 and 5 respectively. Different values for  $B$  apply to rough walls. Unfortunately Equation (4.75) does not apply to separating flows, where both  $U$  and  $\tau_w$  tend to zero. There is a modification for that and it is to calculate the wall shear stress, expressed as:

$$\tau_w = \rho u_\tau^* u_\tau, \quad (4.80)$$

The log-law thus becomes (ANSYS<sup>®</sup>, 2011b):

$$\frac{U}{(\tau_w / \rho)} u_\tau^* = \frac{1}{\kappa} \ln \left( \frac{yu_\tau^*}{\nu} \right) + B, \quad (4.81)$$

This equation is implemented in CFX as a ‘scalable’ wall function with two further modifications. First, the value of  $y$  used is based on one quarter of the distance from the wall to the near wall grid point. According to the CFX-Solver Theory Guide this is done to achieve ‘an optimum performance in terms of accuracy and robustness’. Second, the value of  $y^* (= yu_\tau^*/\nu)$  used is limited to a lower value of 11.06. This allows the wall function approach to be used with arbitrarily fine grids.

#### 4.7.2 Blended high/low Reynolds number formulation

The CFX-Solver includes an ‘automatic’ near wall treatment for  $k-\omega$  or SST based models. As with the wall function formulation in Equation (4.80), here the values of  $u_\tau^*$  and  $u_\tau$  are both blended between sub-layer and log-law relations (ANSYS<sup>®</sup>, 2011b):

$$u_\tau = \left( u_{\tau_{sub}}^4 + u_{\tau_{log}}^4 \right)^{1/4}, \quad (4.82)$$

$$u_\tau^* = \left( u_{\tau_{sub}}^{*4} + u_{\tau_{log}}^{*4} \right)^{1/4}, \quad (4.83)$$

with having the following:

$$u_{\tau_{sub}} = u_{\tau_{sub}}^* = \sqrt{\nu U / y}. \quad (4.84)$$

The log-law velocity scales  $u_{\tau_{log}}$  and  $u_{\tau_{log}}^*$  are defined as per the wall function approach, and the value of  $y$  used is the distance from the wall to the near wall grid point rather than being one quarter as in the previous one.

## 4.8 Numerical schemes

CFX uses Finite Volume Method (FVM) which utilizes finite element shape functions for the discretization of some terms. This involves discretising the spatial domain using a mesh. The mesh is used to construct finite volumes, which are used to conserve relevant quantities such as mass, momentum, and energy. Due to its generality the finite volume method can handle any type of mesh, structured as well as unstructured. In order to resolve the fluid flow inside the turbine motor, a numerical method is applied for solving fluid mechanical equations. We consider here the discretization of the integral mass and momentum conservation equations for a non-deforming control volume as following (ANSYS<sup>®</sup>, 2011b):

$$\frac{d}{dt} \int_V \rho dV + \int_S \rho U_j dS_j = 0, \quad (4.85)$$

$$\frac{d}{dt} \int_V \rho U_i dV + \int_S \rho U_j U_i dn_j = - \int_S P dn_j + \int_S \mu_{eff} \left( \frac{\partial U_i}{\partial x_j} + \frac{\partial U_j}{\partial x_i} \right) dn_j + \int_V S_{U_i} dV \quad (4.86)$$

$$\frac{d}{dt} \int_V \rho \phi dV + \int_S \rho U_j \phi dn_j = - \int_S \mu_{eff} \left( \frac{\partial \phi}{\partial x_j} \right) dn_j + \int_V S_\phi dV, \quad (4.87)$$

where  $V$  and  $S$  denote volume and surface regions of integration respectively, and  $dn_j$  are the differential Cartesian components of the outward normal surface vector. The condition of non-deforming control volumes is necessary for the time derivative to be moved outside of the volume integral in the unsteady terms.

#### 4.8.1 Shape functions

Finite element shape functions are used to approximate solution variables and geometric quantities at integration points from the values stored at the nodes. The variation of a quantity  $\phi$  within an element is calculated from (ANSYS®, 2011b):

$$\phi = \sum_{i=1}^{\text{nodes}} N_i \phi_i, \quad (4.88)$$

where  $N_i$  is the shape function for node  $i$  and  $\phi_i$  is the value of  $\phi$  at node  $i$ . Following the standard finite-element approach, shape functions are used to evaluate spatial derivatives for all the diffusion terms. For example, for a derivative in the  $x$  direction at integration point  $ip$ :

$$\frac{\partial \phi}{\partial x} \Big|_{ip} = \sum_{i=1}^{\text{nodes}} \frac{\partial N_i}{\partial x} \Big|_{ip} \phi_i. \quad (4.89)$$

#### 4.8.2 Advection term

The advection term requires the integration point values of  $\phi$  to be approximated in terms of the nodal values of  $\phi$  (ANSYS®, 2011b):

$$\phi_{ip} = \phi_{up} + \beta \nabla \phi \cdot \Delta \vec{r}, \quad (4.90)$$

where  $\phi_{up}$  is the value at the upwind node, and  $\vec{r}$  is the vector from the upwind node to the  $ip$ . Particular choices for  $\beta$  and  $\nabla \phi$  yield different schemes as described below.

**First order upwind differencing scheme**

A value of  $\beta = 0$  yields a first order Upwind Difference Scheme (UDS). This scheme is very robust, but it will introduce diffusive discretization errors that tend to spread steep spatial gradients (ANSYS<sup>®</sup>, 2011b).

**Specified blend factor**

By choosing a value for  $\beta$  between 0 and 1, and by setting  $\nabla\phi$  equal to the average of the adjacent nodal gradients, the discretization errors associated with the UDS are reduced. The choice  $\beta = 1$  is formally second-order-accurate in space, and the resulting discretization will more accurately reproduce steep spatial gradients than first order UDS. However, this scheme is unbounded, and may introduce dispersive discretization errors that tend to cause non-physical oscillations in regions of rapid solution variation (ANSYS<sup>®</sup>, 2011b).

**High resolution scheme**

The high resolution scheme uses a special nonlinear recipe for  $\beta$  at each node, computed to be as close to 1 as possible. The recipe for  $\beta$  involves first computing a  $\phi_{\min}$  and  $\phi_{\max}$  at each node using a thin sheet of nodes involving adjacent nodes (including the node itself). Next, for each integration point around the node, the Equation (4.90) is solved for  $\beta$  to ensure that it does not undershoot  $\phi_{\min}$  or overshoot. The nodal value for  $\beta$  is taken to be the minimum value of all integration point values surrounding the node. The value of  $\beta$  is also not permitted to exceed 1.

**Transient scheme**

The transient scheme defines the discretization algorithm for the transient term. Options available are in CFX are: First Order Backward Euler, Second Order Backward Euler, and High Resolution. The First Order Backward Euler scheme is an implicit time-stepping scheme that is first-order accurate. Its behaviour is similar to the Upwind differencing scheme for advection terms, and suffers from similar numerical diffusion. Although it is useful for initial studies, its use is not recommended for production runs except for turbulence equations. The Second Order Backward Euler scheme is also an implicit time-stepping scheme, but is second-order accurate, and is the default in CFX. It is applicable for constant and variable timestep sizes. Like second-order advection schemes, is not appropriate for some quantities that must remain bounded, such as turbulence quantities and volume fractions. When running the Second Order Backward Euler scheme, the transient scheme for turbulence equations will remain First Order,

and the transient scheme for volume fraction equations will be set to a bounded second-order scheme, similar to the High Resolution scheme for advection. This scheme is generally recommended for most transient runs. The High Resolution transient scheme uses the second order backward Euler scheme wherever and whenever possible and reverts to the first order backward Euler scheme when required to maintain a bounded solution.

## 4.9 Physical models

Regions of fluid flow and/or heat transfer in CFX are called domains. There can be many domains per model, with each domain defined by separate 3D primitives. When we set up a simulation, we should select which physical models to include. The physical models define the type of simulation we want to perform.

### 4.9.1 Steady state and transient flows

The time dependence of the flow characteristics can be specified as either steady state or transient. Steady state simulations, by definition, are those whose flow characteristics do not change with time and are assumed to have been reached after a relatively long time interval. They require no real time information to describe them. On the other hand, transient simulations require real time information to determine the time intervals at which the CFX solver calculates the flow field. Many flows, particularly those driven by buoyancy, do not have a steady state solution, and may exhibit cyclic behaviour.

Sometimes CFD simulations that are run in steady state mode will have difficulty in converging, and no matter what action you take regarding mesh quality and time step size, the solution does not converge and oscillatory behaviour of the residual plots are seen. This could be an indication of transient behaviour. It can be tested to see if we are observing a transient effect by reducing/increasing the time step size by known factors to see (ANSYS®, 2011a):

- If the period of oscillation of the residual plot changes by changing the time step size, then the phenomenon is most likely a numerical effect.
- If the period stays the same, then it is probably a transient effect.

In transient mode, we should set both physical time steps and the maximum number of coefficient iterations per time step.

### 4.9.2 Automatic timescale

The Auto Timescale option was chosen for this study in the timescale control section of CFX solver. This section describes the way in which a timestep is calculated when using the Auto Timescale option. The following length scales are calculated by CFX (ANSYS®, 2011b):

$$\begin{aligned} L_{\text{vol}} &= \sqrt[3]{V} \\ L_{\text{ext}} &= \max(L_x, L_y, L_z) \\ L_{\text{bc}} &= \min \sqrt{A_{bc}} \end{aligned} \quad (4.91)$$

Where  $V$  is the domain volume (over all domains),  $L_x$ ,  $L_y$  and  $L_z$  are the  $x$ ,  $y$  and  $z$  extents of the domain (over all domains) and  $A_{bc}$  is the area of an ‘open’ boundary (that is, inlets, outlets or openings).

Further length scales are then calculated depending on the Length Scale option parameter, which can be Conservative, Aggressive or Specified Length Scale (ANSYS®, 2011b):

$$L_{\text{scale}} = \begin{cases} \min(L_{\text{vol}}, L_{\text{ext}}) & \text{for Conservative} \\ \max(L_{\text{vol}}, L_{\text{ext}}) & \text{for Aggressive} \\ L_{\text{user}} & \text{for Specified} \end{cases} \quad (4.92)$$

The velocity scales used to calculate a timestep are (ANSYS®, 2011b):

$$\begin{aligned} U_{\text{bc}} &= \max |\bar{U}_{\text{bc}}| \\ U_{\text{node}} &= |\bar{U}_{\text{node}}| \\ U_{\Delta P} &= \sqrt{\frac{P_{\text{bc},\text{max}} - P_{\text{bc},\text{min}}}{\bar{\rho}_{\text{node}}}} \end{aligned} \quad (4.93)$$

Where  $U_{\text{bc}}$  is the arithmetic average of the velocity on a boundary,  $U_{\text{node}}$  is the arithmetic average of the nodal velocities,  $P_{\text{bc},\text{max}}$  and  $P_{\text{bc},\text{min}}$  are the maximum and minimum pressure values on an ‘open’ boundary and  $\bar{\rho}_{\text{node}}$  is the arithmetic average nodal density. The final fluid time scale used here is calculated as (ANSYS®, 2011b):

$$\Delta t = \min(\Delta t_U, \Delta t_{\Delta P}, \Delta t_{\text{rot}}), \quad (4.94)$$

where:

$$\Delta t_U = 0.3 \left[ \frac{L_{\text{scale}}}{\max(U_{\text{bc}}, U_{\text{node}}, U_{\Delta P})}, \frac{\rho L^2_{\text{scale}}}{\mu}, \frac{m}{\dot{m}_{in}} \right], \quad (4.95)$$

with the dynamic viscosity  $\mu$ , the total mass  $m$  and the total mass flow into the system  $\dot{m}_{in}$ .

#### 4.9.3 Heat transfer

A heat transfer model is used to predict the temperature throughout the flow. Heat transfer by conduction, convection, and (where appropriate) turbulent mixing and viscous work are included in CFX. In the “Isothermal” model we enter a uniform temperature for the fluid in absolute temperature terms and in this case, heat transfer is not modelled. In the “Thermal Energy” mode, the transport of enthalpy through the fluid domain is modelled. It differs from the “Total Energy” model in that the effects of mean flow kinetic energy are not included. It consequently reproduces the same results as the Total Energy model when kinetic energy effects vanish, and is therefore adequate for low speed flows where kinetic effects are negligible (ANSYS®, 2011a). The “Total Energy” mode models the transport of enthalpy and includes kinetic energy effects. It should be used where kinetic energy effects become significant. For cases where viscous heating and the effects of turbulence on it are important, it is recommended that we use the Total Energy model (ANSYS®, 2011a).

#### 4.9.4 Buoyancy

Fluid flows in which gravity is important can be modelled by CFX by the inclusion of buoyancy source terms. For an isothermal, single phase, single component flow with constant density, there are no buoyancy forces. For buoyancy calculations, a source term is added to the momentum equations as follows (ANSYS®, 2011a):

$$S_{M,\text{bouy}} = (\rho - \rho_{ref}) g. \quad (4.96)$$

The density difference  $\rho - \rho_{ref}$  is evaluated using either the Full Buoyancy model or the Boussinesq model, depending on the physics. In the Full Buoyancy model,  $\rho - \rho_{ref}$  is evaluated directly. This model is set automatically when the simulation involves multi-component flow, multiphase flow, or a fluid having density set as a function of for instance pressure, temperature, or other field variables. In the Boussinesq model, a constant reference density  $\rho_{ref}$  is used for all terms other than the buoyancy source term. The buoyancy source term is then approximated as (ANSYS®, 2011a):

$$\rho - \rho_{ref} = -\rho_{ref}\beta(T - T_{ref}), \quad (4.97)$$

where  $\beta$  is the thermal expansion coefficient:

$$\beta = -\frac{1}{\rho} \frac{\partial \rho}{\partial T} \Big|_P. \quad (4.98)$$

#### 4.9.5 Non-Newtonian flow

Some fluids are non-Newtonian; that is, they do not obey the simple linear relationship between shear stress and shear strain rate. Many practical fluids fall into this class, and their behaviour is generally described using various mathematical models. CFX has several models for calculating viscosity based on shear strain rate. In this study, only the “Herschel Bulkely” model is used which is a well-known model for drilling fluids. This is a model for viscoplastic fluids that, after yield, exhibits a power law behaviour in shear stress versus shear strain rate, stated as (ANSYS®, 2011b):

$$\mu = \frac{\tau_y}{(\lambda \dot{\gamma})} + K(\lambda \dot{\gamma})^{n-1}, \quad (4.99)$$

where,

$\mu$  = Dynamic viscosity (absolute viscosity), is a measure of the resistance of a fluid to shearing forces (Pa.s),

$\tau_y$  = yield stress (Pa),

$K$  = viscosity Consistency (Pa.s),

$\lambda$  = Time constant,

$n$  = Power law index.

## 4.10 Multiphase flow modelling

Multiphase flow refers to the situation where more than one fluid is present. Each fluid may possess its own flow field, or all fluids may share a common flow field. CFX includes a variety of multiphase models to allow the simulation of multiple fluid streams, bubbles, droplets, solid particles, and free surface flows. Two distinct multiphase flow models are available in CFX, an Eulerian-Eulerian multiphase model and a Lagrangian Particle Tracking multiphase model. All continuous phases should use the Eulerian model. In this study, for the mist flow simulations (mixture of air as continuous phase and water droplets as dispersed fluid particle), a Lagrangian Particle Tracking multiphase model has been used because it gives better details for mass and

heat transfer, and complete information on behaviour of individual particles. This particle transport model is capable of modelling dispersed phases which are discretely distributed in a continuous phase. The modelling involves the separate calculation of each phase with source terms generated to account for the effects of the particles on the continuous phase. Also the separated flow analysis method was used in which each particle represents a sample of particles that follow an identical path. The behaviour of the tracked particles is used to describe the average behaviour of the dispersed phase. The actual number of particles modelled by the representative particle is called the Particle Number Rate. The particle number rate is determined from the mass flow rate assigned to the representative particle divided by the mass of an actual particle. All the particles represented by the sample particle will follow exactly the same track, even if the turbulent particle dispersion is used. Unlike in an Eulerian multiphase calculation, the fraction of volume taken by the particles is not included in the continuous phase calculation. This means that the model is only valid for quite low volume fractions (ANSYS®, 2011a). The turbulence model used here in a particle tracking simulations only applies to the continuous phases. Turbulence can affect the particles through the particle dispersion force, but the particles can have no effect on the turbulence of the continuous phase, other than indirectly by affecting the velocity field.

Here, the objective of using mist as drilling fluid is to add some amount of water to the pumped air to provide cooling to the down hole tools and especially to provide sufficient cooling to the impregnated diamond bit which is cutting the rock by grinding action and produce a large amount of heat on the bit face. The large surface area of the small water droplets leads to high evaporation rates which extract large amounts of heat. In addition, as the water droplets are converted to steam they expand approximately 1700 times.

A particle diameter distribution can optionally be set for a domain (different particle diameters, mass, shape and etc.). If specified, then the distribution applies to all boundaries where particles are injected in that domain. Here, a constant specified particle diameter for all water droplets was set to 100 micron with constant mass and spherical shape.

## **4.11 Lagrangian Particle Transport**

The application of Lagrangian tracking in CFX involves the integration of particle paths through the discretized domain. Individual particles are tracked from their injection

point until they escape the domain or some integration limit criterion is met (ANSYS®, 2011a). Because each particle is tracked from its injection point to final destination, the tracking procedure is applicable to steady state flow analysis. The physical mechanisms by which small particles are transported by a turbulent fluid flow are complex. Here, the particle tracking is carried out by forming a set of differential equations in time for each particle, consisting of equations for position, velocity, temperature, and masses of species. These equations are then integrated using integration methods to calculate the behaviour of the particles as they traverse the flow domain. Here, the particle displacement is calculated using forward Euler integration of the particle velocity over timestep ( $\delta t$ ). The particle displacement is given as (ANSYS®, 2011b):

$$x_p^n = x_p^o + U_p^o \delta t, \quad (4.100)$$

where the superscripts  $o$  and  $n$  refer to old and new values respectively, and  $U_p^o$  is the initial particle velocity. In forward integration, the particle velocity calculated at the start of the timestep is assumed to remain constant over the entire step. At the end of the timestep, the new particle velocity is calculated using the analytical solution to the particle momentum equation (ANSYS®, 2011b):

$$m_p \frac{dU_p}{dt} = F_{all}, \quad (4.101)$$

where  $F_{all}$  is the sum of all forces acting on a particle. In CFX several different forces affect the motion of a particle in a fluid.

In this study, the liquid particle and gas phases were modelled as fully coupled, due to the relatively significant mass of water that interacts with the gas phase (air); that is, the momentum transfers from particles to gas, and from gas to particles, are resolved. One-way coupling simply predicts the particle paths as a post-process based on the flow field and therefore it does not influence the continuous phase flow field. The choice of one-way or full coupling for particles depends on the mass loading, that is, the ratio of the mass flow rate of particles to the mass flow rate of fluid. One-way coupling may be an acceptable approximation in flows with low mass loadings where particles have a negligible influence on the fluid flow. If the particles influence the fluid flow significantly, then full coupling should be used. The particle source terms acting on the fluid phase are proportional to the particle number rate and the convergence of a simulation can be improved if a sufficiently large number of particles are tracked (ANSYS®, 2011b). Full coupling requires that the particle source terms are included in

the continuous phase momentum equations. The momentum sources could be due to turbulent dispersion forces or drag forces.

The CPU cost of tracking particles is proportional to the number of particles tracked multiplied by the number of times tracked. One-way coupled particles are tracked only once, at the end of the solver run. The number of times fully coupled particles are tracked depends on the iteration frequency set on the solver control tab and the number of iterations required for the simulation to converge.

In this study, considering a discrete particle traveling in a continuous fluid medium, three important forces acting on the particle that affect the particle acceleration are viscous drag force, buoyancy force and forces due to domain rotation (Centripetal and Coriolis forces). Therefore, it results at:

$$m_p \frac{dU_p}{dt} = F_D + F_B + F_R, \quad (4.102)$$

where,

$F_D$  = drag force acting on the particle,

$F_B$  = buoyancy force due to gravity,

$F_R$  = forces due to domain rotation (centripetal and Coriolis forces).

For spherical particle used here, the particle mass can be obtained as:

$$m_p = \frac{\pi}{6} d_p^3 \rho_p, \quad (4.103)$$

where  $d_p$  is the particle diameter and  $\rho_p$  is the particle density.

The drag forces between the continuous phase and the particle phase can be modelled with:

- using the Schiller-Naumann, Ishii-Zuber, or Grace correlations, or
- using Particle Transport Drag Coefficient and specify the drag coefficient.

The aerodynamic drag force on a particle is proportional to the slip velocity,  $U_s$ , between the particle and the fluid velocity, resulting at following equation (ANSYS®, 2011b):

$$F_D = \frac{1}{2} C_D \rho_F A_F |U_s| U_s, \quad (4.104)$$

where  $U_s = U_F - U_p$  and  $C_D$  is the drag coefficient and  $A_F$  is the effective particle cross section. The particle momentum source due to drag is calculated from the following equation (ANSYS®, 2011b):

$$\frac{dS}{dt} = -F_D = -\frac{1}{2} C_D \rho_F A_F |U_s| U_s. \quad (4.105)$$

The source,  $S$ , added to the continuous phase is then multiplied with the number rate for that particle.

In this study particle drag force was modelled using the Schiller-Naumann drag model for sparsely distributed, small, and spherical particles. In addition to the buoyancy forces that arise in single phase flows, the difference in density between the particle and the continuous phase results in a buoyancy force. The buoyancy force is the force on a particle immersed in a fluid. The buoyant force is equal to the weight of the displaced fluid and is given by:

$$F_B = (m_p - m_f)g = m_p \left(1 - \frac{\rho_f}{\rho_p}\right)g = \frac{\pi}{6} d_p^3 (\rho_p - \rho_f) g, \quad (4.106)$$

where  $g$  is the gravity vector.

In a rotating frame of reference, the rotation term is an intrinsic part of the acceleration and is the sum of Coriolis and Centripetal forces (ANSYS®, 2011b):

$$F_R = m_p (-2\Omega \times U_p - \Omega^2 \times r_p), \quad (4.107)$$

where,  $\Omega$  is the angular velocity and  $r_p$  is the particle distance with the axis of rotation. In this equation, the first term is the Coriolis force and the second term is Centripetal force. The rotation force has no contribution to the particle momentum source into the continuous phase.

In turbulent particle tracking, the instantaneous fluid velocity is decomposed into a mean,  $\bar{v}_f$ , and a fluctuating,  $v'_f$ , components (ANSYS®, 2011b). The particle trajectories are not deterministic in this situation and two identical particles, injected from a single point, at different times, may follow separate trajectories due to the random nature of the instantaneous fluid velocity. It is the fluctuating component of the fluid velocity which causes the dispersion of particles in a turbulent flow. The model of turbulent dispersion of particles that is used in CFX, assumes that a particle is always within a single turbulent eddy. Each eddy has a characteristic fluctuating velocity,  $v'_f$ , lifetime,  $\tau_e$ , and length,  $l_e$ . When a particle enters the eddy, the fluctuating velocity for that eddy is added to the local mean fluid velocity to obtain the instantaneous fluid velocity. The turbulent fluid velocity,  $v'_f$ , is assumed to remain as long as the particle/eddy interaction time is less than the eddy lifetime and/or the displacement of

the particle relative to the eddy is less than the eddy length. If either of these conditions is exceeded, the particle is assumed to be entering a new eddy with new characteristic  $v'_f$ ,  $\tau_e$  and  $l_e$  (ANSYS<sup>®</sup>, 2011b). The turbulent velocity, eddy length and lifetime are calculated based on the local turbulence properties of the flow as following (ANSYS<sup>®</sup>, 2011b):

$$v'_f = \Gamma(2k/3)^{0.5}, \quad (4.108)$$

$$l_e = \frac{C_\mu^{3/4} k^{3/2}}{\varepsilon}, \quad (4.109)$$

$$\tau_e = l_e / (2k/3)^{0.5}, \quad (4.110)$$

where  $k$  and  $\varepsilon$  are the local turbulent kinetic energy and dissipation, respectively, and  $C_\mu$  is a turbulence constant. The factor  $C_\mu^{3/4}$  was chosen to relate the characteristic length scale to the eddy dissipation length. The variable  $\Gamma$  is a normally distributed random number which accounts for the randomness of turbulence about a mean value.

In this study, the equations of motion of individual particles are solved without considering collisions between particles and as a result the presence of other particles is not taken into account. Highly loaded gas-particle flows are commonly simulated by the two-fluid model where interactions between particles are computed using the Kinetic Theory of Dense Gases. The particle-particle collision model (PPCM) in CFX takes inter-particle collisions and their effects on the particle and gas phase into consideration.

Depending on the flow being solved, particles may introduce very large source terms to the hydrodynamic equations. In heavily laden flows, viscous drag may introduce large source terms in the momentum equations. In some cases, these source terms may have a destabilizing influence on the convergence of the hydrodynamic equations, resulting in oscillations, or in severe cases, divergence.

Heat transfer between the particles and the continuous phase can be modelled. In Interphase heat transfer was modelled with Ranz-Marshall correlations in this study, which are good for spherical particles. The heat transfer model for the continuous phase is set in the same way as for single-phase simulations. The heat transfer option was set to “Total Energy” for air (continuous phase) and to “Particle Temperature” for water droplets.

### 4.11.1 Particle-wall interaction

Dimensional analysis shows that droplet-wall interaction depends on the wall temperature, wall material and roughness, impact angle and impact velocity, the existence of a wall film, and various other parameters (ANSYS<sup>®</sup>, 2011a). In the standard particle-wall interaction model in CFX, the droplet is reflected off a wall and the momentum change across the collision is described using the perpendicular and parallel “Coefficients of Restitution”. It means these restitution coefficients describe the action of particles when they hit a wall. Coefficient values of 1 described an elastic collision, while values less than 1 describe an inelastic collision. The parallel coefficient will almost always be 1. The perpendicular coefficient will depend on the particle material. Particles that bounce off walls will have a perpendicular coefficient close to 1, while particles that stick to walls will have a perpendicular coefficient of close to 0. The following advanced particle-wall interaction models are available in CFX which are not considered here:

- Elsaesser particle-wall interaction model
- Stick-to-wall model

## 4.12 Boundary conditions

The equations relating to fluid flow can be closed (numerically) by the specification of conditions on the external boundaries of a domain. It is the boundary conditions that produce different solutions for a given geometry and set of physical models. Therefore, it is important to set boundary conditions that accurately reflect the real situation to obtain accurate results. The boundary conditions specified should be sufficient to ensure a unique solution. For all of the CFD simulations of the next Chapter this was essentially achieved by specifying a total pressure at the inlet and a mass flow rate at the outlet. The static pressure at the outlet and the velocity at the inlet are part of the solution.

### 4.12.1 Inlet (subsonic)

An inlet boundary condition is used where the flow is predominantly directed into the domain. Here, a “Total Pressure”,  $P_{tot}$ , is specified at an inlet boundary condition and the CFX-Solver computes the static pressure needed to properly close the boundary condition. For rotating frames of reference one usually specifies the stationary frame total pressure instead.

A reasonable value for the turbulence intensity, or  $k$  and  $\varepsilon$  at an inlet boundary should be set. Several options exist for the specification of turbulence quantities at inlets. Here, we use the Medium (Turbulence Intensity = 5%) option. Nominal turbulence intensities range from 1% to 5% but will depend on our specific application. If choose to specify values of  $k$  and  $\varepsilon$  directly, then we can approximate incoming levels for internal flow by using the following relationships (ANSYS<sup>®</sup>, 2011b):

$$k = \frac{3}{2} I^2 U^2 , \quad (4.111)$$

where  $I$  is the specified turbulence intensity. Also  $\varepsilon$  can then be approximated using:

$$\varepsilon = \frac{k^{3/2}}{0.3 D_h} , \quad (4.112)$$

where  $D_h$  is the hydraulic diameter of the inlet.

#### 4.12.2 Outlet (subsonic)

An outlet boundary condition is used where the flow is predominantly directed out of the domain. Here, the boundary condition for the outlet is set to mass flow rate. The mass flux distribution across the outlet is determined by starting with the local mass flow rate distribution calculated by the flow solver at each integration point:

$$\dot{m}_{ip} = \rho_{ip} A_{ip} U_{ip} , \quad (4.113)$$

From that distribution, we calculate the estimated total mass flow rate through the outlet boundary condition (ANSYS<sup>®</sup>, 2011b):

$$\dot{m}_{tot}^{est} = \sum_{all} \dot{m}_{ip} , \quad (4.114)$$

where the summation is over all boundary integration points. A scaling factor is computed at the end of each coefficient loop that is used to scale the local integration point mass flows such that they add up to the specified mass flow rate (ANSYS<sup>®</sup>, 2011b):

$$F = \frac{\dot{m}_{spec}}{\dot{m}_{tot}^{est}} . \quad (4.115)$$

Iteratively, during the computation,  $F$  can be greater than or less than unity. The final integration point mass flows are reset by multiplying the integration point mass flows by the scaling factor (ANSYS<sup>®</sup>, 2011b):

$$\dot{m}_{ip} = F \rho_{ip} A_{ip} U_{ip} . \quad (4.116)$$

In this way, the mass flux profile is an implicit result of the solution and at the same time gives exactly the specified mass flow rate.

#### 4.12.3 Wall boundary

Walls are solid (impermeable) boundaries to fluid flow. The boundary condition for the domain walls were set to Non Slip (not moving, no wall velocity). The velocity of the fluid at the wall boundary is set to zero. Also the heat flux across the wall boundary was set to zero (Adiabatic).

#### 4.12.4 Counter-rotating wall and rotating wall

Rotating Frames of Reference (RFR) are useful for rotating fluid machinery applications. In CFX-Pre we can specify a domain that is rotating about an axis with the domain angular velocity of  $\omega$ . A counter-rotating wall can be specified for walls in rotating frames. In this case, the wall is stationary in the absolute frame; in the relative frame, it moves with a velocity:

$$U_{wall} = -\omega R , \quad (4.117)$$

where  $R$  is the radial vector from the domain axis of rotation to the wall. A rotating wall can be specified in both stationary and rotating frames. This option is useful to use in stationary domains when we would like to create a spinning wall. In this case, we can enter a local rotation axis for the wall boundary and the wall velocity. The solver automatically transforms the specified wall velocity into Cartesian components.

#### 4.12.5 Symmetry plane

A problem is symmetric about a plane when the flow on one side of the plane is a mirror image of flow on the opposite side. By definition, the symmetry plane boundary condition imposes constraints that ‘mirror’ the flow on either side of it. For example, the normal velocity component at the symmetry plane boundary is set to zero, and the scalar variable gradients normal to the boundary are also set to zero.

### 4.13 Interface models

Domain Interfaces provide a way of connecting meshes or domains together. Two methods of connecting meshes exist for interfaces in CFX; these are one-to-one (direct)

and general grid interface (GGI) (ANSYS<sup>®</sup>, 2011a). CFX-Pre automatically chooses whether the connection is direct (one-to-one) or not, based on whether the nodes are coincident on both side of the interface. General Grid Interface (GGI) connections refer to the class of grid connections where the grid on either side of the two connected surfaces does not match. A control surface approach is used to perform the connection across a GGI attachment or periodic condition. A physically based intersection algorithm is employed to provide the complete freedom for changing the grid topology and physical distribution across the interface (ANSYS<sup>®</sup>, 2011a).

If the flow field is repeated in multiple identical regions, then only one region needs to be solved and the boundaries are specified as “Periodic” (via a rotation or translation). The interface model defines the way the solver models flow physics across the interface. The available interface model options are (ANSYS<sup>®</sup>, 2011a):

- Translational Periodicity,
- Rotational Periodicity,
- General Connection.

The periodic condition ensures that the flow out of one side of the interface automatically appears on the other side. In the case of Translational Periodicity, the two sides of the interface must be parallel to each other such that a single translation transformation can be used to map Region 1 to Region 2. In the case of Rotational Periodicity, the two sides of the periodic interface can be mapped by a single rotational transformation about an axis. This is the most common case of periodicity and is used, for example, in the analysis of a single blade passage in a rotating machine, and is the same case we use for the blades model in this study.

The General Connection interface model is a powerful way to connect regions together. A general connection can be used to (ANSYS<sup>®</sup>, 2011a):

- Apply a frame change at the interface between a rotor and stator,
- Connect non-matching grids,
- Apply fully transient sliding interfaces between domains.

Pitch change can also be applied. For example, a domain interface can connect a stator domain with a rotor domain where the number of stator blades is not equal to the number of rotor blades, even if the mesh contains only one blade from each side.

#### 4.13.1 Frame change/mixing model

Each side of the interface must be a surface of revolution and both sides must sweep out the same surface of revolution. There are three types of frame change/mixing models available in CFX (ANSYS<sup>®</sup>, 2011a):

- Frozen Rotor,
- Stage,
- Transient Rotor-Stator.

In the “Frozen Rotor” model, the frame of reference and/or pitch is changed but the relative orientation of the components across the interface is fixed. Frozen Rotor analysis is most useful when the circumferential variation of the flow is large relative to the component pitch (ANSYS<sup>®</sup>, 2011a). This model requires the least amount of computational effort of the three frames change/mixing models. The disadvantage of this model is that the transient effects at the frame change interface are not modelled.

The “Stage” model is an alternative to the Frozen Rotor model for modelling frame and/or pitch change. Instead of assuming a fixed relative position of the components, the stage model performs a circumferential averaging of the fluxes through bands on the interface. Steady state solutions are then obtained in each reference frame. Stage analysis is most appropriate when the circumferential variation of the flow is of the order of the component pitch, and is not appropriate when the circumferential variation of the flow is significant relative to the component pitch (ANSYS<sup>®</sup>, 2011a). The Stage model usually requires more computational effort than the Frozen Rotor model to converge, but not as much as the Transient Rotor-Stator model. In this study for the steady state simulations the stage model is used for the interface between stator row and rotor row.

The “Transient Rotor-Stator” model predicts the true transient interaction of the flow between a stator and rotor passage. In this approach the transient relative motion between the components on each side of the GGI connection is simulated. It accounts for all interaction effects between components that are in relative motion to each other. The interface position is updated each timestep, as the relative position of the grids on each side of the interface changes. The main disadvantage of this method is that the computer resources required may be large, in terms of simulation time, disk space and quantitative post processing of the data. The resource requirement problem is huge if unequal pitch between components occurs. In practice, components of unequal pitch can be treated by solving  $N$  passages on one side and  $M$  passages on the other side, with  $N$

and  $M$  determined such that the net pitch change across the interface is close to unity (ANSYS<sup>®</sup>, 2011a).

#### 4.13.2 Transient blade row modelling

Using conventional methods for modelling transient rotor-stator applications, it is often the case that prohibitive computing resources are required to obtain detailed accurate simulations. The transient blade row models available in CFX make it possible to reduce the size of the computational problem by solving the blade row solution for one or two passages per row, while still obtaining reasonably accurate solutions, thus providing a solution to the unequal pitch problem between the blade passages of neighbouring rows (ANSYS<sup>®</sup>, 2011a). A steady state solution can be used as the initial condition for all transient flow simulations. The transient blade row models available in CFX are (ANSYS<sup>®</sup>, 2011a):

- Profile Transformation,
- Time Transformation,
- Fourier Transformation.

The Profile Transformation method overcomes the unequal pitch problem by scaling the flow profile across the blade row interfaces. In the Time Transformation method, the unequal pitch problem is overcome by applying a time transformation to the flow equations so that we can use simple periodic boundary conditions on the pitch-wise boundaries. In the Fourier Transformation method, a phase-shifted boundary condition with Fourier data compression is used to account for the unequal pitch between the blade rows passages. The Fourier Transformation and Time Transformation methods can be used to apply periodic conditions that are phase-shifted in time in order to account for inequality between signal and domain pitches for boundary disturbance cases.

### 4.14 Grid properties

Grid generation is a major component in setting up a CFD simulation. Despite the numerous available software codes to support the task of grid generation, it still can be a very time-consuming exercise, particularly when dealing with complex geometries such as turbine. Consequently, automatic grid generation, with an adequate control of grid quality, has become one of the major objectives of modern CFD, both for structured as well as unstructured grids. For a given geometrical configuration, many different grid

topologies can be defined. The choice of a mesh topology is often a matter of personal choice and it is therefore of importance to acquire knowledge of the various possibilities offered by grid generation tools.

Structured grids can be considered as most ‘natural’ for flow problems as the flow is generally aligned with the solid bodies. Structured grids compared to unstructured grids, will often be more efficient from CFD point of view, in terms of accuracy, CPU time and memory requirement (ANSYS®, 2011a). The reason behind the development of unstructured CFD codes is essentially connected to the time required to generate good quality block-structured grids on complex geometries.

Depending on the orientation of the grid lines, various configurations can be selected, indicated by the letter to which they resemble the most. We refer in this context to grids of H-type, C-type, O-type, I-type and their various combinations. In H-type mesh, the grid lines are curvilinear, approaching a set of horizontal and vertical lines in a pseudo-orthogonal configuration, with a topology that can be associated to the letter H (see Figure 4.2). For the C-type mesh, the grid lines are curvilinear, surrounding the geometry, with a topology that can be associated to the letter C, on one side (for instance around the leading), but remaining open at the other end of the computational domain. This can be adapted to concentrate grid lines in the wake region (see Figure 4.3). In the O-type mesh, the grid lines are curvilinear, surrounding completely the geometry, with a topology that can be associated to the letter O. This option allows an accurate mesh point distribution around both leading and trailing edges of external aerodynamic configurations (see Figure 4.4). In the particular case of highly staggered turbomachinery blade sections, the quality requirement of nearly orthogonal cells is better fulfilled with grid lines nearly orthogonal to the blade sections, leading to a I-type topology as shown in Figure (4.5).

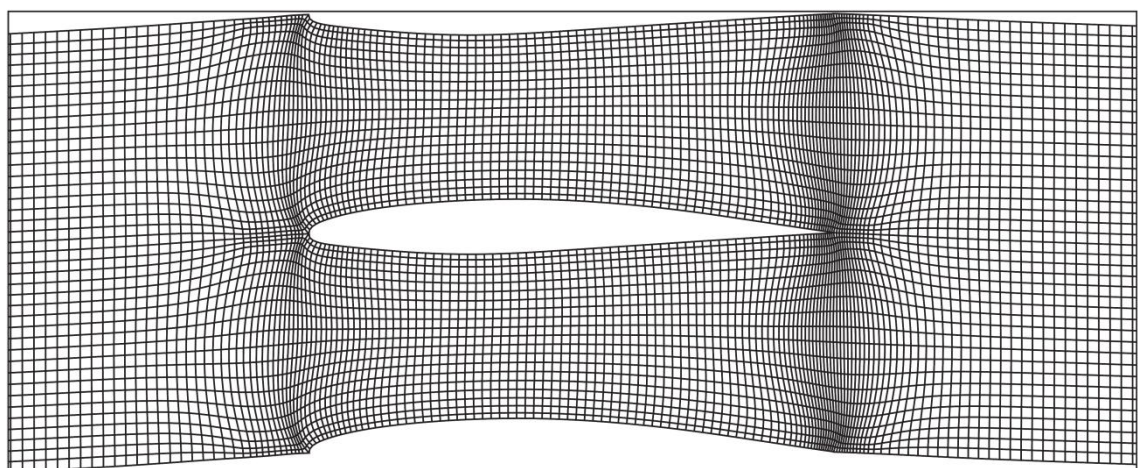


Figure 4.2 Structured curvilinear body-fitted grid of the H-type (Hirsch, 2007).

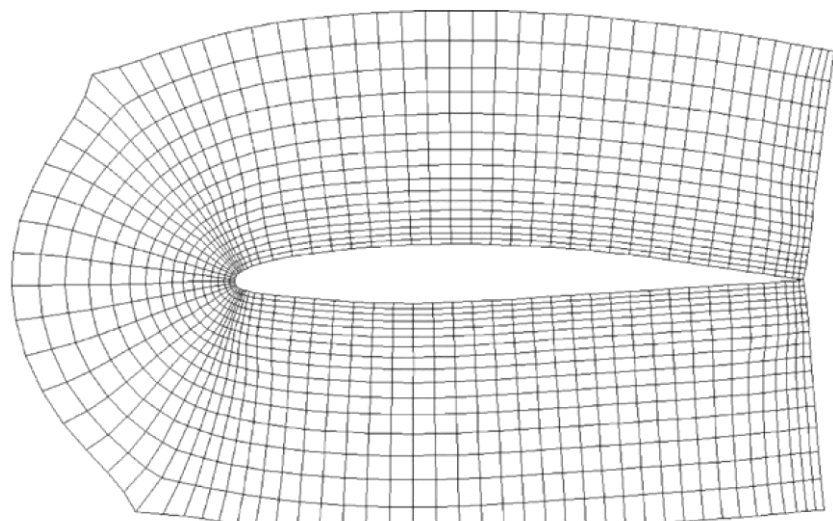


Figure 4.3 Structured curvilinear body-fitted grid of the C-type (Hirsch, 2007).

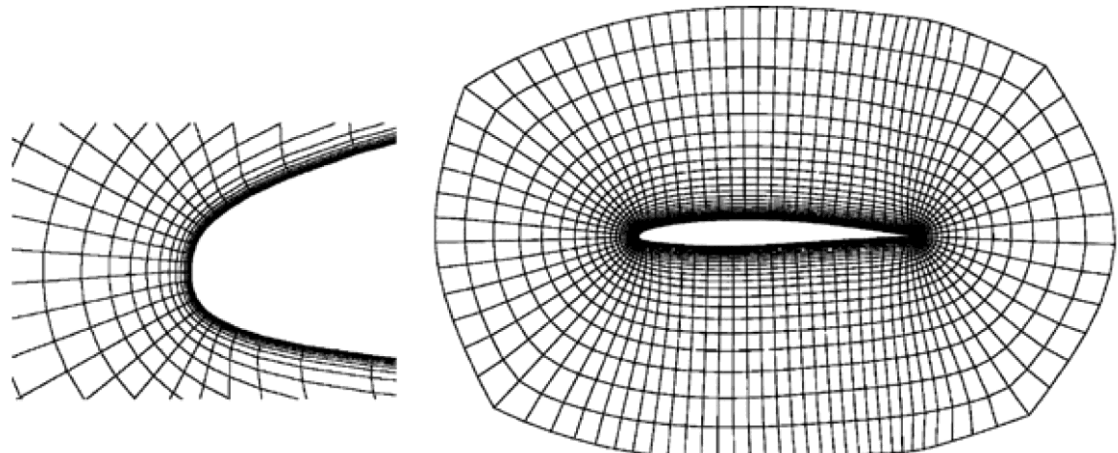


Figure 4.4 Structured curvilinear body-fitted grid of the O-type (Hirsch, 2007).

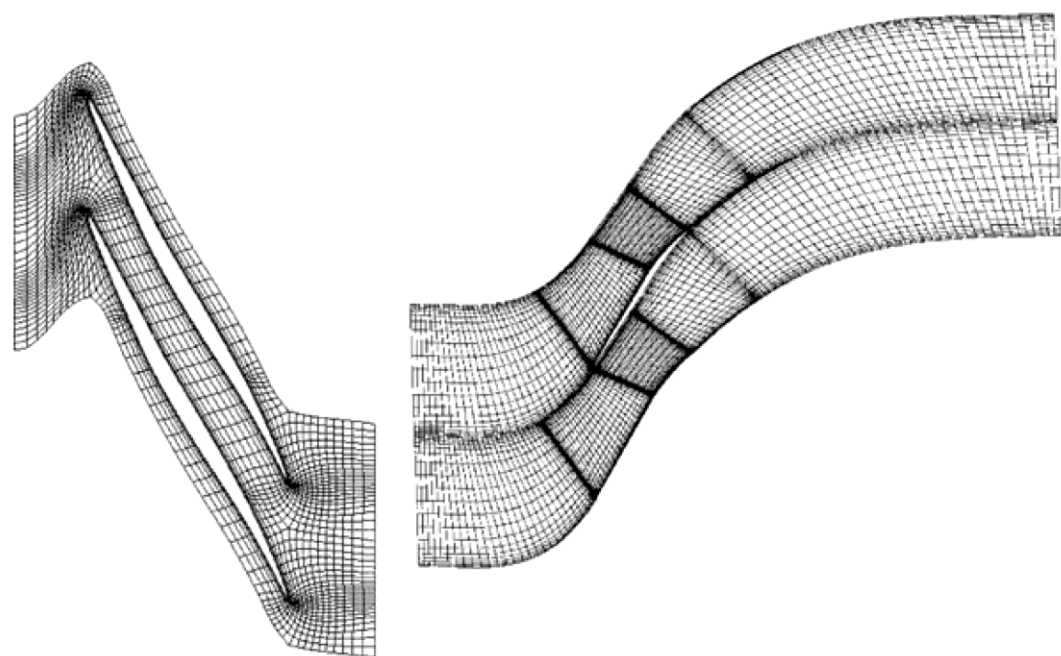


Figure 4.5 Structured curvilinear body-fitted grid of the I-type (Hirsch, 2007).

In order to increase the flexibility, the range of application and the easiness of the meshing process of structured grids, combinations of basic topologies can offer significant advantages. In this strategy, different mesh topologies are applied in different regions of the computational domain, leading to multi-block configurations. For instance the combination of a C-mesh around the body and an H-mesh in the upstream region is C-H mesh as shown in Figure (4.6).

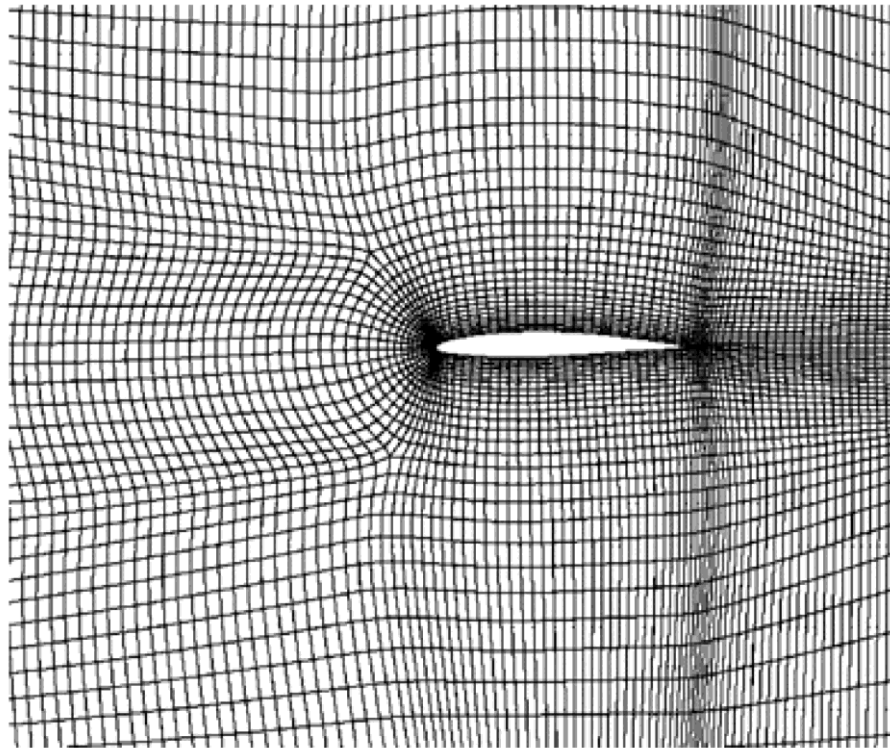


Figure 4.6 Structured curvilinear body-fitted grid of the C-H-type (Hirsch, 2007).

For internal turbomachinery flow simulations, a high degree of mesh flexibility is required and various combinations can be considered to enhance the quality of the grids. For instance, a combination O–H for turbine blades are shown in Figure (4.7).

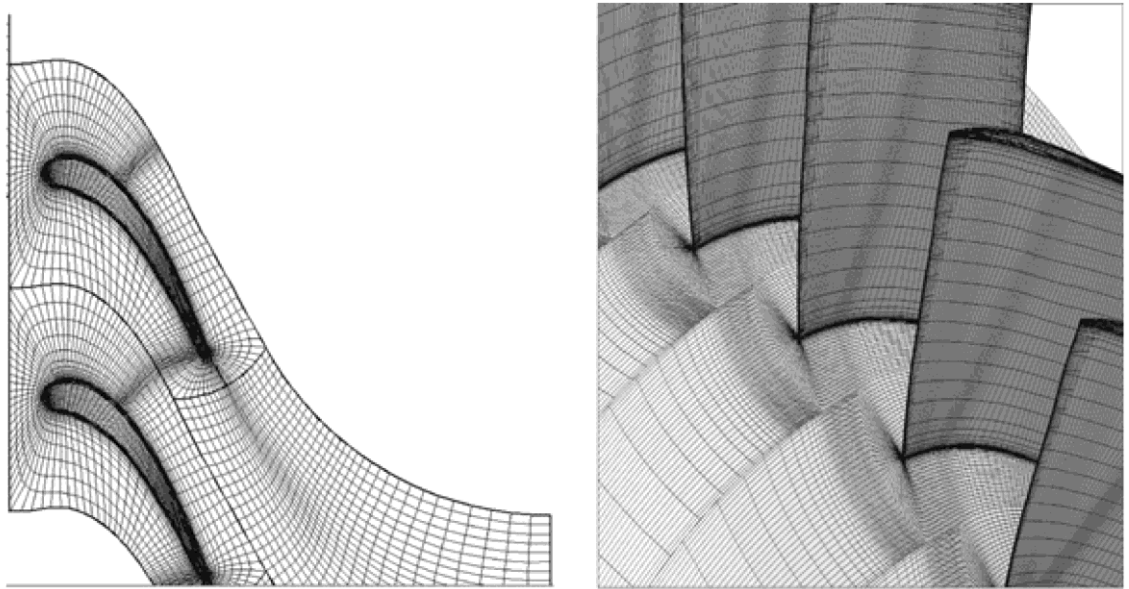


Figure 4.7 Structured curvilinear body-fitted grid of the O-H-type (Hirsch, 2007).

Unstructured grids, formed for instance by triangles in 2D, will tend to have a lower accuracy than the corresponding structured grids. Figure (4.8) shows a two-dimensional unstructured grid with triangular cells, around an airfoil with flaps. The main difficulty with triangular/tetrahedral grids is connected to the boundary layer requirements of high Reynolds number flows, where the grid density in the normal direction has to be adapted to the boundary layer velocity profiles. For solving this problem, hybrid grids have been developed that layers of quadrilaterals or prisms are generated in the near-wall region.

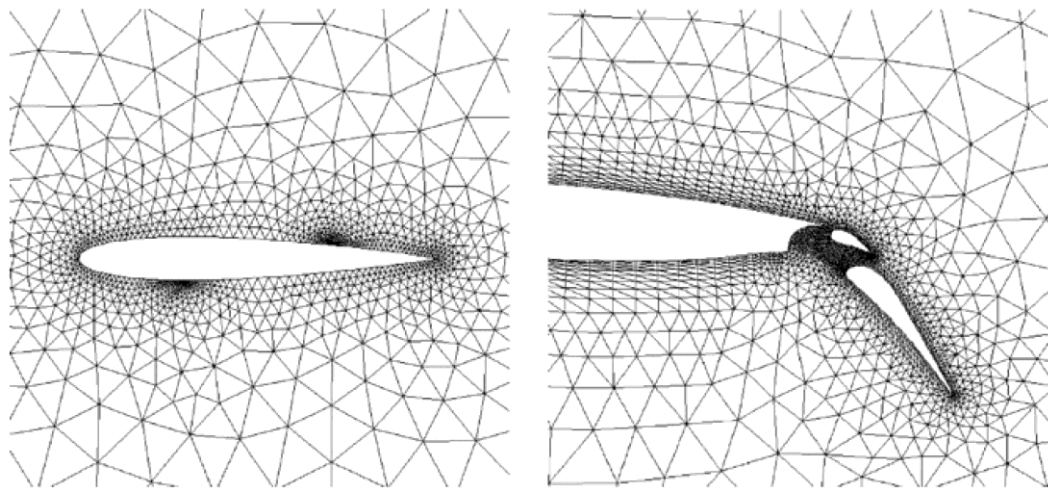


Figure 4.8 Example of an unstructured triangular grid (Hirsch, 2007).

In addition to the grid size continuity, other typical multidimensional quantities influence the global accuracy of the CFD simulation, related to the distortion of a cell from the ideal Cartesian shape. Typical quantities are aspect ratio  $\Delta x/\Delta y$ ; skewness

factor measured by the angle between adjacent sides/faces and their various 3D generalizations.

#### 4.14.1 TurboGrid

ANSYS® TurboGrid is a meshing tool that creates high quality hexahedral meshes for rotating machinery, while preserving the underlying geometry. TurboGrid employs the traditional concept of block-structure (multi-block) mesh generation. The block-structure approach is simple and efficient, allowing the well-known Transfinite Interpolation (TFI) for surface and interior mesh generation to be used (ANSYS®, 2011c). TurboGrid employs an algebraic, semi-isogeometric surface mesh generation procedure (ANSYS®, 2011c).

TurboGrid creates the mesh using the Topology Set and Mesh Data objects. The topology is a structure of blocks that acts as a framework for positioning mesh elements. Topology blocks represent sections of the mesh that contain a regular pattern of hexahedral (hex) elements. They are laid out adjacent to each other without overlap or gaps, with shared edges and corners between adjacent blocks, such that the entire domain is filled. By using topology blocks to control the placement of hex elements, a valid hex mesh can be generated to fill a domain of arbitrary shape. TurboGrid can make two different topology sets: ATM Optimized and Traditional Topologies. ATM Optimized is the default setting and allows high-quality meshes to be easily generated. Traditional Topologies gives more control over mesh generation. ATM is not applicable for blades that have square leading or trailing edges.

When the topology is created, TurboGrid creates a boundary layer control object that provides direct control of the mesh resolution. The near wall element size specification setting controls the method by which the near-wall node spacing is specified on the Passage and Hub/Shroud Tip tabs in the software. The near-wall node spacing is the distance between a wall (e.g., hub, shroud, or blade) and the first layer of nodes from the wall. The  $y^+$  method allows to set the near wall spacing,  $\Delta y$ , in accordance with a target value of  $y^+$ . The following formula relates the near wall spacing to  $y^+$  (ANSYS®, 2011c):

$$\Delta y = L \Delta y^+ \sqrt{80} Re_x^{1/14} \frac{1}{Re_L}, \quad (4.118)$$

where  $L$  is the blade chord,  $\Delta y^+$  is the specified target  $y^+$  value,  $Re_x$  is the Reynolds number based on the distance along the chord (measured from the leading edge), and

$Re_L$  is the Reynolds number based on chord length. TurboGrid approximates  $Re_x$  as being equal to the user specified value of  $Re_L$ .

## 4.15 Errors and uncertainty in CFD modelling

There are several sources of error and uncertainty in a CFD simulation. All of the terms, error, uncertainty, verification and validation have specific meanings which will be introduced below. The AIAA (American Institute of Aeronautics and Astronautics) guide makes a distinction between error and uncertainty, this is (AIAA, 2002):

**Error:** A recognized deficiency that is not due to lack of knowledge.

**Uncertainty:** A potential deficiency that is due to a lack of knowledge.

Error may be subdivided into acknowledged errors and unacknowledged errors. For example discretization error is acknowledged whereas a coding error is not. An acknowledged error (simply called error from now on) can be measured because its origins are fully identified. Quantification of error can proceed by comparison with a test problem or series of test problems and performing a detailed grid convergence study. Convergence studies must be performed in this case. A Grid Convergence Index (GCI), based on Richardson's extrapolation, has been developed to assist in the estimation of grid convergence error. In this manner, error in a CFD calculation typically is defined as (AIAA, 2002):

$$E = u_{exact} - u_{discrete}, \quad (4.119)$$

Here,  $u_{exact}$  is the mathematically correct solution of the exact equations of the conceptual model PDEs for a given set of initial and boundary conditions.  $u_{discrete}$  is the numerical solution of a given discrete approximation of these same PDEs and set of initial and boundary conditions produced by the given code on a given computer.

### 4.15.1 Numerical errors

CFD solves systems of non-linear partial differential equations in discretised form on meshes of finite time steps and finite control volumes that cover the region of interest and its boundaries. Three recognised sources of numerical error are described in following sections.

#### Model error

Modelling errors are defined as the difference between the actual flow and the exact solution to the conservation equations (AIAA, 2002). They arise, essentially, because

the equations are wrong, and it is associated with discrepancies between the real flow and the problem definition within a CFD model. The definition of the domain geometry involves specification of the shape and size of the region of interest. In summary, the macroscopic and microscopic geometry within the CFD model may be somewhat different from the real flow passage, which contributes to input error in the model results.

Apart from the shape and surface state of domain boundaries, it is also necessary to specify the conditions on the surface for all other flow variables, such as velocity, temperature, etc. It can be difficult to acquire this type of input to a high degree of accuracy. Simple assumptions, e.g. given temperature, given heat flux, adiabatic wall, are often made in the computations; the accuracy of these will affect the calculation result.

Moreover, the location of the open boundaries must be sufficiently far from the area of interest so that it does not affect the flow in this region. Solution economy on the other hand dictates that the domain should not be excessively large, therefore a compromise must be found, which may cause discrepancies between the real flow and the CFD model, resulting in a contribution to the input uncertainty.

All fluid properties depend on the local value of flow parameters, such as pressure and temperature. Often the assumption of a constant fluid property is acceptable provided that the spatial and temporal variations of the flow parameters influencing that property are small. CFD models converge more quickly if fluid properties remain constant; however, errors are introduced if the assumption of constant fluid properties is inaccurate. If the fluid properties are allowed to vary as functions of flow parameters we have to struggle with errors due to experimental uncertainty in the relationships describing the fluid properties.

One of the most significant errors in the model error category is generally a result of turbulence modelling assumptions, for example it is well known that the standard  $k-\varepsilon$  model includes the wall function approach. This is a computationally economical method, which avoids having to resolve the entire boundary layer profile by representing the properties of near-wall turbulent boundary layers by means of algebraic relationships. The log-law is itself an empirical description of flow behaviour. It means the standard  $k-\varepsilon$  model will give inaccurate predictions for flow separation determined by boundary layer behaviour in an adverse pressure gradient. These may or may not be due to a lack of knowledge and so they may be errors or uncertainties.

In summary, the empirical nature of the sub-models inside a CFD code, the experimental errors associated with the values of the sub-model constants and the appropriateness of the chosen sub-model for the flow to be studied together determine the level of errors in the CFD results due to physical model errors (AIAA, 2002).

#### **Discretization error**

Discretization errors are defined as the difference between the exact solution of the conservation equations and the exact solution of the algebraic equation system (AIAA, 2002). It is due to the terms neglected when, for example, using finite differences to represent exact derivatives. The error will reduce to zero as the grid spacing and time step decrease. The rate at which this occurs is determined by the order of the finite difference approximation. The reduction in spatial discretization error is known as grid convergence. Control of the magnitude and distribution of discretisation errors through careful mesh design is a major concern in high-quality CFD. In theory, we can make the discretisation error arbitrarily small by progressive reductions of the time step and space mesh size, but this requires increasing amounts of memory and computing time.

Localized sources of error result from the high-order terms that are excluded from the discrete approximations. Both error sources and propagation are affected by the solution and mesh distributions. Reducing the source of solution error is critical if accurate numerical solutions are desired. The two most effective strategies for accomplishing this are to increase the order-accuracy of discrete approximations (for example, using the high resolution rather than the upwind difference advection scheme) and/or to reduce the mesh spacing in regions of rapid solution variation (AIAA, 2002).

Discretisation error is quantified for CFD simulations by systematic refinement of the space and time meshes. In high-quality CFD work we should aim to demonstrate a monotonic reduction of the discretisation error for target quantities of interest and the flow field as a whole on two or three successive levels of mesh refinement.

The most common truncation criterion in CFD is based on so-called residuals. To get an indication of the convergence behaviour across the whole flow field, we define the global residual, which is just the sum of the local residuals over all control volumes within the computational domain. The magnitude of the global residual decreases as we get closer to the final solution. In engineering applications in order to achieve convergence of the solution to an acceptable level, the residual is usually set between four and six orders of magnitude lower than the actual values (Hirsch, 2007).

### Round-off error

Round-off errors are the result of the computational representation of real numbers by means of a finite number of significant digits, which is termed the machine accuracy (AIAA, 2002). The Round-off errors can generally be controlled by careful arrangement of floating-point arithmetic operations to avoid subtraction of almost equalized large numbers or addition of numbers with very large difference in magnitude.

Real numbers can of course only be stored with a finite level of precision. This is generally either ‘single’ i.e. 32 bit or ‘double’ i.e. 64 bit in industrial CFD codes, giving approximately 7 and 16 decimal digits of precision respectively. Round-off error can be assessed by comparing CFD results obtained using different levels of machine accuracy (e.g. in single precision, 7 significant figures; or double precision, 16 significant figures). Round-off errors are significant when calculating small differences between large numbers and so floating point arithmetic operations should be arranged to avoid this. An example of this is the use of gauge pressure in calculations instead of the absolute pressure. All CFD simulations in the next Chapter were run in double precision because of concerns about the accuracy of geometric calculations.

### 4.15.2 Numerical schemes and errors

Consistency, stability and convergence are the requirements to be imposed on a numerical scheme to obtain an acceptable approximation (Hirsch, 2007). They cover different aspects of the relations between the analytical and the discretised equations, and between the numerical solution and the exact, analytical solution of the differential equations which represent the mathematical model. For any mathematical model, we should have the total confidence that the numerical data we obtain indeed are a valid approximation of the ‘exact’ solutions.

Consistency is a condition on the numerical scheme in which the numerical scheme must tend to the differential equation, when time and space steps tend to zero (Hirsch, 2007). Stability is a condition on the numerical solution in which all the errors must remain bounded when the iteration process advances (Hirsch, 2007). That is, for finite values of  $\Delta t$  and  $\Delta x$ , the error has to remain bounded, when the number of time steps  $n$  tends to infinity. If we consider the error  $\bar{\varepsilon}_i^n$  as the difference between the computed solution  $u_i^n$  and the exact solution of the discretised equation  $\bar{u}_i^n$ :

$$\bar{\varepsilon}_i^n = u_i^n - \bar{u}_i^n , \quad (4.120)$$

then, the stability condition can be formulated by the requirement that any error  $\bar{\varepsilon}_i^n$  should remain uniformly bounded for  $n \rightarrow \infty$  at fixed  $\Delta t$ . Hence, the stability condition can be written as (Hirsch, 2007):

$$\lim_{n \rightarrow \infty} |\bar{\varepsilon}_i^n| \leq K \quad \text{at fixed } \Delta t , \quad (4.121)$$

with  $K$  independent of  $n$ .

Convergence is a condition on the numerical solution in which we have to be sure that the output of the simulation is a correct representation of the model we solve, i.e. the numerical solution must tend to the exact solution of the mathematical model, when time and space steps tend to zero. The mathematical formulation of the convergence condition states that the numerical solution  $u_i^n$  should approach the exact solution  $\tilde{u}(x, t)$  of the differential equation, at any point  $x_i = i \cdot \Delta x$  and time  $t^n = n \cdot \Delta t$  when  $\Delta x$  and  $\Delta t$  tend to zero, i.e. when the mesh is refined,  $x_i$  and  $t^n$  being fixed. This condition indicates that  $i$  and  $n$  tend to infinity while  $\Delta x$  and  $\Delta t$  tend to zero, such that the products  $i\Delta x$  and  $n\Delta t$  remain constant. Here we define the error  $\tilde{\varepsilon}_i^n$  as the difference between the computed solution and the exact solution of the analytical equation representing the selected mathematical model, expressed as following (Hirsch, 2007):

$$\tilde{\varepsilon}_i^n = u_i^n - \tilde{u}(i \Delta x, n \Delta t) . \quad (4.123)$$

This error has to satisfy the following convergence condition:

$$\lim_{\substack{\Delta x \rightarrow 0 \\ \Delta t \rightarrow 0}} |\tilde{\varepsilon}_i^n| = 0 \quad \text{at fixed values of } x_i = i \Delta x \text{ and } t^n = n \Delta t . \quad (4.124)$$

Note here that the stability and convergence conditions do not refer to the same errors.

Equivalence Theorem of Lax states that for a well-posed initial value problem and a consistent discretization scheme, stability is the necessary and sufficient condition for convergence. This fundamental theorem suggests two following tasks to be performed for analysing numerical schemes (Hirsch, 2007):

- 1 Analyse the consistency condition; this leads to the determination of the order of accuracy of the scheme and its truncation error,
- 2 Analyse the stability properties.

From these two steps, convergence can be established without additional analysis, and it suffices to test for the stability of a consistent scheme, to ensure that the numerical solution will provide a valid representation of the ‘reality’ we wish to

simulate numerically. These interrelations are summarized in Figure (4.9) which expresses the consistency condition defines a relation between the differential equation and its discrete formulation; and also the stability condition establishes a relation between the computed solution and the exact solution of the discretised equations; while the convergence condition connects the computed solution to the exact solution of the differential equation.

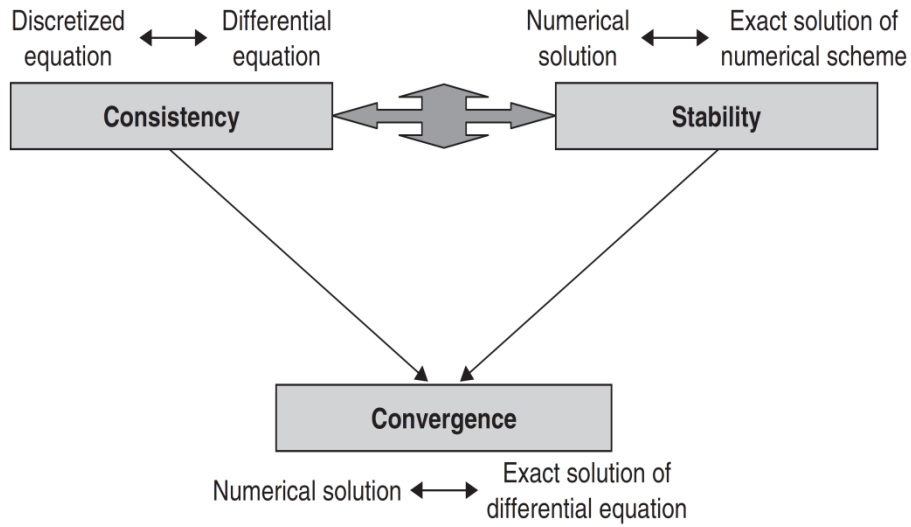


Figure 4.9 Relations between consistency, stability and convergence (Hirsch, 2007).

In order to check for consistency, we consider the discretised equation for the unknown  $u_i^n$ . This equation contains values at other points ( $i+j$ ) and other time levels ( $n+k$ ). The function values  $u_{i+j}^{n+k}$  in the numerical scheme are developed in a Taylor series around the value  $u_i^n$  and the high order terms are maintained in substituting these developments back in the numerical equation. In order to check for consistency, from the Taylor expansion series, the numerical scheme is expressed in the form of the discretised equations for the unknown  $u_i^n$  plus additional terms which called the truncation error, and noted  $\varepsilon_T$ . The truncation error will have the form as:

$$\varepsilon_T = O(\Delta t^q, \Delta x^p), \quad (4.125)$$

where  $p$  and  $q$  are the lowest values occurring in the development of the truncation error. This defines the order of accuracy of the scheme. This equation tells us indeed that the considered scheme is of order  $q$  in time and  $p$  in space. As a result, a scheme is consistent if the truncation error tends to zero for  $\Delta t$  and  $\Delta x$  tending to zero.

## 4.16 Verification and validation

Verification and validation refer to two phases in assessing the quality of a CFD model. The broadly agreed definitions of these terms, taken from the AIAA guide, are (AIAA, 2002):

**Verification:** *The process of determining that a model implementation accurately represents the developer's conceptual description of the model and the solution to the model; or Verification is the assessment of the accuracy of the solution to a computational model by comparison with known solutions.*

**Validation:** *The process of determining the degree to which a model is an accurate representation of the real world from the perspective of the intended uses of the model; or Validation is the assessment of the accuracy of a computational simulation by comparison with experimental data.*

Or in other terms:

**Verification:** *Solving the equations right* (Roache, 1998), a mathematics issue.

**Validation:** *Solving the right equations* (Roache, 1998), a physics issue.

Figure (4.10) shows that verification deals with the relationship between the conceptual model and the computerized model and that validation deals with the relationship between the computerized model and reality. The conceptual model is composed of all information, mathematical modelling data, and mathematical equations that describe the physical system. In CFD, the conceptual model is dominated by the partial differential equations (PDEs) for conservation of mass, momentum, and energy. In addition, the CFD model includes all of the auxiliary equations, such as turbulence models and all of the initial and boundary conditions of the PDEs. The computerized model is an operational computer program that implements a conceptual model.

### 4.16.1 Verification

Verification is defined as verifying that the mathematical model was correctly programmed. It is based on comparing the numerical results with exact, analytical solutions. In verification activities, the accuracy of a computational solution is primarily measured relative to two types of highly accurate solutions: analytical solutions and highly accurate numerical solutions. Therefore, to quantify numerical solution error, a highly accurate, reliable benchmark should be available. Highly accurate solutions refer to either analytical solutions or highly accurate numerical solutions. Figure (4.11) shows the verification process of comparing the numerical solution from the code with various

types of highly accurate solutions. In this essence, verification does not address whether the conceptual model has any relationship to the real world.

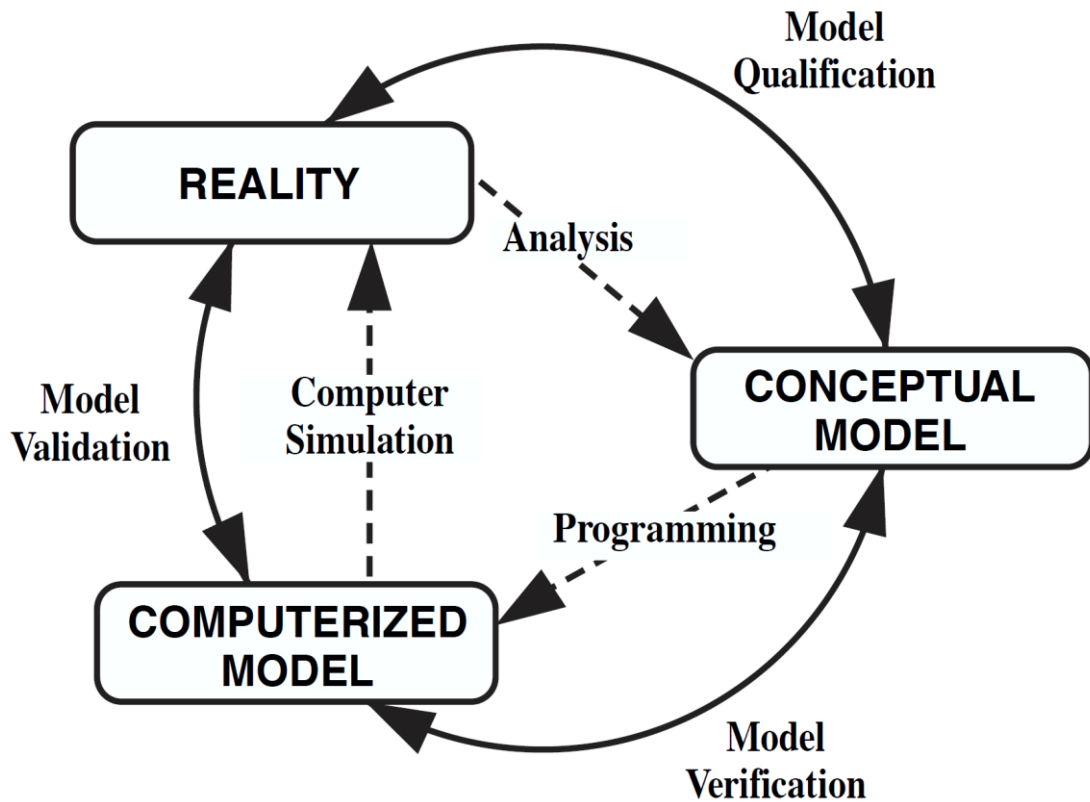


Figure 4.10 Phases of modelling and simulation and the role of verification and validation (AIAA, 2002).

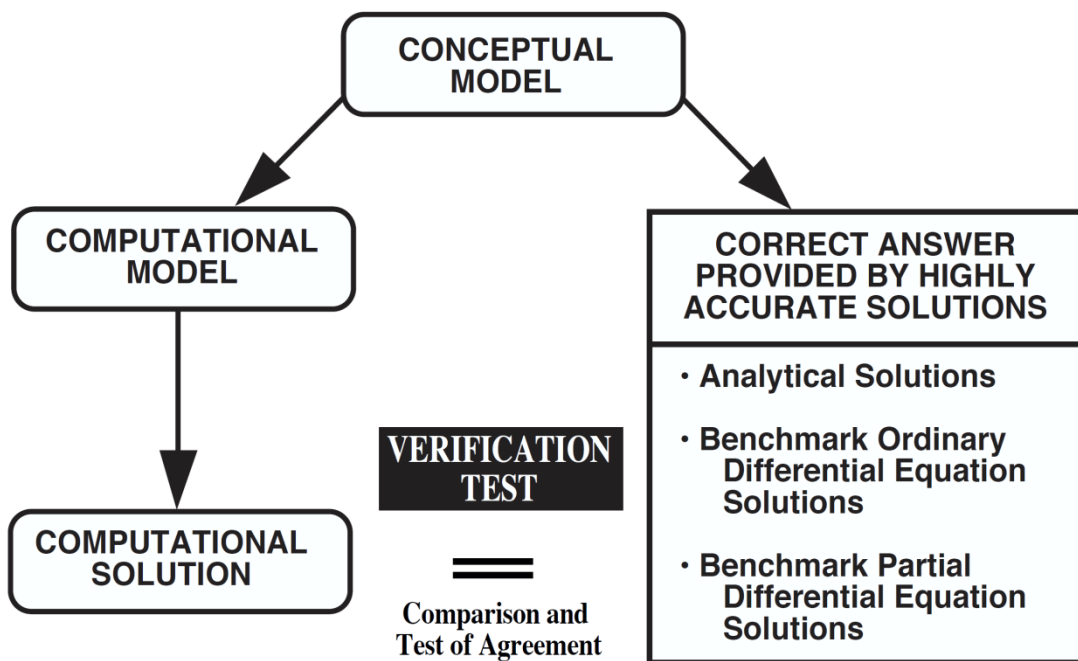


Figure 4.11 Verification process (AIAA, 2002).

Verification involves assessing the error due to insufficiently fine spatial and temporal discretization, insufficient iterative convergence and programming errors. The spatial discretization error is assessed by performing the simulation on a series of grids

of different resolutions, this process being commonly known as a grid convergence study, which is a procedure of successive refinement of an initially coarse grid until certain key results do not change. Then the simulation is grid independent.

The extent of iterative convergence can be assessed by looking at some measure of the equation residuals, namely the differences between the left and right hand sides of the algebraic equation system. The CFX solver gives a normalized value of the maximum and RMS residuals for each of the conservation equations being solved. Whilst reducing the RMS residuals for all equations to less than  $1\times 10^{-6}$  strongly suggests that the solution is tightly converged, i.e. there is negligible iterative error, the reverse is not necessarily true.

#### 4.16.2 Validation

Validation is the process of determining the degree to which a model is an accurate representation of the real world from the perspective of the intended uses of the model. The issue of validation of CFD codes is an extremely complex process as it is hardly possible to generate experimental data at the same level of details as provided by the CFD simulation. In addition, both experimental and numerical data are subjected to many error and uncertainty sources. These uncertainties associated to real life problems, make the verification step even more essential, with the objective to ensure that at least the numerical discretization is full proof and has a controllable accuracy.

Validation involves comparing the results of a verified simulation with experimental data in order to assess the modelling error. This may be difficult if the problem under consideration is particularly complex and the experimental data is limited; in addition the application uncertainty may be significant. This is the case also for this study in which making turbine motor prototype has not yet been funded to then tested with dynamometer test stand in the lab and provide some experimental results and performance data to check the simulation results with them for the validation purposes. Consequently, in this thesis for the simulation errors quantification, mainly the verification process and specially Grid Convergence study is evaluated to check for accuracy of the simulations and the further validation process would be recommended for future studies when turbodrill prototype and laboratory facility for experimental analysis be available for this project.

Under the circumstances that no experimental data are available to perform the validation process, the AIAA guide recommends a ‘building block’ approach to validation, and thus also verification.

The strategy of this building block approach is to progressively decompose the complete system into subsystem cases, benchmark cases and finally unit problems (AIAA, 2002), as shown in Figure (4.12). Each level is characterized by the complexity of the flow physics and geometry. The complete system will feature many interacting flow features and experimental data may be very limited. The subsystem case is the first level of simplification, perhaps achieved by removing some components from the complete system. The experimental data at this level will be somewhat more comprehensive than that for the complete system. Benchmark cases involve a more significant simplification to represent key features of each subsystem case. The aim at this level is to study the interaction between two flow physics features, and to have comprehensive experimental data to compare with. The final simplification is a unit problem, which will only contain a single flow physics feature. Unit problems are characterized by very simple geometries. The geometry features are commonly two-dimensional, but they can be very simple three-dimensional geometries with important geometric symmetry features.

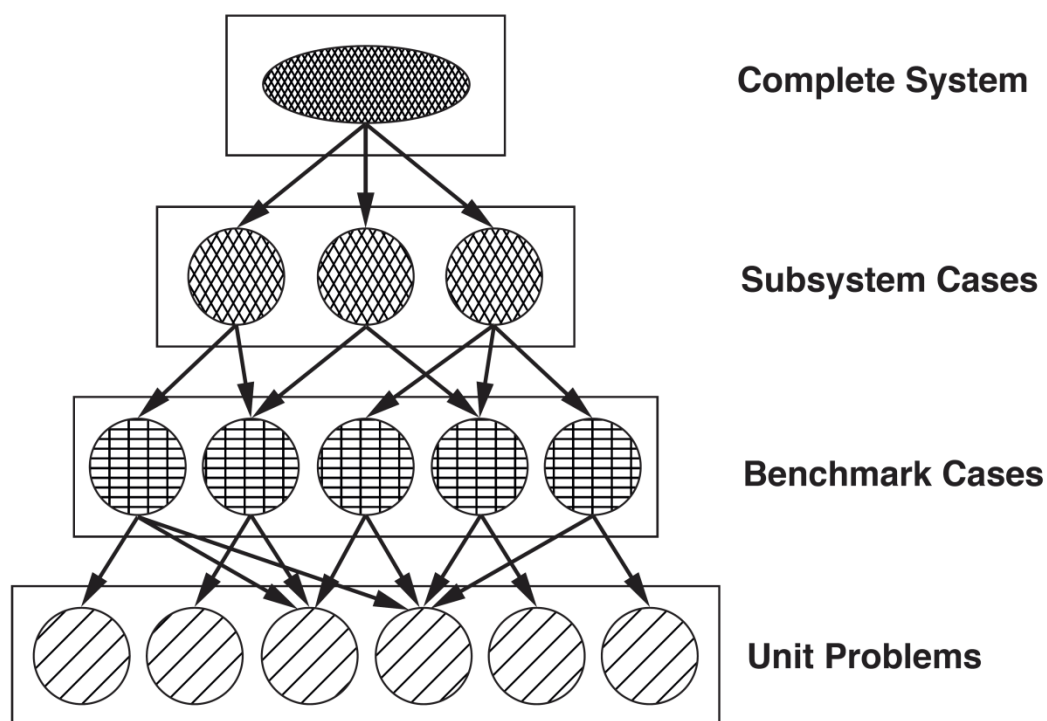


Figure 4.12 Validation phases (AIAA, 2002).

Validation process relates to the verification work. The verification studies as described above can consume a significant amount of CPU time if conducted on the

complete system case. With the building block approach, comprehensive verification studies can be performed on the unit problem and benchmark cases relatively quickly, and the results can then be used to inform the numerical parameters required for the problem setup of the subsystem and complete system cases (AIAA, 2002). Even when verification is required for the more complicated cases, the results from the less complicated cases will guide the choice of the new parameter values, reducing the time taken for verification.

In this study, the complete system is the multistage small diameter turbine motor including shaft and housing with the same hub and shroud diameters for all the stages and both stator rows and rotor rows in all the stages have the same geometrical and dimensional properties. In this case therefore each turbine stage is identical and that the flow rate, pressure drop, rotary speed, generated torque, and power transmitted to the shaft are the same for each of the stages. As a result, the present study is limited to the simulation of one subsystem of the above case, i.e. simulation of one stage of the proposed small turbine motor performance. This subsystem case is a 3D representation of one stage turbine motor with the actual geometrical and dimensional sizes. In the proposed model the number of blades on stator row and also on rotor row is equal and therefore because of the periodic symmetry between the blades on stator row and also on rotor row and having the same number of blades on each row, i.e. pitch ratio of 1, the simulations were conducted for one blade of stator and one blade of rotor interacting with each other. As a result, the benchmark case here is a 3D domain composed of one stator blade and one rotor blade with the transient or oscillating condition. The unit case here is a 3D domain composed of one stator blade and one rotor blade with the steady state condition for which a significant amount of numerical analysis with different accuracy and computation expenses have been done. Here, the result of highly accurate numerical solutions will be the basis for the comparison and for both verification and validation purposes. As a result, starting with the unit case we can go further up in the building block diagram and conduct the more computationally expensive CFD simulations with more confidence concerning the verification and validation issues.

## **4.17 Fluid-Structural Interaction analysis**

During the operation of a turbodrill the fluid mechanical pressure loading on the blades provides the driving torque on the shaft. This fluid loading results in a structural load which in turn causes the blades to deflect. In this study, the mechanical stresses and

deflections caused by the fluid mechanical pressure loading can be analysed by the coupling of solution fields in fluid and solid domains and are calculated by means of Fluid-Structural Interaction (FSI) analysis which applies the pressure distribution on the blade surface calculated by CFD as a major boundary condition. For solving FSI problems there are two options: one-way coupling and two-way coupling. A one-way coupling analysis is performed by running a CFD analysis, extracting the forces acting on a solid surface and then importing them as major boundary conditions to a structural analysis. In a one-way analysis the response from the structural analysis will not affect the CFD analysis. In a two-way coupling analysis, both the flow field and structural response will be taken into account, interacting together and affect the flow simulation. In this study because the turbodrill blades are small and quite stiff, therefore only one-way coupling FSI analyses are considered here in which the response from the structural analysis will not affect the CFD analysis.

In this study, static structural analyses used to determine displacements, stresses, etc. under static loading conditions. A static analysis calculates the effects of steady loading conditions on a structure, while ignoring inertia and damping effects, such as those caused by time-varying loads. A static analysis can, however, include steady inertia loads (such as gravity and rotational velocity), and time-varying loads that can be approximated as static equivalent loads. Here, static structural analyses are performed using the ANSYS® Mechanical APDL solver. APDL solver uses the Finite Element Method (FEM) for finding approximate solutions to partial differential equations and their systems.

The finite element method (FEM) originated from the field of structural analysis. The method is widely used in the analysis of hydraulic turbines. The concept of ‘elements’ go back to the techniques used in stress calculations whereby a structure is subdivided to small substructures with various shape. The FEM is based on the definition of the function values attached to the nodes of the mesh. In this technique the numerical value of the unknown functions, and eventually their derivatives, will have to be determined. The total number of unknowns at the nodes (function values and their derivatives) is called the degrees of freedom (ANSYS®, 2011d). The solution is dependent on the quality of the grid. Therefore size and arrangement of the grid is important in practice. It is desirable with fine grids in areas of stress concentration.

In the ANSYS® APDL solver, stress is related to the strains by:

$$\{\sigma\} = [D]\{\varepsilon^{el}\}, \quad (4.126)$$

where:

$$\{\sigma\} = \text{Stress vector}, [\sigma_x \sigma_y \sigma_z \sigma_{xy} \sigma_{yz} \sigma_{xz}]^T,$$

$[D]$  = Elasticity or elastic stiffness matrix,

$\{\varepsilon^{el}\}$  = Elastic strain vector, which is obtain as following:

$$\{\varepsilon^{el}\} = \{\varepsilon\} - \{\varepsilon^{th}\}, \quad (4.127)$$

$$\{\varepsilon\} = [B]\{u\}, \quad (4.128)$$

$$\{\varepsilon^{el}\} = [B]\{u\} - \{\varepsilon^{th}\}, \quad (4.129)$$

where:

$$\{\varepsilon\} = \text{Total strain vector}, [\varepsilon_x \varepsilon_y \varepsilon_z \varepsilon_{xy} \varepsilon_{yz} \varepsilon_{xz}]^T,$$

$\{\varepsilon^{th}\}$  = Thermal strain vector,

$[B]$  = Strain-displacement matrix evaluated at integration point, based on the element shape functions,

$\{u\}$  = Nodal displacement vector.

The applied loads acting on a body make it move from one position to another (see Figure 4.13). If the position vectors in the “deformed” and “undeformed” state are represented by  $\{x\}$  and  $\{X\}$  respectively, then the displacement vector  $\{u\}$  is computed by:  $\{u\} = \{x\} - \{X\}$ .

The stress vectors are shown in figure 2. The sign convention for direct stresses and strains used throughout the ANSYS® program is that tension is positive and compression is negative. For shear stresses and strains, positive is when the two applicable positive axes rotate toward each other. The following equations between strain and stress components are defined by decomposition of the stiffness matrix, stated as:

The stress vectors are shown in Figure 4.14. The sign convention for direct stresses and strains used throughout the ANSYS® program is that tension is positive and compression is negative. For shear stresses and strains, positive is when the two applicable positive axes rotate toward each other.

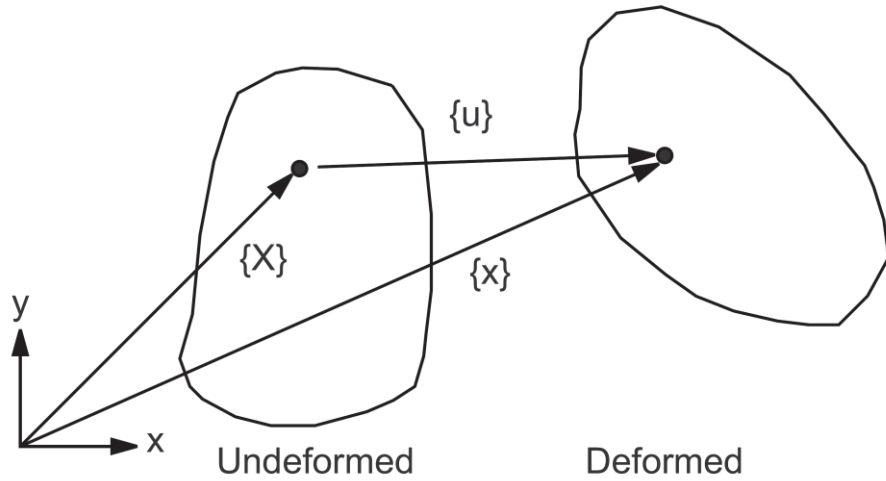


Figure 4.13 Deformation caused by applying loads on a body (ANSYS®, 2011d).

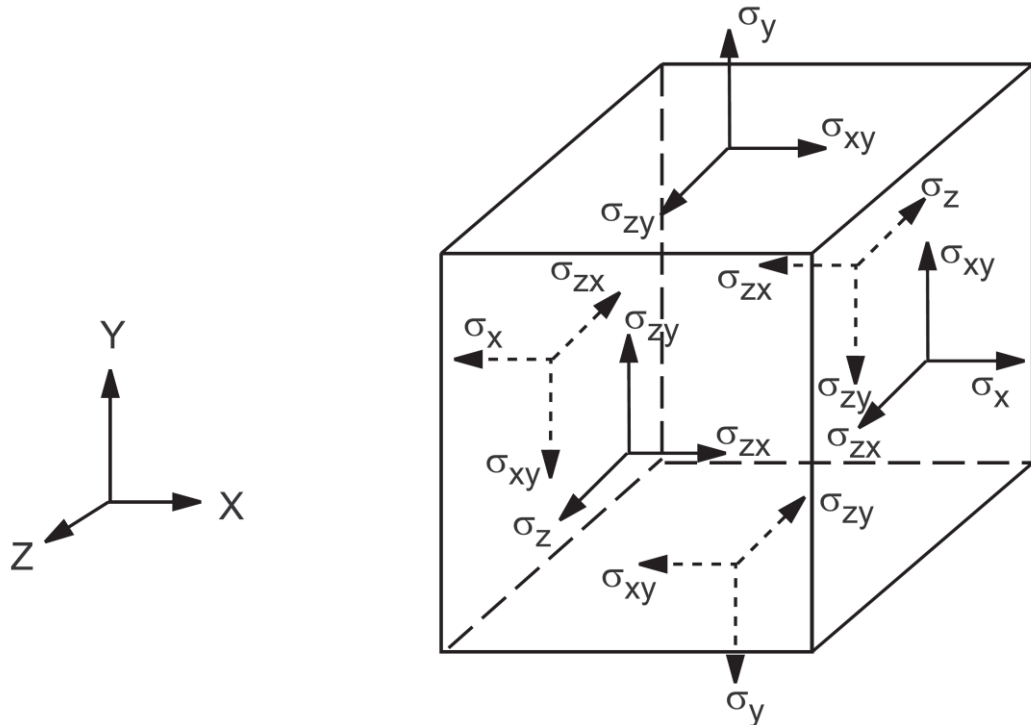


Figure 4.14 The stress vectors (ANSYS®, 2011d).

The following equations between strain and stress components are defined by decomposition of the stiffness matrix, stated as:

$$\varepsilon_x = \alpha_x \Delta T + \frac{\sigma_x}{E_x} - \frac{\nu_{xy} \sigma_y}{E_x} - \frac{\nu_{xz} \sigma_z}{E_x}, \quad (4.130)$$

$$\varepsilon_y = \alpha_y \Delta T + \frac{\sigma_y}{E_y} - \frac{\nu_{xy} \sigma_x}{E_y} - \frac{\nu_{yz} \sigma_z}{E_y}, \quad (4.131)$$

$$\varepsilon_z = \alpha_z \Delta T + \frac{\sigma_z}{E_z} - \frac{\nu_{yz} \sigma_y}{E_z} - \frac{\nu_{xz} \sigma_x}{E_z}, \quad (4.132)$$

$$\varepsilon_{xy} = \frac{\sigma_{xy}}{G_{xy}}, \quad (4.133)$$

$$\varepsilon_{yz} = \frac{\sigma_{yz}}{G_{yz}}, \quad (4.134)$$

$$\varepsilon_{xz} = \frac{\sigma_{xz}}{G_{xz}} \quad (4.135)$$

where:

$\alpha$  = Coefficient of thermal expansion,

$\Delta T$  = Temperature change,

$E$  = Young's modulus,

$G$  = Shear modulus,

$\nu$  = Poisson's ratio,

and also following relations:

$$\sigma_x = \frac{E_x}{h} \left[ 1 - (\nu_{yz})^2 \frac{E_z}{E_y} \right] (\varepsilon_x - \alpha_x \Delta T) + \frac{E_y}{h} \left( \nu_{xy} + \nu_{xz} \nu_{yz} \frac{E_z}{E_y} \right) (\varepsilon_y - \alpha_y \Delta T) + \frac{E_z}{h} (\nu_{xz} + \nu_{yz} \nu_{xy}) (\varepsilon_z - \alpha_z \Delta T), \quad (4.136)$$

$$\sigma_y = \frac{E_y}{h} \left( \nu_{xy} + \nu_{xz} \nu_{yz} \frac{E_z}{E_y} \right) (\varepsilon_x - \alpha_x \Delta T) + \frac{E_y}{h} \left[ 1 - (\nu_{xz})^2 \frac{E_z}{E_x} \right] (\varepsilon_y - \alpha_y \Delta T) + \frac{E_z}{h} \left( \nu_{yz} + \nu_{xz} \nu_{xy} \frac{E_y}{E_x} \right) (\varepsilon_z - \alpha_z \Delta T), \quad (4.137)$$

$$\sigma_z = \frac{E_z}{h} (\nu_{xz} + \nu_{yz} \nu_{xy}) (\varepsilon_x - \alpha_x \Delta T) + \frac{E_z}{h} \left( \nu_{yz} + \nu_{xz} \nu_{xy} \frac{E_y}{E_x} \right) (\varepsilon_y - \alpha_y \Delta T) + \frac{E_z}{h} \left[ 1 - (\nu_{xy})^2 \frac{E_y}{E_x} \right] (\varepsilon_z - \alpha_z \Delta T), \quad (4.138)$$

$$\sigma_{xy} = G_{xy} \varepsilon_{xy}, \quad (4.139)$$

$$\sigma_{yz} = G_{yz} \varepsilon_{yz}, \quad (4.140)$$

$$\sigma_{xz} = G_{xz} \varepsilon_{xz}, \quad (4.141)$$

where:

$$h = 1 - (\nu_{xy})^2 \frac{E_y}{E_x} - (\nu_{yz})^2 \frac{E_z}{E_y} - (\nu_{xz})^2 \frac{E_z}{E_x} - 2 \nu_{xy} \nu_{yz} \nu_{xz} \frac{E_z}{E_x}. \quad (4.142)$$

For isotropic materials, we have following relation:

$$G_{xy} = G_{yz} = G_{xz} = \frac{E_x}{2(1 + \nu_{xy})}. \quad (4.143)$$

The displacements within the element are related to the nodal displacements by:

$$\{w\} = [N]\{u\}, \quad (4.144)$$

where  $[N]$  = matrix of shape functions,  $\{w\}$  = vector of displacements of a general point.

A static structural analysis can be either linear or nonlinear. Material properties can also be linear or nonlinear, isotropic or orthotropic, and constant or temperature-dependent. Stiffness matrix should be defined in an appropriate form (for example, Young's modulus, hyperelastic coefficients, and so on). Geometric nonlinearities refer to the nonlinearities in the structure or component due to the changing geometry as it deflects. That is, the stiffness  $[K]$  is a function of the displacements  $\{u\}$  (ANSYS®, 2011d).

The governing equation of the solid structure motion can be written as (ANSYS®, 2011d):

$$M \frac{d^2u}{dt^2} + C \frac{du}{dt} + Ku = f , \quad (4.145)$$

where  $M$ ,  $C$  and  $K$  are the mass, damping, and stiffness matrices of the solid respectively,  $u$  is the displacement vector and  $f$  is the force exerted on the surface node points of the solid, both can be expressed as:  $u = (u_1 \cdots u_i \cdots u_N)$ ,  $f = (f_1 \cdots f_i \cdots f_N)$ , where  $N$  is the total number of node points of the structural model,  $u_i$  and  $f_i$  are vectors with 3 components in  $x$ ,  $y$ ,  $z$  directions.

## 4.18 Summary

In this Chapter, the numerical simulation process and theories of fluid flow analysis through turbodrill were discussed. Basic equations for computational fluid dynamics (CFD) and fluid-structural interaction (FSI) for applications of this study were presented in detail. Verification and validation process for the numerical methods was also presented and discussed. In the next Chapter, the CFD and FSI simulation results of the turbodrill stage models will be reported in detail with the performance chart for each model.

### Bibliographic note

The most general theories discussed in this chapter are not specifically referenced and come from a number of sources including: An Introduction to Computational Fluid Dynamics (Versteeg and Malalasekera, 2007), Numerical Computation of Internal and External Flows (Hirsch, 2007), Verification and Validation in Computational Fluid Dynamics (AIAA, 2002) and ANSYS® 14.0 software manuals.

# 5

# Numerical simulation results and discussions

In the previous Chapter, basic numerical methodology for Computational Fluid Dynamics (CFD) code used by ANSYS® CFX software in fluid flow analysis of the turbine motor and Fluid-Structural Interaction (FSI) code used by ANSYS® APDL software for structural analysis used in this study were described. Also discussion on verification and validation process in assessing the quality of a CFD model was presented. In this Chapter, CFD and FSI simulation results of the one stage turbine models designed in Chapter 3 will be presented. The grid convergence study is also discussed and the results are presented for water, air and mist as fluids to drive the turbine.

## 5.1 CFD simulation process

ANSYS® CFX 14.0 software was used in this study for fluid flow analysis through turbodrill. When designing and simulating a hydraulic multistage turbodrill, it was assumed that each turbodrill stage is identical and that the flow rate, pressure drop, rotary speed, generated torque, and power transmitted to the shaft are the same for each of the stages. As a result, turbodrill performance is composed of performance of several identical stages stacked close to each other and connected to the turbodrill shaft. In this study, one stage turbodrill performance with different geometrical models presented in Chapter 3 is investigated by CFD and FSI analyses with variety of real working conditions. Each stage is composed of first one stator blade row and then one rotor blade row with plurality of blades on them. The number of blades on each row is equal for both stator and rotor. Based on the interface models included in CFX and described in the previous Chapter, If the flow field is repeated in multiple identical regions, then only one region needs to be solved and the boundaries are specified as “Periodic” (via a rotation or translation). Consequently, here “Rotational Periodicity” can easily be applied due to the same number of blades on each row and then, only one blade on stator row and one blade on rotor row, interacting together, need to be modelled in

which computational expenses will be reduced significantly. Figure 5.1 shows the geometrical domain in green for one of the turbodrill stage models used in this study for simulation purposes.

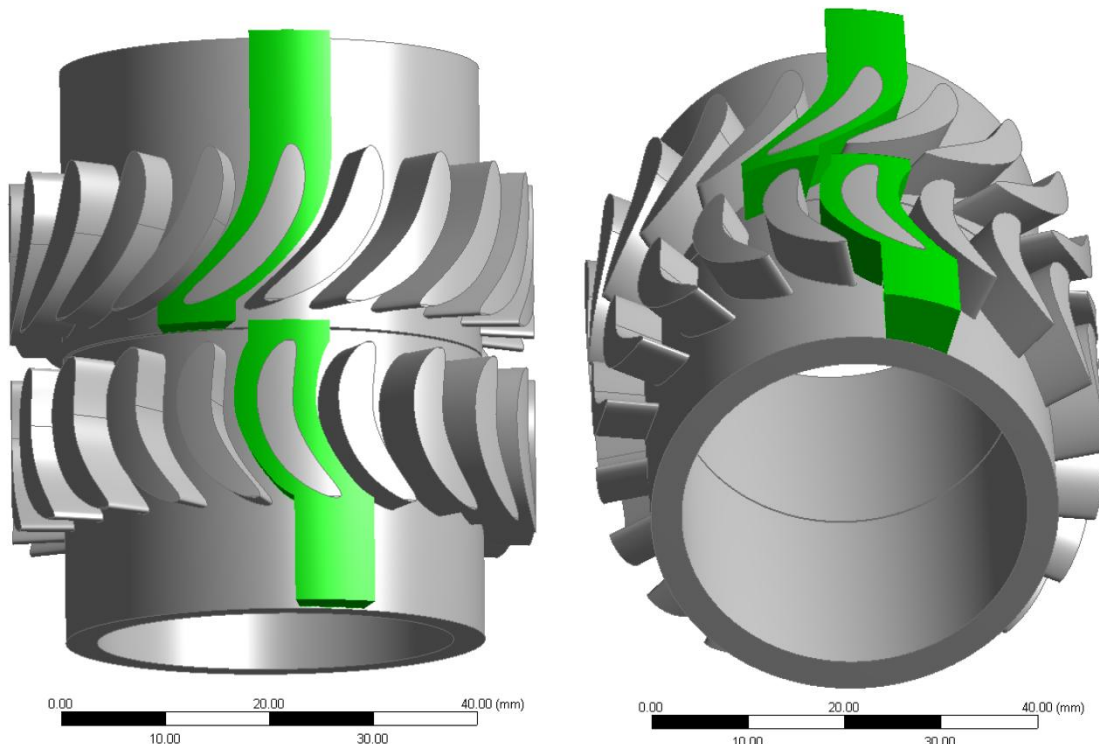


Figure 5.1 Geometrical domain (one blade of stator and rotor) highlighted in green for one of the Turbodrill stage models used in this study for simulation purposes.

### 5.1.1 Fluid type

In this study, for the purpose of hard rocks mineral exploration drilling, clean water was considered as the main drilling fluid and therefore here for the simulation purposes water was used in CFX with following default properties in the software:

*Material:* Water (liquid), constant property liquid, pure substance,

*Dynamic viscosity* =  $8.899 \times 10^{-4}$  (kg/m.s),

*Density* = 997.0 (kg/m<sup>3</sup>),

*Molar mass* = 18.02 (kg/kmol),

*Specific heat capacity* = 4181.7 (J/kg.K),

*Thermal conductivity* = 0.6069 (W/m.K),

*Thermal expansivity* =  $2.57 \times 10^{-4}$  (1/K).

Moreover in this study, air flow and mist flow (mixture of air as continuous phase and water droplets as dispersed fluid particle) were considered and analysed for reaching

higher rotation speeds for the future needs that new bit developments allow high rotation speeds ( $\geq 10,000$  rpm) to be applied delivering high ROP ranges. Here, the objective of using mist as drilling fluid is to add some amount of water to the pumped air to provide cooling to the down hole tools and especially to provide sufficient cooling to the impregnated diamond bit which is cutting the rock by grinding action and produce a large amount of heat on the bit face. The large surface area of the small water droplets leads to high evaporation rates which extract large amounts of heat. In addition, as the water droplets are converted to steam they expand approximately 1700 times. Here, air at  $25^{\circ}\text{C}$  was used in CFX with following software default properties:

*Material:* Air at  $25^{\circ}\text{C}$  (dry gas), constant property gas, pure substance,

*Dynamic viscosity* =  $1.831 \times 10^{-5}$  (kg/m.s),

*Density* = 1.185 (kg/m<sup>3</sup>),

*Molar mass* = 28.96 (kg/kmol),

*Specific heat capacity* = 1004.4 (J/kg.K),

*Thermal conductivity* = 0.0261 (W/m.K),

*Thermal expansivity* =  $3.356 \times 10^{-3}$  (1/K).

### 5.1.2 Boundary conditions

As described in the previous Chapter several boundary conditions were set in CFX. For all of the CFD simulations of this study boundary conditions were specified as a total pressure at the inlet and a mass flow rate at the outlet. The static pressure at the outlet and the velocity at the inlet are therefore part of the solution. For water flow simulations, reference pressure were set to 1000 psi (68.95 bar), the total pressure at the inlet were set to 1500 psi (103.42 bar). For air and mist flow simulations, reference pressure were set to 1 atm (1.01 bar), the total pressure at the inlet were set to 100 psi (6.89 bar). The outlet mass flow rate for each simulation case is varied. Non-slip walls were specified for the domain walls. Detailed descriptions of other boundary conditions set in CFX were provided in the previous Chapter. Figure 5.2 and 5.3 show schematic views of different boundary conditions used in CFX and in this study.

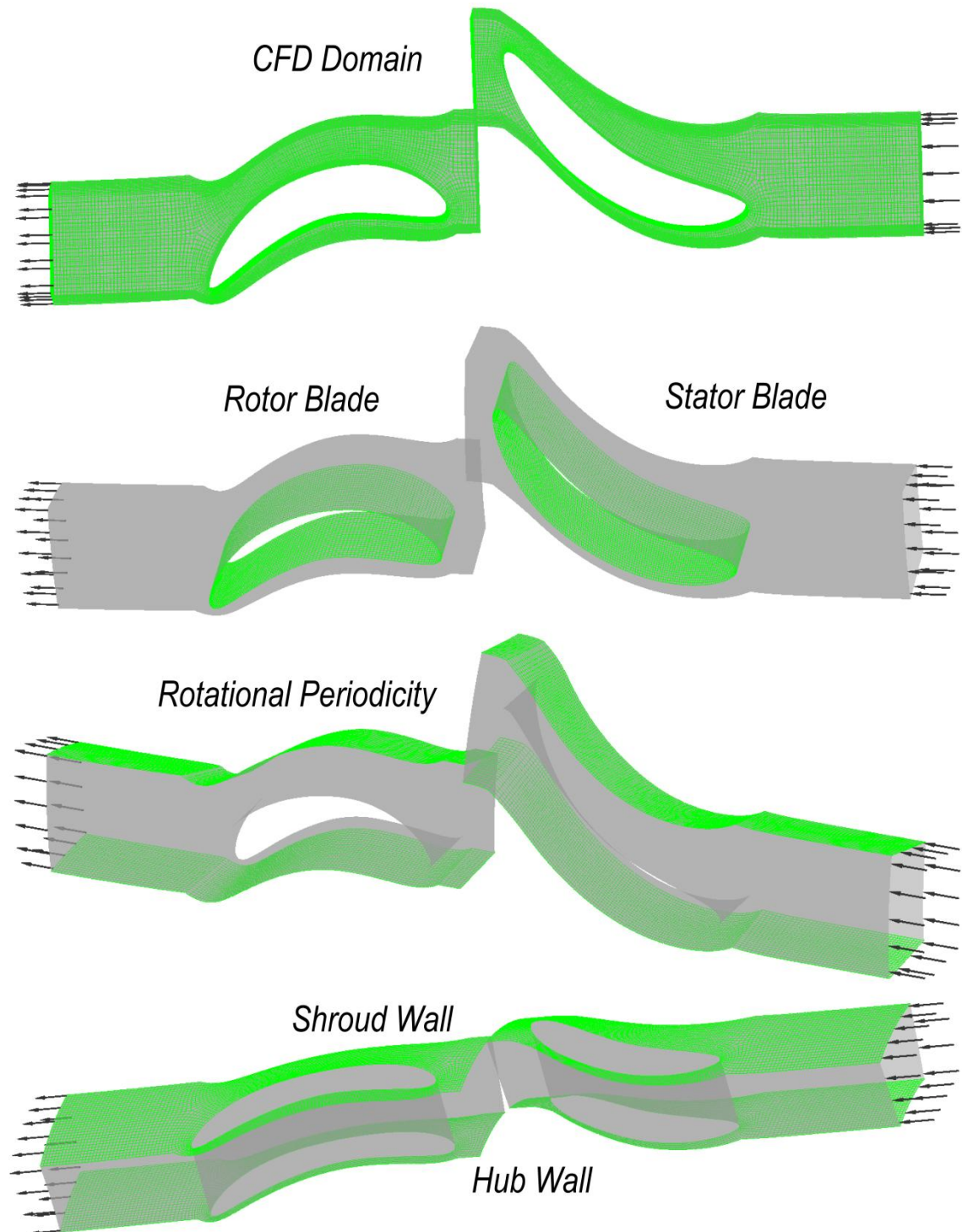


Figure 5.2 Boundary conditions set in CFX for this study (part 1).

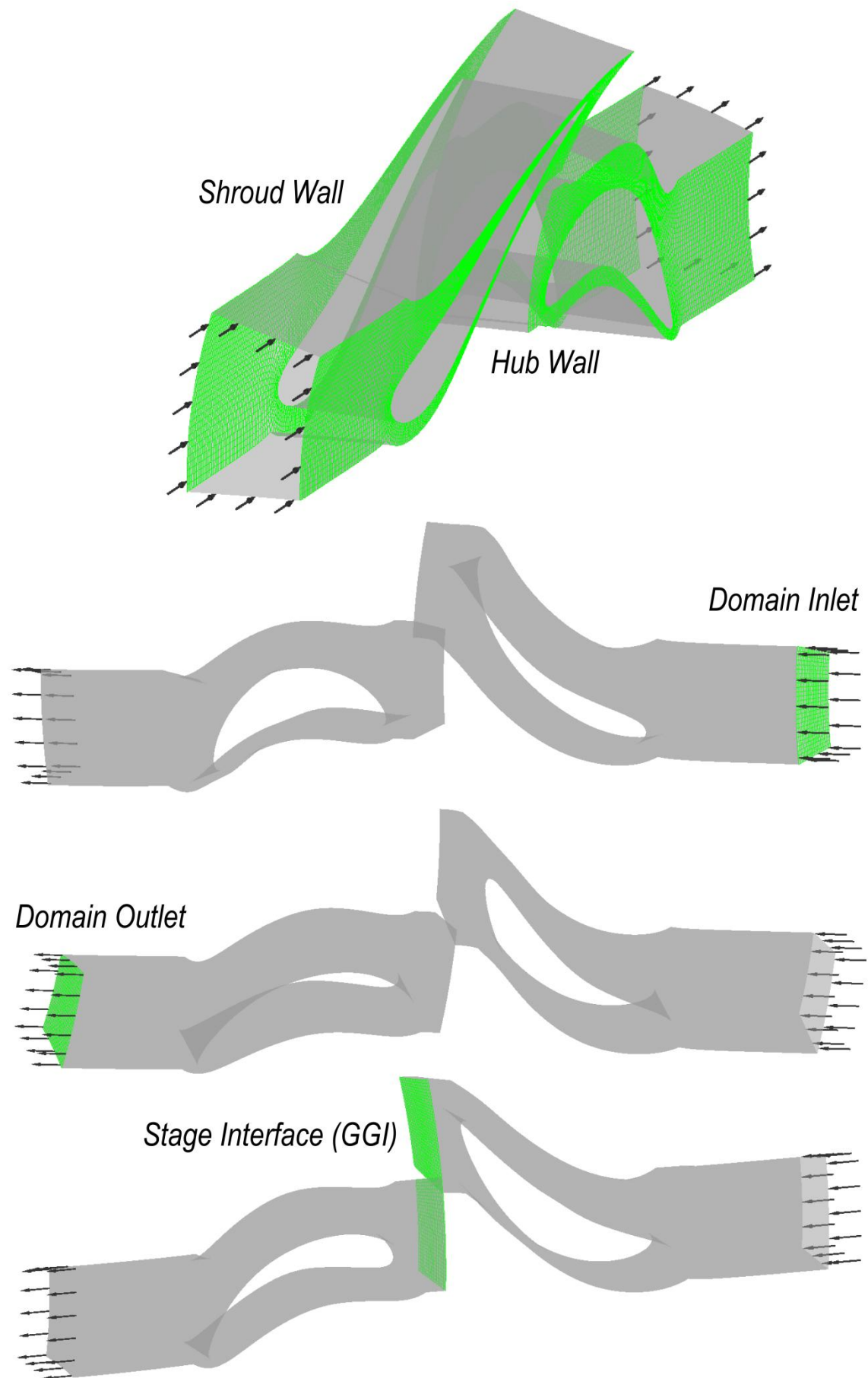


Figure 5.3 Boundary conditions set in CFX for this study (part 2).

## 5.2 Grid convergence study for CFD simulations

After building the geometrical model in the “BladeGen” module of ANSYS®, it needs to be discretised (meshing) to a large number of very small volumes for the purpose of the Finite Volume Method (FVM) and CFD simulation. This process is performed with “TurboGrid” module of ANSYS® that creates high quality hexahedral meshes for rotating machinery. The quality of CFD simulation is highly dependent to the quality of the mesh. According to the discretisation error described in the previous Chapter, the error will reduce to zero as the grid spacing and time step decrease. The reduction in spatial discretisation error is known as grid convergence. In theory, we can make the discretisation error arbitrarily small by progressive reductions of the time step and space mesh size, but this requires increasing amounts of memory and computing time.

In high-quality CFD work we should aim to demonstrate a monotonic reduction of the discretisation error for the target quantities of interest and the flow field as a whole on several successive levels of mesh refinement. To get an indication of the convergence behaviour across the whole flow field, we define the global residual, which is the sum of the local residuals over all control volumes within the computational domain. The magnitude of the global residual decreases as we converge to the final solution. In this study in order to achieve convergence of the solution to an acceptable level, the global root mean square (RMS) residual was set as the convergence criterion and it was set to  $1 \times 10^{-6}$ .

Here for two of the turbodrill stage models (A1W20 and A1G25) used in this study, comprehensive grid convergence study for both water and air flows are reported. Two turbulence models of  $k-\varepsilon$  and SST were used for water flow study. For air flow only SST turbulence model was used.

In TurboGrid the “Target Passage Mesh Size” method was used to set number of nodes in the domain. Then for the boundary layer “Edge Refinement Factor” method was used to set a factor that controls the boundary layer refinement. This refinement factor is especially important for the SST turbulence model. For the near wall element sizes ( $y^+$ ) method and Reynolds number were used. A series of several mesh models were used in the study for both water and air flow studies, each having a defined refinement ratio from the previous model.

### 5.2.1 Water flow grid convergence study

For the grid convergence study of water flow through a turbodrill stage, model “A1W20” was used. Table 5.1 shows several hexahedral mesh configurations generated for this model in “TurboGrid”. The objective here is to demonstrate accuracy and convergence of the analysis to the “exact numerical solution” with progressive mesh refinement.

Table 5.1: Mesh models generated for water flow grid convergence study.

Target Passage Mesh Size (=N×50,000)	Edge Refinement Factor (F)	Total Nodes	Total Elements
N=1 (=50,000)	1	58,560	49,546
	2	60,165	51,688
	3	71,310	62,202
N=2 (=100,000)	1	108,972	94,979
	2	110,736	97,835
	3	103,482	91,919
N=4 (=200,000)	1	214,682	192,544
	2	212,037	191,950
	3	208,886	190,278
N=8 (=400,000)	1	420,384	385,392
	2	418,760	386,932
	3	423,893	393,848
N=20 (=1,000,000)	1	1,041,400	976,638
	2	1,048,240	989,430
	3	1,040,480	985,686
N=40 (=2,000,000)	1	2,084,850	1,981,756
	2	2,078,300	1,984,696
	3	2,056,400	1,969,653
N=80 (=4,000,000)	1	4,118,751	3,955,662
	2	4,087,251	3,939,914
	3	4,090,464	3,952,438

Different mesh models generated for water flow grid convergence study for the stator blade are shown in cut plots in Figures 5.4 to 5.24.

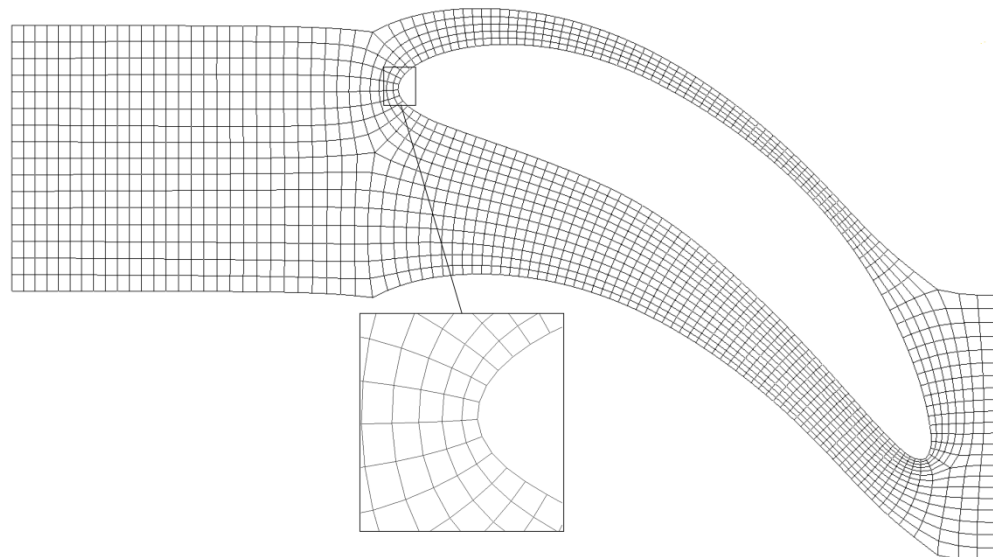


Figure 5.4 Mesh model with  $N=1$  and  $F=1$  for the stator blade at span surface 0.5.

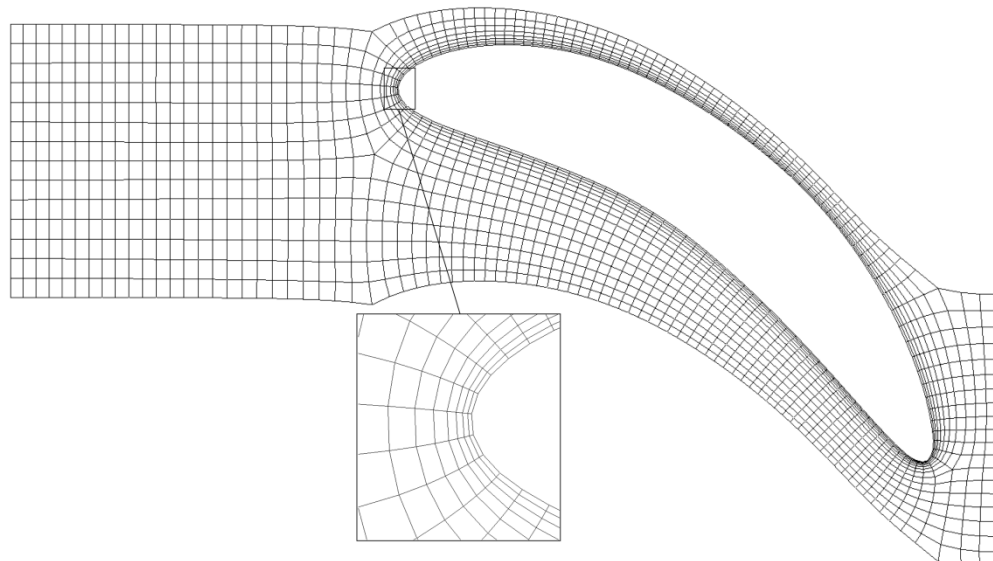


Figure 5.5 Mesh model with  $N=1$  and  $F=2$  for the stator blade at span surface 0.5.

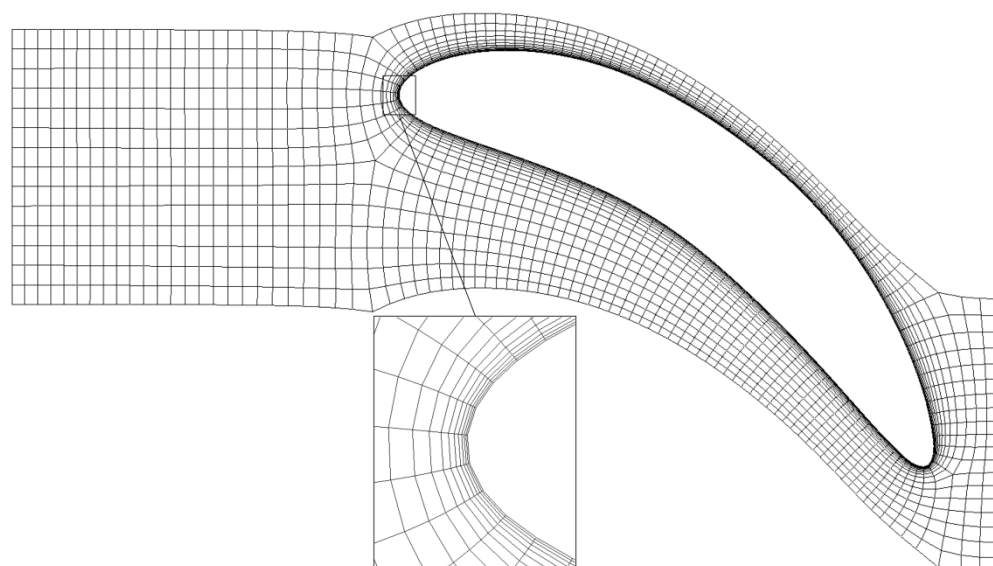


Figure 5.6 Mesh model with  $N=1$  and  $F=3$  for the stator blade at span surface 0.5.

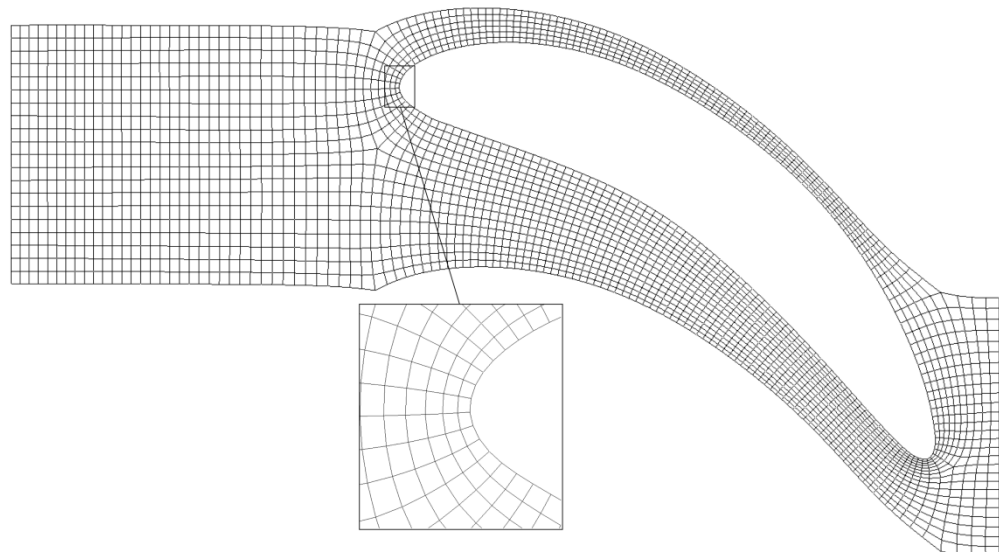


Figure 5.7 Mesh model with  $N=2$  and  $F=1$  for the stator blade at span surface 0.5.

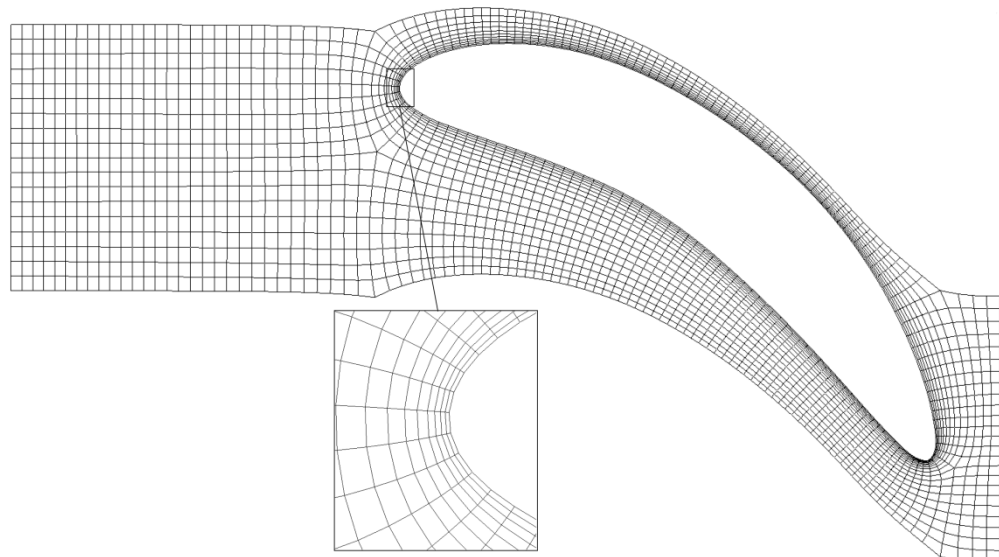


Figure 5.8 Mesh model with  $N=2$  and  $F=2$  for the stator blade at span surface 0.5.

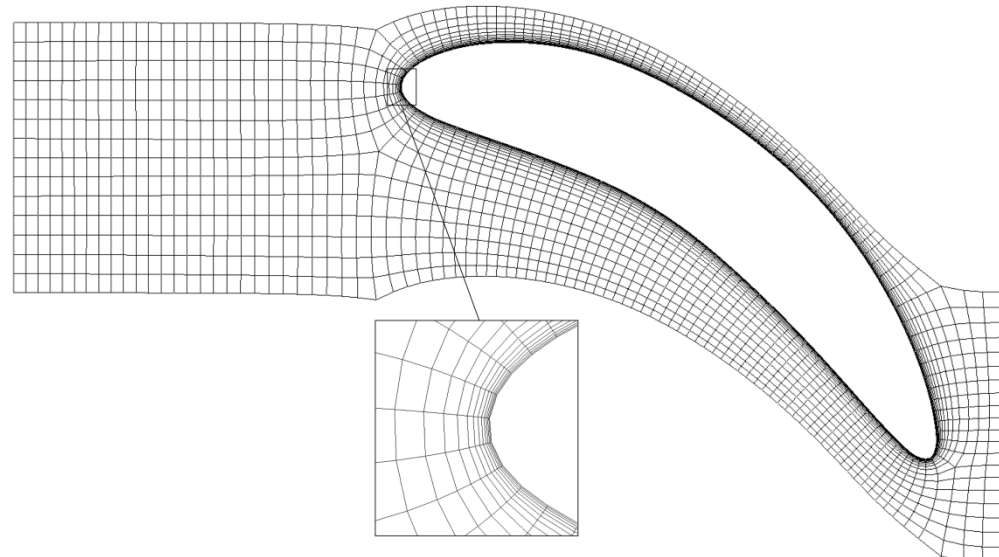


Figure 5.9 Mesh model with  $N=2$  and  $F=3$  for the stator blade at span surface 0.5.

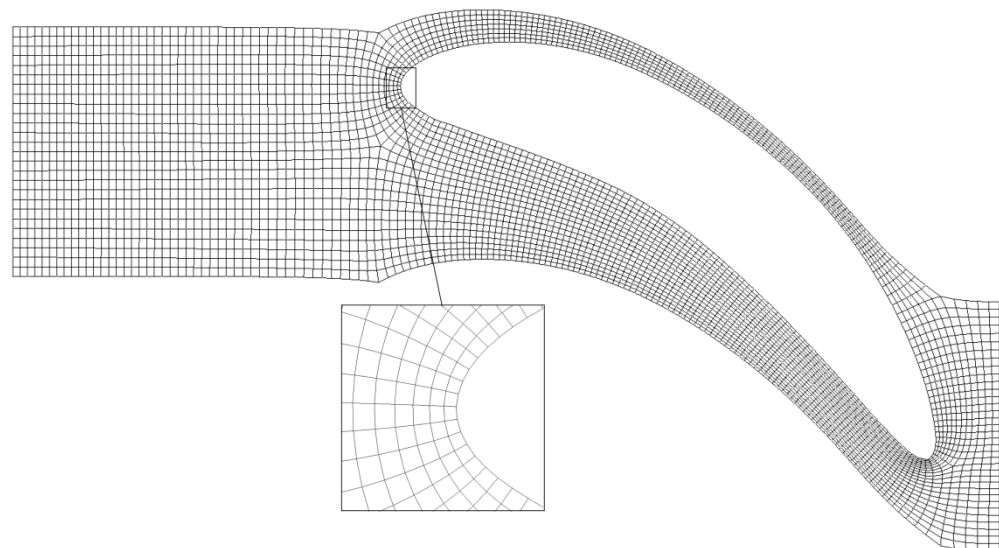


Figure 5.10 Mesh model with  $N=4$  and  $F=1$  for the stator blade at span surface 0.5.

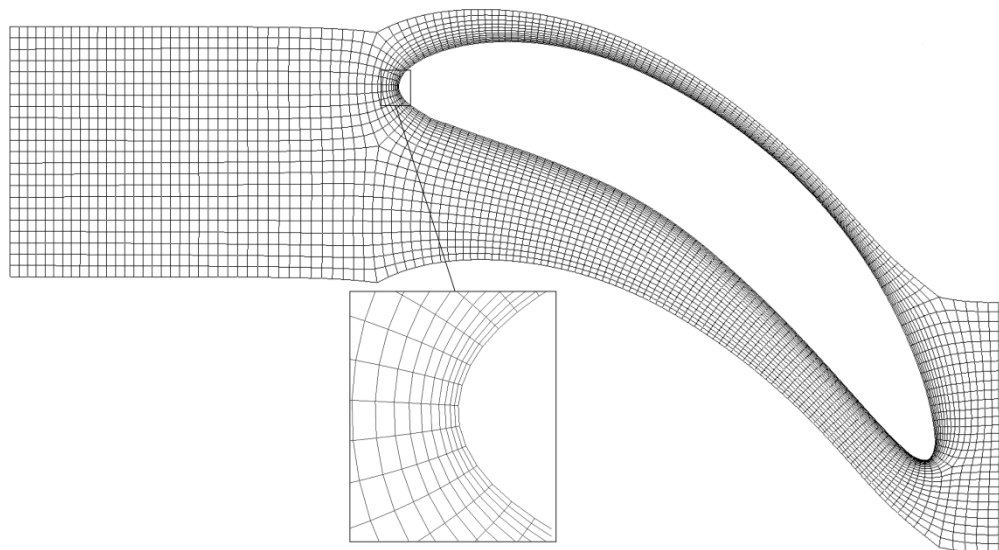


Figure 5.11 Mesh model with  $N=4$  and  $F=2$  for the stator blade at span surface 0.5.

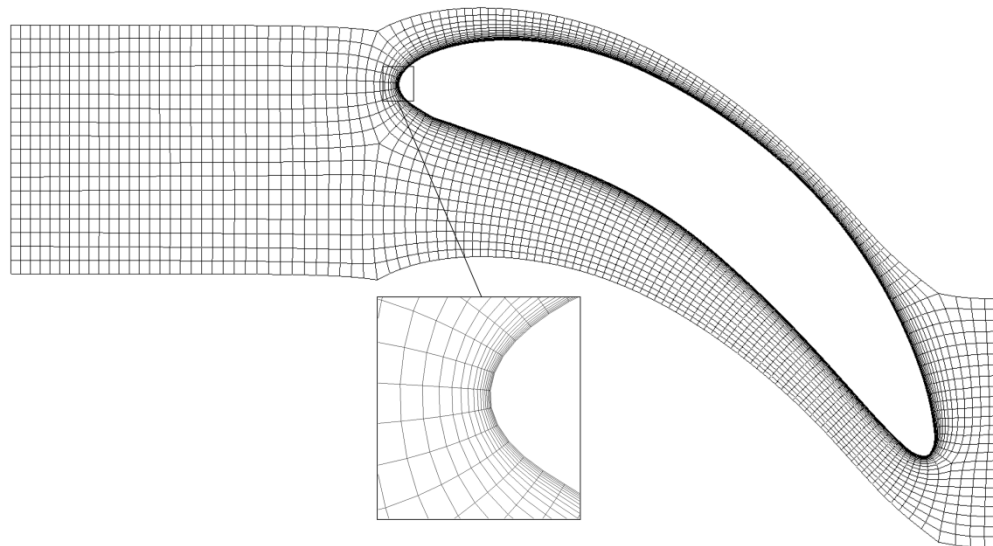


Figure 5.12 Mesh model with  $N=4$  and  $F=3$  for the stator blade at span surface 0.5.

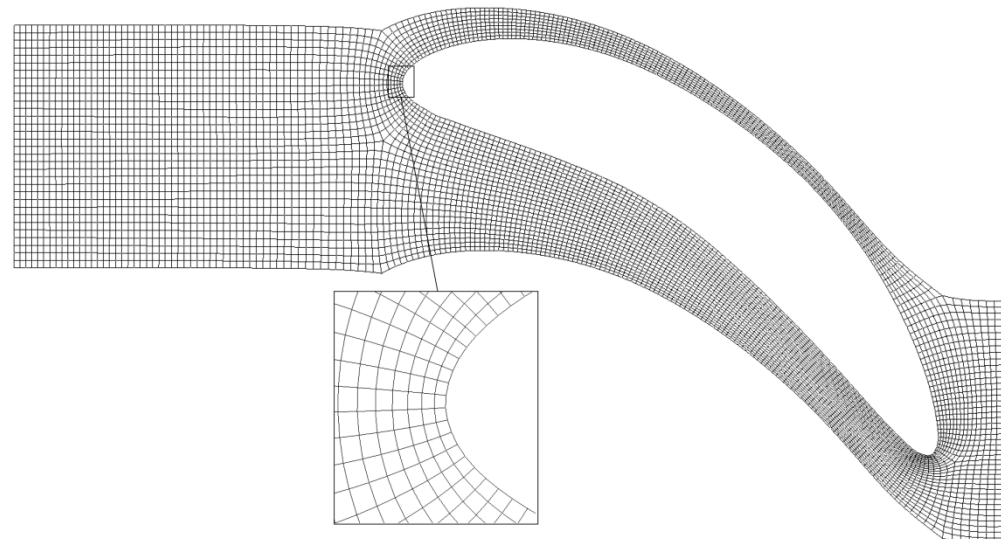


Figure 5.13 Mesh model with  $N=8$  and  $F=1$  for the stator blade at span surface 0.5.

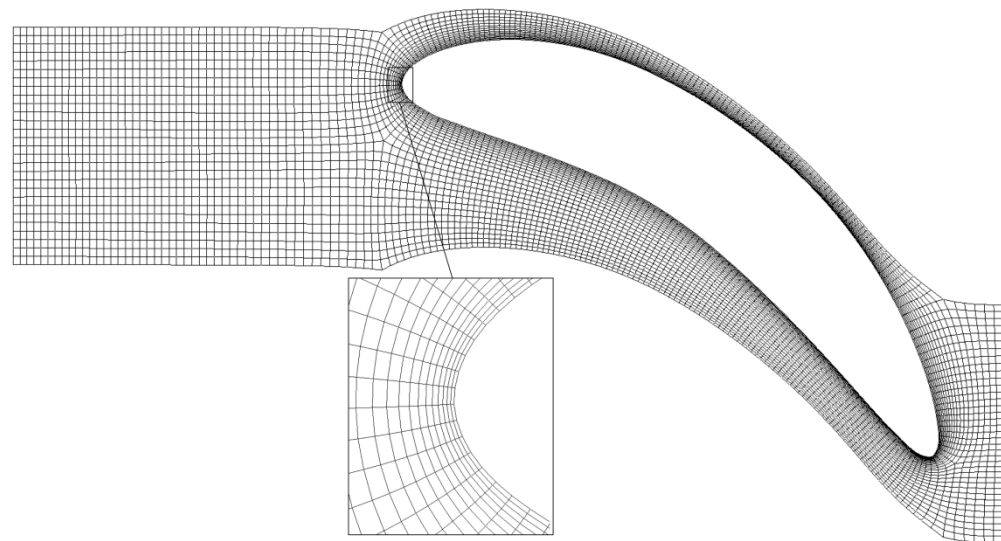


Figure 5.14 Mesh model with  $N=8$  and  $F=2$  for the stator blade at span surface 0.5.

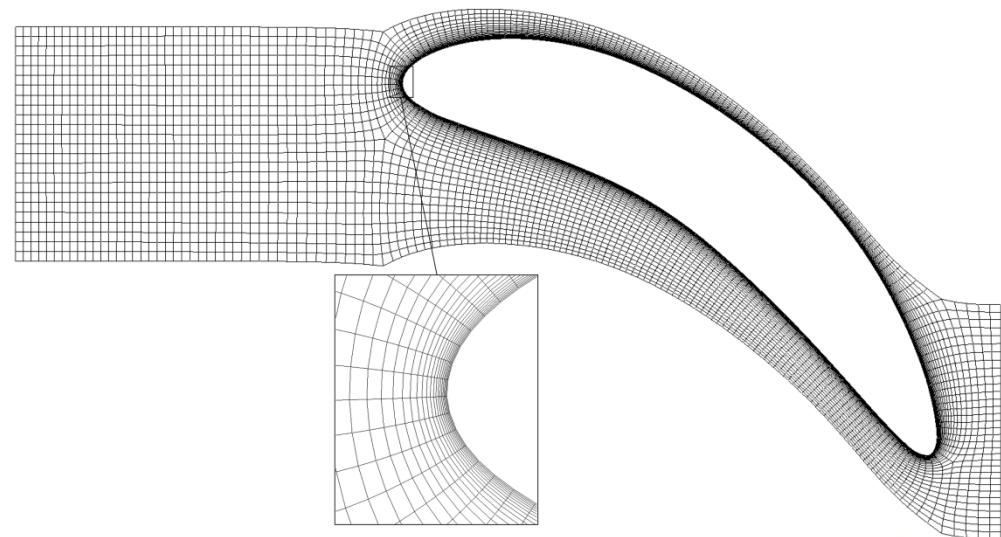


Figure 5.15 Mesh model with  $N=8$  and  $F=3$  for the stator blade at span surface 0.5.

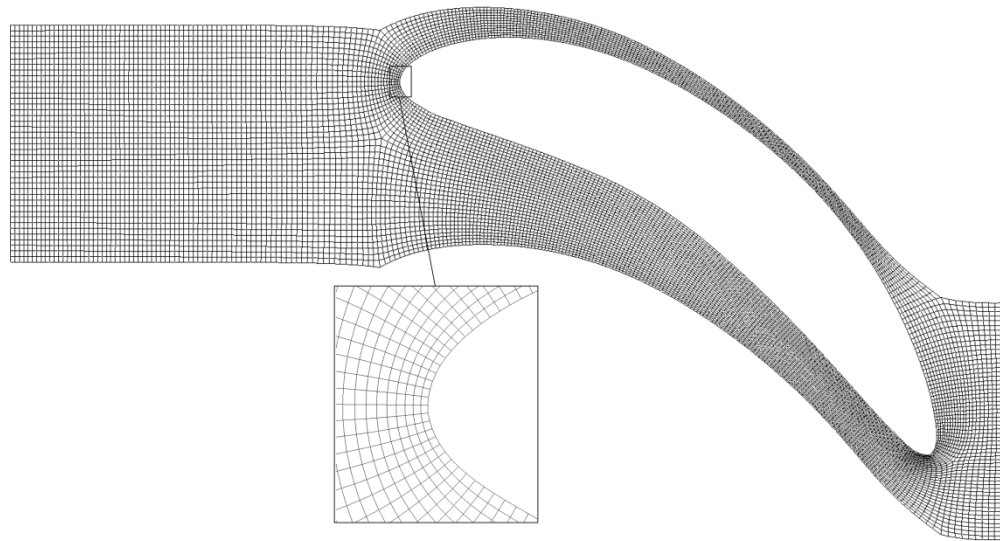


Figure 5.16 Mesh model with  $N=20$  and  $F=1$  for the stator blade at span surface 0.5.

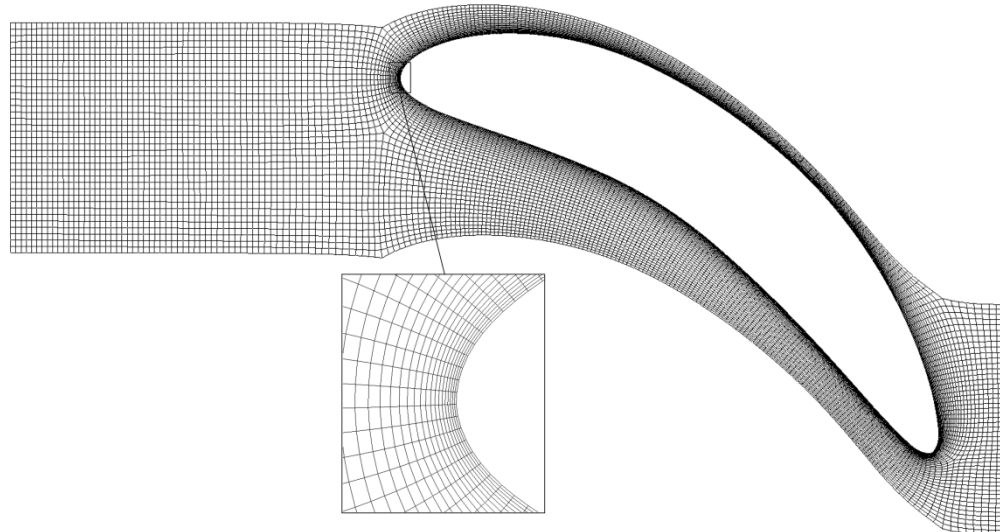


Figure 5.17 Mesh model with  $N=20$  and  $F=2$  for the stator blade at span surface 0.5.

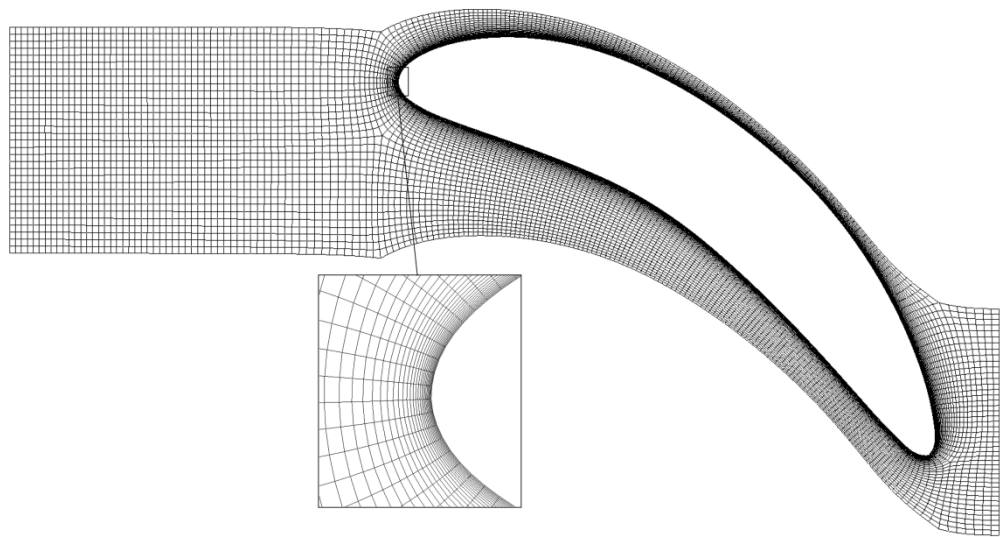


Figure 5.18 Mesh model with  $N=20$  and  $F=3$  for the stator blade at span surface 0.5.

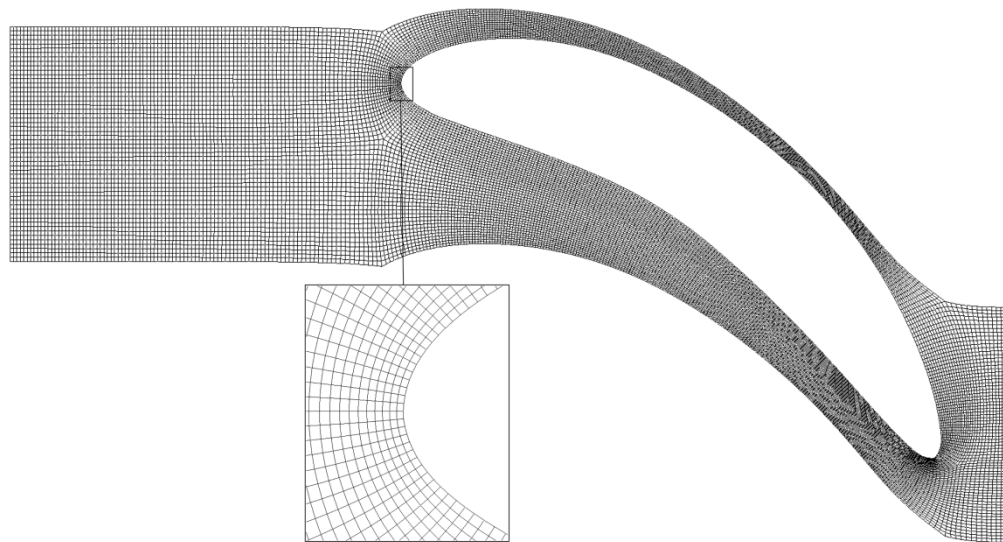


Figure 5.19 Mesh model with  $N=40$  and  $F=1$  for the stator blade at span surface 0.5.

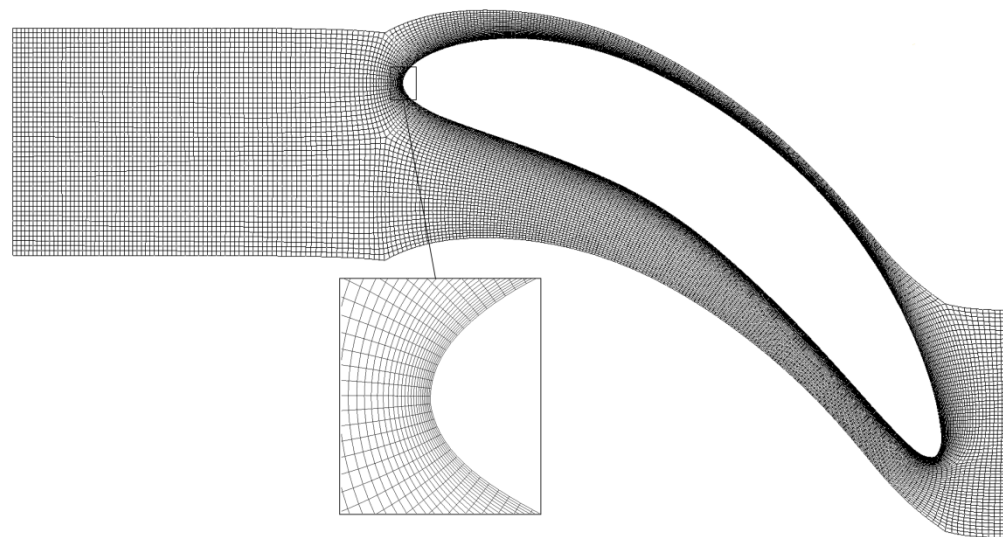


Figure 5.20 Mesh model with  $N=40$  and  $F=2$  for the stator blade at span surface 0.5.

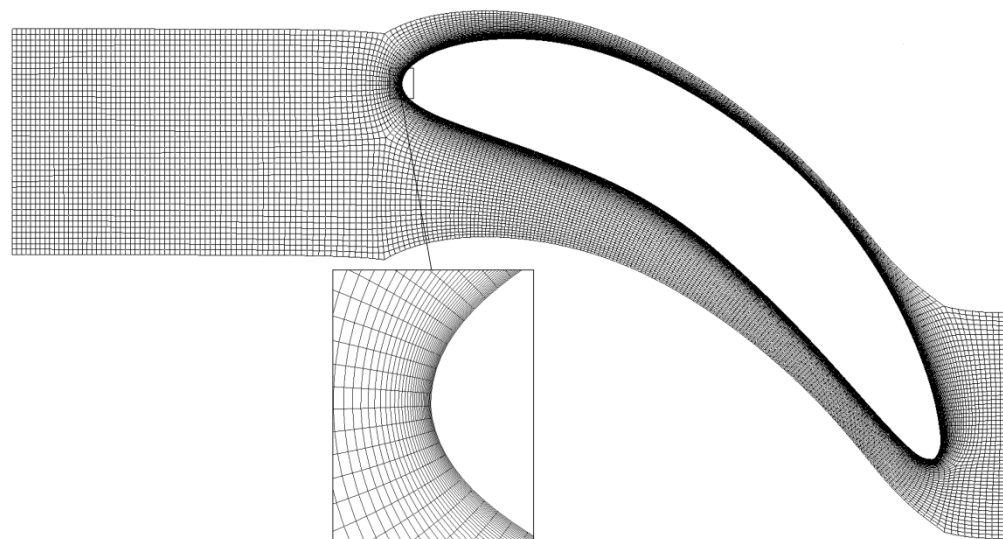


Figure 5.21 Mesh model with  $N=40$  and  $F=3$  for the stator blade at span surface 0.5.

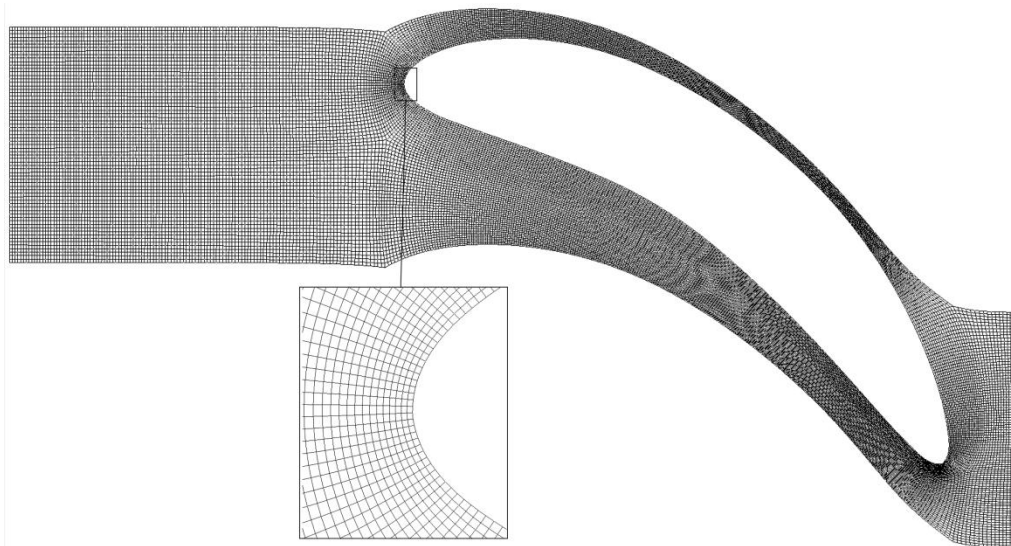


Figure 5.22 Mesh model with  $N=80$  and  $F=1$  for the stator blade at span surface 0.5.

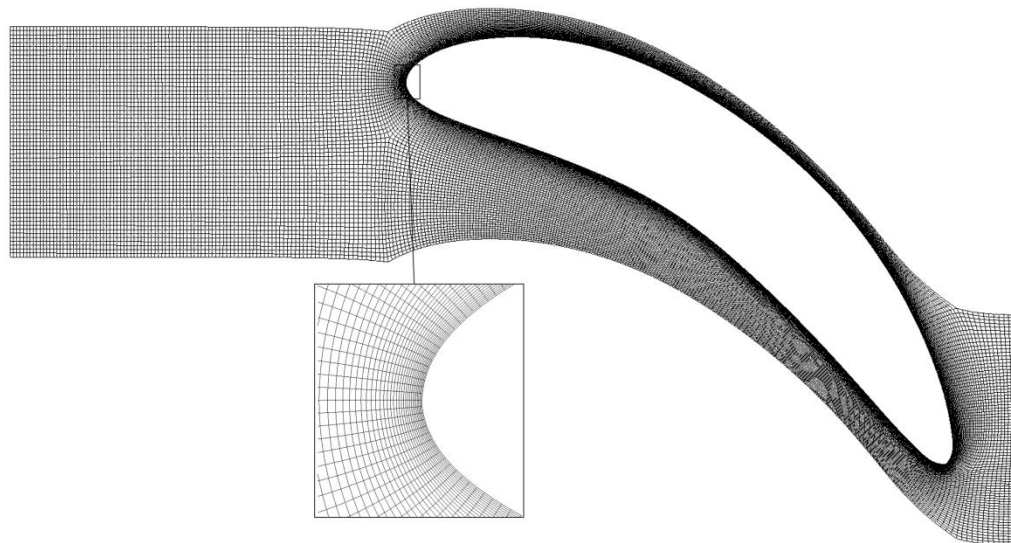


Figure 5.23 Mesh model with  $N=80$  and  $F=2$  for the stator blade at span surface 0.5.

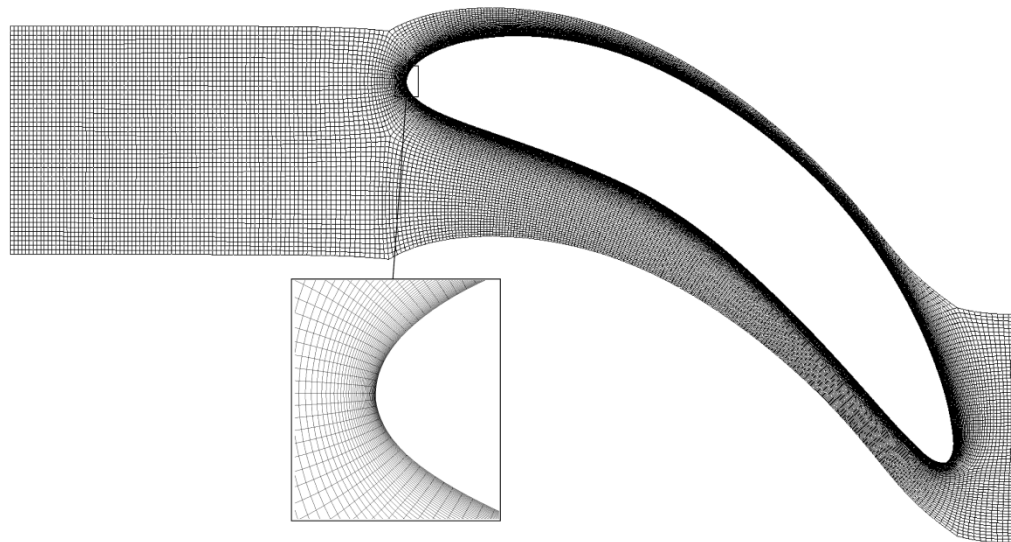


Figure 5.24 Mesh model with  $N=80$  and  $F=3$  for the stator blade at span surface 0.5.

The solver control parameters, boundary conditions and all the CFD parameters are fixed for mesh convergence study. Table 5.2 shows the CFD simulation results of water flow with 4 Kg/s mass flow rate and 6,000 rpm rotation speed for different mesh resolutions and steady state (stage interface model) condition and with the  $k-\varepsilon$  turbulence model. Two last columns show the minimum Turbulence Kinetic Energy (TKE) at the stator and rotor. Table 5.3 shows the CFD simulation results of water flow with 4 Kg/s mass flow rate and 6,000 rpm rotation speed for different mesh resolutions and steady state condition and with the SST turbulence model. Table 5.4 shows the transient CFD simulation results of water flow for similar case with transient rotor-stator modelling and with the SST turbulence model. The existing converged steady state and stage interface simulations are modified to define the transient rotor-stator simulation. Here, we modify the domain to define a transient simulation for a time interval that the rotor blades pass through 1 pitch ( $2\pi$  rad / Blade No.), using 200 time steps. The time step size was calculated as follows:

$$\text{Rotation speed} = 6,000 \text{ rpm} (628.319 \text{ rad/s})$$

$$\text{Rotor pitch modelled} = 2\pi \text{ rad} / 20 \approx 0.3142 \text{ rad}$$

$$\text{Time to pass through 1 pitch} \approx (0.3142 \text{ rad}) / (628.319 \text{ rad/s}) \approx 5 \times 10^{-4} \text{ s}$$

$$\text{Time step size} = 5 \times 10^{-4} / 200 = 2.5 \times 10^{-6} \text{ s}$$

Table 5.2: CFD simulation results for water flow grid convergence study with 4 Kg/s mass flow rate and 6,000 rpm rotation speed and with the  $k-\varepsilon$  turbulence model.

Grid Model	CPU Time ( $\times 10^4$ S)	Power (W)	Reaction	Min. TKE at Stator ( $\times 10^{-2}$ )	Min. TKE at Rotor
N=1, F=1	1.58	659.881	0.8613	3.73	$8.52 \times 10^{-2}$
N=1, F=2	0.47	641.500	0.8418	3.72	0.11
N=2, F=1	1.99	677.307	0.865	3.73	0.11
N=2, F=2	0.97	656.749	0.8479	3.73	0.13
N=4, F=1	1.78	696.430	0.8673	3.72	0.13
N=4, F=2	1.69	667.349	0.8526	3.73	0.14
N=8, F=1	3.21	698.709	0.8677	3.73	0.16
N=8, F=2	3.30	670.187	0.8529	3.74	0.16
N=20, F=1	7.30	698.089	0.8658	3.73	0.18
N=20, F=2	6.86	670.358	0.8536	3.74	0.18
N=40, F=1	12.40	691.582	0.8622	3.74	0.19
N=40, F=2	16.20	669.819	0.8543	3.75	0.19
N=80, F=1	22.60	684.995	0.8586	3.75	0.21
N=80, F=2	38.50	669.476	0.8519	3.75	0.20

Table 5.3: CFD simulation results for water flow grid convergence study with 4 Kg/s mass flow rate and 6,000 rpm rotation speed and with the SST turbulence model.

Grid Model	CPU Time ( $\times 10^4$ S)	Power (W)	Reaction	Min. TKE at Stator	Min. TKE at Rotor
N=1, F=1	0.46	617.099	0.8418	$3.81 \times 10^{-2}$	0.24
N=1, F=2	0.75	673.296	0.8557	$3.81 \times 10^{-2}$	$2.52 \times 10^{-2}$
N=1, F=3	0.67	719.891	0.8620	$1.61 \times 10^{-3}$	$1.72 \times 10^{-3}$
N=2, F=1	0.80	617.159	0.8394	$3.80 \times 10^{-2}$	0.23
N=2, F=2	1.26	717.308	0.8710	$3.64 \times 10^{-2}$	$1.88 \times 10^{-2}$
N=2, F=3	0.79	725.322	0.8710	$5.76 \times 10^{-4}$	$1.46 \times 10^{-3}$
N=4, F=1	1.66	624.931	0.8392	$3.79 \times 10^{-2}$	0.22
N=4, F=2	2.79	724.164	0.8683	$3.79 \times 10^{-2}$	$1.28 \times 10^{-2}$
N=4, F=3	2.26	731.211	0.8729	$3.46 \times 10^{-4}$	$2.24 \times 10^{-4}$
N=8, F=1	3.09	656.386	0.8465	$3.78 \times 10^{-2}$	0.23
N=8, F=2	4.83	732.953	0.8742	$3.78 \times 10^{-2}$	$3.05 \times 10^{-3}$
N=8, F=3	3.68	733.959	0.8745	$3.04 \times 10^{-4}$	$5.25 \times 10^{-5}$
N=20, F=1	6.44	686.313	0.8539	$3.77 \times 10^{-2}$	0.14
N=20, F=2	12.70	742.424	0.8779	$6.10 \times 10^{-3}$	$1.62 \times 10^{-4}$
N=20, F=3	4.43	734.586	0.8720	$4.97 \times 10^{-5}$	$1.97 \times 10^{-5}$
N=40, F=1	14.00	707.958	0.8616	$3.76 \times 10^{-2}$	$4.65 \times 10^{-2}$
N=40, F=2	24.00	744.905	0.8781	$3.88 \times 10^{-3}$	$1.38 \times 10^{-5}$
N=40, F=3	23.80	738.678	0.8820	$2.02 \times 10^{-5}$	$4.21 \times 10^{-6}$
N=80, F=1	26.03	709.781	0.8624	$3.76 \times 10^{-2}$	$2.48 \times 10^{-2}$
N=80, F=2	29.40	738.106	0.8751	$1.48 \times 10^{-3}$	$1.44 \times 10^{-4}$
N=80, F=3	23.80	738.831	0.8629	$1.21 \times 10^{-6}$	$2.90 \times 10^{-6}$

Table 5.4: Transient CFD simulation results for water flow grid convergence study with 4 Kg/s mass flow rate and 6,000 rpm rotation speed and with the SST turbulence model.

Grid Model	CPU Time ( $\times 10^4$ S)	Power (W)	Reaction	Min. TKE at Stator	Min. TKE at Rotor
N=8, F=2	3.92	738.199	0.8742	$3.78 \times 10^{-2}$	$3.05 \times 10^{-3}$
N=20, F=2	9.72	760.665	0.8795	$6.25 \times 10^{-3}$	$1.62 \times 10^{-4}$
N=40, F=2	20.80	758.747	0.8770	$3.12 \times 10^{-3}$	$1.34 \times 10^{-5}$
N=40, F=3	19.10	745.439	0.8775	$1.51 \times 10^{-5}$	$4.21 \times 10^{-6}$

Figure 5.25 shows the CFD simulation results for output power generated by one stage turbodrill model “A1W20” with different mesh and turbulence models used in water flow grid convergence study and with steady state analysis. This Figure shows that using SST turbulence model instead of  $k-\varepsilon$  model in CFD, generally will results at more accurate results, especially with blade boundary layer refinement. Using  $k-\varepsilon$  turbulence model, the grid model of (N=8) with no blade boundary layer refinement yields good quality CFD results within a reasonable CPU time for the purpose of this study. This grid geometry was used for CFD simulations in the next sections. Using SST turbulence model, the grid model of (N=8) with blade boundary layer refinement

yields in good quality CFD results within a reasonable CPU time for the purpose of this study and therefore this grid geometry was used for CFD simulations in the next sections.

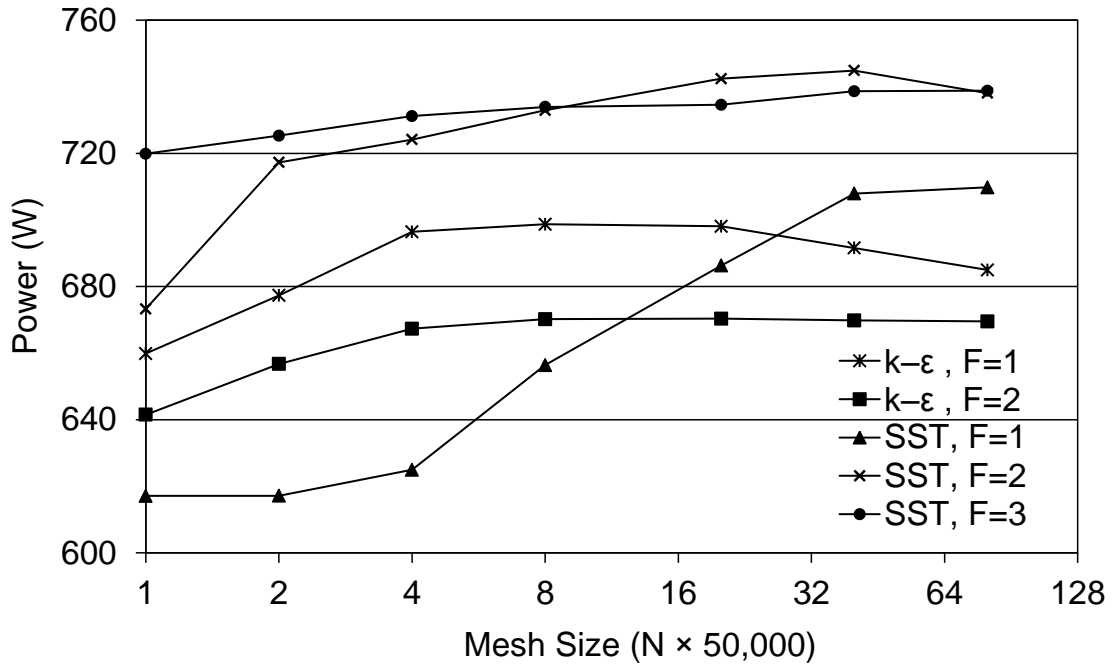


Figure 5.25 CFD simulation results of water flow grid convergence study for one stage power with different mesh and turbulence models and steady state analysis.

### 5.2.2 Air flow grid convergence study

For the grid convergence study of air flow through turbodrill stage, model “A1G25” was used. Table 5.5 shows several hexahedral mesh configurations generated for this model in “TurboGrid”. The objective here is to demonstrate accuracy and convergence of the analysis to the “exact numerical solution” with progressive mesh refinement.

The solver control parameters, boundary conditions and all the CFD parameters are fixed for mesh convergence study. Table 5.6 shows the CFD simulation results of air flow with 0.07 Kg/s mass flow rate at 100 psi (6.89 bar) inlet pressure and 10,000 rpm rotation speed for different mesh resolutions and steady state (stage interface model) condition and with the SST turbulence model.

Table 5.7 shows the transient CFD simulation results of air flow for similar case with transient rotor-stator modelling and with the SST turbulence model. The existing converged steady state and stage interface simulations are modified to define the transient rotor-stator simulation. Here, we modify the domain to define a transient simulation for a time interval that the rotor blades pass through 1 pitch ( $2\pi$  rad / blade no.), using 200 time steps. The time step size is calculated as follows:

$$\text{Rotation speed} = 10,000 \text{ rpm} (1047.2 \text{ rad/s})$$

*Rotor pitch modelled =  $2\pi$  rad / 25  $\approx 0.2513$  rad*

*Time to pass through 1 pitch  $\approx (0.2513 \text{ rad}) / (1047.2 \text{ rad/s}) \approx 2.4 \times 10^{-4} \text{ s}$*

*Time step size =  $2.4 \times 10^{-4} / 200 = 1.2 \times 10^{-6} \text{ s}$*

Table 5.5: Mesh models generated for air flow grid convergence study.

Target Passage Mesh Size (=N×50,000)	Edge Refinement Factor (F)	Total Nodes	Total Elements
N=1 (=50,000)	1	56,430	46,998
	2	61,845	52,696
	3	61,680	52,934
	4	73,425	63,896
	6	96,915	85,820
N=2 (=100,000)	1	114,804	99,433
	2	108,738	94,894
	3	108,036	95,149
	4	106,938	94,775
	6	116,298	104,210
N=4 (=200,000)	1	215,073	191,400
	2	224,227	201,762
	3	217,166	196,548
	4	212,474	193,204
	6	206,609	188,892
N=8 (=400,000)	1	438,886	400,428
	2	420,442	386,232
	3	412,119	380,156
	4	428,301	397,236
	6	419,717	391,188
N=20 (=1,000,000)	1	1,044,960	975,234
	2	1,089,000	1,023,945
	3	1,027,560	968,526
	4	1,030,560	974,493
	6	1,016,240	964,782
N=40 (=2,000,000)	1	2,089,600	1,978,865
	2	2,063,400	1,962,940
	3	2,063,600	1,969,408
	4	2,042,450	1,953,434
	6	2,035,650	1,953,532
N=80 (=4,000,000)	1	4,121,208	3,945,432
	2	4,139,478	3,979,408
	3	4,105,080	3,955,972
	4	4,111,758	3,969,736
	6	4,053,105	3,922,802

## Chapter 5 Numerical simulation results and discussions

Table 5.6: CFD simulation results for air flow grid convergence study with 0.07 Kg/s mass flow rate at 100 psi (6.89 bar) inlet pressure and 10,000 rpm rotation speed using the SST turbulence model.

Grid Model	CPU Time ( $\times 10^4$ S)	Power (W)	Reaction	Tot. pressure Ratio	Tot. Temp. Ratio	Min. TKE at Stator	Min. TKE at Rotor
N=1, F=1	0.52	631.502	4.1875	1.0337	1.0311	9.37	74.30
N=1, F=2	0.54	678.292	4.4790	1.0451	1.0334	9.40	2.08
N=1, F=3	0.29	708.713	4.7582	1.0501	1.0350	0.35	0.53
N=1, F=4	0.26	710.729	4.7829	1.0518	1.0350	$5.73 \times 10^{-4}$	$4.34 \times 10^{-4}$
N=1, F=6	0.47	714.887	4.7347	1.0544	1.0353	$1.82 \times 10^{-10}$	$2.20 \times 10^{-10}$
N=2, F=1	0.71	632.902	4.1786	1.0332	1.0311	9.34	68.70
N=2, F=2	0.16	688.471	4.2924	1.0418	1.0328	9.36	3.63
N=2, F=3	0.94	714.523	4.7354	1.0485	1.0353	0.27	0.43
N=2, F=4	0.39	714.951	4.8445	1.0507	1.0353	$4.73 \times 10^{-5}$	$3.88 \times 10^{-5}$
N=2, F=6	0.44	712.051	4.7833	1.0525	1.0352	$2.50 \times 10^{-10}$	$1.80 \times 10^{-10}$
N=4, F=1	1.53	635.578	4.1751	1.0336	1.0313	9.32	69.00
N=4, F=2	2.41	709.036	4.7096	1.0447	1.0350	2.36	9.32
N=4, F=3	1.66	721.693	4.8447	1.0483	1.0356	$6.25 \times 10^{-2}$	$5.26 \times 10^{-2}$
N=4, F=4	1.08	723.642	4.8721	1.0494	1.0357	$1.79 \times 10^{-5}$	$7.48 \times 10^{-6}$
N=4, F=6	0.90	723.196	4.8559	1.0504	1.0357	$1.52 \times 10^{-8}$	$1.50 \times 10^{-8}$
N=8, F=1	3.39	649.496	4.2604	1.0350	1.0320	9.30	71.30
N=8, F=2	2.23	728.308	4.9092	1.0465	1.0360	0.86	1.70
N=8, F=3	2.65	729.111	4.9326	1.0479	1.0360	$2.14 \times 10^{-2}$	$1.68 \times 10^{-2}$
N=8, F=4	6.16	731.982	4.9704	1.0491	1.0362	$7.12 \times 10^{-6}$	$1.19 \times 10^{-5}$
N=8, F=6	2.69	731.986	4.9248	1.0502	1.0362	$5.31 \times 10^{-11}$	$3.98 \times 10^{-9}$
N=20, F=1	8.57	663.025	4.3664	1.0365	1.0327	9.28	77.50
N=20, F=2	8.78	730.738	4.9438	1.0466	1.0361	0.67	0.13
N=20, F=3	7.15	733.975	4.9915	1.0480	1.0363	$2.09 \times 10^{-3}$	$5.04 \times 10^{-3}$
N=20, F=4	4.16	734.089	5.0172	1.0479	1.0363	$7.01 \times 10^{-6}$	$7.17 \times 10^{-7}$
N=20, F=6	5.28	734.329	4.9841	1.0488	1.0363	$2.22 \times 10^{-11}$	$2.42 \times 10^{-11}$
N=40, F=1	17.20	686.135	4.5443	1.0390	1.0339	9.26	30.70
N=40, F=2	29.00	732.678	4.9705	1.0476	1.0362	0.40	$2.00 \times 10^{-2}$
N=40, F=3	25.90	734.753	5.0219	1.0476	1.0363	$8.37 \times 10^{-4}$	$5.96 \times 10^{-4}$
N=40, F=4	28.10	735.539	5.0401	1.0474	1.0363	$1.85 \times 10^{-6}$	$1.02 \times 10^{-7}$
N=40, F=6	27.80	734.560	5.0168	1.0482	1.0363	$2.24 \times 10^{-11}$	$7.18 \times 10^{-12}$
N=80, F=1	32.60	699.892	4.6446	1.0412	1.0346	9.24	18.50
N=80, F=2	34.80	734.211	4.9840	1.0483	1.0363	0.17	$4.47 \times 10^{-3}$
N=80, F=3	42.10	735.179	5.0363	1.0476	1.0365	$1.09 \times 10^{-4}$	$1.99 \times 10^{-5}$
N=80, F=4	28.50	735.642	5.0523	1.0476	1.0363	$2.06 \times 10^{-7}$	$5.37 \times 10^{-8}$
N=80, F=6	18.40	734.953	5.0446	1.0479	1.0363	$3.26 \times 10^{-14}$	$3.42 \times 10^{-12}$

Table 5.7: Transient CFD simulation results for air flow grid convergence study with 0.07 Kg/s mass flow rate at 100 psi (6.98 bar) inlet pressure and 10,000 rpm rotation speed using the SST turbulence model.

Grid Model	CPU Time ( $\times 10^4$ S)	Power (W)	Reaction	Tot. pressure Ratio	Tot. Temp. Ratio	Min. TKE at Stator	Min. TKE at Rotor
N=4, F=6	7.19	726.543	4.8633	1.0507	1.0369	$1.66 \times 10^{-8}$	$1.27 \times 10^{-8}$
N=20, F=6	3.13	736.549	4.9227	1.0504	1.0383	$1.70 \times 10^{-11}$	$2.27 \times 10^{-11}$
N=40, F=3	3.22	739.772	4.9556	1.0497	1.0391	$1.53 \times 10^{-3}$	$5.78 \times 10^{-4}$
N=80, F=3	2.92	735.376	5.0389	1.0474	1.0360	$1.29 \times 10^{-4}$	$3.45 \times 10^{-6}$

Figure 5.26 shows the CFD simulation results for output power generated by one stage turbodrill model “A1G25” with different mesh models and SST turbulence model used in air flow grid convergence study and using steady state analysis. This Figure shows that using SST turbulence model, generally the CFD results will be more accurate with blade boundary layer refinement. This Figure shows that the grid model of N=8 with blade boundary layer refinement will results in good quality CFD results within a reasonable CPU time for the purpose of this study. As a result this model was used for the CFD simulations in the next sections.

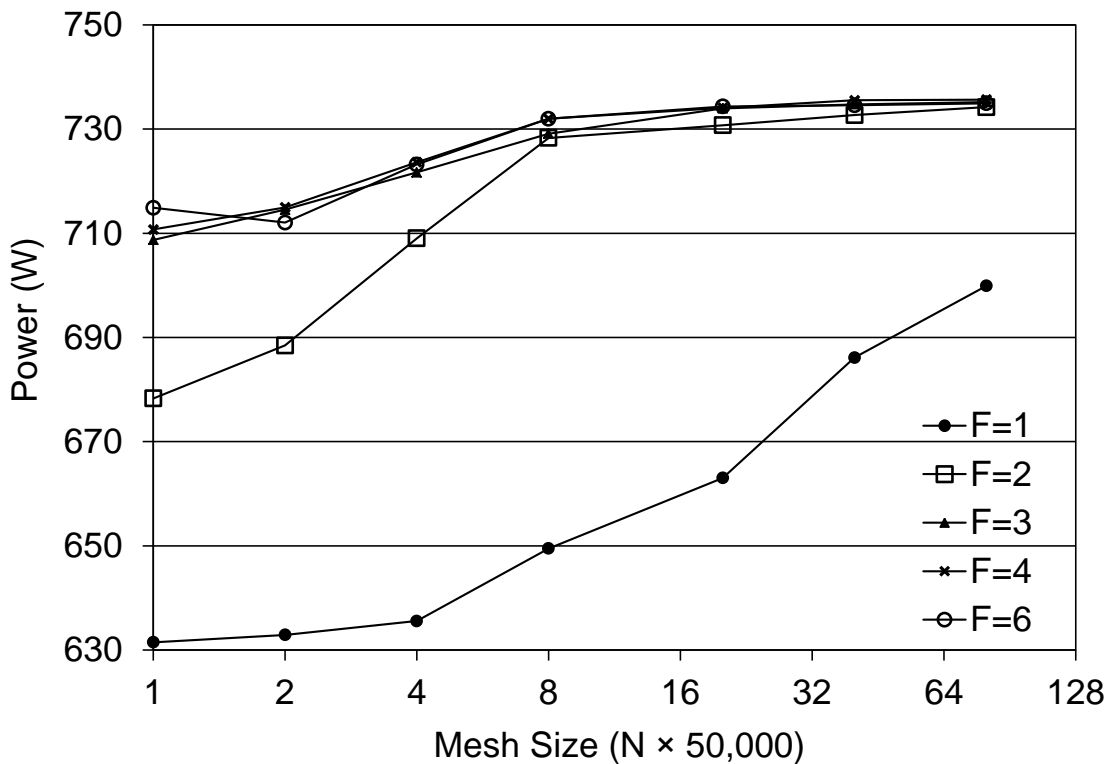


Figure 5.26 CFD simulation results of air flow grid convergence study for one stage power with different mesh models with SST turbulence and steady state analysis.

### 5.3 FSI simulation process

ANSYS® Mechanical APDL 14.0 software was used in this study for Fluid-Structural Interaction (FSI) analysis of the fluid flow through turbodrill. After performing CFD simulation for the selected domain (one blade of both stator and rotor interacting together), to evaluate the mechanical stresses and deflections caused by the fluid mechanical pressure loading, one-way coupling of solution fields in fluid and solid domains are calculated by means of FSI analysis. Consequently in this study, static structural analyses were used to determine displacements, stresses, etc. under static loading conditions. In this way, one-way coupling analyses were performed by running

a CFD analysis, extracting the forces acting on a solid surface and then importing them as major boundary conditions to a structural analysis.

Blades on the stator and rotor row are both connected to the hub and housing and there is no hub or shroud tip for them. Therefore in this study to evaluate the mechanical loading effects on the blades, both hub and shroud for the turbodrill stage were modelled as fixed supports for the blades. Figure 5.27 shows the geometry domain of the turbodrill model “A1W20” used for structural analysis. Here, one blade of stator and rotor is shown in green with the blends or fillets on their interface with hub and shroud to reduce the stress concentrations.

For the purpose of structural analysis in this study, stainless steel form the general material library of ANSYS® software with following default properties was assigned for the blade body:

*Young's Modulus* = 193 GPa,

*Shear Modulus* = 73.7 GPa,

*Bulk Modulus* = 169 GPa,

*Poisson's Ratio* = 0.31,

*Yield Strength* = 207 MPa.

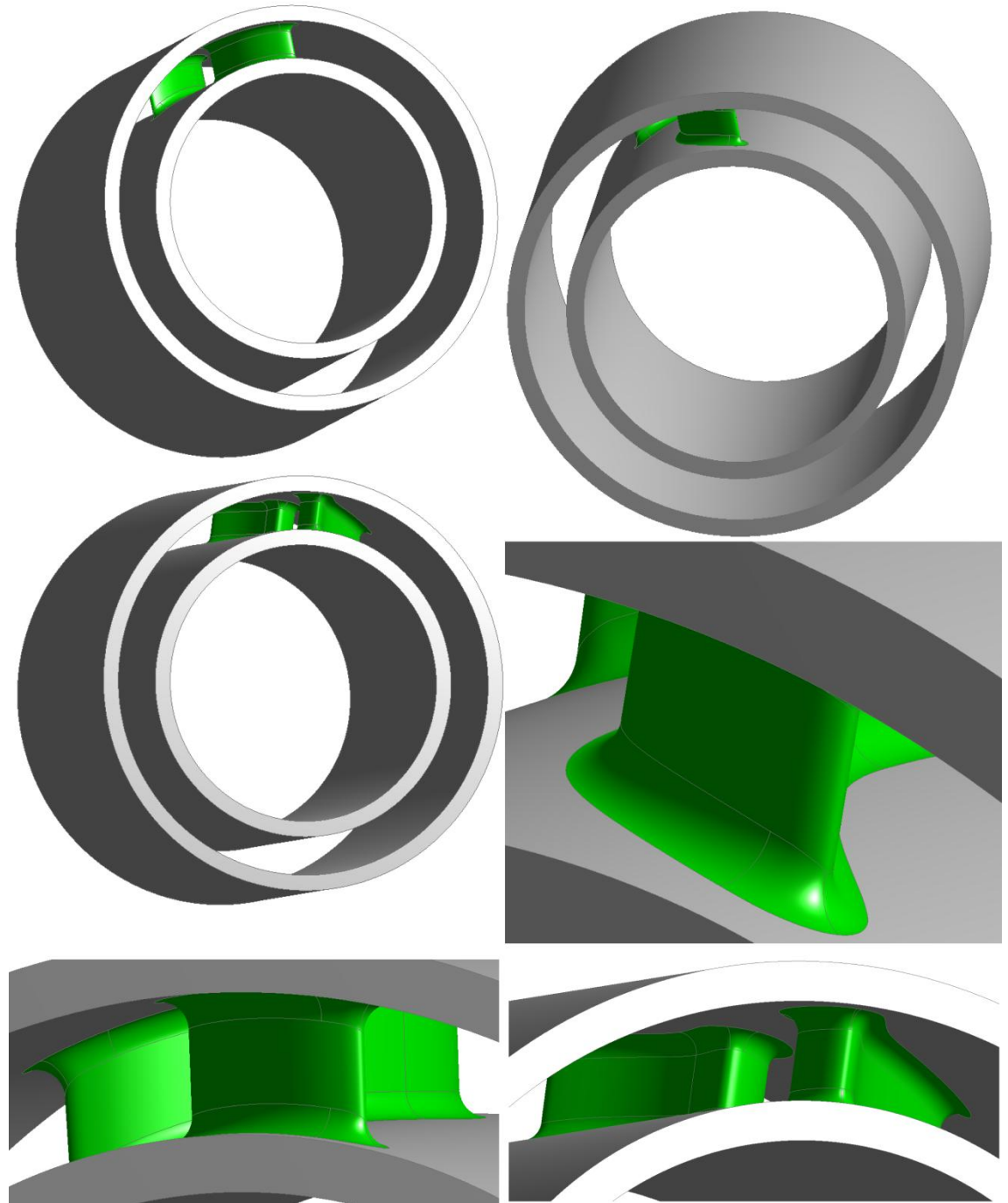


Figure 5.27 Geometry domain of the turbodrill model “A1W20” used for structural analysis, with one blade of stator and rotor in green with the blends or fillets on their interfaces with hub and shroud.

## 5.4 Grid convergence study for FSI simulations

The quality of FSI simulation is dependent to the quality of the structural mesh on the blade body. Here, for the purpose of grid convergence study for structural analysis, 4 mesh models with the default mesh options of the mesh module in ANSYS® for the whole domain and 4 levels of mesh refinements for the blades body of the turbodrill stage model “A1W20” with blend radius of 0.5 mm, were generated and are shown in

Figures 5.28 to 5.31. The blends on the intersection of blades with hub and shroud surfaces with different blend or fillet radius were located to reduce the stress concentration on the sharp interfaces.

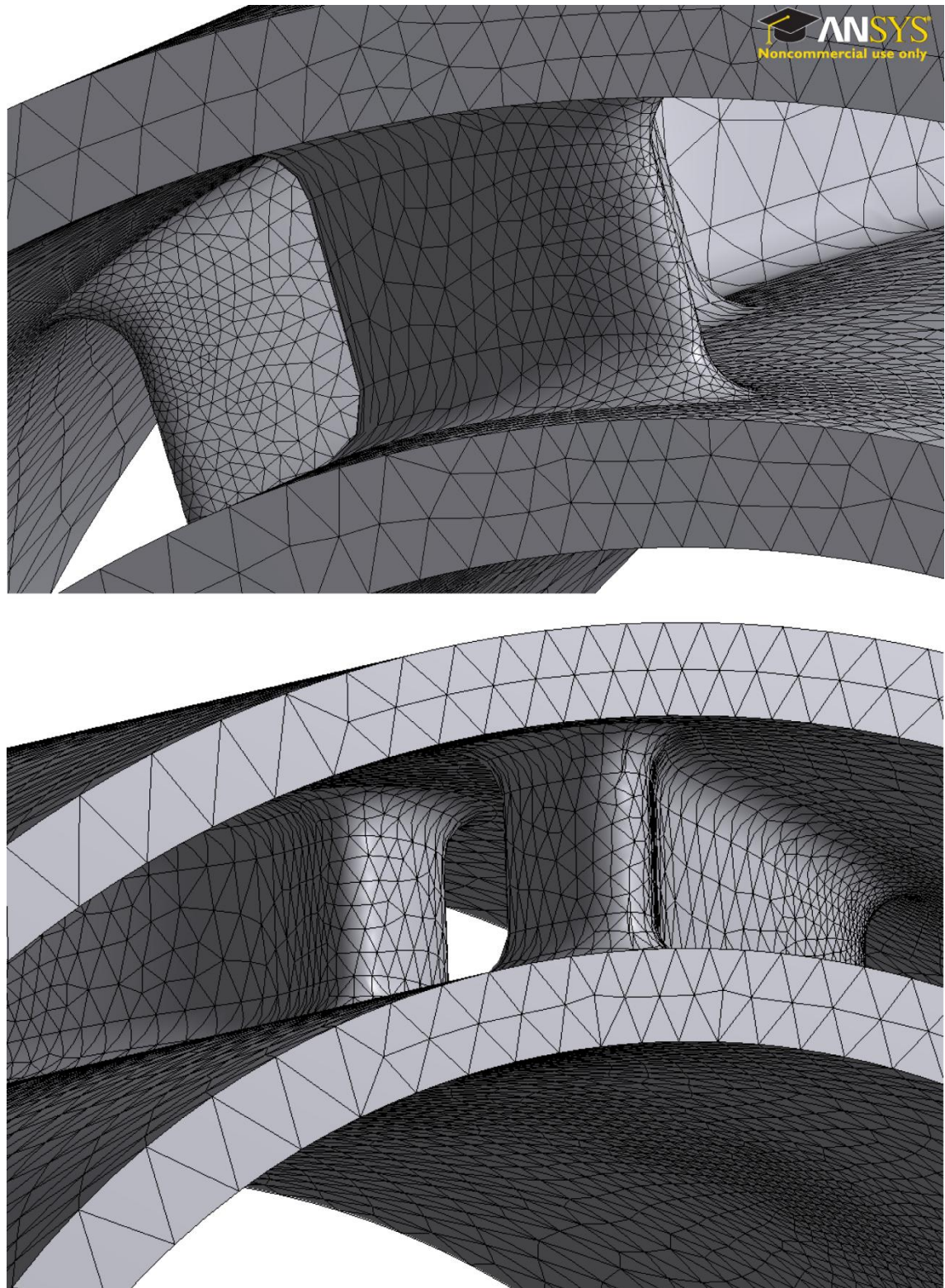


Figure 5.28 Mesh model for FSI grid convergence study with zero refinement on the blades body (mesh model 0).

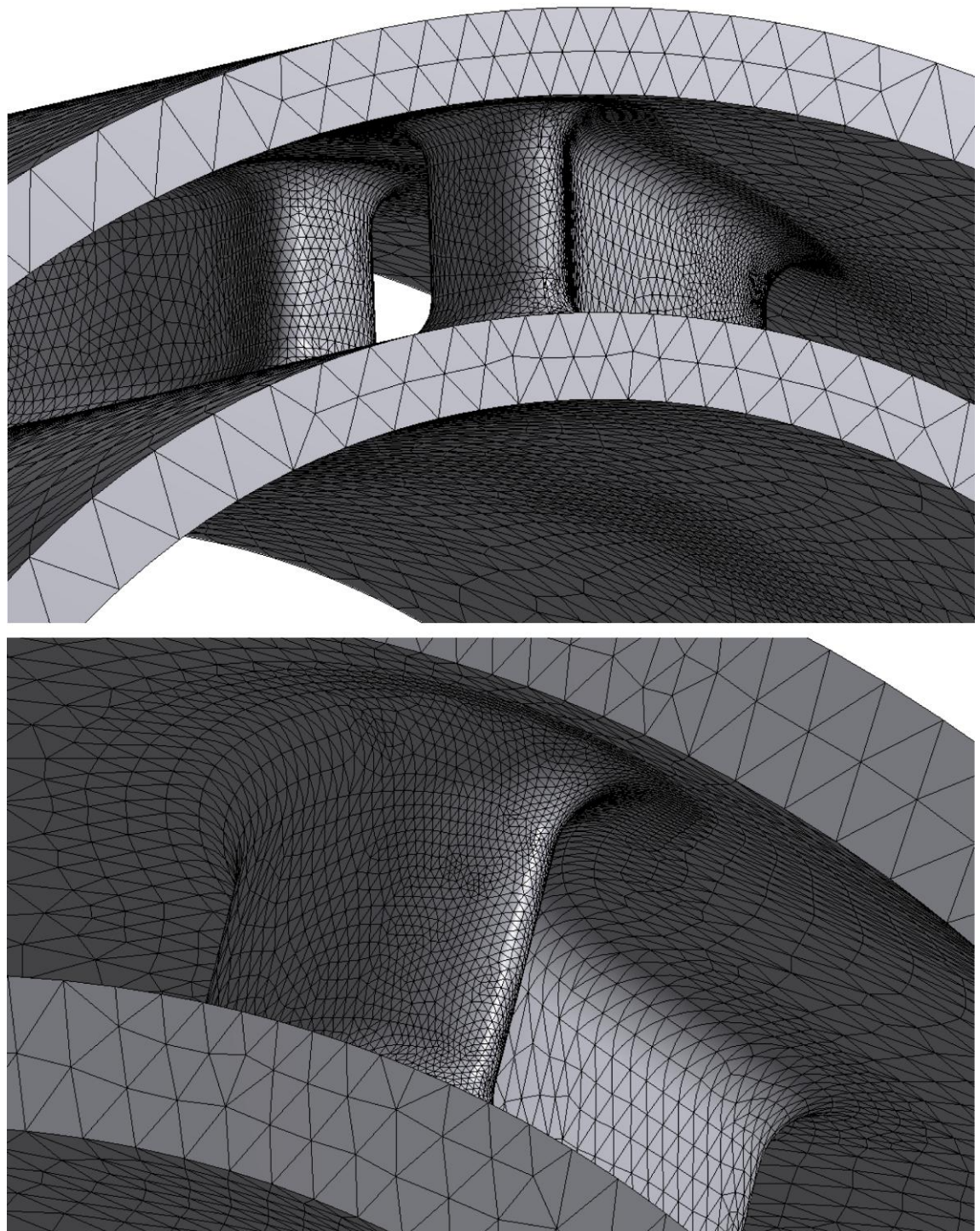


Figure 5.29 Mesh model for FSI grid convergence study with one level refinement on the blades body (mesh model 1).

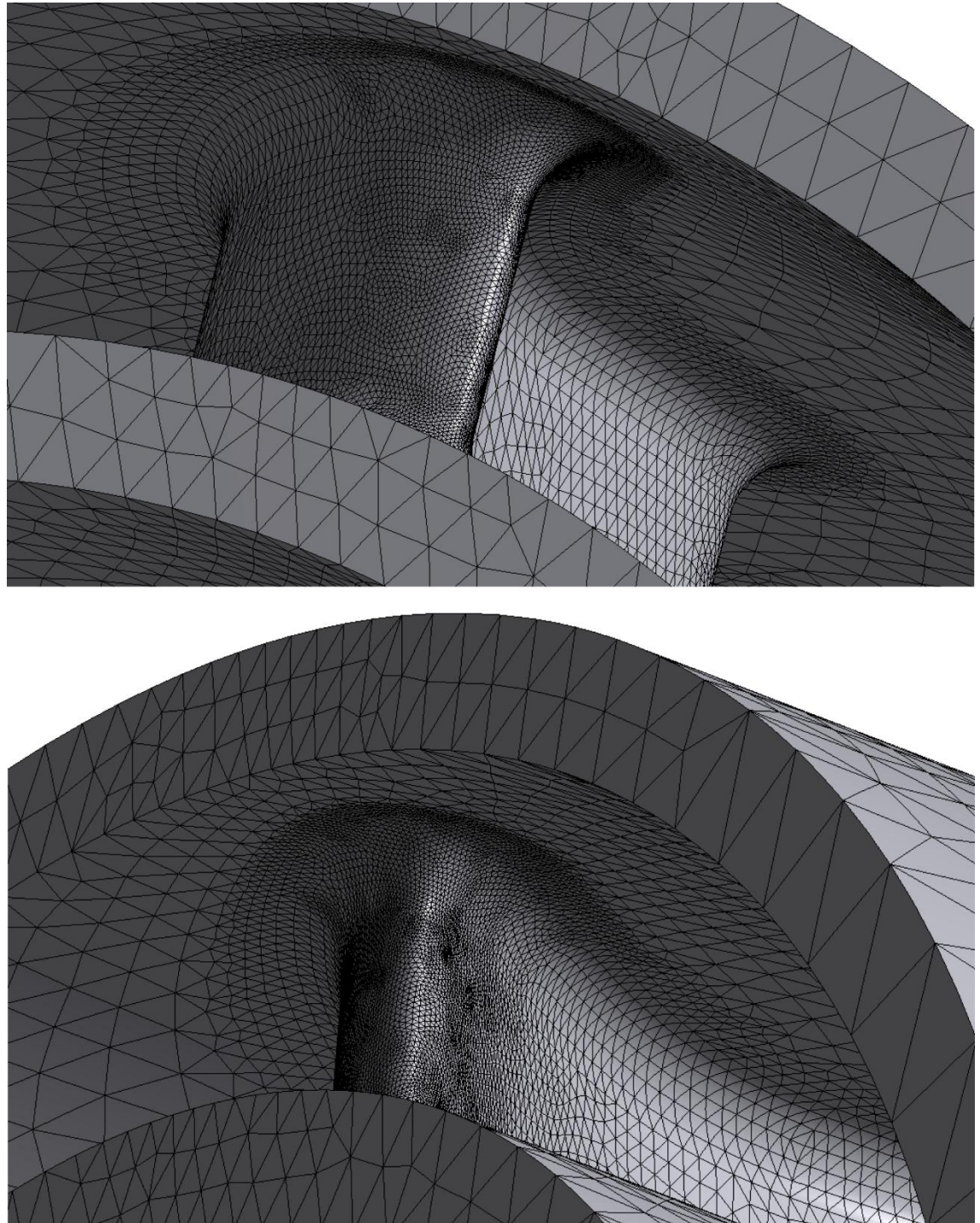


Figure 5.30 Mesh model for FSI grid convergence study with two level refinements on the blades body (mesh model 2).

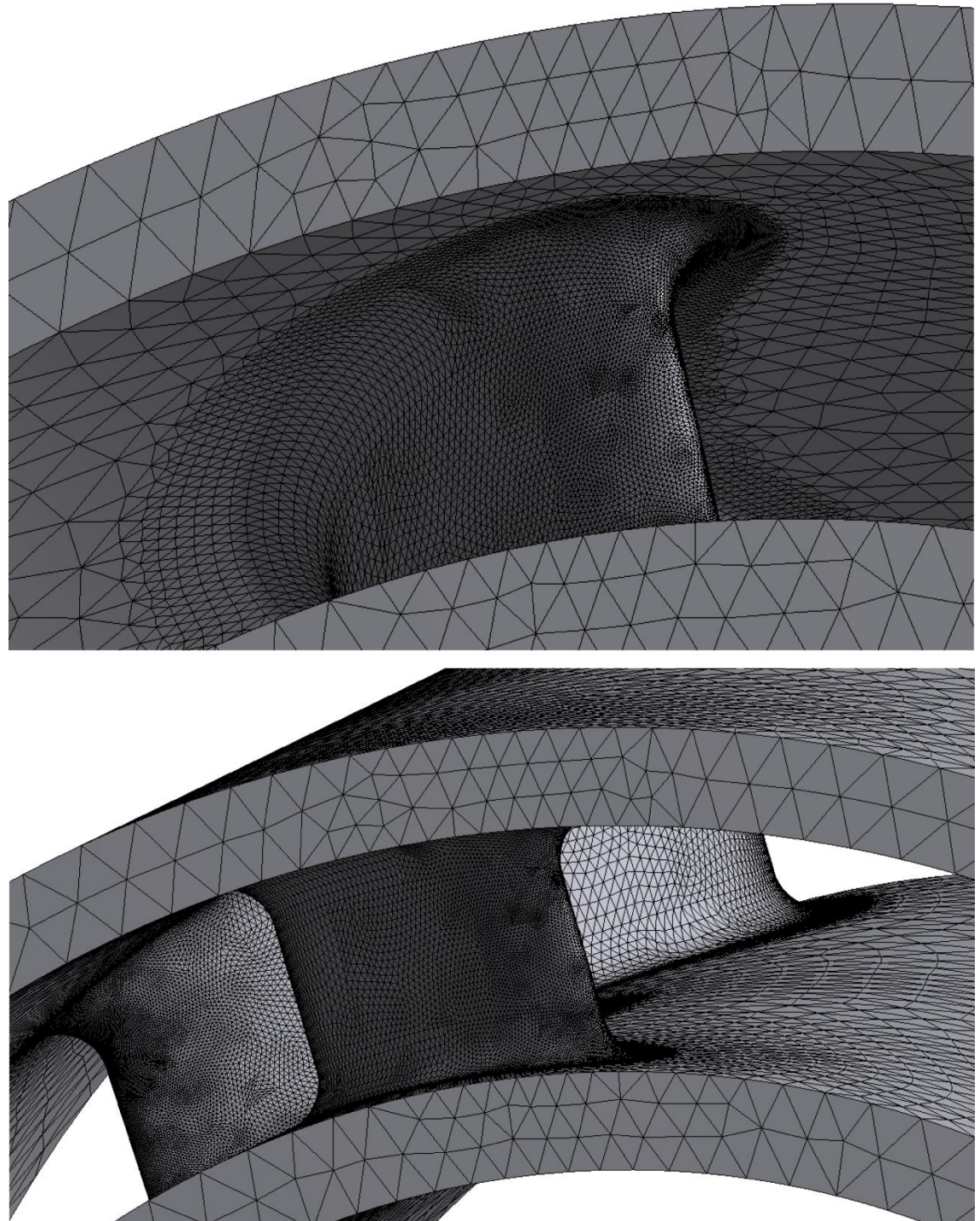


Figure 5.31 Mesh model for FSI grid convergence study with three level refinements on the blades body (mesh model 3).

Table 5.8 shows the mesh models information and structural analysis results for the four mesh models generated for FSI grid convergence study. This table shows that the mesh model 2 will result in a good quality simulation results with moderate mesh density on the blades body and then within a reasonable CPU time for the purpose of this study. As a result, this mesh model was used for the FSI analyses in the next sections.

Table 5.8: Simulation results for FSI grid convergence study for four mesh models.

Mesh Model	Total Nodes	Total Elements	Minimum Maximum	Equivalent (von-Mises) Stress (MPa)	Equivalent Elastic Strain ( $\times 10^{-4}$ mm/mm)	Total Deformation ( $\times 10^{-3}$ mm)
0	96,631	62,371	Min	8.597	0.471	0
			Max	181.144	9.440	2.711
1	322,474	221,602	Min	9.068	0.471	0
			Max	191.100	9.903	2.732
2	683,000	477,477	Min	9.048	0.472	0
			Max	193.784	10.320	2.737
3	1,646,698	1,177,216	Min	9.030	0.469	0
			Max	194.319	10.960	2.739

## 5.5 Water flow simulation results

In the previous sections, CFD and FSI simulation process and grid convergence study for one stage turbodrill were discussed. In following sections, comprehensive CFD and FSI simulations results for water flow through one stage of different turbodrill models are presented.

### 5.5.1 Water flow simulation results for Turbodrill stage model “A1”

Water flow simulation results for one stage turbodrill models with 5 cm shroud diameter and 5 mm blade height (span) which are known here as stage model “A1” are presented in this section.

#### Simulation results through stage model “A1W20” with water flow rate of 3 L/s

Table 5.9 shows water flow CFD simulation results for one stage turbodrill model with 5 cm shroud diameter, 5 mm blade height and 20 blades on each blade row (stage model “A1W20”) with water flow rate of 3 L/s.

Table 5.9: CFD simulation results for one stage turbodrill model “A1W20” with water flow rate of 3 L/s.

Speed (rpm $\times 100$ )	Power (W)	Torque (N.mm)	Inlet Flow Coefficient	Stage Reaction
1	13.572	1296.078	24.554	15.526
10	123.138	1175.968	2.281	2.029
20	212.036	1012.472	1.054	1.289
30	268.066	853.343	0.669	1.034
40	295.613	705.776	0.490	0.905
50	294.641	562.764	0.395	0.834
60	260.810	415.123	0.340	0.789
70	180.864	246.750	0.310	0.748
80	70.434	84.081	0.300	0.708

Figure 5.32 shows the CFD simulation results for power and torque produced by one stage turbodrill model “A1W20” with water flow rate of 3 L/s at its reference radius of 22.5987 mm. Each set of power and torque data at specific rotation speed is a result of one CFD simulation run. Non-linear regression analysis was applied to the calculated power values, and this was found to be highly correlated to second-order dependence on speed as evidenced by the high resultant correlation coefficients ( $R^2$ ). For the resulted torque data, there is a linear relation with high correlation coefficient. The maximum stage efficiency and power for this case is at around 4,000 revolutions per minute (rpm) rotation speed. One stage power and torque at maximum efficiency condition are around 300 W and 705 N.mm, respectively. In this case, the runaway turbine speed is almost over 8,000 rpm, and stalled torque is around 1300 N.mm.

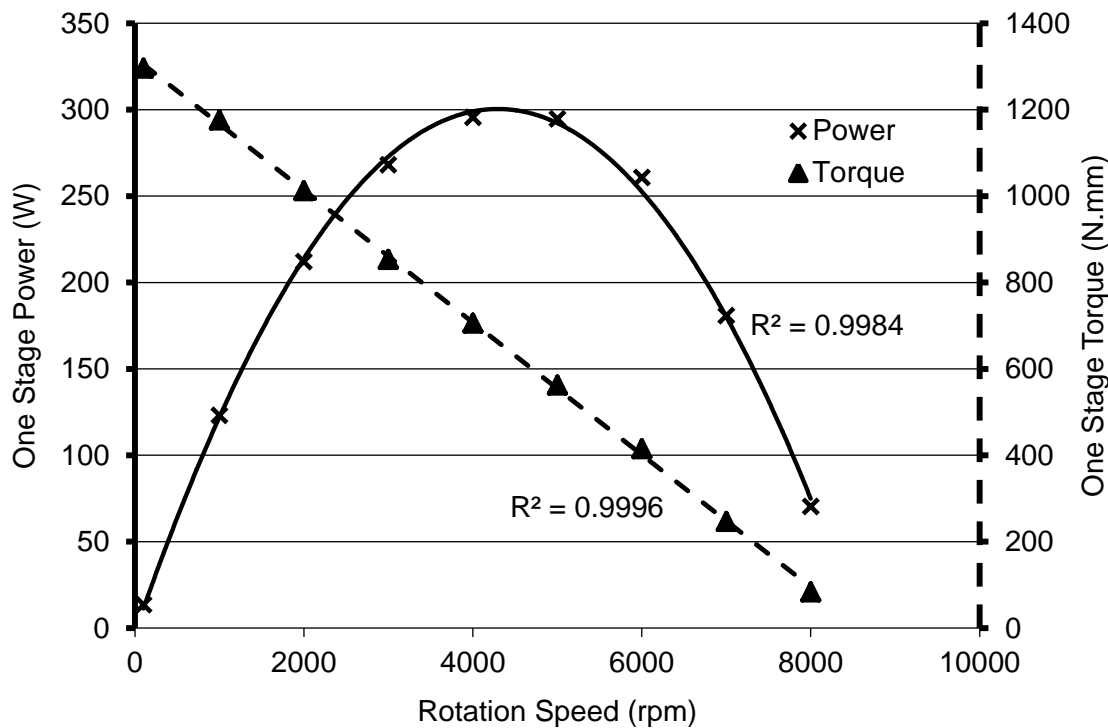
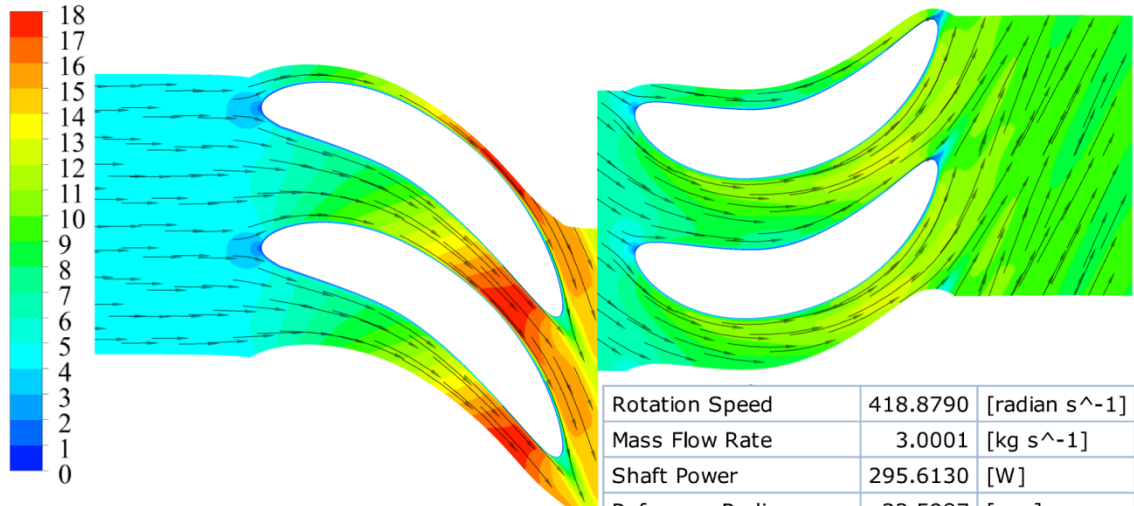


Figure 5.32 CFD simulation results for one stage turbodrill model “A1W20” with water flow rate of 3 L/s at reference radius of 22.5987 mm.

Figure 5.33 shows the CFD simulation results for one stage turbodrill model “A1W20” with water flow rate of 3 L/s at the optimum rotation speed of 4,000 rpm. This figure shows the velocity profile in the blade to blade view at the span surface 0.5 (half way between hub and shroud). The first blade row is the stator blade row that shows increasing velocity. The second blade row is the rotor blade row that shows changing in velocity vectors, in turn, cause rotation. Some flow separations are visible on the leading and trailing edges of the blades. Also this figure shows the pressure and meridional velocity profiles at meridional surface (axi-symmetric surface between hub

and shroud). The pressure and velocity profiles show the maximum velocity and minimum pressure is occurred near the stator blade trailing edge. The other simulation outputs are also provided in the figure.

Velocity [m/s] at Span Surface 0.5



Rotation Speed	418.8790	[radian s <sup>-1</sup> ]
Mass Flow Rate	3.0001	[kg s <sup>-1</sup> ]
Shaft Power	295.6130	[W]
Reference Radius	22.5987	[mm]
Inlet Flow Coefficient	0.4904	
Reaction	0.9050	
Total Pressure Ratio	1.0075	
Nozzle Loss Coefficient	2.3622	
Nozzle Efficiency %	78.5882	

Pressure [MPa] at Meridional Surface

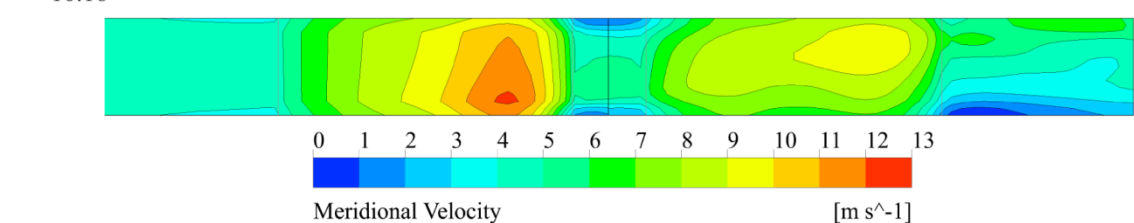
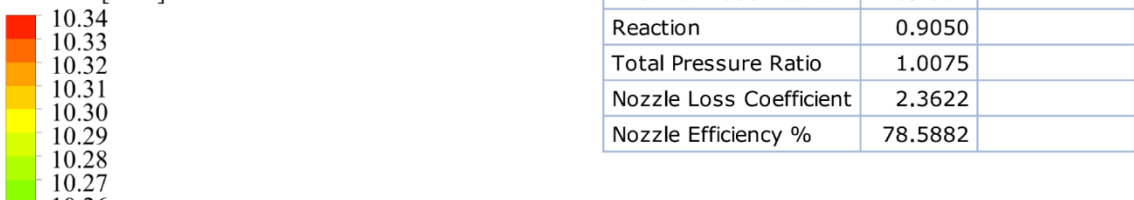


Figure 5.33 CFD simulation results for one stage turbodrill model “A1W20” with water flow rate of 3 L/s at 4,000 rpm rotation speed.

Figures 5.34 and 5.35 show the velocity and pressure values versus normalized streamwise length of stator and rotor at span surface 0.5 for water flow rate of 3 L/s at 4,000 rpm rotation speed through turbodrill stage model “A1W20”. These figures show the velocity and pressure data on the both blade surfaces (suction and pressure surfaces) which therefore show the velocity and pressure range on the both sides of the stator and rotor blade.

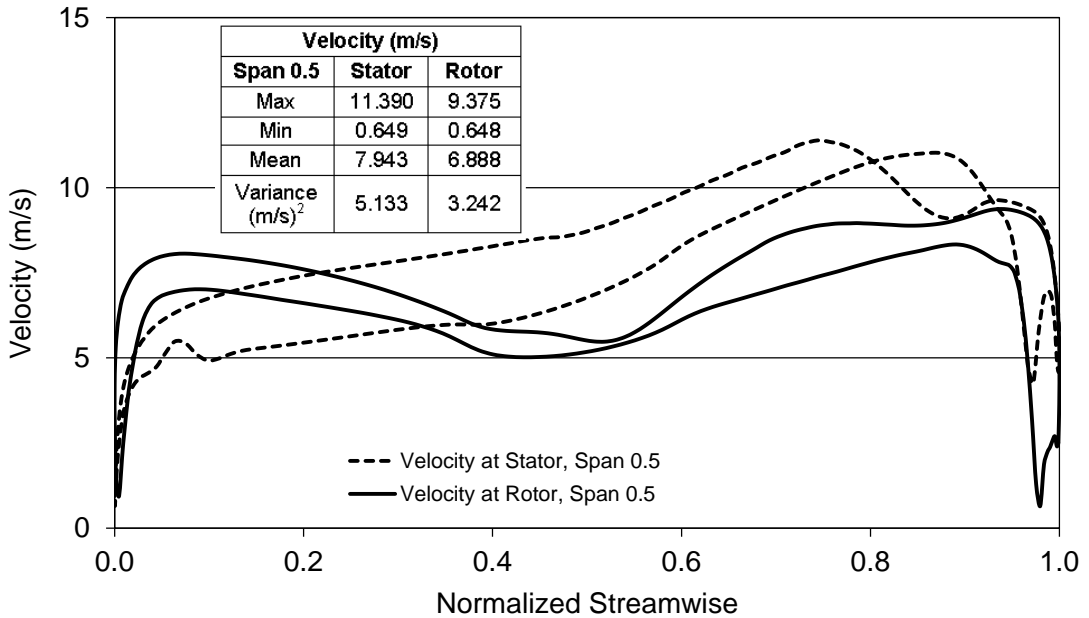


Figure 5.34 Velocity profile versus normalized streamwise for water flow rate of 3 L/s at 4,000 rpm rotation speed through turbodrill stage model “A1W20”.

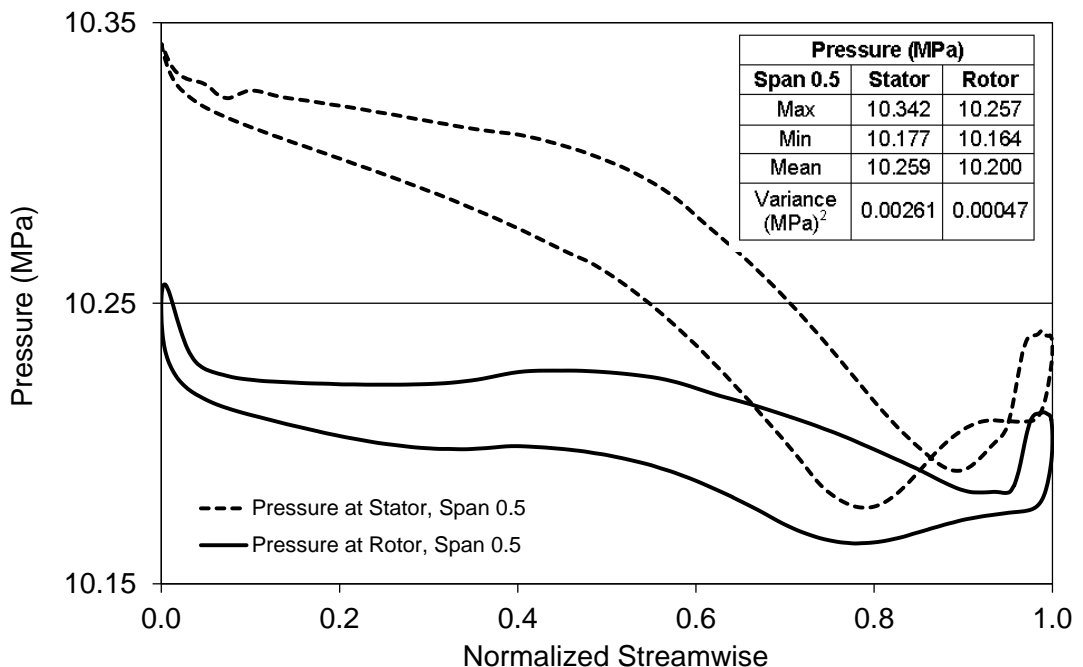


Figure 5.35 Pressure profile versus normalized streamwise for water flow rate of 3 L/s at 4,000 rpm rotation speed through turbodrill stage model “A1W20”.

After the CFD simulation was performed the FSI analysis is carried out by importing the CFD simulation results (pressure data on the blade’s surfaces) as the main boundary conditions for the static structural analysis. Table 5.10 shows the structural (FSI) simulation results for water flow rate of 3 L/s at 4,000 rpm rotation speed through turbodrill stage model “A1W20”. This table shows the minimum and maximum stress, strain and deformation caused by water flow on the blades with different blend or fillet radius. The blends on the intersection of blades with hub and shroud surfaces with

different blend radius were located to reduce the stress concentration on the sharp interfaces. The blade's material was set to the default stainless steel which its properties were reported in the previous Chapter.

Table 5.10: FSI simulation results for water flow rate of 3 L/s at 4,000 rpm rotation speed through turbodrill stage model “A1W20”.

Static Structural Analysis		Equivalent (Von-Mises) Stress (MPa)	Equivalent Elastic Strain ( $\times 10^{-4}$ mm/mm)	Total Deformation ( $\times 10^{-3}$ mm)
Blend Radius = 0.0 mm	Min	8.847	0.479	0
	Max	302.649	24.655	2.812
Blend Radius = 0.5 mm	Min	9.109	0.474	0
	Max	193.599	10.353	2.732
Blend Radius = 1.0 mm	Min	7.274	0.381	0
	Max	132.608	8.027	2.179

Figures 5.36 and 5.37 show the equivalent (Von-Mises) stress and the equivalent elastic strain profiles, respectively, for water flow rate of 3 L/s at 4,000 rpm rotation speed through turbodrill stage model “A1W20” with blend radius of 0.5 mm. These figures show that maximum equivalent stress of 193.599 MPa and maximum equivalent elastic strain of  $10.353 \times 10^{-4}$  mm/mm are both occurred on the trailing edge of the stator blade at its interface with shroud. Figure 5.38 shows the total deformation profile for water flow rate of 3 L/s at 4,000 rpm rotation speed through turbodrill stage model “A1W20” with blend radius of 0.5 mm. This figure also shows that maximum total deformation of  $2.732 \times 10^{-3}$  mm is occurred on the trailing edge of the stator blade at the middle distance between the hub and shroud.

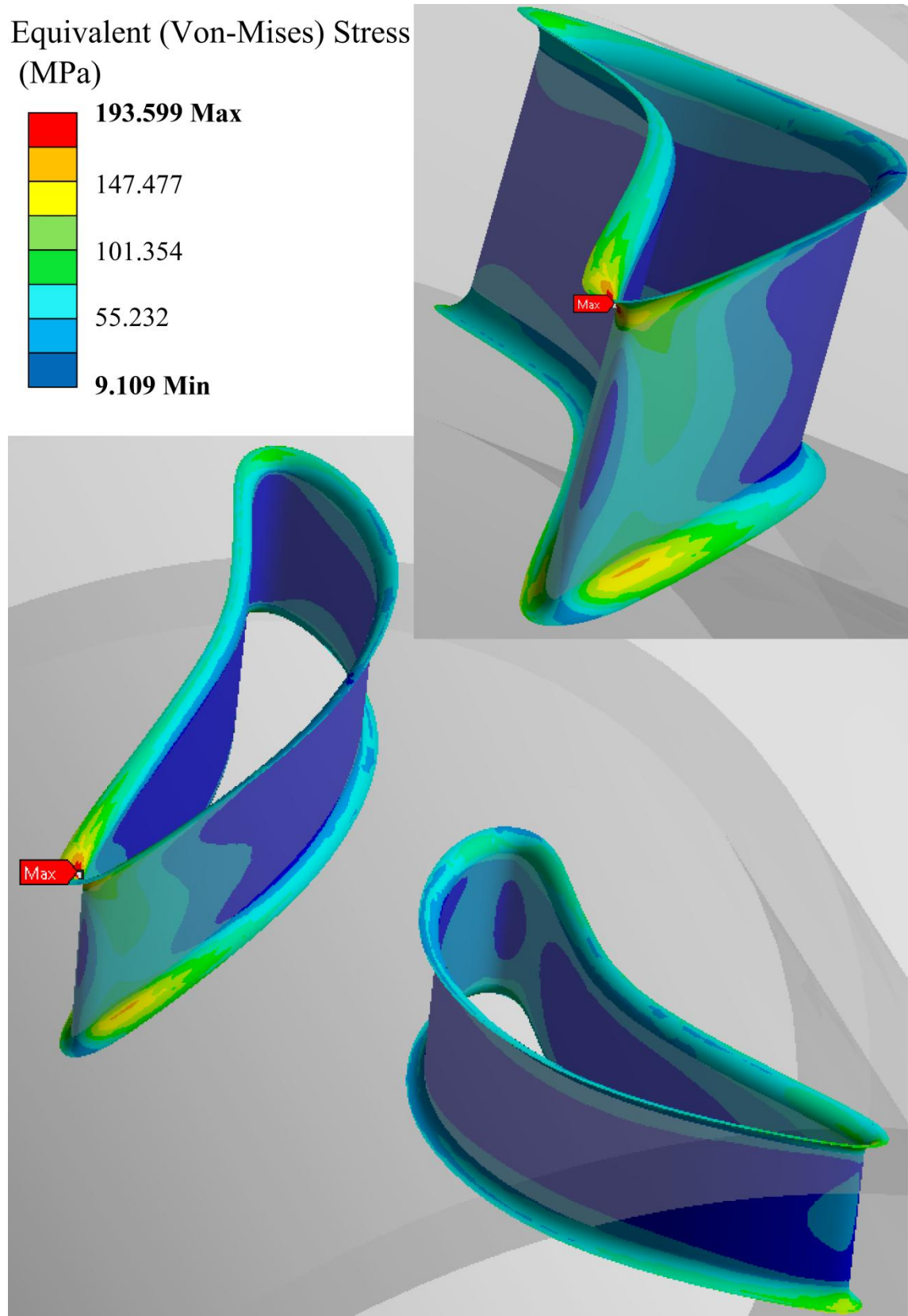


Figure 5.36 Equivalent (Von-Mises) stress profile for water flow rate of 3 L/s at 4,000 rpm rotation speed through turbodrill stage model "A1W20" with blend radius of 0.5 mm.

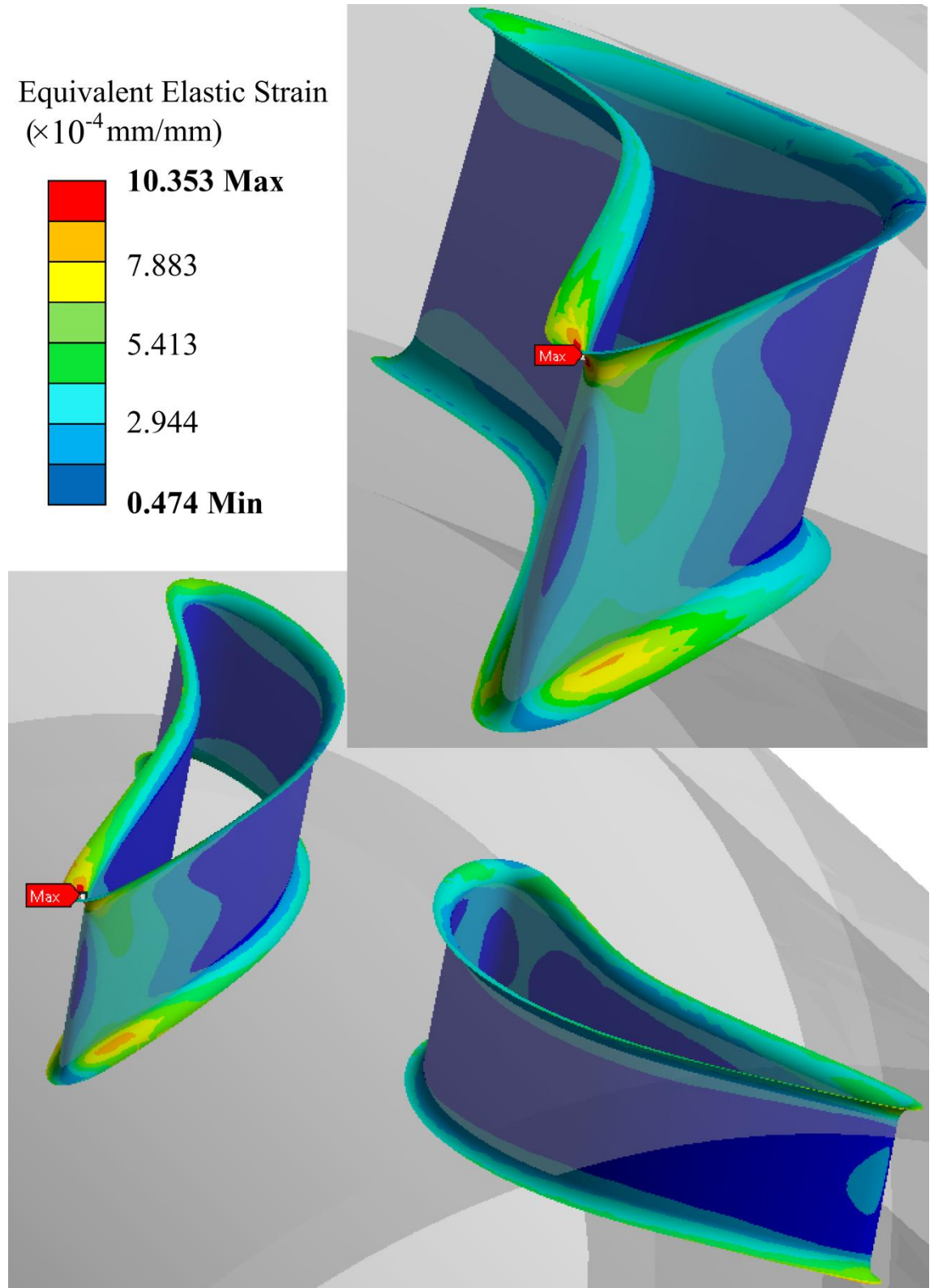


Figure 5.37 Equivalent elastic strain profile for water flow rate of 3 L/s at 4,000 rpm rotation speed through turbodrill stage model "A1W20" with blend radius of 0.5 mm.

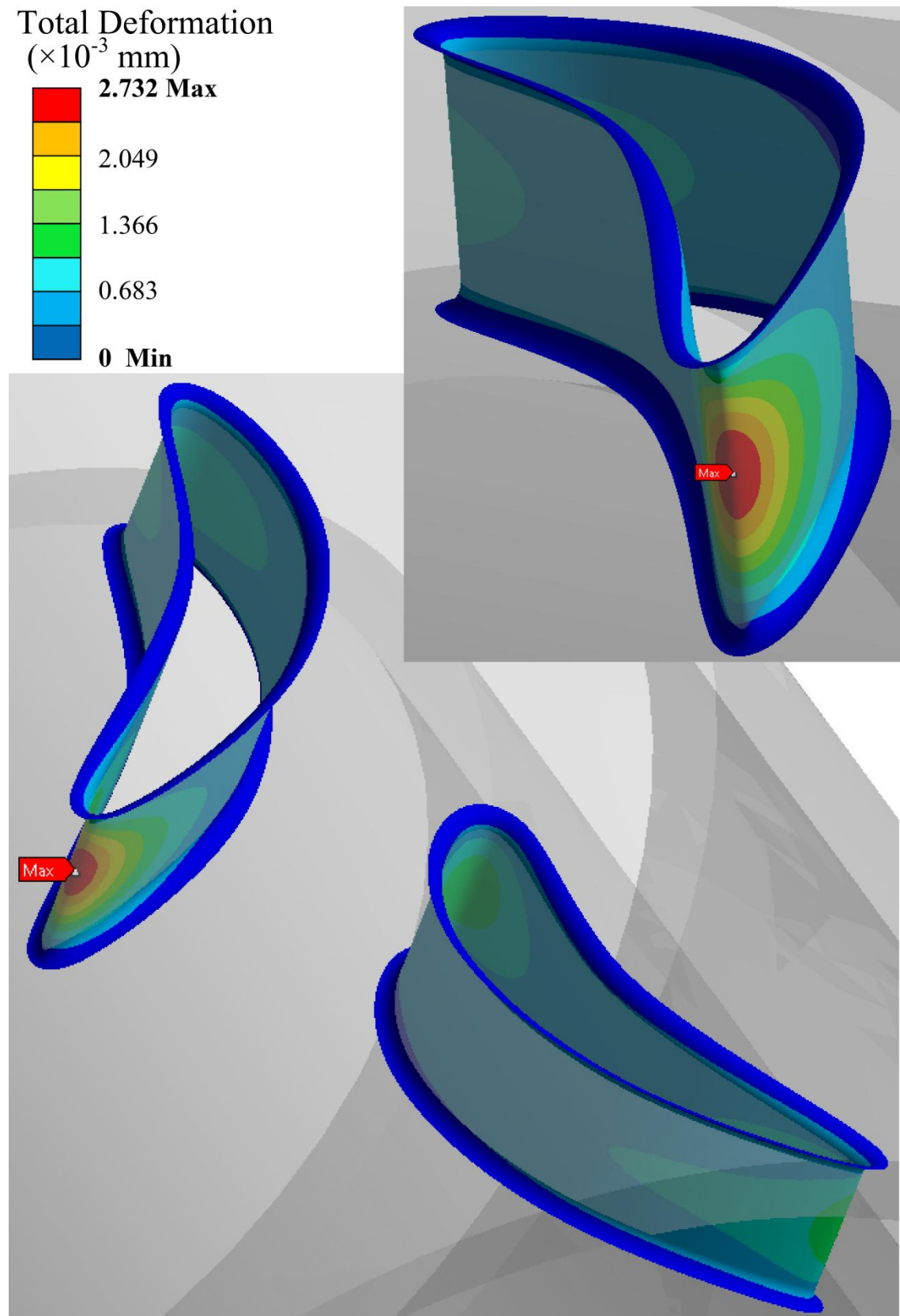


Figure 5.38 Total deformation profile for water flow rate of 3 L/s at 4,000 rpm rotation speed through turbodrill stage model "A1W20" with blend radius of 0.5 mm.

Figure 5.39 shows the CFD simulation results for one stage turbodrill model "A1W20" with water flow rate of 3 L/s at the rotation speed of 100 rpm. This figure shows the velocity profile in the blade to blade view at the span surface 0.5 and also

shows the pressure and meridional velocity profiles at meridional surface. The pressure and velocity profiles show the maximum velocity and minimum pressure is occurred near the stator blade trailing edge. The other simulation outputs are also provided in the figure.

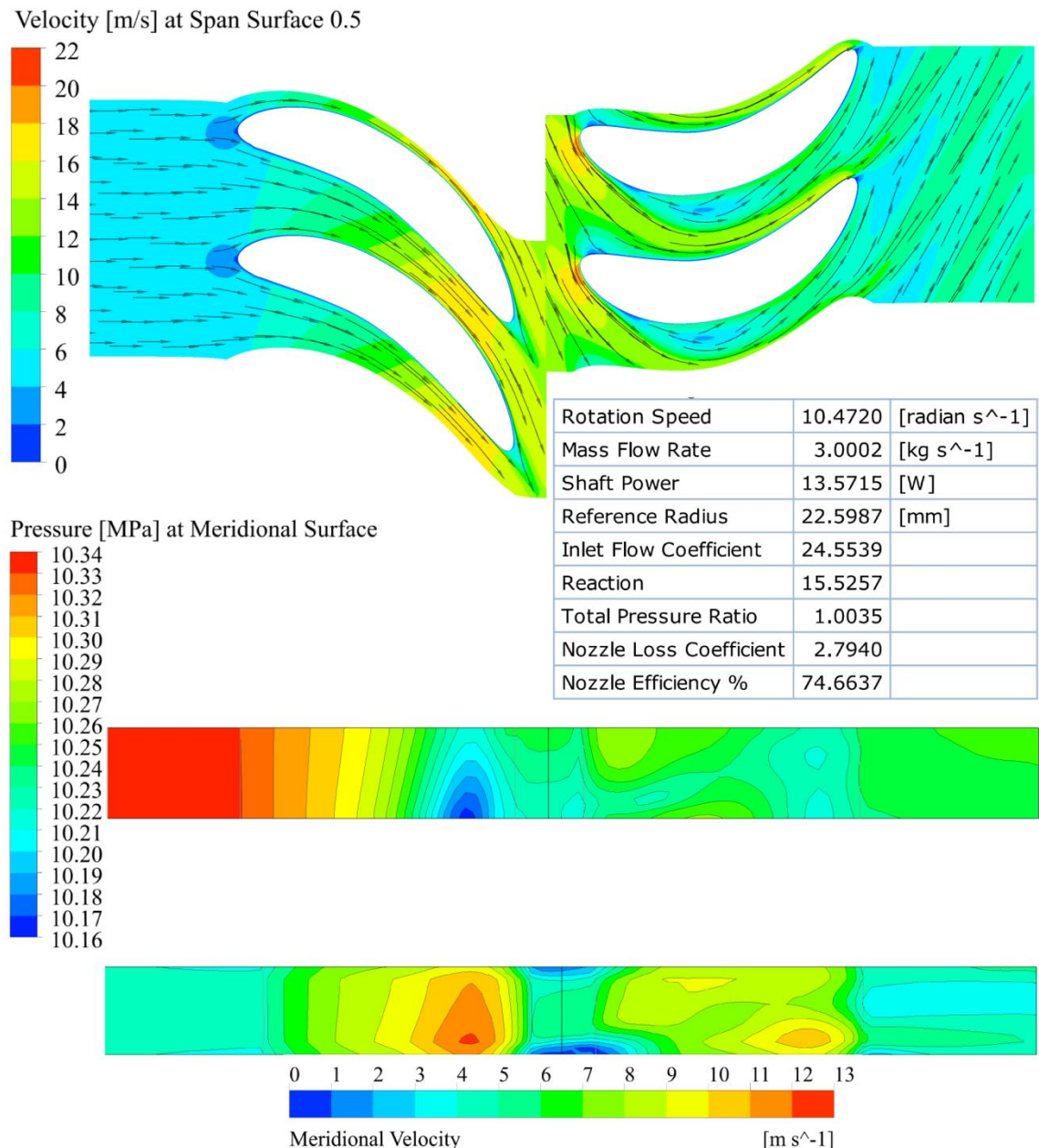


Figure 5.39 CFD simulation results for one stage turbodrill model "A1W20" with water flow rate of 3 L/s at 100 rpm rotation speed.

Figures 5.40 and 5.41 show the velocity and pressure values versus normalized streamwise length of stator and rotor at span surface 0.5 for water flow rate of 3 L/s at 100 rpm rotation speed through turbodrill stage model "A1W20". These figures show the velocity and pressure data on the both blade surfaces.

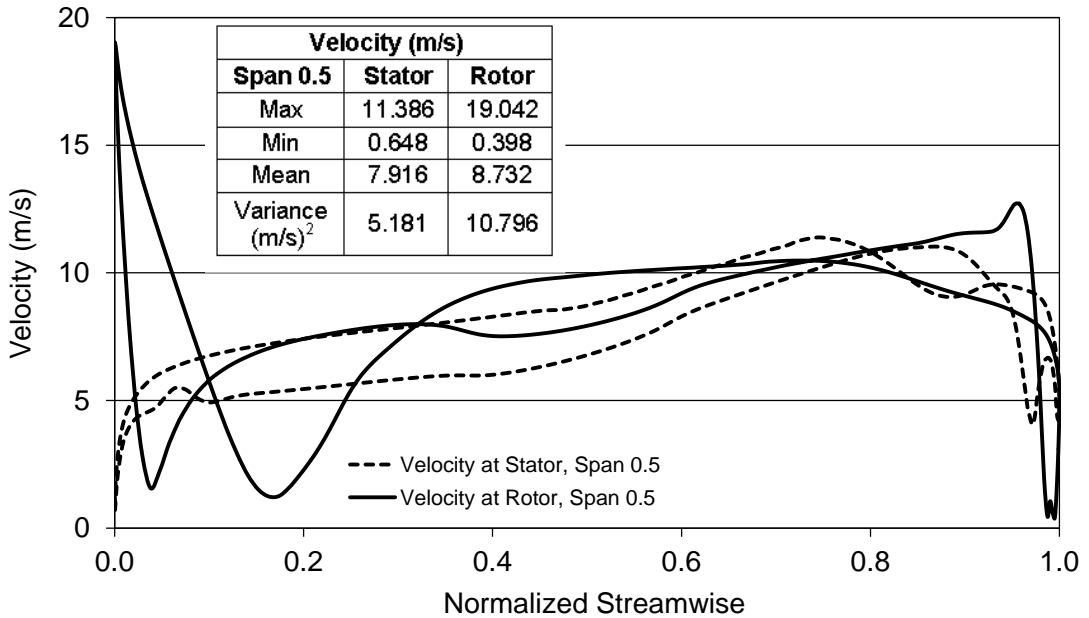


Figure 5.40 Velocity profile versus normalized streamwise for water flow rate of 3 L/s at 100 rpm rotation speed through turbodrill stage model “A1W20”.

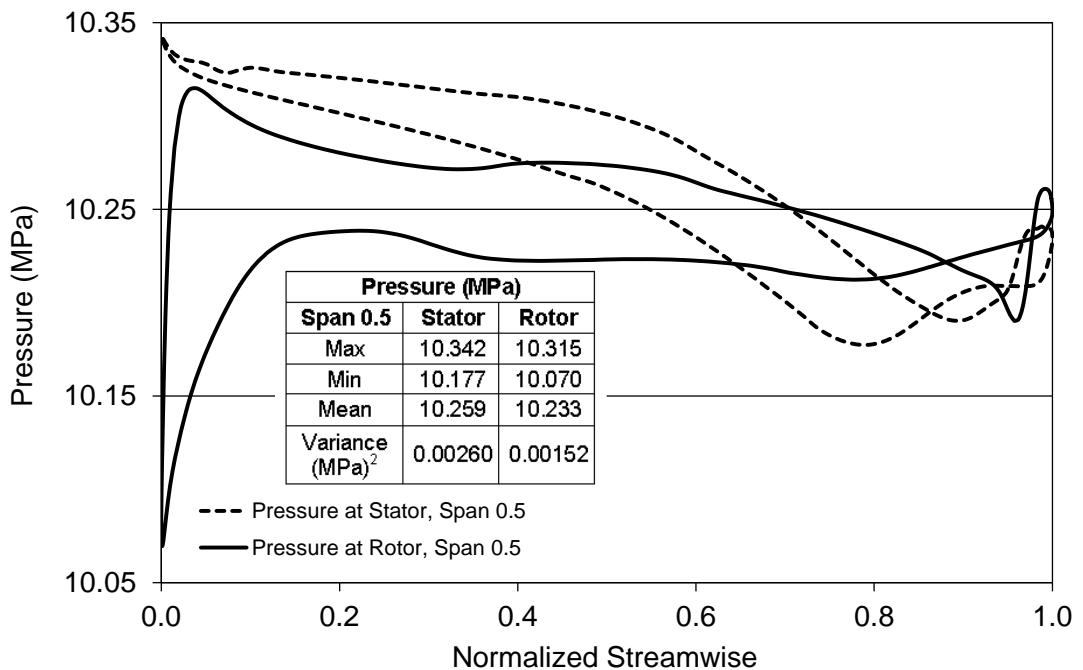


Figure 5.41 Pressure profile versus normalized streamwise for water flow rate of 3 L/s at 100 rpm rotation speed through turbodrill stage model “A1W20”.

Table 5.11 shows the structural (FSI) simulation results for stress, strain and deformation on the blades for water flow rate of 3 L/s at 100 rpm rotation speed through turbodrill stage model “A1W20” for two different blend radius. The structural simulation results at 100 rpm are almost similar to the results at 4,000 rpm provided in Table 5.10 with water flow rate of 3 L/s.

Table 5.11: FSI simulation results for water flow rate of 3 L/s at 100 rpm rotation speed through turbodrill stage model “A1W20”.

Static Structural Analysis		Equivalent (Von-Mises) Stress (MPa)	Equivalent Elastic Strain ( $\times 10^{-4}$ mm/mm)	Total Deformation ( $\times 10^{-3}$ mm)
Blend Radius = 0.5 mm	Min	9.048	0.472	0
	Max	193.784	10.320	2.737
Blend Radius = 1.0 mm	Min	7.165	0.381	0
	Max	126.017	6.530	2.181

Figure 5.42 shows the CFD simulation results for one stage turbodrill model “A1W20” with water flow rate of 3 L/s at the rotation speed of 8,000 rpm.

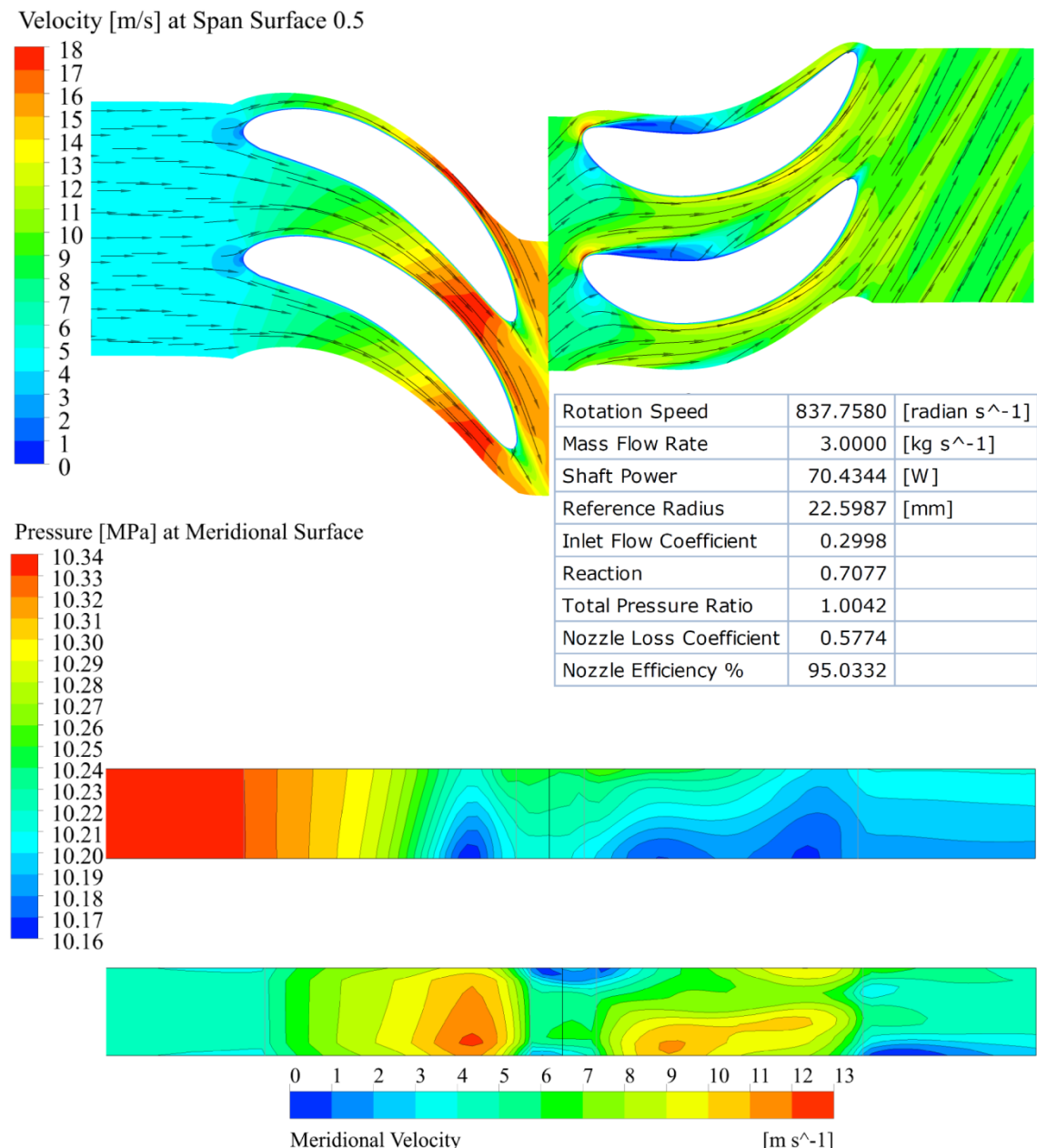


Figure 5.42 CFD simulation results for one stage turbodrill model “A1W20” with water flow rate of 3 L/s at 8,000 rpm rotation speed.

In Figure 4.42, it can be seen that velocity vectors are not directed to the right direction at the rotor blade leading edge due to high blade rotation speed which is close to the turbine runaway speed with 3 L/s water flow rate. Figures 5.43 and 5.44 show the velocity and pressure values versus normalized streamwise length of stator and rotor at span surface 0.5 for water flow rate of 3 L/s at 8,000 rpm rotation speed through turbodrill stage model “A1W20”.

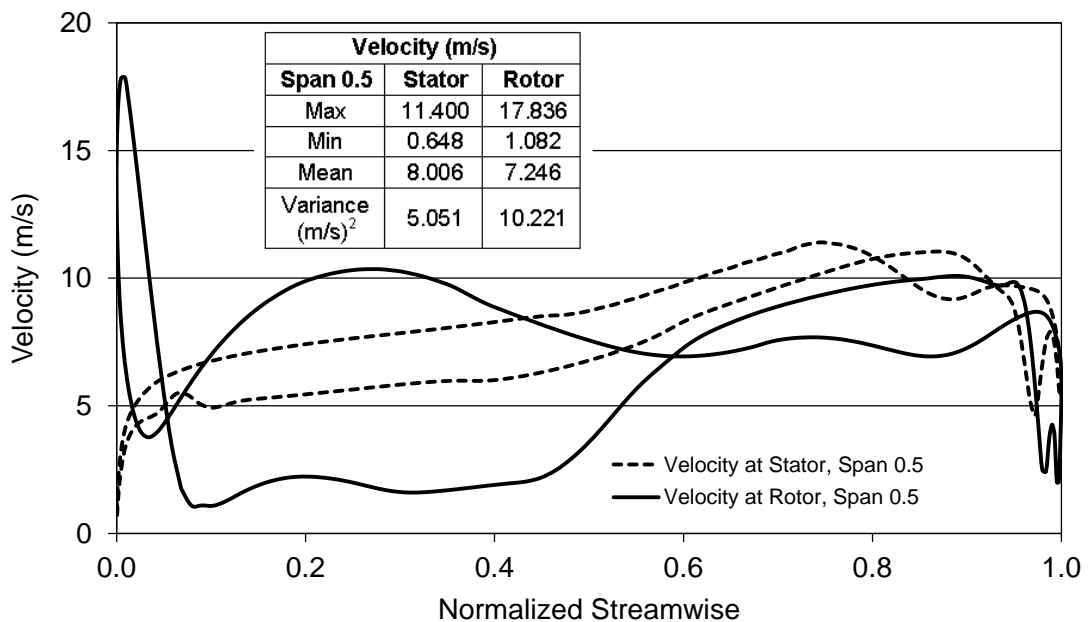


Figure 5.43 Velocity profile versus normalized streamwise for water flow rate of 3 L/s at 8,000 rpm rotation speed through turbodrill stage model “A1W20”.

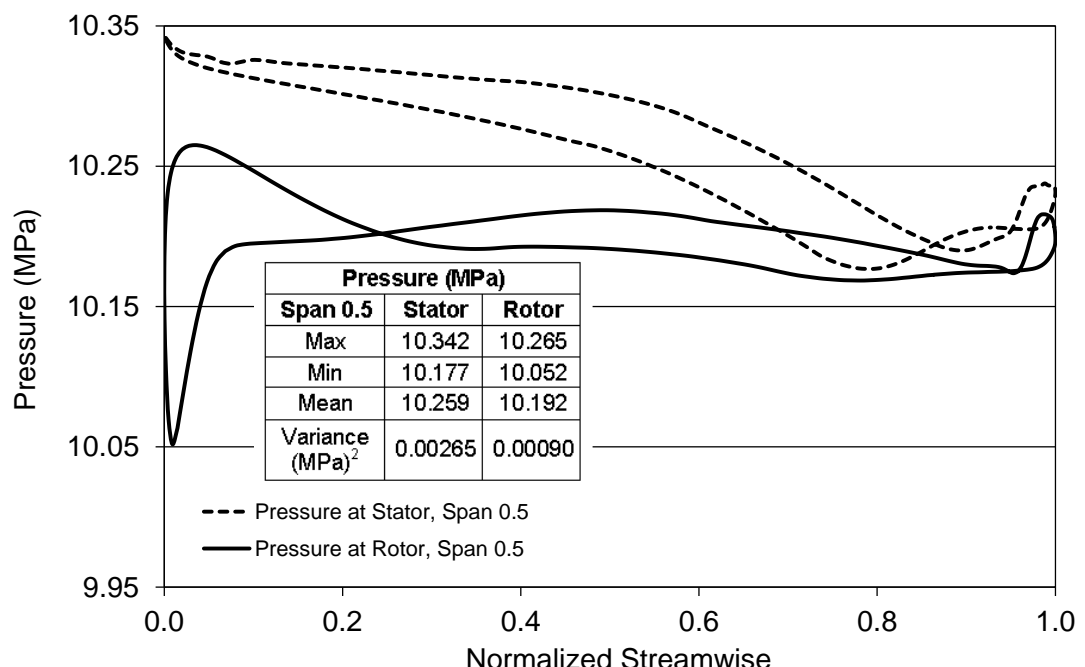


Figure 5.44 Pressure profile versus normalized streamwise for water flow rate of 3 L/s at 8,000 rpm rotation speed through turbodrill stage model “A1W20”.

CFD simulation results for 3 L/s water flow rate through one stage turbodrill model “A1W20” were reported at three rotation speeds of 100, 4,000 and 8,000 rpm for further comparison. For the next CFD simulations, only the results at optimum rotation speed are reported.

Table 5.12 shows the structural (FSI) simulation results for stress, strain and deformation on the blades for water flow rate of 3 L/s at 8,000 rpm rotation speed through turbodrill stage model “A1W20” for two different blend radius.

Table 5.12: FSI simulation results for water flow rate of 3 L/s at 8,000 rpm rotation speed through turbodrill stage model “A1W20”.

Static Structural Analysis		Equivalent (Von-Mises) Stress (MPa)	Equivalent Elastic Strain ( $\times 10^{-4}$ mm/mm)	Total Deformation ( $\times 10^{-3}$ mm)
Blend Radius = 0.5 mm	Min	9.162	0.477	0
	Max	194.235	10.350	2.740
Blend Radius = 1.0 mm	Min	7.328	0.383	0
	Max	139.643	8.285	2.185

The structural simulation results at 100, 4,000 and 8,000 rpm are almost similar with water flow rate of 3 L/s. Therefore the FSI simulation results for the next cases are only reported at their optimum rotation speed.

#### **Simulation results through stage model “A1W20” with water flow rate of 4 L/s**

Table 5.13 shows water flow CFD simulation results for one stage turbodrill model with 5 cm shroud diameter, 5 mm blade height and 20 blades on each blade row (stage model “A1W20”) with water flow rate of 4 L/s.

Table 5.13: CFD simulation results for one stage turbodrill model “A1W20” with water flow rate of 4 L/s.

Speed (rpm×100)	Power (W)	Torque (N.mm)	Inlet Flow Coefficient	Stage Reaction
1	24.275	2318.215	32.962	20.078
10	230.000	2196.500	3.122	2.612
20	416.303	1987.847	1.466	1.565
30	549.827	1750.283	0.924	1.208
40	644.139	1537.882	0.669	1.039
50	703.623	1343.920	0.524	0.936
60	723.508	1151.584	0.434	0.870
70	701.762	957.404	0.376	0.824
80	636.879	760.274	0.337	0.792
90	509.162	540.277	0.313	0.762
100	334.589	319.532	0.299	0.731
110	103.218	89.612	0.297	0.697

Figure 5.45 shows the CFD simulation results for power and torque produced by one stage turbodrill model “A1W20” with water flow rate of 4 L/s at its reference radius of 22.5987 mm. Each set of power and torque data at specific rotation speed is a result of one CFD simulation run. Non-linear regression analysis was applied to the calculated power values, and this was found to be highly correlated to second-order dependence on speed as evidenced by the high resultant correlation coefficients ( $R^2$ ). For the resulted torque data, there is a linear relation with high correlation coefficient. The maximum stage efficiency and power for this case is at around 6,000 revolutions per minute (rpm) rotation speed. One stage power and torque at maximum efficiency condition are around 725 W and 1152 N.mm, respectively. In this case, the runaway turbine speed is almost over 11,000 rpm, and stalled torque is around 2320 N.mm.

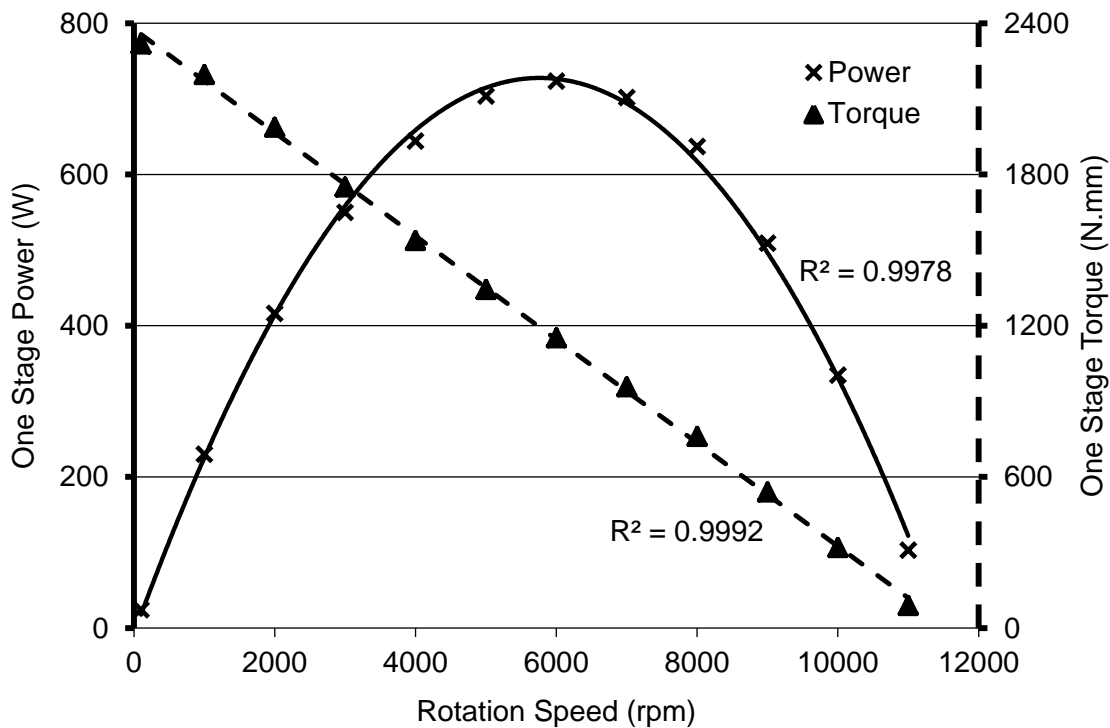


Figure 5.45 CFD simulation results for one stage turbodrill model “A1W20” with water flow rate of 4 L/s at reference radius of 22.5987 mm.

Figure 5.46 shows the CFD simulation results for one stage turbodrill model “A1W20” with water flow rate of 4 L/s at the rotation speed of 6,000 rpm. This figure shows the velocity profile in the blade to blade view at the span surface 0.5 and also shows the pressure and meridional velocity profiles at meridional surface. The pressure and velocity profiles show the maximum velocity and minimum pressure is occurred near the stator blade trailing edge. The other simulation outputs are also provided in the figure.

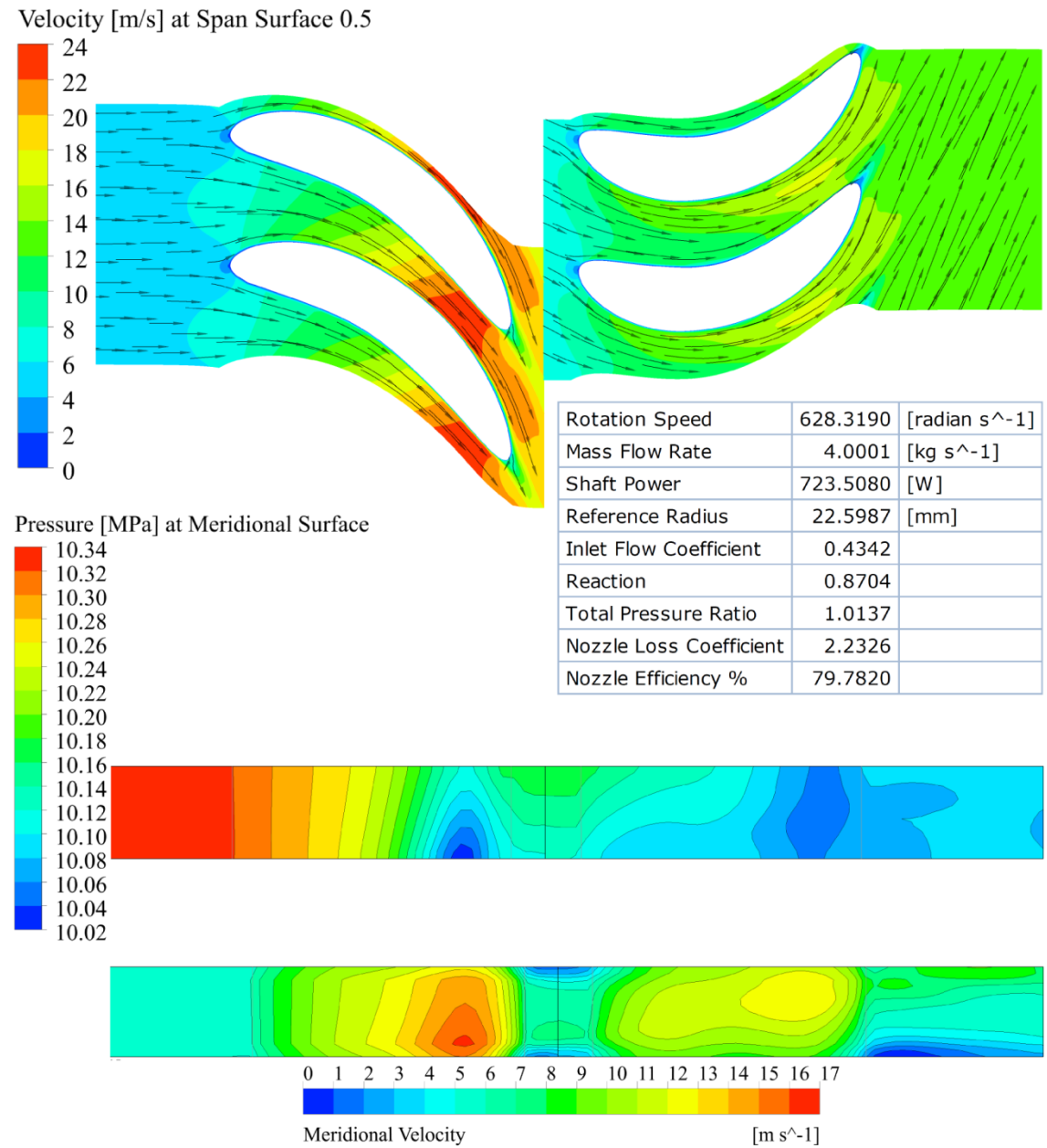


Figure 5.46 CFD simulation results for one stage turbodrill model "A1W20" with water flow rate of 4 L/s at 6,000 rpm rotation speed.

Figures 5.47 and 5.48 show the velocity and pressure values versus normalized streamwise length of stator and rotor at span surface 0.5 for water flow rate of 4 L/s at 6,000 rpm rotation speed through turbodrill stage model "A1W20". These figures show the velocity and pressure data on the both blade surfaces.

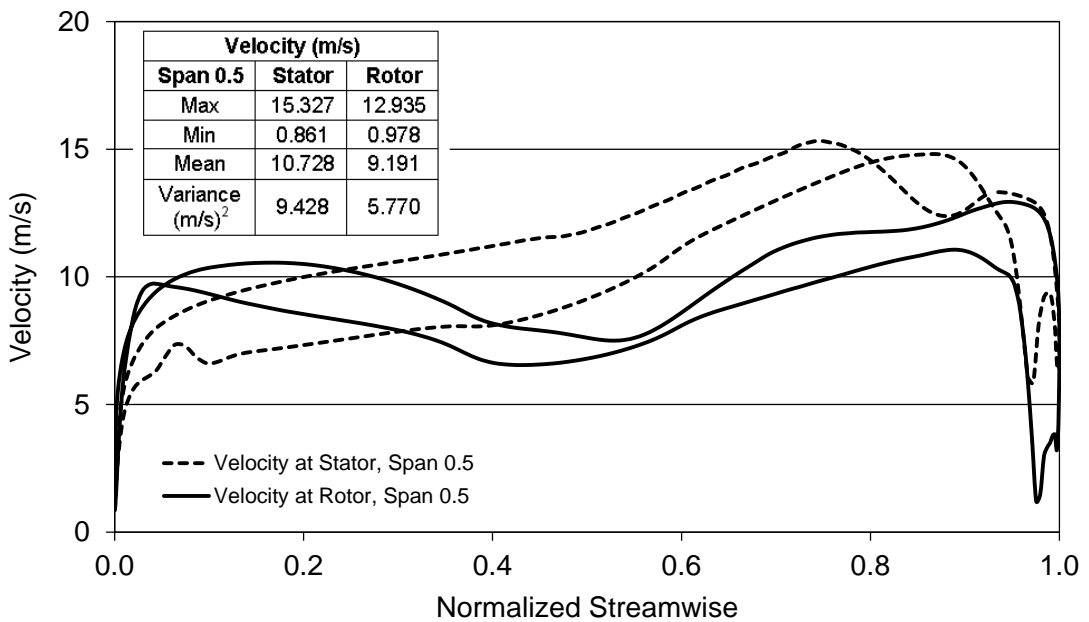


Figure 5.47 Velocity profile versus normalized streamwise for water flow rate of 4 L/s at 6,000 rpm rotation speed through turbodrill stage model “A1W20”.

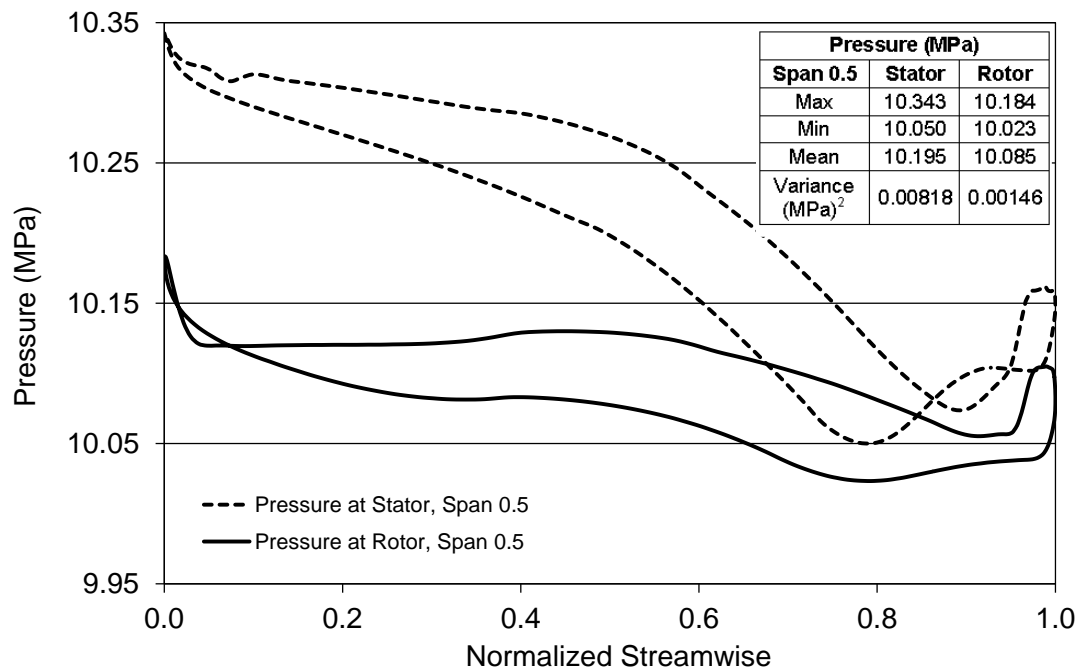


Figure 5.48 Pressure profile versus normalized streamwise for water flow rate of 4 L/s at 6,000 rpm rotation speed through turbodrill stage model “A1W20”.

Table 5.14 shows the structural (FSI) simulation results for stress, strain and deformation on the blades for water flow rate of 4 L/s at 6,000 rpm rotation speed through turbodrill stage model “A1W20” for two different blend radius.

Table 5.14: FSI simulation results for water flow rate of 4 L/s at 6,000 rpm rotation speed through turbodrill stage model “A1W20”.

Static Structural Analysis		Equivalent (Von-Mises) Stress (MPa)	Equivalent Elastic Strain ( $\times 10^{-4}$ mm/mm)	Total Deformation ( $\times 10^{-3}$ mm)
Blend Radius = 0.5 mm	Min	9.092	0.473	0
	Max	190.350	9.864	2.699
Blend Radius = 1.0 mm	Min	7.137	0.382	0
	Max	125.033	6.479	2.153

#### Simulation results through stage model “A1W20” with water flow rate of 4 L/s and different viscosity

In this section, simulation results for water flow rate of 4 L/s through stage model “A1W20” with different viscosity are reported. Several viscosity models are assumed by adding some amount of polymer to water. The viscosity models here are based on the Hershel-Bulkley method as a non-Newtonian fluid expressed as:

$$\tau = \tau_0 + K\gamma^n, \quad (5.1)$$

where  $\tau$  is the shear stress,  $\gamma$  is the shear rate,  $\tau_0$  is the yield stress, and  $K$  and  $n$  are regarded as the model factors. The default water dynamic viscosity used in the CFD simulations in the CFX is  $8.899 \times 10^{-4}$  kg/m.s. Here, to see the effect of different viscosity parameters on the turbine motor performance, following quantities are assumed as the base viscosity model.

$$\tau_0 = \text{yield stress} = 0.1312 \text{ Pa}$$

$$\gamma = \text{shear rate} = 0 - 1021$$

$$K = 0.1115 \text{ Pa.s}$$

$$n = 0.7053$$

Table 5.15 shows water flow CFD simulation results for one stage turbodrill model with 5 cm shroud diameter, 5 mm blade height and 20 blades on each blade row (stage model “A1W20”) with water flow rate of 4 L/s, using a mixture of water and polymer with the base viscosity parameters given above.

Table 5.16 and 5.17 show water flow CFD simulation results for one stage turbodrill stage model “A1W20” with water flow rate of 4 L/s, using the base viscosity parameters with different values of  $n$ . Table 5.16 shows the results for  $n = 0.5$  and Table 5.17 shows the results for  $n = 0.9$ .

Table 5.15: CFD simulation results for one stage turbodrill model “A1W20” with water flow rate of 4 L/s and using the base viscosity model.

Speed (rpm×100)	Power (W)	Torque (N.mm)	Inlet Flow Coefficient	Stage Reaction
1	20.075	1917.201	29.569	15.847
10	184.358	1760.619	2.813	2.117
20	328.669	1569.394	1.349	1.352
30	431.606	1373.946	0.875	1.092
40	494.461	1180.526	0.648	0.958
50	518.258	989.873	0.518	0.875
60	500.786	797.084	0.435	0.817
70	439.738	599.928	0.379	0.775
80	343.457	410.002	0.343	0.748
90	232.495	246.703	0.315	0.734
100	57.094	54.525	0.294	0.718

Table 5.16: CFD simulation results for one stage turbodrill model “A1W20” with water flow rate of 4 L/s and using the base viscosity model with  $n=0.5$ .

Speed (rpm×100)	Power (W)	Torque (N.mm)	Inlet Flow Coefficient	Stage Reaction
1	20.600	1967.300	30.903	15.486
10	193.680	1849.644	2.944	2.204
20	351.671	1679.229	1.410	1.403
30	468.202	1490.443	0.907	1.125
40	540.202	1289.732	0.664	0.980
50	575.654	1099.499	0.528	0.893
60	571.694	909.946	0.444	0.835
70	523.182	713.770	0.391	0.792
80	437.973	522.830	0.358	0.762
90	304.101	322.685	0.337	0.741
100	104.630	99.922	0.325	0.716

Table 5.17: CFD simulation results for one stage turbodrill model “A1W20” with water flow rate of 4 L/s and using the base viscosity model with  $n=0.9$ .

Speed (rpm×100)	Power (W)	Torque (N.mm)	Inlet Flow Coefficient	Stage Reaction
1	20.797	1986.142	28.786	17.089
10	189.269	1807.519	2.756	2.249
20	337.927	1613.601	1.328	1.430
30	447.970	1426.038	0.864	1.152
40	519.461	1240.213	0.641	1.002
50	549.425	1049.402	0.511	0.908
60	537.513	855.542	0.426	0.845
70	479.945	654.782	0.368	0.801
80	386.438	461.310	0.327	0.765
90	238.428	252.999	0.299	0.743
100	49.771	47.531	0.279	0.727

Table 5.18 and 5.19 show water flow CFD simulation results for one stage turbodrill stage model “A1W20” with water flow rate of 4 L/s, using the base viscosity parameters with different values of  $K$ . Table 5.18 shows the results for  $K = 0.2$  and Table 5.19 shows the results for  $K = 0.05$ .

Table 5.18: CFD simulation results for one stage turbodrill model “A1W20” with water flow rate of 4 L/s and using the base viscosity model with  $K=0.2$  Pa.s.

Speed (rpm×100)	Power (W)	Torque (N.mm)	Inlet Flow Coefficient	Stage Reaction
1	20.456	1953.519	29.226	16.767
10	187.032	1786.156	2.783	2.217
20	334.298	1596.273	1.336	1.405
30	441.646	1405.906	0.867	1.128
40	509.184	1215.677	0.642	0.986
50	536.318	1024.367	0.512	0.898
60	521.438	829.955	0.428	0.837
70	464.296	633.432	0.370	0.789
80	367.386	438.567	0.330	0.756
90	242.474	257.292	0.303	0.740
100	64.676	61.765	0.284	0.729

Table 5.19: CFD simulation results for one stage turbodrill model “A1W20” with water flow rate of 4 L/s and using the base viscosity model with  $K=0.05$  Pa.s.

Speed (rpm×100)	Power (W)	Torque (N.mm)	Inlet Flow Coefficient	Stage Reaction
1	19.499	1862.145	30.330	14.833
10	182.819	1745.921	2.901	2.114
20	332.014	1585.367	1.392	1.363
30	441.599	1405.757	0.899	1.101
40	507.984	1212.812	0.663	0.966
50	536.160	1024.066	0.529	0.884
60	523.191	832.746	0.448	0.826
70	467.265	637.483	0.396	0.782
80	375.794	448.604	0.363	0.756
90	244.617	259.566	0.342	0.741
100	37.092	35.423	0.330	0.720

Figure 5.49 shows the CFD simulation results for power produced by one stage turbodrill model “A1W20” with water flow rate of 4 L/s at its reference radius of 22.5987 mm using the base viscosity parameters and also with different values  $n$  and  $K$ . Table 5.18 and 5.19 show that changes in  $K$  result at very close simulation results. Therefore simulation data with  $K = 0.05$  are shown only in Figure 5.49. The effect of changing  $n$  on the one stage power is considerable rather than changing  $K$  values. In compare to simulation results using only water with same flow rate (4 L/s) and default viscosity in CFX shown in Figure 4.45, the optimum rotation speed with changing the viscosity reduces to around 5,000 rpm. Also the produced power was reduced by changing the default water viscosity to a non-Newtonian viscosity model used here.

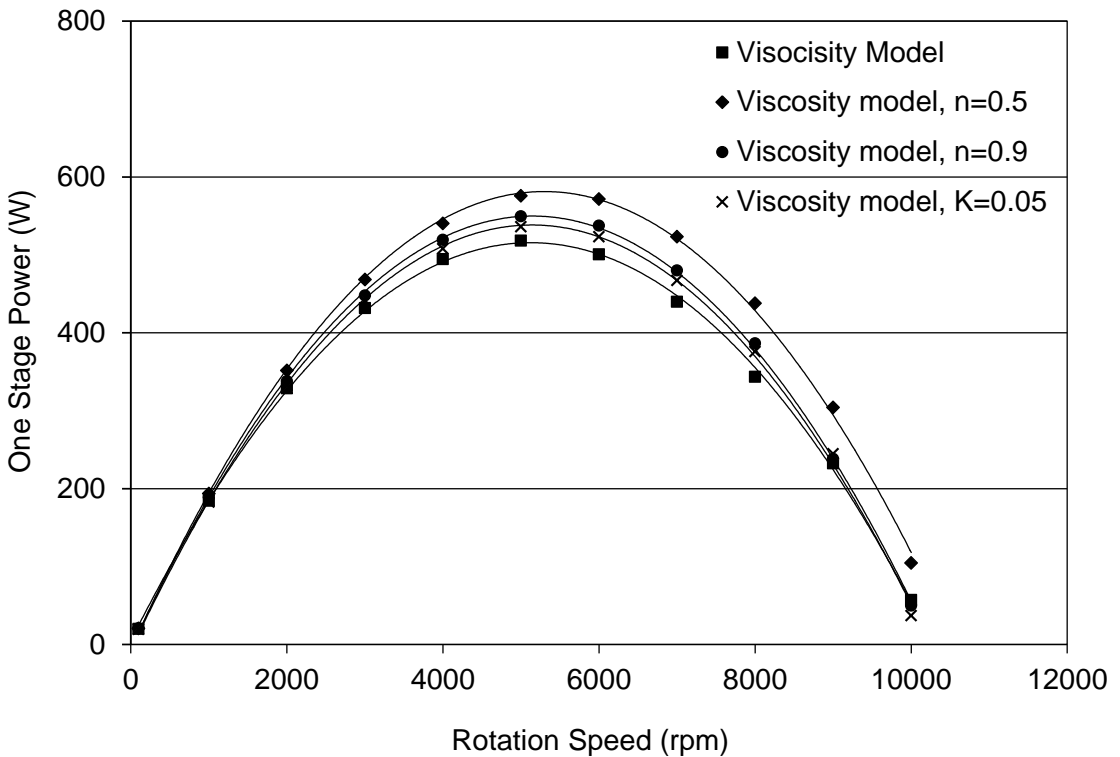


Figure 5.49 CFD simulation results for one stage turbodrill model “A1W20” with water flow rate of 4 L/s and various viscosity models at reference radius of 22.5987 mm.

**Simulation results through stage model “A1W20” with water flow rate of 4 L/s and stator outlet blade angle of 60 degree**

Table 5.20 shows water flow CFD simulation results for one stage turbodrill model “A1W20” and stator outlet blade angle of 60 degree with water flow rate of 4 L/s.

Table 5.20: CFD simulation results for one stage turbodrill model “A1W20” with water flow rate of 4 L/s and stator outlet blade angle of 60 degree.

Speed (rpm×100)	Power (W)	Torque (N.mm)	Inlet Flow Coefficient	Stage Reaction
1	19.807	1891.559	29.180	19.595
10	176.173	1682.452	2.797	2.401
20	306.034	1461.312	1.349	1.485
30	394.649	1256.299	0.879	1.161
40	450.749	1076.163	0.656	1.011
50	462.319	883.029	0.533	0.918
60	435.263	692.794	0.457	0.856
70	369.402	503.970	0.410	0.815
80	238.672	284.915	0.382	0.765
90	49.759	52.799	0.367	0.722

Figure 5.50 shows the CFD simulation results for power and torque produced by one stage turbodrill model “A1W20” with water flow rate of 4 L/s and with stator outlet blade angle of 60 degree at reference radius of 22.5987 mm. Each set of power and torque data at specific rotation speed is a result of one CFD simulation run. Non-linear

regression analysis was applied to the calculated power values, and this was found to be highly correlated to second-order dependence on speed as evidenced by the high resultant correlation coefficients ( $R^2$ ). For the resulted torque data, there is a linear relation with high correlation coefficient. The maximum stage efficiency and power for this case is at around 5,000 revolutions per minute (rpm) rotation speed. One stage power and torque at maximum efficiency condition are around 463 W and 883 N.mm, respectively. In this case, the runaway turbine speed is almost over 9,000 rpm, and stalled torque is around 1892 N.mm.

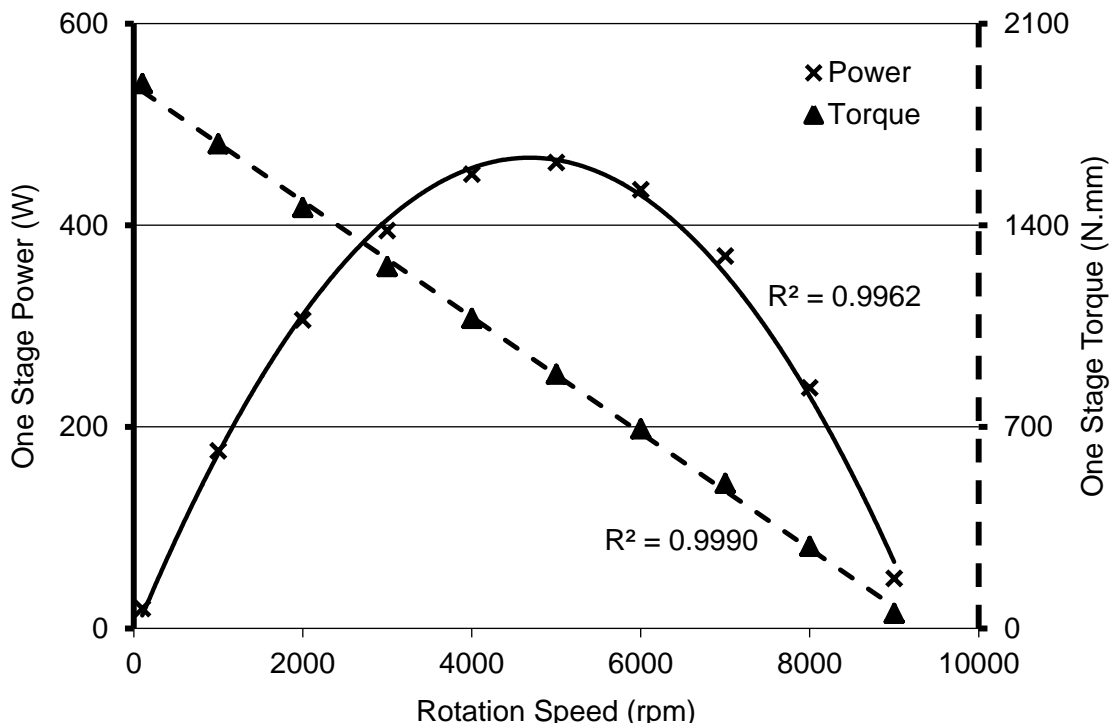


Figure 5.50 CFD simulation results for one stage turbodrill model "A1W20" with water flow rate of 4 L/s and with stator outlet blade angle of 60 degree at reference radius of 22.5987 mm.

Figure 5.51 shows the CFD simulation results for one stage turbodrill model "A1W20" with water flow rate of 4 L/s and with stator outlet blade angle of 60 degree at the rotation speed of 5,000 rpm. This figure shows the velocity profile in the blade to blade view at the span surface 0.5 and also shows the pressure and meridional velocity profiles at meridional surface. The pressure and velocity profiles show the maximum velocity and minimum pressure is occurred near the stator blade trailing edge. The other simulation outputs are also provided in the figure.

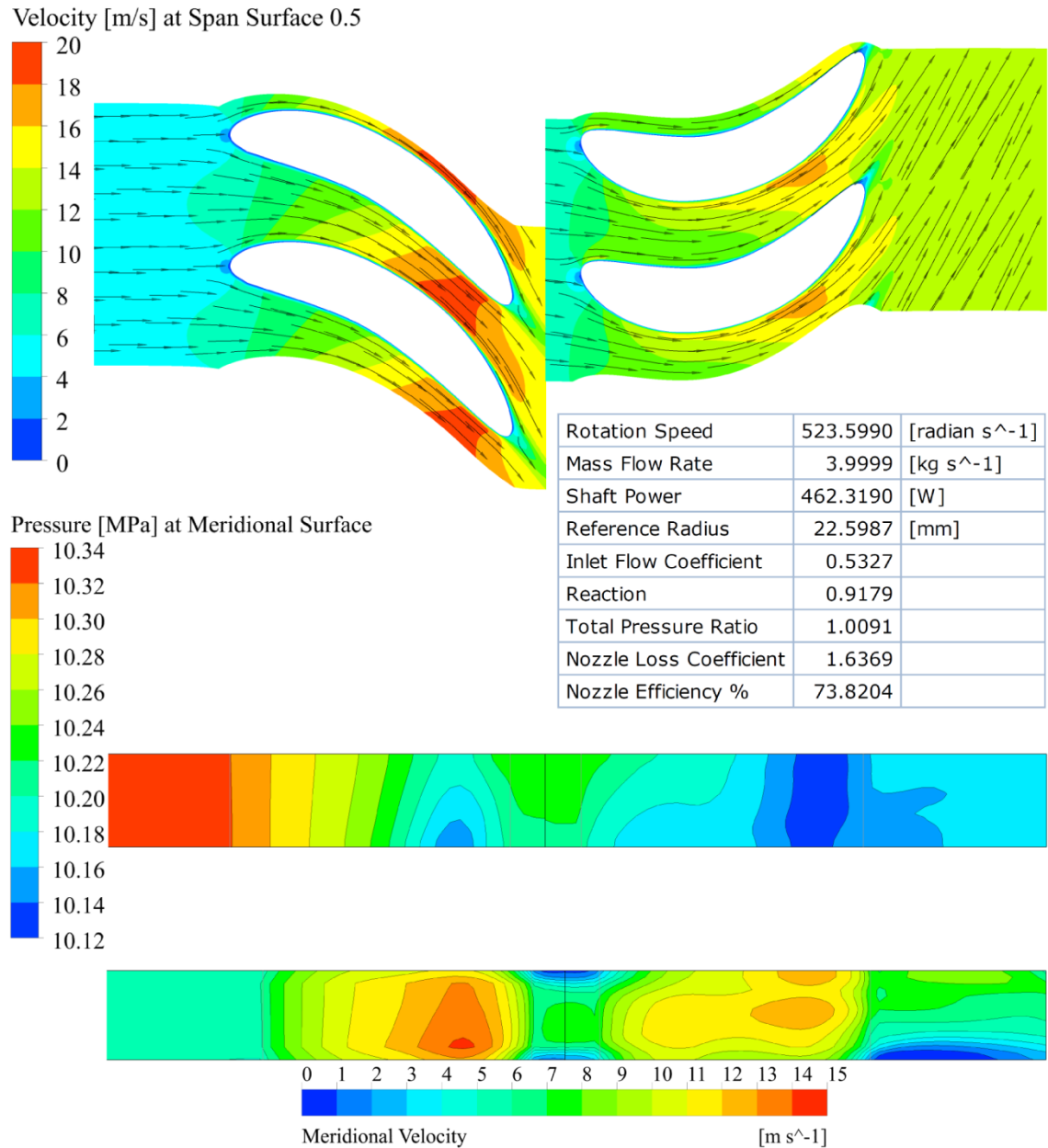


Figure 5.51 CFD simulation results for one stage turbodrill model "A1W20" with water flow rate of 4 L/s and stator outlet blade angle of 60 degree at 5,000 rpm rotation speed.

Figures 5.52 and 5.53 show the velocity and pressure values versus normalized streamwise length of stator and rotor at span surface 0.5 for water flow rate of 4 L/s at 5,000 rpm rotation speed through turbodrill stage model "A1W20" and with stator outlet blade angle of 60 degree. These figures show the velocity and pressure data on the both blade surfaces.

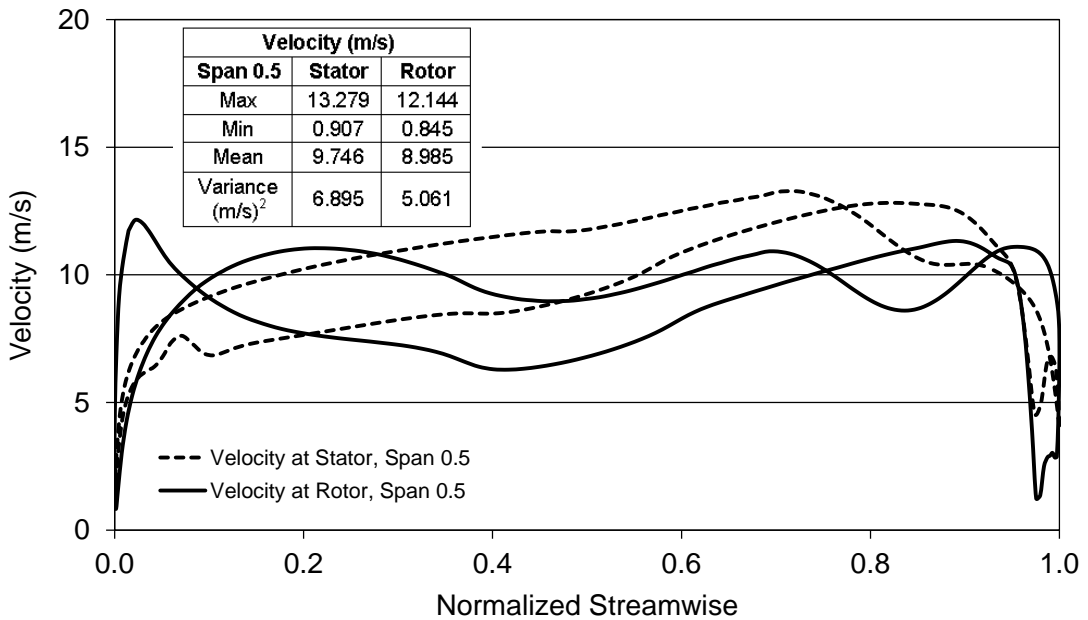


Figure 5.52 Velocity profile versus normalized streamwise for water flow rate of 4 L/s at 5,000 rpm rotation speed through turbodrill stage model "A1W20" with stator blade outlet angle of 60 degree.

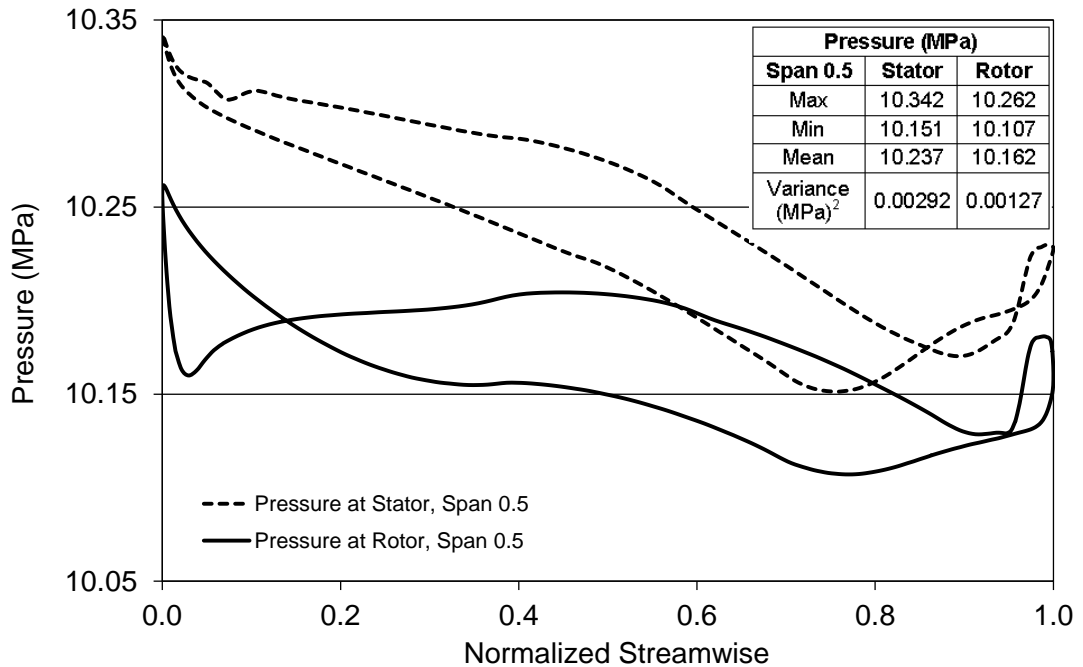


Figure 5.53 Pressure profile versus normalized streamwise for water flow rate of 4 L/s at 5,000 rpm rotation speed through turbodrill stage model "A1W20" with stator blade outlet angle of 60 degree.

Table 5.21 shows the structural (FSI) simulation results for stress, strain and deformation on the blades for water flow rate of 4 L/s at 5,000 rpm rotation speed through turbodrill stage model "A1W20" with stator outlet blade angle of 60 degree for two different blend radius.

Table 5.21: FSI simulation results for water flow rate of 4 L/s at 5,000 rpm rotation speed through turbodrill stage model “A1W20” with stator outlet blade angle of 60 degree.

Static Structural Analysis		Equivalent (Von-Mises) Stress (MPa)	Equivalent Elastic Strain ( $\times 10^{-4}$ mm/mm)	Total Deformation ( $\times 10^{-3}$ mm)
Blend Radius = 0.5 mm	Min	9.923	0.516	0
	Max	178.094	9.237	2.641
Blend Radius = 1.0 mm	Min	9.523	0.498	0
	Max	134.887	8.176	2.132

#### Simulation results through stage model “A1W16” with water flow rate of 4 L/s

Table 5.22 and Figure 5.54 show water flow CFD simulation results for one stage turbodrill model with 5 cm shroud diameter, 5 mm blade height and 16 blades on each blade row (stage model “A1W16”) with water flow rate of 4 L/s.

Table 5.22: CFD simulation results for one stage turbodrill model “A1W16” with water flow rate of 4 L/s.

Speed (rpm×100)	Power (W)	Torque (N.mm)	Inlet Flow Coefficient	Stage Reaction
1	18.189	1737.011	28.519	16.142
10	161.857	1545.734	2.733	2.105
20	276.095	1318.354	1.315	1.293
30	347.715	1106.893	0.856	1.030
40	379.399	905.815	0.638	0.903
50	369.388	705.531	0.515	0.827
60	307.608	489.609	0.439	0.772
70	192.851	263.104	0.389	0.725
80	37.979	45.337	0.354	0.694

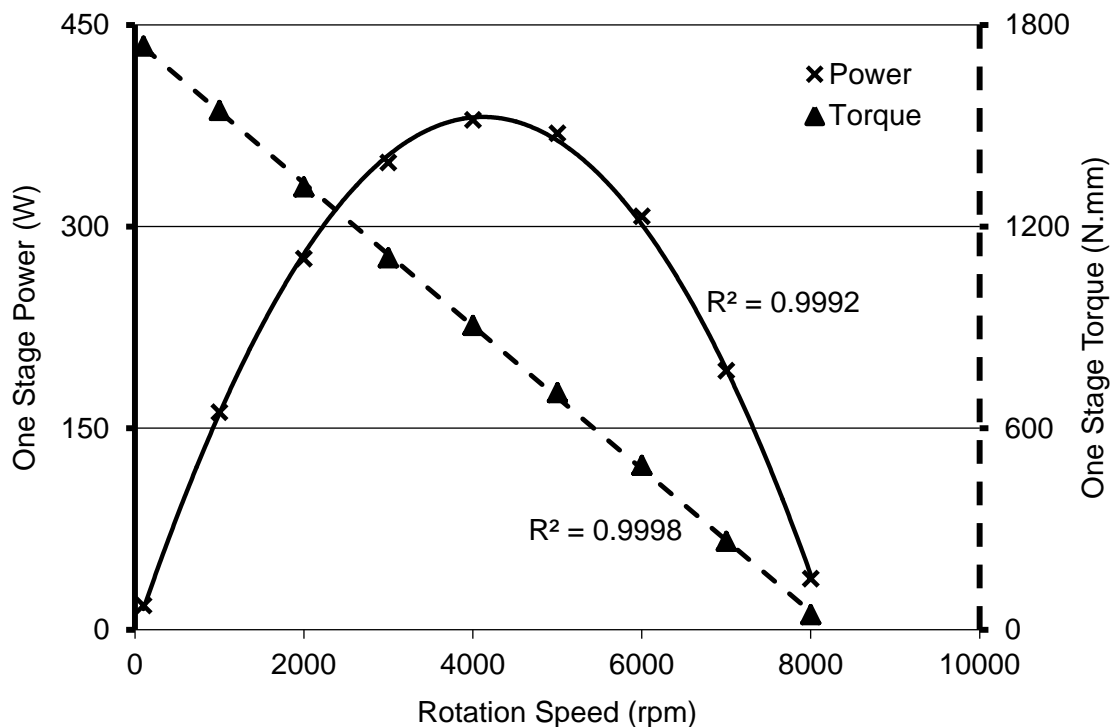


Figure 5.54 CFD simulation results for one stage turbodrill model “A1W16” with water flow rate of 4 L/s at reference radius of 22.5972 mm.

Figure 5.54 shows that the maximum stage efficiency and power for this case is at around 4,000 rpm rotation speed. One stage power and torque at maximum efficiency condition are around 380 W and 906 N.mm, respectively. In this case, the runaway turbine speed is almost over 8,000 rpm, and stalled torque is around 1737 N.mm. Figure 5.55 shows the CFD simulation results for one stage turbodrill model “A1W16” with water flow rate of 4 L/s at the rotation speed of 4,000 rpm. This figure shows the velocity profile in the blade to blade view at the span surface 0.5 and also shows the pressure and meridional velocity profiles at meridional surface. The other simulation outputs are also provided in the figure.

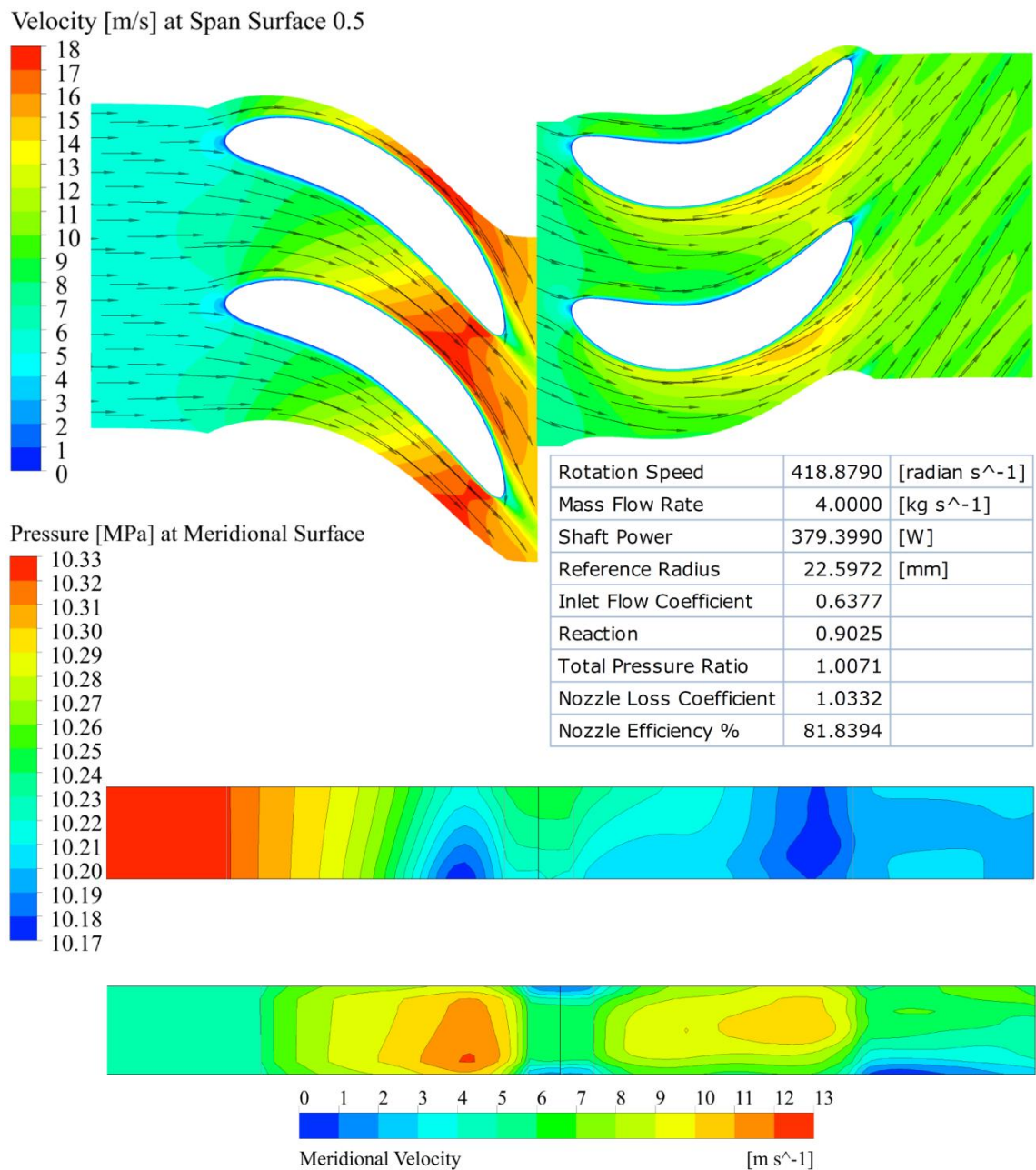


Figure 5.55 CFD simulation results for one stage turbodrill model “A1W16” with water flow rate of 4 L/s at 4,000 rpm rotation speed.

Figures 5.56 and 5.57 show the velocity and pressure values versus normalized streamwise length of stator and rotor at span surface 0.5 for water flow rate of 4 L/s at 4,000 rpm rotation speed through turbodrill stage model “A1W16”. These figures show the velocity and pressure data on the both blade surfaces.

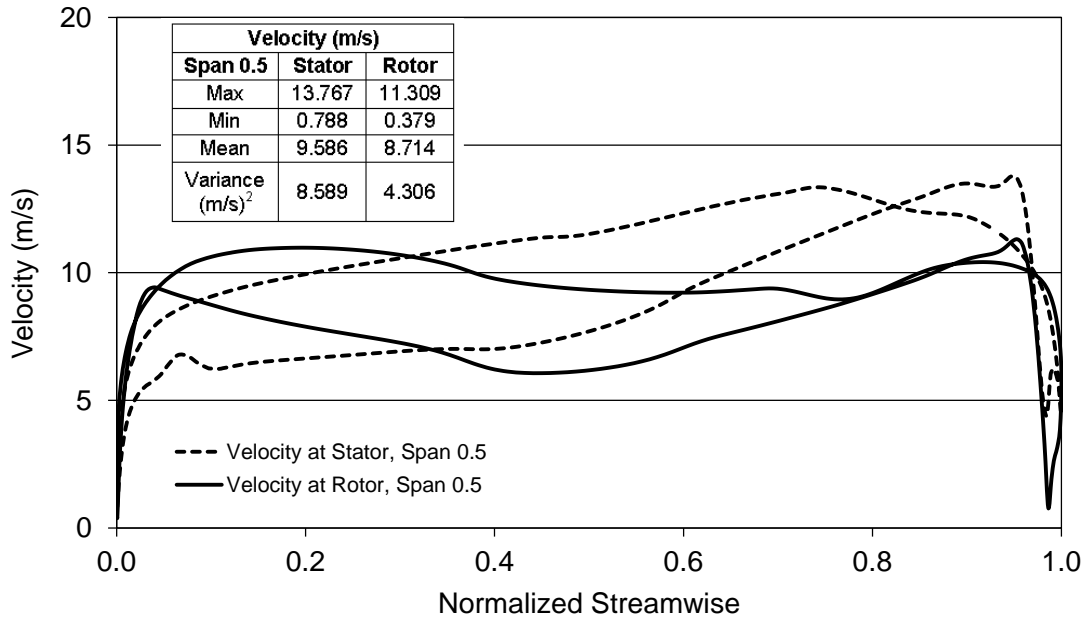


Figure 5.56 Velocity profile versus normalized streamwise for water flow rate of 4 L/s at 4,000 rpm rotation speed through turbodrill stage model “A1W16”.

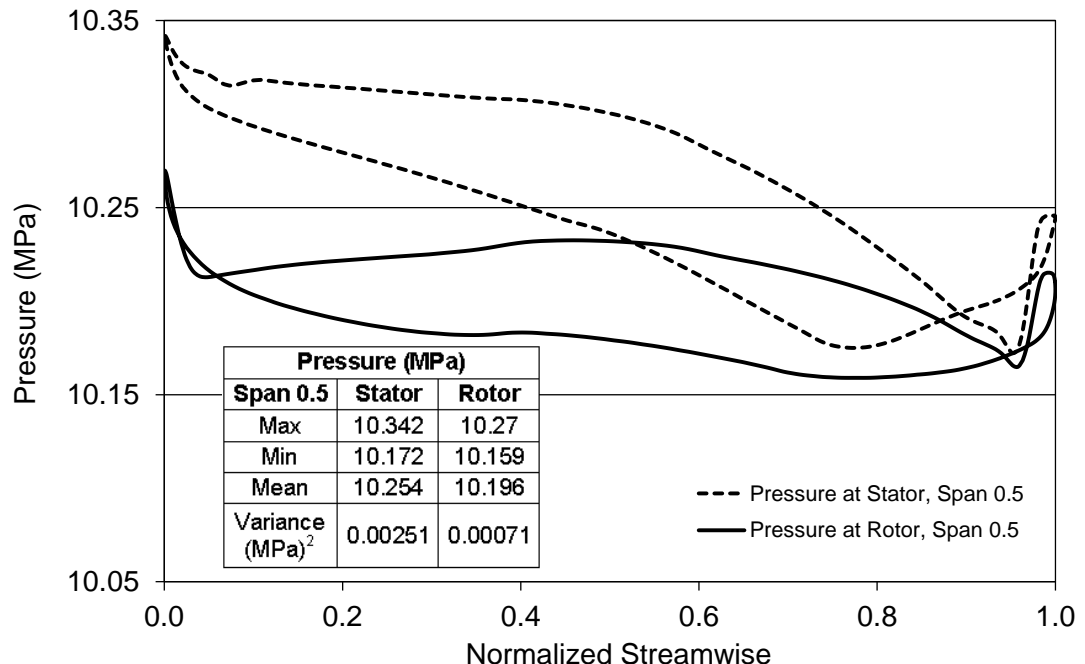


Figure 5.57 Pressure profile versus normalized streamwise for water flow rate of 4 L/s at 4,000 rpm rotation speed through turbodrill stage model “A1W16”.

Table 5.23 shows the structural (FSI) simulation results for stress, strain and deformation on the blades for water flow rate of 4 L/s at 4,000 rpm rotation speed through turbodrill stage model “A1W16” for two different blend radius.

Table 5.23: FSI simulation results for water flow rate of 4 L/s at 4,000 rpm rotation speed through turbodrill stage model “A1W16”.

Static Structural Analysis		Equivalent (Von-Mises) Stress (MPa)	Equivalent Elastic Strain ( $\times 10^{-4}$ mm/mm)	Total Deformation ( $\times 10^{-3}$ mm)
Blend Radius = 0.5 mm	Min	9.175	0.482	0
	Max	190.558	9.877	2.722
Blend Radius = 1.0 mm	Min	7.098	0.377	0
	Max	125.559	6.506	2.172

#### Conclusion remarks for simulation results of water flow through stage model “A1”

Figure 5.58 shows the water flow simulation results for one stage power with different turbodrill stage models with 5 cm shroud diameter and 5 mm blade height (model “A1”). The effect of different geometrical and flow properties on the turbodrill stage “A1” performance is shown in this Figure. It can be inferred that flow rate has significant effect on the turbodrill performance. After that, the numbers of blades on each row, the outlet stator blade angle and fluid viscosity have considerable influence on the turbodrill performance. As a result, the turbodrill performance should be evaluated for each different and possible condition, separately.

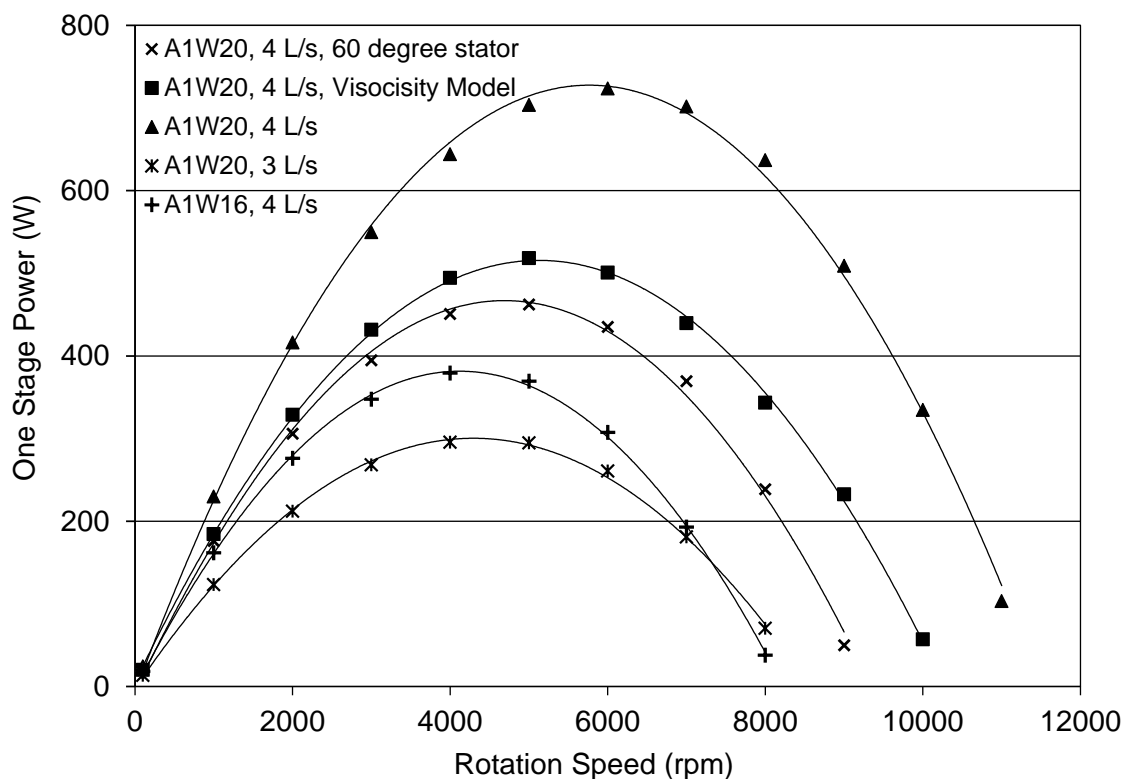


Figure 5.58 CFD simulation results of water flow through one stage turbodrill stage model “A1”.

### 5.5.2 Water flow simulation results for Turbodrill stage model “A2”

Water flow simulation results for one stage turbodrill models with 5 cm shroud diameter and 8 mm blade height (span) which are known here as stage model “A2” are presented in this section.

#### Simulation results through stage model “A2W20” with water flow rate of 3 L/s

Table 5.24 and Figure 5.59 show water flow CFD simulation results for one stage turbodrill model with 5 cm shroud diameter, 8 mm blade height and 20 blades on each blade row (stage model “A2W20”) with water flow rate of 3 L/s.

Table 5.24: CFD simulation results for one stage turbodrill model “A2W20” with water flow rate of 3 L/s.

Speed (rpm×100)	Power (W)	Torque (N.mm)	Inlet Flow Coefficient	Stage Reaction
1	8.761	836.704	17.850	9.636
10	77.036	735.689	1.648	1.600
20	128.376	612.995	0.743	1.077
30	155.662	495.524	0.472	0.910
40	151.112	360.780	0.357	0.822
50	111.359	212.696	0.307	0.762
60	47.915	76.264	0.302	0.737

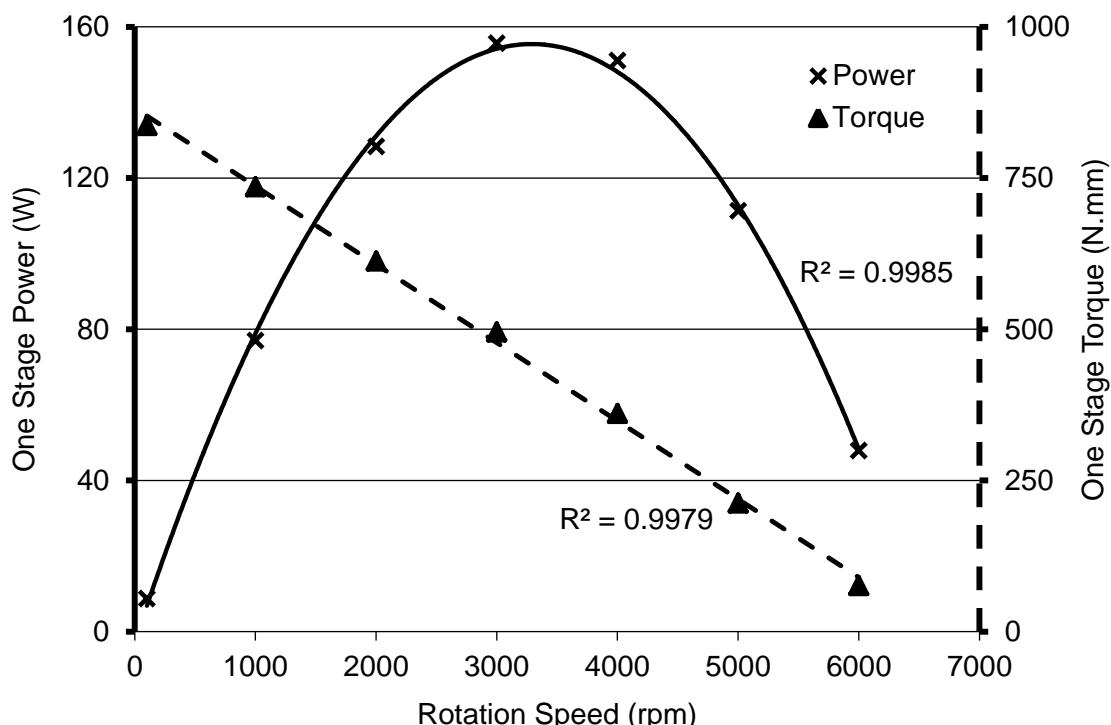


Figure 5.59 CFD simulation results for one stage turbodrill model “A2W20” with water flow rate of 3 L/s at reference radius of 21.2716 mm.

Figure 5.60 shows that the maximum stage efficiency and power for this case is at around 3,000 rpm rotation speed. One stage power and torque at maximum efficiency condition are around 156 W and 496 N.mm, respectively. In this case, the runaway turbine speed is almost over 6,000 rpm, and stalled torque is around 837 N.mm. Figure 5.60 shows the CFD simulation results for one stage turbodrill model “A2W20” with water flow rate of 3 L/s at the rotation speed of 3,000 rpm. This figure shows the velocity profile in the blade to blade view at the span surface 0.5 and also shows the pressure and meridional velocity profiles at meridional surface.

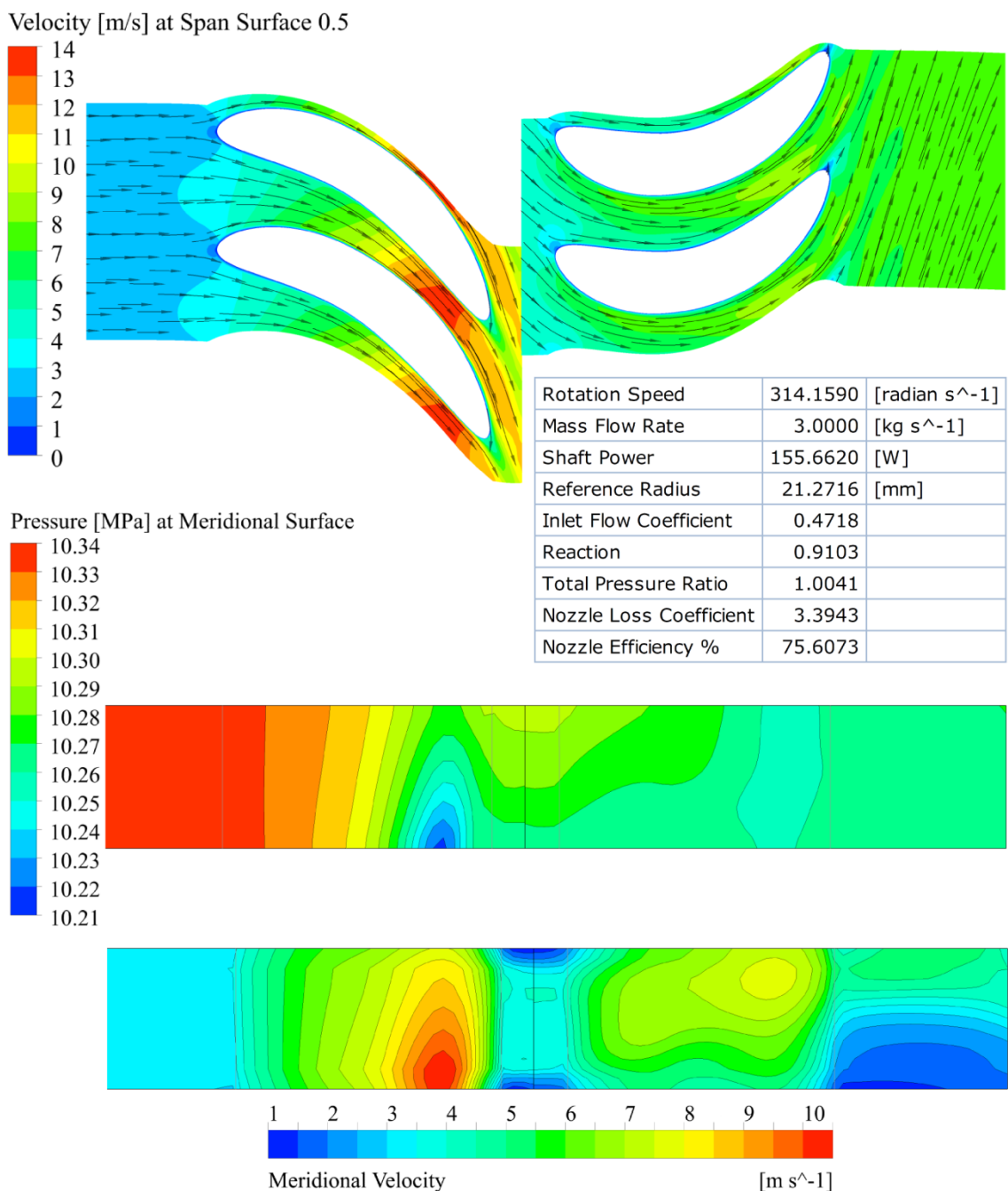


Figure 5.60 CFD simulation results for one stage turbodrill model “A2W20” with water flow rate of 3 L/s at 3,000 rpm rotation speed.

Figures 5.61 and 5.62 show the velocity and pressure values versus normalized streamwise length of stator and rotor at span surface 0.5 for water flow rate of 3 L/s at 3,000 rpm rotation speed through turbodrill stage model “A2W20”. These figures show the velocity and pressure data on the both blade surfaces.

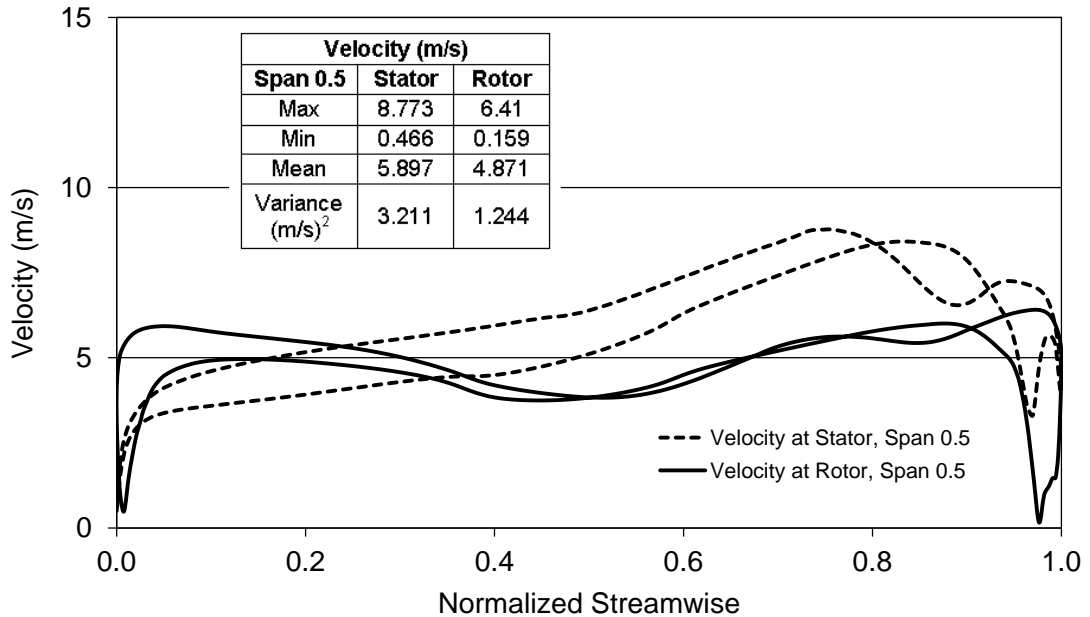


Figure 5.61 Velocity profile versus normalized streamwise for water flow rate of 3 L/s at 3,000 rpm rotation speed through turbodrill stage model “A2W20”.

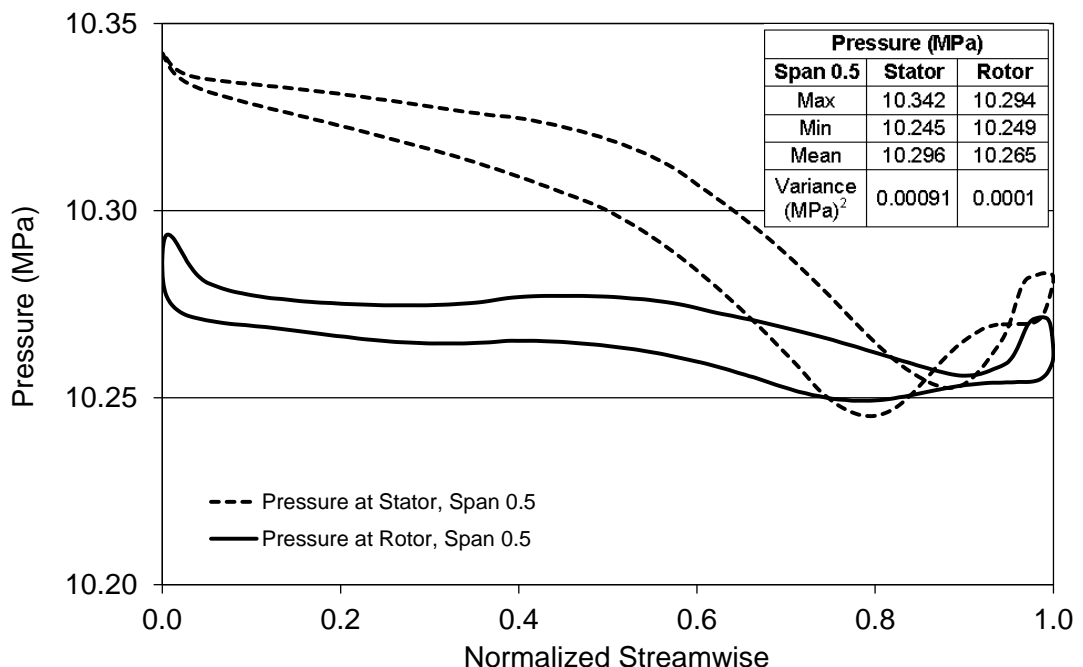


Figure 5.62 Pressure profile versus normalized streamwise for water flow rate of 3 L/s at 3,000 rpm rotation speed through turbodrill stage model “A2W20”.

Table 5.25 shows the structural (FSI) simulation results for stress, strain and deformation on the blades for water flow rate of 3 L/s at 3,000 rpm rotation speed through turbodrill stage model “A2W20” for two different blend radius.

Table 5.25: FSI simulation results for water flow rate of 3 L/s at 3,000 rpm rotation speed through turbodrill stage model “A2W20”.

Static Structural Analysis		Equivalent (Von-Mises) Stress (MPa)	Equivalent Elastic Strain ( $\times 10^{-4}$ mm/mm)	Total Deformation ( $\times 10^{-3}$ mm)
Blend Radius = 0.5 mm	Min	11.348	0.590	0
	Max	343.800	17.821	7.677
Blend Radius = 1.0 mm	Min	11.605	0.603	0
	Max	245.043	12.697	6.553
Blend Radius = 2.0 mm	Min	10.388	0.545	0
	Max	149.706	7.758	4.392

Figures 5.63 to 5.65 show the equivalent (Von-Mises) stress, the equivalent elastic strain profiles, and total deformation, respectively, for water flow rate of 3 L/s at 3,000 rpm rotation speed through turbodrill stage model “A2W20” with three different blend radius. These figures show that the blend radius has considerable influence on the maximum stress and strain which are occurred on the trailing edge of the stator blade at its interface with shroud. Also the blend radius is effective on the maximum total deformation which is occurred on the trailing edge of the stator blade at the middle distance between hub and shroud.

### Equivalent (Von-Mises) Stress (MPa)

Blend Radius = 0.5 mm

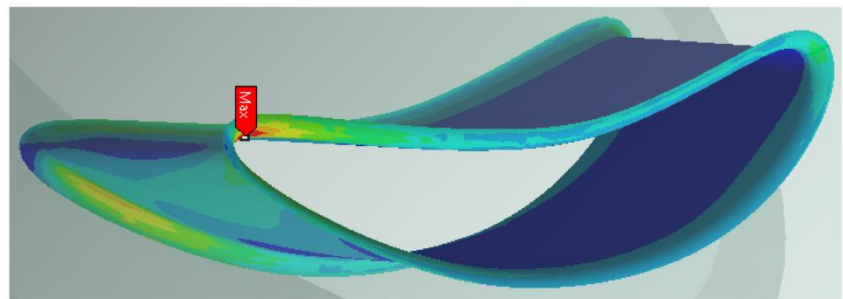
**343.800 Max**

260.687

177.574

94.461

**11.348 Min**



Blend Radius = 1 mm

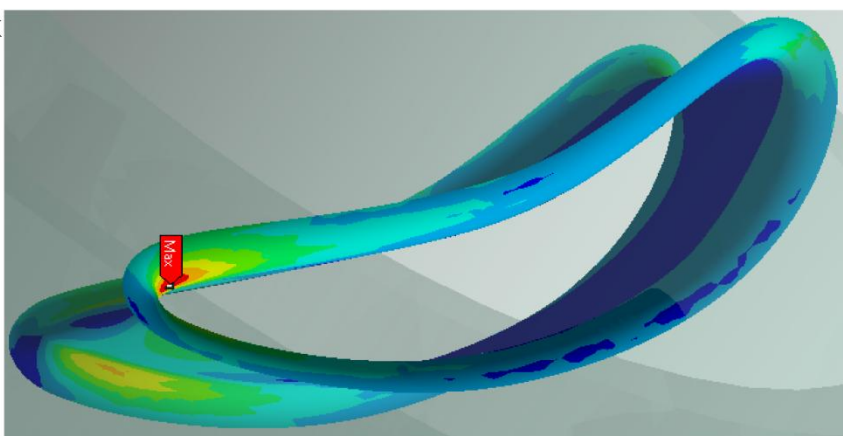
**245.043 Max**

186.683

128.324

69.964

**11.605 Min**



Blend Radius = 2 mm

**149.706 Max**

114.877

80.047

45.217

**10.388 Min**

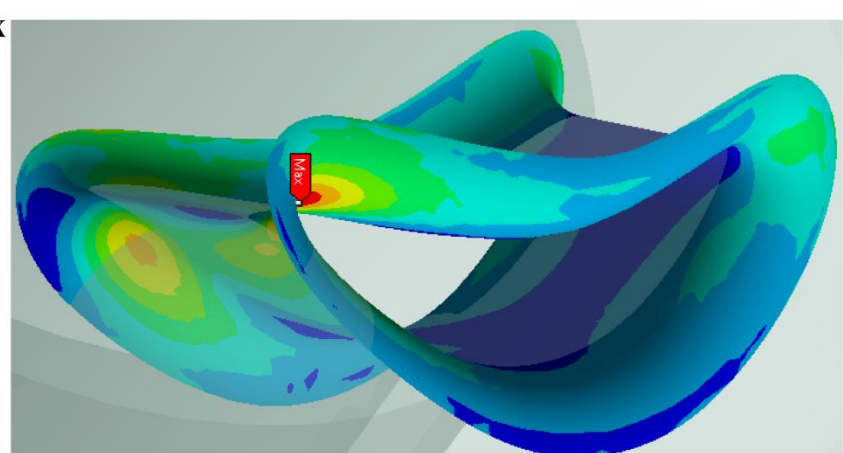
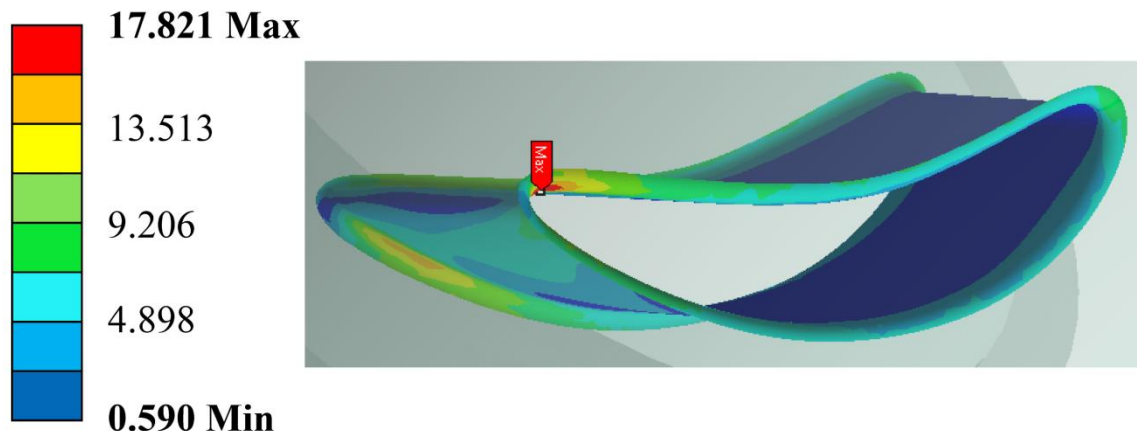


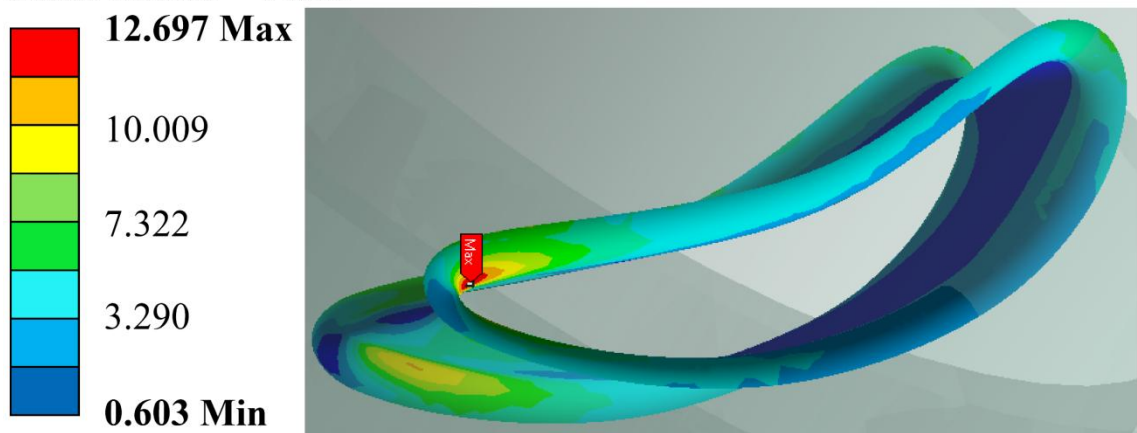
Figure 5.63 Equivalent (Von-Mises) stress profile for water flow rate of 3 L/s at 3,000 rpm rotation speed through turbodrill stage model "A2W20" with different blend radius.

### Equivalent Elastic Strain ( $\times 10^{-4}$ mm/mm)

Blend Radius = 0.5 mm



Blend Radius = 1 mm



Blend Radius = 2 mm

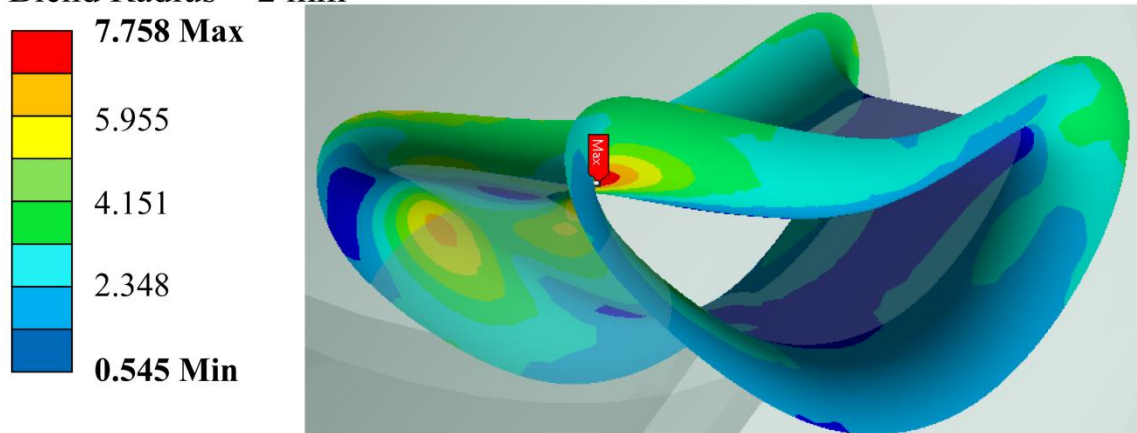
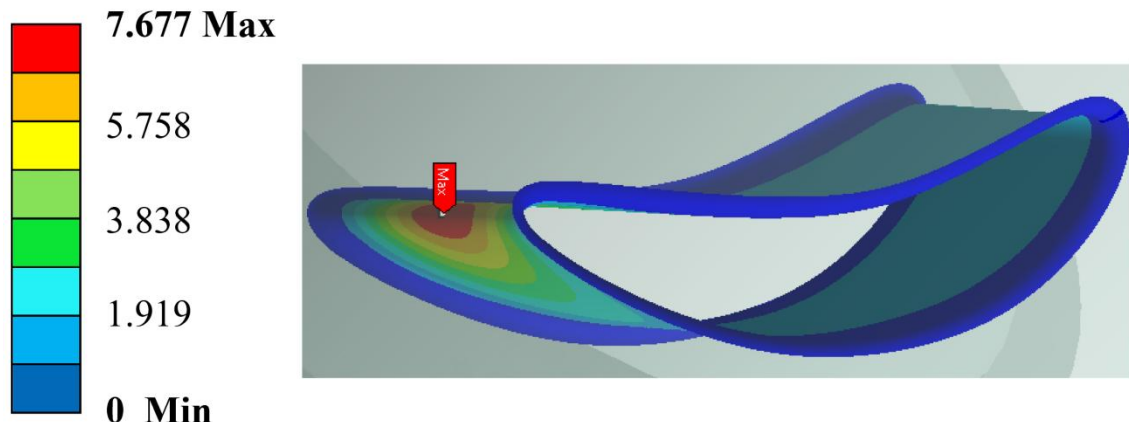


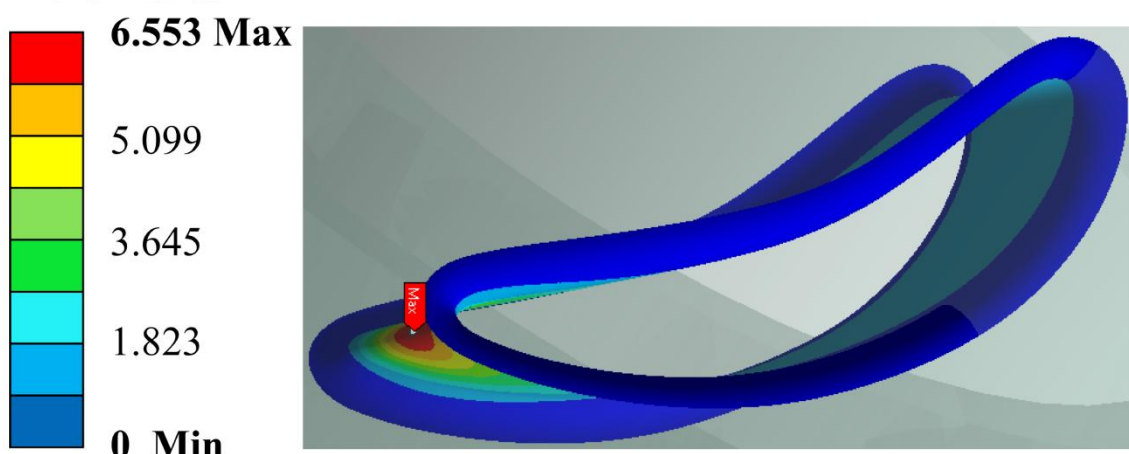
Figure 5.64 Equivalent elastic strain profile for water flow rate of 3 L/s at 3,000 rpm rotation speed through turbodrill stage model “A2W20” with different blend radius.

Total Deformation  
( $\times 10^{-3}$  mm)

Blend Radius = 0.5 mm



Blend Radius = 1 mm



Blend Radius = 2 mm

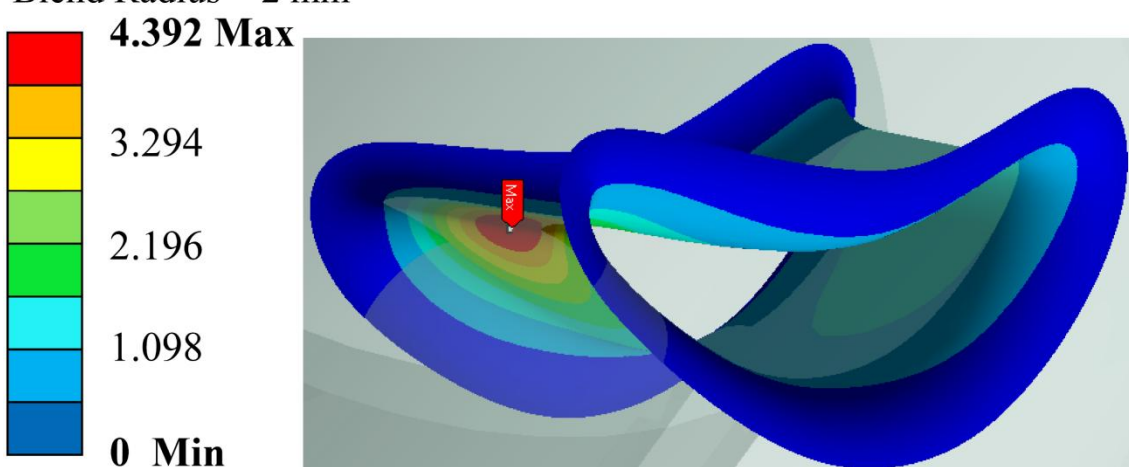


Figure 5.65 Total deformation profile for water flow rate of 3 L/s at 3,000 rpm rotation speed through turbodrill stage model "A2W20" with different blend radius.

**Simulation results through stage model “A2W20” with water flow rate of 4 L/s**

Table 5.26 and Figure 5.66 show water flow CFD simulation results for one stage turbodrill model with 5 cm shroud diameter, 8 mm blade height and 20 blades on each blade row (stage model “A2W20”) with water flow rate of 4 L/s.

Table 5.26: CFD simulation results for one stage turbodrill model “A2W20” with water flow rate of 4 L/s.

Speed (rpm×100)	Power (W)	Torque (N.mm)	Inlet Flow Coefficient	Stage Reaction
1	15.725	1501.690	23.847	12.826
10	144.167	1376.795	2.265	1.947
20	256.752	1225.991	1.049	1.272
30	332.847	1059.563	0.651	1.027
40	377.681	901.713	0.472	0.915
50	377.943	721.871	0.377	0.846
60	334.035	531.672	0.324	0.792
70	245.914	335.497	0.301	0.752
80	131.378	156.832	0.299	0.740
90	16.001	16.979	0.298	0.726

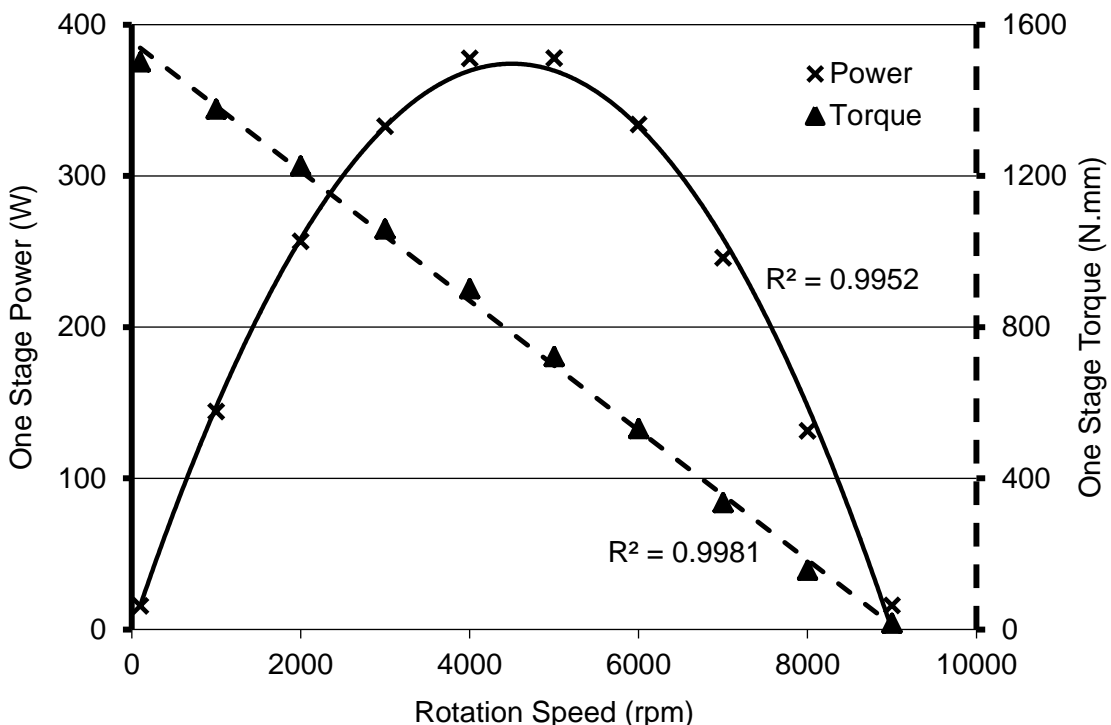


Figure 5.66 CFD simulation results for one stage turbodrill model “A2W20” with water flow rate of 4 L/s at reference radius of 21.2716 mm.

Figure 5.66 shows that the maximum stage efficiency and power for this case is at around 5,000 rpm rotation speed. One stage power and torque at maximum efficiency condition are around 378 W and 722 N.mm, respectively. In this case, the runaway turbine speed is almost over 9,000 rpm, and stalled torque is around 1502 N.mm. Figure

5.67 shows the CFD simulation results for one stage turbodrill model “A2W20” with water flow rate of 4 L/s at the rotation speed of 5,000 rpm. This figure shows the velocity profile in the blade to blade view at the span surface 0.5 and also shows the pressure and meridional velocity profiles at meridional surface. The pressure and velocity profiles show the maximum velocity and minimum pressure is occurred near the stator blade trailing edge. The other simulation outputs are also provided in the figure.

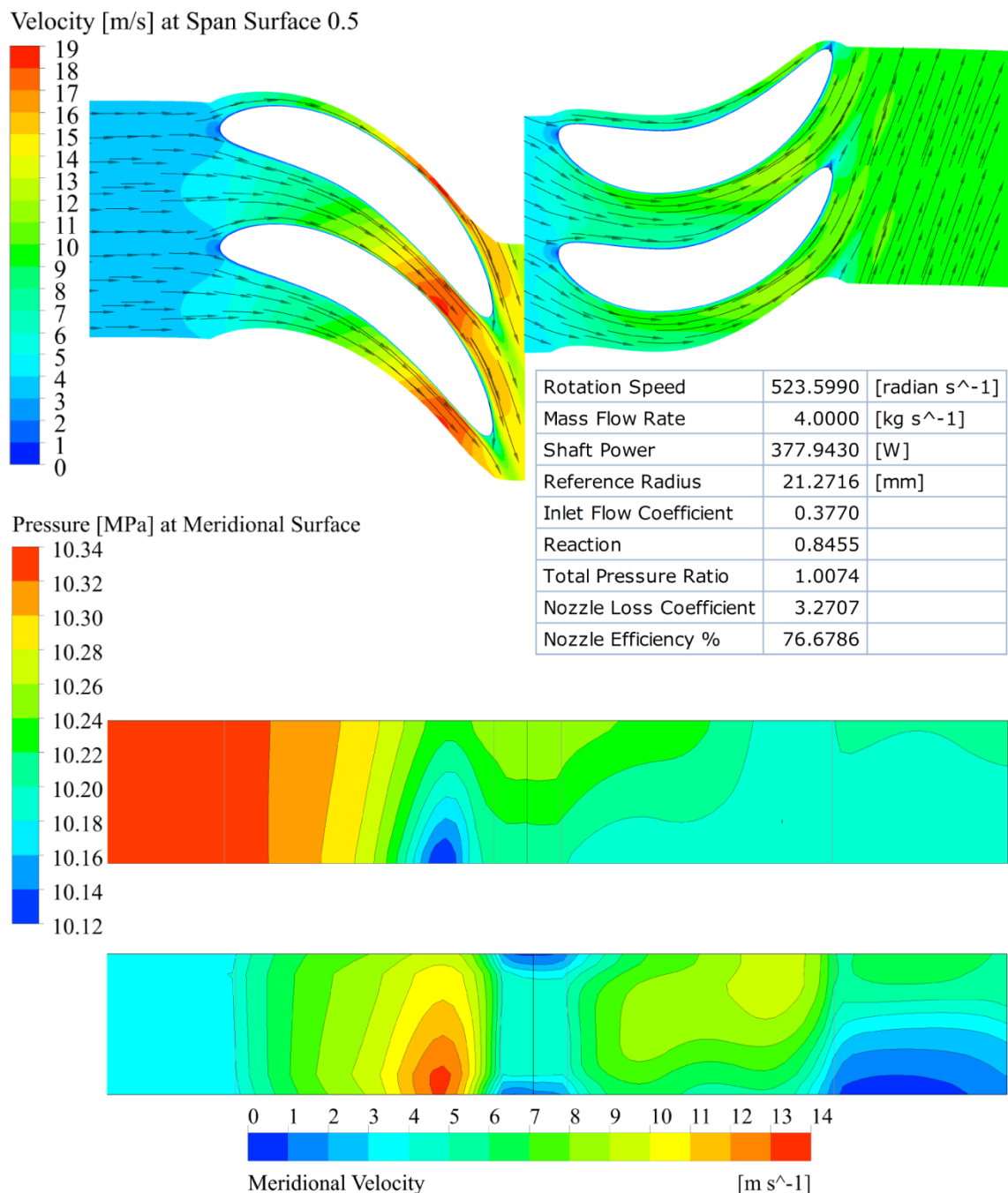


Figure 5.67 CFD simulation results for one stage turbodrill model “A2W20” with water flow rate of 4 L/s at 5,000 rpm rotation speed.

Figures 5.68 and 5.69 show the velocity and pressure values versus normalized streamwise length of stator and rotor at span surface 0.5 for water flow rate of 4 L/s at 5,000 rpm rotation speed through turbodrill stage model “A2W20”. These figures show the velocity and pressure data on the both blade surfaces.

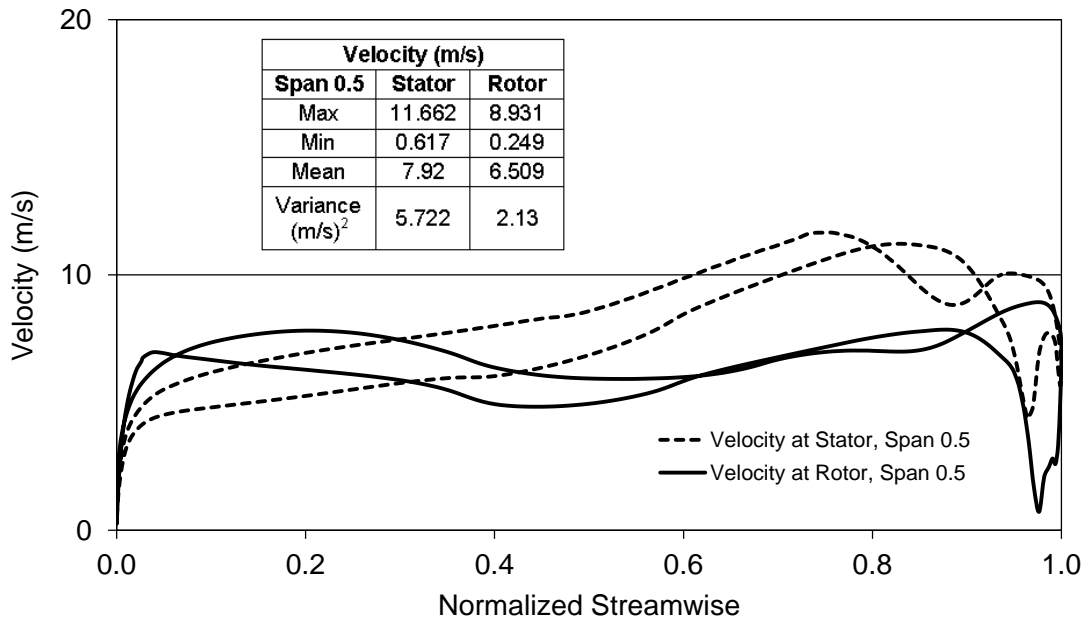


Figure 5.68 Velocity profile versus normalized streamwise for water flow rate of 4 L/s at 5,000 rpm rotation speed through turbodrill stage model “A2W20”.

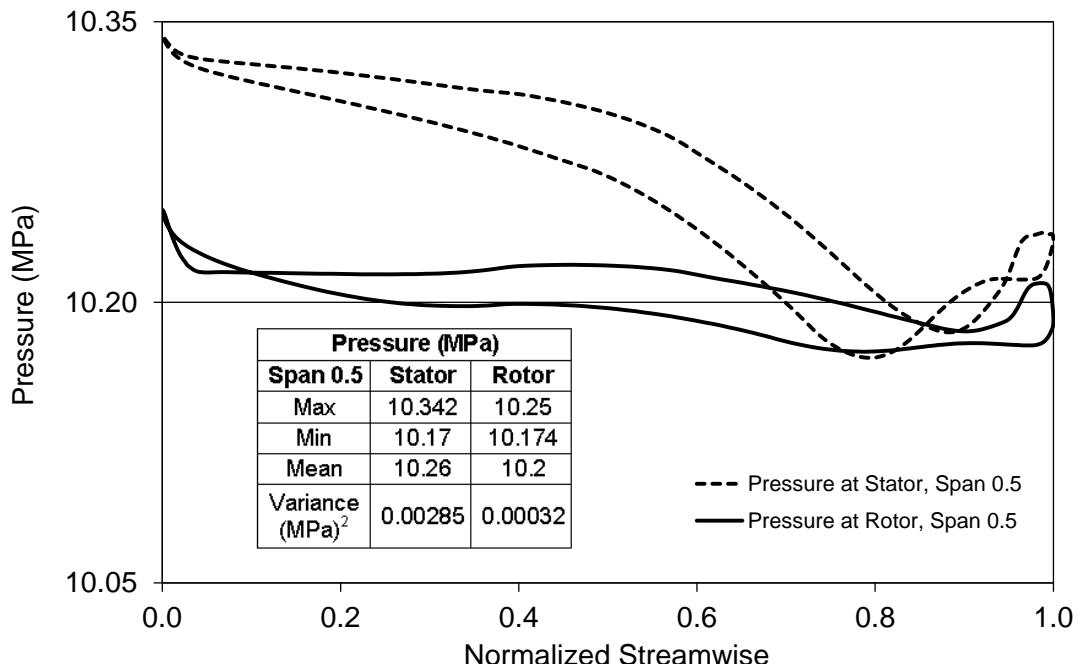


Figure 5.69 Pressure profile versus normalized streamwise for water flow rate of 4 L/s at 5,000 rpm rotation speed through turbodrill stage model “A2W20”.

Table 5.27 shows the structural (FSI) simulation results for stress, strain and deformation on the blades for water flow rate of 4 L/s at 5,000 rpm rotation speed through turbodrill stage model “A2W20” for two different blend radius.

Table 5.27: FSI simulation results for water flow rate of 4 L/s at 5,000 rpm rotation speed through turbodrill stage model “A2W20”.

Static Structural Analysis		Equivalent (Von-Mises) Stress (MPa)	Equivalent Elastic Strain ( $\times 10^{-4}$ mm/mm)	Total Deformation ( $\times 10^{-3}$ mm)
Blend Radius = 0.5 mm	Min	11.649	0.605	0
	Max	344.499	17.860	7.632
Blend Radius = 1.0 mm	Min	11.501	0.597	0
	Max	243.483	12.616	6.514

#### Simulation results through stage model “A2W20” with water flow rate of 5 L/s

Table 5.28 and Figure 5.59 show water flow CFD simulation results for one stage turbodrill model with 5 cm shroud diameter, 8 mm blade height and 20 blades on each blade row (stage model “A2W20”) with water flow rate of 5 L/s.

Table 5.28: CFD simulation results for one stage turbodrill model “A2W20” with water flow rate of 5 L/s.

Speed (rpm×100)	Power (W)	Torque (N.mm)	Inlet Flow Coefficient	Stage Reaction
1	24.636	2352.700	29.859	15.941
10	231.107	2207.072	2.875	2.259
20	424.209	2025.598	1.361	1.444
30	575.377	1831.617	0.854	1.163
40	680.951	1625.771	0.606	1.002
50	746.313	1425.458	0.472	0.917
60	753.989	1200.099	0.391	0.860
70	704.075	960.559	0.341	0.812
80	601.808	718.408	0.309	0.774
90	463.174	491.479	0.299	0.751
100	276.698	264.247	0.298	0.741
110	59.789	51.908	0.298	0.728

Figure 5.70 shows that the maximum stage efficiency and power for this case is at around 6,000 rpm rotation speed. One stage power and torque at maximum efficiency condition are around 754 W and 1200 N.mm, respectively. In this case, the runaway turbine speed is almost over 11,000 rpm, and stalled torque is around 2353 N.mm. Figure 5.71 shows the CFD simulation results for one stage turbodrill model “A2W20” with water flow rate of 5 L/s at the rotation speed of 6,000 rpm. This figure shows the velocity profile in the blade to blade view at the span surface 0.5 and also shows the pressure and meridional velocity profiles at meridional surface. The pressure and

velocity profiles show the maximum velocity and minimum pressure is occurred near the stator blade trailing edge. The other simulation outputs are also provided in the figure.

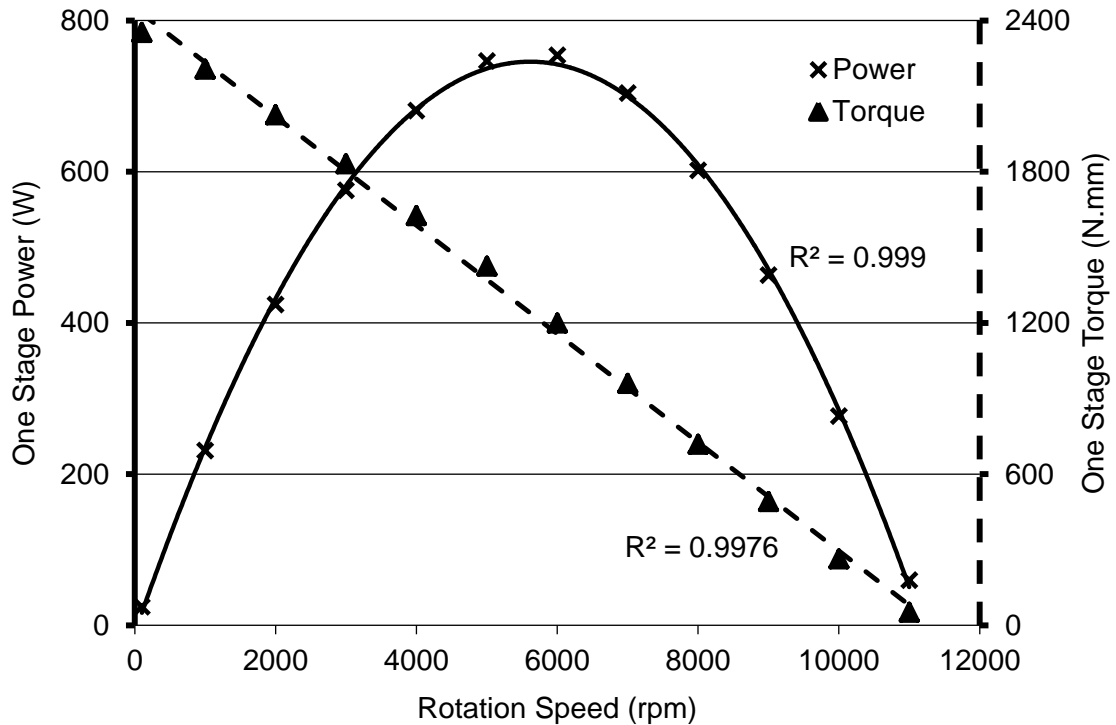


Figure 5.70 CFD simulation results for one stage turbodrill model "A2W20" with water flow rate of 5 L/s at reference radius of 21.2716 mm.

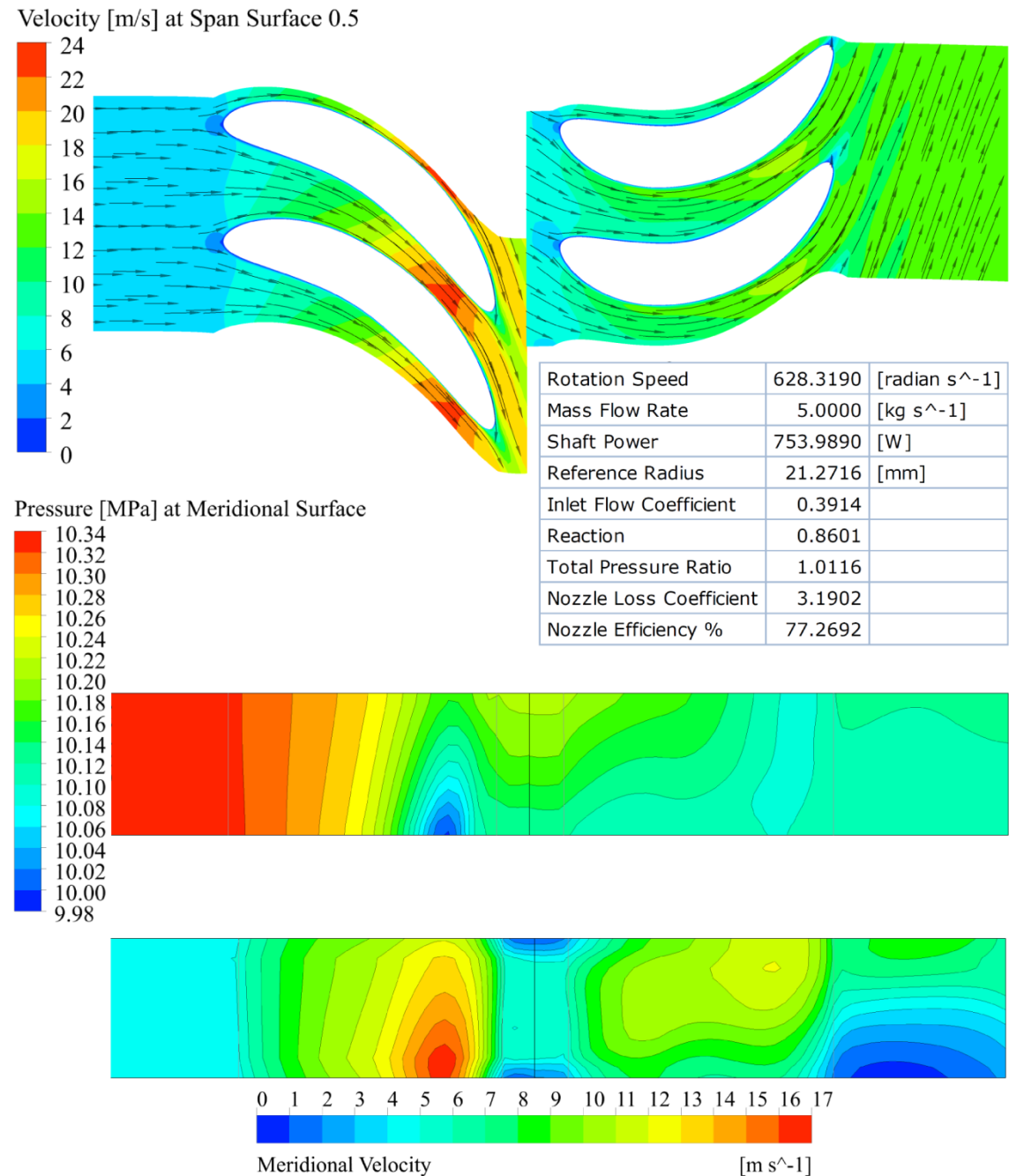


Figure 5.71 CFD simulation results for one stage turbodrill model “A2W20” with water flow rate of 5 L/s at 6,000 rpm rotation speed.

Figures 5.72 and 5.73 show the velocity and pressure values versus normalized streamwise length of stator and rotor at span surface 0.5 for water flow rate of 5 L/s at 6,000 rpm rotation speed through turbodrill stage model “A2W20”. These figures show the velocity and pressure data on the both blade surfaces.

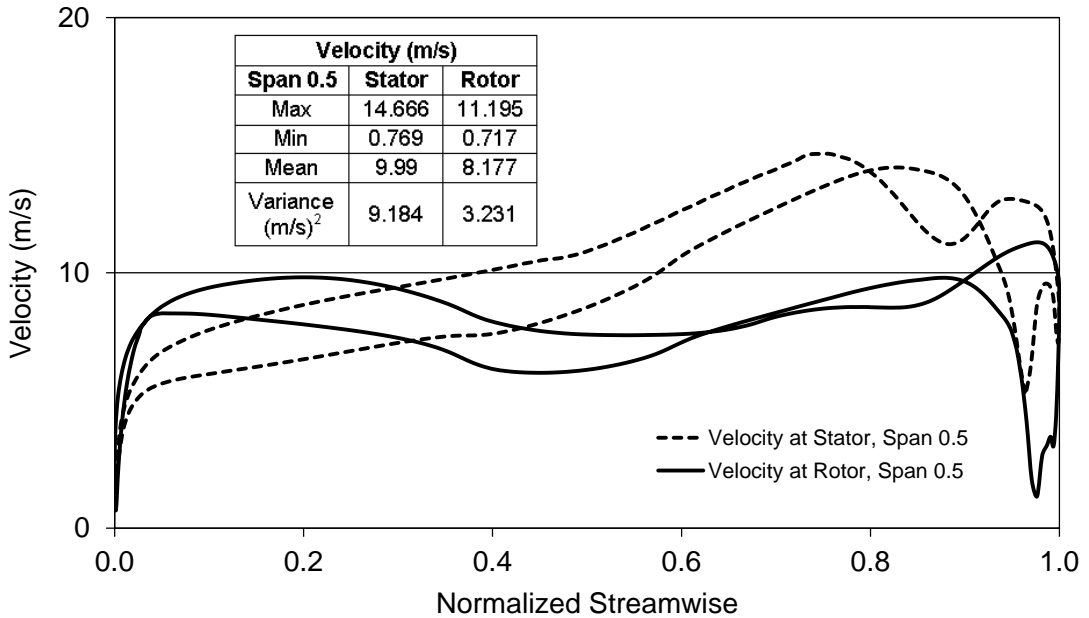


Figure 5.72 Velocity profile versus normalized streamwise for water flow rate of 5 L/s at 6,000 rpm rotation speed through turbodrill stage model “A2W20”.

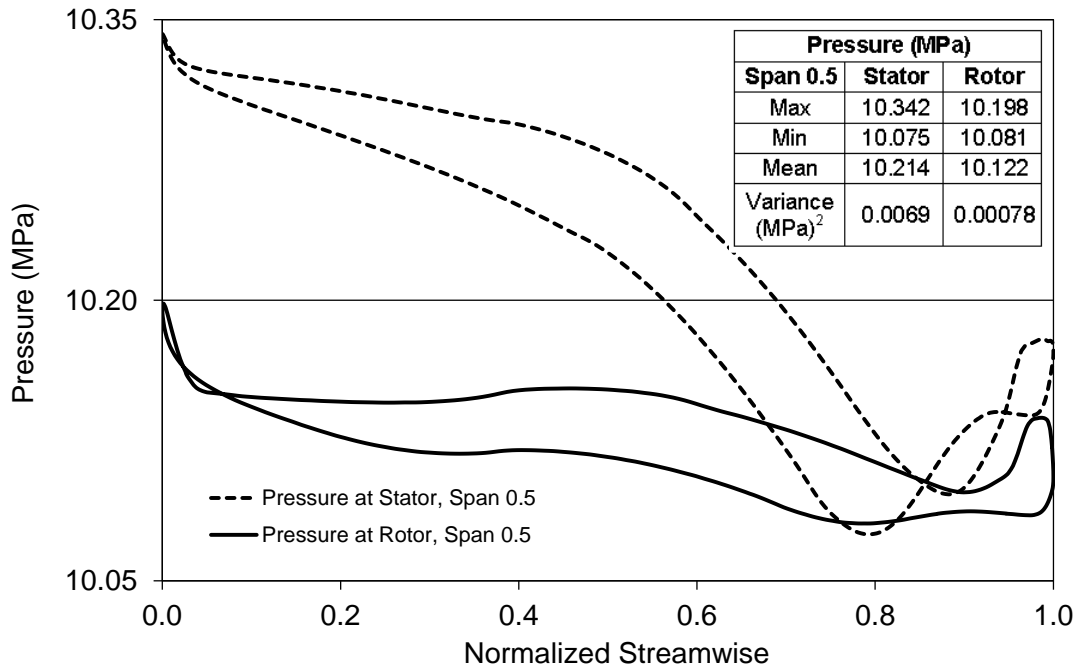


Figure 5.73 Pressure profile versus normalized streamwise for water flow rate of 5 L/s at 6,000 rpm rotation speed through turbodrill stage model “A2W20”.

Table 5.29 shows the structural (FSI) simulation results for stress, strain and deformation on the blades for water flow rate of 5 L/s at 6,000 rpm rotation speed through turbodrill stage model “A2W20” for two different blend radius.

Table 5.29: FSI simulation results for water flow rate of 5 L/s at 6,000 rpm rotation speed through turbodrill stage model “A2W20”.

Static Structural Analysis		Equivalent (Von-Mises) Stress (MPa)	Equivalent Elastic Strain ( $\times 10^{-4}$ mm/mm)	Total Deformation ( $\times 10^{-3}$ mm)
Blend Radius = 0.5 mm	Min	11.620	0.603	0
	Max	341.476	17.700	7.571
Blend Radius = 1.0 mm	Min	11.423	0.593	0
	Max	241.112	12.493	6.462

#### Conclusion remarks for simulation results of water flow through stage model “A2”

Figure 5.74 shows the water flow simulation results for one stage power with different turbodrill stage models with 5 cm shroud diameter and 8 mm blade height (model “A2”). The effect of three different flow rates on the turbodrill stage “A2” performance is shown in this Figure. It can be concluded that flow rate has significant effect on the turbodrill performance.

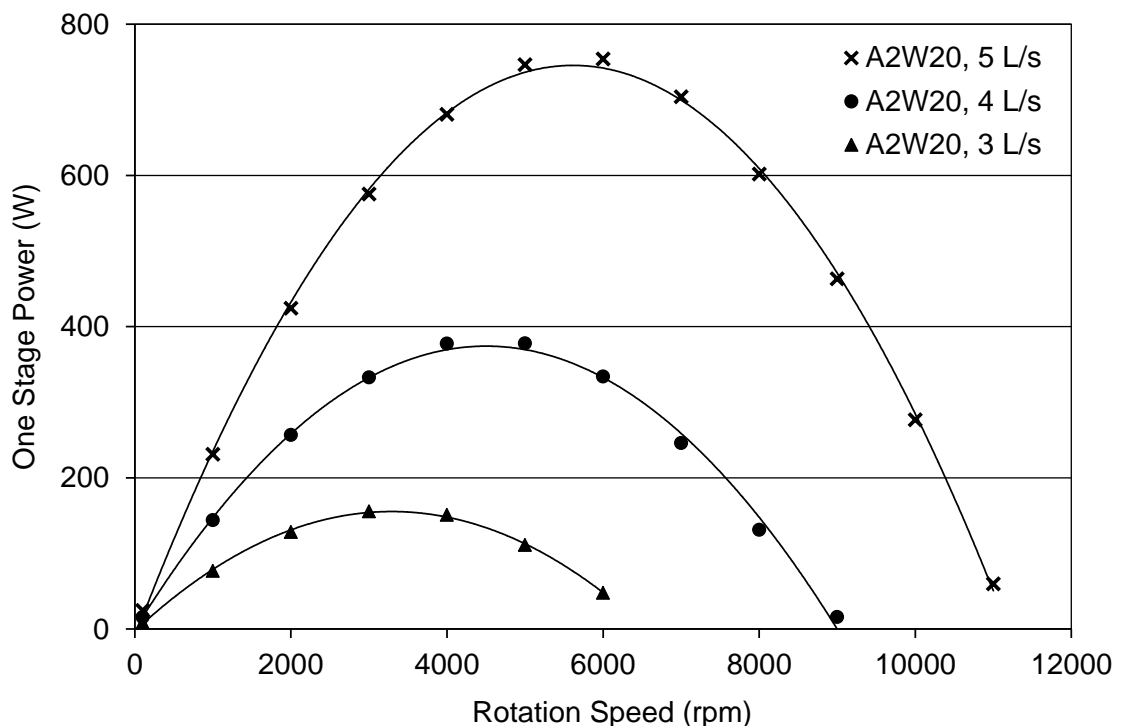


Figure 5.74 CFD simulation results of water flow through one stage turbodrill stage model “A2”.

### 5.5.3 Water flow simulation results for Turbodrill stage model “A3”

Water flow simulation results for one stage turbodrill models with 5 cm shroud diameter and 12 mm blade height (span) which are known here as stage model “A3” are presented in this section.

**Simulation results through stage model “A3W22” and 65 degree stator outlet blade angle with water flow rate of 5 L/s**

Table 5.30 and Figure 5.75 show water flow CFD simulation results for one stage turbodrill model with 5 cm shroud diameter, 12 mm blade height and 22 blades on each blade row (stage model “A3W22”) and 65 degree stator outlet blade angle with water flow rate of 5 L/s.

Table 5.30: CFD simulation results for one stage turbodrill model “A3W22” and 65 degree stator outlet blade angle with water flow rate of 5 L/s.

Speed (rpm×100)	Power (W)	Torque (N.mm)	Inlet Flow Coefficient	Stage Reaction
1	14.786	1412.034	26.150	12.692
10	133.472	1274.658	2.435	1.843
20	229.542	1096.063	1.121	1.208
30	286.076	910.675	0.698	0.964
40	306.908	732.743	0.498	0.857
50	272.853	521.149	0.396	0.790
60	173.728	276.517	0.344	0.738
70	19.897	27.145	0.319	0.690

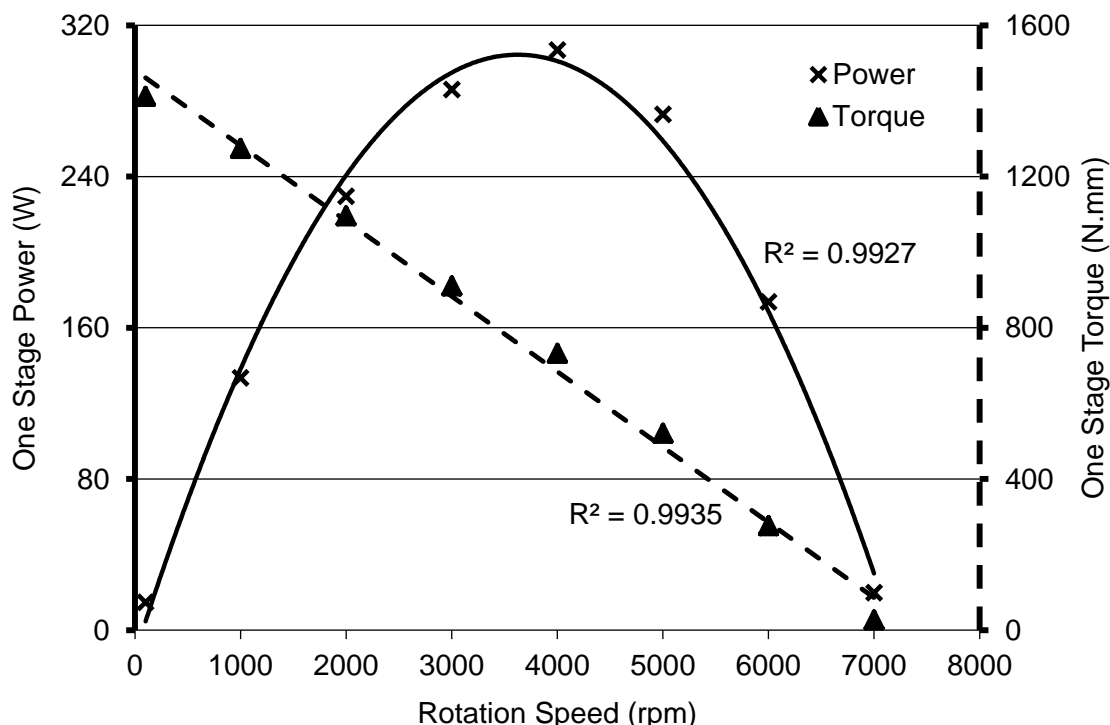


Figure 5.75 CFD simulation results for one stage turbodrill model “A3W22” and 65 degree stator outlet blade angle with water flow rate of 5 L/s at reference radius of 19.6776 mm.

Figure 5.75 shows that the maximum stage efficiency and power for this case is at around 4,000 rpm rotation speed. One stage power and torque at maximum efficiency condition are around 307 W and 733 N.mm, respectively. In this case, the runaway turbine speed is almost over 7,000 rpm, and stalled torque is around 1412 N.mm. Figure 5.76 shows the CFD simulation results of velocity and pressure profiles for one stage turbodrill model “A3W22”.

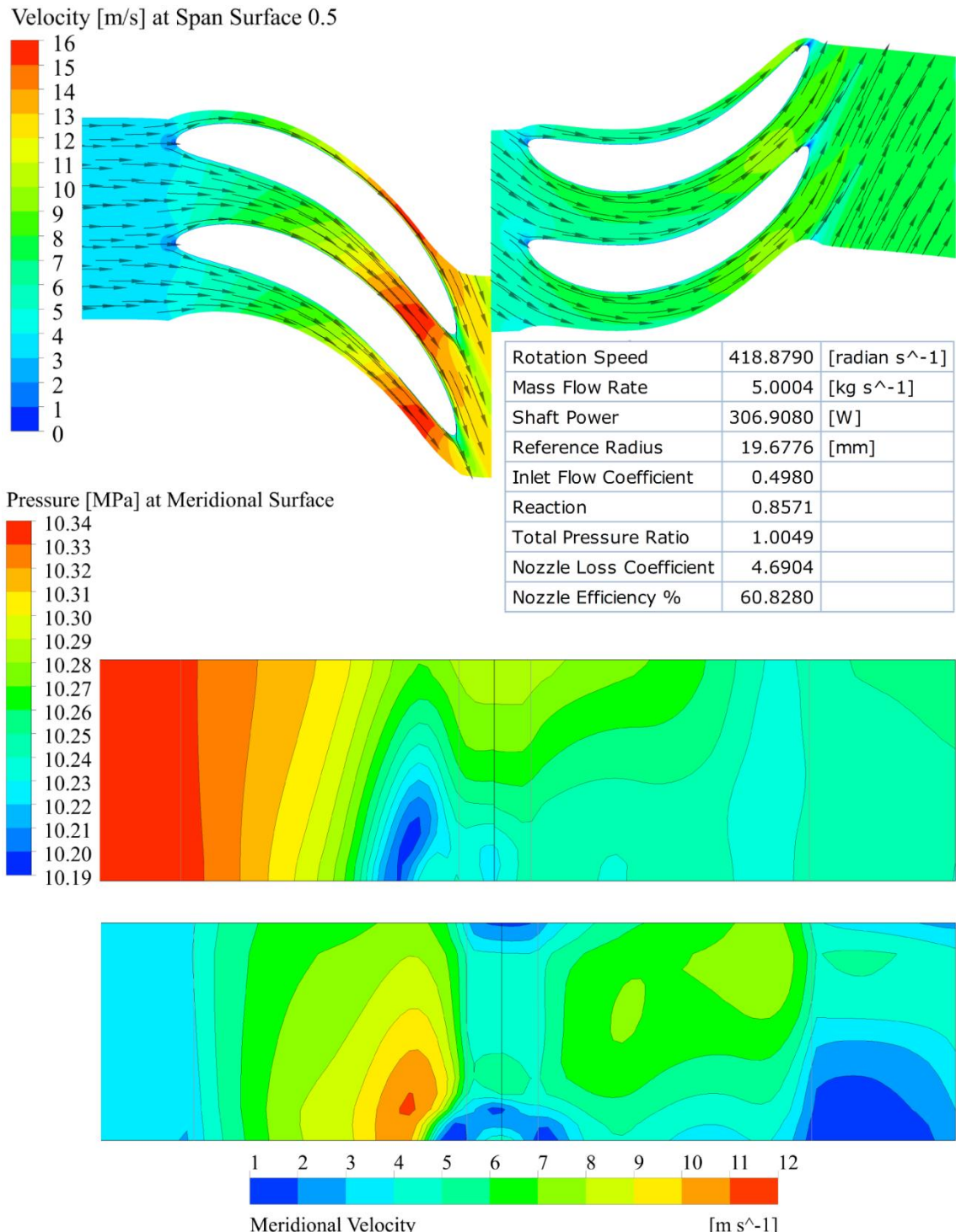


Figure 5.76 CFD simulation results for one stage turbodrill model “A3W22” and 65 degree stator outlet blade angle with water flow rate of 5 L/s at 4,000 rpm rotation speed.

Figures 5.77 and 5.78 show the velocity and pressure values versus normalized streamwise length of stator and rotor at span surface 0.5 for water flow rate of 5 L/s at 4,000 rpm rotation speed through turbodrill stage model “A1W20” and 65 degree stator outlet blade angle. These figures show the velocity and pressure data on the both blade surfaces.

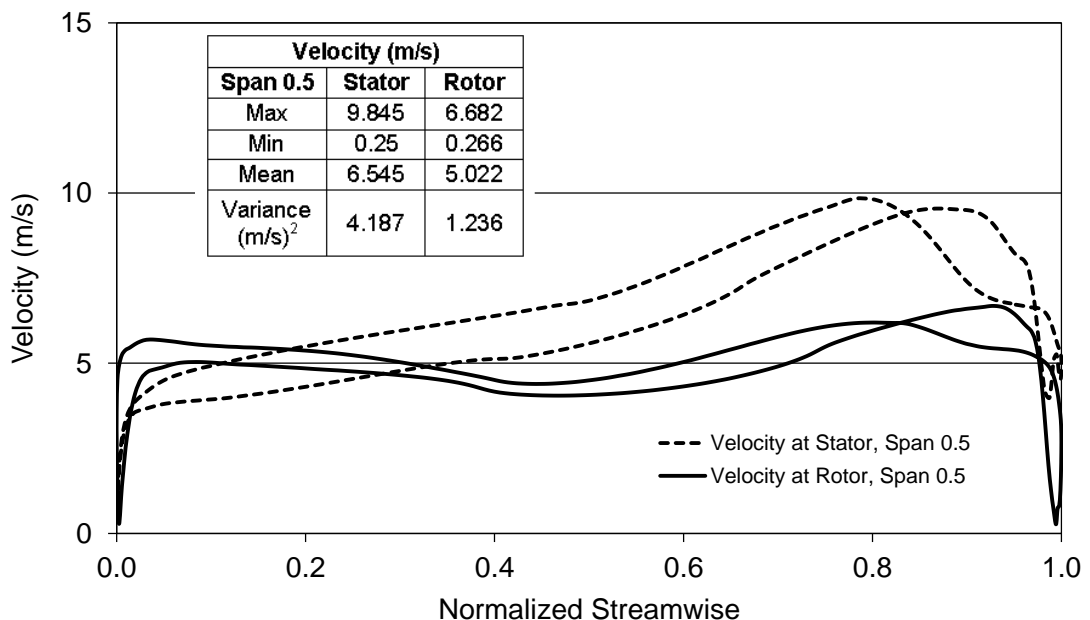


Figure 5.77 Velocity profile versus normalized streamwise for water flow rate of 5 L/s at 4,000 rpm rotation speed through turbodrill stage model “A3W22” and 65 degree stator outlet blade angle.

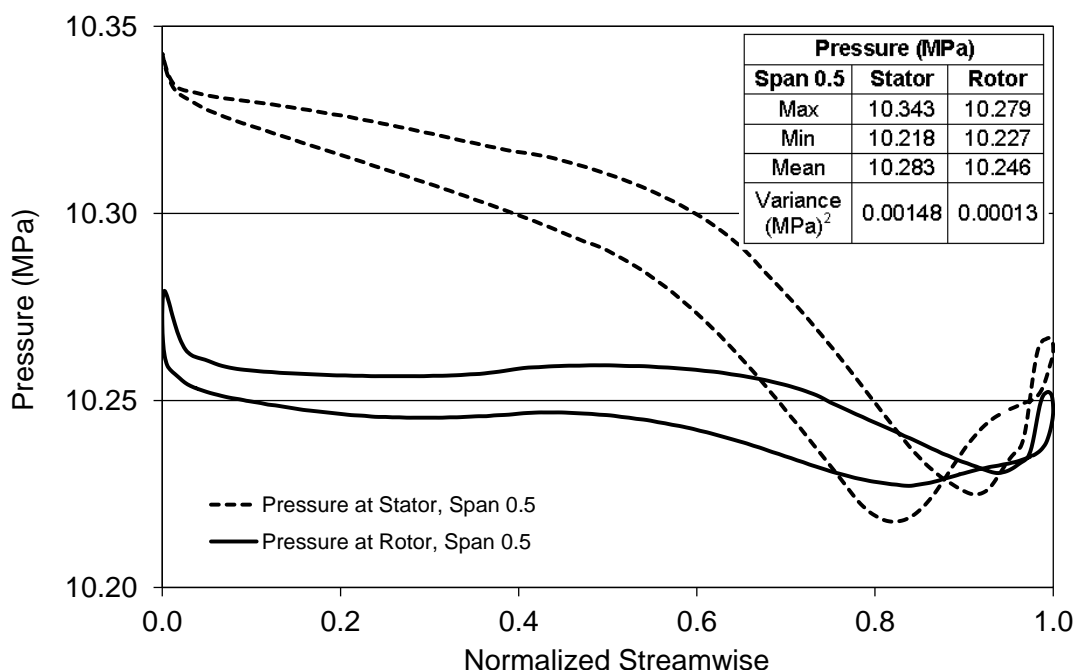


Figure 5.78 Pressure profile versus normalized streamwise for water flow rate of 5 L/s at 4,000 rpm rotation speed through turbodrill stage model “A3W22” and 65 degree stator outlet blade angle.

Table 5.31 shows the structural (FSI) simulation results for stress, strain and deformation on the blades for water flow rate of 5 L/s at 4,000 rpm rotation speed through turbodrill stage model “A3W22” and 65 degree stator outlet blade angle for two different blend radius.

Table 5.31: FSI simulation results for water flow rate of 5 L/s at 4,000 rpm rotation speed through turbodrill stage model “A3W22” and 65 degree stator outlet blade angle.

Static Structural Analysis		Equivalent (Von-Mises) Stress (MPa)	Equivalent Elastic Strain ( $\times 10^{-4}$ mm/mm)	Total Deformation ( $\times 10^{-3}$ mm)
Blend Radius = 0.5 mm	Min	11.292	0.629	0
	Max	962.224	49.860	38.140
Blend Radius = 1.0 mm	Min	10.556	0.608	0
	Max	711.745	36.878	33.223

**Simulation results through stage model “A3W22” and 65 degree stator outlet blade angle with water flow rate of 6 L/s**

Table 5.32 and Figure 5.79 show water flow CFD simulation results for one stage turbodrill model with 5 cm shroud diameter, 12 mm blade height and 22 blades on each blade row (stage model “A3W22”) and 65 degree stator outlet blade angle with water flow rate of 6 L/s.

Table 5.32: CFD simulation results for one stage turbodrill model “A3W22” and 65 degree stator outlet angle with water flow rate of 6 L/s.

Speed (rpm $\times 100$ )	Power (W)	Torque (N.mm)	Inlet Flow Coefficient	Stage Reaction
1	21.572	2060.078	31.595	15.272
10	197.812	1889.105	2.983	2.092
20	354.642	1693.416	1.383	1.352
30	459.661	1463.254	0.864	1.072
40	523.945	1250.919	0.614	0.925
50	538.766	1029.043	0.473	0.849
60	484.966	771.904	0.393	0.792
70	354.267	483.321	0.348	0.747
80	27.945	33.360	0.315	0.686

Figure 5.79 shows that the maximum stage efficiency and power for this case is at around 5,000 rpm rotation speed. One stage power and torque at maximum efficiency condition are around 539 W and 1029 N.mm, respectively. In this case, the runaway turbine speed is almost over 8,000 rpm, and stalled torque is around 2060 N.mm.

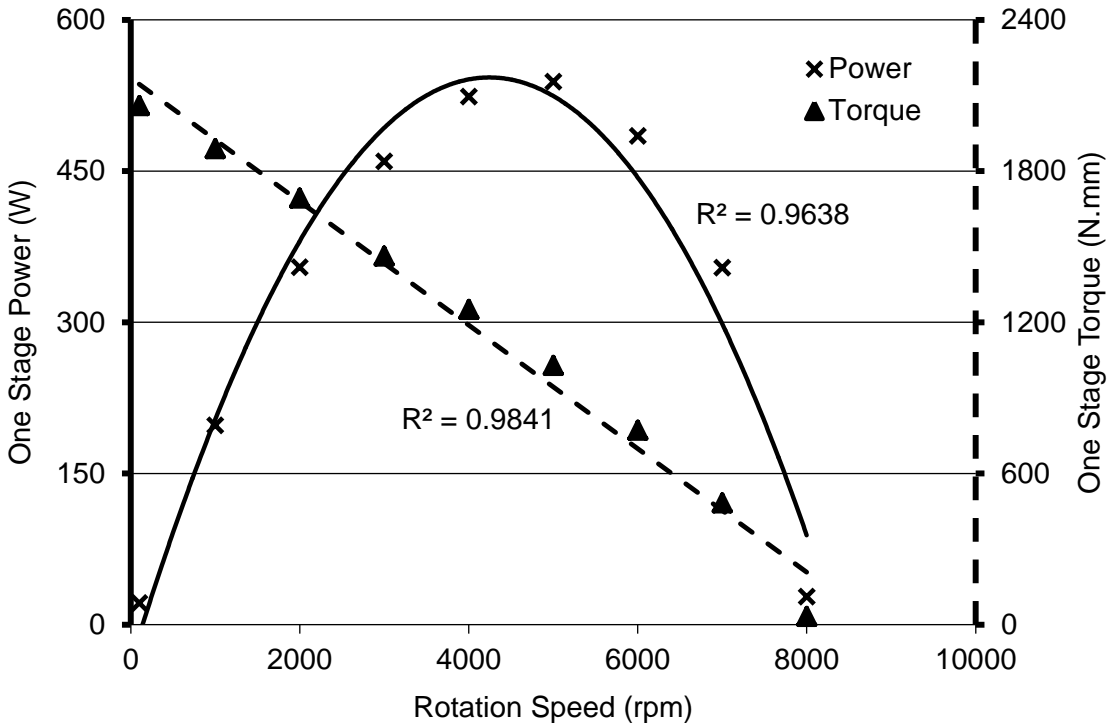


Figure 5.79 CFD simulation results for one stage turbodrill model “A3W22” and 65 degree stator outlet blade angle with water flow rate of 6 L/s at reference radius of 19.6776 mm.

Figure 5.80 shows the CFD simulation results for one stage turbodrill model “A3W22” and 65 degree stator outlet blade angle with water flow rate of 6 L/s at the rotation speed of 5,000 rpm. This figure shows the velocity profile in the blade to blade view at the span surface 0.5 and also shows the pressure and meridional velocity profiles at meridional surface. The pressure and velocity profiles show the maximum velocity and minimum pressure is occurred near the stator blade trailing edge. The other simulation outputs are also provided in the figure.

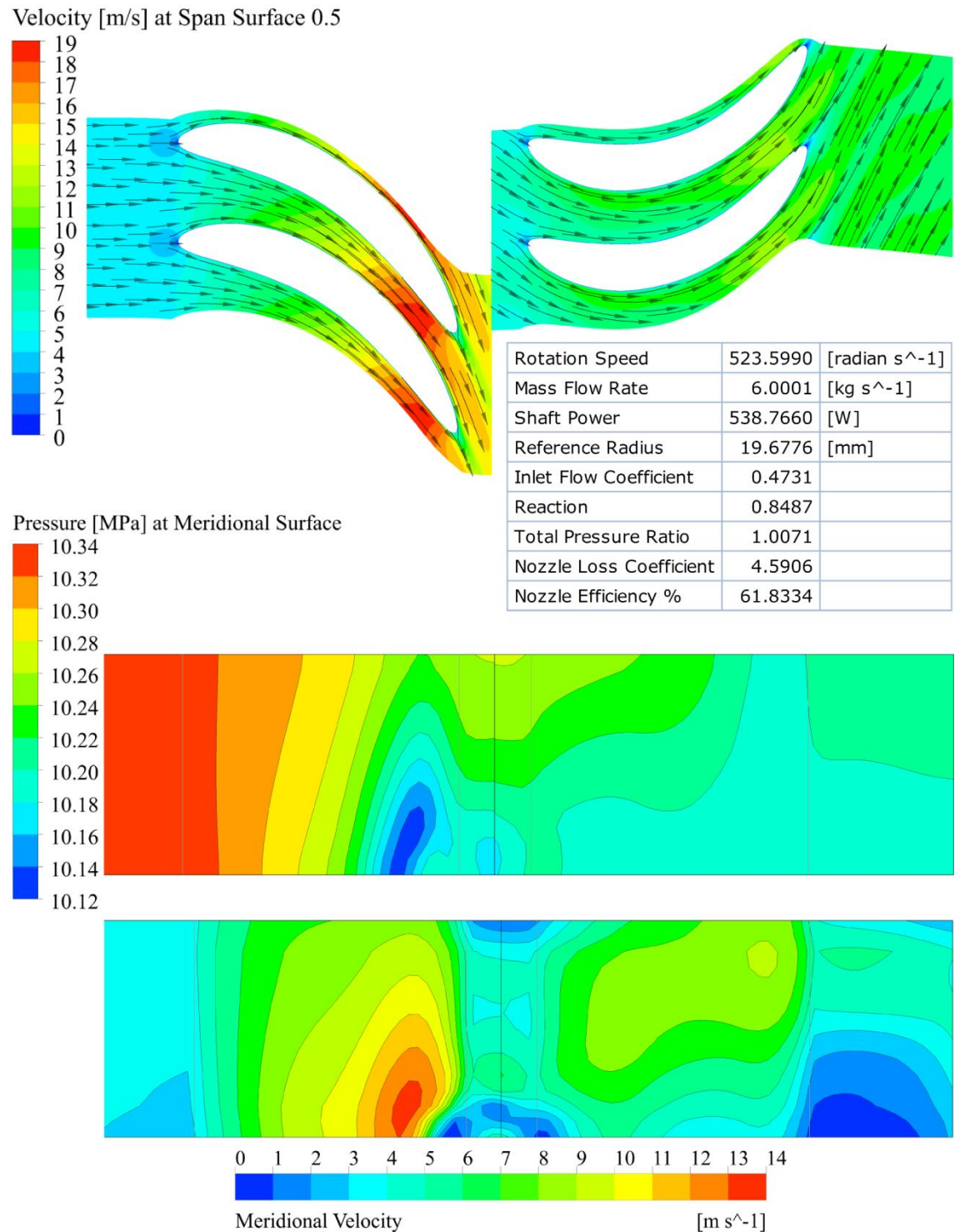


Figure 5.80 CFD simulation results for one stage turbodrill model "A3W22" and 65 degree stator outlet blade angle with water flow rate of 6 L/s at 5,000 rpm rotation speed.

Figures 5.81 and 5.82 show the velocity and pressure values versus normalized streamwise length of stator and rotor at span surface 0.5 for water flow rate of 6 L/s at 5,000 rpm rotation speed through turbodrill stage model "A3W22" and 65 degree stator outlet blade angle. These figures show the velocity and pressure data on the both blade surfaces.

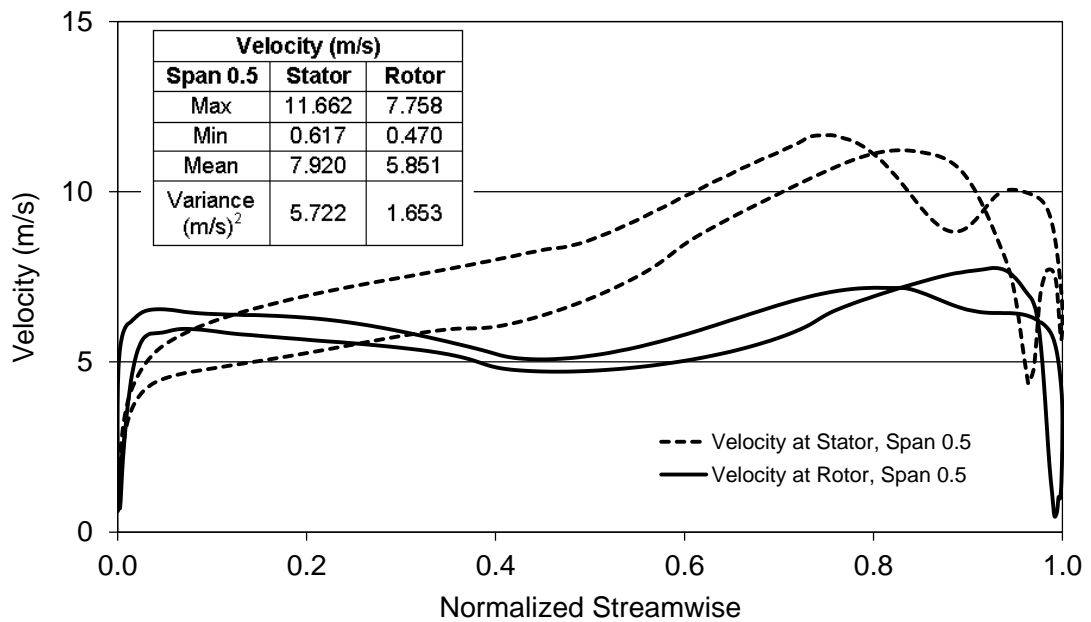


Figure 5.81 Velocity profile versus normalized streamwise for water flow rate of 6 L/s at 5,000 rpm rotation speed through turbodrill stage model "A3W22" and 65 degree stator outlet blade angle.

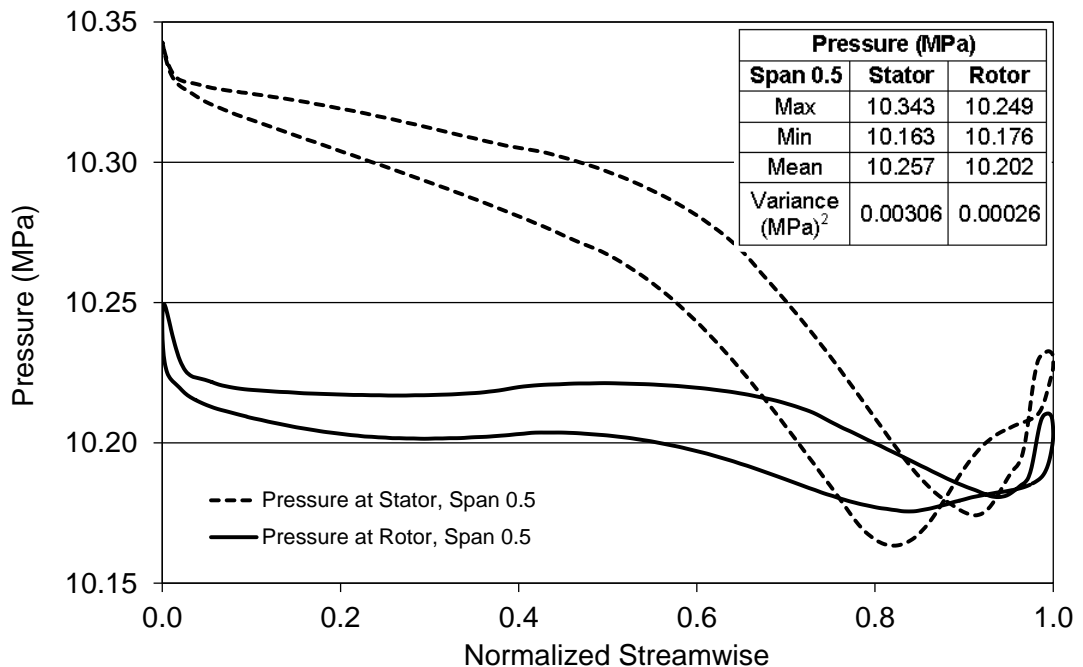


Figure 5.82 Pressure profile versus normalized streamwise for water flow rate of 6 L/s at 5,000 rpm rotation speed through turbodrill stage model "A3W22" and 65 degree stator outlet blade angle.

Table 5.33 shows the structural (FSI) simulation results for stress, strain and deformation on the blades for water flow rate of 6 L/s at 5,000 rpm rotation speed through turbodrill stage model "A3W22" and 65 degree stator outlet blade angle for two different blend radius.

Table 5.33: FSI simulation results for water flow rate of 6 L/s at 5,000 rpm rotation speed through turbodrill stage model “A3W22” and 65 degree stator outlet blade angle.

Static Structural Analysis		Equivalent (Von-Mises) Stress (MPa)	Equivalent Elastic Strain ( $\times 10^{-4}$ mm/mm)	Total Deformation ( $\times 10^{-3}$ mm)
Blend Radius = 0.5 mm	Min	11.267	0.630	0
	Max	962.828	49.890	37.990
Blend Radius = 1.0 mm	Min	10.136	0.6096	0
	Max	708.076	36.688	33.088

#### Simulation results through stage model “A3W22” and 50 degree stator outlet blade angle

Table 5.34 and Figure 5.83 show water flow CFD simulation results for one stage turbodrill model with 5 cm shroud diameter, 12 mm blade height and 22 blades on each blade row (stage model “A3W22”) and 50 degree stator outlet blade angle with water flow rate of 6 L/s.

Table 5.34: CFD simulation results for one stage turbodrill model “A3W22” and 50 degree stator outlet blade angle with water flow rate of 6 L/s.

Speed (rpm×100)	Power (W)	Torque (N.mm)	Inlet Flow Coefficient	Stage Reaction
1	15.061	1438.278	22.780	17.219
10	131.251	1253.447	2.226	2.265
20	209.238	999.111	1.111	1.388
30	241.234	767.928	0.749	1.085
40	211.314	504.512	0.577	0.931
50	119.369	227.995	0.488	0.844
55	33.109	57.490	0.458	0.791

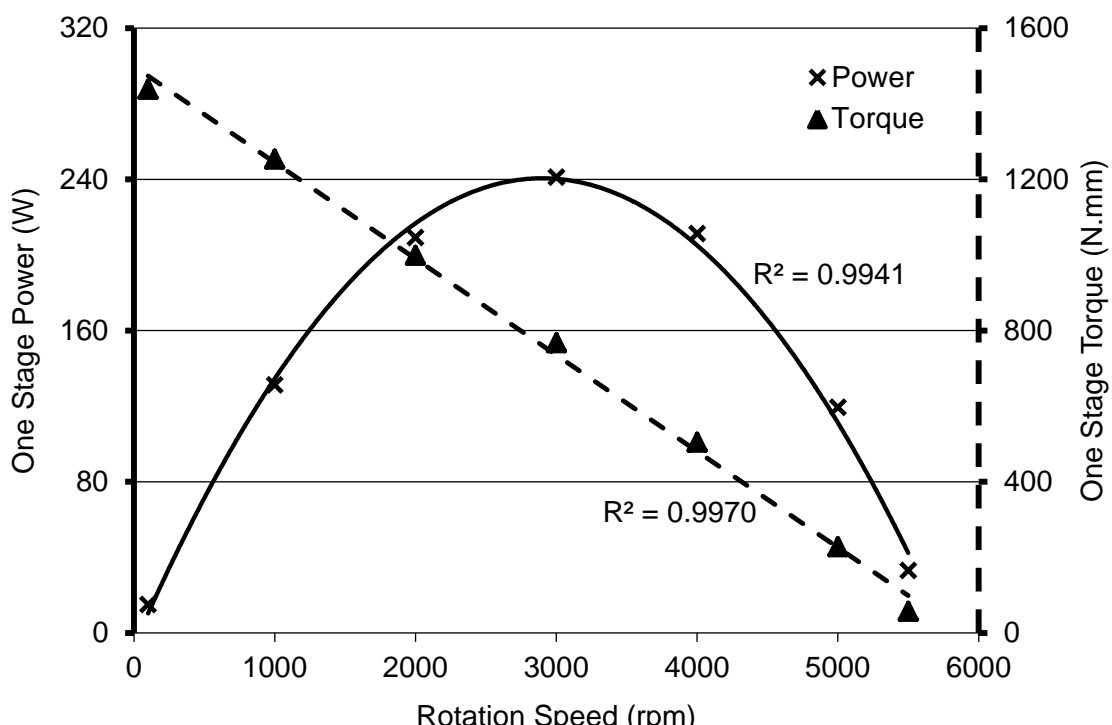


Figure 5.83 CFD simulation results for one stage turbodrill model “A3W22” and 50 degree stator outlet blade angle with water flow rate of 6 L/s at reference radius of 19.6734 mm.

Figure 5.83 shows that the maximum stage efficiency and power for this case is at around 3,000 rpm rotation speed. One stage power and torque at maximum efficiency condition are around 241 W and 768 N.mm, respectively. In this case, the runaway turbine speed is almost over 5,500 rpm, and stalled torque is around 1438 N.mm. Figure 5.84 shows the CFD simulation results for this case at the rotation speed of 3,000 rpm.

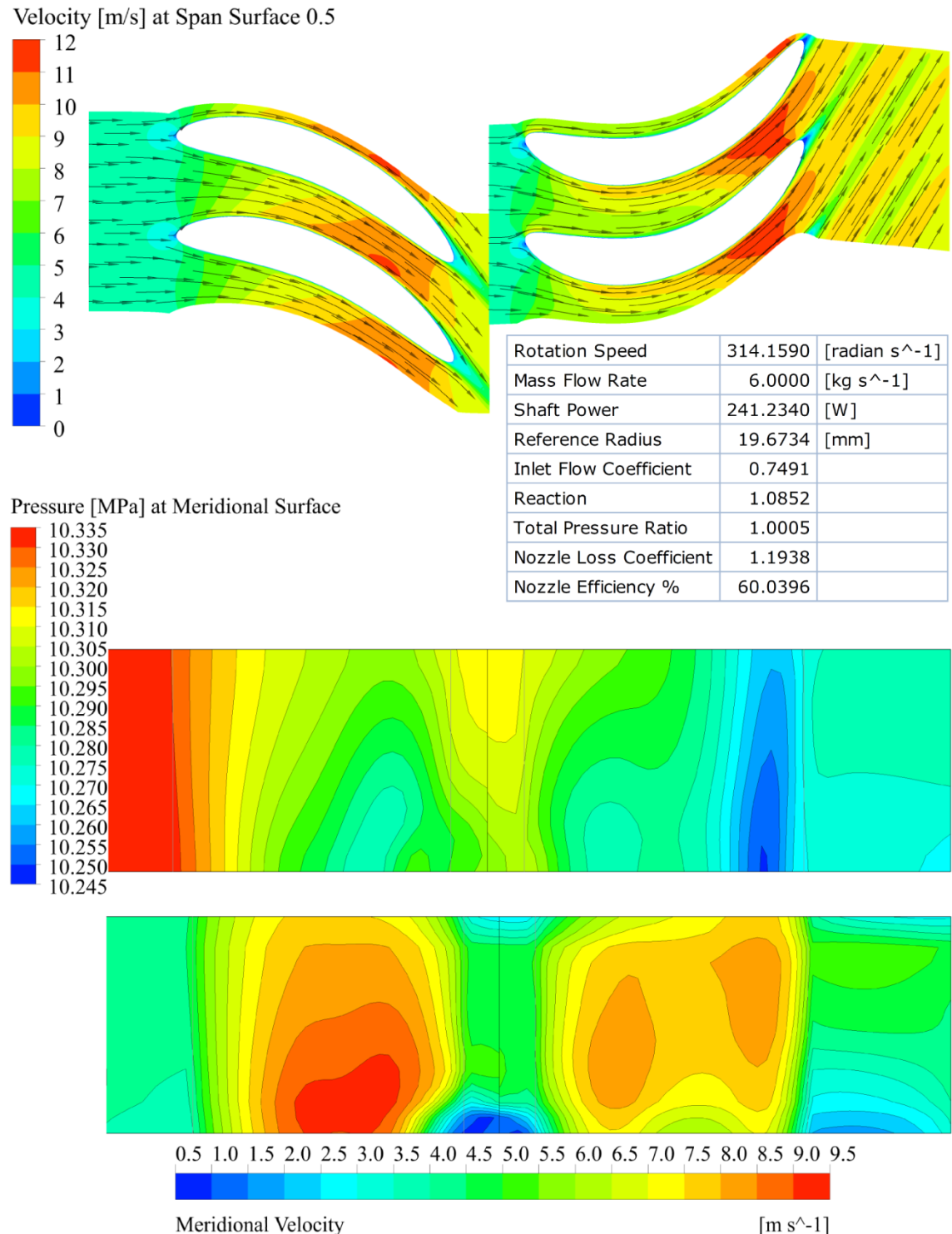


Figure 5.84 CFD simulation results for one stage turbodrill model "A3W22" and 50 degree stator outlet blade angle with water flow rate of 6 L/s at 3,000 rpm rotation speed.

Figures 5.85 and 5.86 show the velocity and pressure values versus normalized streamwise length of stator and rotor at span surface 0.5 for water flow rate of 6 L/s at 3,000 rpm rotation speed through turbodrill stage model “A3W22” and 50 degree stator outlet blade angle. These figures show the velocity and pressure data on the both blade surfaces.

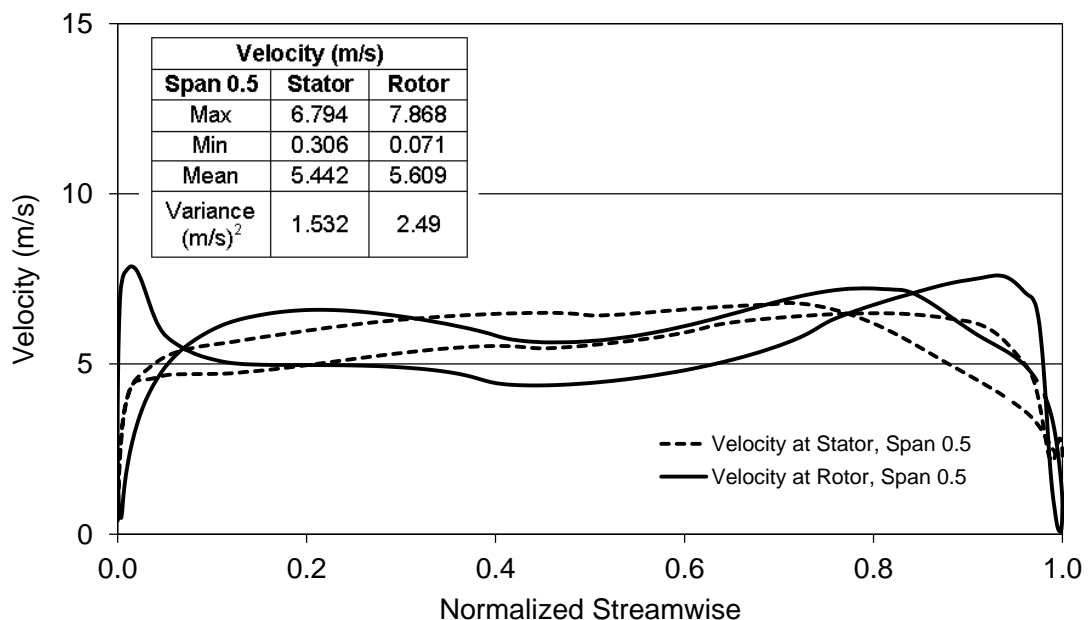


Figure 5.85 Velocity profile versus normalized streamwise for water flow rate of 6 L/s at 3,000 rpm rotation speed through turbodrill stage model “A3W22” and 50 degree stator outlet blade angle.

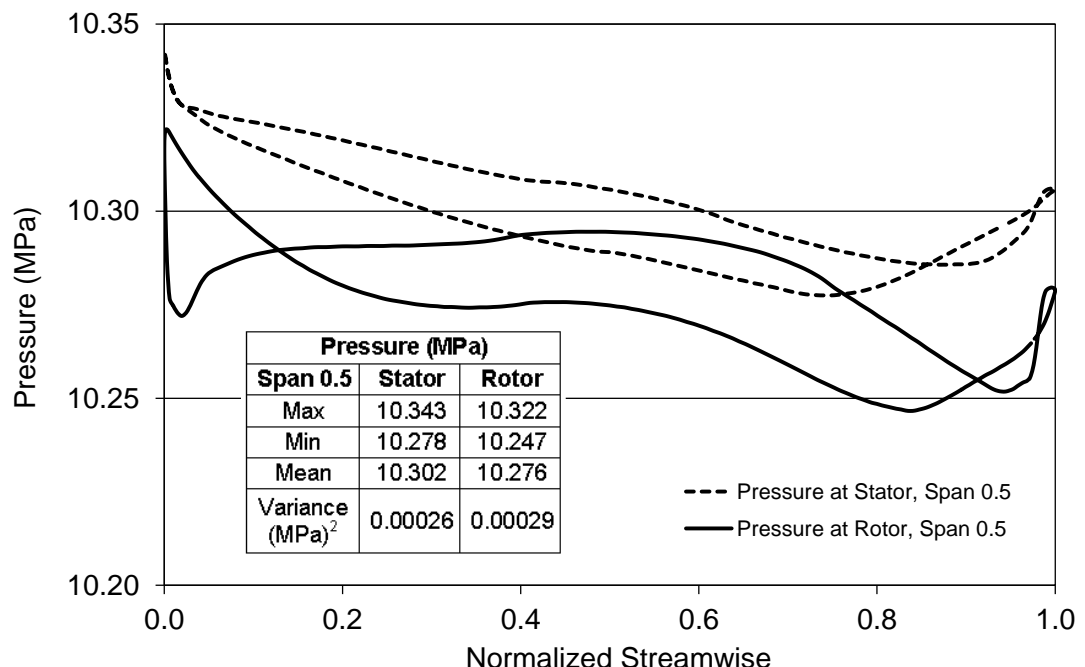


Figure 5.86 Pressure profile versus normalized streamwise for water flow rate of 6 L/s at 3,000 rpm rotation speed through turbodrill stage model “A3W22” and 50 degree stator outlet blade angle.

Table 5.35 shows the structural (FSI) simulation results for stress, strain and deformation on the blades for water flow rate of 6 L/s at 3,000 rpm rotation speed through turbodrill stage model “A3W22” and 50 degree stator outlet blade angle for two different blend radius.

Table 5.35: FSI simulation results for water flow rate of 6 L/s at 3,000 rpm rotation speed through turbodrill stage model “A3W22” and 50 degree stator outlet blade angle.

Static Structural Analysis		Equivalent (Von-Mises) Stress (MPa)	Equivalent Elastic Strain ( $\times 10^{-4}$ mm/mm)	Total Deformation ( $\times 10^{-3}$ mm)
Blend Radius = 0.5 mm	Min	12.252	0.635	0
	Max	693.806	35.970	31.010
Blend Radius = 1.0 mm	Min	12.193	0.632	0
	Max	518.624	26.874	27.521

#### Conclusion remarks for simulation results of water flow through stage model “A3”

Figure 5.87 shows the water flow simulation results for one stage power with different turbodrill stage models with 5 cm shroud diameter and 12 mm blade height (model “A3”). The effect of different geometrical and flow properties on the turbodrill stage “A3” performance is shown in this Figure. It can be inferred that flow rate and the outlet stator blade angle have significant effects on the turbodrill performance.

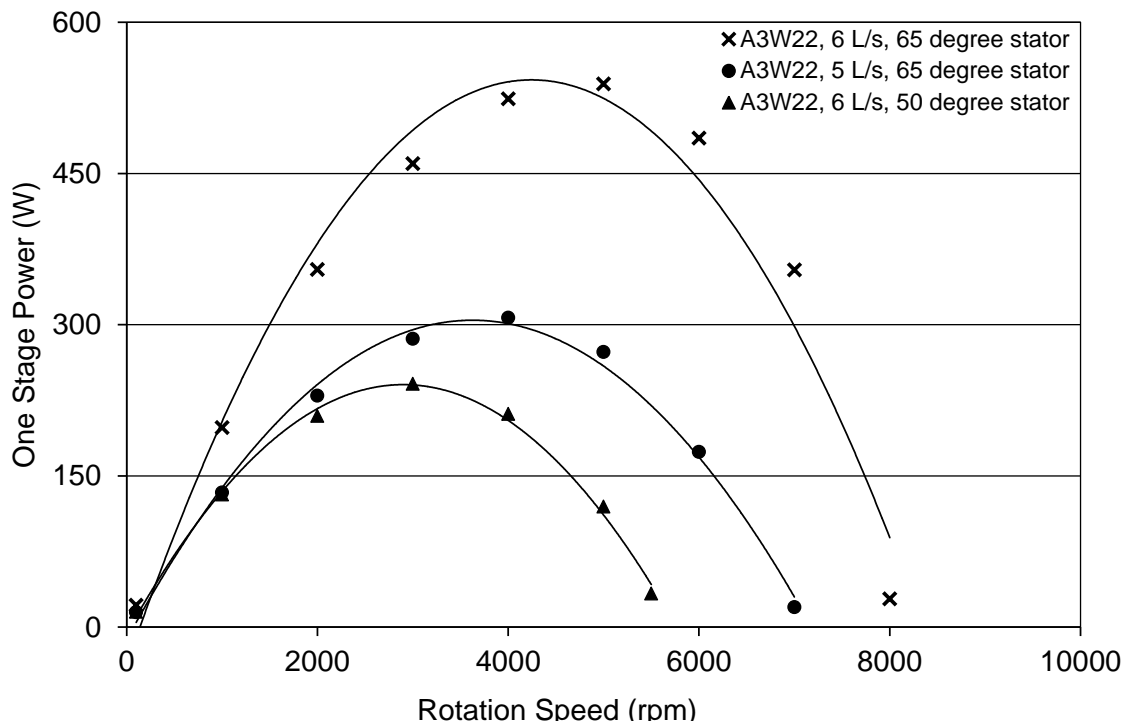


Figure 5.87 CFD simulation results of water flow through one stage turbodrill stage model “A3”.

### 5.5.4 Water flow simulation results for Turbodrill stage model “B1”

Water flow simulation results for one stage turbodrill models with 4 cm shroud diameter and 3 mm blade height (span) which are known here as stage model “B1” are presented in this section.

#### Simulation results through stage model “B1W20” with water flow rate of 2 L/s

Table 5.36 and Figure 5.88 show water flow CFD simulation results for one stage turbodrill model with 5 cm shroud diameter, 3 mm blade height and 20 blades on each blade row (stage model “B1W20”) with water flow rate of 2 L/s.

Table 5.36: CFD simulation results for one stage turbodrill model “B1W20” with water flow rate of 2 L/s.

Speed (rpm×100)	Power (W)	Torque (N.mm)	Inlet Flow Coefficient	Stage Reaction
1	15.301	1461.207	51.807	36.672
10	142.195	1357.962	5.022	3.905
20	270.021	1289.350	2.393	1.929
40	472.684	1128.533	1.050	1.301
60	613.477	976.451	0.640	1.020
80	698.055	833.303	0.444	0.908
100	759.791	725.600	0.334	0.855
120	756.127	601.751	0.276	0.794
140	655.863	447.392	0.249	0.757
160	526.462	314.232	0.238	0.727
180	258.851	137.335	0.240	0.708
190	86.453	43.454	0.246	0.693

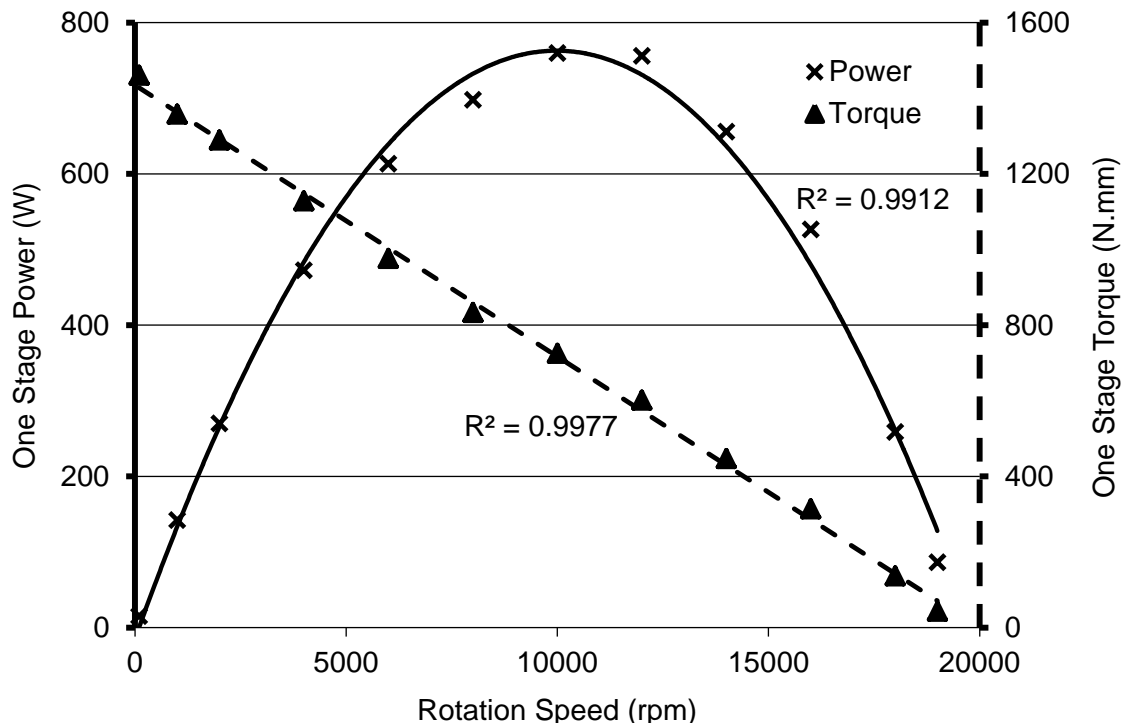


Figure 5.88 CFD simulation results for one stage turbodrill model “B1W20” with water flow rate of 2 L/s at reference radius of 18.5438 mm.

Figure 5.88 shows that the maximum stage efficiency and power for this case is at around 10,000 rpm rotation speed. One stage power and torque at maximum efficiency condition are around 760 W and 726 N.mm, respectively. In this case, the runaway turbine speed is almost over 19,000 rpm, and stalled torque is around 1461 N.mm. Figure 5.89 shows the CFD simulation results for one stage turbodrill model “B1W20” with water flow rate of 2 L/s at the rotation speed of 10,000 rpm. This figure shows the velocity profile in the blade to blade view at the span surface 0.5 and also shows the pressure and meridional velocity profiles at meridional surface. The pressure and velocity profiles show the maximum velocity and minimum pressure is occurred near the stator blade trailing edge.

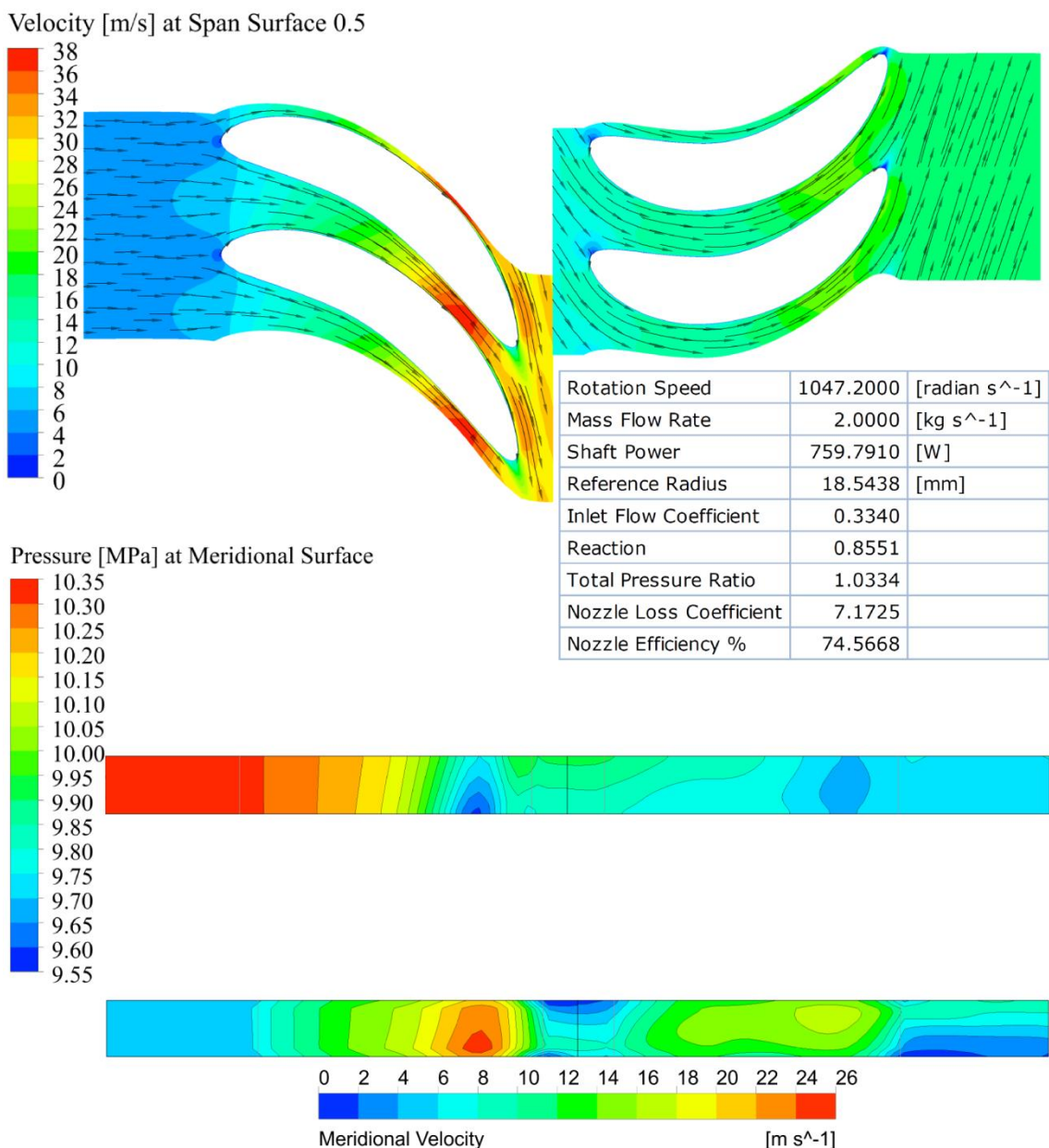


Figure 5.89 CFD simulation results for one stage turbodrill model “B1W20” with water flow rate of 2 L/s at 10,000 rpm rotation speed.

Figures 5.90 and 5.91 show the velocity and pressure values versus normalized streamwise length of stator and rotor at span surface 0.5 for water flow rate of 2 L/s at 10,000 rpm rotation speed through turbodrill stage model “B1W20”. These figures show the velocity and pressure data on the both blade surfaces.

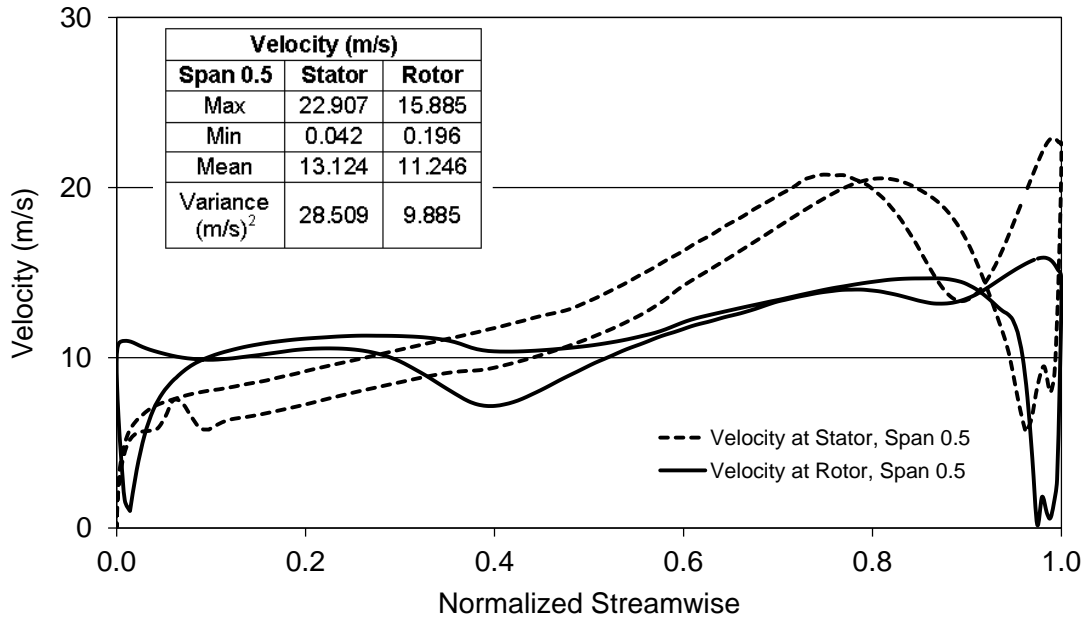


Figure 5.90 Velocity profile versus normalized streamwise for water flow rate of 2 L/s at 10,000 rpm rotation speed through turbodrill stage model “B1W20”.

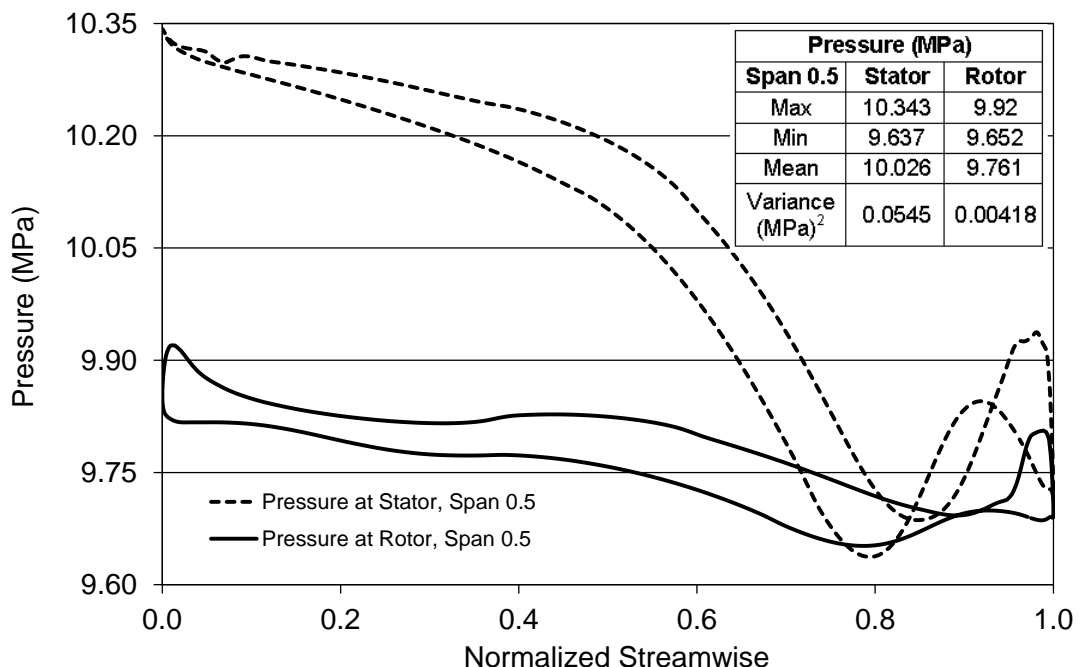


Figure 5.91 Pressure profile versus normalized streamwise for water flow rate of 2 L/s at 10,000 rpm rotation speed through turbodrill stage model “B1W20”.

Table 5.37 shows the structural (FSI) simulation results for stress, strain and deformation on the blades for water flow rate of 2 L/s at 10,000 rpm rotation speed through turbodrill stage model “B1W20” for two different blend radius.

Table 5.37: FSI simulation results for water flow rate of 2 L/s at 10,000 rpm rotation speed through turbodrill stage model “B1W20”.

Static Structural Analysis		Equivalent (Von-Mises) Stress (MPa)	Equivalent Elastic Strain ( $\times 10^{-4}$ mm/mm)	Total Deformation ( $\times 10^{-3}$ mm)
Blend Radius = 0.5 mm	Min	4.859	0.253	0
	Max	105.108	6.346	0.933
Blend Radius = 1.0 mm	Min	4.814	0.254	0
	Max	84.152	5.166	0.674

#### Simulation results through stage model “B1W16” with water flow rate of 2 L/s

Table 5.38 and Figure 5.92 show water flow CFD simulation results for one stage turbodrill model with 4 cm shroud diameter, 3 mm blade height and 16 blades on each blade row (stage model “B1W16”) with water flow rate of 2 L/s.

Table 5.38: CFD simulation results for one stage turbodrill model “B1W16” with water flow rate of 2 L/s.

Speed (rpm×100)	Power (W)	Torque (N.mm)	Inlet Flow Coefficient	Stage Reaction
1	9.779	933.914	39.475	24.161
10	91.941	878.038	3.796	2.874
20	169.537	809.539	1.819	1.696
40	277.583	662.729	0.843	1.087
60	339.498	540.368	0.540	0.931
80	341.236	407.350	0.406	0.834
100	255.295	243.807	0.344	0.764
120	138.182	109.970	138.182	0.715

Figure 5.92 shows that the maximum stage efficiency and power for this case is at around 8,000 rpm rotation speed. One stage power and torque at maximum efficiency condition are around 341 W and 407 N.mm, respectively. In this case, the runaway turbine speed is almost over 12,000 rpm, and stalled torque is around 934 N.mm. Figure 5.93 shows the CFD simulation results for one stage turbodrill model “B1W16” with water flow rate of 2 L/s at the rotation speed of 8,000 rpm. This figure shows the velocity profile in the blade to blade view at the span surface 0.5 and also shows the pressure and meridional velocity profiles at meridional surface. The pressure and velocity profiles show the maximum velocity and minimum pressure is occurred near the stator blade trailing edge.

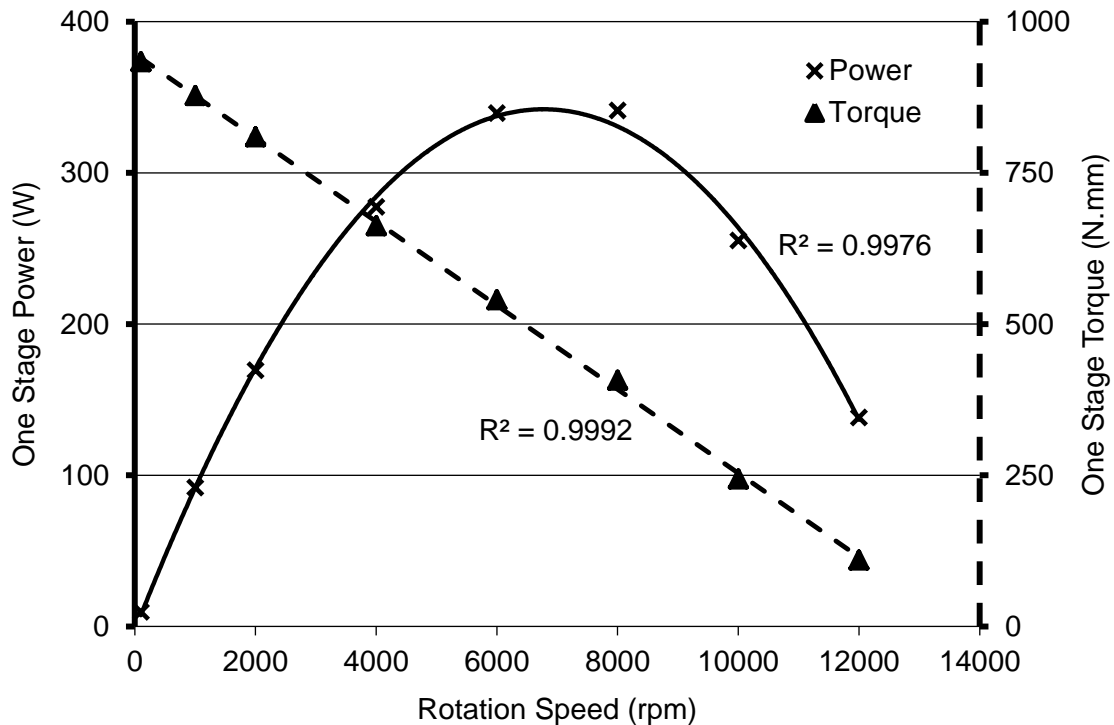


Figure 5.92 CFD simulation results for one stage turbodrill model "B1W16" with water flow rate of 2 L/s at reference radius of 18.5431 mm.

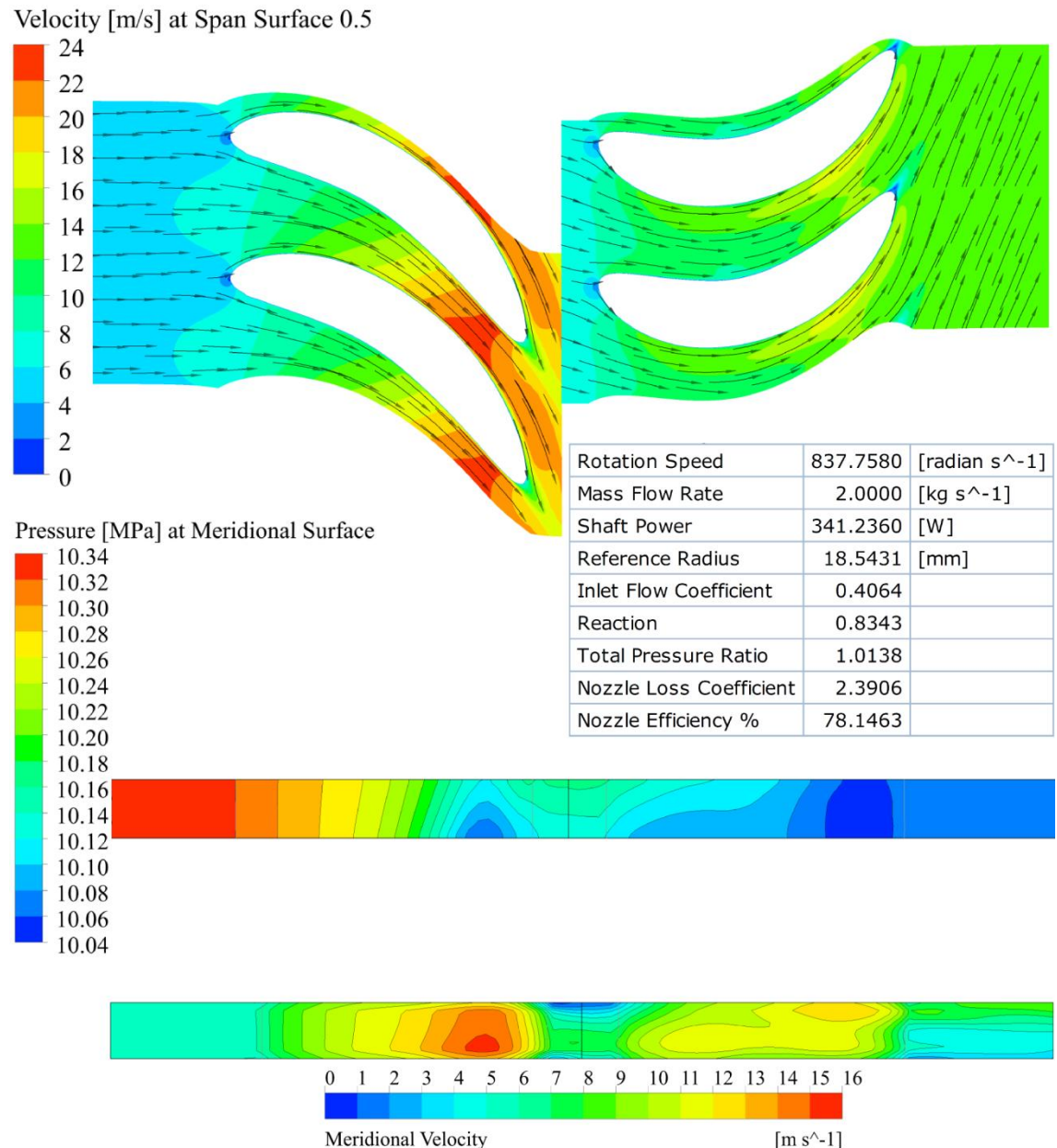


Figure 5.93 CFD simulation results for one stage turbodrill model "B1W16" with water flow rate of 2 L/s at 8,000 rpm rotation speed.

Figures 5.94 and 5.95 show the velocity and pressure values versus normalized streamwise length of stator and rotor at span surface 0.5 for water flow rate of 2 L/s at 8,000 rpm rotation speed through turbodrill stage model "B1W16". These figures show the velocity and pressure data on the both blade surfaces.

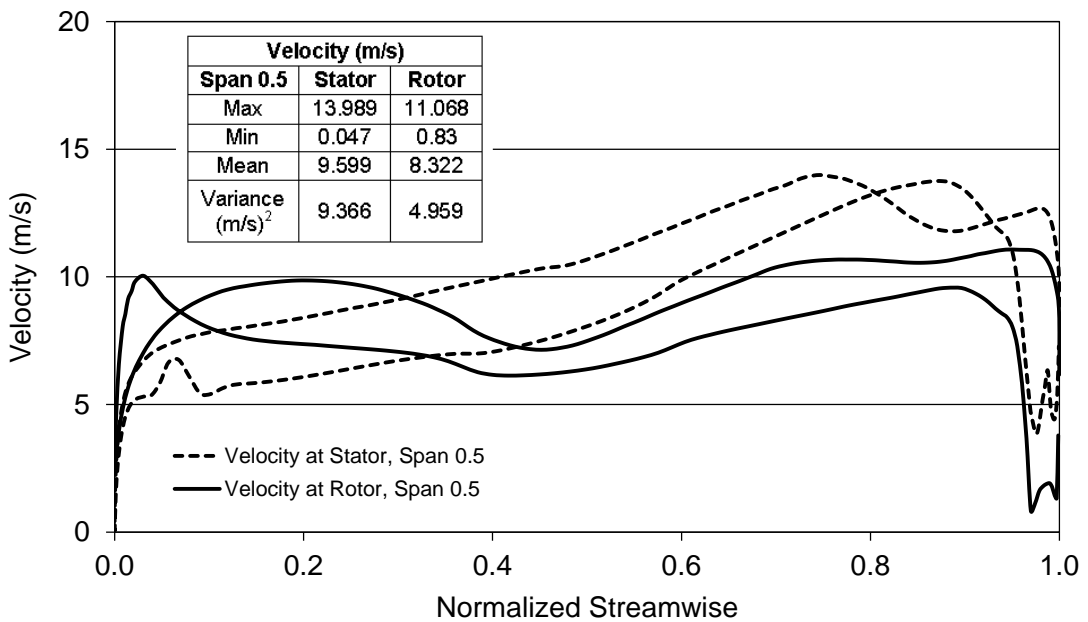


Figure 5.94 Velocity profile versus normalized streamwise for water flow rate of 2 L/s at 8,000 rpm rotation speed through turbodrill stage model “B1W16”.

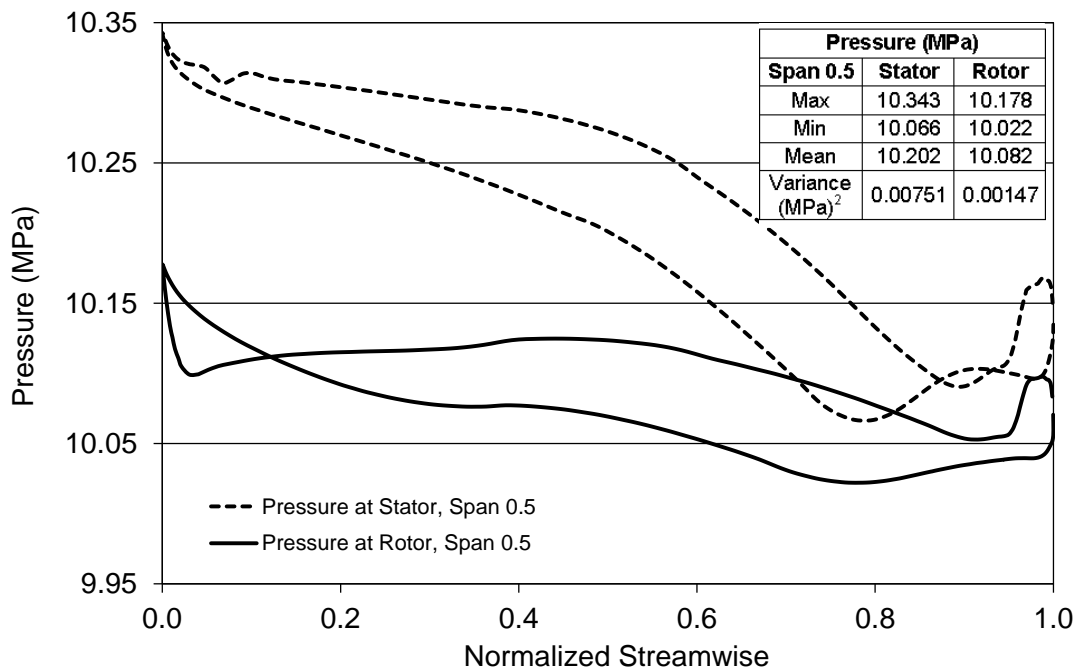


Figure 5.95 Pressure profile versus normalized streamwise for water flow rate of 2 L/s at 8,000 rpm rotation speed through turbodrill stage model “B1W16”.

Table 5.39 shows the structural (FSI) simulation results for stress, strain and deformation on the blades for water flow rate of 2 L/s at 8,000 rpm rotation speed through turbodrill stage model “B1W16” for two different blend radius.

Table 5.39: FSI simulation results for water flow rate of 2 L/s at 8,000 rpm rotation speed through turbodrill stage model “B1W16”.

Static Structural Analysis		Equivalent (Von-Mises) Stress (MPa)	Equivalent Elastic Strain ( $\times 10^{-4}$ mm/mm)	Total Deformation ( $\times 10^{-3}$ mm)
Blend Radius = 0.5 mm	Min	4.908	0.255	0
	Max	108.584	6.686	0.960
Blend Radius = 1.0 mm	Min	4.66	0.242	0
	Max	93.82	5.469	0.694

#### Simulation results through stage model “B1W16” with water flow rate of 3 L/s

Table 5.40 and Figure 5.96 show water flow CFD simulation results for one stage turbodrill model with 4 cm shroud diameter, 3 mm blade height and 16 blades on each blade row (stage model “B1W16”) with water flow rate of 3 L/s.

Table 5.40: CFD simulation results for one stage turbodrill model “B1W16” with water flow rate of 3 L/s.

Speed (rpm×100)	Power (W)	Torque (N.mm)	Inlet Flow Coefficient	Stage Reaction
1	22.033	2104.161	59.319	34.093
10	208.744	1993.505	5.802	3.947
20	400.323	1911.542	2.809	2.259
40	714.371	1705.561	1.334	1.380
60	938.798	1494.253	0.844	1.079
80	1098.130	1310.893	0.614	0.973
100	1180.530	1127.406	0.484	0.895
120	1155.950	919.944	0.407	0.836
140	961.228	655.695	0.360	0.783
160	759.970	453.607	0.334	0.753
180	400.688	212.587	0.322	0.731
200	18.069	8.628	0.318	0.703

Figure 5.96 shows that the maximum stage efficiency and power for this case is at around 10,000 rpm rotation speed. One stage power and torque at maximum efficiency condition are around 1181 W and 1127 N.mm, respectively. In this case, the runaway turbine speed is almost over 20,000 rpm, and stalled torque is around 2104 N.mm. Figure 5.97 shows the CFD simulation results for one stage turbodrill model “B1W16” with water flow rate of 3 L/s at the rotation speed of 10,000 rpm. This figure shows the velocity profile in the blade to blade view at the span surface 0.5 and also shows the pressure and meridional velocity profiles at meridional surface. The pressure and velocity profiles show the maximum velocity and minimum pressure is occurred near the stator blade trailing edge.

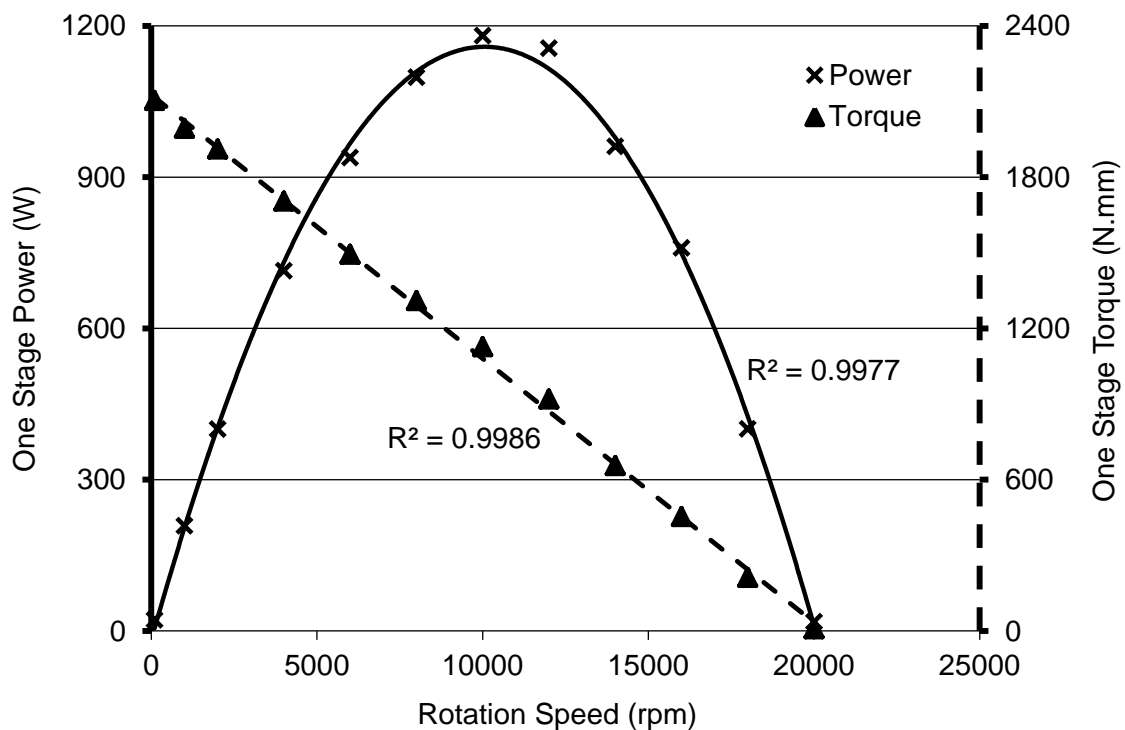


Figure 5.96 CFD simulation results for one stage turbodrill model "B1W16" with water flow rate of 3 L/s at reference radius of 18.5431 mm.

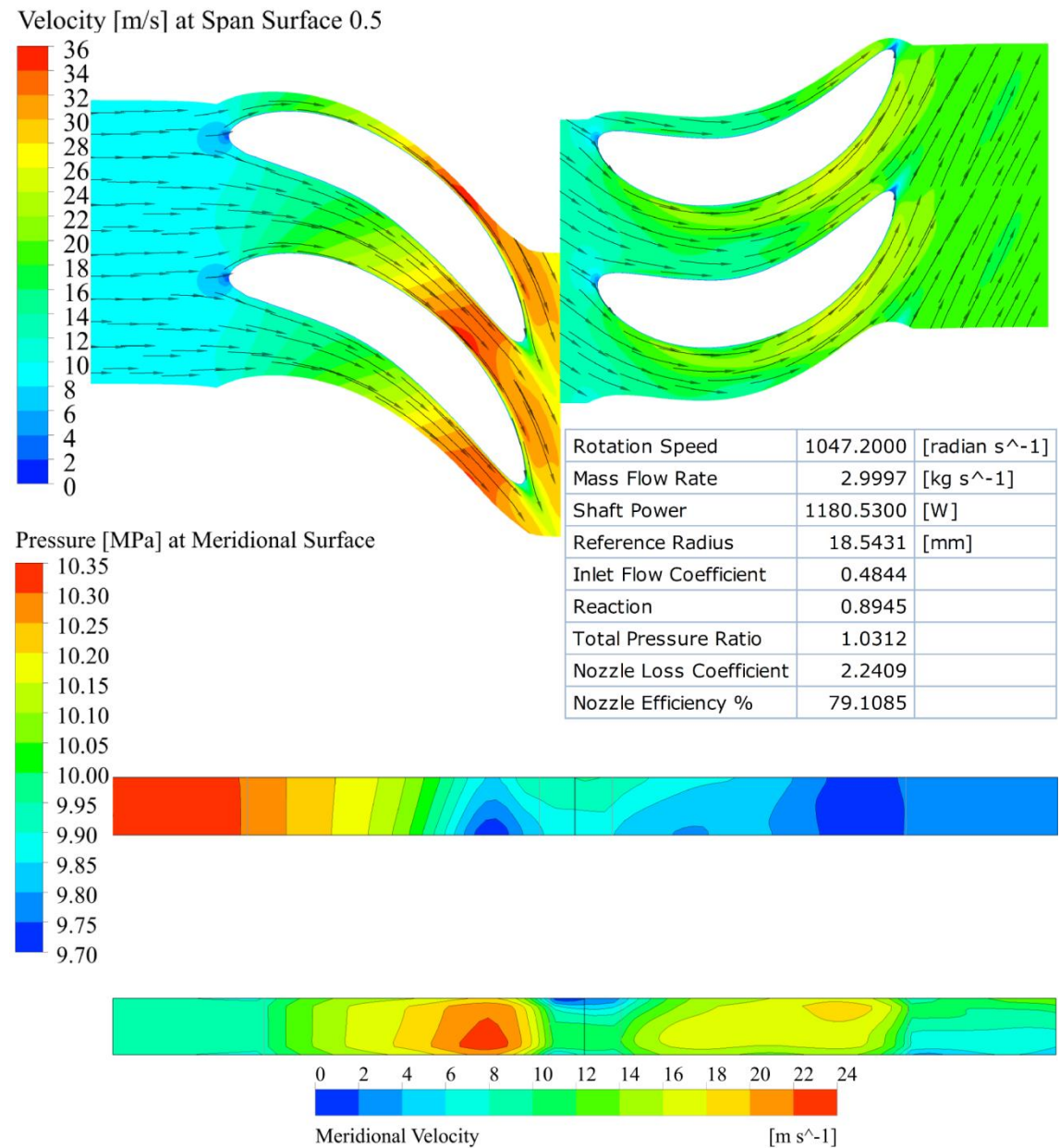


Figure 5.97 CFD simulation results for one stage turbodrill model “B1W16” with water flow rate of 3 L/s at 10,000 rpm rotation speed.

Figures 5.98 and 5.99 show the velocity and pressure values versus normalized streamwise length of stator and rotor at span surface 0.5 for water flow rate of 3 L/s at 10,000 rpm rotation speed through turbodrill stage model “B1W16”. These figures show the velocity and pressure data on the both blade surfaces.

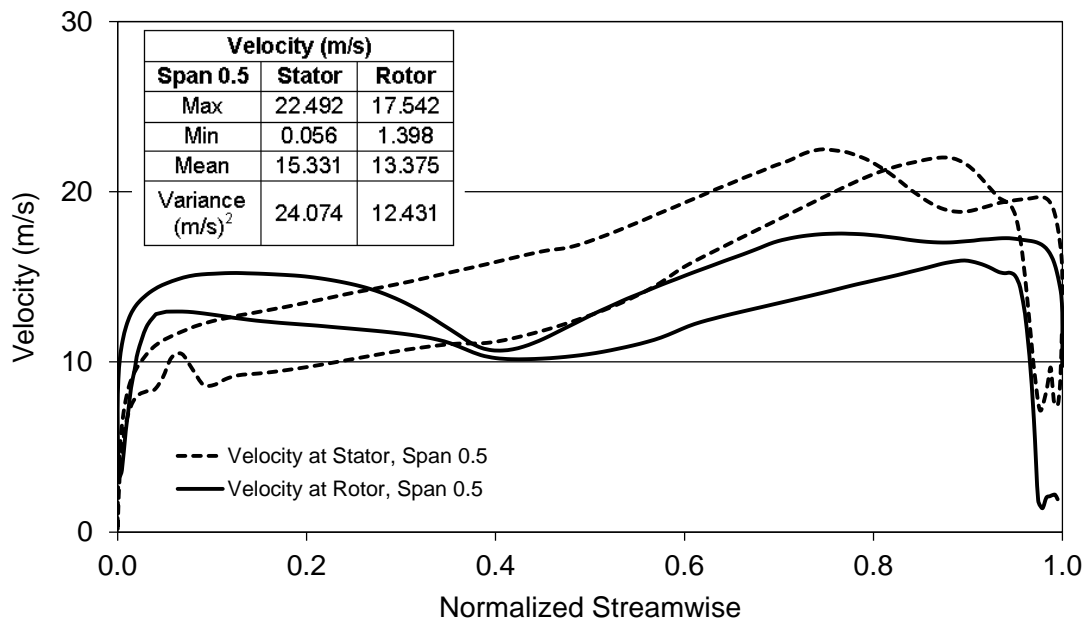


Figure 5.98 Velocity profile versus normalized streamwise for water flow rate of 3 L/s at 10,000 rpm rotation speed through turbodrill stage model “B1W16”.

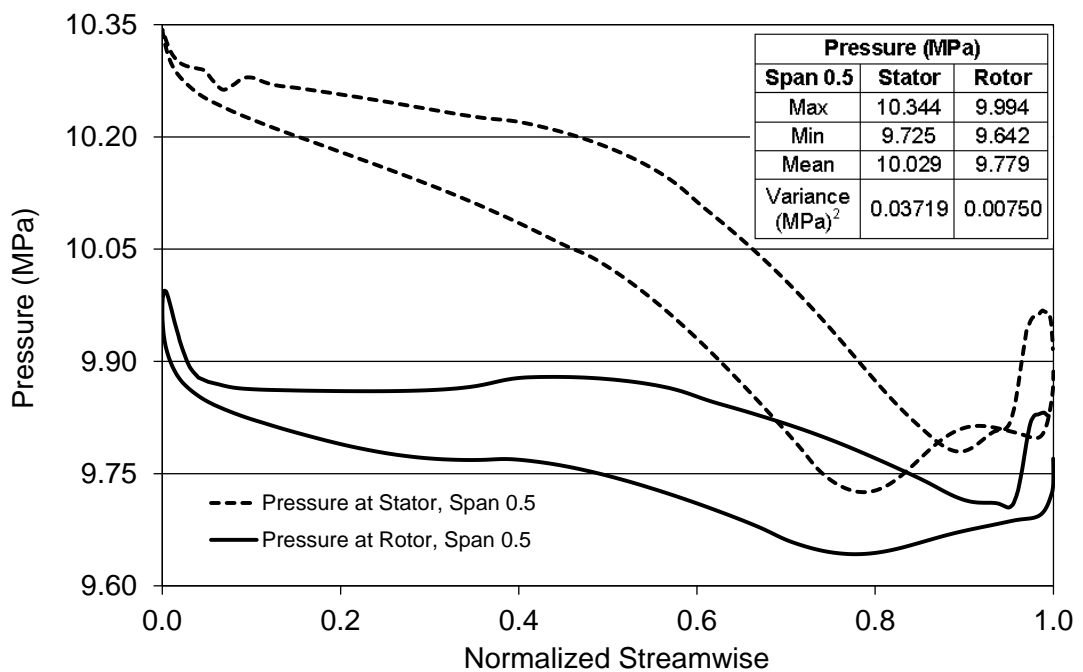


Figure 5.99 Pressure profile versus normalized streamwise for water flow rate of 3 L/s at 10,000 rpm rotation speed through turbodrill stage model “B1W16”.

Table 5.41 shows the structural (FSI) simulation results for stress, strain and deformation on the blades for water flow rate of 3 L/s at 10,000 rpm rotation speed through turbodrill stage model “B1W16” for two different blend radius.

Table 5.41: FSI simulation results for water flow rate of 3 L/s at 10,000 rpm rotation speed through turbodrill stage model “B1W16”.

Static Structural Analysis		Equivalent (Von-Mises) Stress (MPa)	Equivalent Elastic Strain ( $\times 10^{-4}$ mm/mm)	Total Deformation ( $\times 10^{-3}$ mm)
Blend Radius = 0.5 mm	Min	4.772	0.248	0
	Max	105.369	6.494	0.930
Blend Radius = 1.0 mm	Min	4.515	0.235	0
	Max	91.143	5.313	0.673

#### Conclusion remarks for simulation results of water flow through stage model “B1”

Figure 5.100 shows the water flow simulation results for one stage power with different turbodrill stage models with 4 cm shroud diameter and 3 mm blade height (model “B1”). The effect of different geometrical and flow properties on the turbodrill stage “B1” performance is shown in this Figure. It can be inferred that flow rate and the blade numbers on each row have significant effects on the turbodrill performance.

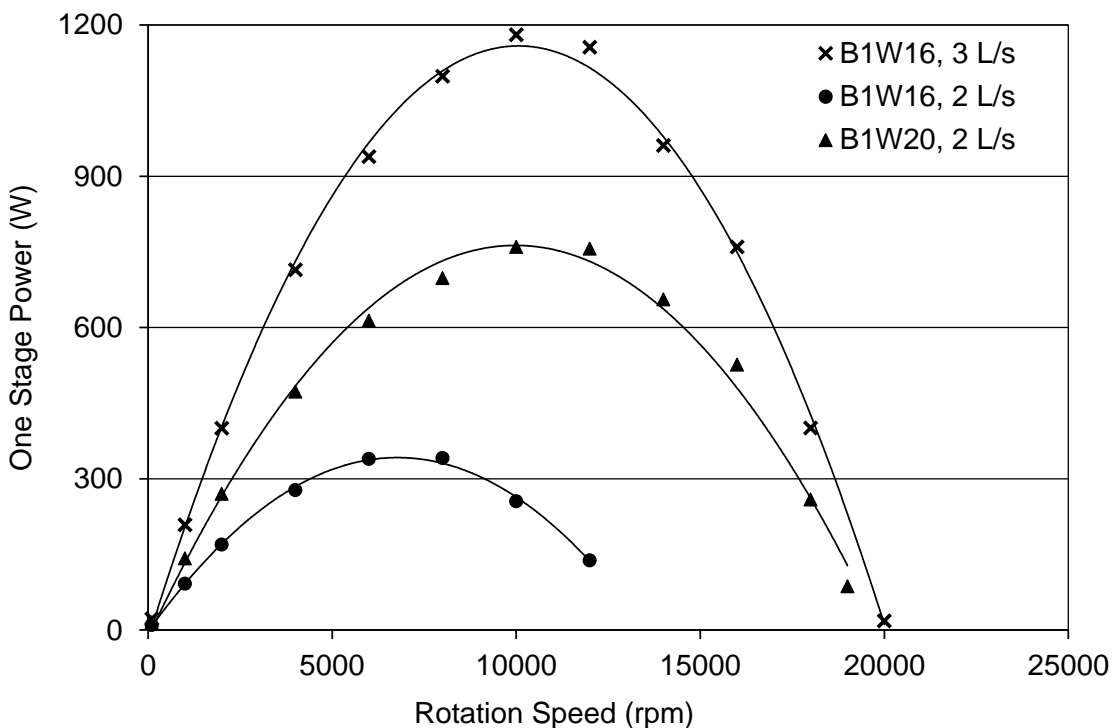


Figure 5.100 CFD simulation results of water flow through one stage turbodrill stage model “B1”.

#### 5.5.5 Water flow simulation results for Turbodrill stage model “B2”

Water flow simulation results for one stage turbodrill models with 4 cm shroud diameter and 5 mm blade height (span) which are known here as stage model “B2” are presented in this section.

**Simulation results through stage model “B2W20” with water flow rate of 2 L/s**

Table 5.42 and Figure 5.101 show water flow CFD simulation results for one stage turbodrill model with 4 cm shroud diameter, 5 mm blade height and 20 blades on each blade row (stage model “B2W20”) with water flow rate of 2 L/s.

Table 5.42: CFD simulation results for one stage turbodrill model “B2W20” with water flow rate of 2 L/s.

Speed (rpm×100)	Power (W)	Torque (N.mm)	Inlet Flow Coefficient	Stage Reaction
1	9.759	932.013	37.032	23.306
10	92.327	881.727	3.409	2.888
20	172.411	823.263	1.608	1.744
40	289.231	690.539	0.703	1.118
60	361.389	575.211	0.407	0.935
80	383.438	457.729	0.283	0.851
100	359.435	343.260	0.230	0.784
120	269.170	214.214	0.229	0.753
140	70.449	48.056	0.248	0.719

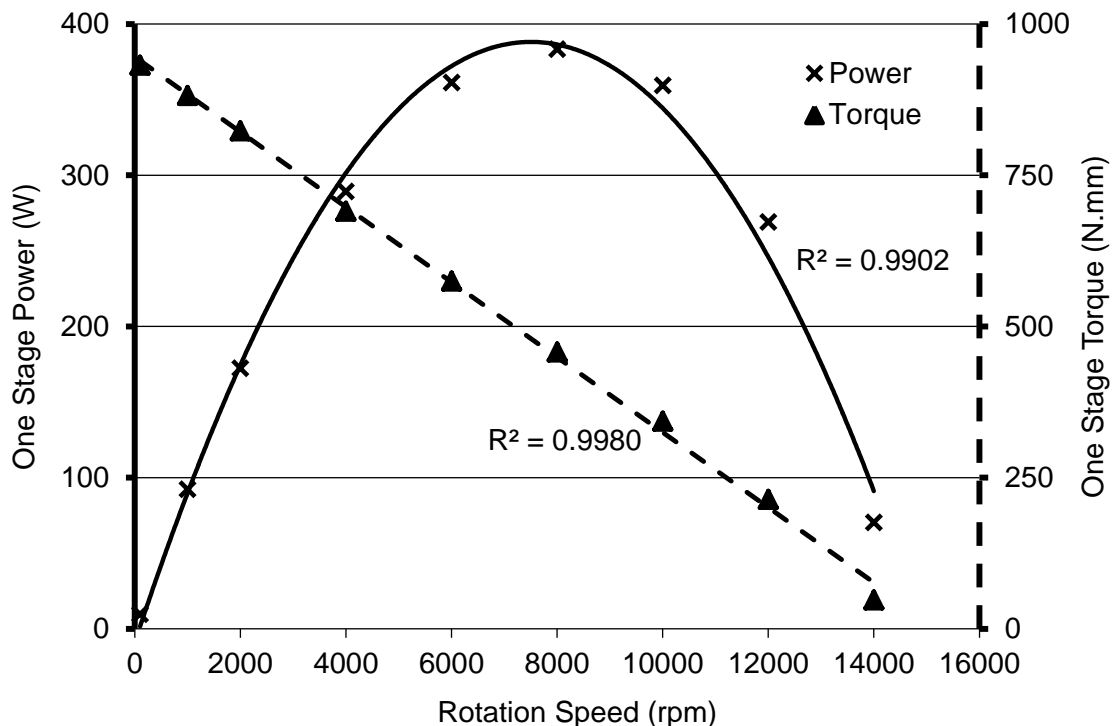


Figure 5.101 CFD simulation results for one stage turbodrill model “B2W20” with water flow rate of 2 L/s at reference radius of 17.6290 mm.

Figure 5.101 shows that the maximum stage efficiency and power for this case is at around 8,000 rpm rotation speed. One stage power and torque at maximum efficiency condition are around 383 W and 458 N.mm, respectively. In this case, the runaway turbine speed is almost over 14,000 rpm, and stalled torque is around 932 N.mm. Figure 5.102 shows the CFD simulation results for one stage turbodrill model “B2W20” with

water flow rate of 2 L/s at the rotation speed of 8,000 rpm. This figure shows the velocity profile in the blade to blade view at the span surface 0.5 and also shows the pressure and meridional velocity profiles at meridional surface.

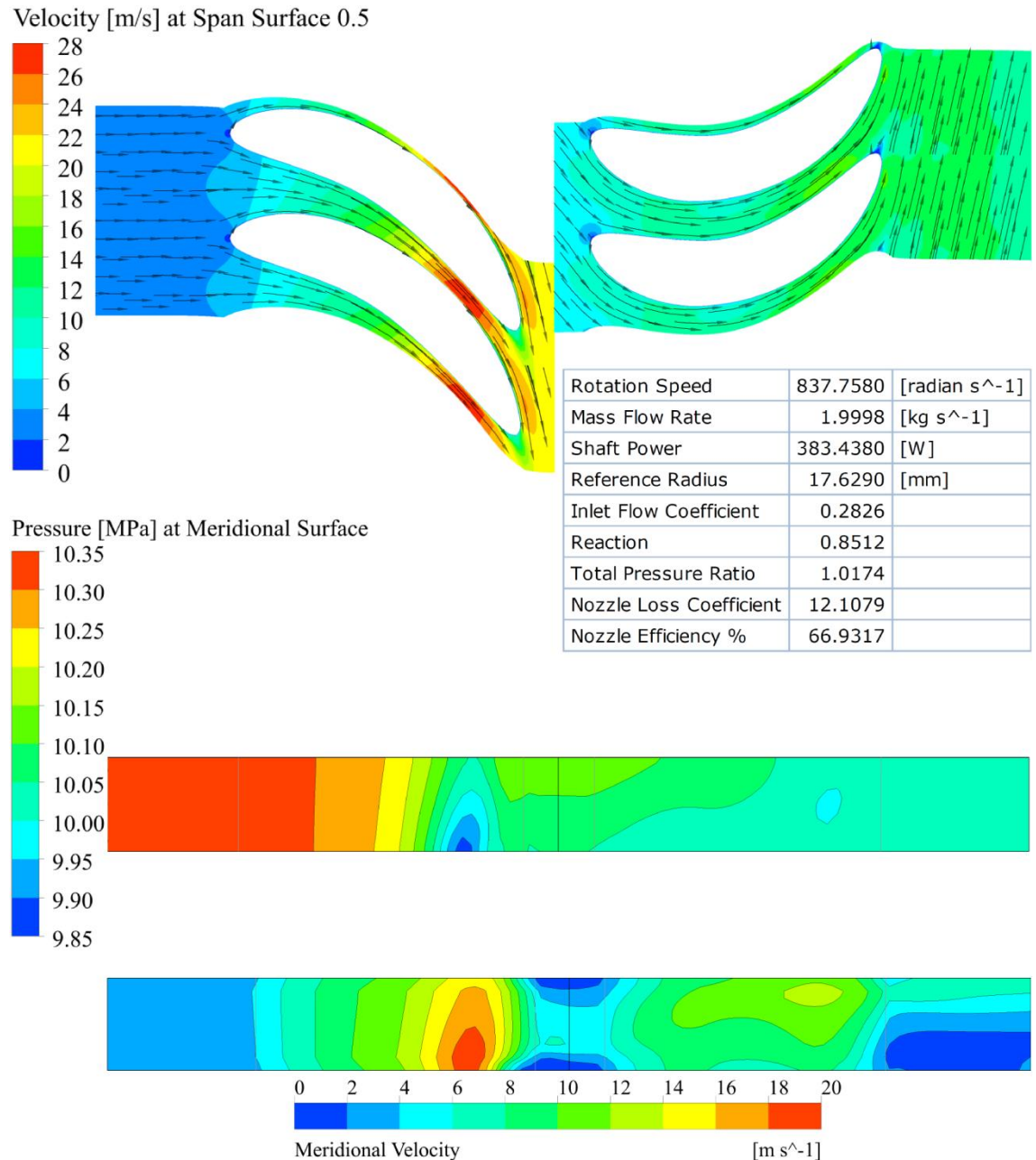


Figure 5.102 CFD simulation results for one stage turbodrill model “B2W20” with water flow rate of 2 L/s at 8,000 rpm rotation speed.

Figures 5.103 and 5.104 show the velocity and pressure values versus normalized streamwise length of stator and rotor at span surface 0.5 for water flow rate of 2 L/s at 8,000 rpm rotation speed through turbodrill stage model “B2W20”. These figures show the velocity and pressure data on the both blade surfaces.

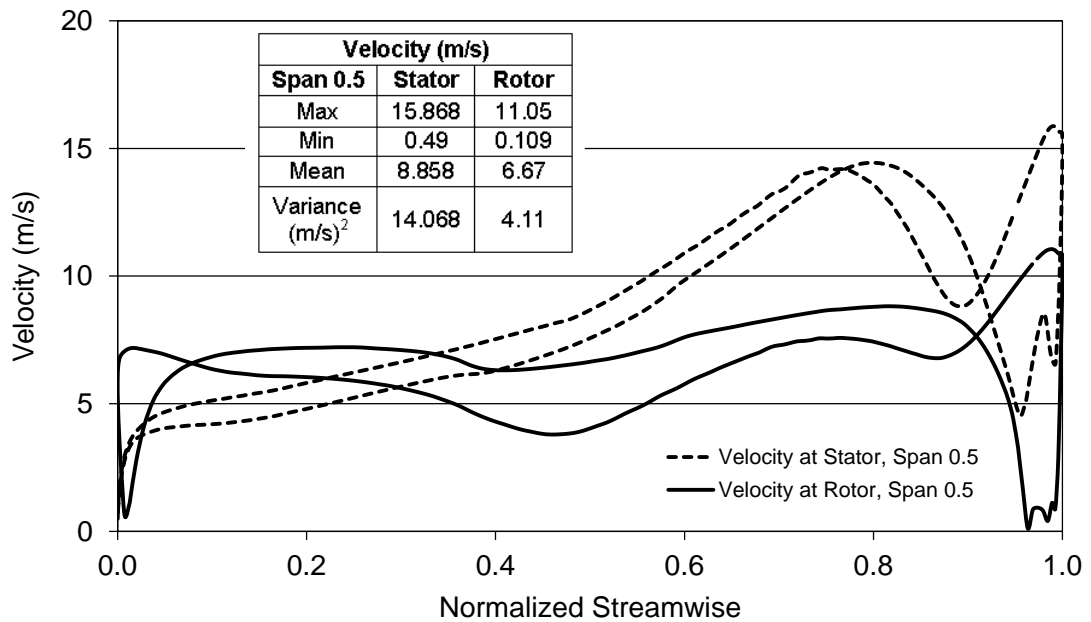


Figure 5.103 Velocity profile versus normalized streamwise for water flow rate of 2 L/s at 8,000 rpm rotation speed through turbodrill stage model “B2W20”.

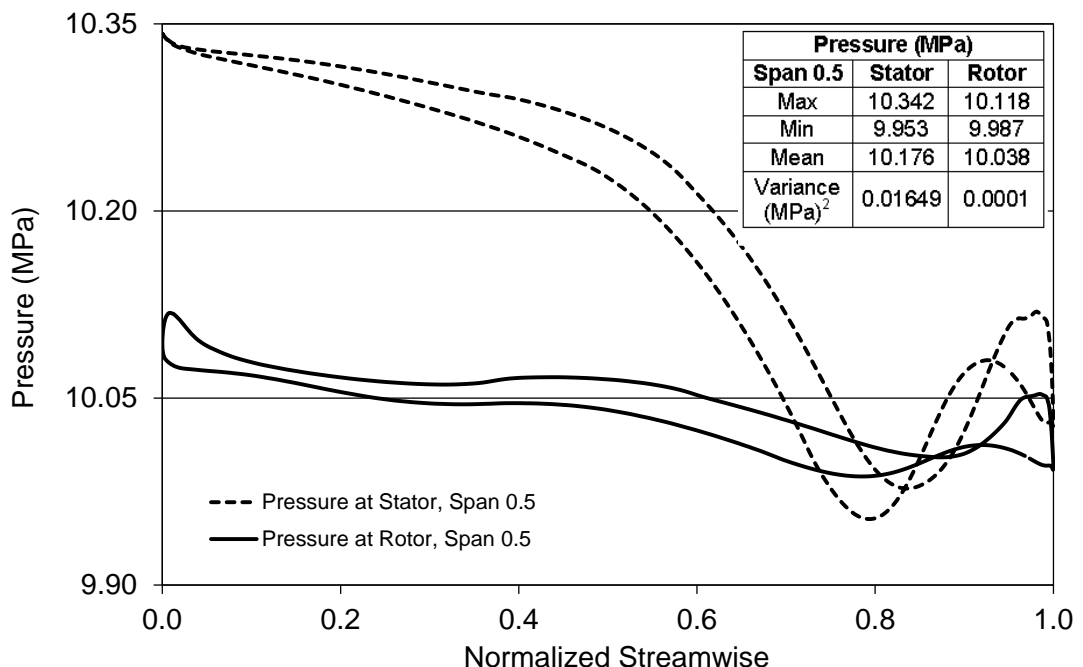


Figure 5.104 Pressure profile versus normalized streamwise for water flow rate of 2 L/s at 8,000 rpm rotation speed through turbodrill stage model “B2W20”.

Table 5.43 shows the structural (FSI) simulation results for stress, strain and deformation on the blades for water flow rate of 2 L/s at 8,000 rpm rotation speed through turbodrill stage model “B2W20” for two different blend radius.

Table 5.43: FSI simulation results for water flow rate of 2 L/s at 8,000 rpm rotation speed through turbodrill stage model “B2W20”.

Static Structural Analysis		Equivalent (Von-Mises) Stress (MPa)	Equivalent Elastic Strain ( $\times 10^{-4}$ mm/mm)	Total Deformation ( $\times 10^{-3}$ mm)
Blend Radius = 0.5 mm	Min	9.395	0.495	0
	Max	192.510	9.977	2.691
Blend Radius = 1.0 mm	Min	7.646	0.399	0
	Max	126.124	6.628	2.131

#### Simulation results through stage model “B2W16” with water flow rate of 2 L/s

Table 5.44 and Figure 5.105 show water flow CFD simulation results for one stage turbodrill model with 4 cm shroud diameter, 5 mm blade height and 16 blades on each blade row (stage model “B2W16”) with water flow rate of 2 L/s.

Table 5.44: CFD simulation results for one stage turbodrill model “B2W16” with water flow rate of 2 L/s.

Speed (rpm×100)	Power (W)	Torque (N.mm)	Inlet Flow Coefficient	Stage Reaction
1	6.176	589.818	26.976	17.761
10	55.556	530.557	2.534	2.238
20	95.404	455.552	1.187	1.337
30	126.771	403.554	0.752	1.108
40	145.187	346.634	0.548	0.968
50	152.230	290.759	0.437	0.886
60	144.480	229.964	0.374	0.828
70	120.210	164.001	0.339	0.789
80	82.136	98.049	0.324	0.756

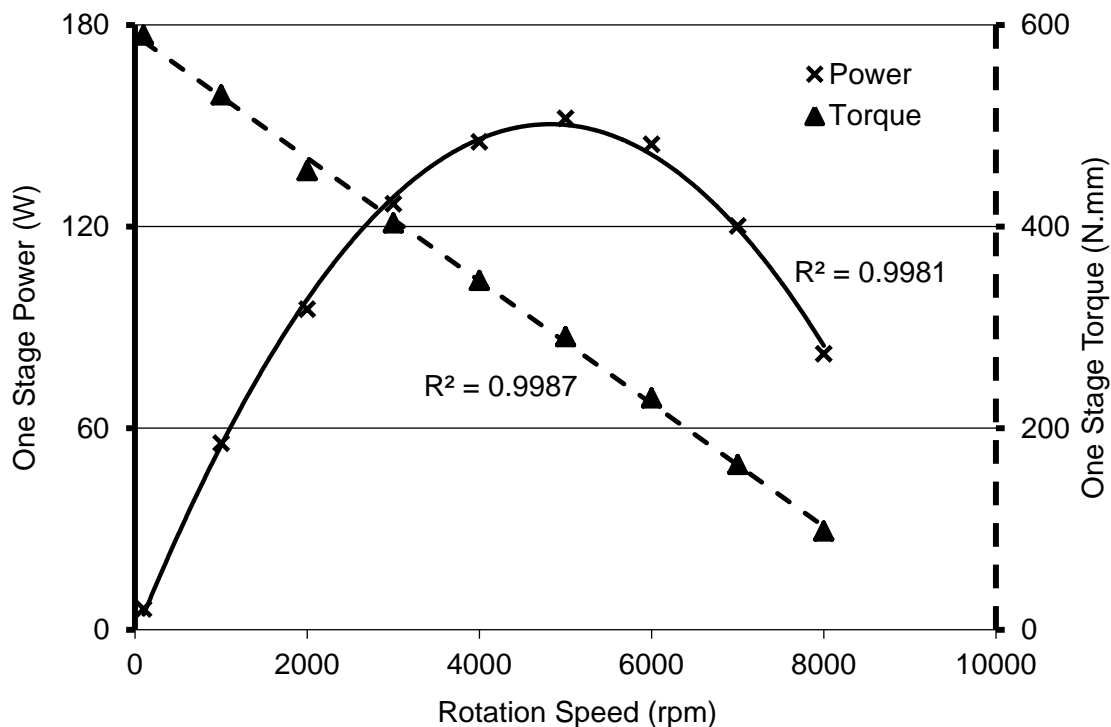


Figure 5.105 CFD simulation results for one stage turbodrill model “B2W16” with water flow rate of 2 L/s at reference radius of 17.6266 mm.

Figure 5.105 shows that the maximum stage efficiency and power for this case is at around 5,000 rpm rotation speed. One stage power and torque at maximum efficiency condition are around 152 W and 291 N.mm, respectively. In this case, the runaway turbine speed is almost over 8,000 rpm, and stalled torque is around 590 N.mm. Figure 5.106 shows the CFD simulation results for one stage turbodrill model “B2W16” with water flow rate of 2 L/s at the rotation speed of 5,000 rpm. This figure shows the velocity profile in the blade to blade view at the span surface 0.5 and also shows the pressure and meridional velocity profiles at meridional surface.

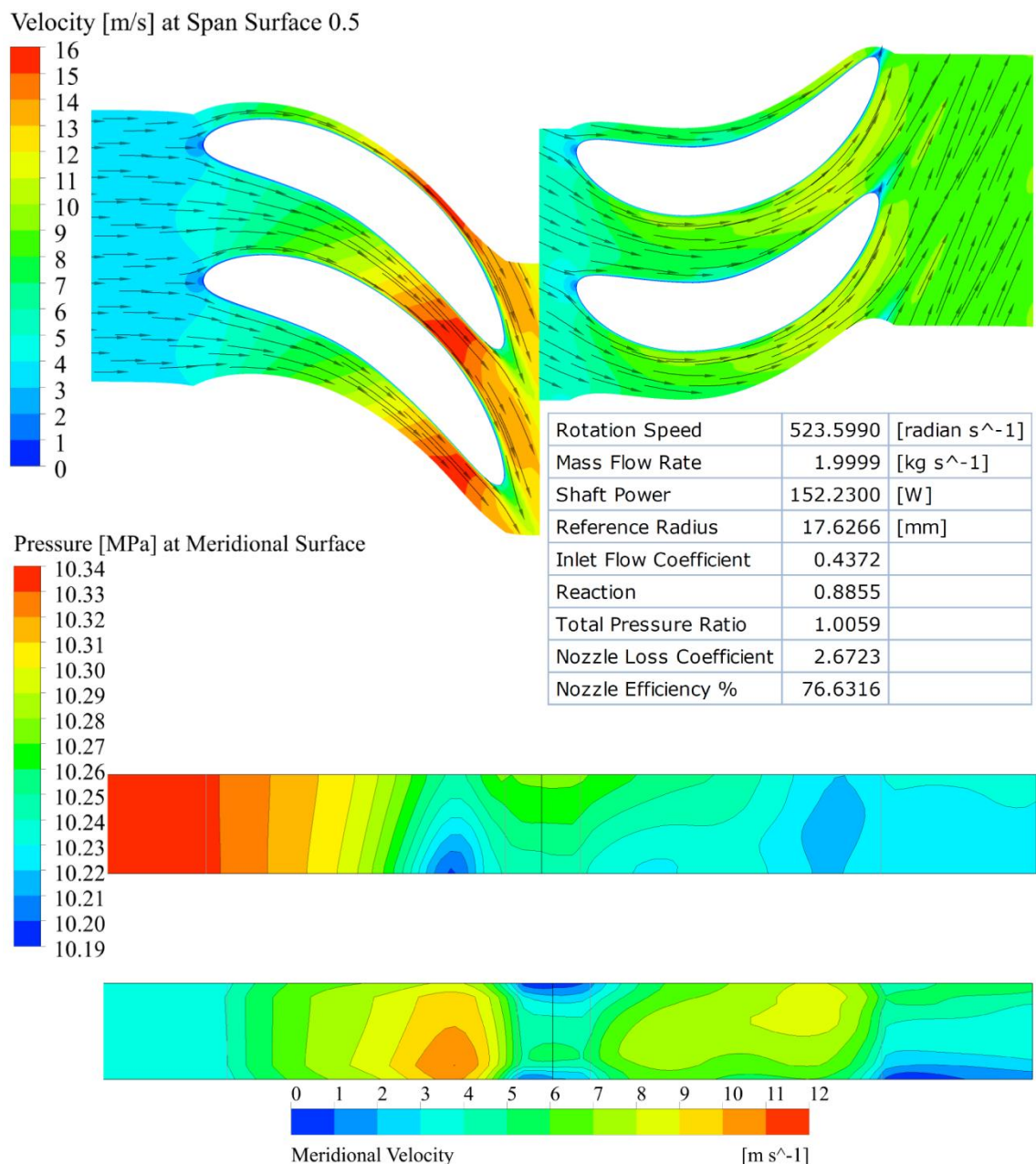


Figure 5.106 CFD simulation results for one stage turbodrill model “B2W16” with water flow rate of 2 L/s at 5,000 rpm rotation speed.

Figures 5.107 and 5.108 show the velocity and pressure values versus normalized streamwise length of stator and rotor at span surface 0.5 for water flow rate of 2 L/s at 5,000 rpm rotation speed through turbodrill stage model “B2W16”. These figures show the velocity and pressure data on the both blade surfaces.

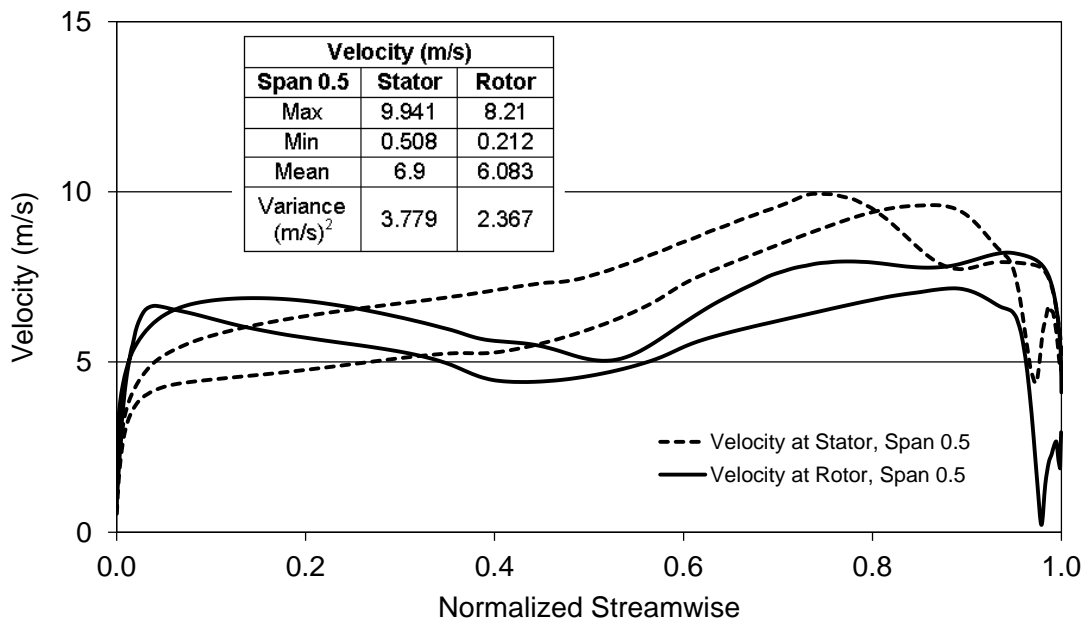


Figure 5.107 Velocity profile versus normalized streamwise for water flow rate of 2 L/s at 5,000 rpm rotation speed through turbodrill stage model “B2W16”.

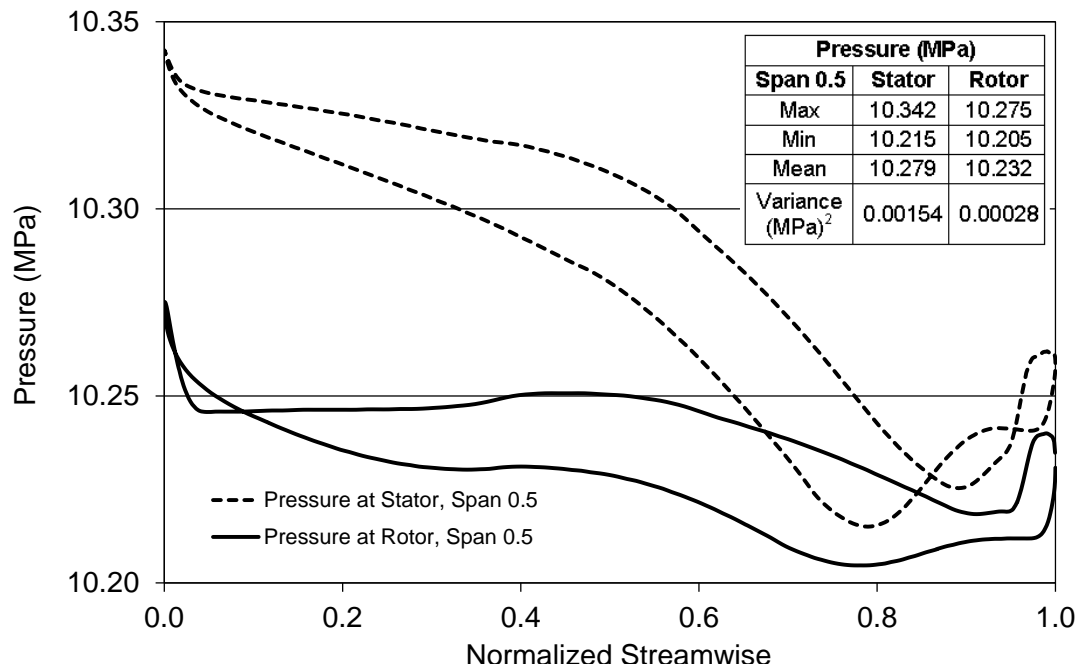


Figure 5.108 Pressure profile versus normalized streamwise for water flow rate of 2 L/s at 5,000 rpm rotation speed through turbodrill stage model “B2W16”.

Table 5.45 shows the structural (FSI) simulation results for stress, strain and deformation on the blades for water flow rate of 2 L/s at 5,000 rpm rotation speed through turbodrill stage model “B2W16” for two different blend radius.

Table 5.45: FSI simulation results for water flow rate of 2 L/s at 5,000 rpm rotation speed through turbodrill stage model “B2W16”.

Static Structural Analysis		Equivalent (Von-Mises) Stress (MPa)	Equivalent Elastic Strain ( $\times 10^{-4}$ mm/mm)	Total Deformation ( $\times 10^{-3}$ mm)
Blend Radius = 0.5 mm	Min	9.563	0.503	0
	Max	195.797	10.150	2.739
Blend Radius = 1.0 mm	Min	7.849	0.409	0
	Max	128.327	7.597	2.169

#### Simulation results through stage model “B2W16” with water flow rate of 3 L/s

Table 5.46 and Figure 5.109 show water flow CFD simulation results for one stage turbodrill model with 4 cm shroud diameter, 5 mm blade height and 16 blades on each blade row (stage model “B2W16”) with water flow rate of 3 L/s.

Table 5.46: CFD simulation results for one stage turbodrill model “B2W16” with water flow rate of 3 L/s.

Speed (rpm×100)	Power (W)	Torque (N.mm)	Inlet Flow Coefficient	Stage Reaction
1	14.100	1346.569	40.915	26.864
10	132.750	1267.763	3.922	3.192
20	239.933	1145.680	1.875	1.773
30	333.467	1061.537	1.187	1.365
40	409.778	978.345	0.856	1.188
50	464.654	887.489	0.668	1.067
60	503.441	801.310	0.547	0.978
70	524.879	716.085	0.465	0.917
80	525.237	627.002	0.410	0.871
90	504.831	535.682	0.371	0.835
100	462.474	441.663	0.344	0.808
110	408.109	354.313	0.326	0.785
120	322.290	256.489	0.317	0.761
130	171.155	125.733	0.323	0.732

Figure 5.109 shows that the maximum stage efficiency and power for this case is at around 7,000 rpm rotation speed. One stage power and torque at maximum efficiency condition are around 525 W and 716 N.mm, respectively. In this case, the runaway turbine speed is almost over 13,000 rpm, and stalled torque is around 1347 N.mm. Figure 5.110 shows the CFD simulation results for one stage turbodrill model “B2W16” with water flow rate of 3 L/s at the rotation speed of 7,000 rpm. This figure shows the

velocity profile in the blade to blade view at the span surface 0.5 and also shows the pressure and meridional velocity profiles at meridional surface.

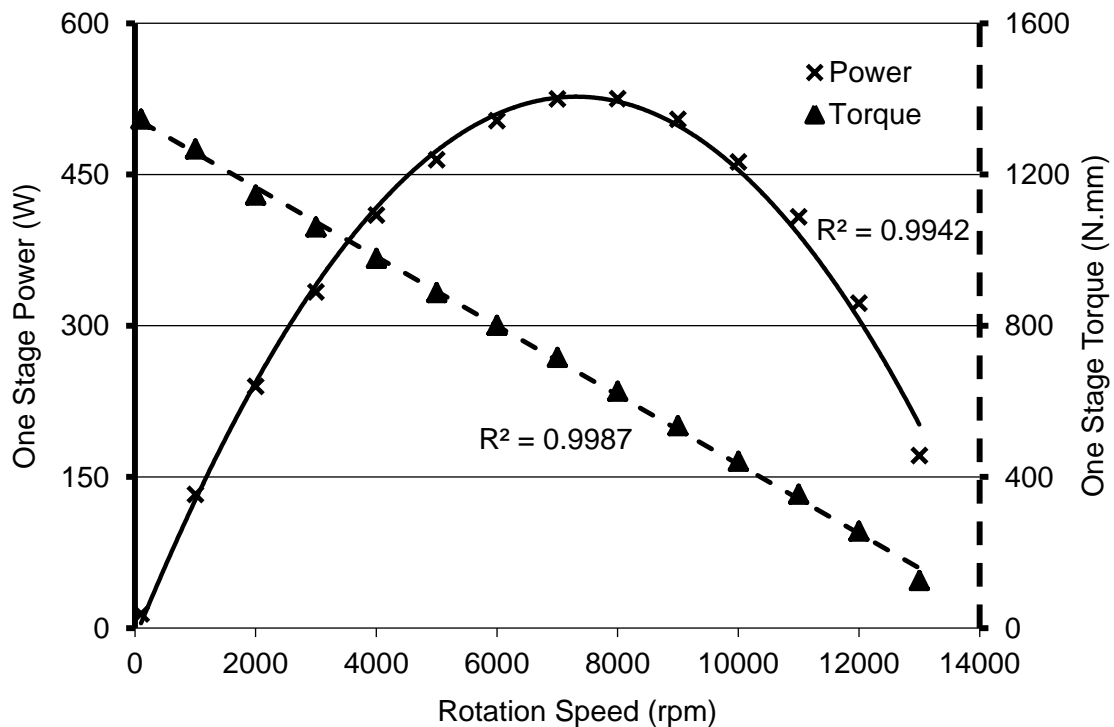


Figure 5.109 CFD simulation results for one stage turbodrill model "B2W16" with water flow rate of 3 L/s at reference radius of 17.6266 mm.

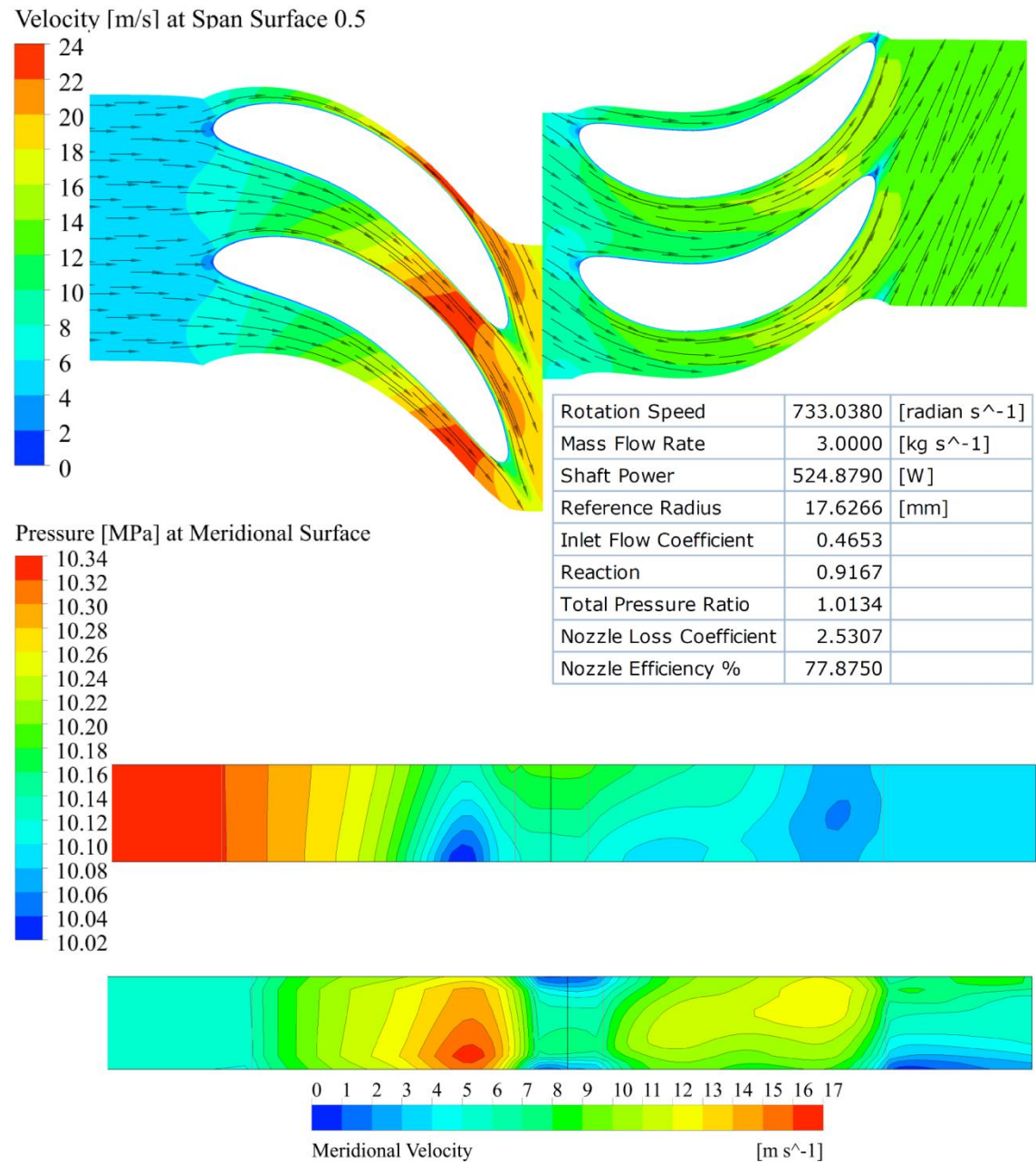


Figure 5.110 CFD simulation results for one stage turbodrill model "B2W16" with water flow rate of 3 L/s at 7,000 rpm rotation speed.

Figures 5.111 and 5.112 show the velocity and pressure values versus normalized streamwise length of stator and rotor at span surface 0.5 for water flow rate of 3 L/s at 7,000 rpm rotation speed through turbodrill stage model "B2W16". These figures show the velocity and pressure data on the both blade surfaces.

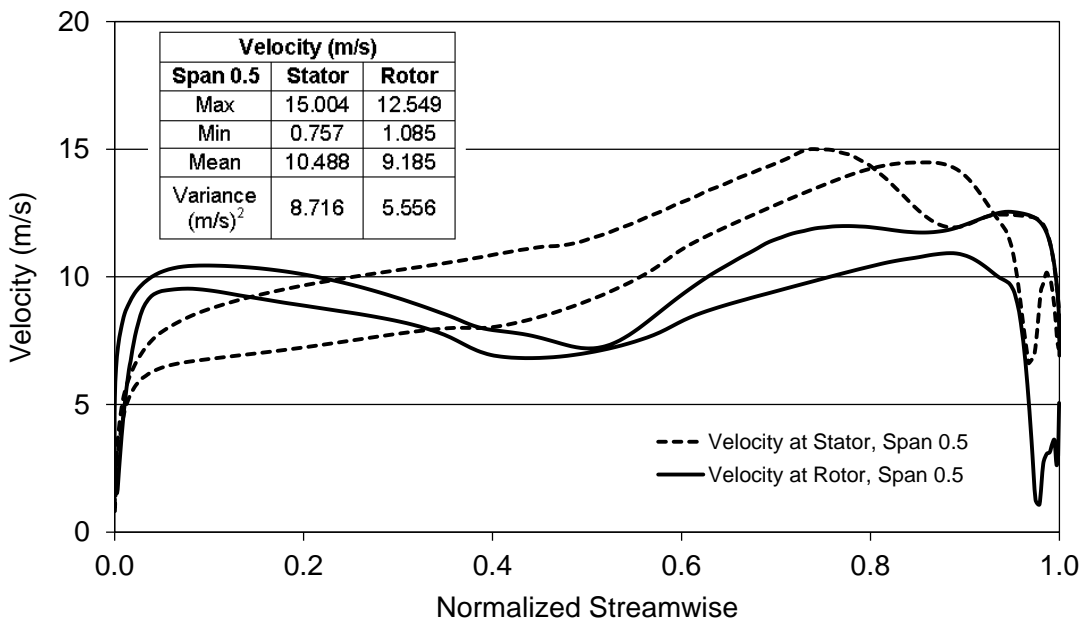


Figure 5.111 Velocity profile versus normalized streamwise for water flow rate of 3 L/s at 7,000 rpm rotation speed through turbodrill stage model “B2W16”.

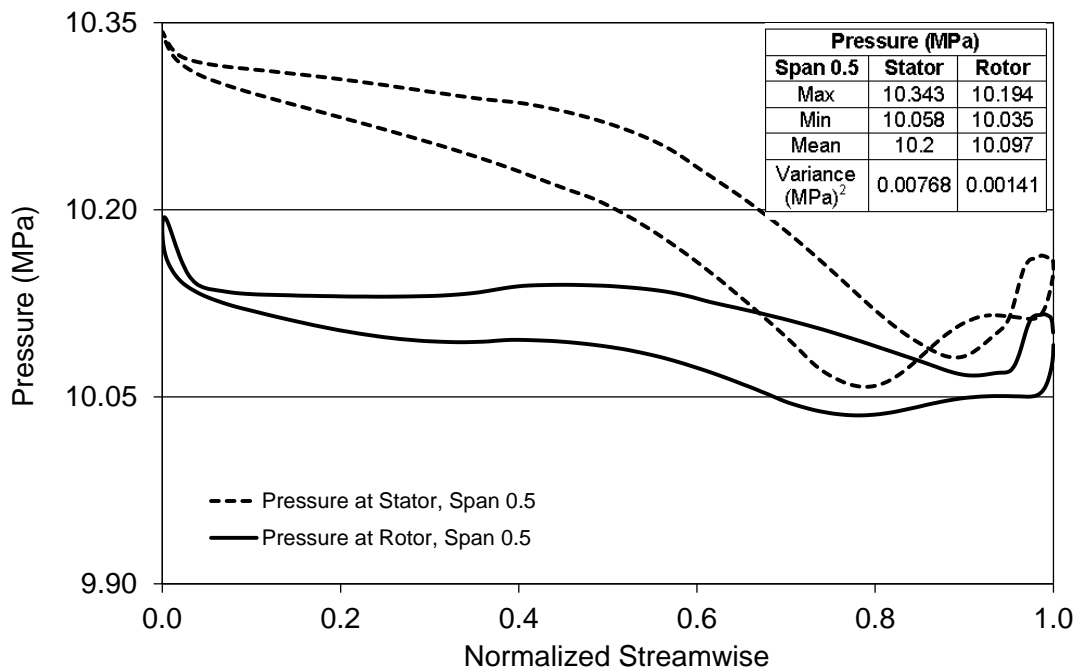


Figure 5.112 Pressure profile versus normalized streamwise for water flow rate of 3 L/s at 7,000 rpm rotation speed through turbodrill stage model “B2W16”.

Table 5.47 shows the structural (FSI) simulation results for stress, strain and deformation on the blades for water flow rate of 3 L/s at 7,000 rpm rotation speed through turbodrill stage model “B2W16” for two different blend radius.

Table 5.47: FSI simulation results for water flow rate of 3 L/s at 7,000 rpm rotation speed through turbodrill stage model “B2W16”.

Static Structural Analysis		Equivalent (Von-Mises) Stress (MPa)	Equivalent Elastic Strain ( $\times 10^{-4}$ mm/mm)	Total Deformation ( $\times 10^{-3}$ mm)
Blend Radius = 0.5 mm	Min	9.456	0.499	0
	Max	193.214	10.010	2.702
Blend Radius = 1.0 mm	Min	7.767	0.405	0
	Max	126.775	6.687	2.139

#### Simulation results through stage model “B2W16” with water flow rate of 4 L/s

Table 5.48 and Figure 5.113 show water flow CFD simulation results for one stage turbodrill model with 4 cm shroud diameter, 5 mm blade height and 16 blades on each blade row (stage model “B2W16”) with water flow rate of 4 L/s.

Table 5.48: CFD simulation results for one stage turbodrill model “B2W16” with water flow rate of 4 L/s.

Speed (rpm×100)	Power (W)	Torque (N.mm)	Inlet Flow Coefficient	Stage Reaction
1	25.117	2398.702	54.897	35.275
10	240.307	2294.932	5.313	4.049
20	451.903	2157.837	2.564	2.252
40	810.323	1934.646	1.190	1.418
60	1056.540	1681.660	0.750	1.133
80	1209.320	1443.626	0.545	0.984
100	1263.170	1206.327	0.434	0.896
120	1211.160	963.882	0.369	0.837
140	1052.630	718.044	0.331	0.798
160	792.746	473.170	0.315	0.762
180	275.695	146.272	0.321	0.718

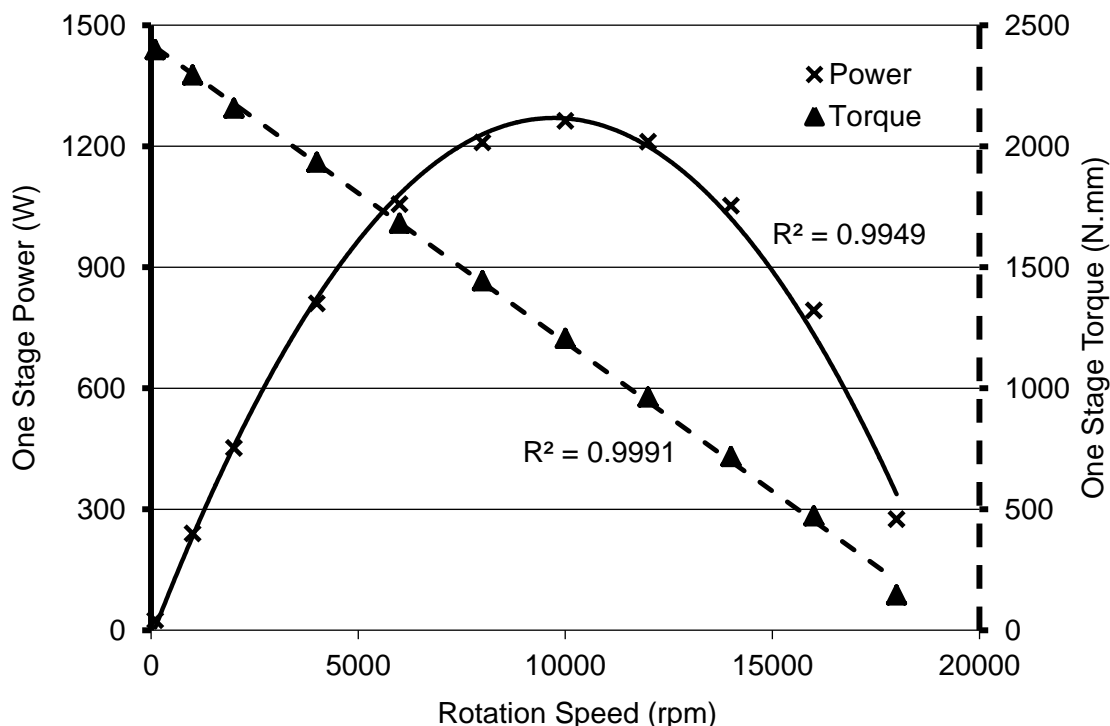


Figure 5.113 CFD simulation results for one stage turbodrill model “B2W16” with water flow rate of 4 L/s at reference radius of 17.6266 mm.

Figure 5.113 shows that the maximum stage efficiency and power for this case is at around 10,000 rpm rotation speed. One stage power and torque at maximum efficiency condition are around 1263 W and 1206 N.mm, respectively. In this case, the runaway turbine speed is almost over 18,000 rpm, and stalled torque is around 2399 N.mm. Figure 5.114 shows the CFD simulation results for one stage turbodrill model “B2W16” with water flow rate of 4 L/s at the rotation speed of 10,000 rpm. This figure shows the velocity profile in the blade to blade view at the span surface 0.5 and also shows the pressure and meridional velocity profiles at meridional surface.

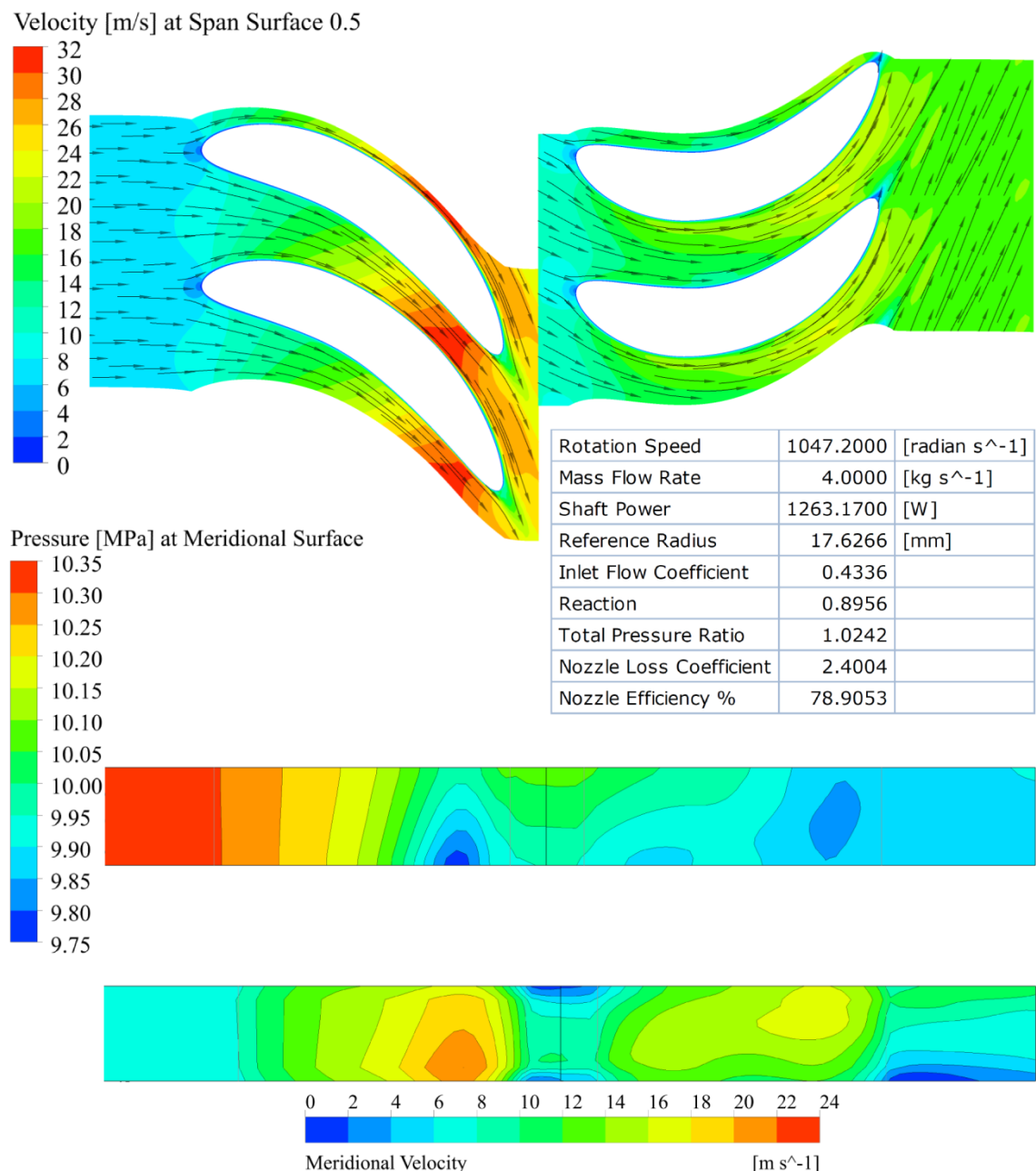


Figure 5.114 CFD simulation results for one stage turbodrill model “B2W16” with water flow rate of 4 L/s at 10,000 rpm rotation speed.

Figures 5.115 and 5.116 show the velocity and pressure values versus normalized streamwise length of stator and rotor at span surface 0.5 for water flow rate of 4 L/s at 10,000 rpm rotation speed through turbodrill stage model “B2W16”. These figures show the velocity and pressure data on the both blade surfaces.

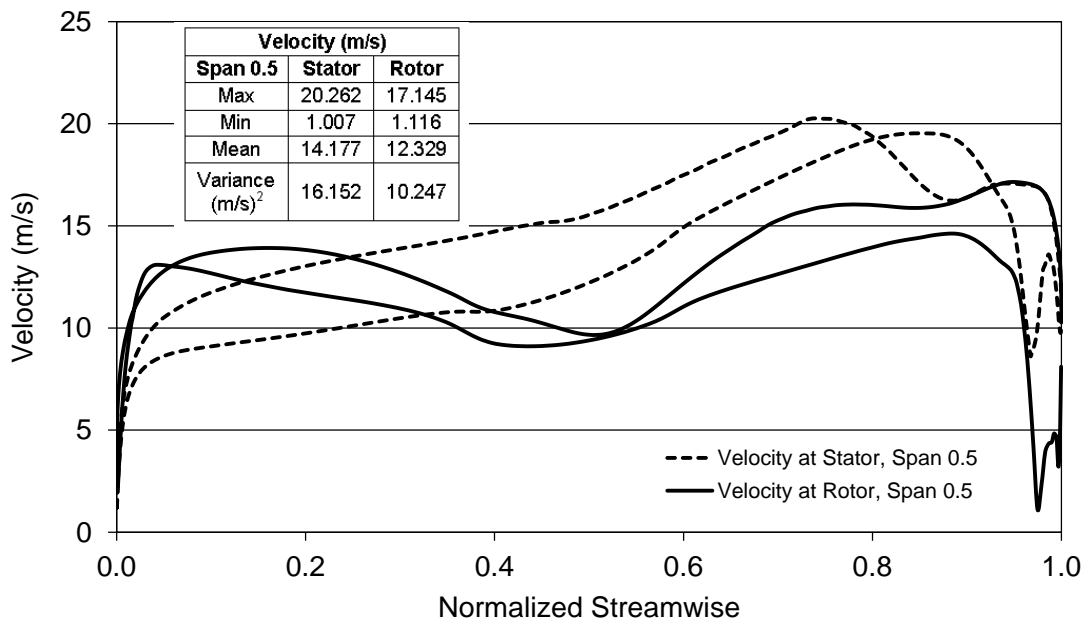


Figure 5.115 Velocity profile versus normalized streamwise for water flow rate of 4 L/s at 10,000 rpm rotation speed through turbodrill stage model “B2W16”.

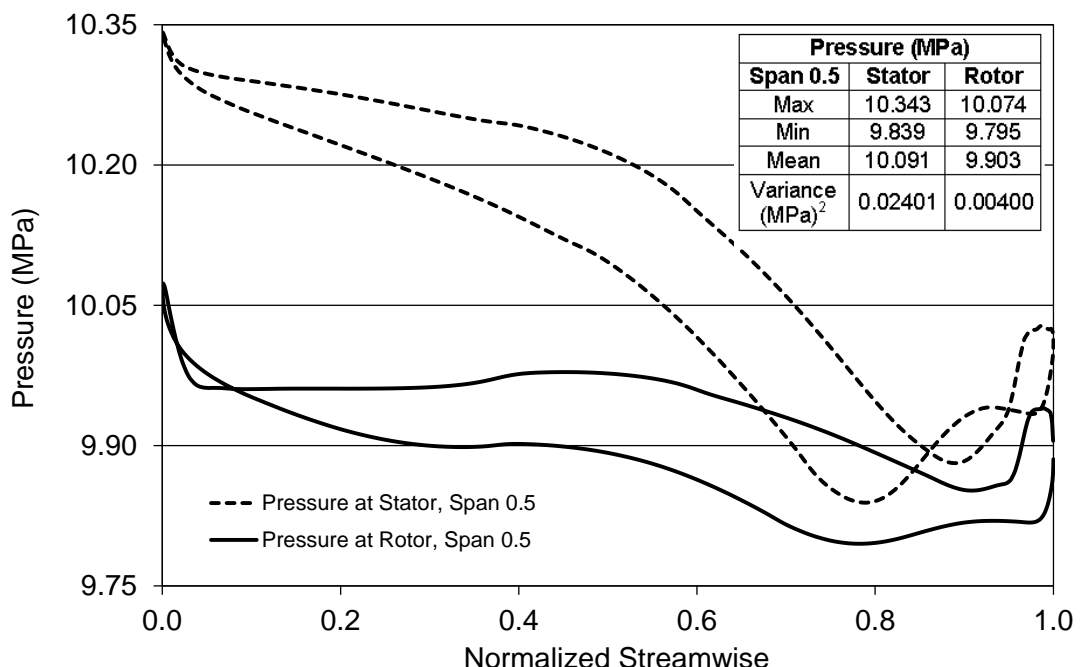


Figure 5.116 Pressure profile versus normalized streamwise for water flow rate of 4 L/s at 10,000 rpm rotation speed through turbodrill stage model “B2W16”.

Table 5.49 shows the structural (FSI) simulation results for stress, strain and deformation on the blades for water flow rate of 4 L/s at 10,000 rpm rotation speed through turbodrill stage model “B2W16” for two different blend radius.

Table 5.49: FSI simulation results for water flow rate of 4 L/s at 10,000 rpm rotation speed through turbodrill stage model “B2W16”.

Static Structural Analysis		Equivalent (Von-Mises) Stress (MPa)	Equivalent Elastic Strain ( $\times 10^{-4}$ mm/mm)	Total Deformation ( $\times 10^{-3}$ mm)
Blend Radius = 0.5 mm	Min	9.345	0.493	0
	Max	190.326	9.866	2.649
Blend Radius = 1.0 mm	Min	7.626	0.400	0
	Max	124.229	6.437	2.097

#### Conclusion remarks for simulation results of water flow through stage model “B2”

Figure 5.117 shows the water flow simulation results for one stage power with different turbodrill stage models with 4 cm shroud diameter and 5 mm blade height (model “B2”). The effect of different geometrical and flow properties on the turbodrill stage “B2” performance is shown in this Figure. It can be inferred that flow rate and the blade numbers on each row have significant effects on the Turbodrill performance.

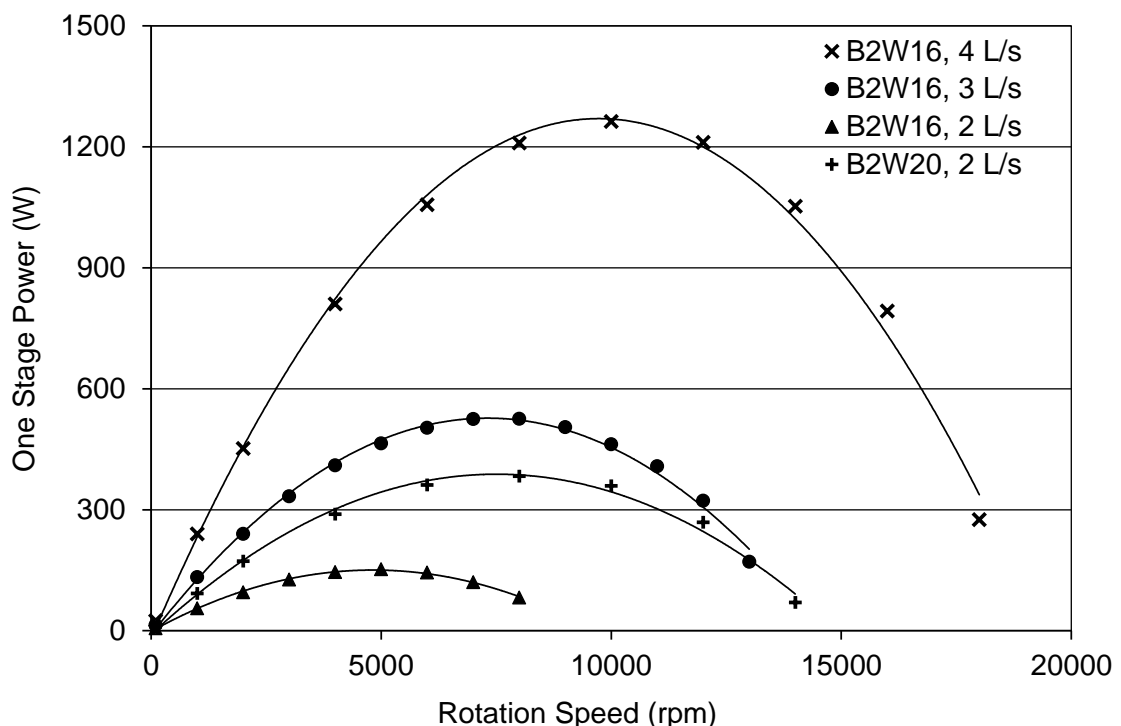


Figure 5.117 CFD simulation results of water flow through one stage turbodrill stage model “B2”.

## 5.6 Air and mist flow simulation results

Air and mist (mixture of air as continuous phase and water droplets as dispersed fluid particle) flow analyses through turbodrill have been considered in this research for seeking ultra-high rotation speeds ( $\geq 10,000$  rpm) with turbine down hole motor. Here, the objective of using mist as drilling fluid is to add some amount of water to the pumped air to provide cooling to the down hole tools and especially to provide sufficient cooling to the impregnated diamond bit which is cutting the rock by grinding action and produce a large amount of heat on the bit face. In following sections air and mist flow simulation results for some of turbodrill stages are reported.

### 5.6.1 Air and mist flow simulation results for Turbodrill stage model “A1”

Air and mist flow simulation results for one stage turbodrill models with 5 cm shroud diameter and 5 mm blade height (span) which are known here as stage model “A1” are presented in this section.

#### **Stage model “A1G25” with air mass flow rate of 0.05 Kg/s**

Table 5.50 shows air flow CFD simulation results for one stage turbodrill model with 5 cm shroud diameter, 5 mm blade height and 25 blades on each blade row (stage model “A1G25”) with air mass flow rate of 0.05 Kg/s.

Table 5.50: CFD simulation results for one stage turbodrill model “A1G25” with air mass flow rate of 0.05 Kg/s.

Speed (rpm $\times 1000$ )	Power (W)	Torque (N.mm)	Inlet Flow Coefficient	Stage Reaction
1	37.814	361.124	33.093	29.386
5	183.040	349.606	6.434	6.276
10	346.169	330.591	3.087	3.336
15	502.113	319.679	2.014	2.475

Table 5.51 shows mist flow CFD simulation results for one stage turbodrill model “A1G25” for mist flow with air mass flow rate of 0.05 Kg/s and different water flow rate at 10,000 rpm rotation speed. Here, perpendicular restitution coefficient (PRC) for the blade’s surfaces are considered to be equal to 1 (PRC=1). The restitution coefficients describe the action of particles when they hit a wall. Coefficient values of 1 described an elastic collision. The parallel restitution coefficient will always be 1.

Table 5.51: CFD simulation results for one stage turbodrill model “A1G25” for mist flow with air mass flow rate of 0.05 Kg/s and different water flow rate for PRC=1 at 10,000 rpm rotation speed.

Water Flow (L/s)	Power (W)	Torque (N.mm)	Inlet Flow Coefficient	Stage Reaction
0.5	347.325	331.695	3.064	3.385
2	339.521	324.243	3.011	3.376
4	325.469	310.823	2.953	3.226
6	316.291	302.058	2.911	3.087
12	295.129	281.848	2.871	2.762
15	290.366	277.300	2.864	2.653
18	287.911	274.955	2.858	2.560

Figure 5.118 shows the CFD simulation results for one stage turbodrill model “A1G25” for mist flow with air mass flow rate of 0.05 Kg/s and water flow rate of 12 L/s for PRC=1 at 10,000 rpm rotation speed. This figure shows the velocity profile in the blade to blade view at the span surface 0.5, and the pressure and meridional velocity profiles at meridional surface. This figure also shows the averaged water droplets volume fraction in the blade to blade view at the span surface 0.5.

Figures 5.119 and 5.120 show the velocity and pressure values versus normalized streamwise length of stator and rotor at span surface 0.5 for mist flow with air mass flow rate of 0.05 Kg/s and water flow rate of 12 L/s for PRC=1 at 10,000 rpm rotation speed through turbodrill stage model “A1G25”. These figures show the velocity and pressure data on the both blade surfaces.

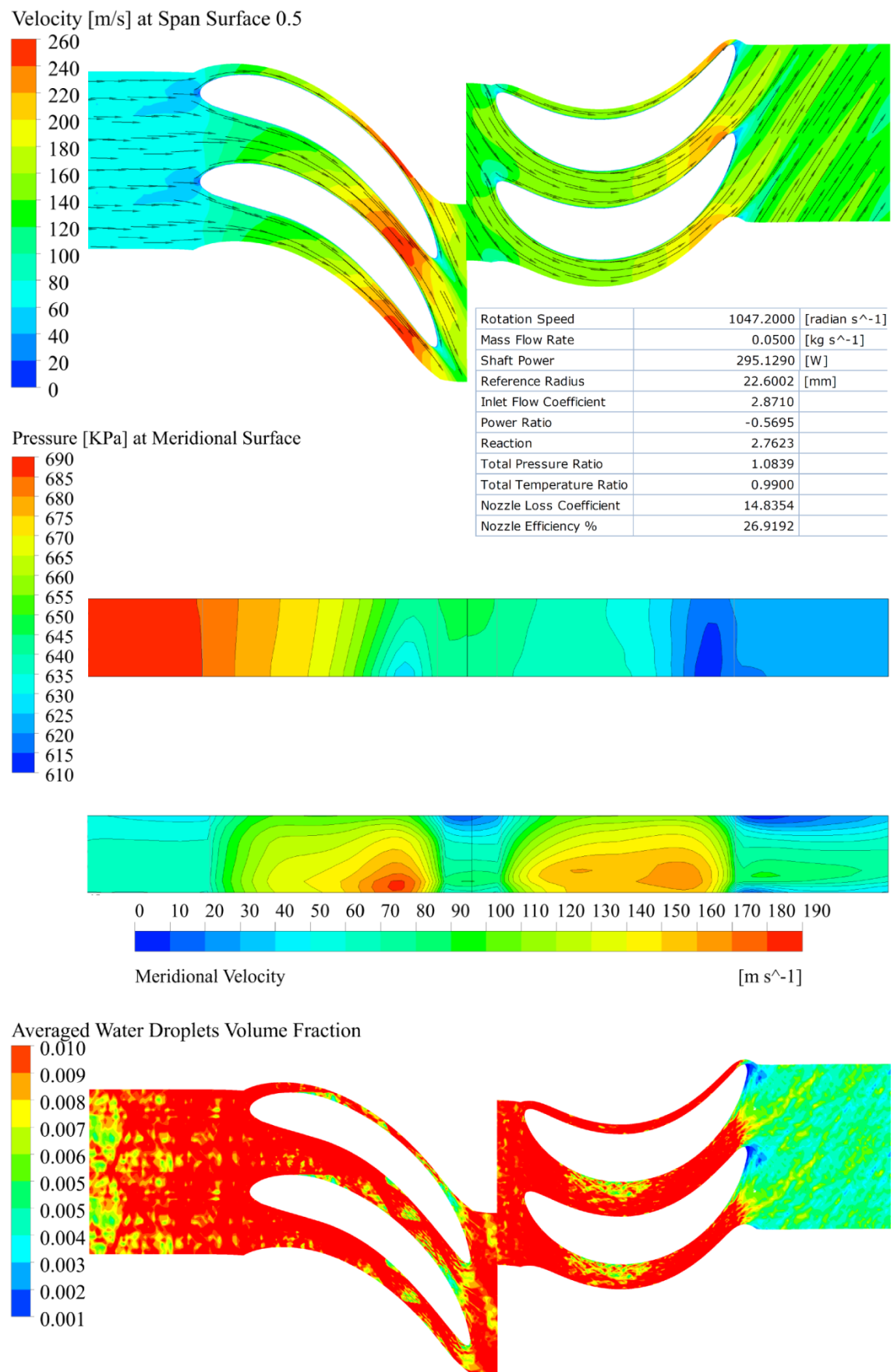


Figure 5.118 CFD simulation results for one stage turbodrill model "A1G25" for mist flow with air mass flow rate of 0.05 Kg/s and water flow rate of 12 L/s for PRC=1 at 10,000 rpm rotation speed.

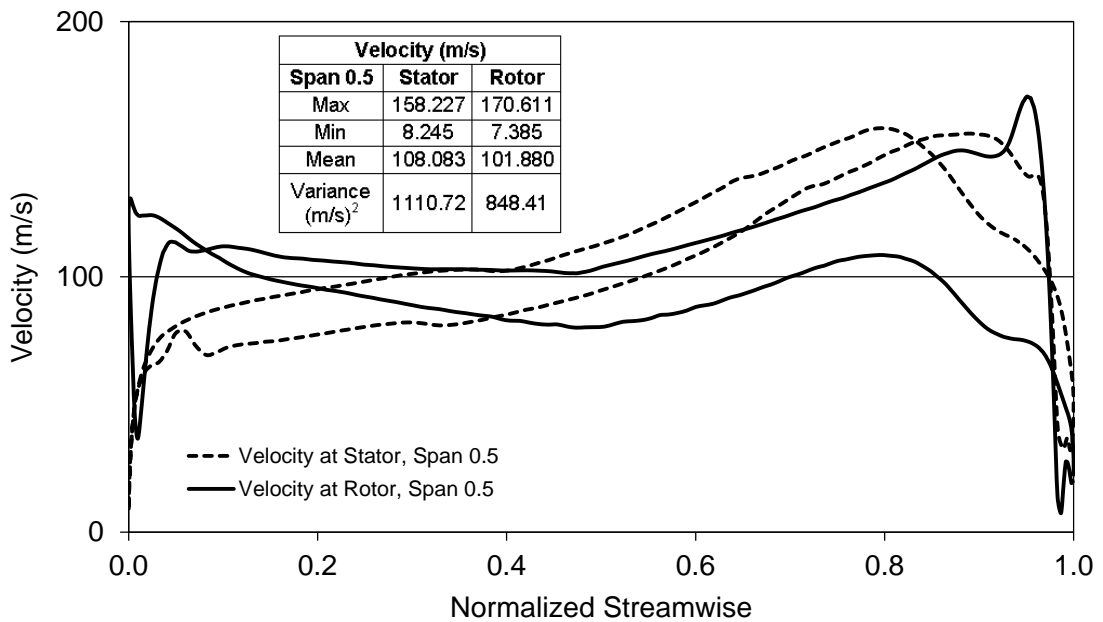


Figure 5.119 Velocity profile versus normalized streamwise for mist flow with air mass flow rate of 0.05 Kg/s and water flow rate of 12 L/s for PRC=1 at 10,000 rpm rotation speed through turbodrill stage model "A1G25".

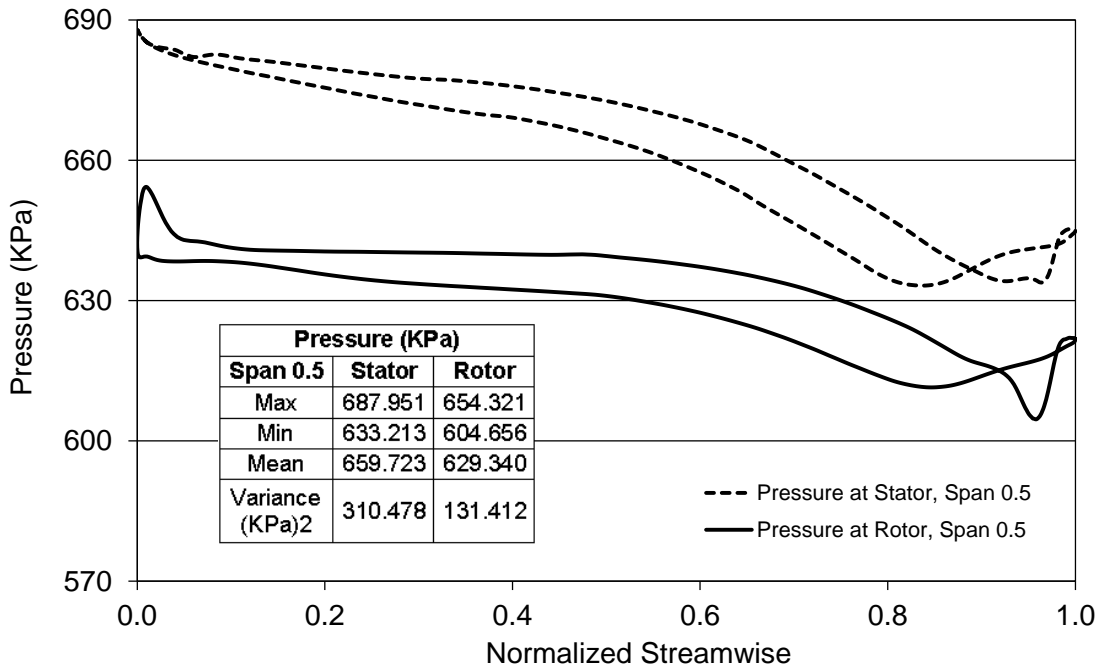


Figure 5.120 Pressure profile versus normalized streamwise for mist flow with air mass flow rate of 0.05 Kg/s and water flow rate of 12 L/s for PRC=1 at 10,000 rpm rotation speed through turbodrill stage model "A1G25".

#### Stage model "A1G25" with air mass flow rate of 0.1 Kg/s

Table 5.52 shows air flow CFD simulation results for one stage turbodrill model with 5 cm shroud diameter, 5 mm blade height and 25 blades on each blade row (stage model "A1G25") with air mass flow rate of 0.1 Kg/s.

Table 5.52: CFD simulation results for one stage turbodrill model “A1G25” with air mass flow rate of 0.1 Kg/s.

Speed (rpm×1000)	Power (W)	Torque (N.mm)	Inlet Flow Coefficient	Stage Reaction
1	149.146	1424.344	64.851	58.654
5	731.015	1396.239	12.768	11.937
10	1412.750	1349.176	6.303	6.045
15	2059.340	1311.113	4.160	4.156

Table 5.53 shows mist flow CFD simulation results for one stage turbodrill model “A1G25” for mist flow with air mass flow rate of 0.1 Kg/s and different water flow rate at 10,000 rpm rotation speed. Here, perpendicular restitution coefficient (PRC) for the blade’s surfaces are considered to be equal to 1 (PRC=1).

Table 5.53: CFD simulation results for one stage turbodrill model “A1G25” for mist flow with air mass flow rate of 0.1 Kg/s and different water flow rate for PRC=1 at 10,000 rpm rotation speed.

Water Flow (L/s)	Power (W)	Torque (N.mm)	Inlet Flow Coefficient	Stage Reaction
0.5	1439.240	1374.474	6.273	6.347
2	1422.570	1358.554	6.222	6.308
6	1340.580	1280.254	6.042	5.998
12	1260.070	1203.367	5.884	5.553
18	1205.360	1151.119	5.814	5.218
30	1150.130	1098.374	5.760	4.755

Figure 5.121 shows the CFD simulation results for one stage turbodrill model “A1G25” for mist flow with air mass flow rate of 0.1 Kg/s and water flow rate of 12 L/s for PRC=1 at 10,000 rpm rotation speed. This figure shows the velocity profile in the blade to blade view at the span surface 0.5, and the pressure and meridional velocity profiles at meridional surface. This figure also shows the averaged water droplets volume fraction in the blade to blade view at the span surface 0.5.

Figures 5.122 and 5.123 show the velocity and pressure values versus normalized streamwise length of stator and rotor at span surface 0.5 for mist flow with air mass flow rate of 0.1 Kg/s and water flow rate of 12 L/s for PRC=1 at 10,000 rpm rotation speed through turbodrill stage model “A1G25”. These figures show the velocity and pressure data on the both blade surfaces.

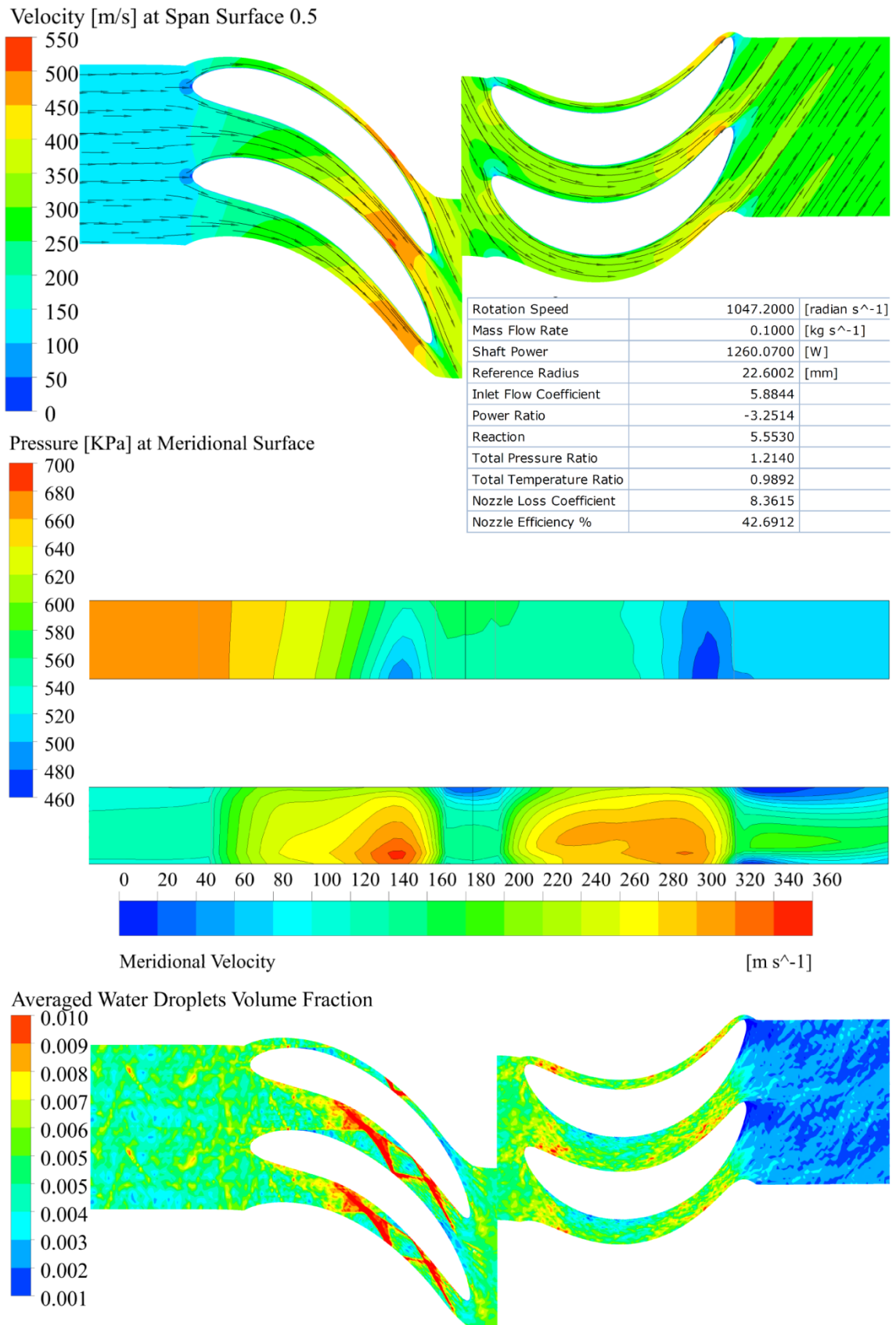


Figure 5.121 CFD simulation results for one stage turbodrill model “A1G25” for mist flow with air mass flow rate of 0.1 Kg/s and water flow rate of 12 L/s for PRC=1 at 10,000 rpm rotation speed.

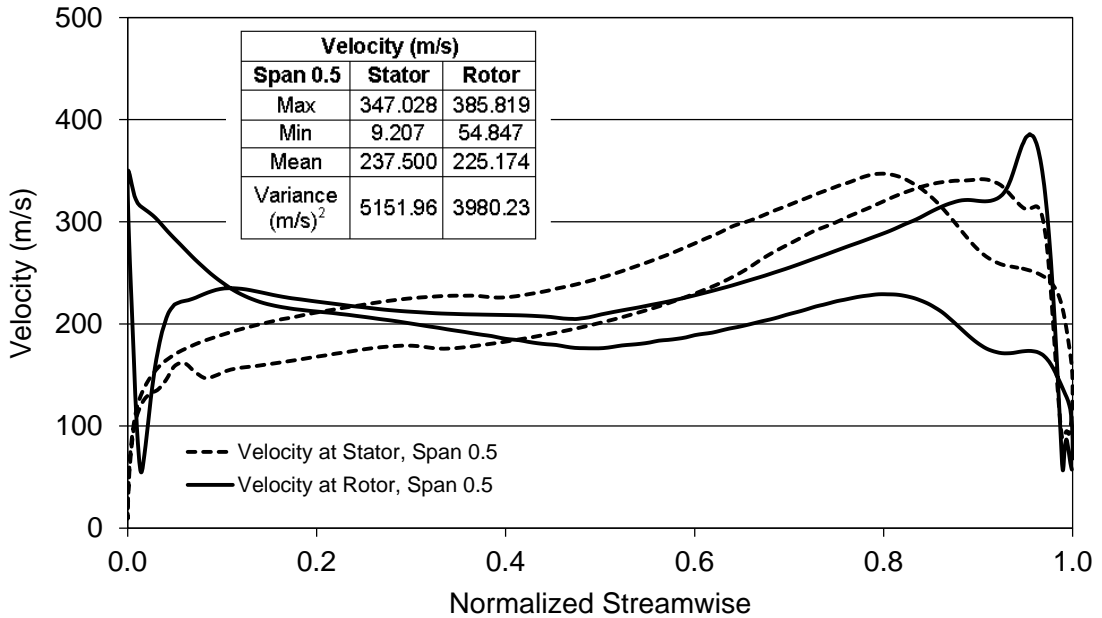


Figure 5.122 Velocity profile versus normalized streamwise for mist flow with air mass flow rate of 0.1 Kg/s and water flow rate of 12 L/s for PRC=1 at 10,000 rpm rotation speed through turbodrill stage model "A1G25".

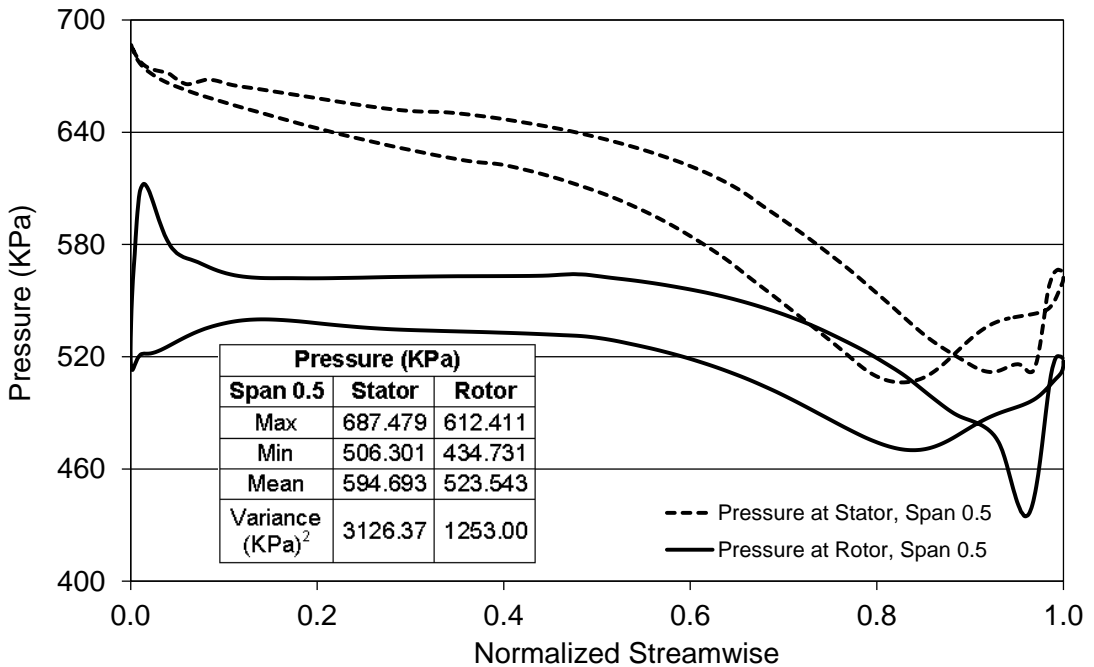


Figure 5.123 Pressure profile versus normalized streamwise for mist flow with air mass flow rate of 0.1 Kg/s and water flow rate of 12 L/s for PRC=1 at 10,000 rpm rotation speed through turbodrill stage model "A1G25".

#### Stage model "A1G25" with air mass flow rate of 0.07 Kg/s

Table 5.54 shows mist flow CFD simulation results for one stage turbodrill model "A1G25" for mist flow with air mass flow rate of 0.07 Kg/s and different water flow rate at 10,000 rpm rotation speed. Here, perpendicular restitution coefficient (PRC) for the blade's surfaces are considered to be equal to 1 (PRC=1).

Table 5.54: CFD simulation results for one stage turbodrill model “A1G25” for mist flow with air mass flow rate of 0.07 Kg/s and different water flow rate for PRC=1 at 10,000 rpm rotation speed.

Water Flow (L/s)	Power (W)	Torque (N.mm)	Inlet Flow Coefficient	Stage Reaction
0.5	694.813	663.546	4.351	4.546
2	682.916	652.185	4.288	4.516
6	639.343	610.573	4.156	4.276
12	598.798	571.852	4.056	3.897
18	573.699	547.883	4.022	3.618
30	557.952	532.844	4.002	3.317

Figure 5.124 shows the CFD simulation results for one stage turbodrill model “A1G25” for mist flow with air mass flow rate of 0.07 Kg/s and water flow rate of 6 L/s for PRC=1 at 10,000 rpm rotation speed. This figure shows the velocity profile in the blade to blade view at the span surface 0.5, and the pressure and meridional velocity profiles at meridional surface. This figure also shows the averaged water droplets volume fraction in the blade to blade view at the span surface 0.5.

Figures 5.125 and 5.126 show the velocity and pressure values versus normalized streamwise length of stator and rotor at span surface 0.5 for mist flow with air mass flow rate of 0.07 Kg/s and water flow rate of 6 L/s for PRC=1 at 10,000 rpm rotation speed through turbodrill stage model “A1G25”. These figures show the velocity and pressure data on the both blade surfaces.

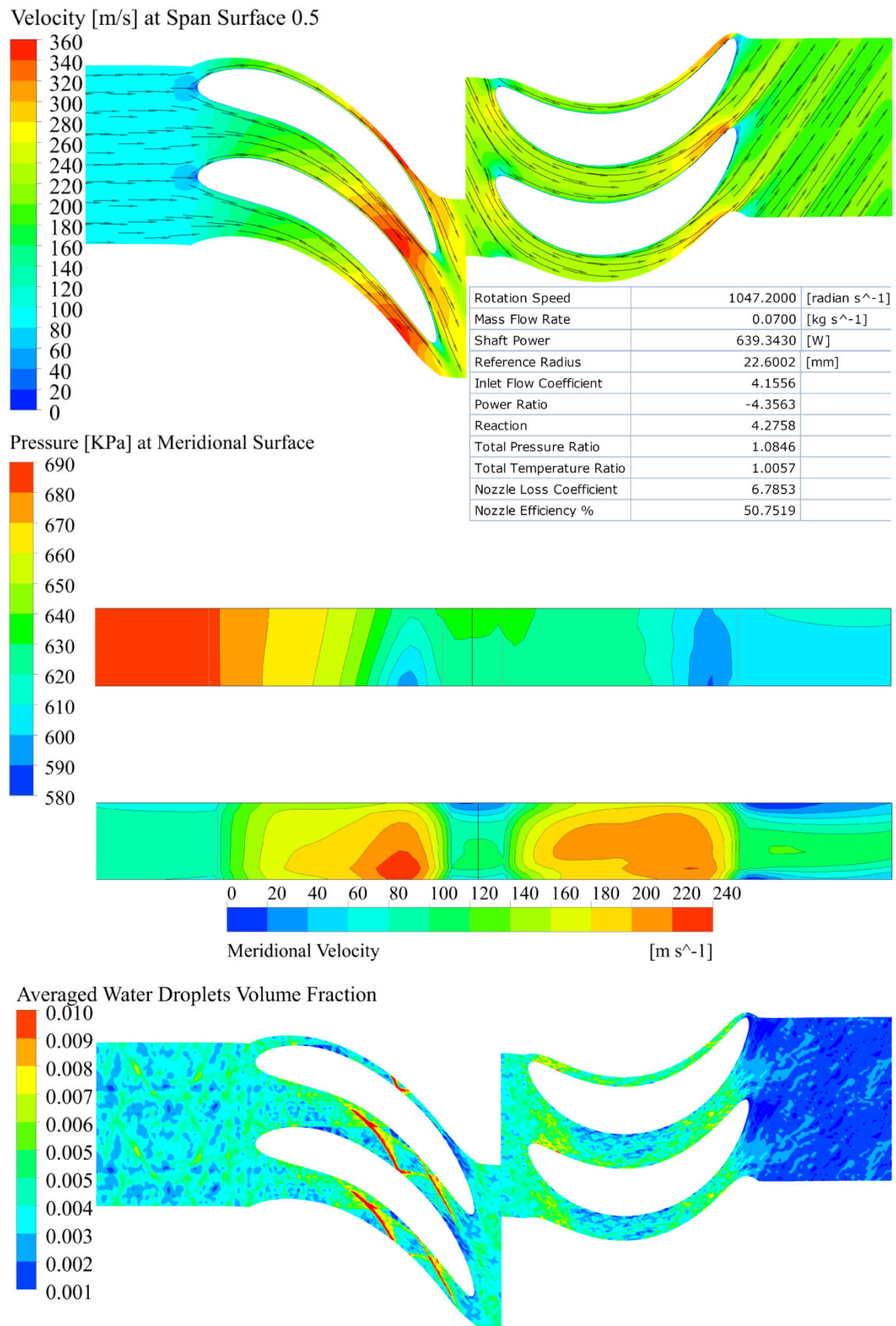


Figure 5.124 CFD simulation results for one stage turbodrill model “A1G25” for mist flow with air mass flow rate of 0.07 Kg/s and water flow rate of 6 L/s for PRC=1 at 10,000 rpm rotation speed.

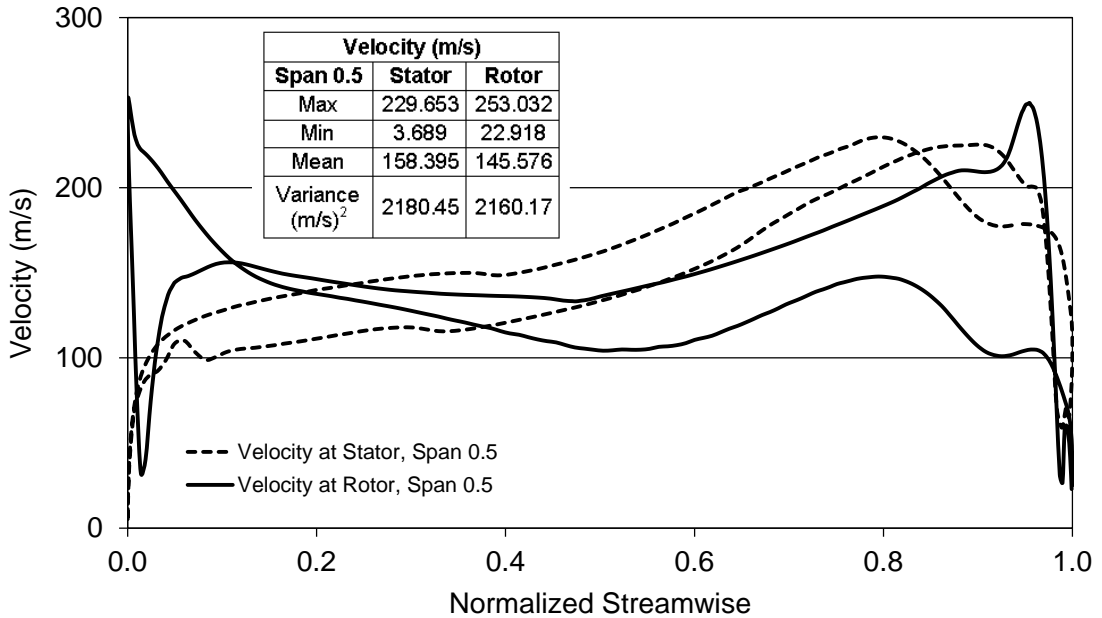


Figure 5.125 Velocity profile versus normalized streamwise for mist flow with air mass flow rate of 0.07 Kg/s and water flow rate of 6 L/s for PRC=1 at 10,000 rpm rotation speed through turbodrill stage model "A1G25".

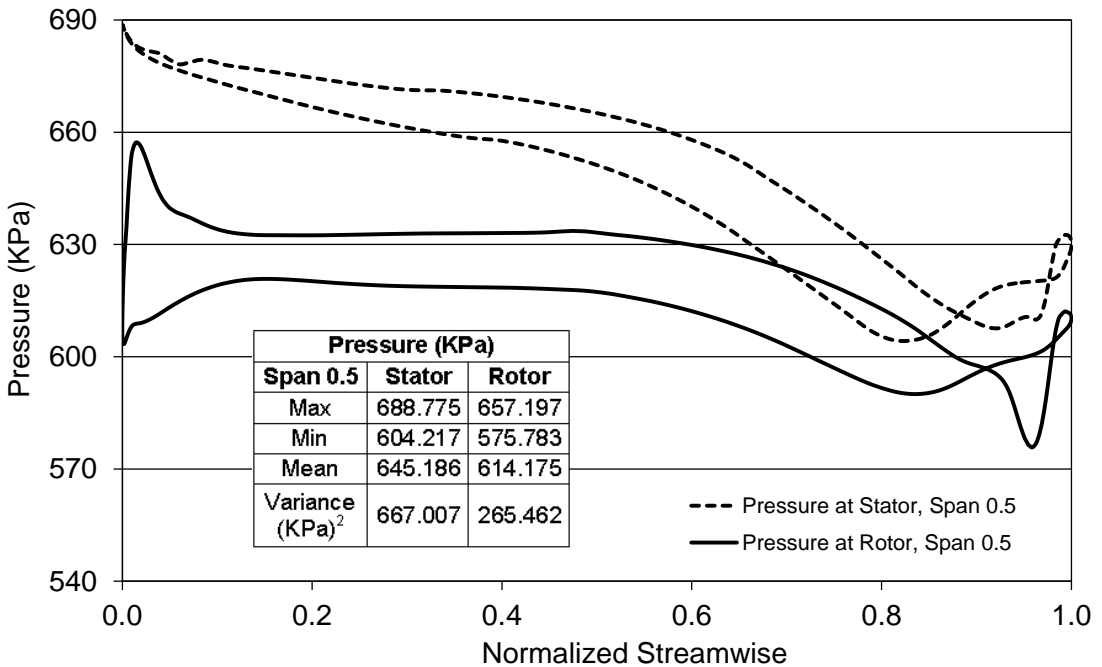


Figure 5.126 Pressure profile versus normalized streamwise for mist flow with air mass flow rate of 0.07 Kg/s and water flow rate of 6 L/s for PRC=1 at 10,000 rpm rotation speed through turbodrill stage model "A1G25".

Figure 5.127 shows the CFD simulation results for one stage turbodrill model "A1G25" for mist flow with air mass flow rate of 0.07 Kg/s and water flow rate of 12 L/s for PRC=1 at 10,000 rpm rotation speed. This figure shows the velocity profile in the blade to blade view at the span surface 0.5, and the pressure and meridional velocity profiles at meridional surface. This figure also shows the averaged water droplets volume fraction in the blade to blade view at the span surface 0.5.

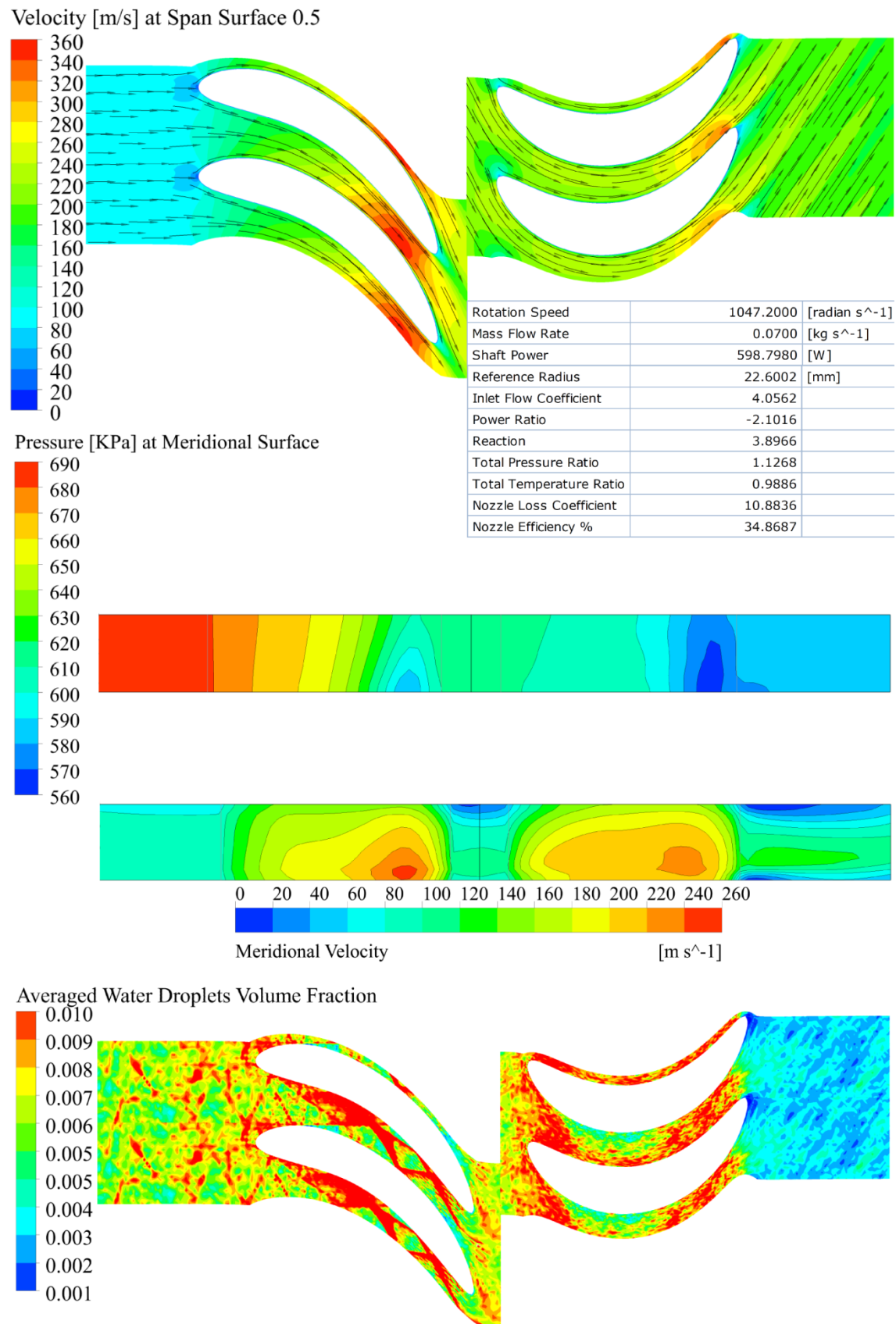


Figure 5.127 CFD simulation results for one stage turbodrill model "A1G25" for mist flow with air mass flow rate of 0.07 Kg/s and water flow rate of 12 L/s for PRC=1 at 10,000 rpm rotation speed.

Table 5.55 shows mist flow CFD simulation results for one stage turbodrill model “A1G25” for mist flow with air mass flow rate of 0.07 Kg/s and different water flow rate at 10,000 rpm rotation speed. Here, perpendicular restitution coefficient (PRC) for the blade’s surfaces are considered to be equal to 0.5 (PRC=0.5).

Table 5.55: CFD simulation results for one stage turbodrill model “A1G25” for mist flow with air mass flow rate of 0.07 Kg/s and different water flow rate for PRC=0.5 at 10,000 rpm rotation speed.

Water Flow (L/s)	Power (W)	Torque (N.mm)	Inlet Flow Coefficient	Stage Reaction
0.5	720.393	687.975	4.399	4.820
2	741.347	707.986	4.370	4.954
6	760.523	726.299	4.311	4.899
12	759.463	725.287	4.213	4.544
18	757.261	723.184	4.165	4.249
30	757.491	723.404	4.094	3.779

Figure 5.128 shows the CFD simulation results for one stage turbodrill model “A1G25” for mist flow with air mass flow rate of 0.07 Kg/s and water flow rate of 12 L/s for PRC=0.5 at 10,000 rpm rotation speed. This figure shows the velocity profile in the blade to blade view at the span surface 0.5, and the pressure and meridional velocity profiles at meridional surface. This figure also shows the averaged water droplets volume fraction in the blade to blade view at the span surface 0.5.

Figures 5.129 and 5.130 show the velocity and pressure values versus normalized streamwise length of stator and rotor at span surface 0.5 for mist flow with air mass flow rate of 0.07 Kg/s and water flow rate of 12 L/s for PRC=0.5 at 10,000 rpm rotation speed through turbodrill stage model “A1G25”. These figures show the velocity and pressure data on the both blade surfaces.

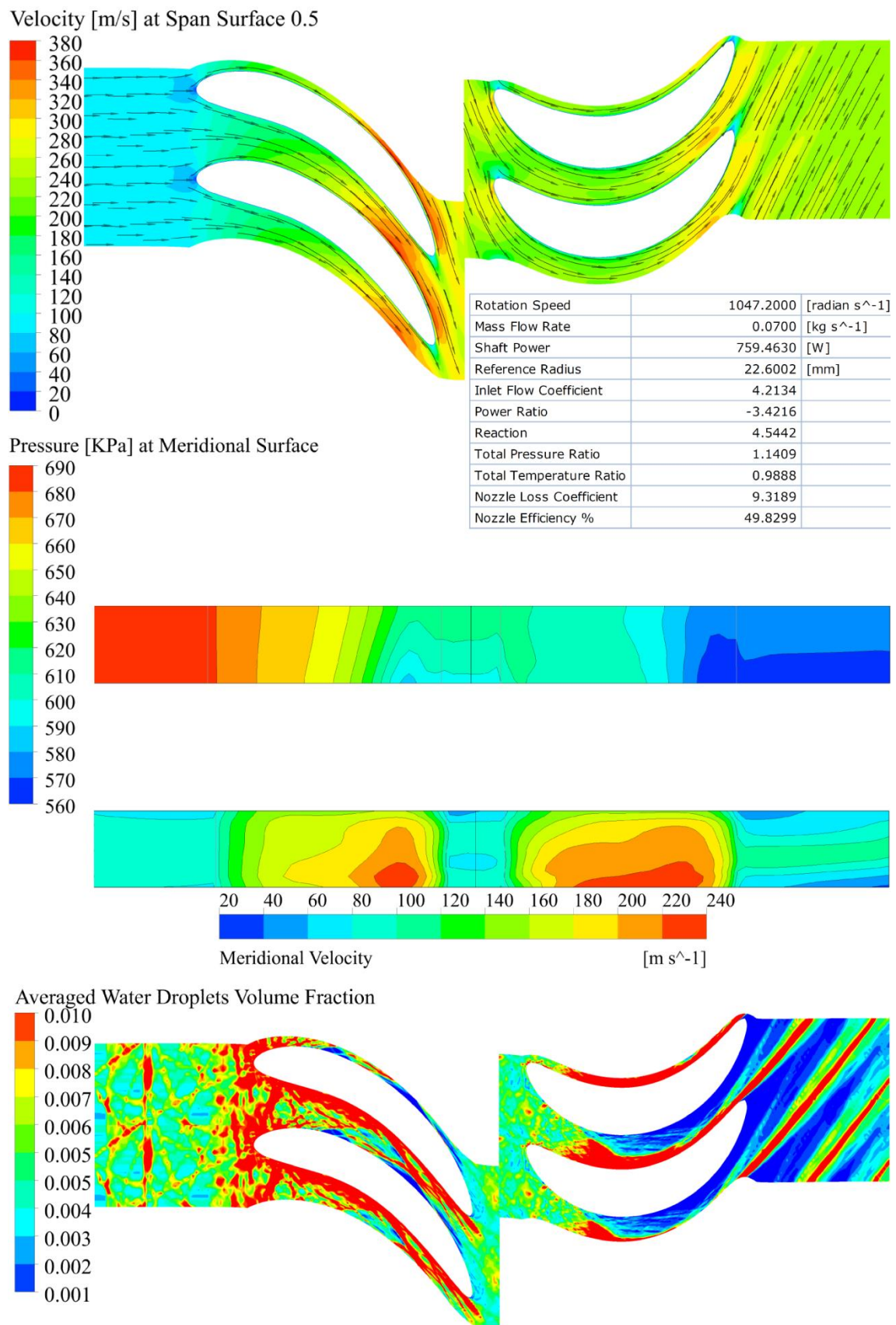


Figure 5.128 CFD simulation results for one stage turbodrill model "A1G25" for mist flow with air mass flow rate of 0.07 Kg/s and water flow rate of 12 L/s for PRC=0.5 at 10,000 rpm rotation speed.

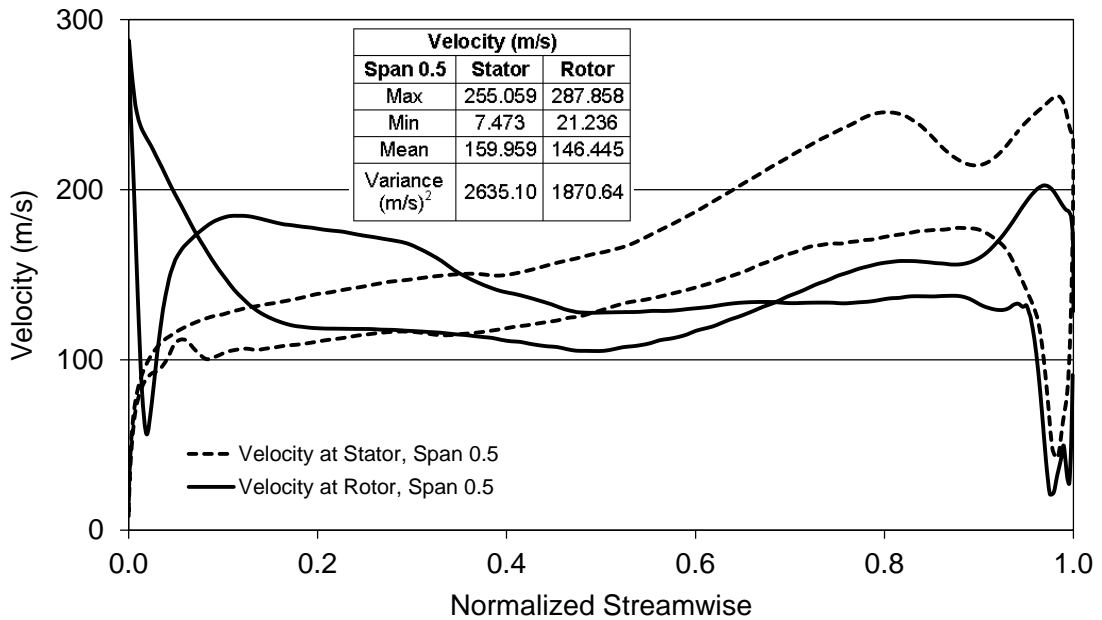


Figure 5.129 Velocity profile versus normalized streamwise for mist flow with air mass flow rate of 0.07 Kg/s and water flow rate of 12 L/s for PRC=0.5 at 10,000 rpm rotation speed through turbodrill stage model "A1G25".

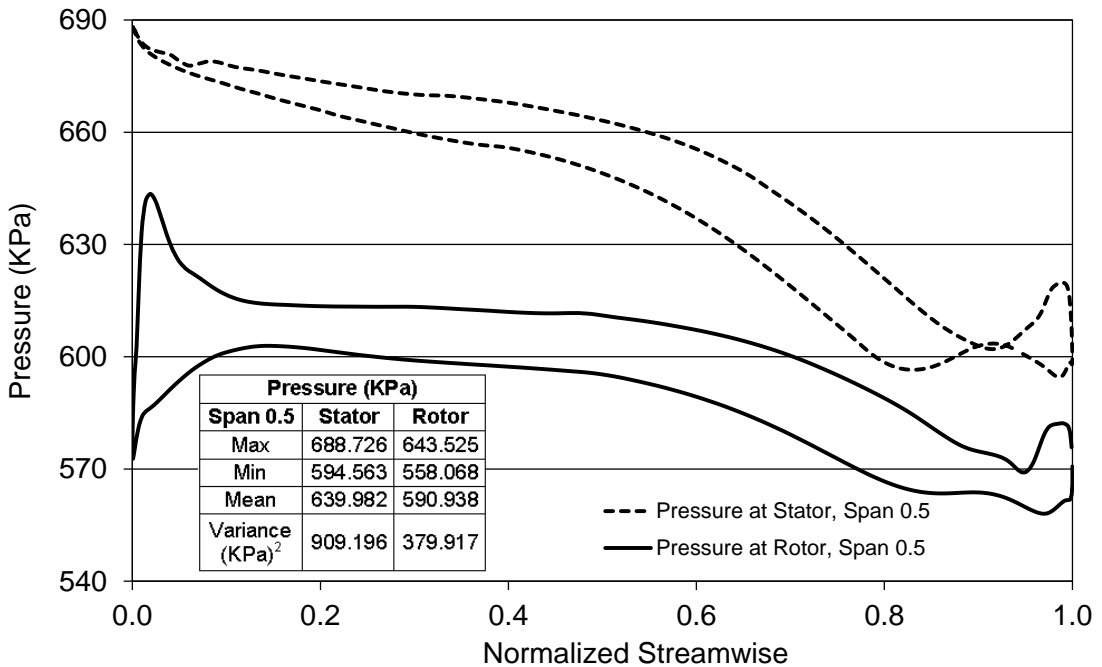


Figure 5.130 Pressure profile versus normalized streamwise for mist flow with air mass flow rate of 0.07 Kg/s and water flow rate of 12 L/s for PRC=0.5 at 10,000 rpm rotation speed through turbodrill stage model "A1G25".

Table 5.56 shows mist flow CFD simulation results for one stage turbodrill model "A1G25" for mist flow with air mass flow rate of 0.07 Kg/s and different water flow rate at 10,000 rpm rotation speed. Here, perpendicular restitution coefficient (PRC) for the blade's surfaces are considered to be equal to 0.1 (PRC=0.1).

Table 5.56: CFD simulation results for one stage turbodrill model “A1G25” for mist flow with air mass flow rate of 0.07 Kg/s and different water flow rate for PRC=0.1 at 10,000 rpm rotation speed.

Water Flow (L/s)	Power (W)	Torque (N.mm)	Inlet Flow Coefficient	Stage Reaction
0.5	721.534	689.065	4.409	4.655
2	758.612	724.474	4.452	4.930
6	775.106	740.226	4.387	4.768
12	769.934	735.287	4.293	4.329
18	719.010	686.655	4.147	4.050

Figure 5.131 shows the CFD simulation results for one stage turbodrill model “A1G25” for mist flow with air mass flow rate of 0.07 Kg/s and water flow rate of 12 L/s for PRC=0.1 at 10,000 rpm rotation speed. This figure shows the velocity profile in the blade to blade view at the span surface 0.5, and the pressure and meridional velocity profiles at meridional surface. This figure also shows the averaged water droplets volume fraction in the blade to blade view at the span surface 0.5.

Figures 5.132 and 5.133 show the velocity and pressure values versus normalized streamwise length of stator and rotor at span surface 0.5 for mist flow with air mass flow rate of 0.07 Kg/s and water flow rate of 12 L/s for PRC=0.1 at 10,000 rpm rotation speed through turbodrill stage model “A1G25”. These figures show the velocity and pressure data on the both blade surfaces.

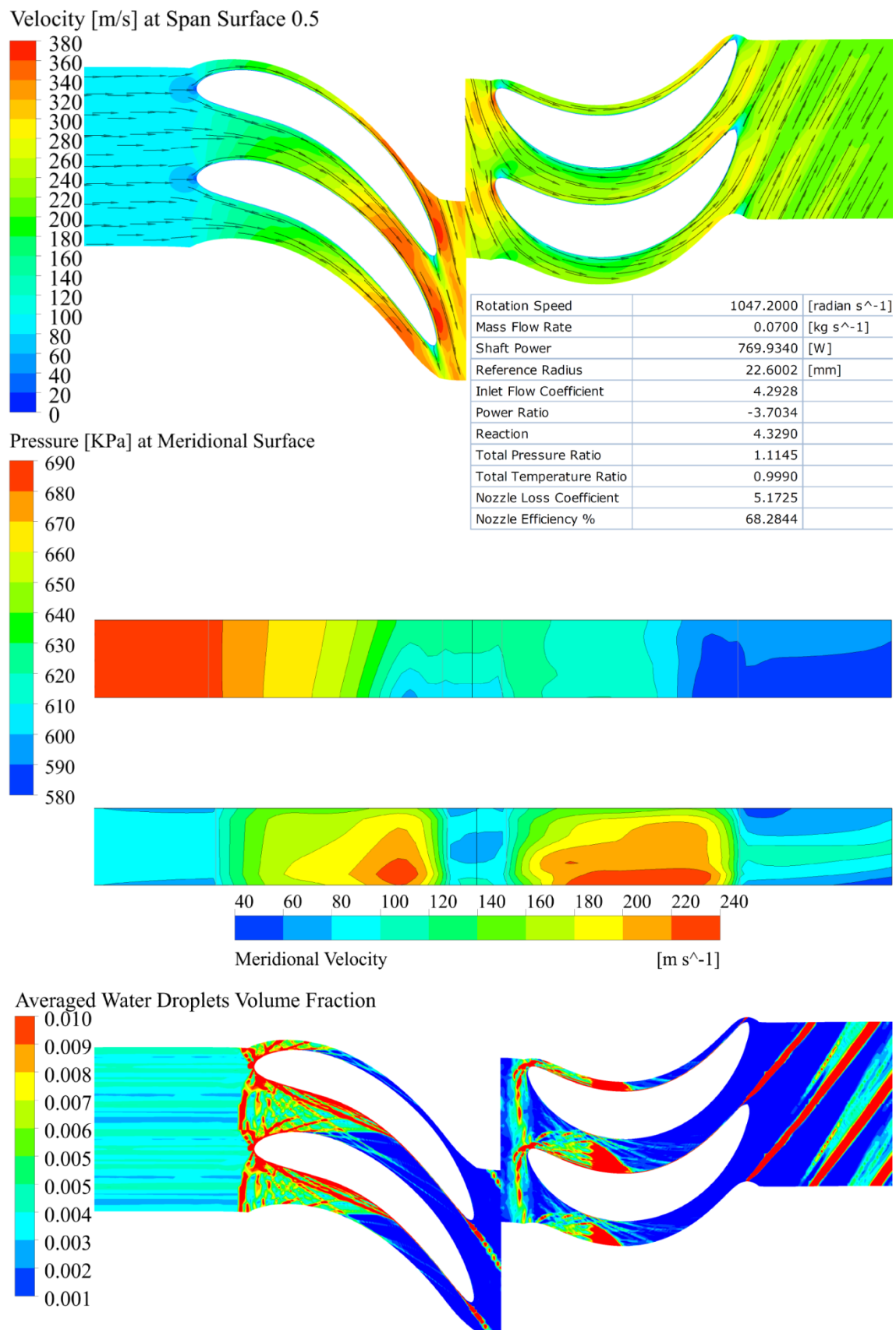


Figure 5.131 CFD simulation results for one stage turbodrill model "A1G25" for mist flow with air mass flow rate of 0.07 Kg/s and water flow rate of 12 L/s for PRC=0.1 at 10,000 rpm rotation speed.

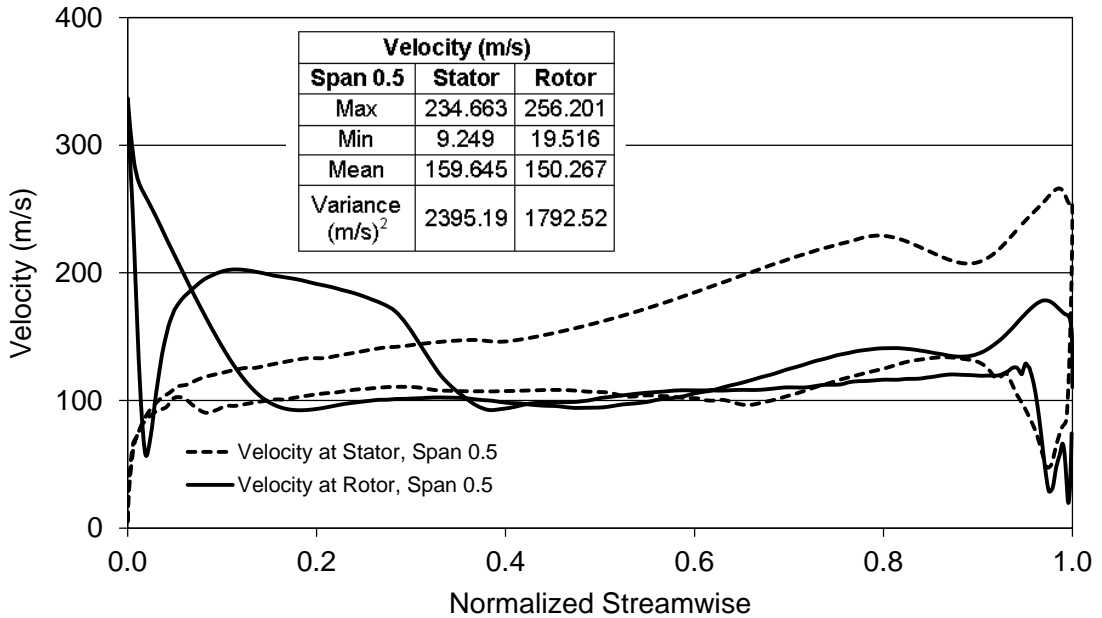


Figure 5.132 Velocity profile versus normalized streamwise for mist flow with air mass flow rate of 0.07 Kg/s and water flow rate of 12 L/s for PRC=0.1 at 10,000 rpm rotation speed through turbodrill stage model "A1G25".

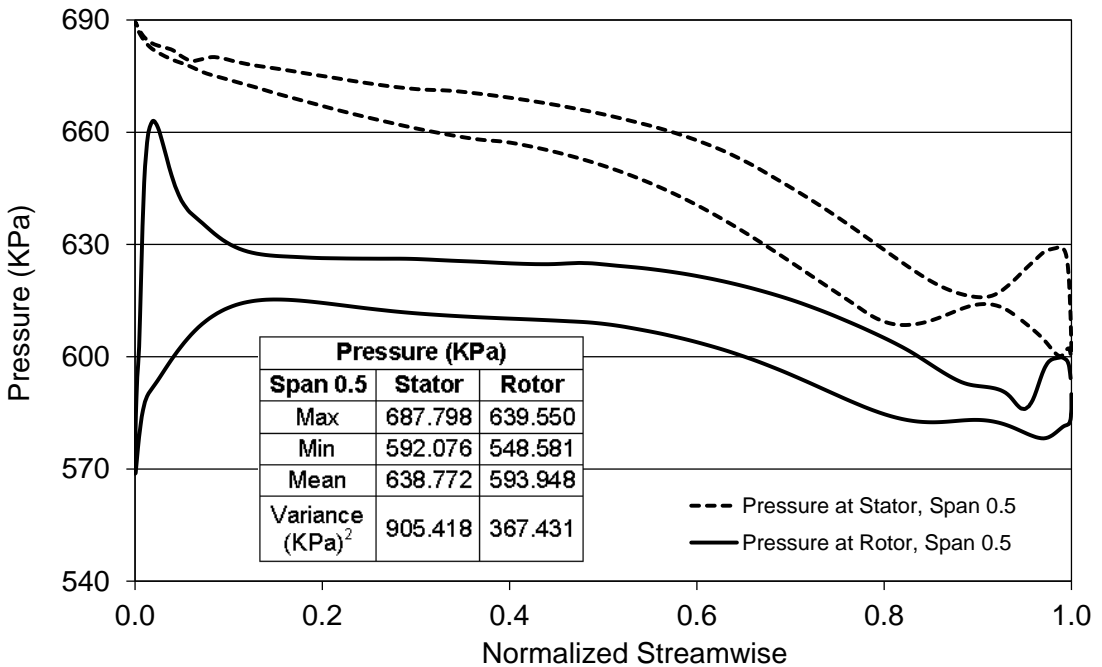


Figure 5.133 Pressure profile versus normalized streamwise for mist flow with air mass flow rate of 0.07 Kg/s and water flow rate of 12 L/s for PRC=0.1 at 10,000 rpm rotation speed through turbodrill stage model "A1G25".

#### Stage model "A1G22" with air mass flow rate of 0.1 Kg/s

Table 5.57 shows mist flow CFD simulation results for one stage turbodrill model "A1G22" for mist flow with air mass flow rate of 0.1 Kg/s and different water flow rate at 10,000 rpm rotation speed. Here, perpendicular restitution coefficient (PRC) for the blade's surfaces are considered to be equal to 1 (PRC=1).

Table 5.57: CFD simulation results for one stage turbodrill model “A1G22” for mist flow with air mass flow rate of 0.1 Kg/s and different water flow rate for PRC=1 at 10,000 rpm rotation speed.

Water Flow (L/s)	Power (W)	Torque (N.mm)	Inlet Flow Coefficient	Stage Reaction
2	1228.800	1173.504	5.901	5.670
6	1150.160	1098.403	5.778	5.233
12	1086.390	1037.502	5.683	4.791
18	1040.140	993.334	5.640	4.469

Figure 5.134 shows the CFD simulation results for one stage turbodrill model “A1G22” for mist flow with air mass flow rate of 0.1 Kg/s and water flow rate of 12 L/s for PRC=1 at 10,000 rpm rotation speed. This figure shows the velocity profile in the blade to blade view at the span surface 0.5, and the pressure and meridional velocity profiles at meridional surface. This figure also shows the averaged water droplets volume fraction in the blade to blade view at the span surface 0.5.

Figures 5.135 and 5.136 show the velocity and pressure values versus normalized streamwise length of stator and rotor at span surface 0.5 for mist flow with air mass flow rate of 0.1 Kg/s and water flow rate of 12 L/s for PRC=1 at 10,000 rpm rotation speed through turbodrill stage model “A1G22”. These figures show the velocity and pressure data on the both blade surfaces.

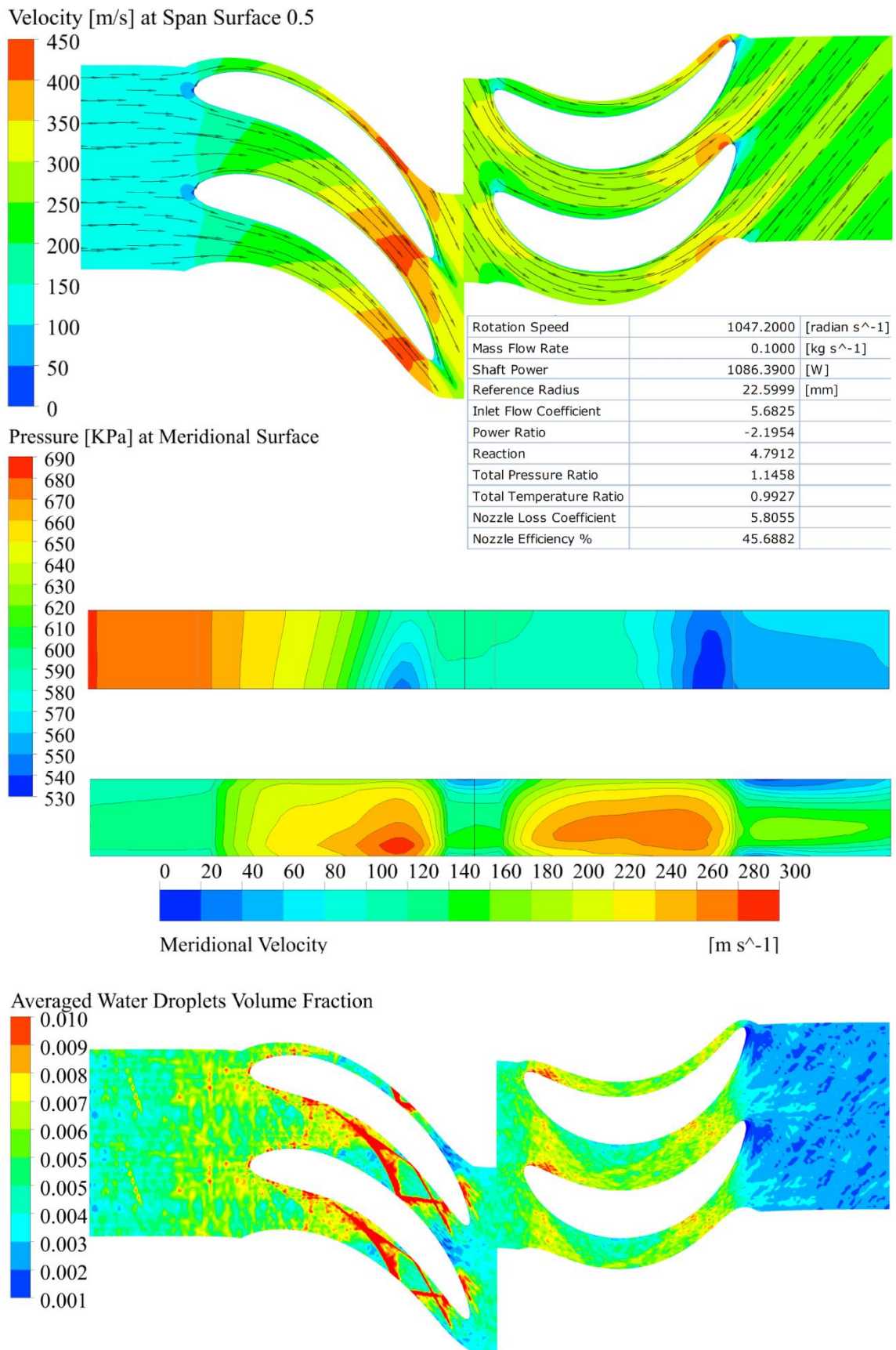


Figure 5.134 CFD simulation results for one stage turbodrill model "A1G22" for mist flow with air mass flow rate of 0.1 Kg/s and water flow rate of 12 L/s for PRC=1 at 10,000 rpm rotation speed.

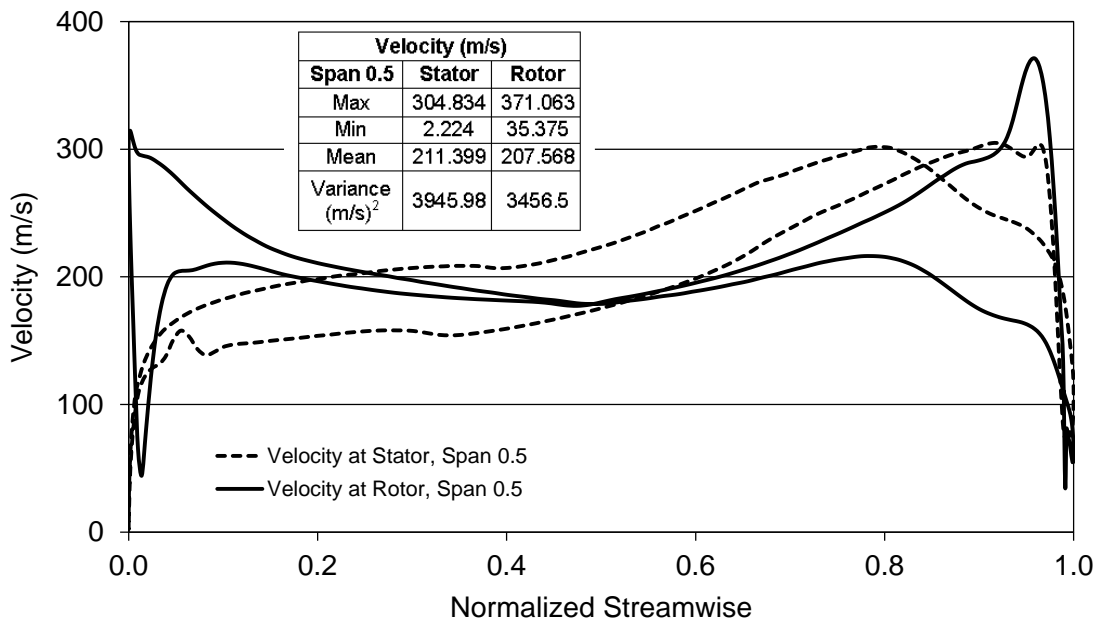


Figure 5.135 Velocity profile versus normalized streamwise for mist flow with air mass flow rate of 0.1 Kg/s and water flow rate of 12 L/s for PRC=1 at 10,000 rpm rotation speed through turbodrill stage model "A1G22".

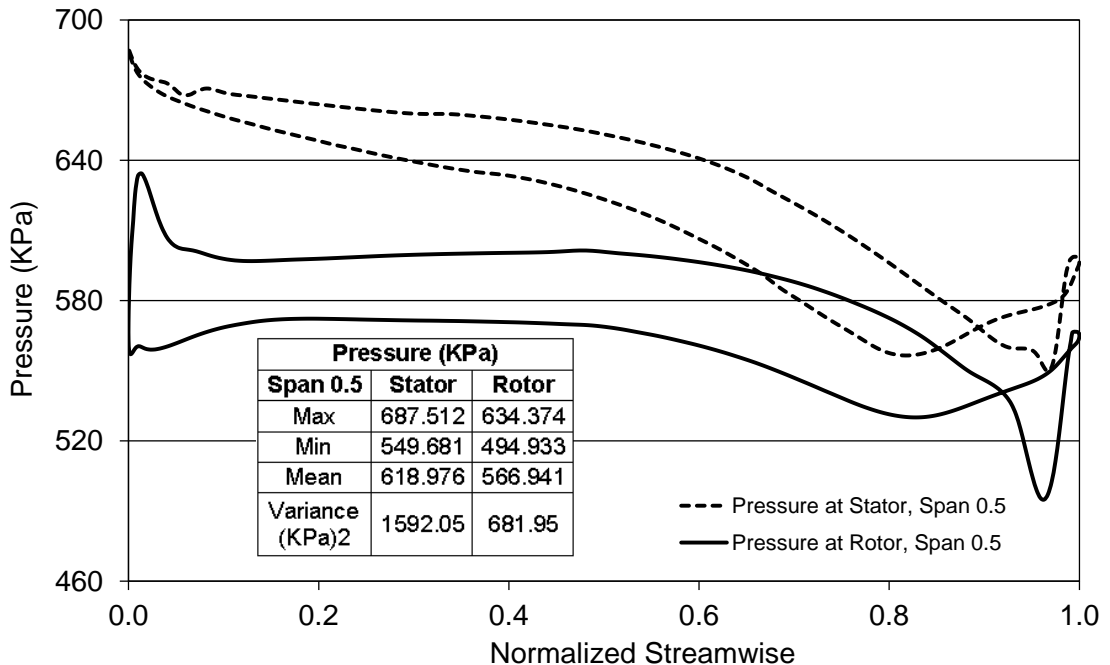


Figure 5.136 Pressure profile versus normalized streamwise for mist flow with air mass flow rate of 0.1 Kg/s and water flow rate of 12 L/s for PRC=1 at 10,000 rpm rotation speed through turbodrill stage model "A1G22".

### 5.6.2 Conclusion remarks for air and mist flow simulation results

With applicable air and mist mass flow rates through turbodrill, much higher rotation speeds and output power are resulted in comparison with applicable water flow rates. In the mist flow analyses, different water particle flow rates and perpendicular restitution coefficient values have considerable influence on the turbodrill performance.

## 5.7 Summary

In the first part of this Chapter, CFD and FSI simulation processes were discussed for fluid flow analysis through turbodrill. Grid convergence studies for CFD and FSI simulations were reported. Comprehensive simulation results for water, air and mist flow through different turbodrill stage models were presented in detail with the performance chart for each stage model. The performance chart for each turbodrill stage model helped us to compare and proposed the proper stage model for applications of this study. Similar approaches can be adopted for designing an optimised turbodrill for any other drilling conditions and drilling fluid properties.

# 6

# Conclusions and future work

In this thesis, for the first time, several small diameters (5-6 cm OD) down hole turbine motors with ultra-high optimum rotation speeds (5-10 thousand rpm) were designed. This was done through a comprehensive full scale (3D) numerical fluid flow analyses with the aid of Computational Fluid Dynamics (CFD) and Fluid-Structural Interaction (FSI) analyses. The effects of various design specifications, fluid types and properties on the turbodrill performance with real drilling conditions were evaluated. The design platform and approach in this study is applicable to any turbodrill size and specifications to be optimised for any complex fluid flow properties for both petroleum and mining drilling applications.

Proposed turbodrill stage models for water flow are presented in Section 6.1. In addition the prototyped turbodrill stage and the opportunities for future study and work are reported in Sections 6.2 and 6.3, respectively.

## 6.1 Proposed Turbodrill stage models

This thesis concludes that in drilling deep hard rocks with low weight on bit coiled tubing system, to maximize the rate of penetration (ROP) through the drilling interval, high rotation speed (RPM) is the key driver. Therefore turbodrill (turbine motors) was identified as the best choice to be used for these applications which results in a smooth and good quality borehole with little vibrational effects during drilling. In addition, in this study, based on the down hole power and speed requirements for small size coiled tubing drilling in deep hard rocks, a small diameter turbodrill composed of several stages was designed specifically to provide the required power and speed at shortest possible length with applicable range of the flow rates.

When designing and simulating a hydraulic multistage turbodrill, it was assumed that each turbodrill stage is identical and that the flow rate, pressure drop, rotary speed, generated torque, and power transmitted to the shaft are the same for each of the stages. As a result, turbodrill performance is composed of performance of several identical stages stacked close to each other and connected to the turbodrill shaft. In this study, performance of one stage turbodrill with different geometrical models was investigated

using CFD and FSI analyses with variety of real working conditions (see Chapter 3). Each stage is composed of first one stator blade row and then one rotor blade row with plurality of blades on them. The number of blades on each row is equal for both the stator and the rotor.

In this study, for the purpose of hard rocks mineral exploration drilling, clean water was considered as the main drilling fluid for the simulation purposes. In addition, air flow and mist flow (mixture of air as continuous phase and water droplets as dispersed fluid particle) were considered and analysed for reaching higher rotation speeds for the future needs once the new bit developments allow high rotation speeds ( $\geq 10,000$  rpm) to be applied. Here, the objective of using mist as drilling fluid is to add some amount of water to the pumped air to provide cooling to the down hole tools and especially to provide sufficient cooling to the impregnated diamond bit which is cutting the rock by grinding action and producing a large amount of head force on the bit face.

The results of this study also showed that the quality of CFD simulation is highly dependent to the quality of the mesh. Here, the reduction in spatial discretisation error which is known as grid convergence study for both water and air flows and for the two turbulence models of  $k-\varepsilon$  and SST were reported in Chapter 5. The objective was to demonstrate accuracy and convergence of the analysis to the “exact numerical solution” with progressive mesh refinement. The results also showed that using SST turbulence model instead of  $k-\varepsilon$  model in CFD, generally yields more accurate results, especially with blade boundary layer refinement.

According to the CFD results presented in Chapter 5, for water flow, amongst all the stage models presented in Chapter 3, two selected turbodrill stage models with two different outer diameters and blade heights are proposed for the small coiled tubing assembly in hard rocks mineral exploration drilling. The selected turbodrill stage model should provide the highest optimum rotation speed, power and efficiency with the lowest flow capacity.

Based on the CFD simulations, it was concluded that the flow rate has a significant effect on the turbodrill performance. After that, the numbers of blades on each row, the outlet stator blade angle and fluid viscosity have the most considerable influence on the turbodrill performance. As a result, the turbodrill performance should be evaluated for each operation condition, separately.

The length of the turbine motor section is dependent to the number of stages needed to provide the required range of power and torque with a specific water flow rate. The

required power and torque are dependent to several drilling conditions and formation properties. A brief calculation of the power and torque for drilling typical hard rocks for two hole sizes with 60 mm and 70 mm diameters were reported in Section 3.1. As a result, the number of identical turbine stages for generating the required power for any specific conditions is calculated by dividing the overall power required based on the rock-bit interaction laws to the power generated by each stage.

The first model proposed here is the stage model of “A1W20” with 50 mm shroud diameter and blade height or span of 5 mm. The geometrical specifications of this turbodrill stage model were shown in Figure 3.7 that has an outer diameter of 60 mm. Water flow CFD simulation results for one stage turbodrill model “A1W20” with water flow rate of 3 L/s and 4 L/s at the reference radius of 22.5987 mm were shown in Figures 5.32 and 5.45, respectively. With 3 L/s water flow rate, the optimum rotation speed is around 4,000 rpm, and one stage power and torque at maximum efficient condition are around 300 W and 705 N.mm, respectively. With 4 L/s water flow rate, the optimum rotation speed is around 6,000 rpm, and one stage power and torque at maximum efficient condition are around 725 W and 1152 N.mm, respectively.

The second proposed model is the stage model of “B1W20” with 40 mm shroud diameter and blade height or span of 3 mm. The geometrical specifications of this turbodrill stage model were shown in Figure 3.24 that has an outer diameter of 48 mm. Water flow CFD simulation results for one stage turbodrill model “B1W20” with water flow rate of 2 L/s at the reference radius of 18.5438 mm were shown in Figure 5.88. With 2 L/s water flow rate, the optimum rotation speed is around 10,000 rpm, and one stage power and torque at maximum efficient condition are around 760 W and 726 N.mm, respectively.

As a result, for the water flow driven motor the small diameter turbodrill stage model with smaller blade’s height produces higher rotation speed and power with less torque by even less water flow rate comparing to the larger diameter one. This also suits more to the application of this study with the small bit diameter, the higher rotation speeds can be applied for faster drilling. Therefore, the turbodrill stage model of “B1W20” is more suitable for application of this study in which with low flow rate produces the required output for small low weight on bit coiled tubing system.

In addition, air and mist flow simulation results for one stage turbodrill models with 5 cm shroud diameter and 5 mm blade height (span) which are known here as stage model “A1” were also presented in Chapter 5. The simulation results showed that with

applicable air and mist mass flow rates through turbodrill, much higher rotation speeds and output power are resulted in comparison with applicable water flow rates. Furthermore, in the mist flow analyses, different water particle flow rates and perpendicular restitution coefficient values have considerable influence on the turbodrill performance.

Finally, after performing the CFD simulations, to evaluate the mechanical stresses and deflections caused by the fluid mechanical pressure loading, one-way coupling of solution fields in fluid and solid domains were calculated by means of FSI analysis. In this way, the forces acting on solid surfaces were extracted from CFD simulations and then imported as major boundary conditions to the structural analyses. For the purpose of the structural analyses, general stainless steel was assigned as the material for the blade body. The quality of FSI simulation was studied and reported in Chapter 5 based on the quality of the structural mesh (mesh convergence study) on the blade body. The FSI results showed that the maximum stress, strain and deformation caused by the fluid flow were in a reasonable margin and could be managed with a suitable type of stainless steel. Surface treatments are needed for the blade surfaces to be wear resistance against the unavoidable solid particles present in water flow.

## **6.2 Turbodrill stage prototype**

The proposed turbodrill stage models for the applications of this study were prototyped by 3D printing machine (rapid prototyping) for demonstration purposes. In the 3D printer, the 3D model is read from Computer Aided Design (CAD) software, then transformed into thin, virtual, horizontal cross-sections and subsequently creates successive layers until the model is complete. The standard data interface between CAD software and the 3D printer is the Standard Template Library (STL) file format. An STL file approximates the shape of a part or assembly using triangular facets. Smaller facets produce a higher quality surface. Figure 6.1 shows the prototyped turbodrill stage model which was made of polymer powder. The model shown here has a cut through for better illustration.

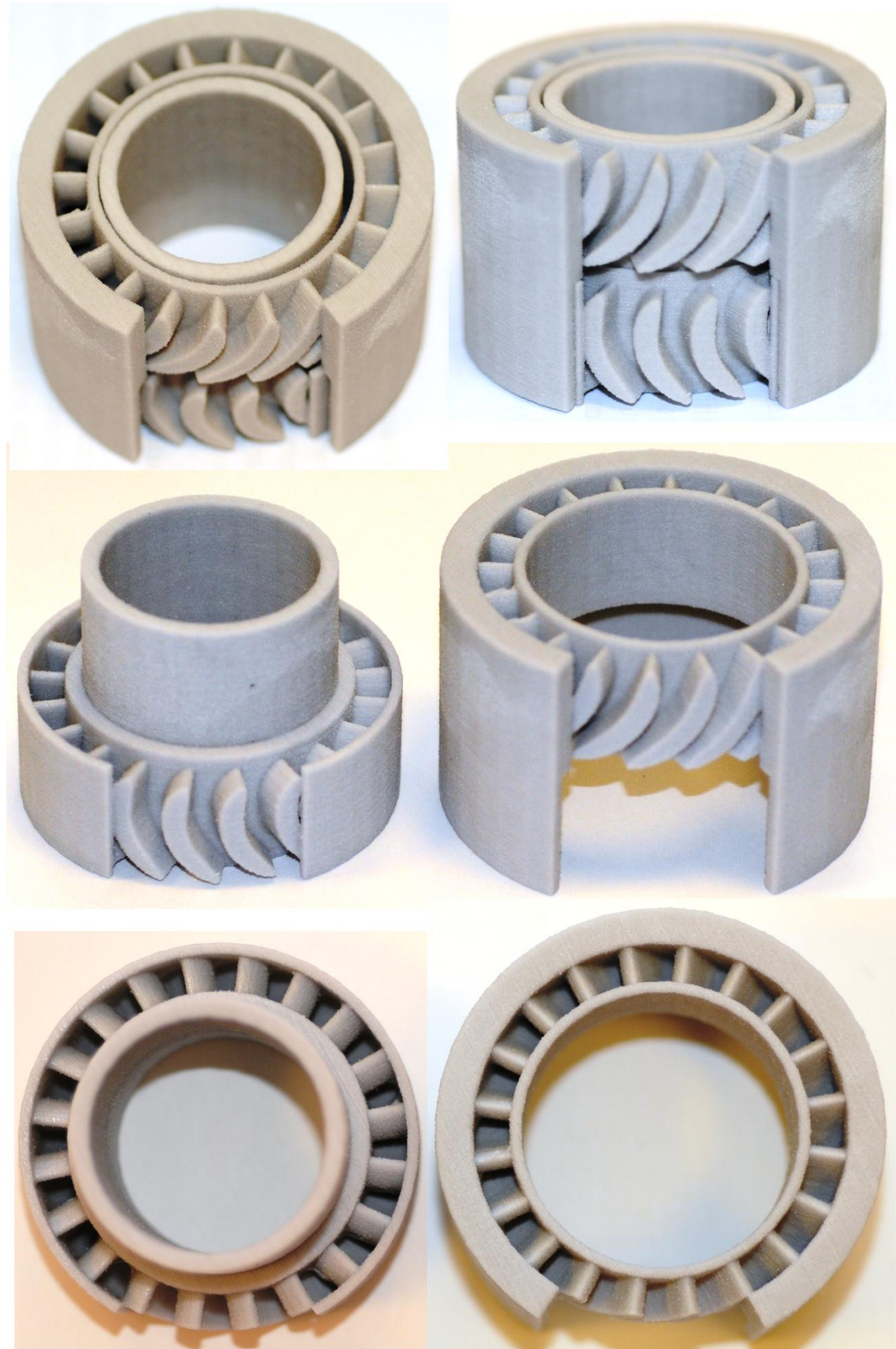


Figure 6.1 Prototyped turbodrill stage model made with 3D printing.

### 6.3 Recommendations for future work

The design process of the small diameter turbine stages for high speed turbodrill have been performed successfully for applications of this study and the proposed stage model was prototyped (not with the actual material). In the next step, the proposed turbine motor composed of the required number of the optimised turbodrill stage model needs to be manufactured with actual material (wear resistance stainless steel) and then tested with the drilling dynamometer test stand in the lab. Prototype testing provides valuable comparison and validation of the simulation results. Besides, the software platform capable of designing turbodrill with any desired configuration and predicting turbodrill performance and flow properties passing motor is now developed and ready for analysis of any complex drilling fluid (multiphase flow, multi-components fluid) in different working conditions. This makes the drilling optimization more straightforward in comparison with the previous platforms that are passive and only check the turbodrill performance through limited lab experiment flow test with limited fluid properties and flow observations.

In turbodrilling, rotary speed and torque at the turbine motor are difficult to control while drilling, making it difficult to optimize the turbine energy characteristics. The only means of control is to change the bit torque and the mud flow rate. In addition, the rotation speed and/or torque cannot be measured using normal surface data (i.e., standpipe pressure, weight on bit); therefore a measure-while-drilling instrument should be used to monitor the efficient turbodrill use: this is by itself related new future development. This also needs to provide data for accurate surface feed control that is required to maintain the particular weight on bit.

High flow rates and the resulting pressure drops through the turbine motor require relatively large mud flow rate and pressure capacity. The pumping capacity existing on the current available mining drilling rigs is relatively small, and so the efficiency of the turbo-motor must be maximized by design so as to minimize the required input flow rate whilst delivering the necessary bit-turning speed and power. Obviously, there are limits to efficiency gains; pumping requirements of the best designs may still exceed installed rig capacities, necessitating auxiliary pumping systems or retrofitting larger pumps.

The focus of this study was only on the simulation of the turbine stages performance and specifically on the blade configurations. There are several other components in the turbodrill including turbine shaft, bearing assembly, bend sub and

tool face adjustments, that all need to be designed specifically for this project. The vibration issues of the turbine motor and specifically turbine shaft need to be addressed for this project. For the bearing assembly, the PDC (polycrystalline diamond compact) bearing system should be engineered and specifically configured for this application. These bearings have low friction coefficients with the diamond-to-diamond contact that provide long working life at high load capacities.

There is another main application of turbodrill suitable for mineral exploration drilling which is the ability for coring during drilling. This is an area of product development for the turbodrill that includes the core tube assembly inside the turbine shaft and with the suitable core bit. If successfully designed, the system can drill and produce a suitable core sample of the rock. Directional core drilling with turbodrill also offers a complete record of the geology, with significant product cost reduction compared to currently available methods.

# References

- AIAA, 2002, Verification and Validation in Computational Fluid Dynamics: SAND2002-0529, California, U.S.A., Sandia National Laboratories.
- Albright, J., Dreesen, D. and Anderson, D., 2003, Road Map For A 5000-Ft Microborehole, Los Alamos National Laboratory (LANL).
- Albright, J.N., Clough, J.G. and Dreesen, D.S., 2003, The Application of Microhole Technology to the Development of Coalbed Methane Resources at Remote Locations, Los Alamos National Laboratory, Division of Geological & Geophysical Surveys, Department of Natural Resources.
- Anderson, D.R., Dorel, A. and Martin, R., 1997, A New, Integrated, Wireline-Steerable, Bottom Hole Assembly Brings Rotary Drilling-Like Capabilities to Coiled Tubing Drilling: Paper Presented at the SPE/IADC Drilling Conference (SPE/IADC 37654), Amsterdam, The Netherlands.
- ANSYS®, 2011a, ANSYS® CFX-Solver Modelling Guide, <http://www.ansys.com>.
- ANSYS®, 2011b, ANSYS® CFX-Solver Theory Guide, <http://www.ansys.com>.
- ANSYS®, 2011c, ANSYS® TurboGrid User's Guide, <http://www.ansys.com>.
- ANSYS®, 2011d, ANSYS® Mechanical APDL Theory Reference, <http://www.ansys.com>.
- APIRP-13D, 2010, Rheology and Hydraulics of Oil-well Fluids: API Recommended Practice 13D, American Petroleum Institute. Sixth Edition.
- APS, 2008, Novel High-Speed Drilling Motor for Oil Exploration & Production: US Department of Energy, Final Report, National Energy Technology Laboratory.
- Atlas-Copco, 2010, Exploration Drilling: First Edition, Sweden.
- Barton, S., Baez, F. and Gee, R., 2011, Downhole Matched Solutions: Innovative Scientific Approach to More Efficient Assemblies: Paper Presented at the SPE Asia Pacific Oil and Gas Conference and Exhibition (SPE 145980), Jakarta, Indonesia.
- Beaton, T. and Seale, R., 2004, The Use of Turbodrills in Coiled Tubing Applications: Paper Presented at the SPE/ICoTA Coiled Tubing Conference (SPE 89434), Houston, Texas, U.S.A.
- Beaton, T., Seale, R. and Beaird, J., 2004, Development of a Geared Turbodrilling System and Identifying Applications: Paper Presented at the Petroleum Society's 5th Canadian International Petroleum Conference (55th Annual Technical Meeting), Calgary, Alberta, Canada.
- Blount, C.G., et al., 1998, Weight on Bit in Coiled Tubing Drilling: Collection and Analysis of Field Data: Paper Presented at the SPE/ICoTA Coiled Tubing Roundtable (SPE 46008), Houston, Texas.
- Bourgoine, J.A.T., et al., 1986, Applied Drilling Engineering, Society of Petroleum Engineers, Richardson, TX, U.S.A.
- Byrom, T.G., 1999, Coiled Tubing Drilling in Perspective: Journal of Petroleum Technology, Vol. 51 (SPE 51792).
- Calnan, D., Seale, R. and Beaton, T., 2007, Identifying Applications for Turbodrilling and Evaluating Historical Performances in North America: Journal of Canadian Petroleum Technology, Vol. 46(6).
- Cavo, 2005, Motor Operations Manual: Fourth Edition, Houston, Texas, U.S.A.
- Chen, D.C-K., Gaynor, T. and Comeaux, B., 2002, Hole Quality: Why It Matters: Paper Presented at the SPE International Petroleum Conference and Exhibition (SPE 74403), Villahermosa, Mexico.

- Cohen, J.H.and Deskins, G., 2005, Advanced High-Pressure Coiled-Tubing Drilling System: Final Report, Maurer Technology Inc.
- CTES, L.P., 2005, Coiled Tubing Manual, U.S.A.
- Dagestad, V., et al., 2006, First Field Results for Extended-Reach CT-Drilling Tool: Paper Presented at the The SPE/ICoTA Coiled Tubing Conference and Exhibition, (SPE 100108), The Woodlands, Texas, U.S.A.
- Davis, J.R., 2002, Surface Hardening of Steels: Understanding the Basics: United States of America, ASM International.
- DeLucia, F.V., 1989, Benefits, Limitations, and Applicability of Steerable System Drilling: Paper Presented at the SPE/IADC Drilling Conference (SPE 18656), New Orleans, Louieiana, U.S.A.
- DeLucia, F.V.and Herbert, R.P., 1984, PDM vs. Turbodrill: A Drilling Comparison: Paper Presented at the 59th Annual Technical Conference and Exhibition (SPE 13026), Houston,Texas.
- Detournay, E.and Defourny, P., 1992, A Phenomenological Model for the Drilling Action of Drag Bits: international Journal of Rock Mechanics and Mining Science & Geomechanics Abstract, Vol. 29(1), PP. 13-23.
- Detournay, E., Richard, T.and Shepherd, M., 2008, Drilling response of drag bits: Theory and experiment: international Journal of Rock Mechanics and Mining Science, Vol. 45, PP. 1347-1360.
- Dietrich, J., et al., 2009, A Feasibility Study Regarding Micro-Drilling Technology, Germany, E.ON Energy Research Center. vol 1.
- Dixon, S.L.and Hall, C.A., 2010, Fluid Mechanics and Thermodynamics of Turbomachinery: The United States of America, Elsevier Inc.
- Elsborg, C., Carter, J.and Cox, R., 1996, High Penetration Rate Drilling with Coiled Tubing: Paper Presented at the SPE International Conference on Horizontal Well Technology (SPE 37074), Calgary, Canada.
- Eskin, M.and Maurer, W.C., 1997, Advanced Downhole Drilling Motors, Maurer Engineering Inc.
- Fleckenstein, W.W.and Eustes, A.W., 2003, Novel Wireline Coring System: Paper Presented at the SPE Annual Technical Conference and Exhibition, (SPE 84358), Denver, Colorado, U.S.A.
- Franca, L.F.P.and Lamine, E., 2010, Cutting Action of Impregnated Diamond Segments: Modelling and Experimental Validation: Paper Presented at the The 44th U.S. Rock Mechanics Symposium and 5th U.S.-Canada Rock Mechanics Symposium (ARMA 10-439), Salt Lake City, UT, U.S.A.
- Galbierz, B.E.and Oglesby, K.D., 2005, Advanced Mud System for Microhole Coiled Tubing Drilling, Final Report, U.S. Department of Energy, Bandera Petroleum Exploration LLC, Impact Technologies LLC.
- Gaynor, T.M., 1988, Downhole Control of Deviation with Steerable Straight-Hole Turbodrills: SPE Drilling Engineering.
- Georgi, D.T., Harville, D.G.and Robertson, H.A., 1993, Advances in Cuttings Collection and Analysis: Paper Presented at the SPWLA 34th Annual Logging Symposium.
- Gleitman, D.D., et al., 1998, Newly applied BHA Elements Contribute to Mainstreaming of Coiled-Tubing Drilling Applications: SPE Drilling & Completion(SPE 35130).
- Govier, G.W.and Aziz, K., 1972, The flow of complex mixtures in pipes, Van Nostrand Reinhold Co.
- Grigor, C., Conroy, D.and Henderson, M., 2008, Expanding the Use of Turbodrills in Coiled Tubing and Workover Applications: Paper Presented at the SPE/ICoTA Coiled Tubing

- and Well Intervention Conference and Exhibition (SPE 113721), The Woodlands, Texas, U.S.A.
- Hirsch, C., 2007, Numerical Computation of Internal and External Flows: Oxford, Great Britain, John Wiley & Sons, Ltd.
- ICoTA, 2005, An introduction to Coiled tubing: History, Applications, and Benefits: <http://www.icota.com>.
- IT, 2007, Advanced Ultra-High Speed Motor for Drilling: Tulsa, Oklahoma, Final Report, US Department of Energy, National Energy Technology Laboratory (NETL).
- Judzis, A., et al., 2006, Investigation of Smaller-Footprint Drilling System; Ultrahigh-Rotary-Speed Diamond Drilling Has Potential for Reduced Energy Requirements: Paper Presented at the IADC/SPE Drilling Conference (IADC/SPE 99020), Miami, Florida, U.S.A.
- Langille, P., Deen, A. and Klassen, J., 2009, Minimizing Risks, Maximizing On-Bottom Drilling Time: Turbodrilling with Impregnated Bits Improve Efficiency and Circumvents Trouble Time, Southern Oklahoma: Paper Presented at the SPE/IADC Drilling Conference and Exhibition (SPE/IADC 119230), Amsterdam, The Netherlands.
- Leising, L.J. and Newman, K., 1993, Coiled-Tubing Drilling: SPE Drilling and Completion, Vol. 8(4), 24594-PA.
- Leising, L.J. and Walton, I.C., 2002, Cuttings-Transport Problems and Solutions in Coiled-Tubing Drilling: SPE Drilling & Completion, Vol. 17(No. 1), PP: 54-66.
- Littleton, B., Nicholson PE, S. and Blount, C., 2010, Improved Drilling Performance and Economics Using Hybrid Coiled Tubing Unit on the Chittim Ranch, West Texas: Paper Presented at the IADC/SPE Drilling Conference and Exhibition, (IADC/SPE 128926), New Orleans, Louisiana, U.S.A.
- Lyons, W.C. and Plisga, G.J., 2005, Standard Handbook of Petroleum & Natural Gas Engineering: United States of America, Elsevier Inc.
- Maehs, J., Law, A. and Pruitt, R., 2005, Drilling With Success: BHA Optimization for Coiled-Tubing Drilling in Harsh Environment: Paper Presented at the SPE/ICoTA Coiled Tubing Conference and Exhibition (SPE 94162), The Woodlands, Texas, U.S.A.
- Maranuk, C.A., et al., 2000, A Concept of a New Steerable Drilling System for Coiled Tubing: Paper Presented at the SPE/ICoTA Coiled Tubing Roundtable (SPE 60752), Houston, U.S.A.
- Marjoribanks, R., 2010, Geological Methods in Mineral Exploration and Mining: Berlin Heidelberg, Springer-Verlag.
- Maurer-Engineering-Inc., 2000, Advanced Geothermal Turbodrill: Final Report, Houston, TX, U.S. Department of Energy.
- Maurer, W.C., et al., 1977, Downhole Drilling Motors: Technical Review, Houston, Texas, Maurer Engineering Inc.
- Melamed, Y., et al., 2000, Hydraulic Hammer Drilling: Journal of Energy Resources Technology, Vol. 122 (1), PP. 1-7.
- Menter, F.R., Kuntz, M. and Langtry, R., 2003, Ten Years of Industrial Experience with the SST Turbulence Model: Turbulence, Heat and Mass Transfer 4: Proceedings of the Fourth International Symposium on Turbulence, Heat and Mass Transfer, Begell House, Antalya, Turkey.
- Mokaramian, A., Rasouli, V. and Cavanagh, G., 2012, Coiled Tube Turbodrilling: a proposed technology to optimise drilling deep hard rocks for mineral exploration: International Journal of Mining and Mineral Engineering, Vol.4 (3), PP. 224-248. DOI: 10.1504/IJMME.2013.053171.

- Mokaramian, A., Rasouli, V. & Cavanough, G., 2013, Fluid Flow Investigation through Small Turbodrill for optimal Performance: Mechanical Engineering Research, Vol. 3 (1), Canadian Center of Science and Education. Doi: 10.5539/mer.v3npl.
- Mokaramian, A. and Rasouli, V. and Cavanough, G., 2012, A hydraulic specific energy performance indicator for coiled tube turbodrilling: American Rock Mechanics Association (ARMA), 46th US Rock Mechanics / Geomechanics Symposium, June 24-27 2012. Chicago, Illinois.
- Mokaramian, A., Rasouli, V. and Cavanough, G., 2012, Adapting oil and gas downhole motors for deep mineral exploration drilling: Deep Mining 2012: Proceedings of the sixth International Seminar on Deep and High Stress Mining, Australian Centre for Geomechanics (ACG), Perth, Western Australia, pp. 475-486.
- Mokaramian, A., Rasouli, V. and Cavanough, G., 2012, A feasibility study on adopting coiled tubing drilling technology for deep hard rock mining exploration: Deep Mining 2012: Proceedings of the sixth International Seminar on Deep and High Stress Mining, Australian Centre for Geomechanics (ACG), Perth, Western Australia, pp. 487-499.
- Mushovic, T., et al., 2009, Beyond the Technical Limit: Turbodrilling—A Paradigm Shift to World Class Horizontal Well Construction: Paper Presented at the SPE/IADC Drilling Conference and Exhibition (SPE/IADC 118809), Amsterdam, The Netherlands.
- Natanael, M., et al., 2008, Turbodrill with asymmetric stator and rotor vanes: U.S.A, Smith International, Inc.
- NETL, 2005, Coiled Tubing: State of the Industry and Role for NETL: U.S. Department of Energy.
- Newman, K., Kelleher, P. and Smalley, E., 2007, Friction Reduction for Microhole CT Drilling: Final Technical Report, CTES, L.P., U.S. Department of Energy.
- NOV, 2011, Motor Handbook, National Oilwell Varco, ([www.nov.com](http://www.nov.com)). Seventh Edition.
- Ohlinger, J.J., Gantt, L.L. and McCarty, T.M., 2002, A Comparison of Mud Pulse and E-Line Telemetry in Alaska CTD Operations: Paper Presented at the SPE/ICoTA Coiled Tubing Conference and Exhibition, (SPE 74842), Houston, Texas, U.S.A.
- PES, 2000, (Precision Energy Services), Directional Drilling 1, Operational Manual.
- Pierce, K.G., Livesay, B.J. and Finger, J.T., 1996, Advanced Drilling Systems Study, SAND95-033, U.S. Department of Energy (DOE).
- Radtke, R., et al., 2011, High-Power Turbodrill And Drill Bit For Drilling With Coiled Tubing, Technology International, Inc., US Department of Energy, National Energy Technology Laboratory (NETL).
- Regener, T., et al., 2005, Latest Positive Displacement Motor and Drill Bit Developments for Drilling Hard and Abrasive Formations: Paper Presented at the SPE/IADC Drilling Conference (SPE/IADC 92542), Amsterdam, The Netherlands.
- Reich, M., et al., 2000, Competitive Performance Drilling with High-Speed Downhole Motors in Hard and Abrasive Formations: Paper Presented at the IADC/SPE Drilling Conference (IADC/SPE 59215), New Orleans, Louisiana.
- RIO, 2004, Current Capabilities of Hydraulic Motors, Air/Nitrogen Motors, and Electric Downhole Motors: Final Report, US Department of Energy.
- Roache, P.J., 1994, Perspective: A method for the uniform reporting of grid refinement studies: ASME Journal of Fluids Engineering, Vol. 116, PP. 405-413.
- Roache, P.J., 1998, Verification and Validation of Computational Fluid Dynamics Simulations: Albuquerque, NM.
- Sanchez, A., Samuel, G.R. and Johnson, P., 1996, An Approach for the Selection and Design of Slim Downhole Motors for Coiled Tubing Drilling: Paper Presented at the SPE Horizontal Drilling Conference (SPE 37054), Calgary, Canada.

- Santarelli, F.J.and Dusseault, M.B., 1991, Core quality control in petroleum engineering: Rock Mechanics as a Multidisciplinary Science.
- Schlumberger, 2010, Smaller Footprint Drilling System for Deep and Hard Rock Environments; Feasibility of Ultra-High-Speed Diamond Drilling: Salt Lake City, UT, USA, Final Edition, US Department of Energy (DOE), National Energy Technology Laboratory (NETL).
- Seale, R., Beaton, T.and Flint, G., 2004, Optimizing Turbodrill Designs for Coiled Tubing Applications:Paper Presented at the SPE Eastern Regional Meeting (SPE 91453), Charleston, West Virginia, U.S.A, .
- Seale, R.and Conroy, D., 2005, PDC Bits Run on Turbodrills: The History, Facts and Current Developments:Paper Presented at the SPE Latin American and Caribbean Petroleum Engineering Conference (SPE 94826), Rio de Janeiro, Brazil.
- Selnes, K.S., Clemmensen, C.and Reimers, N., 2009, Drilling Difficult Formations Efficiently With the Use of an Antistall Tool: SPE Drilling & Completion(SPE 111874).
- Staley, C., et al., 2011, Turbodrill BHA Solves Build Section Challenges, Anadarko Basin: Paper Presented at the SPE/IADC Drilling Conference and Exhibition (SPE/IADC 140245), Amsterdam, The Netherlands.
- Theimer, K.and Kollé, J., 2007, Microhole High-Pressure Jet Drill For Coiled Tubing: Final Report, Tempress Technologies Inc., US Department of Energy (DOE).
- Turner, D.R., et al., 1999, Electric Coiled Tubing Drilling: A Smarter CT Drilling System: Paper Presented at the SPE/IADC Drilling Conference (SPE/IADC 52791), Amsterdam, Holland.
- Turner, D.R., et al., 1999, The All Electric BHA: Recent Developments toward an Intelligent Coiled-Tubing Drilling System: Paper Presented at the SPE/ICoTA Coiled Tubing Roundtable (SPE 54469), Houston, Texas, U.S.A.
- Versteeg, H.K.and Malalasekera, W., 2007, An Introduction to Computational Fluid Dynamics: The Finite Volume Method, Pearson.
- WWT, 2007, Microhole Drilling Tractor Technology Development: Anaheim, Canada, Final Report, U.S. Department of Energy.
- Zegarra, E., et al., 2002, Intelligent Wireless Orienter for Coiled Tubing Drilling: Development to Field Test: Paper Presented at the SPE/ICoTA Coiled Tubing Conference, (SPE 74836), Houston, Texas, U.S.A.

*Every reasonable effort has been made to acknowledge the owners of copyright material. I would be pleased to hear from any copyright owner who has been omitted or incorrectly acknowledged.*